EXPLORING THE FORMATION OF SPATIALLY MODULATED REGIMES IN QCD AT NON-VANISHING DENSITIES

Dissertation
zur Erlangung des Doktorgrades
der Naturwissenschaften

vorgelegt beim Fachbereich Physik
der Goethe Universität
in Frankfurt am Main

von
MARC WINSTEL
aus Hattersheim am Main, Deutschland

Frankfurt am Main 2025
(D30)

vom Fachbereich Physik der
Goethe Universität als Dissertation angenommen.

Dekan: Prof. Dr. Marc Wagner

Gutachter: Prof. Dr. Marc Wagner
Prof. Dr. Christian Fischer

Datum der Disputation: 11.06.2025

ABSTRACT

The majority of the phase diagram of quantum chromodynamics (QCD), especially at non-vanishing baryon densities, is not explored from the theoretical side. This is caused by the non-applicability of perturbative methods, due to the strong coupling at all temperatures T and quark chemical potentials μ, which are not asymptotically large, and numerical lattice methods, which are valid only for $\mu/T < 1$. A deeper theoretical understanding of the QCD phase structure at intermediate baryon densities has direct implications for the study of matter under extreme conditions, such as in heavy-ion-collisions and the interior of neutron stars. In the absence of first-principle methods, investigations of the phase structure at intermediate chemical potentials and temperature are carried out mostly using effective models, that capture certain, essential features of QCD but not all of them.

This thesis explores mechanisms for the formation of regimes with spatially modulated, chiral observables in QCD at non-vanishing μ using QCD-inspired theories. In particular, we focus on two such regimes: a crystalline phase, the inhomogeneous phase (IP), where the chiral condensate is non-uniform and periodically varying in space, and a liquid-like phase, the quantum pion liquid (QπL), characterized by spatially oscillatory, intermediate-range correlations of mesonic fields. Hints in the literature imply the possible existence of spatially modulated regimes in QCD around the expected critical point (CP), which marks the end of the chiral crossover transition at low and zero μ.

To incorporate new, relevant features of QCD in model studies, we employ renormalizable $2+1$-dimensional four-fermion models and investigate the effects of these features on the phase structure within the mean-field approximation, where bosonic quantum fluctuations are suppressed. In a complementary approach, the influence of bosonic quantum fluctuations on inhomogeneous condensates is investigated with lattice field theory (LFT) simulations of a scalar O(N) model.

A key finding of this thesis is that the novel inclusion of scalar-vector meson mixing induces spatially oscillating, exponentially damped mesonic correlation functions, i.e., a QπL is observed in the phase diagram of the studied four-fermion model. This result aligns with arguments in the literature expecting spatially modulated regimes from the emergent combined symmetry of the model under charge conjugation and complex conjugation, which is also present in QCD at $\mu \neq 0$. Moreover, the stability of homogeneous ground states is proven within the phase diagram of all four-fermion models in two spatial dimensions. We argue that this finding suggests the absence of IPs in these models with the mean-field approximation and in the full quantum theories. Further, Monte-Carlo simulations of a scalar O(N) model, which classically features an IP, reveal that bosonic quantum fluctuations disorder inhomogeneous condensates in finite spatial volumes and, instead, a QπL is observed.

The findings suggest that the scenario of a QπL is more likely to be realized in QCD than an IP, since the presence of bosonic quantum fluctuations, mixing effects between scalar and vector mesons, and emergent symmetries at $\mu \neq 0$ seem to favor the formation of QπLs. A crucial next step to provide quantitative, theoretical predictions for the QCD phase diagram is to incorporate the above mentioned effects in more sophisticated model approaches as well as in functional computations.

PUBLICATIONS

The majority of the content in this thesis, including the central results, is based on the following publications:

[1] Adrian Koenigstein, Laurin Pannullo, Stefan Rechenberger, Martin J. Steil, and Marc Winstel. "Detecting inhomogeneous chiral condensation from the bosonic two-point function in the (1 + 1)-dimensional Gross–Neveu model in the mean-field approximation*." In: *J. Phys. A* 55.37 (2022), p. 375402. DOI: 10.1088/1751-8121/ac820a. arXiv: 2112.07024 [hep-ph] (cit. on pp. 8, 10, 12, 39, 40, 44, 54, 57, 65–68, 76, 89, 102, 104, 109, 128, 144).

[2] Laurin Pannullo and Marc Winstel. "Absence of inhomogeneous chiral phases in (2+1)-dimensional four-fermion and Yukawa models." In: *Phys. Rev. D* 108.3 (2023), p. 036011. DOI: 10.1103/PhysRevD.108.036011. arXiv: 2305.09444 [hep-ph] (cit. on pp. 54, 57, 60, 81, 88, 101, 102, 173, 176, 184, 186, 190, 192).

[3] Marc Winstel. "Spatially oscillating correlation functions in (2+1)-dimensional four-fermion models: The mixing of scalar and vector modes at finite density." In: *Phys. Rev. D* 110.3 (2024), p. 034008. DOI: 10.1103/PhysRevD.110.034008. arXiv: 2403.07430 [hep-ph] (cit. on pp. vi, 81, 106, 163, 189).

[4] Adrian Koenigstein and Marc Winstel. "Revisiting the spatially inhomogeneous condensates in the (1 + 1)-dimensional chiral Gross–Neveu model via the bosonic two-point function in the infinite-N limit." In: *J. Phys. A* 57.33 (2024), p. 335401. DOI: 10.1088/1751-8121/ad6721. arXiv: 2405.03459 [hep-th] (cit. on pp. 14, 54, 57, 74–76).

Furthermore, the following conference proceedings contributions contain results that are presented in this thesis:

[5] Marc Winstel and Laurin Pannullo. "Stability of homogeneous chiral phases against inhomogeneous perturbations in 2+1 dimensions." In: *PoS* LATTICE2022 (2023), p. 195. DOI: 10.22323/1.430.0195. arXiv: 2211.04414 [hep-ph] (cit. on pp. 58, 187).

[6] Marc Winstel and Semeon Valgushev. "Lattice study of disordering of inhomogeneous condensates and the Quantum Pion Liquid in effective $O(N)$ model." In: *Excited QCD 2024 Workshop*. 2024. arXiv: 2403.18640 [hep-lat] (cit. on p. 127).

Also, the following further works and conference contributions additionally were published and/or produced during the time of working on the PhD project. These works are briefly summarized and accordingly cited within this thesis whenever relevant, as, for example, in the introduction, a literature review or in discussions of results:

[7] Laurin Pannullo, Marc Wagner, and Marc Winstel. "Inhomogeneous Phases in the Chirally Imbalanced 2 + 1-Dimensional Gross-Neveu Model and Their Absence in the Continuum Limit." In: *Symmetry* 14.2 (2022), p. 265. DOI: 10.3390/sym14020265. arXiv: 2112.11183 [hep-lat] (cit. on pp. 56, 58, 60, 86, 89, 92–94, 104, 105).

[8] Marc Winstel, Laurin Pannullo, and Marc Wagner. "Phase diagram of the 2+1-dimensional Gross-Neveu model with chiral imbalance." In: *PoS* LATTICE2021 (2022), p. 381. DOI: 10.22323/1.396.0381. arXiv: 2109.04277 [hep-lat] (cit. on pp. 56, 58, 89, 104).

[9] Laurin Pannullo, Marc Wagner, and Marc Winstel. "Inhomogeneous phases in the 3+1-dimensional Nambu-Jona-Lasinio model and their dependence on the regularization scheme." In: *PoS* LATTICE2022 (2023), p. 156. DOI: 10.22323/1.430.0156. arXiv: 2212.05783 [hep-lat] (cit. on pp. 11, 39, 128, 153, 157, 192).

[10] Laurin Pannullo, Marc Wagner, and Marc Winstel. "Regularization effects in the Nambu–Jona-Lasinio model: Strong scheme dependence of inhomogeneous phases and persistence of the moat regime." In: *Phys. Rev. D* 110.7 (2024), p. 076006. DOI: 10.1103/PhysRevD.110.076006. arXiv: 2406.11312 [hep-ph] (cit. on pp. 8, 11, 12, 14, 15, 39, 48, 49, 56, 57, 65, 90, 104, 108, 125, 144, 153, 154, 156, 157).

[11] Zohar Nussinov, Michael C. Ogilvie, Laurin Pannullo, Robert D. Pisarski, Fabian Rennecke, Stella T. Schindler, and Marc Winstel. "Dilepton production from moaton quasiparticles." 2024. arXiv: 2410.22418 [hep-ph] (cit. on pp. 13, 125, 126, 129, 156, 157, 159).

DISCLOSURE

This dissertation has developed from my scientific efforts during my doctoral studies, starting in November 2020, at the *Institute für theoretische Physik* at Goethe University in Frankfurt. The research presented in this manuscript was performed across different scientific projects. Some of these project were initialized by myself, others were established by senior researchers. I had the privilege of working on these projects together with other, highly appreciated researchers, including senior physicists, other doctoral students, and postdocs, and I am immensely thankful for the fruitful and fun collaboration with my collaborators. Many of the results and also my own development as a scientists emerged from joint discussions, shared investigations, and collective thinking associated to individual research projects. Also I profited from many open scientific exchanges throughout various formal and informal occasions.

Given the collaborative nature of most modern physics research, results of joint projects cannot entirely be attributed to a single individual. Nevertheless, I hereby confirm that I contributed the main share of the scientific work in the projects associated with the central findings of this thesis. My contributions encompass the conceptualization and management of the projects, analytical and numerical computations including programming, as well as the writing of original publications. The project associated to the single-author publication [3] was carried out independently by myself, though I acknowledge inspiration and valuable feedback from colleagues within the field. Wherever appropriate, individual contributions of other collaborators are explicitly mentioned, typically at the individual disclosure at the beginning of most chapters.

This manuscript has been typeset in LaTeX, a document preparation software developed by the associated community, utilizing various packages and templates, most prominently: The LaTeXcode for this thesis is based on the `classicthesis` package [12] developed by André Miede, who derived the typo-graphical style from Robert Bringhurst's book "*The Elements of Typographic Style*" [13], which is partially reflected in the type-setting of this manuscript. Moreover, we use the BibLaTeXpackage [14] with the *biber* backend [15], the *glossaries* packages [16, 17] for acronyms, and *cleveref* [18] for cross-referencing.

Plots and figures in this thesis, that were created by me, were made using *Python3* [19] with *Matplotlib* [20]. Numerical computations have been carried out using *Python3*, C++14 [21] and *Matlab* [22].

I have made every effort to identify and provide proper references for all ideas, equations, and techniques that cannot be directly attributed to my own work. Consequently, the original publications for all plots, tables and figures, where I am not an authors, are properly cited in the respective captions.

The text in the manuscript has been entirely written by myself, unless specifically noted otherwise. Whenever text passages might be close to the original publications, upon which the work is based, this is specifically mentioned in the disclosure of the corresponding chapter. Manual revisions and spell-checking of certain paragraphs were conducted using dictionaries of *TeXstudio* [23] and *Visual studio code* [24]. Moreover, the refinement of the language in individual sentences and spellchecking was supported through interactions

with the language model *ChatGPT* 4 [25] and the free version of the AI-pair programmer *GitHub Copilot* [26] in *Visual studio code*. Note that these models were not used to generate logical sentences or paragraphs directly.

ACKNOWLEDGEMENTS

I would like to express my gratitude to a variety of people and organizations who have supported me in finishing the work on and related to this thesis. Foremost, I thank my supervisor, Marc Wagner, for his continuous support and guidance starting from the time I was as a Bachelor's student in 2018 to the completion of my dissertation in 2025. His mentorship has been invaluable in my development as a physicist but also in my personal growth over these years. Thereby, he exceptionally well transitioned from being a scientific teacher – helping me acquire relevant skills for a theoretical physicist and providing the input for my Bachelor's and Master's theses and various research projects, to the role of a mentor fostering my personal and professional development. His continued encouragement and trust in my abilities had a significant impact on my journey.

I express my gratitude to Prof. Christian Fischer for being the second supervisor of my thesis and fruitful, scientific discussions in the past years. Moreover, my thanks go to Dr. Michael Buballa for serving as the second supervisor of my PhD Committee, as well as for many insightful discussions and for sharing his knowledge on inhomogeneous chiral condensates and related phenomena in the past years. Additionally, I thank Prof. Owe Philipsen and Prof. Christoph Blume for joining the examination committee.

I am grateful to my collaborateurs for their input, inspiration and joint work on numerous projects. The countless fruitful discussions, shared knowledge and the inspiration from all of them had a huge beneficial impact on this thesis. In particular, I would like to thank Laurin Pannullo, with whom I have worked together since we both were master students to the completion of my dissertation (and along the way, his as well). Over the years, we had an uncountable number of fruitful discussions and completed multiple joint projects. I could not have asked for a better companion to work with throughout this time and I am grateful for the open work environment, where every issue could be openly discussed, and all the fun I had during this time. I also would like to thank Adrian Koenigstein, who is not only a well-appreciated collaborator but also for sharing his vast knowledge in physics throughout multiple discussions. Moreover, I want to thank all my other collaborators, namely Michael Buballa, Lennart Kurth, Zohar Nussinov, Michael C. Ogilvie, Robert D. Pisarski, Fabian Rennecke, Stella T. Schindler, Martin J. Steil, Semeon Valgushev and Marc Wagner. The stimulating discussions and fruitful collaborations were invaluable to the completion of this dissertation.

Next, I want to thank a variety of people at the *Institut für theoretische Physik* and members of the CRC-TR 211 for the stimulating research environment and enjoyable time. I like to thank my office mates Alfredo D'Ambrosio, Fabian Geiger, Berkan Kuepeli and Carolin Schlosser for the good times shared in room 02.105. Special thanks go to Alfredo for many fun conversations, ranging from physics to differences between German and Italian culture. I also thank the current and past members of Marc Wagner's research group for the cherished time together at the ITP and the Lattice Conference in Bonn 2022, as well as for joint efforts in teaching.

Additionally, I would like to thank many members of Dirk Rischke's group for lots of off-topic discussions over lunch but also for the scientific exchange in the context of meetings in the seminar "Special topics in QCD at finite temperature and density", related to projects A03 and A06 of the CRC TR 211, and beyond. I am also grateful to Alessandro Sciarra for helpful programming advice, scientific discussions, and his overall engagement within (and beyond) the CRC-TR 211 regarding good practices in scientific software development.

Moreover, I thank the members of the CRC-TR 211 for a stimulating research environment, offering me with the opportunity to engage with international experts in high energy physics from all over the world. I am grateful to my colleagues in project A03 and other participants of the aforementioned seminar for valuable input and discussions. In addition to the academic environment, I am thankful for the traveling funds and the encouragement to present my research at multiple occasions.

Further, I would like to thank Adrian Koenigstein, Keiwan Jamaly and Laurin Pannullo for proofreading (parts of) this manuscript, and providing invaluable feedback and constructive criticism. In particular, I am grateful to Adrian for his enormous effort in reviewing not only the scientific content and language of the whole thesis but also for helpful comments regarding the formatting, grammar and typesetting. Thanks to all of you for your help in significantly improving this manuscript.

I would like to express my gratitude to all my friends and family for their overwhelming support, as well as for preventing me from going crazy over theoretical physics through enjoyable distractions. I am thankful to Pascal Henkelmann for a dozen years of friendship and uncountable, shared stories. I thank Lisa Georg for her continuous support and love over the past nine years. I look forward to many more years to come. I am also deeply grateful to my parents, Michael and Tanja Winstel, my brother, Timo Winstel, and grand parents, Baldur and Renate Jacobi as well as Gertrud Siener, for their unconditional support and love.

In the end, I acknowledge the support of various organizations. I acknowledge the support of the *Deutsche Forschungsgemeinschaft* (DFG, German Research Foundation) through the collaborative research center trans-regio CRC-TR 211 "Strong-interaction matter under extreme conditions"– project number 315477589 – TRR 211. Furthermore, I acknowledge the support provided by the *Helmholtz Graduate School for Hadron and Ion Research* (HGS-HIRe) for the excellent soft skill courses and the travel funds, providing me with the opportunity to visit multiple conferences all over Europe, and the *Stiftung Giersch* (Giersch foundation) for the financial support and scientific recognition through the Giersch Excellence Award. Calculations on the GOETHE-HLR and on the FUCHS-CSC high-performance computer of the Frankfurt University were conducted for this research. I would like to thank HPC-Hessen, funded by the State Ministry of Higher Education, Research and the Arts, for programming advice.

"FAST READING" GUIDE

The structure of this thesis allows to read only parts of the 163 pages of the main text and still grasp the key findings of this work in the context of the research objectives (**RO**s). The following guide is only recommended for experts in the field familiar with investigations of QCD-inspired models and the mean-field approximation, since technical details as well as detailed discussion of equations, data and figures are omitted. Also, one has to be aware that many minor results of the respective research projects are skipped. The abbreviated version of this thesis (roughly 50 pages) allows experienced readers to grasp the main results and their implications by reading in the following order:

1. Chapter 1 provides the main motivations, the literature context and **RO**s of the thesis.
2. Sections 4.1, 4.4 and 4.5 gives context on the methodology for the investigation of exotic regimes in the QCD-inspired models relevant for this thesis.
3. The introductory paragraphs and last sections of Chapters 5 to 7 summarize the main findings of these chapters and discusses their implications with respect to the **RO**s. Thereby, central results from the main body of the respective chapter are pointed out to the reader for reference. Also, direct improvements and follow-up studies of the respective results are discussed in these sections. Skimming over the used actions provides more context on the respective modeled features of QCD.
4. Chapter 8 provides an overall interpretation of the main findings with respect to the **RO**s, and a contextualization with existing literature.

The author considers the proposed structure a good starting point for people familiar with the theoretical approaches in this thesis, who want to get an overview over the scientific contributions of this thesis.

Readers, who are unfamiliar with the study of QCD-inspired models at non-vanishing temperatures and densities, however, should find proper introductions to the theory and methodology in Chapter 2 and Chapter 4 as well as a specific, in-depth literature review in Chapter 3. Moreover, the reading of Chapters 5 to 7 in full length provides more technical details, but also many minor results of the corresponding research projects.

For more details on the structure of this manuscript, the reader is referred to the following table of contents and the outline section at the end of Chapter 1.

CONTENTS

1

INTRODUCTION

The strong interaction is one of the four established fundamental interactions in nature and part of the *Standard Model of particle physics*. The latter contains all known elementary particles and their interactions. The strong interaction was first observed indirectly as the nuclear force responsible for the binding of protons and neutrons in the atomic nuclei, which accounts for almost the entire mass of ordinary matter that makes up stars, planets, and living organisms such as humans. Of our current understanding, quarks are the fundamental building blocks of matter which are bound together by the strong interaction to form hadrons [27–32]. These hadrons can be baryons, made up of three quarks such as the protons and neutrons, or mesons, for example pions and kaons, which are made up of a quark and an antiquark. Other, more exotic states, such as tetraquarks, are a topic of present research, but are not relevant for this thesis. The strong force is mediated by the massless gluons which are the gauge bosons of QCD, which is a non-abelian gauge theory with gauge group SU(3) and is the quantum field theory (QFT) describing the strong interaction between quarks and gluons [32–35]. Gluons can be understood as the QCD analogue of photons that mediate the electromagnetic force described by quantum electrodynamics (QED). Quarks are massive fermions with spin-1/2 and carry a color charge with possible "values" red, green, and blue, an analogue to the electric charge in QED. Antiquarks carry the corresponding anticolors (for example "antired"). Although the term "color" is used to discuss properties of QCD, it is important to note that this is only a concept to illustrate the mathematical structure of the underlying SU(3) gauge group (there is no overlap with the colors visible to the human eye). Due to the non-Abelian gauge group, gluons carry color charge themselves resulting in self-interactions of gluons and the short-range of the strong interaction – features that are not present in the Abelian QED where photons are chargeless. This property makes the computations of observables in strongly interacting systems rather complicated, as QCD is strongly coupled at energy scales of order 1 GeV and below relevant for the understanding of, e.g., nuclear matter. For illustration, in natural units, where $k_b = \hbar = c = 1$, the mass of the proton is $1\,\mathrm{GeV} = 1000\,\mathrm{MeV}$ and a temperature of 1 MeV corresponds to $10^{10}\,\mathrm{K}$ in SI units, which is three orders of magnitude hotter than the core of our sun.

One peculiar feature of QCD at low energy scales is the phenomenon of *confinement* which means that only color neutral states such as baryons (a combination of three valence quarks with different color charges) and mesons (a combination of a quark and an antiquark with the corresponding color and anticolor) are observed in nature. For example, in a quark-antiquark system the color neutrality is guaranteed by the linear rising potential between the quark-antiquark pair at large distances such that at some point the energy for the separation of the pair is so large that it is energetically favored to create another quark-antiquark pair from the vacuum, such that the overall system remains color neutral.

Asymptotic freedom explains how the strong coupling of color charged quarks at the low energy scales of nuclear matter decreases with increasing energy scales (or momentum transfer), i.e., the quarks are expected to behave as free particles at asymptotically large energy scales [36, 37] where confinement should not be observed anymore.

CHIRAL SYMMETRY BREAKING Another important feature of QCD is spontaneous *chiral symmetry breaking*. Chiral symmetry is a global symmetry of massless fermion fields and is a direct consequence of the Poincaré symmetry of the free Dirac action. It allows the transformation of the fermion fields according to their chirality or handedness. There exist left- and right-handed fermion fields, represented by so-called Weyl spinors, that transform under different representations of the Poincaré group. In the massless QCD action, the chiral symmetry transformations can be written as independent transformations of left- and right-handed quarks in flavor space. In reality, quarks are, however, not massless as they acquire a current mass through the Higgs mechanism [38–40]. Compared to the relevant energy scales of QCD matter or, more intuitive, to observed hadron masses of order $\sim$ GeV the masses of the two light quark flavors (up and down, respectively) are relatively light, with $m_{\text{up}} \approx 2.16\,\text{MeV}$ and $m_{\text{down}} \approx 4.7\,\text{MeV}$ [41].[1] Thus, these masses are often neglected and one speaks of an approximate "two-flavor" chiral symmetry, or of a small explicit breaking of the chiral symmetry. This approximate symmetry is, however, *spontaneously broken* at low energy scales, which is called spontaneous chiral symmetry breaking [42, 43]. Due to this mechanism, the nucleon masses are almost 1 GeV while the bare up and down quarks have masses of only a few MeV such that roughly 99% of the nucleons mass are dynamically generated by the QCD interactions, a highly non-perturbative effect. The breaking of chiral symmetry can be understood as the formation of a chiral condensate $\langle\bar{\psi}\psi\rangle$, which is spatially homogeneous in the vacuum and acts as an effective mass contribution to each of the constituent quarks in the nucleon, through the QCD interaction. In the discussion, we limit ourselves to the two lightest quark flavors such that the bilinear $\bar{\psi}\psi$ can also be understood as an antiquark-quark condensate of the lightest quarks. The breaking of a continuous symmetry leads to the appearance of massless Goldstone bosons [44, 45], which there should be three of in the case of the spontaneous breaking of the axial SU(2) symmetry of the QCD action for two flavors [46]. This beautifully explains the existence of the pions, also called the "pseudo-Goldstone modes of QCD", as the lightest mesons in the hadron spectrum, which are much lighter than the other hadrons [41], but not exactly massless since chiral symmetry is only approximate in QCD.[2]

1.1 THE QCD PHASE DIAGRAM – A LITERATURE OVERVIEW

As described above, the non-Abelian, non-perturbative nature of QCD makes the study of strongly-interacting system extremely challenging. Yet, the behavior of QCD at non-vanishing temperatures and densities is of great interest for the understanding of the early

1 Ref. [41] gives the above mentioned values of current quark masses for up and down quarks at a renormalization scale of 2 GeV in the minimal subtraction scheme. Thus, the light quark mass value is less than 1% of the renormalization scale.

2 The strange quark mass of roughly 95MeV is often also considered to be low enough compared to other energy scales such as, e.g., the hadron masses. The breaking of the resulting SU(3) chiral symmetry gives rise to eight pseudo-Goldstone bosons, the pions, the kaons as well as the eta meson which all are relatively light compared to other hadrons. This thesis focuses on QCD-inspired models that maximally contain two different quark flavors, such that the author decided to keep the discussion simple by focusing on the two-flavor case.

universe as well as the extreme conditions in astrophysical applications like neutron stars, their mergers or the core of supernovae [47–49]. An important experimental tool, besides indirect access by the study of neutron star (mergers)[3], for the investigation of the QCD phase diagram are collider experiments, most prominently the Brookhaven National Laboratory's Relativistic Heavy Ion Collider (RHIC), the Large Hadron Collider (LHC) and the Facility for Antiproton and Ion Research (FAIR), that are able to create extreme conditions by colliding nuclei with each other to reach a large enough energy density [50, 51].

In this thesis, we restrict ourselves to strongly-interacting systems in equilibrium, i.e., we are interested in the thermodynamic properties of QCD. Thereby, we are particularly interested in the conditions of non-vanishing temperatures T as well as baryon densities, where typically the baryon chemical potential μ_B is used to enforce a mean baryon number density in the system. At non-zero T, the baryon density increases monotonically with μ_B, such that most of the phase diagram looks similar. We refer to Ref. [52] for a nice presentation of the phase diagram using the baryon density as a parameter.[4] The phase diagram of QCD in the (μ_B, T) plane is expected to have a complex and rich structure that is neither fully understood theoretically nor explored experimentally. We start the discussion on the relatively well-understood regions of the phase diagram and then move on to conjectures about possibly realized phases or phenomena.

Figure 1.1 is used for visual orientation to guide the discussion in the following, but it should be noted that it represents a sketch. Thus, Fig. 1.1 incorporates a lot of simplifications and conjectures, which are often not based on first-principle calculations. However, the three colored regions in the sketch (a phase made of a gas of hadrons, the quark gluon plasma and color-superconducting phases) represent relatively well-established literature findings on phases of QCD, especially in certain limits of either T or μ_B being asymptotically large or near the vacuum. Moreover, the nuclear liquid-gas transition (the magenta line) is unquestionably realized at zero and low temperatures. Besides this, all features of the sketch are (some more, others less) speculative. Especially, the regimes at intermediate temperatures and densities are not well understood and are the focus of this thesis.

QUARK GLUON PLASMA From the theoretical side, the QCD phase diagram at $\mu_B = 0$ can be investigated using first-principle lattice simulations, which are based on the discretization of the QCD action on a finite Euclidean space-time lattice, see Ref. [58] for a review and Ref. [59] for beginner's introduction to LFT. At low or vanishing temperatures and chemical potential, we know that there is a hadronic phase simply from computations and experimental observations of the hadron spectrum. In this region the thermodynamics of QCD is incredibly well described by statistical models of hadrons, such as the hadron resonance gas. At sufficiently high temperatures, c.f. the red region in Fig. 1.1, as obtained for example in the early universe shortly after the big bang, however, one obtains a so-called *quark-gluon plasma* which is a deconfined phase of free quarks and gluons, i.e., confinement is lost in this regime. This was already expected from the discovery of asymptotic freedom from the nobel prize winning work of Gross, Politzer, and Wilczek in 1973 [36, 37]: the interactions between quarks and gluons becomes weaker at higher energy scales such that they behave like free particles at very high energy scales. The quark-gluon plasma

3 Astrophysical constraints on strongly-interacting matter are currently gaining more relevance due to advances in the precision of gravitational wave detection. However, we are not making any contact with astrophysical observables in this thesis such that a more detailed discussion of these experimental constraints is omitted for brevity.

4 See also the reviews [53–56] for a more detailed discussion of the QCD phase diagram.

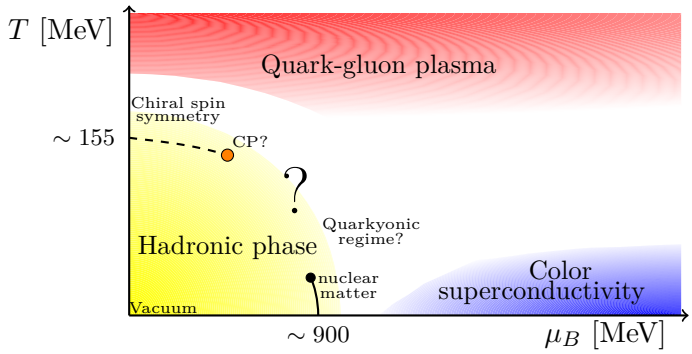

Figure 1.1: Sketch incorporating evidence regarding the phase structure of QCD phase diagram in the (μ_B, T) plane. The sketch is inspired by Refs. [55, 56] and from private communications [57]. The sketch serves to illustrate general features of the phase diagram, such as the quark gluon plasma, the hadronic phase or color superconductivity. These are the three regimes, that are established (in addition to the existence of nuclear matter) at least deep within the respective colored regions. In the intermediate density and temperature region, there exist only conjectures from the community and there is a lot of uncertainty regarding the phase structure. The possibility of exotic, chiral regimes are deliberately not discussed in the main text, as they will be further elaborated upon in Section 1.2. Note that the axes do not necessarily scale linearly.

is the realization of asymptotic freedom in nature through extremely high temperatures and/or densities [60, 61], as in the early universe. In the laboratory, collision experiments are suitable to create such conditions, and hot QCD matter was created for example at RHIC by Au-Au collisions [62]. The most direct approach to the thermodynamics of the quark gluon plasma such as, e.g., the pressure at high temperatures is through perturbation theory which can be performed up to sixth order in the coupling constant [63, 64]. The expansion, however, converges badly and, even with improvements through resummations schemes such as the hard-termal-loop expansion, is reliable only at temperatures of the order of multiple GeV, c.f. Section 4 of Ref. [53] for a review.

FINITE TEMPERATURE PHASE TRANSITION Logically, there must be a phase transition between the hadronic phase and the quark gluon plasma regime at some critical temperature. An indication of such a phase transition in terms of a break-down of the statistical hadronic description of matter was already found in 1965 [65] (before the formulation of QCD in its present form) where a divergence of the partition function of hadrons at a certain temperature is observed. Lattice-QCD simulations reflect this transition by a steep rise in the pressure at a certain temperature [66, 67] and it is by now well-established that the phase transition is a crossover [68]. However, there is still a lot of ongoing research to understand the nature of the transition, especially about the relation of the chiral phase transition and deconfinement. Transitions associated to deconfinement and (approximate) restoration of the chiral symmetry are expected when the system changes from a hadronic regime to a quark-gluon plasma. Currently, it is established from lattice-QCD that the quark condensate decreases from its vacuum value to almost zero at temperatures between 120 and 180MeV with a pseudo-critical temperature of the crossover at $T_{pc} \approx 155$MeV [69, 70]. In earlier investigations of the Polyakov-loop observable, an order parameter for

center symmetry in pure gauge theory[5], it was believed that the deconfinement transition occurs simultaneously the chiral crossover. This is revised in later works [71, 72] using an appropriately renormalized Polyakov-loop observable that does not show any sign of deconfinement. Moreover, LFT simulations around the pseudo-critical temperature show no evidence of deconfinement from the Polyakov-loop either [73, 74]. Since the center symmetry is not a symmetry of QCD but only of pure gauge theory, there is still no reliable order parameter for deconfinement (and, thus, one can argue that a proper theoretical definition of deconfinement is lacking, see Refs. [75, 76] for research on this). Thus, the established phase transition at T_{pc} is a chiral crossover, i.e., one observes a transition from a phase with heavy constituent quarks from dynamical chiral symmetry breaking below T_{pc} to another state with light quarks (where essentially only the bare quark masses from the Higgs mechanism are observed). An important ingredient for the understanding of the relation between the chiral crossover and the deconfinement mechanism is a proper definition of deconfinement in QCD and its relation to chiral symmetry breaking.

CHIRAL SPIN SYMMETRY Only a few year ago it was suggested that above T_{pc} there would still exist a confining regime with hadron-like degrees of freedom [77] that would be characterized by a chiral spin symmetry of QCD correlation functions, see Ref. [78] for a review. However, first indications of hadron-like degrees of freedom above T_c are already discussed for decades [79, 80]. Chiral spin symmetry is a symmetry of the temporal part of the QCD Dirac operator. Measurements of temporal and spatial correlators [81, 82] suggest that between T_c and $3T_c$ this symmetry is approximately realized by the color-electric quark-gluon interaction, mediated by the temporal component of the gluon fields, dominating the color-magnetic interaction and the kinetic Dirac terms, see Ref. [78] for details. See figure 1 in Ref. [83] for a qualitative sketch of the "stringy fluid" regime in the QCD phase diagram. The realization of chiral spin symmetry implies that besides the hadron gas phase and the quark-gluon plasma, there is a third regime of matter at intermediate temperatures with distinctly different symmetry – the regime of chiral spin symmetry – where QCD behaves more like a "stringy fluid" and chirally symmetric quarks are bound by confining color-electric fields. Evidence for the realization of this symmetry comes further from screening mass analysis at temperatures above T_{pc} which are inconsistent with a quark gluon plasma description [78] as well as from hadron-like degrees of freedom in the pseudoscalar spectral function that demonstrate a distinct pion-like state [84].

COLOR SUPERCONDUCTIVITY At asymptotically large densities and low temperatures, one expects a color superconducting phase of quark matter [53, 85–89]. Therein, quarks form a degenerate Fermi gas with a condensate of Cooper pairs near the Fermi surface, as can be obtained from weak-coupling calculations [90, 91]. This is rather natural because the color interaction between quarks is attractive in the anti-symmetric channels and at low temperature a Fermi surface manifest in the quark distribution such that the quarks can form pairs, according to Cooper's theorem. The most attractive pairing channel is antisymmetric in both color and flavor implying that the Cooper pairs consists of pairs with unequal color charge and flavor number. The condensation can occur in different pairing channels, for example the color-flavor locked phase where all three colors and the three lightest quark flavors are paired [92], while in the two-flavor superconducting phase

5 In pure gauge theory, the center symmetry of the gauge group is broken at high temperatures through a non-zero Polyakov loop expectation value and, thus, the Polyakov loop is understood as an order parameter for deconfinement in pure gauge theory.

only up and down quarks condense in a diquark condensate. The former is favored in the weak-coupling limit of QCD with three light quark flavors. At lower densities, however, non-perturbative effects become more important such that this regime is still subject of investigations and the favored pairing mechanism is not settled. In this regime, one mostly relies on effective model calculations [93–100] or functional methods [101, 102] where different pairing mechanisms can occur. Further, crystalline, i.e., spatially dependent order parameters for color superconductivity are discussed [103–107].

NUCLEAR LIQUID-GAS TRANSITION In a proper introduction to the QCD phase diagram, we want to briefly discuss the nuclear phase transition, although nuclear matter is not a central topic of this thesis. Since the nucleon mass is roughly 939 MeV and its binding energy is around 16 MeV, the onset of a non-vanishing density of nuclear matter is at $\mu_B \approx \mu_{\mathrm{NM}} = 923\,\mathrm{MeV}$ at zero temperature. Thus, increasing μ_B from $\mu_B = 0$ towards $\mu_B = \mu_{\mathrm{NM}}$ one obtains a first-order phase transition from a hadron gas, which consists of equal shares of matter and anti-matter, towards a nuclear liquid phase made up predominantly of baryons, forming ordinary nuclear matter as we know it, but also mesons and possibly glueballs. This transition is called the *nuclear liquid-gas transition* and is well established both from experiment and theory [108]. Directly at this threshold, the density varies from zero to the normal nuclear density of $n_0 = 0.16\,\mathrm{fm}^{-3}$. In a phase diagram with the spatially averaged nuclear density $\bar{n}$ and temperature as parameters, nuclear matter would be distributed into droplets of density n_0 when $0 < \bar{n} < n_0$. At non-zero temperatures, the first-order transitions weakens for increasing T and turns second-order at $T_{LG} \approx 15 - 20\,\mathrm{MeV}$ and $\mu_B = \mu_{LG} \approx \mu_{\mathrm{NM}}$. Model investigations for nuclear matter [109, 110] share certain technical similarities with the models for chiral symmetry breaking used in this thesis, but we refrain from presenting their phenomenology in this thesis.

QUARKYONIC MATTER At low temperatures and intermediate densities, i.e., in the region of the phase diagram between the nuclear liquid gas transition and the color superconducting phase, a conjectured regime is the so-called *quarkyonic matter* where densities are high enough that nucleons overlap and the constituent quarks become "free" [111–114]. Then, quarks and light hadrons are the dominant, interacting degrees of freedom. It is expected that possible scenarios for chiral phase transitions and especially regimes of exotic phases, which are discussed below, are compatible with quarkyonic matter [115]. Moreover, quarkyonic matter can exist both in phases with broken and restored chiral symmetry, but its existence suggest that confinement persists at larger densities than chiral symmetry [111, 116].

1.2 CHIRAL PHASES AT INTERMEDIATE DENSITIES: VASTLY UNEXPLORED TERRITORY

The chiral crossover between a phase with a dynamically generated chiral condensate $\langle\bar{\psi}\psi\rangle$, which we will refer to as homogeneous broken phase (HBP) in the following, and so-called symmetric phase (SP), where chiral symmetry is approximately restored, at a temperature of $T_{pc} \approx 155\mathrm{MeV}$ and $\mu_B = 0$ is well established [69, 70].[6]

6 The name SP is not fully accurate, as the chiral symmetry is never exact for physical current quark masses. However, we avoid a differing definition between a phase with an approximate chiral symmetry and an exact chiral symmetry. The term SP is used for both of these phases.

At intermediate and large μ_B/T, there is little evidence with respect to the nature of the chiral phase transition and order parameters related to chiral symmetry breaking at intermediate temperatures and densities in general. This is due to the infamous *sign problem* of QCD at $\mu_B \neq 0$ which spoils the Monte-Carlo simulation techniques from statistical physics in LFT due to the emergence of complex weights, see Ref. [117] for a review. Results from lattice simulations can be extrapolated to up to $\mu_B/T = 3\mu/T \geq 2$ [118, 119] where μ is the quark chemical potential. The findings from LFT predict a decrease of the crossover temperature for increasing μ [120] in consistency with functional approaches such as the functional renormalization group (FRG) [121] and from Dyson-Schwinger equations (DSEs) [122–125]. Functional methods, in general, are a powerful tool as they provide the possibility to study the phase diagram at intermediate temperatures and densities with first principle input.[7] However, DSEs require truncation at a certain order and the FRG requires restrictive ansatzes for the form of the quantum effective action to be solvable, both of which introduces artifacts into the findings which are uncontrolled. Thus, the results from functional approaches carry a systematic error, which is hard to quantify and is expected to increase for larger μ/T. Therefore, results from functional methods must be treated with caution and, ideally, should be cross-checked through investigations of similar observables with different methodologies.

Thus, first principle evidence for the phase structure of QCD at intermediate temperatures and density is scarce. Due to the lack of such evidence, there are many conjectures regarding the (chiral) phase structure of QCD at intermediate temperatures and densities. In Fig. 1.2, two possible scenarios for regimes related to chiral, mesonic order parameters are sketched. The focus of the sketches is solely on chiral phases, while other features of the phase diagram (such as the possibility of a confinement-deconfinement transition or the onset of color superconductivity) are neglected for clarity. These expectations are based on effective model calculations that are inspired by QCD and capture certain, essential features of the theory but not all of them. Within the following discussion and in the sketches, we do not discuss the chiral spin symmetric regime, as it is generated by quantum effects in the QCD partition function. These have, so far, not been studied using model calculations, at least according to the knowledge of the author. Also, this regime is not further investigated within this thesis.

Four-fermion models (such as the well-known Nambu-Jona-Lasinio (NJL) model [42, 43] or the Gross-Neveu (GN) model [36]) and quark-meson (QM) models feature quark interactions with meson fields emerging as auxiliary and dynamical degrees of freedom, respectively,[8] as well as spontaneous chiral symmetry breaking in the vacuum and at low μ and T [137]. In high energy physics, they are often used to model QCD at lower energy scales, see Refs. [93, 138–146] for examples. In these works the gluon dynamics can be treated as

7 Other lattice approaches, like Lefshetz thimble or complex Langevin methods, are prospects to circumvent the sign problem, but so far they are either restricted to very simplistic theories (Lefshetz thimbles) [126–128] or have not yet been shown to provide reliable, physical results [129–131]. Quantum computing is expected to provide the solution to the sign problem of lattice QCD in a few decades, at least if the required hardware and algorithms can be developed [132].

8 NJL-type models can be written as purely fermionic models containing self-interactions of the fermions in terms of a four-fermion contact interaction, that are interpreted as effective vertices for the quark-gluon interaction at lower energy scales [133–135]. Therefore, we use the term NJL-type models interchangeably with four-fermion models in this thesis, although the latter term refers rather to lower-dimensional theories in the literature, while the former name is often used for $3+1$-dimensional models. Mesonic fields emerge as auxiliary bosonic fields which are dynamically formed as $\bar{\psi}\Gamma\psi$ states in four-fermion models [136], where Γ is a matrix with the quantum numbers appropriate for the respective meson field.

integrated out and represented in the reminiscent four-quark and quark-meson couplings.[9] This transition from QCD to degrees of freedom relevant in effective model calculations at low energy is observed in functional methods involving dynamical hadronization methods [121, 147–149]. However, approaches based on NJL and QM models lack the incorporation of the gauge symmetry and, consequently, confinement is not realized in these models. Existing improvements involve including the Polyakov loop as an effective background field in the effective potential [150–152], but this is only a rather crude approximation to the full gluon dynamics and its response to the medium, especially at non-vanishing densities [152–154].

Many of the below discussed scenarios and/or exotic regimes are based on calculations from the aforementioned models. In the following, we want to not only describe the regimes, that are expected to be relevant for QCD from model studies, but also provide and contextualize the underlying literature. Also, the goal is to point out missing evidence in the literature and to motivate the **RO**s and goals of this thesis briefly, before explaining them in more depth in Section 1.3.

CRITICAL POINT The scenario, that is expected by large parts of the community, is the conjecture that the crossover ends in a CP beyond which the chiral phase transition becomes first-order [137, 155], see the red line in the left plot of Fig. 1.2.[10] This expectation is based on model calculations [137, 141, 157, 158] and supported by recent computations using the FRG [121], DSEs [124, 125, 159] as well as reconstructions based on lattice data [160, 161]. Those methods estimate the location of the CP in the range of approximately $T = 90 - 110\,\mathrm{MeV}$ and $\mu = 120 - 210\,\mathrm{MeV}$, a region in the phase diagram that is currently not probed by heavy ion collision experiments. Although the Beam Energy Scan at RHIC studies collisions with a center of mass energy of 3 GeV and 7 GeV, the theoretical prediction for the CP (based on the freezeout chemical potential) could be reached when the collision have a center of mass energy between those two energy scales [162]. The Compressed Baryonic Matter (CBM) experiment at FAIR will in the future have access to the theoretically predicted first-order transition. However, the CP might be difficult to probe directly, since the expected critical scaling is absent even close to the transition [121, 163–165]. Many model calculations find that the first-order line originating from the CP extends until the $T = 0$ axis, although it possibly could have another endpoint at non-vanishing T.

MOAT REGIME There is recent evidence from the FRG [121, 166] and calculations in NJL models [1, 10, 167] for the existence of a so-called moat regime in the phase diagram where the dispersion relation of quark correlations in mesonic channels have a minimum at non-vanishing spatial momenta. For example, pions can exhibit this moat regime dispersion relation in parts of the QCD phase diagram [121]. The moat regime might be present in large regions of the (μ, T) plane including the vicinity of the (to-be) CP, see the blue regions in Fig. 1.2 for illustration. The behavior of the moat dispersion relation is naturally associated to exotic phases featuring spatial modulations, as it favors non-vanishing mo-

9 A nice, although rather simplistic picture is to think of lowering the momentum scale as increasing the relevant length scales that need to be considered. Then, at low enough momentum or energy scale the microscopic gluon exchange between quarks "looks like" a contact interaction between quarks. This picture is, of course, incomplete. It only provides a crude idea for the approximation of relevant terms in QCD.

10 For massless quarks, the chiral crossover becomes a second-order phase transition [156] (since chiral symmetry becomes exactly restored in the SP) such that, precisely speaking, the CP is a tricritical point. However, for simplicity, we will nevertheless refer to it as a CP throughout this work.

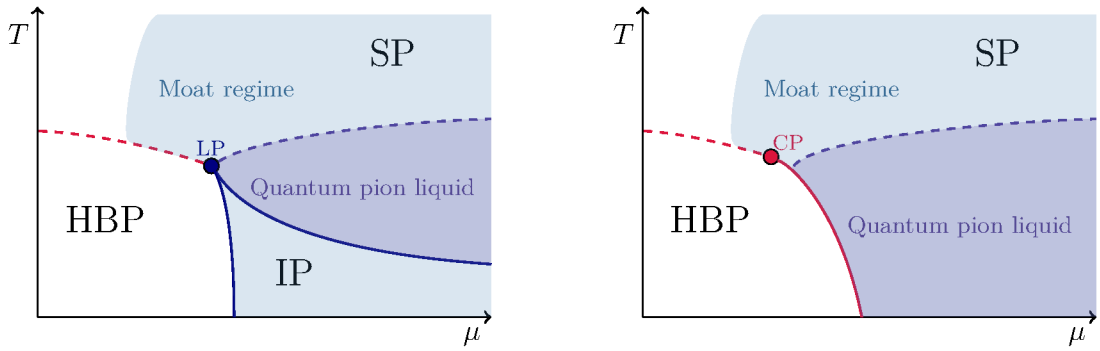

Figure 1.2: Sketches of possible scenarios for the QCD phase diagram with respect to chiral order parameters and exotic phases related to spatially modulated observables. Dense dotted lines are used for the second-order phase transition which is the symmetry restoring transition in the chiral limit from the HBP to the SP – the analogue to the chiral crossover that is obtained for physical current quark masses. The dashed violet line describes the disorder line, which is the onset of the QπL, see the corresponding paragraph in the text. *(Right)* The solid red line is a first-order phase transition between the SP and the HBP that turns second-order in the chiral limit at the CP. *(Left)* The first-order phase transition is replaced by an IP with transitions to the HBP and SP (solid blue lines).

menta of the corresponding (quasi)-particles. Studying the implications of the moat regime for the existence of spatially modulated regimes with full quantum effects is part of the scope of this thesis, as in detail formulated in **RO3** "How do bosonic quantum fluctuations influence exotic regimes?". In QFT, the onset of the moat regime is often associated with the wave function renormalization – the coefficient of the spatial kinetic terms in the quantum effective action – of the respective, (quasi-particle) meson turning negative which must be reflected in the quantum effective action and, consequently, in related observables. While such a moat dispersion relation might be considered exotic in the high energy physics community, it is a well-known and common phenomenon in condensed matter physics, see Refs. [168–171] for original publications and reviews. It occurs for example in models of magnetic materials [168–170], liquid crystals [172, 173] or chemical mixtures and membranes [170] and is often associated with crystallization [174], superconductors [175–177] and quantum Hall systems [178, 179]. Often, the occurrence of the moat regime is associated with certain symmetries, see below, and/or a competitive interplay between repulsive and attractive interactions, although both of these properties are neither necessary nor sufficient conditions for observing the moat dispersion relation.

GENERALIZED $\mathcal{PT}$-SYMMETRY, ITS RELATION TO THE MOAT REGIME AND EXOTIC PHASES Moat regimes naturally arise in (non-Hermitian) theories with a generalized $\mathcal{PT}$ symmetry [180], see Refs. [181–184] for a discussion of $\mathcal{PT}$ symmetry in quantum mechanics and QFT. In this context, $\mathcal{P}$ denotes a generic, linear operation and $\mathcal{T}$ a generic, anti-linear operation. A generalized $\mathcal{PT}$ symmetry is defined as the invariance of a quantity under the action of $\mathcal{P}$ and $\mathcal{T}$ simultaneously, but not individually [181, 184].[11] Such a gener-

11 In non-Hermitian quantum mechanics, this is an often used framework modeling systems with loss and gain in dynamical equilibrium. Thereby, the standard hermiticity conditions for Hamiltonians is replaced by requiring them to commute with the $\mathcal{PT}$ operation where $\mathcal{P}$ and $\mathcal{T}$ in quantum mechanics denotes the parity and time reversal operation [181]. This framework allows to compute a spectrum this is either purely real-valued ("$\mathcal{PT}$-symmetric region") or contains complex-conjugate eigenvalues ("$\mathcal{PT}$-broken region") [181,

alized $\mathcal{PT}$ symmetry is also realized in QCD at $\mu \neq 0$ where the action turns non-Hermitian and the QCD action is invariant under combined operation of charge conjugation $\mathcal{C}$ and complex conjugation $\mathcal{K}$ (but not individually under each of these operations), a $\mathcal{PT}$-type symmetry transformation. Such a symmetry can also be realized in QCD-inspired models [189] but its influence on the phase structure is, so far, mostly neglected. QFTs with a generalized $\mathcal{PT}$ symmetry can give rise to the existence of exotic phases, see, e.g., Refs. [188, 190] where "patterned phases" and "$\mathcal{PT}$-broken phases" are predicted from the properties of propagator poles in scalar mass-mixing theories. Both of these regimes reoccur in this thesis under the terms inhomogeneous phase and quantum pion liquid, respectively. It is a focal aspect of this thesis to investigate the relation between the invariance under a generalized $\mathcal{PT}$ symmetry to the existence of exotic phases in QCD-inspired models, as this aspect is mostly neglected in the literature (exceptions are Refs. [189, 191]). We aim to study the consequences of this symmetry using a four-fermion model with an emergent $\mathcal{CK}$ symmetry at $\mu \neq 0$, see **RO1** "What are the implications of the presence of the combined $\mathcal{CK}$-symmetry at $\mu \neq 0$ for the existence of exotic phases?".

QUANTUM PION LIQUID AND INHOMOGENEOUS CHIRAL CONDENSATES A phenomenon, that is likely related to the moat regime, is the appearance of a so-called *disorder line* [180, 192]. The disorder line separates a regime in the phase diagram where the bosonic two-point correlation functions are dominated by an exponential falloff, such as the SP, from a region in which the spatial correlations behave as an exponential times an oscillatory function, which is defined as quantum pion liquid (QπL) in this thesis. Disorder lines appear in Polyakov-NJL models [191], Polyakov-QM models [189], static quark models at strong coupling [193] and nuclear liquid-gas models [194]. In the QπL the chiral condensate (and other one-point functions) are homogeneous, while the bosonic two-point correlation functions feature spatial inhomogeneities in form of the oscillatory intermediate range behavior. The QπL can be associated to complex-conjugate poles of the bosonic two-point correlation functions in the spatial momenta of the corresponding mesonic channels [189, 190]. The disorder line marks the point where two poles of the correlation functions become degenerate.

If the minimum of the moat dispersion relations at non-vanishing momentum is deep enough, the thermodynamic ground state, given by a condensate of the form $\langle\bar{\psi}\Gamma\psi\rangle$, can be inhomogeneous carrying a non-vanishing momentum. In this so-called inhomogeneous phase (IP), the inhomogeneous chiral condensate breaks chiral symmetry as well as translational symmetry spontaneously. Inhomogeneous chiral condensates are obtained in typical model calculations in the mean-field approximation – an approximation method that suppresses bosonic quantum fluctuations in the path integral – at low $\mu < T$ [195–200], motivated by findings in $1+1$-dimensional four-fermion models where IPs commonly appear [201–203]. We note, however, that inhomogeneous condensation was first studied in nuclear matter model computations in the form of inhomogeneous pion condensation [204] and, later, in strongly-interacting models based on quark degrees of freedom [205, 206].[12]

Inhomogeneous phases can overlap with parts of the moat regime [1]. Typically, one obtains direct transitions from homogeneous phases like the SP and the HBP to the IP, see

183]. A generalization of this symmetry as the above discussed combination of a generic linear and antilinear operation is used both in quantum mechanics and in QFT [185, 186]. This type of symmetries might be useful for resolving the sign problem in lattice-QCD at $\mu \neq 0$ [185, 187, 188].

12 In mean-field nuclear matter models, instabilities of the homogeneous ground states towards perturbations with a non-vanishing momentum are also found in Ref. [207].

the right plot in Fig. 1.2. In model calculations, the CP (and with it the entire region of the first-order phase transition) is then often replaced by a lifshitz point (LP) where both transitions from the homogeneous phases to the IP meet. However, in principle there can also exist a separation of LP and CP [196, 208]. It is important to note that in NJL model calculations the presence of an IP strongly depends upon the regularization scheme and regulator value, while the moat regime is rather robust [9, 10, 167]. Further, the extent of the IP can significantly depend on model details and technical aspects as well as further parameters such as the pion mass [209, 210]. This renders the predictive power of the above mentioned studies questionable with respect to QCD, since there is an inherit ambiguity in the model analysis itself. IPs might only be present in strongly regulated or, equivalently, lower-dimensional four-fermion models [211, 212]. We provide further context on the robustness of IPs in QCD-inspired models by analyzing renormalizable QCD-inspired models, as in detail described under **RO5** "What is the fate of inhomogeneous chiral condensates within $2+1$-dimensional four-fermion models and related QCD-inspired models?". Beyond model investigations, recent analyses of QCD DSEs show that the symmetric solution is instable to inhomogeneities at low T and high μ. This instability, however, exits in a parameter region where the symmetric solution is not preferred [213–215]. While this is an interesting result, these works are not yet conclusive regarding the existence of IPs in the phase diagram of the DSEs model for QCD.

One-dimensional, inhomogeneous condensates are, moreover, instable against fluctuations from the Goldstone modes of the broken translational symmetry (phonons) [216, 217], leading to a power-law decay of the oscillating correlation functions, and can be disordered through the Goldstone bosons of chiral symmetry breaking [218, 219]. The disordering through Goldstone bosons leads to a QπL regime where the chiral condensate is homogeneous but the bosonic two-point correlation functions are oscillatory functions times an exponential fall-off, as described above [219]. Thus, this mechanism is expected to dominate over the disordering from phonon modes. The finding is only relevant in a large-N_s limit of a model for N_s light meson fields, but the mechanism is likely applicable for QCD at non-vanishing μ and T such that we expect the QπL to be favored over an IP in the phase diagram, see Ref. [219] for details. This competition of the above described mechanisms for the disordering of IPs is covered in this thesis under **RO4** "Are inhomogeneous chiral condensates disordered by bosonic fluctuations? Is the QπL the preferred scenario in the full quantum theory?...". Note, however, that magnetic fields can stabilize inhomogeneous condensates against phonon fluctuations through topological effects [220, 221] and might possibly stabilize them also against Goldstone mode fluctuations from chiral symmetry breaking. In general, ordered phases are expected to be weakened by fluctuations, especially by thermal and bosonic quantum fluctuations.[13] The effects of quantum fluctuations on models for these exotic phases is investigated in this thesis under **RO3** using LFT simulations of a scalar QFT, which classically features a moat regime as well as an IP.

13 In one spatial dimension, there even exists a no-go theorem forbidding the breaking of any continuous symmetry, as in a dynamically generated chiral condensate, for non-zero temperatures[222–224]. In present literature, it is still discussed unclear whether an IPs persist at non-zero temperatures in the GN model [225], as indicated by lattice simulations [226]. However, these results directly show the existence of oscillating correlations function in the GN model, but not necessarily the long-range order and true translational symmetry breaking. In the chiral GN model, however, it is rather clear that the inhomogeneous condensate is disordered at non-zero temperatures [227–229].

1.2.1 *Possible scenarios for exotic regimes in the QCD phase diagram*

In Fig. 1.2, two different scenarios for the above discussed phases in the chiral limit are sketched. In the right plot, we present a scenario where exotic regimes like the moat regime exist close to the CP, consistent with Ref. [121]. As discussed above, the first-order transition (solid red line) is depicted as extending until $T = 0$ although it might possibly as well have another endpoint at $T \neq 0$. In addition to the moat regime, which extends over a large region of the (μ, T) plane consistent with model calculations [1, 10], this sketch features the disorder line and a QπL at lower temperatures. This QπL itself might be obtained from the disordering mechanism of inhomogeneous chiral condensates through quantum fluctuations [219, 225, 226] or mixing effects [180]. The location of the disorder line in the sketch admittedly is chosen arbitrarily. At lower temperatures, short range correlations stemming from the oscillations in the QπL are expected to be enhanced compared to larger temperatures (where oscillations might still be present but more suppressed). At almost zero temperature, the decay of correlation functions might even change from an exponential to a power-law suppression (a liquid-crystal like regime). Such a behavior can be observed in perturbative QCD with massless quarks where so-called Friedel oscillations arise at zero temperature, a power-low fall-off times an oscillatory function that is additionally exponentially screened for $T \neq 0$ [230].

In the left plot of Fig. 1.2, we conjecture that the CP and the first-order phase transition is entirely covered by an IP ,as implied by standard model computations [197] (although these computations suffer from regularization artifacts [10, 167]). Thus, also the CP is replaced by an LP – the onset of the IP and meeting point of three transition lines from the respective homogeneous phases to the IP. Alternatively, a splitting of the CP and the LP might also be observed such that there is a first-order transition at temperatures larger than for the IP. The moat regime at larger temperatures is a natural precursor of the an IP. A moat regime often also implies the appearance of a disorder line, such that, again, we expect the existence of a QπL. It is expected that the exponentially suppressed oscillatory behavior in the QπL is present at intermediate temperatures, while the suppression of thermal fluctuations at lower temperatures allows for the formation of crystalline-like inhomogeneous condensates.

1.3 RESEARCH OBJECTIVES AND GOALS OF THIS THESIS

This thesis explores the possibility of exotic phases[14] in QCD at intermediate temperatures T and baryon chemical potential μ_B building upon the current state of the literature summarized above. QCD-inspired models provide starting point for the investigation of relevant mechanisms for chiral observables in QCD at intermediate temperatures and chemical potentials, also due to the lack of first principle calculations. Admittedly, the model approach does not allow for quantitative predictions. Instead, we aim at the identification of novel phenomena relevant for QCD itself. An example for such a phenomenon is the discovery of inhomogeneous chiral condensates in NJL-type theories [195, 202] that further motivated the investigation of IPs using DSEs [213, 214] and FRG [121]. Moreover, an improved understanding of possible exotic phenomena in QCD could aid in developing new methods to study the phase diagram of QCD directly, see Refs. [185, 187, 188] for recent, although still

14 At this point, it should be noted that the term "exotic phase" is not only restricted to phases in a strict thermodynamic classifications. Instead, the term is used for any phase or regime that can be characterized by a distinctly different behavior of a certain observable. For example, the moat regime can be characterized by a non-vanishing, global minimum of the mesonic dispersion relation.

rather academic examples. The discovery of a novel feature of the phase diagram further allows for experimental predictions using model calculations, which can then be tested in heavy-ion collisions. For example, the moat regime dispersion relations leaves its imprints on two-particle correlations for pions [231–234] and leads to an enhanced production of back-to-back dileptons [11]. These signatures are expected to be testable experimentally in the future through the CBM experiment at FAIR.

Given these preliminary remarks, we formulate the **RO**s addressed in this thesis and give some context for the necessity of addressing them:

RO1 What are the implications of the presence of the combined $\mathcal{CK}$-symmetry at $\mu \neq 0$ for the existence of exotic phases?

As outlined above, scalar QFTs with a generalized $\mathcal{PT}$-type symmetry (as is the $\mathcal{CK}$ symmetry) feature moat regimes, QπLs and IPs [180, 188, 190]. However, computations using QCD-inspired models for chiral symmetry breaking have so far neglected modeling the emergent $\mathcal{CK}$-symmetry of QCD at $\mu \neq 0$ and its effect on the phase diagram, besides a few studies [189, 191]. We are going to explore the effect of this symmetry in the framework of four-fermion models avoiding the above described regularization artifacts by studying $2+1$ dimensional models (we further elaborate on this in **RO5**).

RO2 What are the implications of mixing effects between scalar and vector mesons for the existence of exotic phases at $\mu \neq 0$?

Many investigations of QCD-inspired models with respect to chiral phases do not include vector interactions. Exceptions are Refs. [196, 208, 235, 236] which in turn do not consider the emergent $\mathcal{CK}$-symmetry. The fundamental QCD partition function gives rise to such Yukawa-type interactions between fermions and vector mesons, as, for example, the ω meson, arising from a resonance of four-fermion interactions in the corresponding vector channels [133, 148, 237]. In line with **RO1**, we investigate the momentum-dependent mixing effects between scalar and vector mesons using $2+1$-dimensional four-fermion models. In this thesis, we aim to explore the mixing effects of scalar and vector mesons on the phase structure, as generated through the fermionic interactions. We note that the parallel work [189] explores both **RO1** and **RO2** in a similar approach as this work, but only static mixing effects are investigated and the focus is more on phenomenological results.

RO3 How do bosonic quantum fluctuations influence exotic regimes ?

Most of QCD-inspired model computations with respect to the phase diagram rely on certain approximations that either completely suppress bosonic fluctuations or only partially take them into account, while allowing for semi-analytical analyses. In this thesis, we study exotic regimes without any approximation using LFT simulations of a scalar O(N_s) theory. This theory can be seen as a toy model for the light scalar mesons in QCD and is tuned to feature exotic regimes. Such models are applied in the literature already for spontaneous symmetry breaking and phase transitions both in high-energy and condensed matter physics [238, 239]. Note that in QCD the chiral symmetry for two, massless quark flavors amounts to a rotational O(4) symmetry transformation of the mesonic fields describing the sigma meson and the pions. The standard action for O(N_s)-symmetric scalar fields is extended in our analysis by higher-order spatial derivative terms such that a moat regime arises and its classical

equation of motions feature an IP in the parameter region corresponding to the moat regime. The effect of bosonic quantum fluctuations is then investigated in LFT simulations. This approach allows to investigate the existence and possible competition or coexistence of the moat regime, IPs and QπLs in three spatial dimensions without the limitations of particular approximations or regularization artifacts.

RO4 Are inhomogeneous chiral condensates disordered by bosonic fluctuations? Is the QπL the preferred scenario in the full quantum theory? How is translational symmetry breaking in an IP appropriately detected in the infinite-volume limit using lattice field theory?

As outlined for **RO3**, the effect of quantum fluctuations on exotic phases that are obtained in semi-classical approximations of certain theories. In Ref. [219], the above mentioned O(N_s) model is studied in the large-N_s limit. Therein, a QπL is obtained instead of an IP and it is argued that in the full quantum theory the QπL is favored over the IP, since IPs are disordered by the transverse fluctuations from the Goldstone modes of O(N_s) (chiral) symmetry breaking. In this work, we are going to investigate this claim by studying the model for $N_s = 1$ and $N_s = 2$ such that no transverse modes from chiral symmetry breaking are present in the system. This allows to test for the alternative scenario that the disordering of inhomogeneous chiral condensates is a generic effect of quantum fluctuations. Further, the competition of the QπL and the IP is studied for different $N_s = 1, 2, 4, 8$ and different spatial volumes. Thereby, we tackle the technical question on how to appropriately characterize the breaking of the invariance under (the discrete subgroup of) spatial translations using lattice field theory by an external field approach.

RO5 What is the fate of inhomogeneous chiral condensates within $2+1$-dimensional four-fermion models and related QCD-inspired models?

Inhomogeneous chiral condensates in NJL models likely arise as artifacts from the employed regularization scheme in non-renormalizable $3+1$-dimensional four-fermion models [10, 167, 211, 212, 240, 241]. The first hint in this direction stems from the investigation of the $2+1$-dimensional GN model where an IP might exist at finite regulator values depending on the used regularization scheme [242] but vanishes when removing the regulator [240, 241]. This is possible in two spatial dimensions [243, 244]. Refs. [10, 167] demonstrate that the existence of an IP depends on the chosen regularization scheme in the $3+1$-dimensional NJL model, while Refs. [4, 211] suggest that a four-fermion model in $3+1$ dimensions with a finite regulator is equivalent to the same model in lower spatial dimensions (the number of spatial dimensions is not restricted to integers therein). The two latter manuscripts show that in the GN model with a discrete chiral symmetry IPs exist only for non-integer spatial dimensions $1 \leq d < 2$. The regulator artifacts, that are unavoidable in three spatial dimensions, can be in detail explored in two spatial dimensions since the renormalizability allows to in detail study the dependence on the regulator value and used regularization scheme [240, 241]. However, in $1+1$ dimensional four-fermion models larger chiral symmetry groups typically favor the existence of inhomogeneous condensates and, often, more involved inhomogeneous structures arise [201, 245–248]. Thus, a natural question, that arises, is whether IPs exist in $2+1$-dimensional four-fermion models with a larger and continuous chiral symmetry group, that gets spontaneously broken. With respect to QCD, of course, it is also interesting to study a four-fermion model with a

similar SU(2) axial symmetry that gets spontaneously broken by a chiral condensate. Answering this question provides insights into the fate of IP in four-fermion models, in general, since in $3+1$ dimensions four-fermion model investigations with respect to IPs (and exotic phases in general) will always suffer from the ambiguities of the above described regularization artifacts. Moreover, obtaining unambiguous results for the existence of IPs in many $2+1$-dimensional four-fermion models avoids artifacts stemming from details of the chosen model.

REMARKS ON FOUR-FERMION MODELS Four-fermion models are non-renormalizable in $3+1$ dimensions and arise naturally as low-energy effective interaction channels in QCD at certain energy scales, making them a popular choice for investigations of regions of the phase diagram unavailable to first-principle investigations. Thus, keeping a finite regulator in the theory is necessary and predictions from these models are only trustworthy if they are robust against the change of the regulator value and regularization schemes whilst still reproducing expected QCD behavior in certain limits (for example, NJL models are typically tuned such that the pion decay constant and constituent quark mass are close to the physical values in the vacuum). Thus, avoiding these artifacts from regularization is crucial for the investigation of exotic phases at intermediate μ and T, as demonstrated by the observation of the regulator artifacts in the IP of the NJL model [10, 167]. Since the interesting parameter regions for exotic phases are at the order of magnitude of the typically required regulator values in four-fermion models, this work focuses on $2+1$-dimensional four-fermion models which are renormalizable [243, 244] and, thus, avoids the artifacts from regularization completely. In the literature, there are quite a few studies (e.g. Refs. [249–257]) applying $2+1$-dimensional four-fermion models to investigate physical phenomena in high energy physics such as, e.g., color superconductivity in a directly accessible QFT [107, 258–261]. Four-fermion models are interesting themselves for several branches of physics, and are used not only as low-energy effective models for chiral symmetry breaking in QCD but also to study strongly-interacting, fermionic matter under extreme conditions such as isospin imbalance or magnetic fields, condensed matter applications such as spontaneous symmetry breaking in graphene effective field theory [262–267] and other (almost) planar systems [268–271] as well as for the development of techniques and technical aspects in QFT [243, 244, 272–276] (that are also relevant for other aspects of high energy physics such as asymptotic safety [277]). However, we focus on the application of these models to chiral aspects of the QCD phase diagram.

1.4 OUTLINE

This thesis is structured as follows. In Chapter 2 we introduce basic concepts of QFT in thermal equilibrium, which are relevant for the investigations in this thesis. Further, we introduce four-fermion and Yukawa models used as low energy effective, QCD-inspired theories and apply certain techniques, like bosonization and the mean-field approximation, which are relevant multiple times in the results chapters.

Then, an extended literature review on conjectures of the QCD phase diagram at $\mu_B \neq 0$ with particular emphasis on exotic regimes with spatially modulated observables is presented in Chapter 3. We also elaborate on the relation of these expected regimes to QFTs with generalized $\mathcal{PT}$-symmetry and show evidence for the existence of a moat regime from functional methods. This chapter aims at providing a deeper overview over moat regimes,

QπLs, and IPs by presenting selected literature results, which are relevant throughout this thesis.

In Chapter 4, the major tool for our investigations, namely the computation and analysis of bosonic two-point vertex functions in four-fermion and Yukawa models within the mean-field approximation, is presented. Thereby, we discuss its appearance both in the stability analysis of homogeneous condensates and in the analysis of propagator poles from considerations of $\mathcal{PT}$-type symmetry. Also, the computation of the bosonic two-point vertex functions are tested using analytical results for the phase diagram of two different $1+1$-dimensional four-fermion models.

Following these theory and methodology chapters, three result chapters are presented that focus on different aspects of the research objectives posed in Section 1.3. In Chapter 5, the absence of instabilities towards inhomogeneous chiral condensates and the moat regime is shown in all four-fermion and Yukawa models in $2+1$ dimensions with local, scalar interactions (with different, possible further extensions) in the mean-field approximation and, thereby, provides arguments that IPs observed in three spatial dimensions in NJL-type models might very well be artifacts of regularization schemes. An extension of the results to vector interactions (such that all models with local quark-meson interactions are covered) is presented and the absence of instabilities is shown in the SP. Moreover, we argue that the absence of instabilities in general is a strong indication for the non-existence of inhomogeneous chiral condensates in these models. Thus, this directly addresses **RO5**, see Section 1.3. Using existing literature, we also discuss that the absence of the IP and the moat regime is likely valid beyond the mean-field approximation in the studied theories. In Chapter 6, we further investigate the effects of scalar and vector interactions leading to the mixing of scalar and vector mesons in the HBP within one particular four-fermion model. One observes a QπL within the HBP of this model, where bosonic two-point correlation functions are spatially oscillating but exponentially damped. The existence of the QπL aligns with the presence of a generalized $\mathcal{PT}$-symmetry in this model, a similar symmetry that is also present in QCD at non-vanishing μ. We show that our findings are also valid in the context of all four-fermion models that feature scalar-vector mixing effects and local interaction terms. This chapter directly addresses **RO1**, **RO2**, and partially also **RO5**.

The above chapters all apply the mean-field approximation where bosonic quantum fluctuations are suppressed. In Chapter 7, the influence of these quantum fluctuations on exotic regimes is investigated in an effective scalar $\mathrm{O}(N_s)$ model. The used model features spontaneous chiral symmetry breaking as well as moat regime and an IP in classical computations and can directly be simulated on the lattice. The findings demonstrate how quantum fluctuations disorder the inhomogeneous condensates, that are observed in the parameter space of the classical theory, at finite spatial volume independent of N_s. Only a QπL is present in the quantum theory. A proof-of-work of a specifically developed external field technique to investigate translational symmetry breaking in the infinite-volume extrapolation is presented, but no explicit conclusions from this analysis can be derived yet.

A summary of the results as well as a overall interpretation with respect to the **RO**s and a contextualization with the literature can be found in Chapter 8 where also future research directions are discussed.

For a quicker read, experts familiar with the research field may consider following the "fast reading" guide, presented in the front matter of this manuscript.

2

THEORETICAL PREREQUISITES

AGENDA AND RELATION TO THE RESEARCH OBJECTIVES In this chapter, we introduce the theoretical prerequisites which are relevant for the rest of the thesis. As a starting point, we assume that the reader is familiar with basic concepts of QFT, see the textbooks [278–280] as well as the lecture notes [281] for an introduction to these. Due to the nature of such an introduction, there is no direct relation to the **RO**s for this thesis although the theoretical background for their investigation is presented.

DISCLOSURE This chapter provides a brief introduction to thermal QFT and QCD-inspired theories with focus on relevant topics for this thesis. All content can be found in more detail in standard textbooks and lecture notes on the topic, for example in Refs. [64, 282–285]. With respect to the introduction to QCD-inspired models and the approaches used to study them one can refer to the huge amount of literature on four-fermion and Yukawa models. Although bits and pieces of the content presented in this regard can be found in publications working with these QFTs, we are not aware of a comprehensive review in textbooks or review articles. Closely related presentations can be found in the PhD theses [52, 167, 286]. We by no means claim that any of the content presented in this chapter is original. Since the contents of this chapter are textbook knowledge, citations are only spread occasionally for specialized statements, which go beyond the common textbook knowledge.

OUTLINE We start with a brief introduction to the path integral formalism for QFT in a thermal equilibrium and definition of generating functionals for the computation of correlation and vertex functions in this context. Then, the QCD-inspired models of interest for this thesis, i.e., four-fermion and Yukawa-type models, as well as the used techniques for the analysis of this theories, namely the so-called Hubbard-Stratonovich transformation and the mean-field approximation, are presented.

2.1 QUANTUM FIELD THEORY IN THERMODYNAMIC EQUILIBRIUM

The goal of this section is to provide a brief introduction to QFTs in $D = d + 1$ spacetime dimensions in thermal equilibrium. The theories of interest for this thesis are QCD-inspired models in $D = d + 1$ spacetime dimensions that do not contain gauge fields. Thus, the main building blocks of these models are fermionic fields $\bar{\psi}, \psi$ and N_s scalar fields ϕ_j, see Appendix A.4 for a brief introduction of these fields as entities that transform under certain representations of the Poincaré algebra with spin-1/2 and spin-0, respectively. Conventions for the spacetime metric as well as the Dirac matrices are given in Appendix A.2 and

Appendix A.3. Thereby, we assume that the reader is already familiar with the Dirac equation and the free Dirac action.

In the path integral formalism, the computation of the expectation value of an observable O amounts to

$$\langle O \rangle = \tfrac{1}{Z} \int \mathscr{D}\bar{\psi}\mathscr{D}\psi\mathscr{D}\vec{\phi}\, O(\bar{\psi}, \psi, \vec{\phi})\, \mathrm{e}^{\mathrm{i}\mathcal{S}[\bar{\psi},\psi,\vec{\phi}]}, \tag{2.1}$$

where $\mathcal{S}$ is the classical action of the theory and the path integral

$$Z = \mathcal{N} \int \mathscr{D}\bar{\psi}\mathscr{D}\psi\mathscr{D}\vec{\phi}\, \mathrm{e}^{\mathrm{i}\mathcal{S}[\bar{\psi},\psi,\vec{\phi}]}, \tag{2.2}$$

where the operator $\int \mathscr{D}\bar{\psi}\mathscr{D}\psi\mathscr{D}\vec{\phi}$ denotes the integration over all microscopic field configurations of $\bar{\psi}, \psi$ and $\vec{\phi}$, respectively, and $\mathcal{N}$ is a normalization constant. Strictly, such an integration measure is properly defined on a discretized spacetime lattice Λ_a with lattice spacing a. Accordingly, the spacetime coordinates $x = (x_0, \boldsymbol{x})$ are restricted to be elements of Λ, i.e., they can be written as $x = an$ with $n^\nu \in \mathbb{Z}$. Then, the integration measure is defined as

$$\int \mathscr{D}\bar{\psi}\mathscr{D}\psi\mathscr{D}\vec{\phi} = \lim_{a\to 0} \prod_{x\in\Lambda_a} \int \mathrm{d}\bar{\psi}(x)\mathrm{d}\psi(x) \prod_{j=1}^{N_s} \int \mathrm{d}\phi_j(x). \tag{2.3}$$

Thus, Eq. (2.2) is a shorthand notation for an infinite-dimensional integral over all field configurations weighted with the exponential of the action times i. We note that one often implicitly assumes boundary conditions for the functional integral such that the field configurations $\bar{\psi}, \psi, \vec{\phi}$ are fixed at an initial and final time slice t_in and t_f. The path integral (2.2) then corresponds to a transition amplitude between the initial and final state. For example, in scattering processes one typically ensures that the fields are solutions of the free theory, i.e., without interaction terms, in the limits $t_\mathrm{in} \to -\infty$ and $t_\mathrm{f} \to \infty$, respectively.

Although, in principle, the path integral formalism is suitable for computation of observables of any kind, solving Eq. (2.1) is in general often not possible. Thus, one relies on appropriate approximation methods such as, e.g., perturbation theory up to a certain order.

2.1.1 *From Minkowski to Euclidean spacetime*

The path integral (2.2) is particularly hard to solve due to the oscillatory nature of the exponential weight. However, for QFT in thermodynamic equilibrium one often analytically continues from Minkowski spacetime to Euclidean spacetime with metric $\eta_{E,\mu\nu} = \delta_{\mu,\nu}$, which will be outlined below. For the rest of this subsection, we will use the subcript E to denote quantities in Euclidean spacetime and the subscript M for Minkowski spacetime.

The change of coordinates from the Minkowski spacetime coordinates $x_M = (x_0, \boldsymbol{x})^\mathsf{T}$ to Euclidean spacetime coordinates $x_E = (\boldsymbol{x}, \tau)^\mathsf{T}$ is given by the naive substitution

$$\tau = \mathrm{i}x_0, \qquad \text{for the time coordinate,} \tag{2.4}$$

$$\boldsymbol{x}_E = \boldsymbol{x}_M, \qquad \text{for the spatial coordinates,} \tag{2.5}$$

where $\tau \in \mathbb{R}$ such that the time coordinate is taken to be purely imaginary. This process is also known as Wick rotation in the literature [64, 284], (albeit it is only a special case of a Wick rotation [287]) as one rotates into the temporal coordinate from the real to the imaginary axis. The analytical continuation from real to imaginary time implies

$$\mathrm{i}\partial_\tau = \partial_{x_0} \qquad \text{for the time derivative,} \tag{2.6}$$

$$\partial_{x^{E,j}} = \partial_{x_{M,j}},\ j = 1, \ldots, d, \qquad \text{for the spatial derivative.} \tag{2.7}$$

and

$$(\mathrm{d}s_M)^2 = \mathrm{d}x_0^2 - \mathrm{d}\boldsymbol{x}_M^2 = -(\mathrm{d}\tau^2 + \mathrm{d}\boldsymbol{x}_E^2) = -(\mathrm{d}s_E)^2 \tag{2.8}$$

making the Euclidean spacetime metric evident. At this stage, we want to note that performing a Wick rotation is in general more involved than the simplified presentation in this work and is still a topic of active research in mathematical physics.[1] Nevertheless, in the context of this thesis and many common applications in equilibrium QFT, the above substitutions are sufficient and we will not further elaborate on the subtleties of the Wick rotation. The analytical continuation makes it necessary to define an action in Euclidean spacetime, in our case by $\mathcal{S}_E = -\mathrm{i}\mathcal{S}_M$, see Appendix A.2 for examples of specific models. The path integral (2.2) becomes a Euclidean partition function

$$Z = \mathcal{N} \int \mathscr{D}\bar{\psi}\mathscr{D}\psi\mathscr{D}\vec{\phi}\, \mathrm{e}^{-\mathcal{S}_E[\bar{\psi},\psi,\vec{\phi}]}, \tag{2.9}$$

where the fields $\bar{\psi}, \psi$ and $\vec{\phi}$ are now defined in Euclidean spacetime, i.e., transforming under the spin-0 and spin-1/2 representation of the modified Poincaré algebra for Euclidean spacetime, c.f. Appendix A.4. The computation of observables (2.1) is modified in an analogous way, i.e.,

$$\langle O_E \rangle = \tfrac{1}{Z} \int \mathscr{D}\bar{\psi}\mathscr{D}\psi\mathscr{D}\vec{\phi}\, O_E(\bar{\psi}, \psi, \vec{\phi})\, \mathrm{e}^{-\mathcal{S}_E[\bar{\psi},\psi,\vec{\phi}]}, \tag{2.10}$$

where the observables also have to be rotated to Euclidean spacetime quantities. If possible, the analytical continuation to imaginary time is convenient for practical computations, e.g., for LFT methods. However, this procedure can lead to severe difficulties in the computation of dynamical real-time processes [291]. In this thesis, observables are time-independent and, thus, the Wick rotation is a useful tool. Nevertheless, we note that one really has to be careful treating the poles of integrand that lie in the integration contours within this plane.

The transformation to Euclidean spacetime only allows to obtain to interpret Eq. (2.9) as a probability distribution function if $\mathcal{S}_E$ is real-valued. This is the case for the theories studied in this thesis and we assume in the following always that $\mathcal{S}_E$ is real-valued. Note, however, that this is not necessarily true for all QFTs. The most prominent example of a theory with complex-valued action is QCD at non-vanishing baryon chemical potential. Then, typical computational approaches relying on sampling a high-dimensional probability distribution function, such as in LFT, are not directly applicable.[2]

Examples for the consequences of the Wick rotation on the level of the free Dirac action as well as the theories of interest for this thesis are presented in Appendix A.2. In the following, we only work in Euclidean spacetime. Thus, the subscript E is omitted.

2.1.2 *Introduction of temperature*

The Euclidean partition function (2.9) has the form of a probability distribution function and, moreover, its integrand is of similar form as a Boltzmann weight, i.e., it reminds of

1 For example, one has to think about the exchange of contour integrals in the evaluation of observables such as correlation functions using the analytical continuation of the temporal coordinate. This process can become rather complicated when one allows for general observables, since poles, cuts and other non-analyticities in the complex plane need to be considered when changing the integration contour, see Refs. [288–290] for details.

2 Approaches for theories with complex-valued $\mathcal{S}_E$ are under heavy investigation as they pose the possibility to study the phase diagram of QCD at non-vanishing baryon chemical potential, see Refs. [117, 292] for a review of the current status of research.

a partition function in statistical physics. In this section, we will make this analogy more explicit by introducing a non-vanishing temperature to the system, i.e., we are going to construct the QFT analogue of a canonical ensemble.

In a QFT in thermal equilibrium, the temperature T is introduced by compactifying the temporal direction of the Euclidean spacetime to a finite extent $\beta = 1/T$, see, e.g., Refs. [64, 282–285]. This is sensible as the equilibrium implies that there no longer is a global time evolution of the macroscopic system and only local thermal and quantum fluctuations are allowed. Thus, all observables computed by the path integral (2.10) should be time-independent. The spacetime integration over $\mathrm{d}^{d+1}x$ is, consequently modified and rewritten as

$$\int \mathrm{d}^{d+1}x = \int_0^\beta \mathrm{d}\tau \int \mathrm{d}^d x. \tag{2.11}$$

This change of the spacetime manifold is applied particularly in the Euclidean action $\mathcal{S}$ of the theory, but also all other quantities of the respective QFT. Moreover, one has to adjust functional integration in the partition function (2.9). Accordingly, the boundary conditions for the fields have to be modified as the spacetime manifold is compactified. The appropriate modification for the fields must take into account that taking a trace (as needed for the partition function) means to identify the final and initial states. In other words, we need to set

$$\vec{\phi}(\tau+\beta,\boldsymbol{x}) = +\vec{\phi}(\tau,\boldsymbol{x}), \qquad \bar{\psi}(\tau+\beta,\boldsymbol{x}) = -\bar{\psi}(\tau,\boldsymbol{x}), \qquad \psi(\tau+\beta,\boldsymbol{x}) = -\psi(\tau,\boldsymbol{x}), \tag{2.12}$$

i.e, anti-periodic and periodic boundary conditions in the temporal coordinate τ for the bosonic fields $\vec{\phi}$ and the fermionic fields $\bar{\psi}, \psi$, respectively. The necessity of anti-periodic boundary conditions for the fermion fields (instead of periodic as one would expect) can be understood by carefully discretizing the temporal direction and carefully consider the Grassmann nature of fermionic fields when taking the trace which introduces the additional minus sign in Eq. (2.12) for $\bar{\psi}$ and ψ.

In summary, the introduction of a temperature T amounts to compactifying the temporal direction to a cylinder where the temperature is identified with the inverse of the radius of the cylinder. The overall spacetime manifold is then $\mathbb{R}^d \times S^1$, i.e., it is the one of a torus whose radius becomes infinite in the limit of vanishing temperature.

MATSUBARA FREQUENCIES While the introduction of temperature above follows rather hand-waving arguments, one can understand its meaning with reasonable arguments from quantum mechanics. Similar to the quantization of energy levels when studying the Schrödinger equation in a spatial box, the finite temporal extent β produces a discrete spectrum whose resolution is proportional to $1/\beta = T$. This can also read off the Fourier expansions of the fields that hold the boundary conditions (2.12)

$$\chi(\boldsymbol{x},\tau) = T \int \frac{\mathrm{d}^d p}{(2\pi)^d} \sum_{n\in\mathbb{Z}} \tilde{\chi}(\boldsymbol{p}, \mathrm{i}\alpha_n)\, \mathrm{e}^{\mathrm{i}\alpha_n \tau + \mathrm{i}\boldsymbol{p}\boldsymbol{x}}, \tag{2.13}$$

where χ represents either a bosonic or fermionic fields. As the fields obey the (anti-)periodic boundary conditions, the discrete Matsubara frequencies α_n with $n \in \mathbb{Z}$ are given by

$$\alpha_n = \omega_n = 2\pi n T, \qquad \text{for } \chi = \phi_j, \tag{2.14}$$

i.e., for bosonic fields and

$$\alpha_n = \nu_n = 2\pi\,(n + 1/2)\,T, \qquad \text{for } \chi = \psi, \tag{2.15}$$

i.e., for fermionic fields [3]. In the zero temperature limit, the discrete sum over the Matsubara frequencies becomes a continuous integral such that standard QFT after the Wick rotation is recovered. The corresponding, inverse Fourier transformations are

$$\tilde{\chi}(\boldsymbol{p}, \alpha_n) = \int_0^\beta \mathrm{d}\tau \int \mathrm{d}^d x \psi(\boldsymbol{x}, \tau) \mathrm{e}^{-\mathrm{i}\alpha_n \tau - \mathrm{i}\boldsymbol{p}\boldsymbol{x}}. \tag{2.16}$$

2.1.3 *Introduction of a mean fermionic density*

As discussed above, the Euclidean partition function (2.9) reminds of a partition function of a statistical ensemble. In statistical systems, it is common that, e.g., the number of particles in the system fluctuates according to the given probability distribution. In QFT, these fluctuations are naturally incorporated because of the possibility of particle production through quantum fluctuations and, after the introduction of a temperature as discussed above, also through thermal fluctuations. To study systems with a fixed particle number or density, one typically ensures that the particle number of interest is fixed in the statistical average. Mathematically, this can be ensured using Lagrange multipliers [293, 294]. The Lagrange multiplier is introduced into the probability distribution functions to modify the probability of a field configuration according to its corresponding particle number. Physically, this Lagrange multiplier can be identified with the corresponding chemical potential – the energy per additional particle in the system. This chemical potential is treated then as a thermodynamic state variable of the system, analogous to using the grand-canonical ensemble in statistical physics.

In this work, we are interested in QCD-inspired models at non-vanishing fermion densities. Therefore, we define the fermion density

$$n = \bar{\psi}(x)\gamma_{d+1}\psi(x). \tag{2.17}$$

such that the fermion number is given by

$$N = \int \mathrm{d}^d x\, \bar{\psi}(x)\gamma_{d+1}\psi(x). \tag{2.18}$$

This definition is common as it is associated with a conserved charge associated to the temporal component of the vector current $\bar{\psi}\gamma_\mu\psi$ and, thus, is conserved by applying the Noether theorem for a global U(1) symmetry. This conserved charge exists independent of the dimensionality of free fermions in $d+1$ spacetime dimensions, although the respective global symmetry groups of free fermions can differ significantly depending on d, see for example Appendix B.

As described above, the fermion density is expected to be fluctuating according to the statistical distribution. We introduce a fermion chemical potential μ to Eq. (2.9)

$$Z = \mathcal{N} \int \mathscr{D}\bar{\psi}\mathscr{D}\psi\mathscr{D}\vec{\phi}\, \mathrm{e}^{-\mathcal{S}[\bar{\psi},\psi,\vec{\phi}]+\int \mathrm{d}^{d+1}x\, \mu n} \tag{2.19}$$

in order to modify the probability distribution function to account for the fermion number density of a certain field configuration [293, 294]. The above modification is equivalent to modifying the statistical distribution $\sum_r \left(\mathrm{e}^{-\beta E_r}\right)$ in statistical physics to $\sum_r \left(\mathrm{e}^{-\beta(E_r-\mu N_r)}\right)$, where E_r and N_r are the energy and the particle number of the micro state r, respectively.

3 For $\bar{\psi} = \psi^\dagger\gamma_{d+1}$, it is convenient to use the opposite sign to the respective definition for ψ for the Fourier expansion.

As typical in the field, we redefine the action of the theory to include the chemical potential as $\mathcal{S} \to \mathcal{S} - \int \mathrm{d}^{d+1}x\, \mu n$ for the rest of this work and include the chemical potential a priori already in the action.

The expectation value of n can then be computed using the path integral formalism (2.10) which yields the simple relation from statistical physics

$$\langle n \rangle = \frac{1}{\beta V} \frac{\partial \ln Z}{\partial \mu}\bigg|_{T,V}, \tag{2.20}$$

where a finite, spatial volume V is artificially introduced in this definition.

2.1.4 *Finite volume, the thermodynamic limit and phase transitions*

In the context of statistical physics, the thermodynamic limit is taken by letting the volume of the system V go to infinity. In QFT, the situation is more subtle as the volume of the system is often infinite by construction. However, it may occur that the system is put in a finite volume V, e.g., in LFT simulations where periodic boundary conditions are enforced. Then, the momenta of the fields are quantized in each direction, $p_j = 2\pi n_j / L_j$ where L_j is the extent of the respective spatial direction similar to the situation encountered when working at a non-vanishing temperatures.

In this case, a phase transition cannot occur in a strict mathematical sense, where the transition is defined by a diverging correlation length. This is due to the fact that the ordering is already realized in the system when the correlation length approaches the scale set by the by the physical volume. Instead, one can approximate a, e.g., transition temperature by searching for maxima of susceptibilities of the order parameter. These maxima, in principle, approximate the correct behavior and one can estimate the behavior in the thermodynamic limit by finite size scaling of the respectively chosen observable. An extrapolation of this scaling can be used to extract the location of the phase transition in the thermodynamic limit. In Chapter 7 of this thesis, we encounter a situation in LFT simulations of a scalar $\mathrm{O}(N_s)$ field theory where details of the finite size scaling are non-trivial and one has to carefully extract results for the infinite-volume. The respective procedure is special to the investigation in Chapter 7 and is discussed therein.

The definition of certain objects in QFT require the introduction of a spatial volume, which will often implicitly be send to infinity.[4] However, in these cases one typically does not encounter the subtleties of performing the finite-size scaling in the thermodynamic limit as the volume is only introduced for simplification of the analytical computation.

2.2 GENERATING FUNCTIONALS AND CORRELATION FUNCTIONS IN THERMAL QUANTUM FIELD THEORY

The main purpose of this section is to define the generating functionals in the presence of external sources and the (connected) n-point correlation functions and vertex functions properly for QFT in thermal equilibrium. The essence of this objects, however, remains similar to the ones in standard vacuum QFT. Thus, the reader is referred to standard textbooks on QFT for a more detailed discussion of these objects [278, 279, 281, 295].

4 An example is the above definition of a fermion density or the definition of the effective potential of a QFT as the quantum effective action per space-time volume in the following sections. Sometimes the spatial volume will be kept finite in order to ease some computations, but the limit of infinite volume is always properly taken in the end.

2.2.1 *The generating functional of n-point correlation functions*

The partition function (2.19) can be promoted to the generating functional of the thermal QFT by introducing sources $\eta, \bar{\eta}, \vec{J}$ for the fields $\bar{\psi}, \psi, \vec{\phi}$, respectively. The generating functional of n-point correlation functions then reads (after including the fermion chemical potential already in the definition of the action)

$$Z[\bar{\eta}, \eta, \vec{J}] = \mathcal{N} \int \mathscr{D}\bar{\psi}\mathscr{D}\psi\mathscr{D}\vec{\phi}\, \mathrm{e}^{-\mathcal{S}[\bar{\psi},\psi,\vec{\phi}]+\int \mathrm{d}^{d+1}x \left(\eta\bar{\psi}+\bar{\eta}\psi+\vec{J}\cdot\vec{\phi}\right)}, \tag{2.21}$$

where the partition function $Z = Z[0, 0, 0]$. The generating functional $Z[e\bar{t}a, \eta, \vec{J}]$ allows to compute expectation values of any number of fields by taking the appropriate number of derivatives with respect to the sources $\eta, \bar{\eta}, \vec{J}$ and evaluating the result at $\eta = \bar{\eta} = \vec{J} = 0$. If an observable O can be written as an analytic function of the $\bar{\psi}, \psi, \vec{\phi}$, one can be reformulate the formula for its expectation value (2.10). Therefore, one just needs to take the appropriate number of derivatives of the generating functional (2.21) with respect to the sources and setting the sources to zero afterwards. For example, an n-point correlation function of bosonic fields $\phi_{j_1}, \ldots, \phi_{j_n}$, as it is often of interested in this thesis, is given by

$$\langle \phi_{j_1} \ldots \phi_{j_n} \rangle = \frac{1}{Z} \frac{\delta^n Z}{\delta J_{j_1} \ldots \delta J_{j_n}}\bigg|_{\eta,\bar{\eta},\vec{J}=0}. \tag{2.22}$$

Similar expressions can be derived for fermionic n-point correlations as well as for fermionic-bosonic correlations.

2.2.2 *The generating functional of connected n-point functions*

The n-point correlation functions contain the full information about the system. Although they can directly be computed from the generating functional (2.21) using LFT, they are often not the most convenient objects to work with in other approaches. A major reason for this is that the n-point correlation functions contain disconnected contributions, which are often not of interest. We will elaborate on this aspect in the following.

The generating functional for connected n-point correlation functions is defined as the logarithm of the generating functional (2.21),

$$W[\bar{\eta}, \eta, \vec{J}] = \ln Z[\bar{\eta}, \eta, \vec{J}]. \tag{2.23}$$

Again, connected n-point correlation functions can be computed by taking the appropriate number of derivatives with respect to the sources $\eta, \bar{\eta}, \vec{J}$ and evaluating the result at $\eta = \bar{\eta} = \vec{J} = 0$.

First, we compute the one-point function

$$\langle \phi_j \rangle_c = \frac{\delta W[\bar{\eta}, \eta, \vec{J}]}{\delta J_j}\bigg|_{\eta,\bar{\eta},\vec{J}=0} = \frac{1}{Z}\frac{\delta Z[\bar{\eta}, \eta, \vec{J}]}{\delta J_j}\bigg|_{\eta,\bar{\eta},\vec{J}=0} = \langle \phi_j \rangle, \tag{2.24}$$

i.e., the connected one-point function is equal to the one-point function derived from Eq. (2.21).

The difference to the generating functional (2.21) becomes evident when one is interested in the bosonic two-point correlation function

$$\langle \phi_j \phi_k \rangle_c = \frac{\delta^2 W}{\delta J_j \delta J_k}\bigg|_{\eta,\bar{\eta},\vec{J}=0} = \frac{1}{Z}\left[\frac{\delta^2 Z}{\delta J_j \delta J_k} - \frac{1}{Z}\frac{\delta Z}{\delta J_j}\frac{\delta Z}{\delta J_k}\right]\bigg|_{\eta,\bar{\eta},\vec{J}=0} = \langle \phi_j \phi_k \rangle - \langle \phi_j \rangle \langle \phi_k \rangle. \tag{2.25}$$

The quantity $\langle\phi_j\phi_k\rangle_c$ will be of interest at multiple points in this thesis for the classification of phase transition and, for brevity, will also be called the bosonic two-point correlation function. The connected two-point correlation function $\langle\phi_j\phi_k\rangle_c$ only contains information of the correlation between the fields ϕ_j and ϕ_k that is not already contained in the one-point functions $\langle\phi_j\rangle$ and $\langle\phi_k\rangle$. This removal of redundant information is a major advantage of using this formalism and also holds for higher n-point functions.

2.2.3 *The quantum effective action and one-particle-irreducible vertex functions*

While going from the generating functional (2.21) to the generating functional of connected correlation functions (2.23) removes redundant information in terms of disconnected contributions, it is often useful to further simplify the formalism by introducing the quantum effective action Γ. This quantum effective action is defined as the functional Legendre transform of the generating functional of connected correlation functions W with respect to the sources $\vec{J}$, i.e.,

$$\Gamma[\vec{\Phi},\bar{\Psi},\Psi] = \sup_{\vec{J},\eta,\bar{\eta}} \left\{ \int \mathrm{d}^{d+1}x \left(\vec{J}\cdot\vec{\Phi} + \bar{\eta}\bar{\Psi} + \eta\Psi \right) - W[\bar{\eta},\eta,\vec{J}] \right\}, \tag{2.26}$$

where

$$\Phi_j = \frac{\delta W}{\delta J_j}, \qquad \bar{\Psi} = \frac{\delta W}{\delta \eta}, \qquad \Psi = \frac{\delta W}{\delta \bar{\eta}}. \tag{2.27}$$

In the limit of vanishing sources, one consequently obtains

$$\Phi_j = \langle\phi_j\rangle, \qquad \bar{\Psi} = \langle\bar{\psi}\rangle, \qquad \Psi = \langle\psi\rangle. \tag{2.28}$$

As the quantum effective action is a functional of $\Phi_j, \bar{\Psi}$ and Ψ, it still has an implicit dependence on the external sources which in turn can be tuned to obtain certain values of $\Phi_j, \bar{\Psi}$ and Ψ. Thus, the quantum effective action Γ is a functional of the expectation values of the fields. It is a generating functional for the so-called one-particle-irreducible n-point vertex functions, abbreviated with n-point vertex functions in the following, and contains all information about the correlation functions of the theory. The quantum effective action incorporates the effect of quantum fluctuations and, thus, serves as a generalization of the classical action $\mathcal{S}$. An example for this analogue will be given in the following.

Taking derivatives with respect to the field expectation values, one finds the so-called one-point vertex functions

$$\frac{\delta\Gamma}{\delta\Phi_j} = J_j, \qquad \frac{\delta\Gamma}{\delta\bar{\Psi}} = \eta, \qquad \frac{\delta\Gamma}{\delta\Psi} = \bar{\eta} \tag{2.29}$$

directly from Eq. (2.26). In the absence of the artificially introduced sources, the one-point vertex functions are zero implying that the expectation values of the fields are stationary points of the quantum effective action. This is the quantum analogue of the principle of least action in classical mechanics.

Of particular interest in this work, is the bosonic two-point vertex function

$$\Gamma^{(2)}_{\phi_j,\phi_k} = \frac{\delta^2\Gamma}{\delta\Phi_j\delta\Phi_k}, \tag{2.30}$$

which is still a function of the expectation values of the fields $\vec{\Phi}, \bar{\Psi}, \Psi$. The relation to the bosonic two-point correlation function is obtained through

$$\delta_{jk} = \frac{\delta J_j}{\delta J_k} = \frac{\delta J_j}{\delta \Phi_l}\frac{\delta \Phi_l}{\delta J_k} \overset{\vec{J},\bar{\eta},\eta\to 0}{=} \Gamma^{(2)}_{\phi_l,\phi_j}\langle \phi_l \phi_k\rangle_c, \tag{2.31}$$

where in the last step we implicitly send the sources to zero such that the bosonic two-point correlation function could be identified. Thus, $\Gamma^{(2)}_{\phi_l,\phi_k} = \left(\langle \phi_l \phi_k\rangle_c\right)^{-1}$, i.e. the bosonic two-point vertex functions are the inverse of the bosonic two-point correlation functions. Similar relations can be derived for fermionic correlation and vertex functions[5].

2.3 FOUR-FERMION AND YUKAWA MODELS

By now, we established the general setup to study QFTs in a thermal equilibrium, i.e., at non-vanishing temperature and fermion density. However, the rest of this thesis is restricted to the scalar $O(N)$ model (with only bosonic fields), fermionic models with four-fermion interaction terms and Yukawa-type models with both bosonic and fermionic fields. Since multiple chapters of this thesis study four-fermion models, we introduce some basic concepts for these models and important relations to Yukawa-type models.

Hence, we define a generic four-fermion model with the action

$$\mathcal{S}_{\mathrm{FF}}[\bar{\psi},\psi] = \int_0^\beta \mathrm{d}\tau \int \mathrm{d}^d x \left[\bar{\psi}\left(\partial\!\!\!/ + \gamma_{d+1}\mu\right)\psi - \sum_j \frac{\lambda_j}{2N_f}\left(\bar{\psi}\, c_j\, \psi\right)^2\right] \tag{2.32}$$

and partition function

$$Z_{\mathrm{FF}} = \mathcal{N}\int \mathscr{D}\bar{\psi}\mathscr{D}\psi \mathrm{e}^{-\mathcal{S}_{\mathrm{FF}}[\bar{\psi},\psi]}. \tag{2.33}$$

in $d+1$ Euclidean space-time dimensions. The fermion fields $\bar{\psi}, \psi$ describe N_f spinors and the number of respective spinor components is given by the dimension of the Clifford algebra in the respective $d+1$ dimensions.[6] For the purpose of this discussion, the vertices c_j represent matrices in spin space. Later in this work we will study more degrees of freedom for the fermions and the dimensionality of the c_j is then adjusted accordingly.

2.3.1 *Hubbard-Stratonovich transformation*

In order to analytically evaluate the path integral (2.33), one would like to obtain a form of the action that is bilinear in the fermionic fields, i.e. has a form of $\bar{\psi}\mathrm{Q}\psi$ with the so-called Dirac operator Q. Then, one can apply the formula

$$\int \mathscr{D}\bar{\psi}\mathscr{D}\psi \mathrm{e}^{-\int \mathrm{d}^{d+1}x \int \mathrm{d}^{d+1}y \bar{\psi}(x)\mathrm{Q}(x,y)\psi(y)} = \alpha \det \mathrm{Q}(x,y), \tag{2.34}$$

where α is a real normalization parameter, $\int \mathrm{d}^{d+1}x = \int_0^\beta \mathrm{d}\tau \int \mathrm{d}^d x$ and the determinant is understood as a functional determinant over spacetime as well as a matrix determinant over

5 The strategy is rather similar to the above discussion, although one has to be more cautious in the derivations due to the Grassmann nature of the spinors and sources.

6 In the irreducible representation, spinors are two-component objects for $d = 1, 2$ and four-component objects for $d = 3$. However, for the rest of this thesis we consider the reducible, four-component spinor representation for $d = 2$ allowing us to define chiral symmetry in $d = 2$ spatial dimensions, see Appendix A.4 and Appendix A.3 for a discussion of the spinor representation in this work.

the spinor indices. This formula can be derived using the eigenvalue decomposition of the operator Q as well as rewriting the measure $\mathscr{D}\bar{\psi}\mathscr{D}\psi$ as well as the exponent on a discretized spacetime lattice, i.e., into the form of Eq. (2.3), see the discussion from Eqs. (5.23, 5.24) to Eq. (5.43) for scalar fields as well as Eqs. (5.116-5.122) for Grassmann-valued fields in Ref. [281]. An example for the computation of such a matrix determinant can be found in Appendix C.

In order to cast Eq. (2.33) into a fermion bilinear of the form $\bar{\psi}\mathrm{Q}\psi$, a Hubbard-Stratonovich transformation [296, 297] is applied. The transformation can be performed using a Gaussian integral in field space of the form of

$$\mathcal{A} = \int \mathscr{D}\phi\, \mathrm{e}^{-\int \mathrm{d}^{d+1}x \frac{N_f}{2\lambda}\left(\phi + \frac{\lambda}{N_f}\bar{\psi}c\psi\right)^2} = \int \mathscr{D}\phi\, \mathrm{e}^{-\int \mathrm{d}^{d+1}x\left(\frac{N_f}{2\lambda}\phi^2 + \bar{\psi}c\psi\phi\right)} \mathrm{e}^{-\int \mathrm{d}^{d+1}x \frac{\lambda}{2N_f}(\bar{\psi}\, c_j\, \psi)^2}, \tag{2.35}$$

where we omitted the index j for simplicity, the integration measure $\mathscr{D}\phi$ is defined analogous to $\mathscr{D}\bar{\psi}\mathscr{D}\psi$ and $\mathcal{A}$ is a real-valued constant. Inserting this identity iteratively for each of the four-fermion interaction terms in Eq. (2.33) (replacing $\phi \to \phi_j$, $c \to c_j$ et cetera)[7], only changes the partition function by a multiplicative constant (which is without relevance for the computation of observables, compare Eq. (2.10)). Then, the latter exponential factor in Eq. (2.35) cancels the respective four-fermion interaction at the price of introducing two additional terms per four-fermion interaction term. The resulting partition function with auxiliary fields $\vec{\phi}$ reads

$$Z = \mathcal{N}' \int \mathscr{D}\bar{\psi}\mathscr{D}\psi \prod_j \mathscr{D}\phi_j\, \mathrm{e}^{-\mathcal{S}[\bar{\psi},\psi,\vec{\phi}]} \tag{2.36}$$

with the partially bosonized action

$$\mathcal{S}[\bar{\psi},\psi,\vec{\phi}] = \int_0^\beta \mathrm{d}\tau \int \mathrm{d}^d x \left[N_f \sum_j \frac{\phi_j^2}{2\lambda_j} - \bar{\psi}\left(\not{\partial} + \gamma_{d+1}\mu + \sum_j c_j\phi_j\right)\psi\right], \tag{2.37}$$

where $Z \sim Z_{FF}$ and $\mathcal{N}'$ is an arbitrary normalization factor. As one can see, we have hereby exchanged the four-fermion interaction for a Yukawa-type interaction term. Thus, instead of a four-point fermion vertex, a fermion-boson interaction vertex is produced such that fermions interact by the exchange of an auxiliary bosonic field.

EFFECTIVE ACTION Then, one can perform the integration over $\bar{\psi}, \psi$ as described above and obtain the effective theory

$$Z_{\mathrm{Bos}} = \mathcal{N}' \int \prod_j \mathscr{D}\phi_j \mathrm{e}^{-\mathcal{S}_{\mathrm{eff}}[\vec{\phi}]} \tag{2.38}$$

with the so-called effective action

$$\mathcal{S}_{\mathrm{eff}}[\vec{\phi}] = N_f \left(\int \mathrm{d}^{d+1}x \sum_j \frac{\phi_j^2}{2\lambda_j} - \ln \mathrm{Det}\left[\beta\left(\not{\partial} + \gamma_{d+1}\mu + \sum_j c_j\phi_j(\boldsymbol{x})\right)\right]\right). \tag{2.39}$$

Note that the factor of β was introduced to the determinant after integrating out the fermionic fields in order to make the argument of the determinant dimensionless. Thus,

7 If $\bar{\psi}c_j\psi$ has certain non-trivial quantum numbers, one has to introduce a bosonic field that has a similar mathematical structure. For example, if $c_j = \gamma_\nu$ the corresponding bilinear is a vector under (Euclidean) Lorentz transformations and one needs to introduce a vector field in the Hubbard Stratonovich transformation.

Z_{bos} was changed by a multiplicative, temperature-dependent constant factor compared to Eq. (2.36). Moreover, in comparison to Eq. (2.35) one has to note that the Dirac operator is proportional to a Dirac delta in position space. This Dirac delta is omitted in Eq. (2.39) and is implied in the usage of one specific field dependence. One has to keep this in mind when evaluating the functional determinant of the operator for a concrete action.

2.3.2 *Ward identities for the auxiliary bosonic fields*

In QFT, there exist so-called Ward-Takahashi identities (also known as Ward identities) which relate expectation values of different n-point functions to each other and are derived by global or gauge symmetries of the theory. Thus, they are the QFT analogue of classical conservation laws as can be shown using Noether's theorem. The most famous, original Ward-Takahashi identity of quantum electrodynamics relates the electron propagator to the electron-photon vertex leading to the renormalization of the electron charge and canceling the ultra-violet (UV) divergences of theory via the gauge invariance of the theory [298, 299]. In our case, the Ward identities are derived from invariance of the theory under infinitesimal, chiral transformations.[8]

By demanding the invariance of the partition function (2.36) under infinitesimal transformations

$$\phi_j(x) \to \phi_j(x) + \delta\phi_j(x) \tag{2.40}$$

one can derive Ward identities for the expectation values of the auxiliary fields. Inserting this transformation into Eq. (2.36) and assuming invariance of the measure[9] $\mathscr{D}\phi_j$, one obtains

$$\begin{aligned} Z' &= \mathcal{N}' \int \mathscr{D}\bar{\psi}\mathscr{D}\psi \prod_j \mathscr{D}\phi_j \, \mathrm{e}^{-\mathcal{S}[\bar{\psi},\psi,\vec{\phi}+\delta\vec{\phi}]} = \\ &= \mathcal{N}' \int \mathscr{D}\bar{\psi}\mathscr{D}\psi \prod_j \mathscr{D}\phi_j \, \mathrm{e}^{-\mathcal{S}[\bar{\psi},\psi,\vec{\phi}]} \left[1 - \int \mathrm{d}^{d+1}x \sum_k \delta\phi_k(x) \left(\bar{\psi}c_k\psi + N_f \frac{\phi_k}{\lambda_k}\right) + \mathcal{O}\left(\delta\phi^2\right)\right]. \end{aligned} \tag{2.41}$$

Since the transformation $\delta\phi_j(x)$ can be arbitrary, one may choose $\delta\phi_j = \epsilon\phi_j\delta^{(d+1)}(x-z)$ ($\delta^{(d+1)}$ is the $d+1$-dimensional Dirac delta). Demanding $Z' = Z$ implies that the second summand in the square brackets vanishes. Inserting the ansatz for $\delta\phi_j(x)$ into Eq. (2.41) one obtains

$$0 = \mathcal{N}' \int \mathscr{D}\bar{\psi}\mathscr{D}\psi \prod_j \mathscr{D}\phi_j \, \epsilon \left[\bar{\psi}(z)c_k\bar{\psi}(z) + \frac{N_f}{\lambda_k}\phi_k(z)\right] \tag{2.42}$$

and, as ϵ is arbitrary, one concludes after multiplication with $1/Z$

$$\langle\phi_j\rangle = -\frac{\lambda_j}{N_f}\langle\bar{\psi}c_j\psi\rangle. \tag{2.43}$$

Thus, one can directly access the expectation value of fermionic bilinears, such as, e.g., the chiral condensate, by computing the bosonic one-point functions, i.e., the expectation

8 Since we do not deal with a specific theory at this point, the discussion is kept rather generic and transformations are defined on the level of the auxiliary bosonic fields. Thus, it depends on the specific theory whether a certain transformation is chiral in the end. Note that many chiral transformations of fermions correspond to rotations of fermion bilinears and the corresponding auxiliary bosonic fields ϕ_j.

9 The invariance of this measure can only strictly be derived before taking the continuum limit in Eq. (2.3). As common in QFT, we, however, assume that the continuum limit in Eq. (2.3) and Eq. (2.9) can be taken without any complications.

value of the bosonic fields. As the expectation value of bosonic fields are typically easier to compute than fermionic ones, this relation is a powerful tool to study four-fermion models. For example, in a lattice field theory simulations computation of the expectation value of $\bar{\psi}\psi$ would involve measuring the trace over the inverse of the Dirac operator. In contrast, the bosonic field can directly be measured when simulating the partition function (2.38).

Similar relations for two-point functions can be obtained in a similar way demanding invariance of expectation values of one-point functions under Eq. (2.40), instead of the partition function. Application of Eq. (2.40) to the expectation value of the bosonic fields gives

$$\begin{aligned}\langle\phi_j(y)\rangle \to & \mathcal{N}' \int \mathscr{D}\bar{\psi}\mathscr{D}\psi \prod_k \mathscr{D}\phi_k \left(\phi_j(y) + \delta\phi_j(y)\right) \mathrm{e}^{-\mathcal{S}[\bar{\psi},\psi,\vec{\phi}+\delta\vec{\phi}]} = \\ &= \langle\phi_j(y)\rangle - \mathcal{N}' \int \mathscr{D}\bar{\psi}\mathscr{D}\psi \prod_k \mathscr{D}\phi_k \int \mathrm{d}^{d+1}x \sum_l \delta\phi_l(x) \mathrm{e}^{-\mathcal{S}[\bar{\psi},\psi,\vec{\phi}]} \times \\ &\quad \times \left[\delta_{l,j}\, \delta^{(d+1)}(x-y) - \phi_j(y) \left(\bar{\psi}(x) c_l \psi(x) + \frac{N_f \phi_l(x)}{\lambda_l}\right)\right] + \mathcal{O}\left(\delta\phi^2\right).\end{aligned} \tag{2.44}$$

Using again the ansatz $\delta\phi_j(x) = \epsilon\delta^{(d+1)}(x-z)$ this implies the identity

$$\langle\bar{\psi}(z) c_l \psi(z) \phi_j(y)\rangle = -\frac{N_f}{\lambda_l}\langle\phi_j(y)\phi_l(z)\rangle + \delta_{l,j}\, \delta^{(d+1)}(y-z). \tag{2.45}$$

Repeating this procedure for the expectation value of the fermion bilinear $\bar{\psi} c_j \psi$ one obtains an expression for the fermionic four-point function

$$\langle\bar{\psi}(y) c_j \psi(y) \bar{\psi}(z) c_k \psi(z)\rangle = -\frac{N_f}{\lambda_k}\langle\bar{\psi}(y) c_j \psi(y) \phi_k(z)\rangle. \tag{2.46}$$

Combining Eq. (2.45) and Eq. (2.46) one finds

$$\langle\phi_j(y)\phi_k(x)\rangle = \frac{\lambda_j}{N_f}\delta_{jk}\delta(x-y) + \frac{\lambda_j\lambda_k}{N_f^2}\langle\bar{\psi}(y) c_j \psi(y)\, \bar{\psi}(x) c_k \psi(x)\rangle, \tag{2.47}$$

which relates the bosonic two-point correlation functions of the auxiliary bosonic fields to the respective four-point function of the fermion fields.

These Ward identities demonstrate that the partially bosonized partition function (2.36) contains similar information as the original partition function (2.33) with the four-fermion action. Moreover, we explicitly showed that the four-fermion interaction vertex really got replaced by the Yukawa-type interaction between fermion fields and bosonic fields. The above outlined procedure can be performed iteratively to study higher order correlation functions.

2.3.3 *Yukawa models as a generalization of four-fermion models*

In Chapter 5, we are going to study Yukawa-type models where the auxiliary bosonic fields are promoted to dynamical fields by introducing a kinetic term as well as self-interaction terms. Thereby, we restrict ourselves to models that contain local interactions between fermions and the dynamical bosonic fields, i.e., the interaction between fermion fields is modeled through meson exchange, where the mesons themselves can locally self-interact.

Then the action of the resulting Yukawa model can directly be defined using the effective action of the corresponding four-fermion model (2.39), i.e.,

$$\mathcal{S}_{\text{eff,Y}}[\vec{\chi}] = \mathcal{S}_{\text{eff}}[h\vec{\chi}] + \int_0^\beta \mathrm{d}\tau \int \mathrm{d}^d x \left[\frac{1}{2} \left(\partial_\nu \vec{\chi}(\boldsymbol{x})\right)^2 + \sum_{n>1} \kappa_n \left(\sum_j \chi_j^2(\boldsymbol{x}) \right)^n \right], \tag{2.48}$$

where $\vec{\chi}$ contains scalar fields of canonical dimension energy$^{(d+1-2)/2}$, h is the Yukawa coupling of dimension energy$^{(3-d)/2}$, κ_n are the couplings of the self-interaction terms and the sum over n runs over all integers $n > 1$. The corresponding partition function then simply reads

$$Z_{\text{Y}} \sim \int \mathscr{D}\vec{\chi} \mathrm{e}^{-\mathcal{S}_{\text{eff,Y}}[\vec{\chi}]}. \tag{2.49}$$

Due to the additional terms in Eq. (2.48) the Ward identities derived in Section 2.3.2 are not valid for the Yukawa models. Additional contributions from the kinetic terms and self-interactions are contained in the Ward identities. Since the Ward identities for the Yukawa models are not needed throughout this thesis, we do not compute these additional contributions in this section.

2.4 MEAN-FIELD APPROXIMATION AND THE LARGE-N_f LIMIT

Although large parts of this work deals with strongly-interacting four-fermion models at non-vanishing densities instead of fully-fletched QCD, there still exist no direct way to compute the partition function (2.33) or, equivalently, the partition function about the effective action (2.38) in an exact way. A common first approximation for a partition function of a strongly-interacting theory is to use a mean-field approximation. The term mean-field approximation might have different meanings in the literature depending on the respective research field. In the present case, we define the mean-field approximation as the suppression of the quantum fluctuations in the bosonic path integral in Eq. (2.38). Thus, it is a semi-classical approximation where the bosonic fields are treated classically using a variational approach, while the fermionic quantum fluctuations are fully taken into account by integrating them out. Thus, only the global minimum with respect to the bosonic fields $\vec{\phi}$ is taken into account and the partition function is approximated as

$$Z_{\text{bos}} \approx Z_{\text{MF}} = \min_{\vec{\phi}} \mathrm{e}^{-\mathcal{S}_{\text{eff}}[\vec{\phi}]}. \tag{2.50}$$

As a consequence, expectation values of observables can be computed by averaging them over the global minima of the effective action. This can be, in theory, problematic whenever degenerate global minima of the action can be related through a symmetry transformation, which is sponteanously broken by each of these field configurations individually. Often, cancellations occur such that the expectation value does not signal the spontaneous breaking of a symmetry. In the mean-field approximation, it is common and practical to restrict the space of solution such that a degeneracy generated by symmetry transformations cannot occur, i.e., one in practice picks only one of the degenerate minima, cf. Refs. [93, 137, 141, 195, 197, 300].

Terms that are often interchangeably used with the mean-field approximation are the $1/N$-expansion (including the large-N limit), method of steepest descent or the saddle-point approximation. While the relation to the $1/N$-expansion is discussed below, the method of steepest descent or saddle-point method is a general technique to approximate

integrals by evaluating the integrand on contours that go through a saddle point of the integrand. The term saddle-point approximation is a specific example of the method of steepest descent used in statistics where the method of steepest descent is applied to a probability distribution function [301]. In the context of this work, the mean-field approximation amounts to a saddle-point approximation of the partition function (2.38).

Note that we assumed above that there is only one global minimum in the effective action which is not necessarily true, especially in the presence of first-order phase transitions. Moreover, there might be multiple minima that are degenerate but connected through symmetry transformations. Within the mean-field approximation, one typically expresses the effective action as a functional of an invariant order parameter[10] and then minimizes the effective action with respect to this order parameter. In the full QFT, i.e. when evaluating the partition function (2.33) without an approximation using lattice field theory, one typically introduces a small external symmetry breaking parameter which is then continuously removed in the continuum and infinite-volume limit in order to study the spontaneous breaking of the symmetry. In the mean-field approximation, this procedure simply amounts to choosing a specific minimum of the effective action. A simple example for this would be choosing $\phi_j = \delta_{j,0}\sigma$ after minimization with respect to $m = \sqrt{\sum_j \phi_j^2}$, which is typically possible if m is an order parameter for symmetry breaking in the effective action.

2.4.1 *The $1/N$ expansion and the large-N_f limit*

The $1/N$ expansion is a powerful tool to study strongly-interacting theories. Thereby, N describes the number of different kinds of interacting degrees of freedom that are essential ingredient of the respective theory, e.g., the number of colors in QCD or the number of fermion species in a four-fermion model. For an introduction to the $1/N$ expansion, we refer to Ref. [302].

In order for a $1/N$ expansion to be valid, one typically assumes that $1 \ll N$. However, the method has been unexpectedly successful in systems where N is rather small, e.g., in the strong coupling regime. This is caused by the strictly non-perturbative nature of the $1/N$ expansion which is not limited by the convergence radius of the perturbative series in a dimensionless small coupling constant. For example, already the leading order of the $1/N$ expansion can take into account arbitrary high powers of the coupling constant.

In the context of this work, the $1/N$-expansion is particularly important for two use cases. First of all, taking the large-N_f limit of Eq. (2.33), i.e., taking $N_f \to \infty$, amounts to the mean-field approximation of the partition function (2.33). This is most obvious after bosonization when inspecting the partition function over the effective action (2.38). The effective action (2.39) is proportional to N_f such that the partition function is dominated by the global minimum of the effective action in the limit of $N_f \to \infty$. Thus, the leading order $O(N_f^0)$ of the $1/N_f$-expansion amount precisely to the mean-field approximation of the four-fermion model. This is not the necessarily the case for the other models with additional, internal degrees of freedom and one carefully has to examine the impact of taking the limit of infinite number of fermion flavors for the respective theory. For example, in Chapter 7 we study an $O(N_s)$ model of scalar fields using lattice field theory. Thereby, we compare our findings to analytical work in the large-N_s limit of the used $O(N_s)$ model. One finds that the large-N_s limit of scalar $\mathrm{O}(N_s)$ model *does not* correspond to a mean-field approximation, see Section 2.5.

10 With respect to chiral symmetry, this order parameter is typically be the 2-norm of the field vector $\vec{\phi}$.

2.4.2 *Alternative derivation of the mean-field approximation*

An alternative motivation of the mean-field approximation starts from the originally purely fermionic action (2.33). First, one defines the expectation values

$$\langle \bar{\psi} c_j \psi \rangle = \alpha_j, \tag{2.51}$$

and expands the fermion bilinears appearing in the action around these mean-field values $\bar{\psi} c_j \psi = \alpha_j + \Delta\alpha_j$.[11] By neglecting the contributions quadratic in $\Delta\alpha_j$ one obtains the partially bosonized action (2.37) by appropriately relating α_j to ϕ_j. Note that in this procedure one does not integrate over α_j in the partition function from the beginning. Hence, one can directly perform the integration over the fermionic fields and obtain the effective action Eq. (2.39). One then just determines the values of the mean-fields φ_j classically by minimizing the effective action with respect to φ_j, as described above in order to obtain the mean-field approximation. Note that in this subsection we enforced the Ward identities from the beginning by defining the φ_j fields accordingly instead of deriving them as in the Hubbard-Stratonovich transformation, see Section 2.3.1.

This argumentation is based on the drastic assumption that the fluctuations about the classical mean-fields are small. In contrast, the large-N_f limit provides a systematic way to justify and improve upon the mean-field approximation. Note that $1/N_f$-expansion techniques are equivalent to a mean-field approximation specifically in the case of the four-fermion models. In general, this is not necessarily true and one has to carefully perform the $1/N$ expansion.

2.4.3 *Validity of the mean-field approximation*

One might argue that the classical treatment of the bosonic fields, i.e., the complete suppression of the bosonic fluctuations, is a severe simplification of the full QFT. However, it typically allows a first study of the phase structure of theory and, to a certain extent, the computation of observables. Thus, it serves as an appropriate starting point for further investigations that go beyond this approximation. Specifically for the study of phase diagram, the bosonic quantum fluctuations are expected to weaken ordering as present in the HBP where a chiral condensate is formed or the IP where the condensate exhibits a periodic structure. The mean-field approximation can provide first insights about the possible existence of those phases and the phase transitions between them with significantly reduced computational effort compared to functional methods or lattice simulations.

2.4.4 *The homogeneous effective potential and its relation to the mean-field quantum effective action*

In four-fermion and Yukawa models, as introduced in Section 2.3, it is useful to define the homogeneous effective potential $\bar{U}$. The effective potential, in general, is defined as the quantum effective action Γ, see Section 2.2.3 for its definition, per spacetime volume βV, where V is the (typically infinite) spatial volume of the system, and (in the present

11 This replacement is only valid for a generic four-fermion model of the type of Eq. (2.32). For a Yukawa model, one would have to expand the bosonic fields χ_j around their expectation values.

case) per fermion flavor N_f. One can identify after performing a one-loop expansion of the quantum effective action

$$\Gamma[\vec{\phi}] = \mathcal{S}_{\text{eff}}[\vec{\phi}], \tag{2.52}$$

which is exact only in the mean-field approximation. Note this non-trivial result cannot be obtained directly by inserting Z_{MF} into Eq. (2.26) directly, because non-vanishing source terms are present in the definition of $W[\bar{\eta}, \eta, \vec{J}] = \ln Z[\bar{\eta}, \eta, \vec{J}]$ and the fermion fields are not integrated out.

The minimum of Γ in the limit of vanishing external sources is given by $\vec{\Phi}(\boldsymbol{x})$, which is the global minimum of the $\mathcal{S}_{\text{eff}}$ or also called the *ground state* in this thesis. Of course, this assumes that this minimum is unique, which in the presence of internal symmetry transformation formally would have to be ensured via an explicit symmetry breaking term. However, within the mean-field approximation this can be ensured by defining an invariant under the internal symmetry as the parameter to minimize and expressing observables as functions of this invariant order parameter, see also the discussion in the first paragraphs of Section 2.4.

As implied by the name, the homogeneous effective is defined when restricting the expectation values of the $\vec{\phi}$ to be homogeneous, i.e. $\vec{\phi}(x) = \vec{\bar{\phi}}$,

$$\bar{U}(\vec{\bar{\phi}}, \mu, T) = \frac{T}{N_f V} \mathcal{S}_{\text{eff}}[\vec{\bar{\phi}}], \tag{2.53}$$

i.e., it is a function of the variables $\vec{\bar{\phi}}_j$, which are constant in space and time. Note that we additionally also normalize against the number of fermion fields N_f. Under this assumption, the grand potential of the statistical system $\Omega(\mu, T) = -p/N_f$ can be defined as $\Omega(\mu, T) = -(\bar{U}(\vec{\bar{\Phi}}(\mu, T), \mu, T) - \bar{U}(\vec{\bar{\Phi}}(0, 0), 0, 0))$.[12] Throughout this thesis, $\vec{\bar{\Phi}}$ is called the *homogeneous global minimum* or *homogeneous ground state*, i.e., the global mimimum of $\mathcal{S}_{\text{eff}}$ under the restriction $\vec{\phi}(x) = \vec{\bar{\phi}}$. The effective action in the models in this work is of the form of

$$\mathcal{S}_{\text{eff}}[\vec{\bar{\phi}}] = N_f \left(f(\vec{\bar{\phi}}) - \ln \operatorname{Det} \left[\beta \left(\partial\!\!\!/ + \gamma_{d+1} \mu + \sum_j c_j \bar{\phi}_j \right) \right] \right), \tag{2.54}$$

where $f(\vec{\bar{\phi}})$ is a function of the homogeneous fields (typically containing self-interaction terms and / or kinetic terms, see Eq. (2.39) or Eq. (2.48)).

COMPUTATION OF THE FERMION DETERMINANT The fermionic determinant can be computed using the eigenvalue decomposition of the Dirac operator. In the continuum theory, this evaluation is straightforward after Fourier transforming the fermionic and bosonic fields (see Eq. (2.13) for the conventions for Fourier transforms) such that the derivative operator $\partial\!\!\!/$ is replaced by $\mathrm{i}p\!\!\!/\,\delta^{(d+1)}(p-q)$ where p and q are four-momenta whose zero components are given by Matsubara frequencies (2.15). The Dirac operator is, consequently, diagonal in the Fourier space as also $\bar{\phi}_j$ gets replaced by $\tilde{\phi}_j(p-q) = \beta\,(2\pi)^d\,\delta^{(d+1)}(p-q)\bar{\phi}_j$ for homogeneous fields. Thus, it remains to diagonalize the Dirac structure of the operator. Typically, this is possible as the four-fermion models are invariant under certain symmetry operations, e.g., chiral symmetry, which allows to rotate certain

12 The grand potential in turn is generally defined as the difference of the quantum effective action at fixed μ and T and the quantum effective action in the vacuum, evaluated at its minimum.

ϕ_j to zero. Then, depending on the interaction vertices c_j, the dimensionality of space-time $d+1$ and the dimensionality of the Dirac algebra one can determine the eigenvalues $\lambda_\alpha(p,\vec{\phi})$ of the Dirac operator such that the ln Det expression in Eq. (2.54) becomes

$$\ln\left[\prod_p\prod_q\prod_\alpha \delta^{(d+1)}(p-q)\lambda_\alpha(p,\vec{\phi})\right]^{N_f} = N_f T\sum_n\int\frac{\mathrm{d}^d p}{(2\pi)^d}\sum_\alpha \ln\left[\lambda_\alpha(p,\vec{\phi})\right], \tag{2.55}$$

where α runs over the fermionic degrees of freedom and we used that the temporal direction is discretized at finite temperature. Also, we used that the N_f fermion species are decoupled in the determinant. This expression is often further simplified as $\vec{\phi}$ can be rotated through symmetry transformations such that it typically only appears as a mass squared term m^2 in λ_α. Then, one can express the ln Det-term in $\mathcal{S}_{\text{eff}}$ as an integral over the d-dimensional spatial momentum space through standard techniques used to compute the pressure of a free-fermi gas, see Chapter 2.5 of Ref. [64] or Chapter 3.7 of Ref. [285] for details. Consequently, one finds (up to an irrelevant temperature-dependent constant)

$$\begin{aligned}\frac{1}{\beta V}\ln\mathrm{Det}\left[\beta\left(\not{\partial}+\gamma_{d+1}\mu+\sum_j c_j\phi_j\right)\right] = \\ = \tfrac{d_\gamma}{2}\int\tfrac{d^d p}{(2\pi)^d}\left[E_{\boldsymbol{p}}+T\ln\left(1+\mathrm{e}^{-(E_{\boldsymbol{p}}-\mu)/T}\right)+\mu\to-\mu\right]\end{aligned} \tag{2.56}$$

where d_γ represents the number of components of a spinor (see Appendix A.3 for the representations used in this thesis), V is the infinite spatial volume and the energy $E_{\boldsymbol{p}} = \sqrt{\boldsymbol{p}^2+m^2}$. Therein, m^2 is a function of $\vec{\phi}$ and, often, is given by the 2-norm of $\vec{\phi}$ in field space. Note that the vacuum integrand $\sim E_{\boldsymbol{p}}$ yields a divergent contribution, which requires regularization and an appropriate renormalization prescription to remove the divergences. The degree of the divergence depends on the space dimensionality d. An explicit computation of Eq. (2.56) can be found in Appendix C. See the standard textbooks on thermal field theory [64, 282] or Ref. [285] for further reference.

CORRELATION AND VERTEX FUNCTIONS As we already discussed the computation of the generating functional as well as the quantum effective action in the mean-field approximation, we want to briefly comment on the fate of correlation and vertex functions in this approximation.

Determining values of n-point correlation functions when applying the mean-field approximation $Z\approx Z_{\text{MF}}$ can be done in the following way. One needs to compute the expectation value of the respective operator $O(\bar{\psi},\psi,\vec{\phi})$ neglecting the bosonic quantum fluctuations. This can, in general, still be complicated when the operator O contains either $\bar{\psi}$ or ψ. However, as demonstrated in Section 2.3.2, one can relate any fermionic n-point function to purely bosonic expectation values in the case of the four-fermion and Yukawa models in this thesis. Thus, it is sufficient to determine all bosonic n-point correlation functions in order to extract all information of the theory in the mean-field approximation. For bosonic observables one simply finds

$$\langle O(\vec{\phi})\rangle = O(\vec{\Phi}),\quad \text{with}\quad \vec{\Phi}=\arg\min_{\vec{\phi}}\mathcal{S}_{\text{eff}}[\vec{\phi}], \tag{2.57}$$

where $\mathcal{S}_{\text{eff}}$ is the effective action of the theory as outlined in Section 2.3.1 and the minima of the effective action are the expectation values of the respective bosonic fields in the mean

field approximation, as previously discussed. Due to this simple relation, we omit using brackets and simply insert $\vec{\Phi}$ to indicate that we refer to the respective expectation values of fields and observables.

In general, one still has to be careful when studying correlations such as $\langle\phi_j\phi_k\rangle$ in the large-N_f limit, since the definition of bosonic fields includes factors of N_f, compare Eq. (2.35) and Eq. (2.43), which one has to take into account in the power counting when taking $N_f \to \infty$.

The most direct approach to extract relevant observables from the theory is using the quantum effective action, which can be accessed through the effective action in the mean-field approximation according to Eq. (2.52). From this equation, it becomes obvious why $\mathcal{S}_{\text{eff}}$ is called the effective action. The n-point vertex functions are computed via derivatives of the quantum effective action with respect to $\vec{\phi}$ and also contain the full information from the QFT. They can directly be related to the correlation functions of the theory, see Section 2.2.3. Throughout this work, we will compute bosonic two-point vertex function$\Gamma^{(2)}_{j,k}$ in four-fermion and Yukawa models multiple times as a tool to study the phase structure of the respective models with respect to an IP and/or the QπLs. Thus, the entire Chapter 4 with the derivation of $\Gamma^{(2)}_{j,k}$ for homogeneous background $\phi = \bar{\phi}$ and benchmark results is dedicated to the computation of this object.

2.5 LARGE-N_s LIMIT OF SCALAR O(N_s) MODELS

The following discussion is mostly based on the review [302]. For this presentation we define an O(N_s) symmetric Euclidean action

$$\mathcal{S}[\vec{\phi}] = \int \mathrm{d}^d x \left[\frac{1}{2}\left(\partial_\mu \vec{\phi}\right)^2 + + \frac{m^2}{2}\vec{\phi}^2 + \frac{\lambda}{4}(\vec{\phi}^2)^2\right] \tag{2.58}$$

in d spatial dimensions, where $\vec{\phi} = (\phi_1, \ldots, \phi_{N_s})$ is an N_s-component scalar field. Further, m^2 and λ are undetermined bare couplings of the theory. The below discussion is valid for all potentials $V[\vec{\phi}^2]$ that are general polynomials of $\vec{\phi}^2$. The omission of the temporal direction in this section might seem counter-intuitive, but is sensible for the application of this section to Chapter 7. The main statements of this analysis are unaffected by the choice of spacetime dimensions, and we hope that the reader can overlook this inconsistency in the presentation.

MEAN-FIELD APPROXIMATION AS CLASSICAL FIELD THEORY The mean-field approximation, as defined in this thesis, amounts to the complete suppression of bosonic quantum fluctuations. Since the partition function of the above action is

$$Z = \int \prod_{j=1}^{N_s} \mathscr{D}\phi_j \, \mathrm{e}^{-\mathcal{S}[\vec{\phi}]}, \tag{2.59}$$

this approximation amounts to finding the global minimum of $\mathcal{S}$ with respect to $\vec{\phi}$. This minimum is given by the field equations in the Lagrange formalism from classical field theory, see, e.g., Ref. [303]. Thus, the mean-field approximation in terms of scalar field theory amounts to studying classical field theory. The fields $\vec{\phi}$ can be determined by solving the resulting partial differential equations and other observables can be computed by calculating them on the respective global minima of $\mathcal{S}[\vec{\phi}]$.

2.5.1 *Constraint field approach*

The large-N_s limit serves as a tool to include quantum fluctuations in a saddle-point approximation, i.e., to go beyond the classical field theory. Thus, it is *not equivalent* to the mean-field approximation of the scalar field theory in contrast to the large-N_f limit of four-fermion models discussed in Section 2.4. To include quantum fluctuations in analytical computations, a so-called constraint field approach is used. The basic idea is that O(N_s)-invariant quantities self-average for large N_s such that fluctuations are still small. This idea is related to the central limit theorem and also relies on the assumption that the individual components of ϕ_j do not have strong correlations. Anyhow, these small fluctuations suggest that the theory can simplified by studying $\vec{\phi}^2 \sim N_s$ as a dynamical variable for large N_s. Therefore, for each point in space $\boldsymbol{x}_j$, we introduce the identity

$$1 = \int \mathrm{d}\omega_j \, \delta(\omega_j - \vec{\phi}^2(\mathbf{x}_j)) = \frac{1}{4\pi} \int \mathrm{d}\omega_j \mathrm{d}\epsilon_j \, \mathrm{e}^{\mathrm{i}\epsilon_j(\omega_j - \vec{\phi}^2(\mathbf{x}_j))/2} \tag{2.60}$$

with auxiliary fields $w(\boldsymbol{x})$ and $\epsilon(\boldsymbol{x}_j)$ to the partition function (2.59), where the fields are evaluated at $\boldsymbol{x}_j$, i.e., $\omega_j = \omega(\mathbf{x}_j)$ and $\epsilon_j = \epsilon(\mathbf{x}_j)$. Thus, ω is the dynamical field in the following, enforced to have the value $\vec{\phi}^2$ for each spatial coordinate $\mathbf{x}_j$ and ϵ is introduced in the integral representation of the Dirac delta. Functional integration measures of the fields are obtained using the product of Eq. (2.60) over all spacetime points $\mathbf{x}_j$ on a lattice and taking the continuum limit, see Eq. (2.3) for the definition of the functional integration measure in Section 2.1.

The resulting action for constraint fields reads

$$\mathcal{S}_{\text{constr}} = -\int \mathrm{d}^d x \, \frac{\mathrm{i}\epsilon}{2} \left(\omega - \vec{\phi}^2\right) \tag{2.61}$$

and is introduced directly into the partition function (2.59), where each occurrence of $\vec{\phi}^2$ can be replaced by ω due to the insertion of identity (2.60). One obtains the action

$$\mathcal{S}[\vec{\phi}, \epsilon, \omega] = \int \mathrm{d}^d x \left[\frac{1}{2}(\partial_\mu \vec{\phi})^2 + \frac{m^2}{2}\omega + \frac{\lambda}{4N_s}\omega^2 - \frac{\mathrm{i}\epsilon}{2}(\omega - \vec{\phi}^2) \right]$$

and partition function

$$Z = \int \prod_{j=1}^{N_s} \mathscr{D}\phi_j \mathscr{D}\omega \mathscr{D}\epsilon \, \mathrm{e}^{-\mathcal{S}_{\text{eff}}[\vec{\phi}, \epsilon, \omega]}. \tag{2.62}$$

The partition function (2.62) is now gaussian in ϕ such that one can apply the bosonic field version of Eq. (2.35) for each field $\phi_j(\boldsymbol{x})$, i.e.,

$$\int \mathscr{D}\phi_j \, \mathrm{e}^{-\int \mathrm{d}^d x \int \mathrm{d}^d y \phi_j(x) A(x,y) \phi_j(y)} = \alpha \, (\mathrm{Det} A)^{-1/2} \tag{2.63}$$

with a real normalization parameter α. After partial integration of the kinetic term and using Eq. (2.63), one obtains the effective action

$$\mathcal{S}_{\text{eff}}[\omega, \epsilon] = \int \mathrm{d}^d x \left[\frac{m^2}{2}\omega + \frac{\lambda}{4}\omega^2 + \frac{\mathrm{i}\epsilon}{2}\omega + \frac{N_s}{2} \ln \mathrm{Det} \left(-\sum_\mu \partial_\mu^2 + \mathrm{i}\epsilon \right) \right] \tag{2.64}$$

with a path integral going over ω and ϵ. Thus, the functional determinant in Eq. (2.64) encodes the quantum fluctuations of $\vec{\phi}^2$, which are argued to be small for $N_s \to \infty$ according

to the arguments above. So far, we only made mathematical manipulations of the partition function and the action, but solving the full path integral over the remaining degrees of freedom is still a difficult task, in general. Before we discuss how taking $N_s \to \infty$ helps in solving the path integral, let us study condensation of the field ϕ in this setup.

When condensation is involved, it is more practical to define

$$\vec{\phi} = (\sigma, \vec{\chi}) \tag{2.65}$$

such that one can study the condensation of σ while using the constraint field approach. We only allow condensation in σ, i.e., a spontaneously broken symmetry is obtained through $\langle\sigma\rangle \neq 0$. This splitting of field components would need to be introduced through explicit symmetry breaking that is removed in a infinite-volume extrapolation. Without loss of generality, this symmetry breaking external field could be choosen in the direction of $\phi_1 = \sigma$ such that condensation in this direction is implied. In this analytical approach, we assume that a similar procedure was performed by enforcing this condensation pattern by hand. This is common in (semi-)classical approaches, see, e.g., Refs. [93, 137, 141, 197]. Moreover, in this part of the discussion we assume that there is only homogeneous condensation. Similar steps as above lead to

$$\mathcal{S}[\vec{\phi}, \epsilon, \omega] = \int \mathrm{d}^3x \left[\frac{1}{2}\left[(\partial_\mu\sigma)^2 + (\partial_\mu\vec{\chi}^2)\right] + \frac{m^2}{2}\omega + \frac{\lambda}{4}\omega^2 - \frac{\mathrm{i}\epsilon}{2}(\omega - \sigma^2 - \vec{\chi}^2) \right] \tag{2.66}$$

where we use the substitution of ω such that $\vec{\chi}$ appears in bilinears and can be integrated out. One obtains using Eq. (2.63) for $\vec{\chi}$

$$\mathcal{S}_{\text{eff}}[\vec{\phi}, \epsilon, \omega] = \int \mathrm{d}^3x \left\{ \frac{1}{2}(\partial_\mu\sigma)^2 + \frac{m^2}{2}\omega + \frac{\lambda}{4}\omega^2 - \frac{\mathrm{i}\epsilon}{2}(\omega - \sigma^2) + \tfrac{N_s-1}{2} \ln \mathrm{Det}\left[-\sum_\mu \partial_\mu^2 + \mathrm{i}\epsilon \right] \right\}. \tag{2.67}$$

Again, only mathematical manipulations of the path integral were made and no solution to the full partition function was computed. This will be done in the following paragraph.

THE LARGE-N_s LIMIT AS A SADDLE POINT APPROXIMATION Since $\sigma \sim \sqrt{\vec{\phi}^2} \sim \sqrt{N}_s$, $\omega \sim N_s$ and $\epsilon \sim 1$, the remaining degrees of freedom can be calculated in a saddle-point approximation, when N_s is assumed to be large. The overall proportionality of the action to N_s allows to only consider the extrema with respect to the remaining dynamical degrees of freedom when $N_s \to \infty$, given one appropriately rescales the bare couplings with N_s. This is the same argument as in the mean-field approximation of four-fermion models for large-N_f, see Section 2.4. The above detour, however, demonstrates that a large-N expansion must not always be equivalent to the mean-field approximation, which corresponds to the classical field theory for Eq. (2.58). Here, quantum fluctuations are encoded in the functional determinants in Eq. (2.64) and Eq. (2.67).

In the case of the large-N_s limit (or $N_s \to \infty$), the respective, global minimum with respect to σ, ϵ and ω dominates the path integral and can be determined using

$$\frac{\partial \mathcal{S}_{\text{eff}}}{\partial(\sigma, \epsilon, \omega)} = 0. \tag{2.68}$$

This gives a straightforward, analytical approach to a solution of the theory.

The discussed constraint field approach is used extensively in Chapter 7. Depending on the condensation method, it can be also adjusted to account for condensation in more components than just one. Then, the splitting of ϕ in Eq. (2.65) is defined differently but follow-up steps work rather similar.

3

LITERATURE RECAPITULATION ON SPATIALLY MODULATED REGIMES AT NON-VANISHING QUARK CHEMICAL POTENTIAL

ABSTRACT AND RELATION TO THE RESEARCH OBJECTIVES In this chapter, the status of research on the main topic of this thesis, (chiral) phases with spatially modulated observables in QCD at intermediate temperatures and densities, is recapitulated based on a selection of current literature. The focus is on important findings that provide the motivation for the existence of these phases in QCD as well as on relevant examples from QCD-inspired model calculations. Moat regimes, IPs, QπLs, and also liquid-crystal-like phases are covered.

DISCLOSURE This chapter can be seen as a summary of essential literature results on spatially modulated regimes in QCD (mostly from model computations and functional methods) based on the subjective perspective and scientific background of the author. A selection of literature results is necessary for a concise presentation and is designed such that this chapter serves as an additional background for the understanding of results in the subsequent chapters of this thesis. The author had made every effort to provide a comprehensive overview. However, we apologize in advance for any omissions of relevant literature. Due to the nature of this review, none of the content in this chapter is original to this thesis. Accordingly, in each section the respective publications, from which findings are summarized, are properly referenced. Note that the author of this thesis is also an author of some of the mentioned publications; thus, licenses for used figures from these works are already associated with the author. To the best of our knowledge, the content of this chapter has not been compiled in a similar form before, although recapitulations of particular results can certainly be found in literature reviews, theses with a similar focus, or other resources.

OUTLINE We begin the discussion by presenting what we consider the strongest indications for the existence of spatially modulated regimes in QCD in Section 3.1. This includes the findings of the moat regime with the FRG, which is a precursor for all kind of exotic regimes, see Section 1.2, as well as expectations from symmetries arising at non-vanishing chemical potentials in QCD. Then, we discuss the properties of IPs using relevant examples from model computations in Section 3.2. In Section 3.3 we focus on the disordering of inhomogeneous condensates through Goldstone boson fluctuations, which can lead to the emergence of liquid-crystal-like regimes or the QπLs.

3.1 HINTS FOR THE EXISTENCE OF SPATIALLY MODULATED PHASES IN THE QCD PHASE DIAGRAM

In Section 1.2, we give a motivation for the relevance of phases[1] with spatial modulations, including IPs, moat regimes and QπLs, in the QCD phase diagram at intermediate temperatures and baryon densities. Thereby, a selection of the relevant literature with respect to these phenomena and other observations of oscillatory regimes is discussed. In this section, the focus is on references that can be considered as strong arguments or indications for the existence of these exotic regimes in QCD.

There is a variety of literature on QCD-inspired model calculations that identify IPs – the most prominent of the exotic regimes discussed in this thesis – in a region of low to intermediate temperatures and quark chemical potentials of $\geq$ 350MeV [195–198, 304]. However, as outlined in Section 1.2, these computations suffer from their strong dependence on regularization effects that has been discussed recently [10, 240, 241]. A selection of these studies will be mentioned later. We begin the discussion with unambiguous indications for the existence of spatially modulated regimes in the QCD phase diagram.

3.1.1 *Moat regime dispersion relation in QCD*

From the point of view of the author, a strong indication for the existence of inhomogeneities in the QCD phase diagram is the observation of the moat regime in FRG computations of the QCD phase diagram [121, 166]. The moat regime is defined as the region in the phase diagram where the dispersion relation of quark correlations in mesonic channels has a minimum at non-vanishing spatial momenta. For example, pion (quasi-)particles exhibit the moat regime dispersion relation. It is essential that these dispersion relations arise from the thermodynamic ground state of the system, leading to the prediction of, e.g., peaks in two-particle correlations of pions in heavy-ion collisions within the moat regime [233].

Within the FRG framework, and most other available computations [1, 9, 10, 219] the moat regime is often detected from the wave function renormalization Z_ϕ of the respective, dynamically emerging meson field turning negative. This is reflected in the quantum effective action (2.26) of the theory. The wave function renormalization can be extracted from the bosonic two-point vertex function of the respective scalar field at vanishing spatial moments, as will be discussed in Section 4.1. This is often more practical, since not the whole dispersion relation (or bosonic two-point vertex function) has to be computed but only its curvature at zero spatial momentum needs to be extracted.

In the FRG, the meson wave function renormalization is part of modeling the full momentum dependence of the bosonic two-point vertex function of the respective meson fields, and, thus, is computed through solution of flow equations, see, e.g., equation (92) of Ref. [121]. In this work, the wave function renormalization is first computed in an FRG approach to QCD, where a first-principles QCD setup involving the non-trivial gluon dynamics is evolved into a formulation of a quantum effective action resembling the form of many QCD-inspired models, c.f. equation (39) in Ref. [121]. In Fig. 3.1, we show results from Ref. [121], where in the left subfigure the wave function renormalization Z_ϕ is plotted as a function of the temperature for different baryon chemical potentials μ_B. Therein, it is observed that above $\mu_B \sim 400$MeV negative values of Z_ϕ are obtained. This region is identified as

1 Throughout this thesis, the term "phase" is used for a region in the phase diagram that can be characterized through an observable behaving distinctly different than in the rest of the phase diagram.

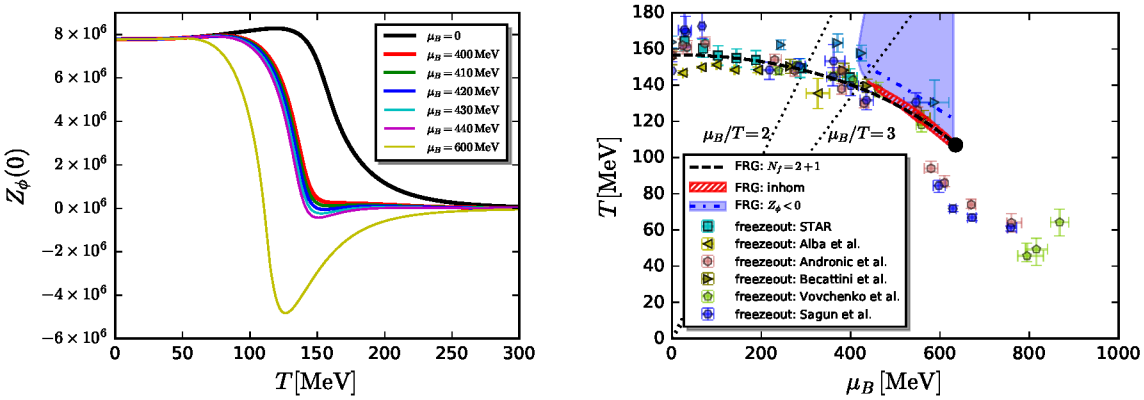

Figure 3.1: Plots regarding the detection of the moat regime with the FRG in Ref. [121]. The figures are taken from Ref. [121] under the *Creative Commons Attribution 4.0 International license. (left)* Value of the mesonic wave function renormalization Z_ϕ as a function of the temperature T for different value of the baryon chemical potential. *(right)* The moat regime within the computed QCD phase diagram. Points represent freeze-out data from the STAR experiment at RHIC [51] and different model computations based on experimental data [50, 305–308]. The dashed line represents the chiral crossover and the black circle represents the CP.

the moat regime, and plotted in the right subfigure of Fig. 3.1. The moat regime ends at roughly $\mu_B \approx 600$MeV, which is just limited by the used truncation scheme in the FRG calculation. This leads to the results having qualitative validity only up to $\mu_B/T \leq 6$.

THE MOAT REGIME AND INHOMOGENEOUS PHASES As discussed in the literature, see Section 1.2, it is expected that, if the global minimum of the moat dispersion relation is deep enough, the ground state is given by a chiral condensate carrying a non-vanishing momentum of roughly the order of the momentum associated with the minimum of the moat dispersion. This is then an inhomogeneous chiral condensate, i.e., IPs are expected to overlap with parts of the moat regime. Often, the moat regime is also called a precursor for IPs. The first finding of a moat regime within an IP (but also in parts of the SP) in the $1+1$-dimensional GN model in the mean-field approximation [1] is discussed in Section 4.2. This computation serves as an important part of testing the methodology of computing the bosonic two-point vertex functions in the results chapters in this thesis such that details of the analysis are presented in Chapter 4. At this point, this work is only mentioned as the first evidence in models from high energy physics that the moat regime indeed can be associated with IPs. In condensed matter physics, the moat regime is, however, often associated with inhomogeneous phenomena, e.g., in crystallization [174] or non-uniform superconductivity [175–177].

3.1.2 *Prediction of spatially modulated phases from $\mathcal{PT}$-symmetric field theory*

Another aspect, that is discussed in the literature of recent years [180, 185, 188, 190, 191, 194, 309], is the emergent $\mathcal{CK}$ symmetry of QCD at non-vanishing quark (or baryon) chemical potential, which is the combined action of charge conjugation $\mathcal{C}$ and complex conjugation $\mathcal{K}$. At $\mu = 0$, the action of QCD can be shown to be Hermitian and real-valued. However, as soon as non-vanishing quark chemical potentials are considered, complex weights appear

in the path integral spoiling statistical simulations, which is the renown *sign problem* of QCD (see Ref. [117] for a review). Moreover, the theory looses the invariance under $\mathcal{C}$ and $\mathcal{K}$ individually while retaining an invariance under the combined action of $\mathcal{CK}$. The emergence of this symmetry and its potential for tackling the complex saddle points appearing in the partition function was to our knowledge first discussed in Ref. [185]. Moreover, the $\mathcal{CK}$ symmetry is of $\mathcal{PT}$-type, i.e., it is a combination of a linear, discrete and an anti-linear, discrete symmetry transformation. There is a whole class of models with generalized $\mathcal{PT}$ symmetry in quantum mechanics [181, 183, 184] and also QFTs with generalized $\mathcal{PT}$ symmetry [186, 310–313]

Recently, it has been discussed that theories with this type of symmetry can feature exotic phases involving moat regimes, IPs and QπLs [185]. Thereby, oscillatory regimes arise naturally in $\mathcal{PT}$-symmetric theories from the behavior of eigenvalues of the Hamiltonian (in quantum mechanics) or transfer matrix (in QFT). These eigenvalues can occur in complex-conjugate pairs, as can be determined by the characteristic polynomial of the corresponding operator having real coefficients [314, 315]. This was recently confirmed in a full QFT investigation by LFT simulations of a scalar model of mixing contributions [180, 188, 190].

We briefly present a generic example of oscillatory behavior in correlation functions using a scalar field theory, taken from Ref. [188]. Therefore, we consider the action in Euclidean spacetime

$$S[\phi_a, \phi_b] = \int \mathrm{d}^{d+1}x \left[\sum_{j=a,b} \frac{1}{2} \left(\partial_\mu \phi_j\right)^2 + V(\phi_a, \phi_b) \right], \tag{3.1}$$

where the potential V is allowed to contain complex masses and couplings. In momentum space, the bare inverse propagator of the scalar fields can be written formally as

$$G^{-1}(q) = q^2 + \mathcal{M}^2 \tag{3.2}$$

with the "$d+1$-momentum" $q_\mu = (\boldsymbol{q}, \omega_n)$ and the mass matrix

$$M_{jk} = \left. \frac{\partial^2 V}{\partial \phi_j \partial \phi_k} \right|_{\phi_a = \bar{\Phi}_a, \phi_b = \bar{\Phi}_b}, \qquad j,k = a,b \tag{3.3}$$

where $\bar{\Phi}_a$ and $\bar{\Phi}_b$ represent homogeneous expectation values of the scalar fields ϕ_a and ϕ_b, respectively. The homogeneity of these expectation values is assumed in this analysis.

MASS MATRIX PROPERTIES AND THEIR IMPLICATIONS In a conventional QFT, $\mathcal{M}$ has positive eigenvalues E_j, such that the position space propagator $G = \langle \phi_j \phi_k \rangle$, $j,k = a,b$, has two exponentially decaying modes if the ground state $(\phi_a, \phi_b) = (\bar{\Phi}_a, \bar{\Phi}_b)$ is stable (instabilities lead to exponentially growing position space propagators). As usual, vanishing eigenvalues can be associated with Goldstone modes. An action with arbitrary complex terms, in general, features positive, negative as well as complex-valued eigenvalues of the mass matrix. Imposing $\mathcal{PT}$ symmetry on such a non-Hermitian theory, the eigenvalues of the mass matrix are better behaved. For the example (3.1), a $\mathcal{PT}$-symmetric version can be obtained by imposing

$$S[\phi_a, \phi_b] = S^*[\phi_a, -\phi_b]. \tag{3.4}$$

For a typical action with linear interactions between the two different fields, the field ϕ_b should be imaginary to fulfill this constraint. Such an imaginary field is actually used in the investigated mixing model in [190] and can also be realized in the four-fermion model studied in Chapter 6. The potential and the mass matrix obey a relation similar to Eq. (3.4).

Eigenvalues λ_j of $\mathcal{M}$	**Position-space propagator behavior**	**Region**
All positive	Exponential decay	Normal
Odd number of $\lambda_j < 0$	Exponential growth	Unstable
Some $\lambda_j = \lambda_k^*$	Sinusoidally-modulated exponential	$\mathcal{PT}$ broken
Even number of $\lambda_j < 0$	$(\bar{\Phi}_a, \bar{\Phi}_b)$ instable against $p \neq 0$	Patterned vacuum

Table 3.1: Properties of the mass matrix of Eq. (3.1) evaluated at homogeneous expansion points $(\phi_a, \phi_b) = (\bar{\Phi}_a, \bar{\Phi}_b)$ under the assumption of a generalized $\mathcal{PT}$ symmetry (3.4) and resulting behavior of the position space propagator. This table is recreated in an almost identical way to Ref. [188].

Inspecting the characteristic equation of the mass matrix, one can make conclusions about the behavior of the position space propagator. The below discussed properties of the mass matrix and the resulting propagator behavior are summarized in Table 3.1. In addition to the typical behavior of position space propagators in an ordinary, hermitian QFT, two novel behaviors can be obtained directly from $\mathcal{M}$. First, when the mass matrix has one (or possibly more) complex-conjugate eigenvalue pairs, the propagator still decays exponentially in position space but with oscillatory modulations from a sine term, i.e., a QπL regime is observed. In Ref. [188] and Table 3.1, this regime is termed the "$\mathcal{PT}$-broken regime", in analogy to the observation of complex-conjugate eigenstates in $\mathcal{PT}$-symmetry quantum mechanics [181].[2] In the QπL, the homogeneous ground state, used in the computation of the mass matrix, is a stable one. The case of multiple complex-conjugate eigenvalue pairs also amounts to a QπL but can only be obtained in a theory with more than two bosonic degrees of freedom; it does not apply for Eq. (3.1).

In the case of an even number of negative eigenvalues, an IP is obtained through an instability of the homogeneous ground state. Since the determinant of $\mathcal{M}$ is positive in this case, the homogeneous ground state $(\bar{\Phi}_a, \bar{\Phi}_b)$ is stable against homogeneous fluctuations $q = 0$ while it is instable for a range of momenta $q \neq 0$. This amounts to an instability towards an inhomogeneous condensate and is again discussed in Section 4.1, in the context of the Hessian matrix of fermionic theories. This is termed a patterned vacuum in Ref. [188] and Table 3.1 and an IP in this work.

The behavior of bare position space propagators, derived from the properties of the mass matrix (i.e, in classical field theory or a semi-classical approximation for the used bosonic fields), must not necessarily be realized generally in the full quantum theory. However, in scalar mass-mixing models all of the predicted (exotic) phases are observed using LFT simulations [180, 188, 190]. The analysis of the mass matrix (or, equivalently, the static Hessian matrix) presented above can be performed equivalently for all theories with a generalized $\mathcal{PT}$-symmetry [185], and is also relevant in Chapter 6.

2 The origin of the term "$\mathcal{PT}$-broken" comes from the observation that the complex-conjugate eigenstates are exchanged under the (generalized) $\mathcal{PT}$ symmetry operation. If the system is in one of the two eigenstates associated with the complex-conjugate eigenvalue pair, it breaks this symmetry spontaneously.

3.2 INHOMOGENEOUS CHIRAL CONDENSATES WITHIN THE MEAN-FIELD APPROXIMATION

In this section, we discuss typical examples of inhomogeneous chiral condensates obtained in $1+1$-dimensional four-fermion models. The found solutions for the condensates are the basis for computations in higher dimensional models, where they are often used as ansatz functions for inhomogeneous condensates. After this discussion, we turn towards the realization of IPs in the NJL model and the recently explored regularization dependence of IPs. For a more in-depth discussion of IPs in QCD-inspired models, we refer to Ref. [197]. In this section, we restrict ourselves to literature employing mean-field approximations, where bosonic fluctuations are suppressed entirely, and focus on the effect of bosonic quantum fluctuations in the following section.

3.2.1 $1+1$-*dimensional Gross-Neveu model and the chiral kink crystal*

The GN model is arguably the simplest fermionic theory with a single quartic self-interaction. The action of this four-fermion model in Euclidean spacetime is

$$\mathcal{S}[\bar{\psi},\psi] = \int_0^\beta \mathrm{d}\tau \int \mathrm{d}^d x \left[\bar{\psi}\left(\not{\partial} + \gamma_{d+1}\mu\right)\psi - \frac{\lambda}{2N_f}\left(\bar{\psi}\psi\right)^2\right] \tag{3.5}$$

at temperature T and quark chemical potential μ, introduced following Section 2.1. Here, ψ and $\bar{\psi}$ contain N_f two-component spinors, see Section 2.3 for an introduction to the generic models and Appendix A.3 for representations of the Clifford algebra. In the rest of this section we discuss the theory in one spatial dimension, i.e., $d=1$. After bosonization according to Section 2.3.1 the action reads

$$\mathcal{S}[\bar{\psi},\psi,\sigma] = \int \mathrm{d}^2 x \left[\frac{\sigma^2}{2\lambda} + \bar{\psi}\left(\not{\partial} + \gamma_2\mu + \sigma\right)\psi\right] \tag{3.6}$$

with an auxiliary bosonic field σ fulfilling the Ward identity (2.43) for $c_j = 1$. The model was introduced in Ref. [36] as a $1+1$-dimensional toy model with features of QCD such as asymptotic freedom and a chiral symmetry (albeit the latter is discrete)

$$\psi \to \gamma_{\mathrm{ch}}\psi, \qquad \bar{\psi} \to -\bar{\psi}\gamma_{\mathrm{ch}}, \tag{3.7}$$

see Appendix B.1 for the breaking of the continuous chiral symmetry in $1+1$ dimensions through the GN interaction term. This symmetry would be explicitly broken by a bare mass term for the fermion fields or spontaneously broken through a non-vanishing expectation value of the field σ.

In the large-N_f limit (or mean-field approximation, see Section 2.4), the *homogeneous phase diagram*, i.e., the phase diagram when restricting only to homogeneous field configurations $\sigma(x) = \bar{\sigma} = \text{const.}$, was first computed in Ref. [316]. It features an HBP at low temperatures and chemical potentials (including the vacuum) where chiral symmetry is spontaneously broken through homogeneous expectation values $\bar{\sigma} = \bar{\Sigma} \neq 0$, similar to QCD. Thereby, $\bar{\Sigma}(\mu,T)$ can be determined as the global minimum of the homogeneous effective potential (2.53).[3] At low chemical potentials and intermediate temperatures (compared to

3 Note that according to the discussion in Section 2.4.4 we do not use brackets for expectation values, but just the capitalization of the respective field.

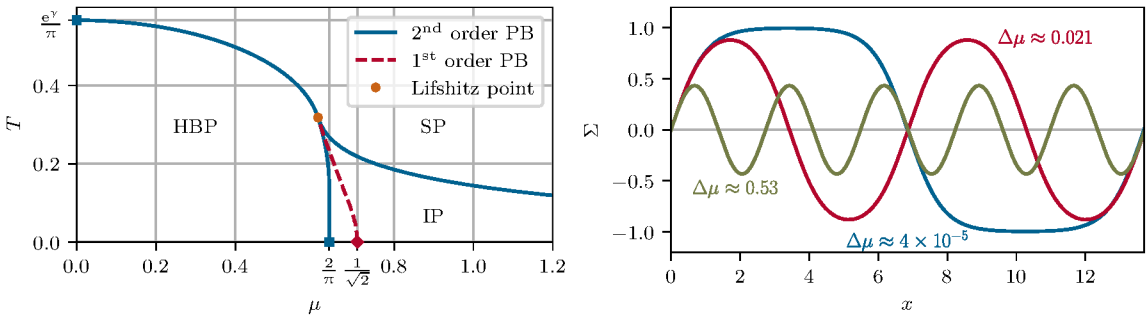

Figure 3.2: Results regarding in IPs in the $1+1$-dimensional GN model from Ref. [202]. *(left)* The phase diagram of the GN in the large-N_f limit. The dashed red curve corresponds to the first-order phase boundary that is obtained in the homogeneous phase diagram, i.e., if only homogeneous field configurations are allowed [316]. The solid blue lines represent second order phase transitions, if inhomogeneous condensates are taken into account [202, 318]. *(right)* Spatial inhomogeneous chiral condensate $\Sigma(\mu, T, x)$ for various chemical potentials $\mu = \mu_c + \Delta\mu$ in the IP where $\mu_c/\bar{\Sigma}_0 = 2/\pi$. Note that in both plots all dimensionful quantities are given in units of the chiral condensate in the vacuum $\bar{\Sigma}_0$. Similar figures can be found in Ref. [1].

the chiral condensate in the vacuum $\bar{\Sigma}_0$) a second order phase transition is obtained to the SP, which turns first-order at a CP, see the dashed red line in Fig. 3.2. Simultaneously, the temperature of the phase transition line decreases until $T = 0$ and $\mu/\bar{\Sigma}_0 = 1/\sqrt{2}$. Later it was shown that the finding of the homogeneous phase diagram is actually a rediscovery of the same phase structure of a model used for spins of electrons in a superconductor under the influence of a magnetic field, found in Ref. [317]. This model can be shown to be mathematically equivalent to the GN model in one spatial dimension [318].

The phase diagram was revised in Ref. [202] where inhomogeneous condensation was taken into account and a solution for the IP was constructed. The full phase diagram including the IP is presented in the left plot of Fig. 3.2. Therein, the CP is replaced by a LP and the entire region of the first-order phase transtion is covered by an IP, that extends to $\mu \to \infty$ at zero temperature. All transitions in this revised phase diagram are of second order. The replacement of the CP and the first-order phase transition through an IP often occurs also in higher-dimensional models. The extension of the inhomogeneous condensation towards $\mu \to \infty$ is, however, rather unique to $1+1$-dimensional models.

In the right plot of Fig. 3.2, we present the form of the chiral condensate $\Sigma(\mu, T)$ as a function of the spatial coordinate x at $T = 0$, the chiral kink. We observe a generic behavior of the condensate when increasing the chemical potential, that remains valid at non-zero temperatures:

- the functional shape of the condensate evolves from a kink-antikink shape, close to the phase transition to the HBP, to a sine-like shape,
- the amplitude of the condensate decreases,
- the frequency of the condensate increases.

The plotted behavior of the chiral condensate can be parameterized using Jacobi-elliptic functions [318] making the Fourier spectrum of the kink solution rather complicated, see [319] for properties of Jacobi elliptic functions. Right at the second order phase transition to the SP, the amplitude of the condensate is always infinitesimal and the oscillation is given

by a sine-wave with fixed frequency. Thus, this transition line can be detected in a stability analysis of the SP with respect to infinitesimal perturbations, as shown in Section 4.2.

The generation of the chiral kink crystal is energetically favored through a mechanism similar to the Peierls instability known from condensed matter models [320] which is applicable to an electron gas in a one-dimensional, infinite lattice structure of atoms. The energy of the system is lowered by applying a spatial perturbation with a momentum that is twice the fermi surface momentum of the electrons. This results in an inhomogeneous, periodic charge density distributed over the one-dimensional lattice, similar to the inhomogeneous condensate [318].

A further, interesting aspect is the alignment of peaks of the baryon density with the zero-crossings of the chiral condensate, see, e.g., Refs. [167, 321] for visualization. This feature also gives rise to the name "baryon crystal" for this particular inhomogeneous condensate and other IPs with a similar alignment.

3.2.2 *Chiral Gross-Neveu model and the chiral spiral*

Before the findings of inhomogeneous condensates in the GN model, it was already shown that IPs ground states exists at non-vanishing μ in the chiral GN model within the mean-field or large-N_f approximation in Ref. [201]. The action of this model reads

$$\mathcal{S}[\bar{\psi},\psi] = \int_0^\beta \mathrm{d}\tau \int \mathrm{d}x \left\{ \bar{\psi}\left(\not{\partial} + \gamma_2\mu\right)\psi + \frac{\lambda}{2N_f}\left[\left(\bar{\psi}\psi\right)^2 + \left(\bar{\psi}\mathrm{i}\gamma_{\mathrm{ch}}\psi\right)^2\right]\right\} \tag{3.8}$$

where, again, ψ and $\bar{\psi}$ contain N_f two-component spinors, see Section 2.3. We refer to Appendix A.3 for the definition of γ_{ch}. This model features a continuous chiral symmetry transformation

$$\psi \to \mathrm{e}^{\mathrm{i}\alpha\gamma_5}\psi, \qquad \bar{\psi} \to \bar{\psi}\mathrm{e}^{\mathrm{i}\alpha\gamma_5}. \tag{3.9}$$

After bosonization the action of the model reads

$$\mathcal{S}[\bar{\psi},\psi,\sigma,\eta] = \int \mathrm{d}^2x \left[\frac{\sigma^2}{2\lambda} + \bar{\psi}\left(\not{\partial} + \gamma_2\mu + \sigma + \mathrm{i}\gamma_{\mathrm{ch}}\eta\right)\psi\right] \tag{3.10}$$

where the auxilary bosonic fields σ and η follow the Ward identity (2.43) for $c_j = 1$ and $c_j = \mathrm{i}\gamma_{\mathrm{ch}}$, respectively. A non-vanishing expectation value of σ and/or η signals the spontaneous breaking of chiral symmetry.

Before the publication of Ref. [201], it was assumed that the phase diagram of the chiral GN model amounts to the homogeneous phase diagram of the GN model with discrete chiral symmetry, as depicted in the left plot of Fig. 3.2. This can be shown through the symmetry transformation (3.9) acting on the bosonic fields

$$\sigma \to \cos(2\alpha)\sigma + \sin(2\alpha)\eta, \quad \eta \to -\sin(2\alpha)\sigma + \cos(2\alpha)\eta\,. \tag{3.11}$$

corresponding to an $O(2)$ symmetry in the (σ,η) plane. This allows to rotate the bosonic fields in the case of homogeneous field configurations $\sigma = \bar{\sigma}$ and $\eta = \bar{\eta}$, such that $\bar{\eta} = 0$. Then, the effective potential and its minima are the same as in the GN model.

Actually, the full phase structure of the chiral GN model is particularly simple when allowing for inhomogeneous condensation. At the critical temperature $T_c = \mathrm{e}^\gamma/\pi$ with the Euler-Mascheroni constant γ, one obtains a second-order phase transition from the SP, with

$\Sigma = H = 0$, to an IP where σ and η form a so-called chiral spiral [201, 246] independent of the value of μ. The critical temperature is the same as the transition temperature in the homogeneous phase diagram for $\mu = 0$. This chiral spiral solution is given by

$$\Sigma(\mu, T, x) = m(T)\cos\left(2\mu(x - x_0)\right), \quad H(\mu, T, x) = m(T)\sin\left(2\mu(x - x_0)\right) \tag{3.12}$$

such that both fields oscillate with a frequency 2μ. Strictly speaking, the chiral spiral solution reduces to an HBP right at $\mu = 0$. The amplitude $m(T)$ goes to zero when T approaches the critical temperature. This chiral spiral solutions is a particularly simple solution, because the norm of field vector (Σ, H) as well as the baryon density remains constant in space. Further, the chiral spiral consists of one dominant Fourier mode such that analytical calculations are particularly simple. This property is of relevance later in the study of disordering of chiral condensates in a different model analysis.

Further, the chiral spiral solution directly implements the linear proportionality of the frequency to the chemical potential μ, in this particular case $k = 2\mu$. A similar proportionality can already be observed in the GN model, although it is less obvious since the chiral kink consists of a Fourier spectrum with multiple, non-vanishing coefficients. However, already this spectrum is dominated by a linear proportionality. The frequency being on the order of the chemical potential is typical for IPs also in more complicated or higher-dimensional models [111, 197].

3.2.3 *Inhomogeneous phases and their regularization dependence in higher dimensions*

Inhomogeneous phases are found in a variety of $3+1$-dimensional models, most of which are NJL models, see, e.g., Refs. [195, 196, 200, 208, 304]. The NJL model and four-fermion models in general are, however, not renormalizable such that regularization effects become part of the model in the sense that the value of the regulator becomes a parameter of the theory. Thus, results become dependent on the regularization scheme such that predictions based on these models should be carefully checked for qualitative agreement amongst different regularization schemes and sensitivity against variations of the regulator [322]. In this subsection, we summarize results that point towards a strong dependence on the used regularization scheme and regulator value of the existence and shape of IPs.

PHASE DIAGRAM OF THE $2+1$-DIMENSIONAL GN MODEL The regularization scheme dependence of IPs was first unveiled through the works [240, 241], which study the phase diagram of the $2+1$-dimensional GN model in the mean-field approximation. The advantage of $2+1$-dimensional four-fermion models, which taken advantage of multiple times throughout this thesis, is their renormalizability in the $1/N_f$-expansion [243, 244]. First, in Ref. [242] an IP was detected within a LFT mean-field computation at one fixed lattice spacing. However, in Ref. [240] it was demonstrated that the obtained IP shrinks when decreasing the lattice spacing such that it is expected to vanish in the continuum limit. An in-depth analysis [241] followed, revealing that inhomogeneous condensates are absent in the model when removing any kind of regulator. In this work, the phase structure of the $2+1$-dimensional GN model was computed using two different lattice discretizations and one continuum approach using a a Pauli-Villars regularization. For one of the two lattice discretizations, no IP was observed at all, independent of the value of the investigated lattice spacing. For the other discretization as well as the continuum approach with a finite value of the Pauli-Villars regulator Λ, an IP is observed at low temperatures and a range of chemical

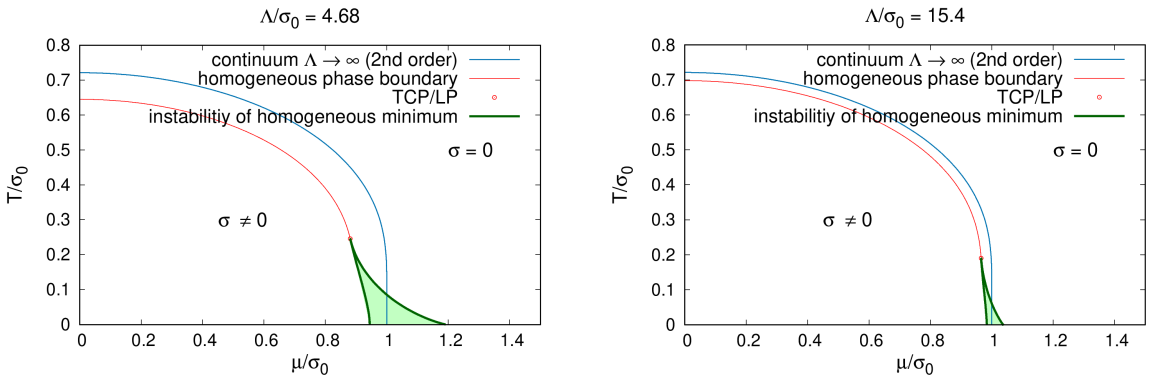

Figure 3.3: Phase diagram of the $2+1$-dimensional GN model in the (μ, T) plane. The blue line is the renormalized result and represents the second-order phase transition between the homogeneous phases. The red line as well as the shaded green region are the results for a finite regulator value Λ and represent the second-order phase transition, ending at an LP (red circle), and the region where the homogeneous ground state is instable, respectively. The latter region corresponds to an IP. The scale is set by the value of the chiral condensate in the vacuum σ_0 (corresponding to $\bar{\Sigma}_0$ in the notation of this thesis). *(Left)* Lower value of the Pauli-Villars regulator $\Lambda/\bar{\Sigma}_0 \approx 4.68$. *(Right)* Higher value of the Pauli-Villars regulator $\Lambda/\bar{\Sigma}_0 \approx 15.4$. This figure is taken from Ref. [241].

potentials, see Fig. 3.3. When the lattice spacing is decreased or the value of Λ is increased, this IP shrinks, however, and finally disappears for all non-vanishing temperatures when removing the regulator. This is demonstrated in Fig. 3.3 where the phase diagram in Pauli-Villars regularization from Ref. [241] is shown for a low value of the regulator (left panel) and a higher value of the regulator (right panel) alongside the renormalized result (blue line in both plots). One can see that the region corresponding to the IP significantly shrinks when increasing the regulator Λ and finally vanishes when removing the regularization by taking the limit $\Lambda \to \infty$, see the blue line in both diagrams. We note that at zero temperature, a degeneracy between homogeneous phases and inhomogeneous condensates might be left at $(\mu/\bar{\Sigma}_0, T/\bar{\Sigma}_0) = (1.0, 0.0)$ where also the homogeneous potential is flat for a range of homogeneous $\bar{\sigma}/\bar{\Sigma}_0 \in [0.0, 1.0]$ [241] ($\bar{\Sigma}_0$ is the value of the chiral condensate in the vacuum). This is in agreement with the analysis in Ref. [321] where this degeneracy is observed in a finite range of baryon densities.

NJL MODEL RESULTS AND THEIR REGULATOR DEPENDENCE In the NJL model in three spatial dimensions and in the chiral limit, the one-dimensional modulations from the $1+1$-dimensional GN and chiral GN model can be embedded leading to the appearance of an IP, which is restricted to an intermediate range of chemical potentials and low temperatures [195, 304]. The shape of the IP looks qualitatively surprisingly similar to the green shaded region in the left panel of Fig. 3.3, i.e., to the phase diagram of the $2+1$-dimensional GN model. Later, we will briefly discuss literature results regarding the dimensionality of four-fermion models and their phase diagram, as well as the relation of regularization effects and dimensionality.

The findings of [195], albeit being robust with respect to the influence of vector interactions and Polyakov-loops [196], already show a certain sensitivity to the value of the regulator used as well as to the parameter fitting. We refer for example to Figure 2 in Ref. [195] where the IP of the NJL model is plotted for three different values of the constituent quark mass implying that different values of the regulator were used according

to the parameter fitting devised in Ref. [138]. A finite regulator is required due to the non-renormalizability of the model and, thus, a regularization scheme inherently becomes part of the theory, in which the regulator scale becomes a parameter. The findings from Refs. [240, 241] triggered the in-depth analysis of regularization effects on IPs but also of moat regimes in the NJL model in Refs. [10, 167]. The main finding of this work is presented in Fig. 3.4. This figure shows the regions of instability from a stability analysis of homogeneous condensate against inhomogeneous ones, corresponding to an IP, in the (M_0, μ) plane for four different regularization schemes, where the constituent quark mass M_0 controls the respective value of the regulator. From this figure it is obvious that there is a strong dependence of both the existence and the extent of IPs on the used regularization scheme as well as on the value of the regulator. For all four of the visualized regularization schemes, the shape and extent of the IP in the (M_0, μ) differs strongly, while the homogeneous phase boundaries are qualitatively similar for the different schemes. There is no single point in the phase diagram where all regularization schemes exhibit an IP simultaneously. Moreover, a fifth regularization scheme was investigated but no IP was observed at all. For small values of the constituent quark mass, that correspond to large values of the regulator due to the used parameter fitting, it is found that IPs are absent within all regularization schemes. These ambiguities in the phase diagram, which are expected to persist to the finite temperature results, indicate that predictions of IPs based on NJL model calculations have limited implications for the phase structure of QCD. The strong regularization artifacts of these findings are not suprising given the typical order of magnitude of regulator values, which are around a few hundred MeV. Thus, the studied chemical potentials and the preferred frequencies of approximately $(1-2)\mu$ of the inhomogeneous condensates are in the same order of magnitude as the regulator (or even above the regulator). These are two quantities, determining the relevant physics of the IP and appearing in corresponding, divergent integral equations. Consequently, this UV regularization strongly influences the phase structure in this parameter region.

ROBUSTNESS OF THE MOAT REGIME A further important finding of the analysis in Ref. [10] is the robustness of the moat regime in the NJL model. This manifest itself in the observed mild scheme dependence of the moat regime. There is qualitative agreement between the applied two regularization schemes that the moat regimes covers a large portion of the SP suggesting that its presence is indeed a consequence of the NJL model action and its symmetries. This in turn implies that it also might exist in QCD, which is strongly supported by the above described FRG computations [121].

GROSS-NEVEU MODEL IN NON-INTEGER SPATIAL DIMENSIONS Inspired by the above findings, the series of works [211, 212] studied the phase diagram of the GN model in non-integer spatial dimensions $1 \leq d < 3$, where four-fermion models are renormalizable [243, 252]. These works make use of a stability analysis (a method that is discussed in Section 4.1 in this thesis) to connect the results regarding IPs from integer spatial dimensions smoothly and demonstrate how the presence of an IP in $d = 1$ turns towards an absence precisely at $d = 2$, i.e., for $1 \leq d < 2$ the IP is still present. For $d \geq 2$, there is no indication for an instability towards an IP. This is visualized in Fig. 3.5, where the phase diagram of the GN model is presented in the (μ, d) plane. Note that the findings for homogeneous phases were originally computed in Ref. [252].

Similar to a finite value of a regulator, the number of spatial dimensions $d < 2$ causes the appearance of a CP and an LP at a non-zero temperature which in turn leads to the

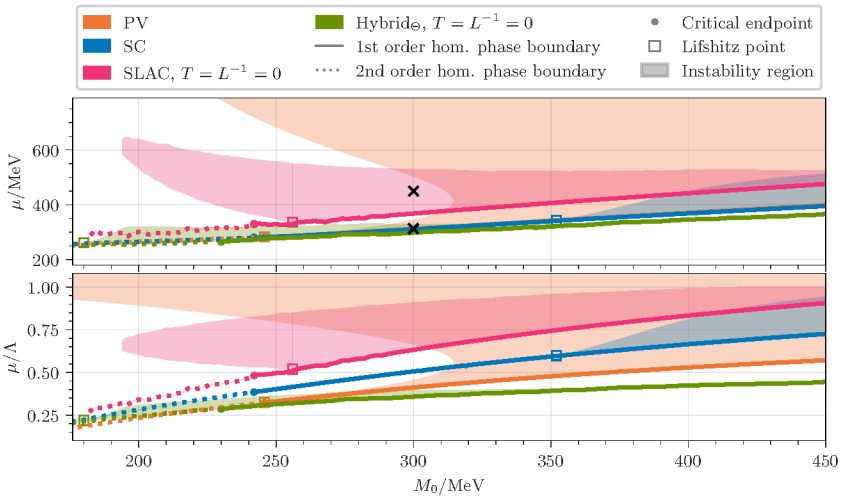

Figure 3.4: Figure 1 from Ref. [10] showing the homogeneous phase boundary and regions of instability of homogeneous minima, corresponding to an IP, in the NJL model in the (M_0, μ) plane at zero temperature for four different regularization schemes. A fifth regularization scheme was investigated but no IP was observed and the homogeneous phase boundary is in agreement with the green line, such that this regularization scheme was not plotted. Thereby, M_0 is the constituent mass in the vacuum and varies the value of the respective regulator according to the standard scale setting approach for the NJL model proposed in Ref. [138]. The pion decay constant was tuned to $f_\pi = 88\text{MeV}$. The model was studied in the chiral limit, i.e., $m_\pi = 0$.

appearance of an IP. This study can be interpreted as a study of the $3+1$-dimensional GN model with dimensional regularization where a small d would correspond to a strongly-regularized theory with a relatively small value of the regulator. In this sense, the results of Ref. [211] can be reinterpreted as a complementary study to Ref. [10], since the expressions appearing in the stability analysis used in both works are mathematically identical for the GN and NJL model independent of the number of spatial dimensions $d = 1, 2, 3$. Thus, this study provides results within another regularization scheme pointing towards the absence of IPs for higher values of the regulator (larger values of d in dimensional regularization).

COMMENT REGARDING IPS IN THE QUARK-MESON MODEL Readers, who are experts in the fields, might comment that there still exist observations of an IP in a QM model. This model is renormalizable and not plagued by regularization artifacts, with dynamical meson fields interacting via a Yukawa-type interaction with the fermions [198]. While it is certainly true that an IP is observed in a renormalized model in the mean-field approximation in Ref. [198], the renormalized theory shows inconsistencies with respect to the important properties of a sensible QFT. In the renormalization procedure a negative coupling of the mesonic, quartic self-interactions as well as an imaginary Yukawa coupling arises at a certain value of the regulator. This leads to an effective potential that is unbounded to $-\infty$ for both large frequencies and amplitudes of the condensates beyond these values of the regulator in the renormalization process. This artifact is ignored in the computation of the phase diagram in the sense that large values of the chiral condensate or large values of the frequencies are neglected. However, at the present stage one might argue that there is no proper ground state in this theory. These technical problems are considered as being caused of the applied mean-field approximation. To date, there is, however, no

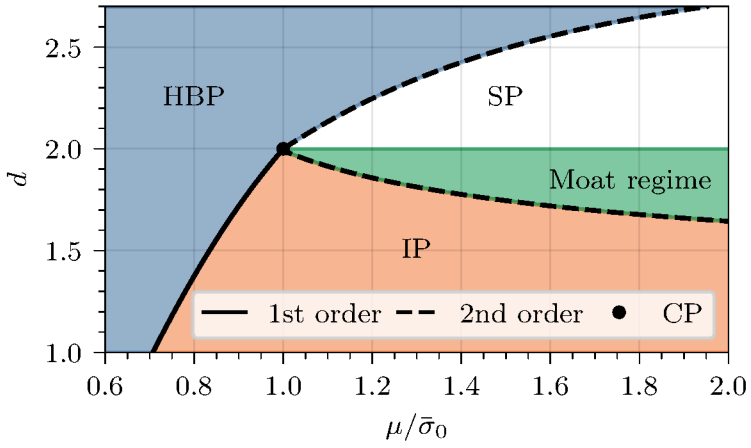

Figure 3.5: Figure 6 from Ref. [211] showing the phase diagram of the GN model in the (μ, d) plane where d is the number of spatial dimensions. The results for the boundary of the HBP was originally obtained in Ref. [252]. This figure is taken from Ref. [211] under the *Creative Commons Attribution 4.0 International license.*

available procedure neither in the mean-field approximation nor beyond to resolve this issue. Thus, while it is certainly true that an IP is observed in the QM model, the predictive power of these findings is also questionable with respect to the discussed technical issues. Since mean-field investigations are typically good starting points for the investigation of the full quantum theory using LFT, see for example Ref. [255], it is questionable how this model could be investigated with Monte Carlo algorithms if such a divergence exists in the action of the model.

3.3 DISORDERING OF INHOMOGENEOUS CHIRAL CONDENSATES

In this section, we present two mechanisms for the disordering of inhomogeneous condensates. Albeit both mechanisms are derived in different contexts and under different conditions, both rely on the appearance of Goldstone modes from symmetry breaking. The quantum fluctuations of these modes lead to the destabilization or, in terms of statistical physics, disordering of the inhomogeneous condensates. IPs break both chiral and translational symmetry spontaneously, such that there exist Goldstone modes from both of these symmetries. Goldstone modes from translational symmetry breaking are also known as phonons, i.e., as collective excitations of vibrational modes in condensed matter systems. First, we discuss the disordering from these phonons, which is also known in condensed matter models as the Landau-Peierls instability [323]. We expect the second mechanism – the disordering due to Goldstone bosons in QCD, i.e., the pions in the chiral limit, to be dominant, as explained in the corresponding subsection.

REMARKS REGARDING QUANTUM FLUCTUATIONS Independent of the specifically proposed mechanisms, there are multiple arguments and literature findings pointing out that bosonic quantum fluctuations as well as thermal fluctuations weaken ordered phases generically. In one spatial dimension, there is even a theorem forbidding the breaking of continuous symmetries at non-vanishing temperatures [222–224]. Note that this no-go theorem is, in principle, violated by the findings in Sections 3.2.1 and 3.2.2. These results are

nevertheless not inconsistent with [222–224] because the large-N_f limit is applied. This limit gives rise to the possibility of infinite range correlations as within the IP, see Ref. [224] where the circumvention of this theorem for $N_f \to \infty$ is discussed for the Thirring model [324]. Further, there is evidence from numerical computations that ordered phases get weaker when going from an approximation that suppresses bosonic fluctuations to the full quantum theory, see, e.g., the computations [52, 225–229, 255, 286, 325–327]. Thus, it is expected that phases with a non-vanishing order parameter such as the HBP and the IP are suppressed or entirely destroyed when incorporating bosonic quantum fluctuations compared to the above mean-field calculations. The two subsections below discuss two different (semi-)analytical approaches to go beyond a mean-field approximation and investigate the effect of quantum fluctuations on IPs.

3.3.1 *Disordering through phonon modes: Liquid crystal regime*

This disordering mechanism is based on the assumption of one-dimensional condensation in the NJL model. It was first published in the context of QCD-inspired models almost at the same time in Ref. [216] and Ref. [217]. The former work uses the chiral spiral, discussed in Section 3.2.2, as an ansatz function, while the latter makes use of the chiral kink ansatz from the GN model, see Section 3.2.1. Both approaches study the Ginzburg-Landau free energy in the mean-field approximation with additional contributions from phonon mode fluctuations of the form

$$\phi_j(\mathbf{x}) = \phi_{j,\text{Ansatz}}(z + u_j(\boldsymbol{x})) = \phi_{j,\text{Ansatz}}(z) + \phi'_{j,\text{Ansatz}}(z)u_j(\boldsymbol{x}) + \frac{1}{2}\phi''_{j,\text{Ansatz}}(z)u_j^2(\boldsymbol{x}) \tag{3.13}$$

where $\vec{\phi}_{\text{Ansatz}}(z)$ is the respective one-dimensional ansatz functions for the condensates in the z-direction and $\vec{u}$ are the phonon mode fluctuations. The specific realization of this ansatz is implemented differently in both works, since for the chiral kink only the σ field needs to be considered while the chiral spiral ansatz requires fluctuations in two field directions. Therefore, Ref. [216] makes use of a specific parametrization of the fluctuations. In any case, $\vec{u}$ parametrizes the fluctuations of the Goldstone modes from translational symmetry breaking in the transverse directions in an attempt to encode the contributions from these particular quantum fluctuations to the mean-field result, that features the respective inhomogeneous condensate.

In the end, quadratic fluctuations of the phonon modes $\vec{u}$ are identified as the leading contribution to the expectation value of the chiral condensate, as is expected in such a saddle-point approximation of the path integral. These low-energy fluctuations destroy the long-range ordering of the inhomogeneous condensate such that the IP is disordered and only homogeneous condensates are obtained. However, a remnant of the spatial inhomogeneities persists in a phase resembling to smectic liquid crystals [173]. This liquid crystal regime is characterized by quasi-long range order, i.e., the order parameter correlation functions $C(\boldsymbol{x})$ decay algebraically according to $C \sim |\boldsymbol{x}|^{-n}$ with $n \in \mathbb{Z}$ and an oscillatory behavior in the z-direction, in which the one-dimensional ansatz function for the IP oscillates, remains. The above described mechanism is known as the Landau-Peierls theorem in condensed matter physics [323], not to be confused with the Peierls instability in one spatial dimensions, see Section 3.2.1. It is demonstrated in both of the works that this mechanism is observed and correlation functions of the chiral condensate decay algebraically but oscillate in the direction of the ansatz function for the inhomogeneous condensate. The transition between a regime with quasi-long range order and an SP is also

called Berezinskii-Kosterlitz-Thouless transition [328–330], and first was discovered in the phase transition of the XY model, which models vector spins in two spatial dimensions.

3.3.2 *Disordering through Goldstone modes from chiral symmetry breaking: Quantum pion liquid*

In Ref. [219], it was demonstrated that there is a mechanism leading to a stronger, exponential suppression of correlation functions, using an $\mathrm{O}(N_s)$ model of N_s scalar fields in the large-N_s limit, see Section 2.5 for a brief introduction to the techniques. For $N_s = 4$, the symmetry breaking pattern of the model is isomorphic to two-flavor QCD in the chiral limit. The disordering mechanism is derived using the fluctuations of Goldstone modes from chiral symmetry breaking, i.e., from the spontaneous breaking of the $\mathrm{O}(N_s)$ symmetry in the IP from a chiral spiral ansatz.

The effective $\mathrm{O}(N_s)$ model, that features both a moat regime and an IP classically, is defined by the Lagrangian

$$L_{\text{eff}} = \frac{Z}{2}\left(\partial_j \vec{\phi}\right)^2 + \frac{1}{2M^2}\left(\sum_j \partial_j^2 \vec{\phi}\right)^2 + \frac{m^2}{2}\vec{\phi}^2 + \frac{\lambda}{4}(\vec{\phi}^2)^2 \tag{3.14}$$

in three Euclidean spatial dimension, where $\vec{\phi}$ is an N_s-component vector of scalar fields ϕ_j. This theory is treated as an effective theory for regimes with spatial modulations at intermediate temperatures and chemical potentials and the temporal direction is treated as integrated out. The bare parameters are thought of as being generated from an underlying (fermionic) theory at non-vanishing temperatures and chemical potentials, i.e., from a gradient and amplitude expansion of a fermion determinant of the form of, e.g., Eq. (2.56).

In the mean-field approximation, which amounts to solving the classical field equations for this scalar theory, three phases are observed: an SP, an HBP and, for negative Z, an IP. In the analytical work [219], the ansatz function for the IP is chosen as the chiral spiral ansatz (3.12), i.e.,

$$\vec{\phi} = \phi_0 \left(\cos(k_0 z), \sin(k_0 z), \vec{\phi}_\perp = \vec{0}\right)^T \tag{3.15}$$

where k_0 and ϕ_0 can be determined from the field equations, as in classical field theory. Thus, the theory features an LP at $m^2 = Z^2 = 0$.

Applying the limit of $N_s \to \infty$ after appropriately rescaling the couplings with N_s, one can treat the model with a constraint field approach, see Ref. [302] for a review and 2.5, allowing to also study quantum fluctuations. Again, the chiral spiral ansatz is used. Ref. [219] shows that double poles arise in the bare propagators of the transverse modes $\vec{\phi}_\perp$, which are expected to disorder the system. Then, indeed, only homogeneous ground states are observed, but, for small positive and negative Z complex-conjugate propagator poles of the scalar fields are detected. These complex-conjugate poles can be interpreted according to the discussion in Section 3.1.2 and correspond to a QπL, i.e., the bosonic propagators are an exponential times an oscillatory sine-like function. A disorder line forms where one transitions from the ordinary SP to the QπL. At this line the purely imaginary poles become degenerate and subsequently develop non-vanishing real parts, responsible for the oscillation. In Ref. [219] it is suggested that these findings are valid for all $N_s > 2$ while for $N_s = 1, 2$ an IP might be present due to the absence of Goldstone modes from chiral symmetry breaking.

The effect of bosonic quantum fluctuations and, particularly, the mechanism of disordering through Goldstone modes from chiral symmetry breaking is topic of **RO3** and **RO4** of this thesis, see Section 1.3. Therefore, the above model (3.14) is studied using LFT simulations in Chapter 7 where also the above results from Ref. [219] are discussed in more detail.

4

DETECTING SPATIALLY MODULATED REGIMES FROM THE BOSONIC TWO-POINT VERTEX FUNCTIONS

ABSTRACT AND RELATION TO THE RESEARCH OBJECTIVES In this chapter, a generic derivation of the bosonic two-point vertex functions for $d+1$-dimensional four-fermion models within the mean-field approximation is presented. We demonstrate that the bosonic two-point vertex functions naturally are obtained in the stability analysis of homogeneous ground states against inhomogeneous fluctuations. Thus, this computation serves as a tool for the detection of IPs. The advantages and drawbacks of the stability analysis itself are also discussed. Moreover, we discuss how the bosonic two-point vertex functions give direct insight in the properties of the bosonic two-point correlation functions in the case of stable homogeneous ground states. Since this is a chapter focused on methodology, none of the **RO**s defined in Section 1.3 are addressed directly. However, the presented computations are applied in Chapters 5 and 6 such that there is an interplay with **RO1**, **RO2** and **RO5**. Reading this chapter is not mandatory for understanding the key findings of this thesis. However, these technical aspects of the computations can be helpful for a in-depth study of Chapters 5 and 6.

DISCLOSURE Computations similar to the presented one can be found in Ref. [1] and Ref. [241] on the example of the $1+1$-dimensional and $2+1$-dimensional GN model or Ref. [2] for generic $2+1$-dimensional four-fermion models. Moreover, we also refer to analyses [211, 212] of the bosonic two-point vertex function in the GN model in non-integer spatial dimensions. The stability analysis based on the bosonic two-point vertex function of the $1+1$-dimensional GN model is published in Ref. [1], while the $1+1$-dimensional chiral GN model is studied in Ref. [4]. The presentation of the findings in this chapter differs from those two publications, but the ideas, computations and figures are taken from the respective publications. Thus, they are attributed in similar shares to me and the respective co-authors A. Koenigstein, L. Pannullo, S. Rechenberger, and M. Steil. The figures in Section 4.2 and Section 4.3 are produced by L. Pannullo and A. Koenigstein, respectively; the underlying data, however, are crosschecked by multiple of the respective authors, and also by myself.

OUTLINE In Section 4.1, the bosonic two-point vertex functions in the mean-field approximation is derived for a generic $d+1$-dimensional four-fermion model using homogeneous auxiliary fields as background fields. Then, the appearance of the bosonic two-point vertex functions in the stability analysis of homogeneous condensates is discussed. Based on this method, we present benchmark computations in the $1+1$-dimensional GN model in Section 4.2 and in the $1+1$-dimensional chiral GN model in Section 4.3, which are both four-fermion models with analytically known phase diagrams in the (μ, T) plane. In

Section 4.4, we discuss how the QπL can be detected using the bosonic two-point vertex function in an analysis related to the one presented in Section 3.1.2.

4.1 THE BOSONIC TWO-POINT VERTEX FUNCTIONS IN FOUR-FERMION MODELS

To provide a rather general derivation of the bosonic two-point vertex function, we use a generic four-fermion model with N_f four-component spinor fields $\bar{\psi}$ and ψ, as defined in Eq. (2.32). We follow Section 2.3 and perform a Hubbard-Stratonovich transformation such that fermion fields appear only in a bilinear of the form $\bar{\psi}\mathrm{Q}\psi$. Then, we integrate over the fermionic degrees of freedom in the path integral in order to obtain the partition function

$$Z_{\mathrm{Bos}} \sim \int \prod_j \mathscr{D}\phi_j \, \mathrm{e}^{-\mathcal{S}_{\mathrm{eff}}[\vec{\phi}]} \tag{4.1}$$

with the effective action

$$\mathcal{S}_{\mathrm{eff}}[\vec{\phi}] = N_f \left[\int \mathrm{d}^{d+1}x \sum_j \frac{\phi_j^2}{2\lambda_j} - \ln \mathrm{Det}\beta\mathrm{Q} \right], \tag{4.2}$$

where the imaginary time direction is restricted to a finite extent , $x_{d+1} = \tau \in [0, \beta)$ and the fields respect (anti-)periodic boundary conditions, see Section 2.1 for context on QFT in thermal equilibrium. We defined in Eq. (4.2) the Dirac operator

$$\mathrm{Q}[\vec{\phi}] = \not{\partial} + \gamma_{d+1}\mu + \sum_j c_j \phi_j \tag{4.3}$$

containing the Yukawa term $\sum_j c_j\phi_j$ with the coupling matrices c_j and the auxiliary bosonic fields ϕ_j. Moreover, λ_j are the coupling constants of the original four-fermion interactions. The sum over j goes over a set of interaction vertices corresponding to the original four-fermion interaction and, for the first part of this derivation, is unspecified. In Chapter 5, two examples for sets of the matrices c_j and, through the Ward identities given in Eq. (2.43), also the auxiliary bosonic fields ϕ_j are presented and studied. For the rest of this chapter, we use $\lambda_j \equiv \lambda$ as this allows to obtain rotational symmetries in the auxiliary field space. These symmetries mostly correspond to chiral symmetry transformations in the fermionic sector, see Appendix B and Section 3.2.2 for examples.

4.1.1 *Computation of the bosonic two-point vertex functions with homogeneous background fields in the mean-field approximation*

The effective action is a functional of $\vec{\phi}(x)$. In the mean-field approximation, one approximates the partition function by the global minimum with respect to $\vec{\phi}$. Since $\Gamma[\vec{\phi}] = \mathcal{S}_{\mathrm{eff}}[\vec{\phi}]$ in the mean-field approximation, cf. Section 2.4.4, one determines $\vec{\Phi}(x)$ by minimizing $\mathcal{S}_{\mathrm{eff}}[\phi_j]$. The computation of observables amounts to evaluating them on the global minimum $\vec{\Phi}(x)$ of the effective action, see Section 2.4. The global minimum is determined by the extremal criterion, also called gap equation

$$\frac{\delta\Gamma[\vec{\phi}]}{\delta\phi_j} = \frac{\delta\mathcal{S}_{\mathrm{eff}}[\vec{\phi}]}{\delta\phi_j} = 0, \tag{4.4}$$

where the functional derivative is used, and reinsertion of all solutions of Eq. (4.4) back into the effective action. The bosonic two-point vertex functions

$$\left.\frac{\delta^2\Gamma[\vec{\phi}]}{\delta\phi_j\delta\phi_k}\right|_{\vec{\phi}=\vec{\Phi}} = \left(\langle\phi_j\phi_k\rangle_c\right)^{-1}, \tag{4.5}$$

where $\langle\phi_j\phi_k\rangle_c$ are the corresponding connected two-point correlation functions in the absence of external sources, also called bosonic two-point correlation functions in this work, see Section 2.2 for the respective definition.

In principle, Eq. (4.5) can directly be computed by performing the second functional derivative with respect to $\vec{\phi}$ and evaluating it on $\vec{\phi} = \vec{\Phi}(x)$. However, determining $\vec{\Phi}(x)$ can become arbitrarily complicated. First of all, the effective action (4.2) requires the computation of the fermionic determinant which can become very involved or (currently) impossible when general shapes of inhomogeneous fields $\vec{\phi}(x)$ are allowed. One can approach this problem using LFT techniques, see, e.g., Refs. [8, 241, 331–333], which requires solving a high-dimensional optimization problem (see Ref. [334] for relevant algorithms) including continuum and infinite-volume limits of non-trivial inhomogeneous modulations. In general, this is a non-trivial, (computer) time consuming task which can usually only be performed in simple approximations of the quantum effective action. A particular setup using mean-field LFT techniques can be and already was applied also by the author [7, 10, 241] but we will later argue that the stability analysis is a more efficient tool to study IPs in model investigations. Even if a (semi)-analytical approach for computing the determinant was available[1], finding global minima of such complicated functionals with respect to arbitrary functions is generically a highly non-trivial task [335, 336].

For similar reasons, evaluating bosonic two-point vertex functions as a curvature of the effective action which is a function of arbitrary inhomogeneous expectation values is not straightforward if one does not make a simple enough ansatz for the inhomogeneous fields, see, e.g., Ref. [337]. This is caused by the necessary, yet complicated evaluation of functional derivatives, even if a form of Γ is found through solving the functional optimization problem.

HOMOGENEOUS BACKGROUND FIELDS A common approach in mean-field model computations, see, e.g., Refs. [99, 141, 249, 252, 316, 338–340] is to assume homogeneous condensation of the bosonic fields, i.e., apply the restriction $\vec{\phi}(\boldsymbol{x}) = \vec{\bar{\phi}} = \text{const.}$. Then, one can express the $\ln\mathrm{Det}$-term in $\mathcal{S}_{\text{eff}}$ as an integral over the d-dimensional spatial momentum space through standard thermal field theory techniques, see for example Chapter 2.5 of Ref. [64] or Chapter 3.7 of Ref. [285] for details. Assuming that the Yukawa-type interactions between the fermion fields and the bosonic fields can be rewritten as a mass term contribution after performing the discrete determinant in Dirac space, one obtains an expression for the effective action where only a momentum integral needs to be performed, see Eq. (2.56) and the discussion in Section 2.4.4. See Appendix C for a calculation in the $2+1$-dimensional GN model where only a single scalar field is present. Using this homogeneous background in the fermion determinant, one finds

$$\Gamma^{(2)}_{\phi_j,\phi_k} = \left.\frac{\partial^2\mathcal{S}_{\text{eff}}}{\partial\bar{\phi}_j\partial\bar{\phi}_k}\right|_{\vec{\phi}=\vec{\bar{\phi}}} \propto \mathrm{Tr}\left(c_j\bar{\mathrm{Q}}^{-1}c_k\bar{\mathrm{Q}}^{-1}\right), \tag{4.6}$$

1 This is the case when one can express the fermion determinant as a low-dimensional integral that can be easily solved numerically. This is an easy task when restricting the bosonic fields to be homogeneous, see Appendix C.

where the proportionality to the inverse of the homogeneous Dirac operator $\bar{\mathrm{Q}} = \mathrm{Q}[\vec{\bar{\phi}}]$ should be understood symbolically at this point. In order to really invert the Dirac structure and perform the functional trace, one typically first performs a Fourier transformation. Further details of the correct mathematical treatment will be discussed in Section 4.1.3. In summary, one evaluates the bosonic two-point vertex functions by performing the second functional derivative of the effective action assuming using homogeneous fields as expansion points. Based on this assumption the functional derivative is equivalent to partial differentiation with respect to the variables $\bar{\phi}_j$, which can be performed in a straightforward manner.

Since the bosonic two-point vertex functions $\Gamma^{(2)}_{\phi_j,\phi_k}$ are the inverse of the bosonic two-point correlation functions $\langle \phi_j \phi_k \rangle_c$, they yield direct information about the bosonic correlations in the system. Note that these correlations solely stem from the fermionic interactions and the bosonic fields are a priori auxiliary fields, i.e., their quantum fluctuations are not included here. In Section 2.3.2, we showed that one can extract information about the fermionic four-point functions from the bosonic two-point vertex functions, cf. Eq. (2.46). We note that the information contained in $\Gamma^{(2)}_{\phi_j,\phi_k}$ is only valid when the global minimum of the effective action is really homogeneous. Otherwise, the computation of $\Gamma^{(2)}$ is based on the wrong expansion point. As we will see in the following, one can directly extract from the bosonic two-point vertex functions whether this is the case.

4.1.2 *Stability analysis and its relation to the bosonic two-point vertex functions*

In general, the assumption of homogeneous background fields is not justified, as spatially dependent condensates can be energetically favored, i.e., the global minimum might be given by $\vec{\phi} = \vec{\Phi}(\boldsymbol{x})$ leading to a lower effective action compared to the homogeneous minimum $\vec{\phi} = \vec{\bar{\Phi}}$ (the minimum when restricting to $\vec{\phi}(\boldsymbol{x}) = \vec{\bar{\phi}} = \text{const.}$). As discussed above, it is difficult to compute the effective action for arbitrary inhomogeneous fields $\vec{\phi}(\boldsymbol{x})$ since there exists no general procedure to diagonalize the Dirac operator Q (4.3). Also, the minimization of a functional with respect to arbitrary functions $\vec{\phi}(\boldsymbol{x})$ is a difficult optimization problem, that has not consistently been solved in the literature [335, 336]. Thus, one refrains to simple ansatz functions with few parameters, in which the effective action can be minimized, ansatz-free minimization using LFT techniques or, alternatively, one performs a so-called stability analysis, which is the strategy adopted for parts of this thesis. The approach of analyzing the stability of homogeneous ground states against inhomogeneous perturbations to detect IPs has been followed in some recent model investigations, for example the works [1, 2, 4, 10, 207, 211, 212, 241, 337, 341–343].[2] A discussion and comparison of the stability analysis with other methods can be found at the end of this subsection.

CENTRAL IDEA The basic concept of the stability analysis is to apply a perturbation to the homogeneous fields $\vec{\bar{\phi}}$ (later to be set to the homogeneous minimum $\vec{\bar{\Phi}}$ of the effective potential) by functions $\delta\phi_j(x)$ of infinitesimal amplitude but arbitrary functional dependence, i.e.,

$$\vec{\phi}(x) = \vec{\bar{\phi}} + \delta\vec{\phi}(x). \tag{4.7}$$

2 Fun fact: Back in the eighties, the community did not expect inhomogeneous condensates to appear in nuclear matter mean-field models. Thus, the appearance of the instability is interpreted in Ref. [207] as a limitation of the validity of relativistic mean-field models for nuclear matter.

Then, one performs an expansion of the effective action in powers of the perturbations $\delta\phi_j$ and determines the sign of the non-vanishing leading-order coefficients in this expansion. It turns out that when choosing $\vec{\phi}$ as an extremum of the effective action, e.g., as $\vec{\phi} = \vec{\bar{\Phi}}$, the first-order terms in the expansion vanish and the leading order is given by the second-order terms. Thus, one can determine the stability of the homogeneous minimum $\vec{\bar{\Phi}}$ by computing the curvature of the effective action at the minimum with respect to the perturbations $\delta\phi_j$. In order to do so, the Hessian matrix in the space of $\delta\vec{\phi}$ needs to be computed and diagonalized to determine the sign of the eigenvalues. If one of the eigenvalues is negative, the homogeneous condensate is unstable against the corresponding perturbation. Such an instability suggests that an inhomogeneous condensate $\vec{\Phi}(\boldsymbol{x})$, whose precise spatial dependence is not determined in this procedure, is energetically favored over the homogeneous $\vec{\bar{\phi}}$. Note that a negative eigenvalue of the Hessian does not imply that all components of the field vector $\vec{\Phi}(\boldsymbol{x})$ have to depend on $\boldsymbol{x}$, but at least one of the components.

Since the Hessian matrix is evaluated on the homogeneous background $\vec{\phi} = \vec{\bar{\phi}}$, it can be computed with standard techniques from thermal field theory, a major advantage of this approach. However, the existence of a negative eigenvalue of the Hessian matrix $H_{\phi_j\phi_k}$ is a sufficient but not necessary condition for the existence of an inhomogeneous condensate when H is evaluated for $\vec{\phi} = \vec{\bar{\Phi}}$. In general, an IP can still exist even if no instability is observed in the stability analysis. This is the case when there is an energy barrier between the local homogeneous minimum $\vec{\bar{\Phi}}$ and the inhomogeneous, global minimum $\vec{\Phi}(\boldsymbol{x})$. However, to the author's knowledge, no phase diagram has been found where an IP does not at least feature a (possibly smaller) *region of instability* in the respective phase diagram – a region where the homogeneous minimum of the effective action is instable with respect to inhomogeneous perturbations. Moreover, all IPs so far observed in the literature are connected to the SP by a second-order phase transition which can always be detected by a stability analysis of the SP. However, when studying the same phase diagram with respect to general inhomogeneous condensates using either ansatz functions or LFT technigues, one finds that these regions of instability are either equivalent to an IP or enclosed by a larger IP, see, e.g., Refs. [5, 7, 8, 241, 344]. Further discussion about the applicability of the stability analysis can be found below.

One can perform a generic expansion of the quantum effective action in terms of inhomogeneous perturbations $\delta\vec{\phi}$ is given by

$$\Gamma[\vec{\bar{\phi}} + \delta\vec{\phi}(\boldsymbol{x})] = \Gamma[\vec{\bar{\phi}}] + \frac{\delta\Gamma[\vec{\bar{\phi}}]}{\delta\phi_j(x)}\delta\phi_j(\boldsymbol{x}) + \frac{1}{2}\frac{\delta^2\Gamma[\vec{\bar{\phi}}]}{\delta\phi_j(\boldsymbol{x})\delta\phi_k(\boldsymbol{y})}\delta\phi_j(\boldsymbol{x})\delta\phi_k(\boldsymbol{y}) + \ldots, \tag{4.8}$$

where in the mean-field approximation this expansion can also be formulated by replacing Γ with $\mathcal{S}_{\text{eff}}$. The first-order term is supposed to vanish at $\vec{\bar{\phi}} = \vec{\bar{\Phi}}$ due to the gap equation $\delta\mathcal{S}_{\text{eff}}/\delta\phi_j = 0$. The coefficient of the second-order term is the Hessian matrix of the effective action evaluated at its minimum. Using the assumption of the homogeneous expansion point $\vec{\bar{\phi}}$ yields

$$H_{\phi_j\phi_k} = \left.\frac{\delta^2\mathcal{S}_{\text{eff}}[\vec{\phi}]}{\delta\phi_j(\boldsymbol{x})\delta\phi_k(\boldsymbol{y})}\right|_{\vec{\phi}=\vec{\bar{\Phi}}} = \left.\frac{\partial^2\mathcal{S}_{\text{eff}}[\vec{\bar{\phi}}]}{\partial\bar{\phi}_j\partial\bar{\phi}_k}\right|_{\vec{\bar{\phi}}=\vec{\bar{\Phi}}} = \Gamma^{(2)}_{\phi_j,\phi_k}, \tag{4.9}$$

where we define the bosonic two-point vertex functions in the mean-field approximation through derivatives of the effective action evaluated at the homogeneous minimum (again, identifying $\mathcal{S}_{\text{eff}}[\vec{\phi}] = \Gamma[\vec{\phi}]$). Note that the last identification implies that the ground state is really given by the homogeneous field values and takes advantage of the mean-field

approximation, see Section 4.1.1 for a more detailed discussion. In case of an instability (or an inhomogeneous, global minimum of the effective potential, in general), also the exact bosonic two-point vertex functions are not given by the bosonic two-point vertex functions at the homogeneous minimum. In Section 4.1.3, we derive $H_{\phi_j\phi_k}$ for the generic four-fermion model (2.39) and also show how to compute negative eigenvalues of H by Fourier transformation of the Dirac operator and $\delta\vec{\phi}(\boldsymbol{x})$ as well as diagonalizing the Hessian matrix in momentum space and field space.

STABILITY ANALYSIS BEYOND MEAN-FIELD In recent efforts [343] the bosonic two-point vertex functions were used to detect instabilities of the symmetric phase towards an IP in the quark-meson model using the functional renormalization group within the local potential approximation to incorporate bosonic quantum fluctuations beyond the mean-field approximation. Moreover, instabilities of the symmetric solution against inhomogeneous condensation were detected in a Dyson-Schwinger study of QCD using a simple model for the quark-gluon interaction [213–215], where an expansion about a homogeneous quark propagator was necessary due to the non-locality of the interaction. One has to note that these instabilities are found in the left spinodal region where the symmetric phase is not preferred over a non-vanishing chiral condensate such that statements about the existence of an IP are not possible.

Note further that the definition of the bosonic two-point vertex functions (4.5) (see Section 2.2.3 for further details) does not involve any kind of approximation. As obvious from Eq. (4.5), the bosonic two-point vertex functions provide all important information about the two-point correlations of bosonic fields in the system. Thus, they are in general interesting observables in all kind of systems and frameworks where bosonization techniques are applied, or dynamical boson fields are present. However, for non-local interaction as in, e.g., QCD the approach for the search of IPs has to be modified, since translational symmetry breaking allows for non-local perturbations of second order. To account for this, an approach based on the two-particle irreducible effective action can be followed [213–215].

GENERAL REMARKS REGARDING THE STABILITY ANALYSIS The idea of analyzing the stability of a homogeneous ground state against inhomogeneous fluctuations is a powerful, yet versatile tool to study the existence of IPs in a model. The general approach can be applied to many theories, in different theoretical frameworks or approximations independent of the space-time dimension. The main reason is that the generic expansion (4.8) is also applicable on the level of the quantum effective action (2.26).

Of course, one has to pay a price for the versatility of the stability analysis such that one, in general, lacks information about the form of the inhomogeneous condensate in case an IP is realized. Also, as discussed above, there are scenarios where an IP is not detected by the stability analysis although an inhomogeneous ground state would be preferred. Both of these drawbacks can be overcome by direct determination of the ground state which in turn is less versatile; often it requires either usage of ansatz functions or LFT techniques. The former method again restricts the form of the inhomogenoeus condensate and introduce a bias to the investigation, the latter is computationally rather time-consuming and involved due to continuum and infinite volume limits that have to be performed on spatially inhomogeneous observables. Both of these alternative methods are only applicable depending on the respective theory and approximation used and can typically be used in a less general manner. For example, a mean-field investigation of the phase diagram of various $2+1$-dimensional four-fermion models with direct numerical minimization using

LFT would be incredibly costly in terms of computing time, while we analyze all kind of local four-fermion models simultaneously with the stability analysis in Chapter 5. This is due to the enormous computational cost of the direct minimization of the effective action for inhomogeneous fields, which also does not guarantee finding the global minimum due to the high dimensionality of the optimization problem, see Refs. [7, 241], compared to the (semi)-analytical computation of the Hessian matrix in the mean-field approximation with standard techniques in thermal field theory.

4.1.3 *Stability analysis in a generic four-fermion model*

In this subsection, we provide a generic algorithm for the computation of the Hessian matrix $H_{\phi_j\phi_k}$ (4.9) using the prototype of a four-fermion model (2.32), rewritten into the effective, bosonized action (4.2) as described in Section 2.3, in the mean-field approximation. One can relatively easily generalize this algorithm to Yukawa models with local interaction terms, see Ref. [2] or Chapter 5.

First, the expansion $\phi_j(\boldsymbol{x}) = \bar{\phi}_j + \delta\phi_j(\boldsymbol{x})$ is inserted into the effective action (4.2) of the model. Then, the effective action is expanded in powers of the perturbations $\delta\phi_j$ of infinitesimal amplitude. Therefore, we split the Dirac operator

$$\mathrm{Q} = \left(\not{\partial} + \gamma_{d+1}\mu + \sum_j c_j\bar{\phi}_j\right) + \sum_k c_k\delta\phi_k(\boldsymbol{x}) = \bar{\mathrm{Q}} + \Delta\mathrm{Q} \tag{4.10}$$

into a homogeneous part $\bar{\mathrm{Q}}$ and a part $\Delta\mathrm{Q} = \sum_k c_k\delta\phi_k(\boldsymbol{x})$ containing the inhomogeneous perturbations. This allows us to express $\ln\mathrm{Det}\beta\mathrm{Q}$ as

$$\ln\mathrm{Det}\beta\mathrm{Q} = \mathrm{Tr}\ln\left[\beta\bar{\mathrm{Q}}\left(1 + \bar{\mathrm{Q}}^{-1}\Delta\mathrm{Q}\right)\right] \tag{4.11}$$

and to expand the logarithm in powers of the small value $\Delta\mathrm{Q}$, i.e.,

$$\ln\mathrm{Det}\beta\mathrm{Q} = \mathrm{Tr}\ln\beta\bar{\mathrm{Q}} - \sum_{n=1}^{\infty}\frac{1}{n}\mathrm{Tr}\left(-\Delta\mathrm{Q}\,\bar{\mathrm{Q}}^{-1}\right)^n. \tag{4.12}$$

Inserting Eq. (4.12) into the effective action (4.2) allows to rewrite $\mathcal{S}_{\mathrm{eff}} = \sum_{n=0}^{\infty}\mathcal{S}_{\mathrm{eff}}^{(n)}$ where $\mathcal{S}_{\mathrm{eff}}^{(n)}$ contains the n-th order terms in $\delta\phi_j$. One finds for the leading three terms

$$\frac{\mathcal{S}_{\mathrm{eff}}^{(0)}}{N_f} = \beta V\sum_j\frac{\bar{\phi}_j^2}{2\lambda_j} - \mathrm{Tr}\ln\beta\bar{\mathrm{Q}}\,, \tag{4.13}$$

$$\frac{\mathcal{S}_{\mathrm{eff}}^{(1)}}{N_f} = \beta\sum_j\frac{\phi_j}{\lambda_j}\int\mathrm{d}^dx\delta\phi_j(\boldsymbol{x}) - \mathrm{Tr}\left(\Delta\mathrm{Q}\,\bar{\mathrm{Q}}^{-1}\right)\,, \tag{4.14}$$

$$\frac{\mathcal{S}_{\mathrm{eff}}^{(2)}}{N_f} = \frac{\beta}{2\lambda_j}\int\mathrm{d}^2x\delta\phi_j^2(\boldsymbol{x}) + \frac{1}{2}\mathrm{Tr}\left(\Delta\mathrm{Q}\,\bar{\mathrm{Q}}^{-1}\Delta\mathrm{Q}\,\bar{\mathrm{Q}}^{-1}\right). \tag{4.15}$$

The zeroth order term $\mathcal{S}_{\mathrm{eff}}^{(0)}$ is proportional to the homogeneous effective potential, see Section 2.4.4, and is minimized by $\vec{\bar{\phi}} = \vec{\bar{\Phi}}$ by definition.

As $\delta\phi_j$ are infinitesimal perturbations, it is reasonable to only consider the first and second-order terms in the expansion as these will be dominating. Therefore, we need to evaluate the functional traces

$$\mathrm{Tr}\left(\Delta\mathrm{Q}\bar{\mathrm{Q}}^{-1}\right)^n = \int\prod_{j=1}^{n}\mathrm{d}^{d+1}x_j\,\mathrm{tr}\left(\Delta\mathrm{Q}\,(x_1)\,\bar{\mathrm{Q}}^{-1}\,(x_1,x_2)\ldots\Delta\mathrm{Q}\,(x_n)\,\bar{\mathrm{Q}}^{-1}\,(x_n,x_1)\right) \tag{4.16}$$

where tr denotes the trace over the discrete degrees of freedom of the Dirac operator, whose number is equivalent to the dimensionality of the matrices c_j, and $x_j = (\boldsymbol{x}_j, \tau_j)$ represents the spacetime coordinates. As the Dirac operator in position space

$$\bar{\mathrm{Q}} = \partial\!\!\!/_x + \gamma_{d+1}\mu + \sum_j c_j \bar{\phi}_j \tag{4.17}$$

is complicated to evaluate and to invert, it is instructive to perform a Fourier transformation of the whole functional trace. The Fourier representation of (the inverse of) the homogeneous Dirac operator is obtained by Fourier-transformation of the respective fermion fields according to Eq. (2.13).

FOURIER REPRESENTATION OF THE INVERSE DIRAC OPERATOR In four-fermion models the Fourier representation of the inverse Dirac operator, i.e., the bare fermion propagator in momentum space, is typically given by

$$\tilde{\bar{\mathrm{Q}}}^{-1}(p) = \frac{-\mathrm{i}\gamma_\nu \left(p_\nu - \mathrm{i}\mu\delta_{\nu,d+1}\right) + \sum_k c_k^\star \bar{\phi}_k}{\tilde{p}^2 + M^2(\bar{\phi}_k^2)} \tag{4.18}$$

where M^2 is a mass generated by the homogeneous fields $\bar{\phi}_k$ and the matrices in Dirac space $c_k^\star$ are proportional to c_k. Those two expressions depend on the choice of the matrices c_j (see Eq. (5.2) for an example of a set of interaction matrices c_j). For many models $M^2 = \vec{\bar{\phi}}^2$ but this must not necessarily be the case, e.g., when including the vertex $c_j = \mathrm{i}\gamma_4\gamma_5$ in two spatial dimensions, see Eq. (5.9). Moreover, one typically finds $\tilde{p} = p - (\mathbf{0}, \mathrm{i}\mu)$ at non-vanishing fermion chemical potential. However, additional modifications to the temporal component of the four-momentum p_{d+1} can stem from condensation of vector fields with, e.g., $c_j \sim \gamma_{d+1}$. As we refrain from specifying the matrices c_j in this general computation, no specific form of $\tilde{\bar{\mathrm{Q}}}^{-1}(p)$ is used. Note however that the assumption of $\tilde{\bar{\mathrm{Q}}}^{-1}$ being diagonal in momentum space[3] is fulfilled for all theories studied in this thesis.

Using the Fourier representation of the Dirac operator one finds for the first-order term (4.14)

$$\frac{\mathcal{S}_{\mathrm{eff}}^{(1)}}{N_f} = \beta \sum_j \left(\int \mathrm{d}^d x \delta\phi_j(\boldsymbol{x}) \right) \left[\frac{\phi_j}{\lambda_j} - T \sum_{n=-\infty}^{\infty} \int \frac{\mathrm{d}^d p}{(2\pi)^d} \mathrm{tr} \left(\tilde{\bar{\mathrm{Q}}}^{-1}(p)\, c_j \right) \right] \tag{4.19}$$

which is proportional to the gap equations in a homogeneous background field

$$\frac{1}{N_f} \frac{\partial \mathcal{S}_{\mathrm{eff}}^{(0)}}{\partial \bar{\phi}_k} \bigg|_{\vec{\phi}=\vec{\phi}'} = \beta \left[\int \mathrm{d}^d x \right] \left[\frac{\bar{\phi}_k}{\lambda_k} - T \sum_{n=-\infty}^{\infty} \int \frac{\mathrm{d}^d p}{(2\pi)^d} \mathrm{tr} \left(\tilde{\bar{\mathrm{Q}}}^{-1}(p)\, c_k \right) \right] \bigg|_{\vec{\phi}=\vec{\phi}'} = 0 \tag{4.20}$$

where $\vec{\phi}'$ is a homogeneous field configuration that is a solution of the gap equations. Note that, most importantly, $\vec{\bar{\Phi}}$ also solves the gap equations. Therefore, the first-order term vanishes at any homogeneous field that solves the gap equations which is the case for $\vec{\phi} = \vec{\bar{\Phi}}$. If these expansion points are used in this derivation, the second-order term is the first non-zero correction. Using the Fourier representation of the inhomogeneous perturbations

$$\delta\phi_j(\boldsymbol{x}) = \int \frac{\mathrm{d}^d q}{(2\pi)^d} \mathrm{e}^{\mathrm{i}\boldsymbol{q}\boldsymbol{x}} \delta\tilde{\phi}_j(\boldsymbol{q}) \tag{4.21}$$

3 This means that the inverse Dirac operator only depends on one momentum variable p that represents the momentum of the bosonic field and not on two external momenta.

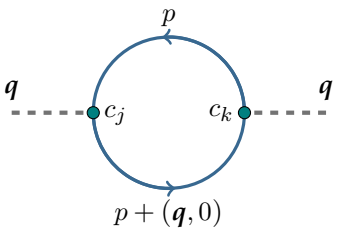

Figure 4.1: Graphical representation of the fermion loop contribution in $\mathcal{S}_{\text{eff}}^{(2)}$ according to Eq. (4.23) and Eq. (4.24). The blue lines represents the bare fermion propagator $\tilde{\bar{\mathrm{Q}}}^{-1}$, the gray dashed lines represent the external, bosonic legs of the auxiliary fields ϕ_j, and the teal circles represents the bare interaction vertices c_j. In the expression for the bosonic two-point vertex functions $\Gamma^{(2)}_{\phi_j,\phi_k}$, the bosonic legs are amputated.

we find for the trace in $\mathcal{S}_{\text{eff}}^{(2)}$

$$\begin{aligned} &\mathrm{Tr}\left[\bar{\mathrm{Q}}^{-1}\Delta\mathrm{Q}\bar{\mathrm{Q}}^{-1}\Delta\mathrm{Q}\right] = \\ &= \int \frac{\mathrm{d}^d p}{(2\pi)^d}\Bigg[\sum_{j,k}\delta\tilde{\phi}_j(-\boldsymbol{q})\,\delta\tilde{\phi}_k(\boldsymbol{q})\left(\sum_n \int \frac{\mathrm{d}^d p}{(2\pi)^d}\mathrm{tr}\left(\tilde{\bar{\mathrm{Q}}}^{-1}\left(p+(0,\boldsymbol{q})\right)c_j\tilde{\bar{\mathrm{Q}}}^{-1}\left(p\right)c_k\right)\right)\Bigg], \end{aligned} \tag{4.22}$$

where $q = |\boldsymbol{q}|$. Inserting this into Eq. (4.15) one obtains

$$\frac{\mathcal{S}_{\text{eff}}^{(2)}}{N_f} = \frac{\beta}{2}\int \frac{\mathrm{d}^d q}{(2\pi)^d}\sum_{j,k}\delta\tilde{\phi}_j(-\boldsymbol{q})\delta\tilde{\phi}_k(\boldsymbol{q})\Gamma^{(2)}_{\phi_j,\phi_k}\left(\vec{\tilde{\phi}},\mu,T,\boldsymbol{q}\right) \tag{4.23}$$

Thereby,

$$\Gamma^{(2)}_{\phi_j,\phi_k}\left(\vec{\tilde{\phi}},\mu,T,\boldsymbol{q}\right) = \frac{\delta_{j,k}}{\lambda_j} + T\sum_n \int \frac{\mathrm{d}^d p}{(2\pi)^d}\mathrm{tr}\left(\tilde{\bar{\mathrm{Q}}}^{-1}\left(p+(\boldsymbol{q},0)\right)c_j\tilde{\bar{\mathrm{Q}}}^{-1}\left(p\right)c_k\right) \tag{4.24}$$

are the the bosonic two-point vertex functions in the mean-field approximation of the generic four-fermion model. The trace over two fermion propagators in this expression can graphically be represented as a fermionic loop with two bare fermion-boson vertices, see Fig. 4.1. The appearance of $\Gamma^{(2)}_{\phi_j,\phi_k}$ in Eq. (4.23) can be anticipated already from the discussion in Section 4.1.2, where the bosonic two-point vertex functions appear in the second-order term in perturbations of the effective action. This is due to the fact that the bosonic two-point vertex functions are proportional to the curvature of the quantum effective action.

Further evaluation of this term requires specifying the interaction matrices c_j and finding the correct expression for $\tilde{\bar{\mathrm{Q}}}^{-1}$, which in all computations in this work is similar to Eq. (4.18) with slight differences between the models in the form of M^2, $c_j^\star$ and $\tilde{p}$. In the following subsections, we will show how this expression is evaluated for the $1+1$-dimensional GN model and the $1+1$-dimensional chiral GN model.

DIAGONALIZING THE HESSIAN MATRIX One can directly use the obtained $\Gamma^{(2)}_{\phi_j,\phi_k}$ to determine the stability of the homogeneous phase against inhomogeneous fluctuations. As derived above, the bosonic two-point vertex functions appear as the Hessian matrix elements in field space. Since the expression is already diagonalized in momentum space

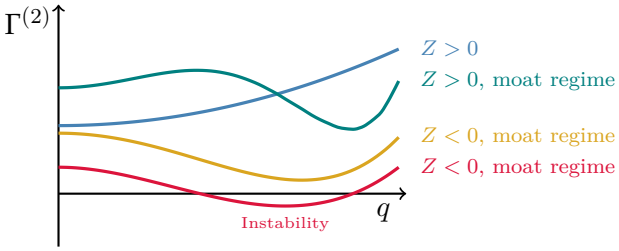

Figure 4.2: Sketches of the bosonic two-point vertex function $\Gamma^{(2)}$ associated with the sign of the bosonic wave function renormalization Z, illustrating its behavior in different cases. The red curve represents the case where the homogeneous ground state is instable against an inhomogeneous condensate such that an IP is detected. The teal and yellow curves represent functional shapes of the bosonic two-point vertex function represented in the moat regime. A negative sign of Z is only present for the yellow curve such that Eq. (4.27) fails to detect the moat regime in a case similar to the teal curve.

(as the integrand only depends on one specific integration variable q), all that is left is to find a basis transformation $\delta\phi_j \to \delta\varphi_j = b_{jk}\delta\phi_k$ where the Hessian matrix $\Gamma^{(2)}_{\phi_j,\phi_k}$ is diagonal. Often, the diagonalization is possible analytically. Since by definition of φ_j the corresponding bosonic two-point vertex functions are diagonal in this basis, i.e., $\Gamma^{(2)}_{\varphi_j,\varphi_k} \sim \delta_{j,k}$, we use the abbreviation $\Gamma^{(2)}_{\varphi_j} = \Gamma^{(2)}_{\varphi_j,\varphi_j}$ for the eigenvalues of the Hessian matrix or, equivalently, the diagonal elements of the Hessian in this basis. We provide a summary of the whole stability analysis:

1. Computation of the homogeneous minimum $\vec{\bar{\Phi}}$ of the effective potential or, equivalently, of $\mathcal{S}_{\text{eff}}[\vec{\phi}]$.

2. Performing an expansion about this minimum $\vec{\phi} = \vec{\bar{\Phi}} + \delta\vec{\phi}(\boldsymbol{x})$ and computation of the Hessian matrix / bosonic two-point vertex functions $\Gamma^{(2)}_{\phi_j,\phi_k}(\vec{\bar{\phi}}, \mu, T, q)$ of the form (4.23), where $q = |\boldsymbol{q}|$ is the absolute value of the spatial momentum of the Fourier mode $\delta\tilde{\phi}_j(\boldsymbol{q})$ of the inhomogeneous perturbation.

3. Determination of the field basis φ_j that diagonalizes the Hessian matrix $\Gamma^{(2)}$ (often analytically possible and sometimes even $\varphi_j = \phi_j$).[4]

4. Searching for negative values of $\Gamma^{(2)}_{\varphi_j}(\vec{\bar{\varphi}}, \mu, T, q)$ at $q \neq 0$ and $\vec{\bar{\phi}} = \vec{\bar{\Phi}}$ which is evidence for the existence of an IP. A possible shape for $\Gamma^{(2)}_{\varphi_j}$ as a function of q, where an instability can be found, is depicted in Fig. 4.2 by the red curve.

4 In Chapter 6 we study a model with both vector and scalar four-fermion interactions which requires the numerical diagonalization of $\Gamma^{(2)}_{\phi_j,\phi_k}$.

4.1.4 *Extracting the bosonic wave function renormalization*

The bosonic wave function renormalizationion Z_ϕ of a bosonic field ϕ is formally defined as the second-order coefficient of the bosonic two-point vertex function $\Gamma^{(2)}_\phi(q)$ in a Taylor expansion around $q = 0$, i.e.,

$$Z_{\varphi_j} = \frac{1}{2}\frac{\mathrm{d}^2}{\mathrm{d}q^2}\Gamma^{(2)}_{\varphi_j}\left(\vec{\bar{\phi}}, \mu, T, \boldsymbol{q}\right)\Big|_{\boldsymbol{q}=0} \tag{4.25}$$

where we used field basis φ_j where $\Gamma^{(2)}_{\varphi_j,\varphi_k} \sim \delta_{j,k}$. More generally, the wave function renormalization encodes the coefficient of the spatial kinetic term $\sim (\nabla\phi_j)^2$ of the quantum effective action Eq. (2.26), see Ref. [121]. Thus, it serves as a measure for the relevance of bosonic fluctuations and gradient driven field configurations in the system. In the mean-field approximation, however, the quantum effective action Γ is given by the classical effective action $\mathcal{S}_{\text{eff}}$ evaluated at its global minimum $\vec{\bar{\Phi}}$. Thus, one can extract the bosonic wave function renormalization Z_{ϕ_j} by expanding the effective action in perturbations around the homogeneous minimum $\vec{\bar{\Phi}}$ and identifying the coefficient of the spatial kinetic term, proportional to the momentum squared $\boldsymbol{q}^2$ of the inhomogeneous fluctuations. From the form of the second-order coefficient in the basis φ_j

$$\frac{1}{N_f}\mathcal{S}^{(2)}_{\text{eff}}[\vec{\bar{\varphi}}, \delta\varphi] = \frac{\beta}{2}\int\frac{\mathrm{d}^d q}{(2\pi)^d}\sum_j \delta\tilde{\bar{\varphi}}_j(-\boldsymbol{q})\Gamma^{(2)}_{\varphi_j}\left(\bar{\varphi}, \mu, T, \boldsymbol{q}\right)\delta\tilde{\bar{\varphi}}_j(\boldsymbol{q}) \tag{4.26}$$

one can directly see that the definition of Z_{φ_j} (4.25) indeed extracts the leading coefficient of the quantum effective action of the term proportional to $q^2\varphi_j^2$, i.e., the spatial kinetic term of the bosonic field φ_j.

Of course, this is no longer the case when one allows for an inhomogeneous expansion point which would break down the association of the order of $\mathcal{S}^{(n)}_{\text{eff}}$ with the Fourier spectrum of the true ground state, which could be composed of the spectrum of the expansion point and, in case of instabilities, the spectrum of inhomogeneous perturbations. For example, already the zeroth order coefficient could contain arbitrary powers of the spatial momenta of the condensates.. Moreover, when going beyond the mean-field approximation one has to be careful with the definition of the wave function renormalization as the quantum effective action in principle contains all kind of non-local contributions also from bosonic fluctuations.

THE WAVE FUNCTION RENORMALIZATION AS A CRITERION FOR THE MOAT REGIME In the literature, a negative value of Z_{φ_j} is discussed as an indication for the presence of an IP [219, 231, 232]. However, a negative wave function renormalization does not yield information whether an instability of the homogeneous phase towards the IP is observed. This would be signaled by $\Gamma^{(2)}_{\varphi_j}(q) < 0$ for any $q \neq 0$, see the discussion in the last paragraph of Section 4.1.3.

Nevertheless, as stated above, the wave functional renormalization is the prefactor of the spatial kinetic term of the quantum effective action in the mean-field approximation. Thus,

$$Z_{\varphi_j} < 0 \tag{4.27}$$

signals a negative curvature of the quantum effective action at $q = 0$ and, thus, also a negative curvature of the dispersion relation E_{φ_j} – which is contained in the quantum

effective action – of the bosonic field φ_j at vanishing momentum, see Fig. 4.2. Consequently, this criterion signals that the dispersion relation of this field has a global minimum at non-vanishing momentum, which is precisely the defining property of the moat regime, see Section 3.1.1 for a detailed discussion. However, it is important to note that Eq. (4.27) is a sufficient, but not a necessary condition, since $\Gamma^{(2)}_{\varphi_j}$ might have a positive curvature at $q = 0$ although a global minimum at $q \neq 0$ exists. This would be caused by higher order terms in q which can be present in the bosonic two-point vertex function and would also result in a moat regime. This behavior is depicted in the teal curve in Fig. 4.2 where the bosonic two-point vertex function features both a maximum and a minimum at $q \neq 0$ such that $Z_{\varphi_j} > 0$ and $q = 0$ is a local minimum, while $q \neq 0$ is the global one. Such a behavior is, however, rather unexpected, see, e.g., Refs. [121, 200], and is typically not observed in any QCD-inspired models relevant in this context.[5] Overall, using Eq. (4.27) is a simple criterion characterizing a moat regime as not the full momentum dependence of $\Gamma^{(2)}_{\varphi_j}$ has to be determined – which is especially advantageous when studying the full phase diagram of a model or the full momentum dependence of the bosonic two-point vertex function is difficult to extract.

4.2 STABILITY ANALYSIS IN THE 1 + 1-DIMENSIONAL GROSS-NEVEU MODEL

In this section, we apply the generic algorithm, presented in Section 4.1.3, for the computation of the bosonic two-point vertex functions in the mean-field approximation to the $1 + 1$-dimensional GN model. This serves as a proof-of principle for this method and tests its applicability for searching IPs on a model with an analytically known phase diagram (in the mean-field approximation), see Ref. [202] and Fig. 3.2. Thereby, we also perform a novel computation of the wave-function renormalization in the GN model which is used to predict the presence of a moat regime in the phase diagram of the model, see Ref. [1] for the original publication of this work.

The $1 + 1$-dimensional GN model can be obtained from the generic four-fermion model in Eq. (2.32) by specifying the spatial dimensions $d = 1$, $\lambda_j = \lambda$ and $\vec{c} = (1)$ where the 1 represents the identity matrix in the two-component spinor space. Then, we obtain

$$\mathcal{S}[\bar{\psi}, \psi] = \int_0^\beta \mathrm{d}\tau \int \mathrm{d}x \left[\bar{\psi}\left(\partial\!\!\!/ + \gamma_2\mu\right)\psi - \tfrac{\lambda}{2N_f}\left(\bar{\psi}\psi\right)^2\right], \tag{4.28}$$

where ψ is a two-component spinor in $1 + 1$ spacetime dimensions, see Eq. (A.16) for the definition of the Gamma matrices and Appendix A.4 for a general discussion of the fermion field as a representation of the Poincaré group. The model is invariant under a U(1) global phase transformation of the spinors $\psi \to \mathrm{e}^{i\alpha}\psi$ with a real-valued parameter α as well as a discrete chiral symmetry transformation (3.7). This symmetry would be explicitly broken by a mass term $m\bar{\psi}\psi$. We note that the γ_μ are proportional to two of the Pauli matrices for $d = 1$ and, thus, $\gamma_{\mathrm{ch}} = -\mathrm{i}\gamma_1\gamma_2$ is proportional to the third Pauli matrix, see Appendix A.3.1.

5 In fact, in the literature there is only one case where a moat regime is observed but the wave function renormalization is not negative. This is the case in the non-renormalizable NJL model in one particular regularization scheme and large chemical potential compared to the regularization scale [10].

Following the Hubbard-Stratonovich transformation in Section 2.3.1, we introduce a bosonic auxiliary field σ to replace the four-fermion interaction term by a Yukawa term between σ and $\bar{\psi}\psi$. This leads to the action

$$\mathcal{S}[\bar{\psi},\psi,\vec{\phi}] = \int_0^\beta \mathrm{d}\tau \int \mathrm{d}^d x \left[N_f \sum_j \frac{\sigma^2}{2\lambda} - \bar{\psi}\left(\partial\!\!\!/ + \gamma_2\mu + \sigma\right)\psi \right], \tag{4.29}$$

i.e., σ acts as a dynamically generated mass term for the fermions. One can directly access the chiral condensate through the Ward identity

$$\langle\sigma\rangle = -\frac{\lambda}{N_f}\langle\bar{\psi}\psi\rangle, \tag{4.30}$$

which can be derived as in Section 2.3.2. Thus, a non-vanishing expectation value of σ implies a spontaneous breaking of the discrete chiral symmetry (3.7) the model. The discrete chiral symmetry transformation (3.7) becomes a reflection symmetry on the level of the auxiliary bosonic field, i.e.,

$$\sigma \to -\sigma. \tag{4.31}$$

In the Hubbard-Stratonovich transformation σ is introduced as a dynamical degree of freedom in the partition function of the model, see Eq. (2.36). As in the partially bosonized action (4.29) the fermions appear only in a bilinear, one can integrate them out in the partition function (compare the explicit calculation in Section 2.3.1). One obtains the effective action of the GN model

$$\mathcal{S}_{\text{eff}}[\sigma] = N_f \int \mathrm{d}^2 x \, \frac{\sigma^2}{2\lambda} - \ln \mathrm{Det}\left[\beta\left(\partial\!\!\!/ + \gamma_2\mu + \sigma\right)\right] \tag{4.32}$$

with the partition function

$$Z = \int \mathscr{D}\sigma \, \mathrm{e}^{-\mathcal{S}_{\text{eff}}[\sigma]} \tag{4.33}$$

which serves as a starting point for the computation of the bosonic two-point vertex functions in the GN model. Note that we use the mean-field approximation, c.f. Section 2.4, such that the computation of the partition function Z is reduced to the computation of the effective action $\mathcal{S}_{\text{eff}}$ evaluated at its global minimum with respect to the bosonic fields.

4.2.1 *The bosonic two-point function in the Gross-Neveu model*

The derivation of the Hessian matrix in the GN model is straightforward using the generic algorithm presented in the previous section. If the reader, however, wants to follow the details of the computation at the example of the GN model, we refer to Refs. [1, 52, 167, 286]. Since there is only one four-fermion interaction in the GN model, the Hessian matrix of the effective action has one element and the second-order correction to the effective action

$$\frac{\mathcal{S}^{(2)}_{\text{eff}}}{N_f} = \frac{\beta}{2}\int \frac{\mathrm{d}q}{2\pi}\, \delta\tilde{\sigma}(-q)\delta\tilde{\sigma}(q)\Gamma^{(2)}_\sigma(\bar{\sigma},\mu,T,q) \tag{4.34}$$

is given by bosonic two-point vertex function $\Gamma^{(2)}_\sigma$ of the auxiliary σ field. In this expression, q is the spatial momentum[6] of the inhomogeneous perturbation $\delta\sigma$. The general form of $\Gamma^{(2)}_\sigma$ according to Eq. (4.24) is

$$\Gamma^{(2)}_\sigma(\bar{\sigma},\mu,T,q) = \frac{1}{\lambda} + T\sum_n \int \frac{\mathrm{d}p}{2\pi} \mathrm{tr}\left(\tilde{\tilde{\mathrm{Q}}}^{-1}\left(p_\nu + (q,0)^T\right)\tilde{\tilde{\mathrm{Q}}}^{-1}\left(p_\nu\right)\right) \tag{4.35}$$

6 For spatial dimensions $d = 1$ we do not adapt the vector notation $\boldsymbol{q} = (q_1)$ from earlier in this chapter.

with

$$\tilde{\mathrm{Q}}^{-1}(p) = \frac{-\mathrm{i}\gamma_2\left(\nu_n - \mathrm{i}\mu\right) - \mathrm{i}\gamma_1 p + \sigma}{\left(\nu_n - \mathrm{i}\mu\right)^2 + p^2 + \sigma^2} \tag{4.36}$$

where $p_\alpha = (p, \nu_n)^T$ for $\alpha = 1, 2$.

The bosonic two-point vertex function can be written as

$$\Gamma_\sigma^{(2)}\left(\bar{\sigma}, \mu, T, q\right) = \frac{1}{\lambda} - \ell_1(\bar{\sigma}, \mu, T) - \ell_2(\bar{\sigma}, \mu, T, q) \tag{4.37}$$

where the momentum-independent integral contribution

$$\begin{aligned}\ell_1(\bar{\sigma}, \mu, T) &= \frac{2}{\pi}\int_0^\infty \mathrm{d}p\, \frac{1}{\beta}\sum_{n=-\infty}^{\infty} \frac{1}{\left(\nu_n - \mathrm{i}\mu\right)^2 + E_p^2} \\ &= \frac{1}{\pi}\int_0^\infty \mathrm{d}p\, \frac{1}{E_p}\left[1 - n_F(E_p) - n_{\bar{F}}(E_p)\right].\end{aligned} \tag{4.38}$$

also appears in the gap equation of the GN model, see Appendix C for a discussion in $2+1$ spacetime dimension, with the Fermi-Dirac distribution functions $n_F(x)$ and $n_{\bar{F}}(x)$, see Eq. (C.18) for their definition. The momentum-dependent integral contribution is

$$\ell_2(\bar{\sigma}, \mu, T, q) \equiv \tfrac{2}{\pi}\int_0^\infty \mathrm{d}p\, \tfrac{1}{\beta}\sum_{n=-\infty}^{\infty} \frac{p\,q - 2\,\bar{\sigma}^2}{(\nu_n - \mathrm{i}\mu)^2 + E_{p+q}^2}\frac{1}{(\nu_n - \mathrm{i}\mu)^2 + E_p^2}\,. \tag{4.39}$$

At this point we want to note that $\Gamma_\sigma^{(2)}$ still contains a UV divergence stemming from the momentum integral ℓ_1. However, this divergence is removed by treating the integral with, e.g., a sharp momentum cutoff scheme and the renormalization condition that the homogeneous global minimum $\bar{\Sigma}$ in the vacuum assumes a non-vanishing value $\bar{\Sigma}_0$, i.e., $\bar{\Sigma}(\mu = 0, T = 0) = \bar{\Sigma}_0$. This renormalization condition ensures that the chiral condensate is non-vanishing in the vacuum and, thus, the fermions acquire a dynamical mass in the vacuum due to the spontaneous chiral symmetry breaking. We note that such a regularization and renormalization prescription is also needed when solving the gap equation of the GN model, see Section II.C of Ref. [1] for details on the $1+1$-dimensional GN model or Appendix C for the procedure in two spatial dimensions. With this renormalization prescription, one can insert

$$\frac{1}{\lambda} - \ell_1(\bar{\sigma}, \mu, T) = \frac{1}{\pi}\left[\frac{1}{2}\ln\frac{\bar{\sigma}^2}{\bar{\Sigma}_0^2} + \int_0^\infty \mathrm{d}p \frac{1}{E_p}\left(n_F(E_p) + n_{\bar{F}}(E_p)\right)\right] \tag{4.40}$$

into Eq. (4.37) and obtain the renormalized bosonic two-point vertex functions in the GN model which is free of UV divergences. In two spatial dimensions ℓ_1 contains a linear divergence and not a logarithmic one as in Eq. (4.38). Thus, resulting formulae in Appendix C obviously differ from Eq. (4.40). Conceptually, both computations are, however, rather similar such that we do not in depth discuss the renormalization of the $1+1$-dimensional GN model and, instead, refer to Ref. [1] for details.

In order to evaluate ℓ_2 further, one carries out the Matsubara sum at non-vanishing q, which yields

$$\begin{aligned}&\ell_2(\bar{\sigma}, \mu, T, q) = \\ &= -\left(\frac{q^2}{2} + \bar{\sigma}^2\right)\frac{2}{\pi}\int_0^\infty \mathrm{d}p\, \frac{1}{E_p}\left(\frac{1}{E_{p+q}^2 - E_p^2} + \frac{1}{E_{p-q}^2 - E_p^2}\right)\left[1 - n(E_p, \mu) - n(E_p, -\mu)\right].\end{aligned} \tag{4.41}$$

and for $q = 0$ one finds[7], one finds

$$\ell_2(\bar{\sigma}, \mu, T, 0) = -\bar{\sigma}^2 \frac{2}{\pi} \int_0^\infty \mathrm{d}p \, \frac{1}{4E_p^3} \Big(1 - (1 + \beta E_p) \Big[n(E_p, \mu) + n(E_p, -\mu) \Big] + \\ + \beta E_p \Big[n^2(E_p, \mu) + n^2(E_p, -\mu) \Big] \Big). \tag{4.42}$$

We note that for the evaluation of Eq. (4.41) one needs to take care of a pole at $p = q/2$ requiring a Cauchy principal value prescription. For the evaluations of both expressions (4.41) and (4.42) in special cases of the thermodynamic variables μ and T, we refer to Appendix A of Ref. [1].

4.2.2 *The bosonic wave function renormalization in the Gross-Neveu model*

The bosonic wave function renormalization can be computed directly from the bosonic two-point vertex function $\Gamma_\sigma^{(2)}$ via Eq. (4.25). Performing the derivative with respect to q in Eq. (4.37) and evaluating at $q = 0$ yields

$$Z_\sigma(\bar{\sigma}, \mu, T) = \frac{1}{\pi} \int_0^\infty \mathrm{d}p \frac{1}{\beta} \sum_{n=-\infty}^{\infty} \frac{1}{(\nu_n - \mathrm{i}\mu)^2 + E_p^2} \left(1 - \frac{4}{3} \frac{\bar{\sigma}^2}{(\nu_n - \mathrm{i}\mu)^2 + E_p^2} \right), \tag{4.43}$$

where the Matsubara summation can be evaluated in the standard way using the residue theorem and contour integration, see the last paragraphs of Appendix C.4. The result is given by

$$Z_\sigma(\bar{\sigma}, \mu, T) = \tag{4.44}$$
$$= \frac{1}{4\pi} \Bigg(\frac{1}{3\bar{\sigma}^2} - \int_0^\infty \mathrm{d}p \frac{1}{E_p^2} \left[n(E_p) + \bar{n}(E_p) - \frac{E_p}{T} \Big(n^2(E_p) + \bar{n}^2(E_p) - n(E_p) - \bar{n}(E_p) \Big) \right] + \\ + \bar{\sigma}^2 \int_0^\infty \mathrm{d}p \frac{1}{E_p^5} \left[n(E_p) + \bar{n}(E_p) - \frac{E_p}{T} \Big(n^2(E_p) + \bar{n}^2(E_p) - n(E_p) - \bar{n}(E_p) \Big) \right] + \\ + \frac{1}{3} \frac{E_p^2}{T^2} \Big[2n^2(E_p) + 2\bar{n}^3(E_p) - 3n^2(E_p) - 3\bar{n}^2(E_p) + n(E_p) + \bar{n}(E_p) \Big] \Bigg).$$

Further analysis of this expression in the limit of vanishing T, μ and/or $\bar{\sigma}$ can be found in Appendix B of Ref. [1].

4.2.3 *Results*

With the expressions for ℓ_1 and ℓ_2 at hand we can proceed by studying the stability of homogeneous condensates in the GN model. We start by analyzing the momentum dependence of $\Gamma_\sigma^{(2)}$ for various values of the chemical potential μ and the temperature T. Before going in this discussion, we refer the reader to the discussion of Fig. 3.2 in Section 3.2.1 where the analytical solution to the phase diagram of the GN model is presented.

7 It is recommended to set $q = 0$ before evaluating the Matsubara summation instead of taking the limit of $q \to 0$ in Eq. (4.41) because the two propagator poles in Eq. (4.39) become degenerate. When taking the $q \to 0$ limit first, one can apply a standard Matsubara frequency summation formula [345], see the last paragraphs of Appendix C.4.

In Fig. 4.3, $\Gamma_\sigma^{(2)}(q)$ is plotted as a function of the external momentum q for different values of μ and T. The figure allows to analyze bosonic two-point vertex function in different regions of the phase diagram. In the top left plot in Fig. 4.3, $\Gamma_\sigma^{(2)}$ is presented for vanishing chemical potential and four different values of T evaluated at the respective homogeneous minimum $\bar{\sigma} = \bar{\Sigma}(0, T)$ of the effective potential as relevant for analyzing the stability of the homogeneous phase. As one would expect, the bosonic two-point vertex function is positive for all values of q and T at $\mu = 0$. This is the case for zero and non-zero temperatures in the HBP ($T/\bar{\Sigma}_0 = 0.0, 0.3$), in the SP ($T/\bar{\Sigma}_0 = 1.0$) and on the phase boundary between the two phases ($T/\bar{\Sigma}_0 = T_c/\bar{\Sigma}_0 = \mathrm{e}^\gamma/\pi$), compare Fig. 3.2 for the homogeneous phase diagram.

In the bottom left subfigure, we analyze the bosonic two-point vertex function at $\mu/\bar{\Sigma}_0$ and five different values of the temperature T. This allows to inspect the behavior of $\Gamma_\sigma^{(2)}$ within the IP of the model. The corresponding homogeneous expansion point is always zero, i.e., $\bar{\Sigma}(\mu, T) = 0$. As expected, we find a positive $\Gamma_\sigma^{(2)}$ with unique minimum at $q = 0$ for high T at $\mu/\bar{\Sigma}_0 = 0.75$, i.e., in the SP. According to our discussion in Section 4.4, such a behavior implies that the long-range behavior spatial propagator of the σ field $\langle\sigma(x_1)\sigma(0)\rangle$ is proportional to $\exp(-mx_1)$ where m is given by the purely imaginary propagator pole. When lowering the temperature to, e.g., $T/\bar{\Sigma}_0 \in [0.2, 0.3]$, one finds that $\Gamma_\sigma^{(2)}$ develops a non-trivial minimum at $q = Q \neq 0.0$ albeit $\Gamma_\sigma^{(2)}(q) > 0.0$ for all q where

$$Q = \arg\min_q \Gamma_\sigma^{(2)}(\bar{\Sigma}(\mu, T), \mu, T, q). \tag{4.45}$$

One can infer that at these intermediate temperatures a moat regime is present in the GN model as the bosonic two-point vertex function has a global minimum at $q = Q \neq 0$ and, also, the more practical criterion of a negative bosonic wave function renormalization (curvature of $\Gamma_\sigma^{(2)}$ with respect to q at $q = 0$) is fulfilled. More details about the value of the bosonic wave function renormalization will be discussed later. For even lower temperatures, this non-trivial minimum becomes negative signaling the presence of an IP in the GN model.

The on-set of the instability (here roughly $T/\bar{\Sigma}_0 = 0.2$) corresponds to the phase transition between the SP to the IP, cf. Fig. 3.2. Since the stability analysis describes the inhomogeneous condensate as a small perturbation about (in this case) $\bar{\sigma} = 0$, it is expected that this second-order phase transition can accurately be captured by the stability analysis as is described in following paragraphs. At this point in the phase diagram, $\Gamma_\sigma^{(2)}(\bar{\Sigma}(\mu, T), \mu, T, Q)$ vanishes and the value of Q corresponds to the wave vector of the inhomogeneous condensate in the full analytical solution, which at the phase transition indeed is a sine wave of infinitesimal amplitude, see Ref. [202] and the discussion in Section 3.2.1 for details. When lowering the temperature further, the minimum of the bosonic two-point vertex function $\Gamma_\sigma^{(2)}(q = Q)$ gets more and more negative. At zero temperature, this minimum finally turns into a pole at $q = 2\mu$. This momentum scale is expected of inhomogeneous condensates as the antifermion-fermion pairs are formed in the vicinity of the Fermi surface $\sim \mu$, see Refs. [111, 197].

Next, the top right plot in Fig. 4.3 is discussed where $\Gamma_\sigma^{(2)}$ at $\mu/\bar{\Sigma}_0 = 0.6$ and $T = 0.0$ is plotted for two different values of the homogeneous expansion point $\bar{\sigma} = 0.0$ and $\bar{\sigma} = \bar{\Sigma}(\mu, 0.0) \neq 0$, i.e., these values of μ and T correspond to the HBP. This plot demonstrates that it is crucial to evaluate the bosonic two-point vertex function at the correct homogeneous expansion point as the evaluation of $\Gamma_\sigma^{(2)}$ at $\bar{\sigma} = 0$ leads to negative values of $\Gamma_\sigma^{(2)}$ signaling an instability which, however, does not provide evidence for the existence of an IP. For this test case scenario, this point seems rather trivial. However, for more

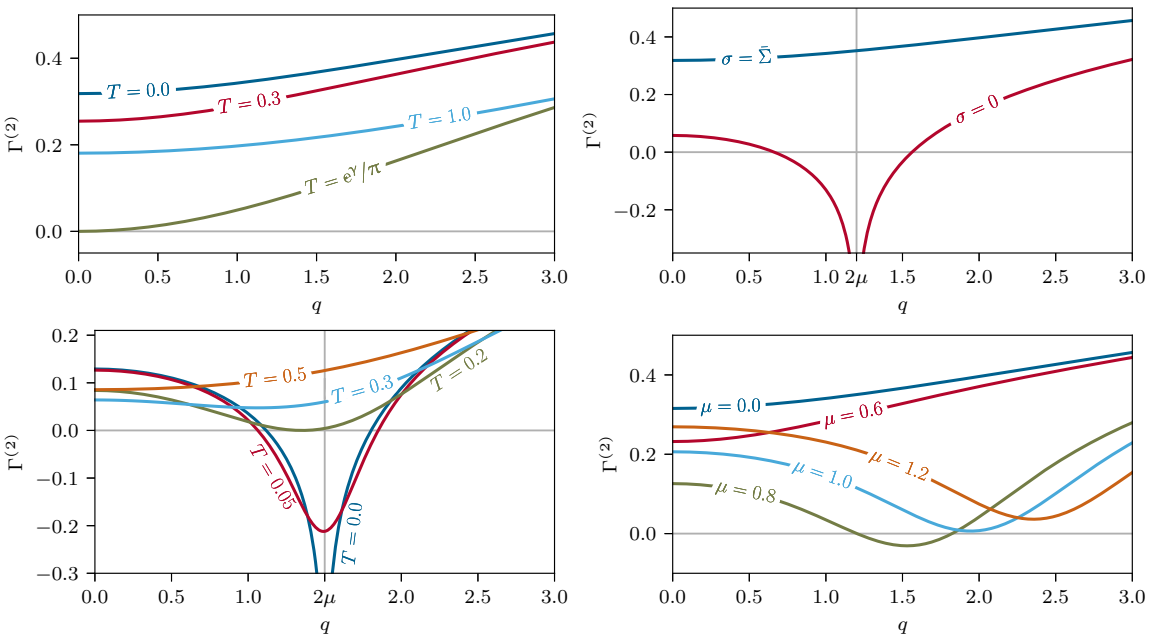

Figure 4.3: The bosonic two-point vertex function $\Gamma_\sigma^{(2)}(q)$ as a function of the external momentum q. The different colors in the same subfigure correspond to different values of the respectively varied quantity. Except for the subfigure in the top right, $\Gamma_\sigma^{(2)}(q)$ is evaluated at the respective homogeneous minimum $\bar{\sigma} = \bar{\Sigma}(\mu, T)$ of the effective potential. *(top left)* $\mu = 0$ and $T/\bar{\Sigma}_0 \in \{0.0, 0.3, e^{\gamma}/\pi, 1.0\}$ (γ is the Euler-Mascheroni constant). *(top right)* $\mu/\bar{\Sigma}_0 \in \{0.6\}$ and $T = 0$. The two different curves correspond to the homogeneous, local minimum $\bar{\sigma} = 0.0$ and the global minimum $\bar{\sigma} = \bar{\Sigma}(\mu, T)$ of the effective potential. *(bottom left)* $\mu/\bar{\Sigma}_0 = 0.75$ and $T/\bar{\Sigma}_0 \in \{0.0, 0.05, 0.2, 0.3, 0.5\}$. *(bottom right)* $\mu\bar{\Sigma}_0 \in \{0.0, 0.6, 0.8, 1.0, 1.2\}$ and $T/\bar{\Sigma}_0 = 0.15$.

involved computations of the bosonic two-point vertex functions in more complicated models or approximations, such as, e.g., Functional Renormalization Group calculations, the determination of the correct evaluation point can be a difficult task.

Finally, in the bottom right plot in Fig. 4.3 the behavior of $\Gamma_\sigma^{(2)}$ is presented at $T/\bar{\Sigma}_0 = 0.15$ and five different values of μ. This particular temperature slice allows to study all three phases present in the phase diagram. Within the HBP at $\mu = 0$ and $\mu/\bar{\Sigma}_0 = 0.6$, the bosonic two-point vertex function is positive for all q with the minimum located at $Q = 0$ as expected. The bosonic curvature mass, i.e. $\Gamma_\sigma^{(2)}(q = 0)$ decreases when increasing the chemical potential μ within the HBP. As soon as one crosses the first-order boundary line between the HBP and the SP, which is present when studying spatially homogeneous condensates, cf. Fig. 3.2, the bosonic two-point vertex function develops a non-trivial, negative minimum at $Q \neq 0$ signaling the instability of $\bar{\Sigma} = 0.0$ against inhomogeneous fluctuations. Thus, at $\mu/\bar{\Sigma}_0 = 0.8$ a spatially inhomogeneous condensate is favored. Further increasing the chemical potential, shifts the $\Gamma_\sigma^{(2)}$ curve to larger values such that roughly at $\mu/\bar{\Sigma}_0 = 1.0$ the minimum of $\Gamma_\sigma^{(2)}(q)$ is positive again. Consequently, at $\mu/\bar{\Sigma}_0 = 1.2$ the bosonic two-point vertex function is positive for all q again as one would expect for the SP. However, the $\Gamma_\sigma^{(2)}$ is not convex such that one still observes a non-trivial global minimum at $q \neq 0$. This curve corresponds again to a moat regime as we will further demonstrate in the following by computing the wave function renormalization Z_σ.

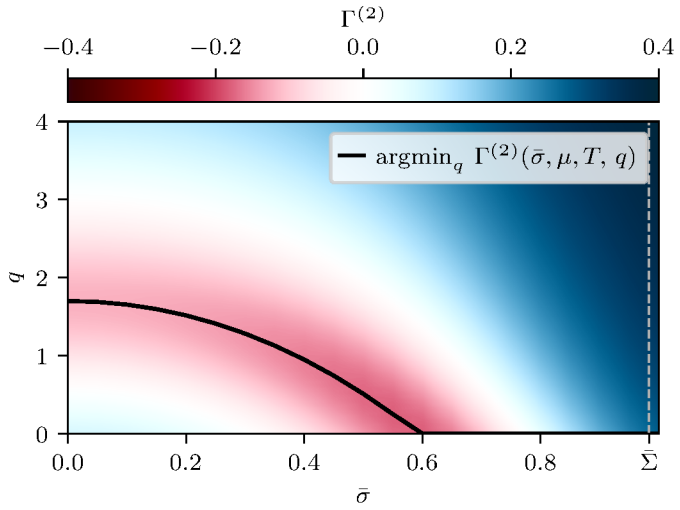

Figure 4.4: The bosonic two-point vertex function $\Gamma^{(2)}_\sigma(q)$ in the $(\bar{\sigma}, q)$ plane for the point $(\mu, T)/\bar{\Sigma}_0 = (0.67, 0.1)$ as a color map. The solid black line marks the non-trivial minima. The dashed white line corresponds to the homogeneous, global minimum $\bar{\sigma} = \bar{\Sigma}$ at this point in the phase diagram.

SHORTCOMINGS OF THE STABILITY ANALYSIS In Fig. 4.4 the bosonic two-point vertex function $\Gamma^{(2)}_\sigma(q)$ is plotted in the $(\bar{\sigma}, q)$-plane for the point $(\mu, T)/\bar{\Sigma}_0 = (0.67, 0.1)$ where the value of $\Gamma^{(2)}_\sigma$ is encoded in a color map. This μ, T point in the phase diagram is located close to the first-order transition line (see the red line in Fig. 3.2) but is within the HBP. The minimum of the effective potential there is roughly $\bar{\sigma}/\bar{\Sigma}_0 = \bar{\Sigma}/\bar{\Sigma}_0 \approx 1$ while $\bar{\sigma} = 0$ is a local minimum. Inspecting Fig. 3.2 reveals that in this region of the phase diagram actually the IP is energetically preferred over the HBP if one allows for spatial modulations of the condensate. However, when performing the stability analysis around the correct homogeneous expansion point $\bar{\sigma} = \bar{\Sigma}$ one finds a positive value of $\Gamma^{(2)}_\sigma$ for all q. Thus, the stability analysis fails to detect the IP in this region of the phase diagram. As can also be inferred from Fig. 4.4, one still finds instabilities when decreasing $\bar{\sigma}$ below the correct expansion point. These instabilities cannot be interpreted with respect to the presence of an IP as they only appear for a homogeneous field value $\bar{\sigma} < \bar{\Sigma}$ that is not relevant for the detection of an IP. We have seen instabilities of this kind in multiple selected sample point in the phase diagram where, e.g., at $\bar{\sigma} = 0.0$ the bosonic two-point vertex function exhibits instabilities while the correct expansion point $\bar{\sigma} = \bar{\Sigma}(\mu, T)$ is stable. The reason for this failure is that the non-trivial homogeneous minimum $\bar{\sigma} = \bar{\Sigma}(\mu, T)$ and the spatially oscillating inhomogeneous ground state are separated by an "energy barrier" in the effective potential. This leads to a positive curvature around $\bar{\sigma} = \bar{\Sigma}$ and the homogeneous minima do no longer turn into saddle points with an unstable direction in momentum space when studying inhomogeneous perturbations. In this region of the phase diagram, the oscillating ground state is described by Jacobi-elliptic functions which oscillates between the two global minima of the effective potential $\pm\bar{\Sigma}(\mu, T)$, see Section 3.2.1. Thus, this condensate can no longer be described by a small perturbation around one of these minima.

PHASE DIAGRAM VIA THE STABILITY ANALYSIS Based on the previous discussion, we present Fig. 4.5 which presents the insights into the (μ, T) phase diagram that can

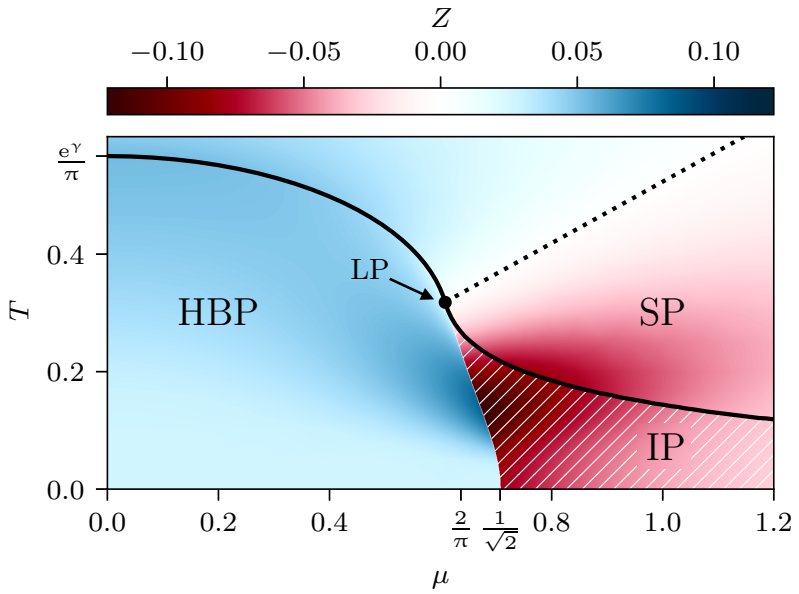

Figure 4.5: The wave function renormalization $Z_\sigma(\bar{\Sigma}(\mu,T),\mu,T)$, line of $Z_\sigma = 0$ (dotted black line) and the boundary of the region with instability of the GN model in the μ-T-plane. In the region marked by the diagonal hatching using thin black solid lines we find $\Gamma^{(2)}_\sigma(\bar{\Sigma}(\mu,T),\mu,T,Q) < 0$, i.e. the homogeneous minimum is unstable with respect to inhomogeneous fluctuations.

be gained from the bosonic two-point vertex functions and the bosonic wave function renormalization in the GN model. The main result – which will be further elaborated on in the following – is that the stability analysis correctly detects the known phase transition line between the SP and the IP while it fails in the region between the HBP and the IP transition line and the homogeneous first-order phase transition, cf. Fig. 3.2.

As discussed above, the stability analysis is trustworthy in regions of the phase diagram where the homogeneous expansion point is trivial, i.e., $\bar{\sigma} = \bar{\Sigma}(\mu,T) = 0$ and, especially, where the inhomogeneous condensate has a small amplitude. This is the case near the second-order phase transition between the SP and the IP. The reliability near this phase transition is expected since the stability analysis itself is based on expanding the field $\sigma(x)$ around the homogeneous background $\bar{\sigma}$. These expectations are matched by our numerical results in Fig. 4.5. The solid black line in Fig. 4.5 marks the line where $\Gamma^{(2)}_\sigma(\bar{\Sigma}(\mu,T),\mu,T,Q) = 0$, which is the unique minimum of the bosonic two-point vertex function for fixed μ and T at $q = Q$, in the external bosonic minimum. This line extends from the LP to larger chemical potentials and is identical to the exact phase boundary from Fig. 3.2 within out numerical precision $\sim 0.005\bar{\Sigma}_0$ within the (μ,T) plane. The method also detects the second-order boundary line between the SP and the HBP which is not surprising since the bosonic curvature mass vanishes at this line. The curvature mass, however, is proportional to $\Gamma^{(2)}_\sigma(\bar{\Sigma}(\mu,T),\mu,T,q=0)$ and consequently also vanishes.

The phase boundary between the HBP and the IP is not correctly detected by the stability analysis. This is caused by the large amplitude of the inhomogeneous oscillation in this region which is not connected to the homogeneous expansion point $\bar{\sigma} = \bar{\Sigma}(\mu,T)$ by a small perturbation. The initial assumption in the stability analysis of small perturbations Eq. (4.7) is violated in this region of the phase diagram. The analysis starts to fail when crossing the first-order phase transition between the HBP and the SP that is present when

studying spatially homogeneous condensates. We note that this failure might be avoided by using the so-called fermion double trick, as in Ref. [337], which takes into account also higher order coefficients in the stability analysis, i.e., higher order n-point vertex functions, at the drawback that it requires an harmonic ansatz for the chiral condensate. The results of Ref. [337] can be interpreted as a sign that one would need to compute higher-order n-point functions in order to correctly detect the IP in the region near the IP↔HBP phase transition line. In Ref. [346], it is demonstrated that a modified stability analysis using the inverse spatial period of the inhomogeneous perturbation as expansion parameter can correctly detect this transition line, which, however, requires computing the effective potential for a single baryon ansatz for $\bar{\sigma}(x)$.

THE WAVE FUNCTION RENORMALIZATION IN THE GROSS-NEVEU MODEL In Fig. 4.5 the wave function renormalization $Z_\sigma(\bar{\Sigma}(\mu,T),\mu,T)$ computed using Eq. (4.44) is visualized through a color map in the (μ,T)-plane. The results in Fig. 4.5 are also cross-checked using a numeric evaluation of the q-derivatives of $\Gamma_\sigma^{(2)}$ at $q=0$. As depicted in this figure the wave function renormalization is positive for small values of μ and T within the HBP. However at larger μ in the region around the first-order phase transition between SP and HBP when studying spatially homogeneous condensates, the wave function renormalization jumps to a negative value. Interestingly, this is also the region where the stability analysis fails to detect the IP. Thus, it seems that also the wave function renormalization signals the importance of bosonic fluctuations of all orders in this phase diagram. This is expected near a first-order phase transition where correlation lengths typically diverge such that all orders of fluctuations become equally important. At larger temperatures, in contrast, Z_σ changes more smoothly from positive to negative values when increasing the chemical potential. In the SP one can observe the line of $\mu/T = 1.91$ where $Z_\sigma = 0$ marked by the black dashed line in Fig. 4.5. The region of negative Z_σ corresponds to the region where the GN model exhibits a moat regime. Such a regime is also present in Functional Renormalization Group studies starting from first-principles [121] and is a precursor for all kind of spatially inhomogeneous observables, see the discussion in Chapter 3.

4.3 STABILITY ANALYSIS IN THE 1 + 1-DIMENSIONAL CHIRAL GROSS-NEVEU MODEL

The second test for the stability analysis is performed on the phase diagram of the $1+1$-dimensional chiral GN model. This model is obtained by setting $\lambda_j = \lambda$, $d = 1$ and $\vec{c} = (1, \mathrm{i}\gamma_5)$. The resulting Euclidean action is

$$\mathcal{S}[\bar{\psi},\psi] = \int_0^\beta \mathrm{d}\tau \int \mathrm{d}x \left\{ \bar{\psi}\left(\partial\!\!\!/ + \gamma_2\mu + \mathrm{i}\gamma_1\tilde{\mu}\right)\psi + \frac{\lambda}{2N_f}\left[\left(\bar{\psi}\psi\right)^2 + \left(\bar{\psi}\mathrm{i}\gamma_{\mathrm{ch}}\psi\right)^2\right]\right\} \tag{4.46}$$

where $\bar{\psi}$ and ψ are N_f two-component Dirac spinors in 1+1 dimensions (see Appendices A.3 and A.4 for details on spinor representation in $1+1$ dimensions). The chiral GN model with both chiral and fermion chemical potential serves as an adequate, additional benchmark model for the stability analysis as it 1.) is a model with a well-known phase diagram featuring an IP in the mean-field approximation, 2.) features a continuous chiral symmetry that is spontaneously broken and 3.) contains two bosonic fields. The two latter aspects of the theory provide a contrast to the GN model which is invariant under a discrete chiral

symmetry operation and has only one bosonic field. Also, the Hessian matrix containing the bosonic two-point vertex functions $\Gamma^{(2)}_{\phi_j,\phi_k}$ needs to be diagonalized in the chiral GN model which is not the case in the GN model.

In addition to the fermion chemical potential μ which couples to the temporal component of the vector current $\bar{\psi}\gamma_\mu\psi$ – the fermion number – we also allow for a non-vanishing chiral chemical potential $\tilde{\mu}$ coupling via conserved charge of the axial vector current $\bar{\psi}\gamma_\mu\gamma_{\text{ch}}\psi$.[8] Remember that $\gamma_{\text{ch}} = \mathrm{i}\gamma_1\gamma_2$ such that the chiral chemical potential is introduced by adding the term $\bar{\psi}\mathrm{i}\tilde{\mu}\gamma_1\psi$ to the above action.

After following the usual bosonization method, the resulting effective action is given by

$$\mathcal{S}_{\text{eff}}[\sigma,\eta] = \int_0^\beta \mathrm{d}\tau \int \mathrm{d}x \left[\frac{N_f}{2\lambda}\left(\sigma^2+\eta^2\right)\right] - \ln\mathrm{Det}\left[\beta\left(\partial\!\!\!/ + \gamma_2\mu + \mathrm{i}\gamma_1\tilde{\mu} + \sigma + \mathrm{i}\gamma_{\text{ch}}\eta\right)\right] \quad (4.47)$$

where the auxiliary bosonic fields σ and η were introduced. See Eq. (3.10) for an intermediate step where σ and η are introduced before integrating out the fermions. The scalar fields follow the Ward identities

$$\langle\sigma\rangle = -\frac{\lambda}{N_f}\langle\bar{\psi}\psi\rangle, \qquad \langle\eta\rangle = -\frac{\lambda}{N_f}\langle\bar{\psi}\mathrm{i}\gamma_{\text{ch}}\psi\rangle \quad (4.48)$$

following the derivation of Eq. (2.43) in Section 2.3.2. The four-fermion action (4.46) is invariant under the chiral symmetry transformation acting on the fermion fields (3.9), which is a continuous symmetry in contrast to the discrete chiral symmetry in the GN model. On the level of the effective bosonic action (4.47), this symmetry is realized by the transformation (3.11) which is an O(2) symmetry acting on the bosonic fields. A non-vanishing expectation value of either σ or η breaks this symmetry spontaneously signaling also the breaking of the chiral symmetry (3.9) and generates a Goldstone mode [44, 45].

4.3.1 *The bosonic two-point vertex functions in the chiral Gross-Neveu model*

In the basis of the auxiliary fields σ and η, the second-order correction in $\delta\sigma$ and $\delta\eta$ are expressed by the Hessian matrix $\Gamma^{(2)}_{\phi_j,\phi_k}(\bar{\rho},\mu,T,q)$ with $\vec{\phi} = (\sigma,\eta)$ and $\bar{\rho} = \bar{\sigma}^2 + \bar{\eta}^2$

$$\frac{\mathcal{S}^{(2)}_{\text{eff}}}{N_f} = \frac{\beta}{2}\int\frac{\mathrm{d}q}{2\pi}\left(\delta\sigma(-q),\delta\eta(-q)\right)\cdot\Gamma^{(2)}(\bar{\rho},\mu,\tilde{\mu},T,q)\cdot\begin{pmatrix}\delta\sigma(q)\\ \delta\eta(q)\end{pmatrix} \quad (4.49)$$

where $\Gamma^{(2)}$ is defined by the matrix elements (recall $\vec{c} = (1,\mathrm{i}\gamma_5)$)

$$\Gamma^{(2)}_{\phi_j,\phi_k}(\bar{\rho},\mu,T,q) = \frac{\delta_{j,k}}{\lambda} + 2T\sum_n\int\frac{\mathrm{d}p}{(2\pi)}\mathrm{tr}\left(\tilde{\mathrm{Q}}^{-1}\left(p+(q,0)^T\right)c_j\,\tilde{\mathrm{Q}}^{-1}\left(p\right)c_k\right). \quad (4.50)$$

Note that $\tilde{\mathrm{Q}}^{-1}$ is given by Eq. (4.36) when using the continuous symmetry (3.11) to choose the homogeneous expansion as $\bar{\eta} = 0$ such that $\bar{\rho} = \bar{\sigma}^2$. Consequently, the Hessian matrix explicitly has non-vanishing off-diagonal elements $\Gamma^{(2)}_{\sigma,\eta} = \Gamma^{(2)}_{\eta,\sigma}$ when one takes into account that the trace over $\gamma_\mu\gamma_5$ is non-vanishing for the Dirac matrices in $d = 1$ spatial dimensions,

8 In terms of testing the stability analysis for QCD-inspired models at non-vanishing baryon density, the introduction of this additional imbalance is not very insightful. However, in the underlying work [4], it is introduced as an extension of the analysis of the model itself. Thus, the author decided to keep it in this section for consistency with the original work [4]. A chiral imbalance is relevant in physical systems such as heavy-ion collision or compact stars.

see Appendix A.3 for their definition. Thus, the diagonalization of the Hessian matrix requires a basis change. The corresponding field transformation was already used in studies of the chiral GN model [203, 227, 347] and is given by

$$\Delta = \sigma + \mathrm{i}\eta, \qquad \Delta^* = \sigma - \mathrm{i}\eta, \qquad \rho = \Delta^*\Delta \tag{4.51}$$

such that

$$\sigma + \mathrm{i}\gamma_{\mathrm{ch}}\eta = \gamma_L\Delta^* + \gamma_R\Delta, \tag{4.52}$$

see Eq. (A.17) for the definition of $\gamma_{L/R}$. In the matrix-vector notation, this reads as

$$\vec{\varphi} = M\vec{\phi}, \qquad \vec{\varphi}^\dagger = \vec{\phi}^T M^{-1}, \qquad M = \begin{pmatrix} 1 & -\mathrm{i} \\ 1 & \mathrm{i} \end{pmatrix} \tag{4.53}$$

where $\vec{\varphi} = (\Delta^*, \Delta)^T$ and $\vec{\varphi}^\dagger = (\Delta, \Delta^*)$. With the definition of the matrix M the Hessian matrix can be transformed as

$$\Gamma^{(2)}_{\varphi_j^\dagger,\varphi_k} = M_{jl}\Gamma^{(2)}_{\phi_l,\phi_m}(M^{-1})_{mk}\,. \tag{4.54}$$

By inserting the identity $1 = MM^{-1}$ left and right of the Hessian matrix we rewrite Eq. (4.49) in terms of the fields Δ and Δ^* as

$$\frac{\mathcal{S}^{(2)}_{\mathrm{eff}}}{N_f} = \frac{\beta}{2}\int\frac{\mathrm{d}q}{2\pi}\left[\delta\varphi_j^\dagger(-q)\Gamma^{(2)}_{\varphi_j^\dagger,\varphi_k}\delta\varphi_k(q)\right] \tag{4.55}$$

with $\delta\varphi = (\delta\Delta^*, \delta\Delta)^T$. This is the so-called complex Hessian matrix in field space, as it also appears in multi-dimensional analysis with complex variables. It is defined such that it contains information invariant under holomorphic coordinate changes. Note $\varphi_1^\dagger = \varphi_2 = \Delta$ and $\varphi_2^\dagger = \varphi_1 = \Delta^*$ such that $\Gamma^{(2)}_{\Delta,\Delta^*}$ and $\Gamma^{(2)}_{\Delta^*,\Delta}$ are the diagonal entries of $\Gamma^{(2)}_{\varphi_j^\dagger,\varphi_k}$. Since off-diagonal elements $\Gamma^{(2)}_{\Delta,\Delta} = \Gamma^{(2)}_{\Delta^*,\Delta^*}$ vanish, the diagonal entries correspond to the eigenvalues. This basis for $\Gamma^{(2)}$ arises naturally as a consequence of the definition of the fields in Eq. (4.51) as a complex-conjugate pair. Note that $\Gamma^{(2)}_{\varphi_j^\dagger,\varphi_k}$ could be directly obtained by taking functional derivatives of the effective action (4.47) with respect to $\vec{\varphi}$ and $\vec{\varphi}^\dagger$ instead of $(\sigma, \eta)^T$ and (σ, η). We define the obtained eigenvalues as $\Gamma^{(2)}_{\varphi_1} = \Gamma^{(2)}_{\Delta,\Delta^*}$ and $\Gamma^{(2)}_{\varphi_2} = \Gamma^{(2)}_{\Delta^*,\Delta}$.

The bosonic two-point vertex functions are given by

$$\Gamma^{(2)}_{\varphi_{1/2}}(\bar{\rho}, \mu, \tilde{\mu}, T, q) = \frac{1}{\lambda} + 2T\sum_n\int\frac{\mathrm{d}p}{(2\pi)}\mathrm{tr}\left(\tilde{\bar{\mathrm{Q}}}^{-1}\left(p + (0, q)\right)\gamma_{R/L}\tilde{\bar{\mathrm{Q}}}^{-1}\left(p\right)\gamma_{L/R}\right) \tag{4.56}$$

with $\tilde{\bar{\mathrm{Q}}}^{-1}(p) = \left(\mathrm{i}\gamma_0(\nu_n - \mathrm{i}\mu) + \mathrm{i}\gamma_1(p + \tilde{\mu}) + \gamma_L\bar{\Delta}^* + \gamma_R\bar{\Delta}\right)^{-1}$ as the fermion propagator for constant fields $\bar{\Delta} = \bar{\sigma} + \mathrm{i}\bar{\eta}$. Since we are interested in using the stability analysis to find the critical temperature, where a phase transition between the SP and the IP occurs independently of μ, only the stability of the SP, i.e., for $\bar{\Delta} = \bar{\Delta}^* = 0$ such that also $\bar{\rho} = \bar{\Delta}\bar{\Delta}^* = 0$, is investigated. See Section 3.2.2 for a discussion of the phase diagram of the chiral GN model. This significantly simplifies the analysis (details can be found in Ref. [4]) such that one finds

$$\Gamma^{(2)}_{\varphi_{1/2}}(0, \mu, T, q) = \frac{1}{\lambda} + T\sum_n\int_{-\infty}^{\infty}\frac{\mathrm{d}p}{(\pi)}\frac{1}{\left[\nu_n + \mathrm{i}(\mu \pm \frac{q}{2})\right]^2 + p^2}\,. \tag{4.57}$$

Note that this equation no longer depends on $\tilde{\mu}$. This is a consequence of the chiral chemical potential coupling via $\mathrm{i}\gamma_1$, i.e., to the spatial momentum p and can, thus, simply be shifted away in the momentum integral. In fact also the effective potential of the theory only contains the term $-\tilde{\mu}^2/2\pi$ [4] such that the phase diagram, is independent of $\tilde{\mu}$, as first discussed in Ref. [246].[9]

Performing the Matsubara sum in Eq. (4.57), one finds

$$\Gamma^{(2)}_{\varphi_{1/2}}(0,\mu,T,q) = \frac{1}{\lambda} + \int \frac{\mathrm{d}p}{\pi}\frac{1}{p}\left[1 - n\left(p,\mu\pm\frac{q}{2}\right) - n\left(p,-\left(\mu\pm\frac{q}{2}\right)\right)\right], \tag{4.58}$$

where the term $1/p$ is not finite but the logarithmic UV divergence is canceled by the renormalization prescription of the four-fermion coupling λ. The renormalization can be done in the same way as in the GN model, compare Eq. (4.40) for the respective formula in the GN model and Appendix C for the entire renormalization procedure in $2+1$ spacetime dimensions.[10] The renormalization is done in the vacuum where homogeneous condensation is preferred and, thus, one can use the chiral rotation (3.11) to rotate homogeneous field configurations such that $\bar{\eta} = 0$. In the integrand of Eq. (4.58), a pole is present that needs to be taken care by a proper infra-red (IR) regularization. Using this IR cutoff one can show that the IR divergence of the first term cancels against the divergence of the latter two terms such that the bosonic two-point vertex functions are finite. Moreover, note that a similar mathematical structure appears in the GN model as one can recover the ℓ_1 integral (4.38) but with a shifted chemical potential $\mu \to \mu \pm q/2$. Incomplete polylogarithms can be identified (see, e.g, Ref. [348] for a summary of these functions) such that we end up within

$$\Gamma^{(2)}_{\varphi_{1/2}}(0,\mu,T,q) = \frac{1}{\pi}\left[\frac{1}{2}\ln\left(\frac{4T^2}{\bar{\rho}_0}\right) - \mathrm{DLi}_0\left(\frac{\mu\pm\frac{q}{2}}{T}\right) - \gamma\right] \tag{4.59}$$

where

$$\begin{aligned}\mathrm{DLi}_{2n}(y) &= \left[\frac{\partial}{\partial s}\mathrm{Li}_s(-\mathrm{e}^{y}) + \tfrac{\partial}{\partial s}\mathrm{Li}_s(-\mathrm{e}^{-y})\right]_{s=2n} \\ &= -\delta_{0,n}(\ln(2\pi)+\gamma) + (-1)^{1-n}(2\pi)^{2n}\,\mathrm{Re}\,\psi^{(-2n)}\left(\frac{1}{2}+\frac{\mathrm{i}}{2\pi}y\right).\end{aligned} \tag{4.60}$$

Here, Li_s is the polylogarithm function and $\psi^{(n)}$ the polygamma function, while γ is the Euler-Mascheroni constant. This result is in agreement with taking derivatives of the free energy from Refs. [228, 229].

Evaluating Eq. (4.59) numerically using *Mathematica* [349] (crosschecks by the authors are done using *Python3* [19] and the *Numpy* package [350]) for different values of μ and T reveals the behavior of the bosonic two-point vertex functions in the chiral GN model. Thereby, $\bar{\rho}_0 = \bar{\Sigma}^2(\mu=0,T=0) + \bar{H}^2(\mu=0,T=0)$, the value of the chiral condensate in the vacuum squared, is used to set the scale in the following ($\bar{\Sigma}(\mu,T)$ and $\bar{H}(\mu,T)$ are the homogeneous, global minima of the effective potential with respect to $\bar{\sigma}$ and $\bar{\eta}$, respectively). In Fig. 4.6, we investigate $\Gamma^{(2)}_{\varphi_2}$ for different values of T at fixed $\mu/\sqrt{\bar{\rho}_0} = 1$ as a function of the external momentum q. Since $\Gamma^{(2)}_{\varphi_1}(q) = \Gamma^{(2)}_{\varphi_2}(-q)$ this plot is sufficient to understand the complete behavior of both bosonic two-point vertex functions. The bosonic two-point

9 More precisely, the condensates Σ and H do not depend on $\tilde{\mu}$.

10 The formulae obtained after momentum space integration are obviously different in two spatial dimensions compared to one due to the additional factor of p in the Jacobi determinant of polar coordinates. Conceptually, however, the procedure is similar to the one in $1+1$ dimensions. More details for the $1+1$-dimensional GN model are discussed in-depth in Ref. [1].

vertex functions are positive for all q when $T/\sqrt{\bar{\rho}_0} > T_c/\sqrt{\bar{\rho}_0} = \mathrm{e}^\gamma/\pi$ where T_c is the critical temperature of the phase transition between the SP and the IP in the chiral GN model, see Section 3.2.2. Precisely at $T = T_c$, the bosonic two-point vertex functions develop a root at $q = 2\mu$ indicating the onset of the instability of the homogeneous phase against inhomogeneous fluctuations. Consequently, the stability analysis successfully detects the phase transition between the SP and the IP in the chiral GN model. Moreover, $q = 2\mu$ is precisely the momentum of the chiral spiral at $T = T_c$ and below. The latter can, of course, not be predicted using the bosonic two-point vertex functions, which however still always have a minimum at $q = \pm 2\mu$. Rather, it is an interesting observation that the minimum of the bosonic two-point vertex functions corresponds to the true wave vector of the chiral spiral, cf. Eq. (3.12). The minimum of the $\Gamma^{(2)}_{\varphi_2}$ finally turns into a pole at $q = \pm 2\mu$ when lowering the temperature further to $T = 0$. This effect is also observed in the GN model, see the bottom left graph in Fig. 4.3.

CONNECTION TO THE INNER SPINODAL LINE Inspecting Fig. 4.6, we find that for $T < T_c$ there exists an interval in q for which the bosonic two-point vertex functions are negative. The roots, i.e., the boundaries of this interval, are related to the inner spinodal line of the homogeneous phase boundary of the GN model (or chiral GN model when the inhomogeneous chiral condensates are neglected). The inner spinodal line is defined as the line where the second derivative of the effective potential (or effective action) with respect to the homogeneous order parameter vanishes at vanishing homogeneous fields. However, the second derivative of the homogenoeus effective potential with respect to $\sqrt{\bar{\rho}}$ is proportional to the bosonic two-point vertex function of the GN model $\Gamma^{(2)}_\sigma(q)$ at $q = 0$ and vanishing homogeneous fields. Since the phase diagram is symmetric with respect to $\mu \to -\mu$, there are always two values $\mu = \pm\mu_{\text{spinodal}}$ of the chemical potential for each $T < T_c$ where $\Gamma^{(2)}_\sigma(q = 0)$ vanishes. These two values correspond to two combinations of μ and q given by $\pm(\mu \pm q/2)$ where the bosonic two-point vertex functions $\Gamma^{(2)}_{\varphi_j}$ in the chiral GN model vanishes exactly. There are two roots for each of the bosonic two-point vertex functions, which can be related to each other by sign reflection according to the combinations of $\pm(\mu \pm q/2)$ or, vice versa, by $\Gamma^{(2)}_{\varphi_1}(q) = \Gamma^{(2)}_{\varphi_2}(-q)$. For fixed chemical potential, these roots are the respective end points of the interval in q where one of the bosonic two-point vertex functions is negative.

4.4 DETECTING THE QUANTUM PION LIQUID FROM HESSIAN MATRIX WITH GENERALIZED $\mathcal{PT}$ SYMMETRY

As discussed above, the bosonic two-point vertex functions $\Gamma^{(2)}_{\phi_j,\phi_k}$ can be interpreted as a Hessian matrix which contains information about the curvature of the (quantum) effective action with respect to (inhomogeneous) perturbation. This is explicitly computed in Section 4.1.2 with Eq. (4.24) as the Hessian matrix within the mean-field approximation. In Section 2.2.3, we show, however, that the $\Gamma^{(2)}_{\phi_j,\phi_k} = (\langle\phi_j\phi_k\rangle_c)^{-1}$, i.e., the bosonic two-point vertex functions are the inverse of the bosonic two-point correlation functions. Thus, one can extract information about the propagator and its poles directly from $\Gamma^{(2)}_{\phi_j,\phi_k}$. For the present analysis, one has to mention that $\Gamma^{(2)}_{\phi_j,\phi_k}$ computed in Eq. (4.24) only are the exact bosonic two-point vertex functions of the system when the ground state is homogeneous. With the presented analysis, we have to assume that this is the case when no instabilities

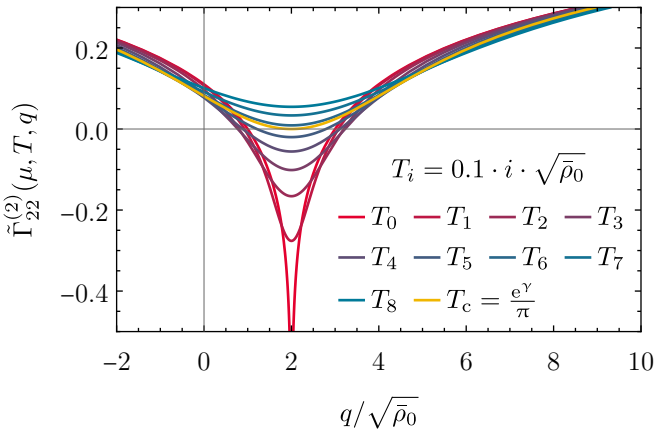

Figure 4.6: Eigenvalue of the bosonic two-point function (4.59), $\tilde{\Gamma}^{(2)}_{22} = \Gamma^{(2)}_{\varphi_2}$, for different T at fixed quark chemical potential $\mu = \sqrt{\bar{\rho}_0}$ as a function of the external momentum q. This plot was produced using *Mathematica* [349].

are detected in the stability analysis, although in principle one would need to determine the true ground state by minimizing the quantum effective action, see the discussion in the paragraph about "general remarks regarding the stability analysis" in Section 4.1.2. Whether this assumption is justified depends on the studied theory and must be checked in each individual case. To perform the search for instabilities, the full Hessian matrix $\Gamma^{(2)}_{\phi_j,\phi_k}$ has to be diagonalized by finding an appropriate basis φ_j and instabilities towards an IP have to be excluded, i.e. $\Gamma^{(2)}_{\varphi_j}(\vec{\varphi}, \mu, T, q) > 0$.

Assuming this analysis was already performed and no IP is observed, one can examine the existence of a QπL in the following way. The basis of our investigation is the discussion in Section 3.1.2. Therein, we explained that propagator poles of ordinary, homogeneous phases, such as the HBP or the SP, typically are purely imaginary leading to an exponential decay of the position space propagators. This is a standard result for QFT in Euclidean spacetime after Wick rotation [64, 282]. However, in theories with a generalized $\mathcal{PT}$ symmetry one may observe a so-called disorder line, where two or more propagator poles first become degenerate and, when crossing the disorder line, these poles develop a non-vanishing real and imaginary part [185, 191], see Section 3.1.2. In finite density QCD, this symmetry transformation corresponds to the combined operation of a charge conjugation $\mathcal{C}$ and complex conjugation $\mathcal{K}$ leaving the QCD action invariant at $\mu \neq 0$ (while it is not invariant under $\mathcal{C}$ or $\mathcal{K}$ individually), see Section 3.1.2 for details. A disorder line is also observed in a study of the stability of an inhomogeneous chiral spiral condensate against flcutuations of Goldstone bosons of O(N_s) symmetry breaking [219].

The disorder line corresponds to a transition towards a so-called $\mathcal{PT}$-broken phase with position space propagators that feature short- and/or intermediate-range oscillations, induced by the real part of the pole, in addition to the exponential decay, stemming from the imaginary part of the pole as discussed above, that dominates the behavior for large distances. In this thesis, this regime is called a QπL, see Section 1.2 or Chapter 3. From the computation and analysis of the mass matrix (the static Hessian matrix) in a scalar field theory with dynamical scalar fields, one can anticipate the appearance of complex-conjugate propagator poles [188], see Section 3.1.2 for details, and the QπL can also be observed in LFT simulations [180, 188, 190]. In a four-fermion model, one uses that the bosonic two-point correlation function are the inverse of the Hessian matrix $\Gamma^{(2)}_{\phi_j,\phi_k}$ in the

mean-field analysis from the previous sections. Also the Hessian matrix in the mean-field approximation $\Gamma^{(2)}_{\phi_j,\phi_k}$ can have complex-conjugate eigenvalues which can be shown to be the characterizing behavior in a QπL [189], see below.

In the analysis of $\Gamma^{(2)}_{\varphi_j}$, however, we at first only consider real momenta q and, therefore, are not in the position to find the roots of the bosonic two-point vertex functions in the complex plane in order to directly determine the respective poles of $\langle\varphi_j\varphi_j\rangle_c(q)$. Although it is possible to repeat the computation of $\Gamma^{(2)}_{\phi_j,\phi_k}$ with $q \in \mathbb{C}$, we perform a simpler, exploratory analysis of the bosonic two-point vertex functions based on the assumption that the ground state is homogeneous. A low-momentum expansion of the bosonic two-point vertex functions in the diagonalizing field basis

$$\Gamma^{(2)}_{\varphi_j}(q) \approx Z_{\varphi_j} q^2 + \Gamma^{(2)}_{\varphi_j}(q=0)\,, \tag{4.61}$$

with the bosonic wave function renormalitzation Z_{φ_j} (4.25), yields an effective kinetic term $\sim q^2$ in the quantum effective action and can be used as an approximation of $\Gamma^{(2)}_{\varphi}$ for small $|q|$. Note that $\Gamma^{(2)}_{\varphi_j}(q=0)$ just corresponds to the mass matrix in its diagonal basis. Setting the low-momentum expansion (4.61) to zero, allows to search for propagator poles in this range. Especially, when

$$\Gamma^{(2)}_{\varphi_j}(q=0) = \left(\Gamma^{(2)}_{\varphi_k}(q=0)\right)^*, \qquad j \neq k, \tag{4.62}$$

i.e., complex-conjugate eigenvalues of $\Gamma^{(2)}(q=0)$ appear, one can directly compute the propagator poles when the imaginary part of Z_{φ_j} is small enough. These poles then also appear as complex-conjugate pairs. Details on this procedure are discussed in Chapter 6. In this chapter, a QπL is observed in the phase diagram of a four-fermion model using this expansion. Analytical benchmarks for this procedure are currently not available, since to our knowledge there exist no simple, analytical result on the existence of QπLs in four-fermion theories in the literature.

4.5 IMPLICATIONS FOR THE FOLLOWING RESULT CHAPTERS

In this chapter, a general derivation of the bosonic two-point vertex functions within the mean-field approximation in a generic four-fermion model in $d+1$ Euclidean spacetime dimensions at non-vanishing temperatures and chemical potentials was presented. We established the appearance of the bosonic two-point vertex functions in the Hessian matrix when applying inhomogeneous fluctuations to homogeneous condensates and demonstrated how the stability of homogeneous condensates can be analyzed by studying the bosonic two-point vertex functions in an appropriate field basis. Moreover, the bosonic wave-function renormalization was computed as the second derivative of the bosonic two-point vertex functions with respect to the external momentum q evaluated at $q=0$. This method was then applied and benchmarked on the phase diagram of the GN model and the chiral GN model in $1+1$ dimensions. Thereby, we demonstrated that the stability analysis is successful in determining the phase transition between an IP and the SP, although it is not guaranteed that the region of instabilities, that is obtained from the analysis of the bosonic two-point vertex functions, is identical to an IP that is obtained from computing the true ground state of the theory (although it is often extremely difficult or impossible to truely determine the ground state). In the GN model, we showed that the method fails to detect parts of the IP when there is an energy barrier between the homogeneous expansion point

and the true, inhomogeneous ground state. In the chiral GN model, the method succeeds in detecting the correct phase boundary between the SP and the IP.

In the case of stable homogeneous ground states, we discussed further the potential of the bosonic two-point vertex functions to analyze properties of the corresponding bosonic two-point correlation functions. Finding complex-conjugate root pairs of the bosonic two-point vertex functions in momentum space yields the existence of a QπL – a regime where the position space propagators are oscillatory but exponentially suppressed. The existence of this regime is based on symmetry arguments from QFTs with generalized $\mathcal{PT}$ symmetry, a framework that also applies to QCD at non-vanishing μ. We outlined how these complex roots can be obtained from a low momentum expansion of the bosonic two-point vertex functions, a method that is applied to a four-fermion model in Chapter 6.

The presented analysis of the bosonic two-point vertex functions in four-fermion models is used as a general framework in the following Chapter 5 and Chapter 6 in order to study the phase diagams of the respective theories with respect to the existence of exotic phases.

5

ABSENCE OF INHOMOGENEOUS CONDENSATES IN (2 + 1)-DIMENSIONAL QCD-INSPIRED MODELS

DISCLOSURE The central findings of this chapter have been published in Ref. [2] and Ref. [3]. To be specific, the results in Section 5.2 stem from Ref. [2] and were obtained in collaborative work with L. Pannullo. They can be associated to both of us in similar shares. The figure in Section 5.2 was produced by L. Pannullo. All other figures were produced by myself. These findings were extended and build upon in Ref. [3] by including the quartic vector interactions. The results including vector interactions in Section 5.3 can, thus, solely be attributed to the author of this thesis. The majority of the presentation of the findings has been rewritten and restructured in the context of this manuscript. However, parts of the description of the tables and central equations are close to the respective references.

ABSTRACT AND RELATION TO THE RESEARCH OBJECTIVES In this chapter, we show that homogeneous condensates are stable against IPs in $2+1$-dimensional four-fermion and Yukawa-type models. The technique of stability analysis, which was introduced in Chapter 4, is applied to these models at non-vanishing baryon chemical potential. We argue that the absence of instabilities is strong evidence for the absence of IPs in these models at any non-vanishing temperature.[1] Thereby, we naturally arrive at conclusive evidence with respect to the part of **RO5**: "What is the fate of inhomogeneous chiral condensates within $2+1$-dimensional four-fermion theories and related QCD-inspired models?". The latter part regarding related QCD-inspired models can only partially be tackled using also context from other findings in the literature.

OUTLINE After a brief definition of the models in Section 5.1, the absence of instabilities is proven for four-fermion models with a complete basis in the local local, (Euclidean) Lorentz-scalar interaction channels at all values of the chemical potential and non-vanishing temperatures in Section 5.2. This finding is shown to be valid also for corresponding Yukawa models that can be obtained from a generalization of the four-fermion models. Moreover, the absence of instabilities is shown for models subjected to multiple chemical potentials, but with a restricted set of scalar interactions.. In Section 5.3, we extend the analysis to four-fermion models with vector interactions and show the absence of instabilities towards inhomogeneous fluctuations within the SP of the theories. This analysis is restricted to the SP since a non-vanishing chiral condensate leads to mixing effects between scalar and vector modes and the appearance of a QπL – an effect that is investigated in Chapter 6. In Section 5.4, the findings are summarized in a compact way and contextualized with the

1 A degeneracy between a HBP and an IP can be observed at $T = 0$ according to Ref. [321]. This degeneracy is specifically excluded from the argumentation.

literature and the **RO**s defined in Section 1.3. Further, we provide research perspectives building on the results and methodology developed in this chapter.

5.1 MODELS

We start by studying four-fermion models in $2+1$-dimensions with the action

$$\mathcal{S}[\bar{\psi},\psi] = \int_0^\beta \mathrm{d}\tau \int \mathrm{d}^2x \left[\bar{\psi}\left(\not{\partial} + \gamma_3\mu\right)\psi - \left[\sum_{c_j\in\vec{\mathcal{C}}} \tfrac{\lambda_j}{2N_f} \left(\bar{\psi}\, c_j\, \psi\right)^2 \right] \right], \tag{5.1}$$

where ψ contains $2N_f$ four-component fermion fields (the factor of 2 comes from an isospin degree of freedom) and T and μ are introduced as discussed in Section 2.1, see Section 2.3 for a more detailed discussion of four-fermion models. The interaction vertices c_j are 8×8 matrices in isospin and spin space. We study two different tupels of local interaction channels, i.e., either only scalar interactions

$$\vec{\mathcal{C}} = \vec{\mathcal{C}}_s = (\mathbb{1}, \mathrm{i}\gamma_4, \mathrm{i}\gamma_5, \gamma_{45}, \vec{\tau}, \mathrm{i}\vec{\tau}\gamma_4, \mathrm{i}\vec{\tau}\gamma_5, \vec{\tau}\gamma_{45}) \tag{5.2}$$

or the full basis of four-fermion interaction channels

$$\vec{\mathcal{C}} = \vec{\mathcal{C}}_c = \vec{\mathcal{C}}_s \times (1, \mathrm{i}\gamma_\nu)\,. \tag{5.3}$$

Vector interactions are contained in

$$\vec{\mathcal{C}}_v = \vec{\mathcal{C}} \setminus \vec{\mathcal{C}}_s. \tag{5.4}$$

Note that $\vec{\mathcal{C}}_c$ is the full set of local four-fermion interactions for two flavors of fermions in $2+1$ and also in $3+1$ dimensions, since the bilinears $\gamma_\nu\gamma_4$ and $\gamma_\nu\gamma_{45}$ correspond to the commonly known tensors $c_j \sim [\gamma_\alpha,\gamma_\beta]$ in $3+1$ dimensions. Thus, the 16 different, linear independent Dirac matrices contained in Eq. (5.3) are a basis of the 4×4 matrices in spinor space. The coupling constants λ_j have the inverse mass dimension. We choose either $\lambda_j = \lambda_S$ or $\lambda_j = 0$ for $\vec{\mathcal{C}} = \vec{\mathcal{C}}_s$, while $\lambda_j = \lambda_S$ or $\lambda_j = 0$ for scalar interactions and $\lambda_j = \lambda_V$ or $\lambda_j = 0$ for vector interactions when studying $\vec{\mathcal{C}} = \vec{\mathcal{C}}_c$. This choice allows us to study different actions with different chiral symmetry groups.

Note that differing conventions for the Gamma matrices and the Wick rotation from Minkowski spacetime can result in differing prefactors in front of the respective interaction terms (especially factors of i and the correct signs can easily be messed up in this procedure), specifically with respect to the vector interactions. The Wick rotation for an action containing both scalar and vector interactions is performed in Appendix A.2.2.

PARTIAL BOSONIZATION Auxiliary bosonic fields are introduced using a Hubbard Stratonovich transformation following Section 2.3.1. This allows to eliminate the four-fermion interaction terms and obtain Yukawa-type interactions between the fermion fields and the auxiliary fields, see Eq. (2.35). Thereby, the auxiliary fields $\vec{\phi}$ and $\vec{v}_\nu$ are introduced to eliminate the scalar and vector interactions, respectively.[2] Following Eq. (2.43),

2 One has to be careful when performing the Hubbard Stratonovich transformation for the vector interactions to ensure the correct signs are used in order to ensure the convergence of Eq. (2.35).

the auxiliary bosonic fields $\vec{\phi}$ (spin quantum number $S = 0$) and $\vec{v}_\nu$ ($S = 1$) obey the Ward identities

$$\langle \phi_j \rangle = -\frac{\lambda_j}{N_f} \langle \bar{\psi} c_j \psi \rangle, \qquad \langle v_{j,\nu} \rangle = -\mathrm{i} \frac{\lambda_j}{N_f} \langle \bar{\psi} c_j \gamma_\nu \psi \rangle, \qquad \forall c_j \in \vec{\mathcal{C}}_s \tag{5.5}$$

relating the respective auxiliary fields to the fermion bilinears. We list the quantum numbers of spin S, parity (P_4, P_5) and isospin I of the auxiliary fields and the corresponding fermion bilinears in Tables 5.1 and 5.2. Note that two different parity transformations labeled (P_4, P_5) exist on the level of fermion fields in $2+1$-dimension in the reducible 4×4 representation of the Dirac algebra, see Eqs. (B.25) and (B.26) for their definition. Parity in odd spacetime dimensions is defined as the inversion of an odd number of cartesian axis, otherwise it is an element of the continuous Lorentz group. The different behavior of bilinears under the two parity transformations is relevant in certain condensed matter systems, e.g., in graphene, see Ref. [351] for a comprehensive, yet brief summary.

After the partial bosonization, one can integrate out the fermionic fields in the path integral in order to obtain

$$\frac{1}{N_f} \mathcal{S}_{\mathrm{eff}}[\vec{\phi}, \vec{v}_\nu] = \int \mathrm{d}^3 x \sum_{j, c_j \in \vec{\mathcal{C}}_s} \left[\frac{v_{j,\nu} v_{j,\nu}}{2\lambda_j} + \frac{\phi_j^2}{2\lambda_j} \right] - \mathrm{Tr} \ln \beta \mathrm{Q} \tag{5.6}$$

with the Dirac operator

$$\mathrm{Q}[\vec{\phi}, \vec{v}_\nu] = \gamma_\nu \partial_\nu + \gamma_3 \mu + \sum_{c_j \in \vec{\mathcal{C}}_s} \left(c_j \phi_j + \mathrm{i} c_j \gamma_\nu v_{j,\nu} \right). \tag{5.7}$$

Thereby, we introduced a temperature-dependent multiplicative factor to the partition function in order to ensure a dimensionless argument in the logarithm.

5.2 ABSENCE OF INHOMOGENEOUS CONDENSATES FOR SCALAR INTERACTIONS

For this part of the chapter, we set $\lambda_j = 0$ when $c_j \in \vec{\mathcal{C}}_v$, i.e., we disregard all vector interactions. This amounts to enforcing $v_{j,\nu} = 0$ in Eq. (5.6). For the scalar fields, we set either $\lambda_j = \lambda_S$ or $\lambda_j = 0$ in order to study different models and allow for different symmetry groups in the action (5.1). First, we turn towards the stability analysis as discussed in Section 4.1.2 with a baryon chemical potential before turning towards the more complicated case with multiple chemical potentials. Finally, we discuss the generalization of our findings to Yukawa-type models based on actions of the form Eq. (2.48).

5.2.1 *Stability analysis at non-vanishing baryon chemical potential*

The stability analysis can be performed in a straightforward way without particular emphasis on the diagonalization of the Hessian matrix, see Section 4.1.2. The study is based on the expansion about the homogeneous field configuration $\vec{\phi}(\boldsymbol{x}) = \vec{\bar{\phi}}$, i.e., $\vec{\phi}(\boldsymbol{x}) = \vec{\bar{\phi}} + \delta\vec{\phi}(\boldsymbol{x})$. The leading-order contribution is of second-order in the perturbations $\delta\vec{\phi}$ when the homogeneous expansion points are extrema of the effective action. This ensures that the first-order terms in the expansion vanish, see Section 4.1.2 and Eq. (4.19) for details. However, in this subsection, we will specifically allow for arbitrary homogeneous expansions points in

S	(P_4, P_5)	I	ϕ_j	CORRESPONDING FERMION BILINEAR
0	$(+,+)$	0	σ	$\bar{\psi}\psi$
0	$(+,+)$	1	$\vec{a}_0$	$\bar{\psi}\vec{\tau}\psi$
0	$(+,-)$	0	η_4	$\bar{\psi}\mathrm{i}\gamma_4\psi$
0	$(+,-)$	1	$\vec{\pi}_4$	$\bar{\psi}\mathrm{i}\gamma_4\vec{\tau}\psi$
0	$(-,+)$	0	η_5	$\bar{\psi}\mathrm{i}\gamma_5\psi$
0	$(-,+)$	1	$\vec{\pi}_5$	$\bar{\psi}\mathrm{i}\gamma_5\vec{\tau}\psi$
0	$(-,-)$	0	η_{45}	$\bar{\psi}\gamma_{45}\psi$
0	$(-,-)$	1	$\vec{\pi}_{45}$	$\bar{\psi}\gamma_{45}\vec{\tau}\psi$

Table 5.1: The quantum numbers for spin S, parity (P_4, P_5) (B.25) and (B.26) and isospin I of the auxiliary scalar fields ϕ_j and the fermion bilinears that are related to the auxiliary fields via Eq. (5.5).

S	(P_4, P_5)	I	$v_{j,\nu}$	CORRESPONDING FERMION BILINEAR
1	$(-,-)$	0	ω_ν	$\bar{\psi}\mathrm{i}\gamma_\nu\psi$
1	$(-,-)$	1	$\vec{\rho}_\nu$	$\bar{\psi}\mathrm{i}\gamma_\nu\vec{\tau}\psi$
1	$(-,+)$	0	$f_{1,4}$	$\bar{\psi}\mathrm{i}\gamma_\nu\mathrm{i}\gamma_4\psi$
1	$(-,+)$	1	$\vec{a}_{1,4}$	$\bar{\psi}\mathrm{i}\gamma_\nu\mathrm{i}\gamma_4\vec{\tau}\psi$
1	$(+,-)$	0	$f_{1,5}$	$\bar{\psi}\mathrm{i}\gamma_\nu\mathrm{i}\gamma_5\psi$
1	$(+,-)$	1	$\vec{a}_{1,5}$	$\bar{\psi}\mathrm{i}\gamma_\nu\mathrm{i}\gamma_5\vec{\tau}\psi$
1	$(+,+)$	0	$f_{1,45}$	$\bar{\psi}\mathrm{i}\gamma_\nu\gamma_{45}\psi$
1	$(+,+)$	1	$\vec{a}_{1,45}$	$\bar{\psi}\mathrm{i}\gamma_\nu\gamma_{45}\psi$

Table 5.2: The quantum numbers for spin S, parity (P_4, P_5) (B.25) and (B.26) and isospin I of the auxiliary vector fields $v_{j,\nu}$ and the fermion bilinears that are related to the auxiliary fields via Eq. (5.5).

order to demonstrate the stability of all possible homogeneous field configurations against inhomogeneous perturbations in the whole phase diagram. Obviously, this analysis includes the (homogeneous) extrema of the effective action such that the stability of homogeneous condensates in the phase diagram is explicitly shown. The main result of this subsection is the *absence of any instability of homogeneous condensates against inhomogeneous fluctuations* for non-vanishing temperatures and chemical potentials in the models defined by Eq. (5.1) with $\vec{\mathcal{C}} = \vec{\mathcal{C}}_s$ and $\lambda_j = \lambda_S$ or $\lambda_j = 0$. We present arguments that this finding is strong evidence for the absence of IPs.

SECOND-ORDER CONTRIBUTION After expanding $\mathcal{S}_{\text{eff}}$ in $\delta\vec{\phi}$ around the homogeneous field configuration $\vec{\phi}(\boldsymbol{x}) = \bar{\vec{\phi}}$, the second-order contribution reads (using Eq. (4.23) and following Appendix D.1)

$$\frac{\mathcal{S}^{(2)}_{\text{eff}}}{N_f} = \frac{\beta}{2} \int \frac{\mathrm{d}^2 q}{(2\pi)^2} \left[\sum_{j \in \vec{\mathcal{C}}} |\delta\tilde{\phi}_j(\boldsymbol{q})|^2 \, \Gamma^{(2)}_{\phi_j} \left(M^2, \mu, T, q \right) \right], \tag{5.8}$$

where $\delta\tilde{\phi}(\boldsymbol{q})$ are the Fourier coefficients of the inhomogeneous perturbations $\delta\phi(\boldsymbol{x})$, see Eq. (4.7). The magnitude of the perturbation's momentum is $q = |\boldsymbol{q}|$ and the fermion mass, that is dynamically generated through the homogeneous expansion point $\vec{\phi}$, can generally be written as

$$M^2\left(\vec{\phi}\right) = \sum_{j \in \vec{\mathcal{C}}_s} c_j^\star c_j (\bar{\phi}_j)^2 \equiv M^2, \qquad \text{with} \qquad c_j^\star = \begin{cases} c_j & \text{for } c_j = 1, \vec{\tau}, \\ -c_j & \text{otherwise .} \end{cases} \tag{5.9}$$

The expression for M^2 manifests the invariance under chiral symmetry transformations of the model (see Appendix B.2 for details) can be mapped onto rotational symmeties of the auxiliary fields. Thereby, η_{45} and $\vec{\pi}_{45}$ do not transform under $\mathrm{U}_\gamma(2N_f)$ and enter as a term $\sim -\phi_j^2$ in Eq. (5.9). However, both of these fields can be shown to have vanishing expectation values in the homogeneous ground state, see the paragraph about the homogeneous expansion point below. Details on the derivation of Eq. (5.8) can be found in Appendix D.1.

DIAGONALIZATION AND HOMOGENEOUS EXPANSION POINT Note that Eq. (5.8) is diagonal with respect to the auxiliary fields ϕ_j such that no diagonalization procedure is necessary (see Section 4.1.2 for a broad discussion about the diagonalization of the Hessian matrix when this is not the case). Therefore, the homogeneous field configuration $\bar{\vec{\phi}}$ must be chosen in a specific way such that only $\bar{\sigma}$ is non-vanishing. This is possible for the homogeneous ground state $\bar{\vec{\Phi}}$ according to the symmetries of the model, as will be elaborated on in the following.

The homogeneous condensate for all possible models, that can be obtained from Eq. (5.1) with $\vec{\mathcal{C}} = \vec{\mathcal{C}}_s$ (5.2) by setting $\lambda_j = \lambda_S$ or $\lambda_j = 0$, can be rotated such that only $\bar{\sigma}$, $\bar{\vec{\pi}}_{45}$ and $\bar{\eta}_{45}$ develop a non-vanishing expectation value, see Appendix B.2 for a discussion of all relevant symmetry transformations. This is due to the fact that the chiral symmetry transformations act as rotations of the field vector $\vec{\phi}$, specifically excluding $\bar{\eta}_{45}$ and $\bar{\vec{\pi}}_{45}$. An example is discussed in Eq. (B.4) in $d = 1$ spatial dimensions with the axial $\mathrm{U}_{\gamma_5}(1)$ transformation. Thereby, one needs to recall that the bilinears appearing in Eq. (B.4) are connected by Ward identities (5.5) to $\vec{\phi}$ such that they are also rotated under the chiral transformations. By analyzing the homogeneous effective action, one can additionally show that $\bar{\eta}_{45} = \bar{\vec{\pi}}_{45} = 0$ for all temperatures and chemical potentials. First, we discuss this

restrictring ourselves to isoscalar channels, i.e., allowing only for non-vanishing auxiliary fields $\sigma, \eta_4, \eta_5, \eta_{45}$. Using the chiral transformations Eq. (B.18) one can rotate the auxiliary fields such only $\bar{\sigma}$ and $\bar{\eta}_{45}$ develop non-vanishing expectation values. Then, we analyze the fermion contribution $\mathrm{Tr}\ln \mathrm{Q}$, which can be represented in a block-diagonal form with 2×2 blocks corresponding to the irreducible spin representation in $2+1$ dimensions, see Eq. (A.22) for the concrete representation chosen. These blocks can be interpreted as GN model contributions in the irreducible fermion representation with chemical potential μ and homogeneous fields $\bar{\phi}_{L/R} \equiv \bar{\sigma} \pm \bar{\eta}_{45}$, see the theory section of Ref. [7] for an in-depth discussion of these irreducible blocks. The model decomposes into two independent GN models with the same chemical potential and temperature, which gives us identical homogeneous expectation values, $\bar{\phi}_L = \bar{\phi}_R$, and, thus $\bar{\eta}_{45} = 0$. Analogous arguments involving additional isospin rotations are valid when additionally considering $\vec{\pi}_{45}$. As a side note, this shows that no spontaneous parity breaking in the four-fermion models for all μ and T occurs within this analysis.[3]

Correspondingly, Eq. (5.6) with $\vec{\mathcal{C}} = \vec{\mathcal{C}}_s$ and homogeneous fields $\vec{\phi} = \vec{\bar{\phi}}$ has a gap equation for $\bar{\sigma}$ equivalent to the $2+1$-dimensional GN model, see Appendix C.2.1 for a in-depth presentation. Thus, the homogeneous condensates are given by $\bar{\phi}_j = \delta_{j,0}\bar{\sigma}$, $M^2 = \bar{\sigma}^2$ and the homogeneous phase diagram, i.e., the phase diagram when restricting the fields to homogeneous field configurations, is given by the phase diagram of the GN model. The homogeneous phase diagram of the $2+1$-dimensional GN model, as first obtained in Ref. [249], features a phase at low temperatures and chemical potentials where the discrete chiral symmetry is spontaneously broken by a non-zero chiral condensate [243, 249]. At finite temperature this phase is separated from the chirally symmetric phase by a second-order phase transition. At $(\mu, T)/\mathcal{M}_0 = (1, 0)$ one obtains a first-order transition point, where degenerate minima with $\mathcal{M}/\mathcal{M}_0 \in [0, 1]$ have the same minimal effective potential, which becomes flat. The phase diagram is presented in Fig. 6.1 of Chapter 6 where it is obtained in a specific limit of the model investigation. In this chapter, however, we are going to focus on the stability of homogeneous condensates against inhomogeneous perturbations, where the exact solution for $\bar{\mathbf{\Phi}} = (\bar{\sigma}, 0)$ as a function of T and μ is not needed.

EVALUATION OF THE BOSONIC TWO-POINT VERTEX FUNCTIONS According to Eq. (5.8), $\Gamma^{(2)}_{\phi_j}(M^2, \mu, T, q^2)$ describes the eigenvalue of Hessian matrix in field space, compare Eq. (4.23) for a general form of such a Hessian matrix. Consequently, $\Gamma^{(2)}_{\phi_j}(M^2, \mu, T, q^2)$ encodes the curvature of the effective action with respect to $|\delta\tilde{\phi}_j(\boldsymbol{q})|$ and, thus, its sign needs to be studied at non-vanishing q in order to determine the stability of the homoge-

3 As described above, this is the case when all couplings are either 0 or λ_S. For a condensed matter system, one would have to think about the relevant parameter space, which is likely to incorporate different couplings for the parity-breaking mass terms. Specifically, if the couplings of the terms involving γ_{45} differ from the scalar ones (which is not forbidden by symmetry constraints), also the corresponding condensates might be generated

neous condensates against inhomogeneous fluctuations. Performing the Dirac traces with the above choice of homogeneous fields in Eq. (4.23) yields, see Appendix D.1 for details,

$$\begin{aligned}
&\Gamma^{(2)}_{\phi_j}\left(M^2,\mu,T,\boldsymbol{q}\right) = \qquad (5.10)\\
&= \frac{1}{\lambda} + \frac{8}{\beta}\sum_n \int \frac{\mathrm{d}^2 p}{(2\pi)^2}\left(\frac{-1}{\tilde{\nu}_n^2+\boldsymbol{p}^2+M^2} + \frac{1}{2}\frac{q^2+a_{\phi_j}M^2}{[\tilde{\nu}_n^2+\boldsymbol{p}^2+M^2][\tilde{\nu}_n^2+(\boldsymbol{p}+\boldsymbol{q})^2+M^2]}\right) \equiv\\
&\equiv \frac{1}{\lambda} - \ell_1\left(M^2,\mu,T\right) + \frac{1}{2}\left(q^2+a_{\phi_j}M^2\right)\ell_2\left(M^2,\mu,T,q\right)\\
&\equiv \frac{1}{\lambda} - \ell_1\left(M^2,\mu,T\right) + L_{2,\phi_j}(M^2,\mu,T,q),
\end{aligned}$$

where $\tilde{\nu}_n = (\nu_n - \mathrm{i}\mu)$ with the fermionic Matsubara frequencies $\nu_n = 2\pi(n+1/2)T$, see Eq. (2.15) for their introduction. We find $a_{\phi_j} = a_+ = 4$ for fields ϕ_j with parity quantum number $(P_4,P_4) \in \{(+,+),(-,-)\}$ and $a_{\phi_j} = a_- = 0$ for fields with $(P_4,P_5) \in \{(-,+),(+,-)\}$. Accordingly, we find two possible momentum dependent contributions

$$L_{2,+}(M^2,\mu,T,q) = \frac{1}{2}\left(q^2+4M^2\right)\ell_2(M^2,\mu,T,q)\ , \qquad (5.11)$$

$$L_{2,-}(M^2,\mu,T,q) = \frac{1}{2}q^2\ell_2(M^2,\mu,T,q) \qquad (5.12)$$

to the bosonic two-point vertex functions. The integral ℓ_2 evaluated at $T=0$ yields the closed form expression

$$\ell_2(M^2,\mu,T=0,q^2) = \frac{2}{\pi q}\begin{cases} 0\,, & \mu^2 > M^2+q^2/4\\ \arctan\left(\frac{\sqrt{q^2+4(M^2-\mu^2)}}{2\mu}\right)\,, & M^2 \le \mu^2 \le M^2+q^2/4\,. \\ \arctan\left(\frac{q}{2|M|}\right)\,, & \mu^2 < M^2 \end{cases} \qquad (5.13)$$

Note that the integral ℓ_1 is also obtained in the fermionic trace in the gap equation (C.16) of the GN model, see Appendix C.2.1. The gap equation and, correspondingly, ℓ_1 is typically used as a renormalization condition in the vacuum for the coupling constant λ. Further expressions for ℓ_1 for various cases of μ, T, M^2 can be found in Appendix C.2.1. For $L_{2,\pm}$ and ℓ_2 different cases of μ, T, M^2, q^2 can be found in Appendix D.1.1.

ABSENCE OF INSTABILITIES The global homogeneous minimum, i.e., the global minimum of the homogeneous effective potential, see Section 2.4.4, of the theory is the relevant expansion point when searching for an IP via the stability analysis. It is by definition stable against *homogeneous fluctuations* at all temperatures and chemical potentials, i.e. $\Gamma^{(2)}_{\phi_j}(M^2,\mu,T,q^2=0) \ge 0$. Thus, an instability towards inhomogeneous fluctuations is ruled out if the momentum-dependent terms in $\Gamma^{(2)}_{\phi_j}$ are monotonically increasing functions of q. This is the case for the relevant terms $L_{2,\pm}(M^2,\mu,T,q^2)$ for all values of T,μ,M^2. From the analytical form (5.13) the monotonically increasing behavior of ℓ_2 and, consequently, also $L_{2,\pm}$ is obvious at zero temperature. The same is true for all values of T, μ, M^2 which can be verified from numerical evaluation of the integral expressions ℓ_1 and ℓ_2 in Appendix C.2.1 and Appendix D.1.1, respectively. In Fig. 5.1 an exemplary color plot of $L_{2,\pm}$ for $T/M_0 = 0.0, 0.05$ and $\mu/M_0 = 1.0$ as a function of q and M is shown. Consequently, no instabilities towards IPs are observed in the general model defined by Eq. (5.1)

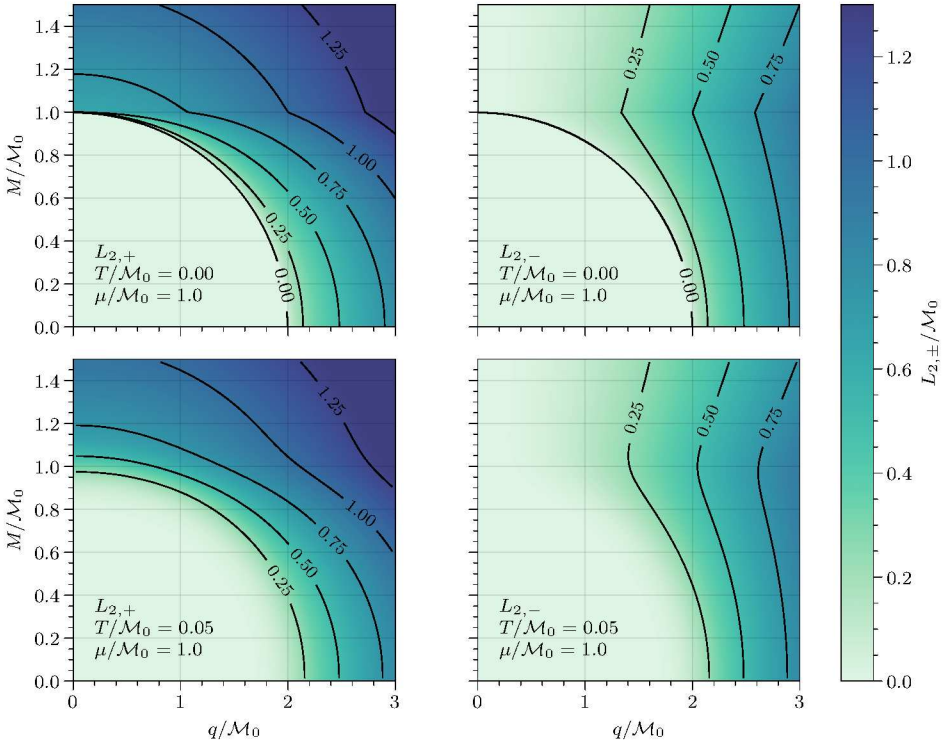

Figure 5.1: $L_{2,+}$ and $L_{2,-}$ for $T/M_0 = 0, 0.05$ and $\mu/M_0 = 1.0$ as a function of q and M. The 0.0 contour line and its label are not shown, because they would be obscured by the axis. In the ancillary files to Ref. [2], we provide a *Python3* script for the numerical computation of $L_{2,\pm}$ for arbitrary values of (M^2, μ, T, q^2) and the production of figures similar to this one. See Eqs. (5.10) and (5.11) for the definition of $L_{2,\pm}$.

with $\vec{\mathcal{C}} = \vec{\mathcal{C}}_s$ and $\lambda_j = \lambda_S$ or $\lambda_j = 0$ is stable against inhomogeneous fluctuations for all temperatures and chemical potentials. Moreover, these models also do not feature a moat regime where $\Gamma^{(2)}_{\phi_j}$ develops a global minimum at $q \neq 0$, see Section 3.1.1 and Section 4.1.4 for a more detailed introduction of the moat regime. The monotonically increasing behavior of $L_{2,\pm}$ implies that the wave function renormalization Z, the curvature of the bosonic two-point vertex function with respect to q, see Eq. (4.25), is always ≥ 0, and the moat regime is absent in these models.

At zero temperature, one finds $\ell_2 \sim \Theta\left(\mu^2 - M^2 - q^2/4\right)$ resulting in the observation of a plateau with $\Gamma^{(2)}_{\phi_j}(M^2, \mu, T = 0, q = 0) = \Gamma^{(2)}_{\phi_j}\left(M^2, \mu, T = 0, q^2 \leq 4\left(\mu^2 - M^2\right)\right)$. In this area, the bosonic wave function renormalization Z but also higher derivatives of the bosonic two-point vertex functions vanish. The flatness itself is a consequence of the behavior of the fermionic distribution functions (see Eq. (C.18) for their definition) at zero temperature. However, when also the contribution $1/\lambda - \ell_1$ vanishes, the whole bosonic two-point function $\Gamma^{(2)}_{\phi_j}$ vanishes for $0 \leq q^2/4 \leq \mu^2 - M^2$ implying a degeneracy between the homogeneous global minimum and inhomogeneous condensates that can be built up by infinitesimal inhomogeneous perturbations with $q^2/4 \leq \mu^2 - M^2$ according to Eq. (5.8). Such a degeneracy was observed in the $(2+1)$-dimensional GN model at $T = 0$ and $\mu/M_0 = 1.0$ using a one-dimensional ansatz for the inhomogeneous condensate [321]. Interestingly, this ansatz

is the so-called chiral kink, build by Jacobi-elliptic functions, and the found parameters for this ansatz allow for rather large amplitudes of the inhomogeneous condensate, see Fig. 3.2 for a plot of exemplary field configurations of the chiral kink. Moreover, at $T = 0$ and $\mu/M_0 = 1.0$ the homogeneous effective action and, consequently, also the effective potential of the GN model is flat for homogeneous field values $M/M_0 \in [0.0, 1.0]$. This point in the phase diagram was termed a first-order phase transition in the past, but rather this behavior corresponds to a CP. As discussed above, the homogeneous phase diagram of all models described by Eq. (5.8) with $\vec{\mathcal{C}} = \vec{\mathcal{C}}_s$ and $\lambda_j = \lambda_S$ or $\lambda_j = 0$ is identical to the one of the $(2+1)$-dimensional GN model.

At this point, it is important to mention that the absence of instabilities towards inhomogeneous fluctuations does not completely rule out the existence of an IP. As shown in Ref. [1] at the example of the $(1+1)$-dimensional GN model, it is possible that an energy barrier exists between the homogeneous minimum, i.e., the minimum of the homogeneous effective potential and, thus, the appropriate expansion point for the stability analysis, and the global inhomogeneous minimum. Then, the homogeneous condensate is metastable and, thus, the IP is not detected by the stability analysis although the inhomogeneous condensate is energetically favored. Such a phase can only be detected by calculations with a guess of an ansatz function, reducing the minimization of the effective action for inhomogeneous condensates to the minimization of a few parameters, or by numerical brute-force minimization of the effective action using lattice discretizations of the theory. For the $(2+1)$-dimensional GN model, there is evidence that an IP can also not be found by explicit lattice minimizations of the effective actions [7, 8, 240, 241, 344]. In these works, only IPs are found at finite lattice spacings which are also detected using the stability analysis, see Refs. [7, 241, 344] for detailed descriptions. It is crucial to note that these IPs vanish when taking the continuum limit [240, 241] as the bosonic two-point vertex function converges toward a momentum dependence proportional to $L_{2,+}$. These findings in the $(2+1)$-dimensional GN model suggest that the stability analysis applied to the general four-fermion model (5.1) with Lorentz-scalar interactions also does not miss an IP. Also, to the best of our knowledge, all IPs in effective model investigations can at least in some parameter region be detected by the stability analysis. Typically, one observes a transition between the SP and the IP which is of second-order. This implies that at least this second-order transition can be detected by analyzing the stability of the SP against inhomogeneous fluctuations. Finding the stability of all homogeneous expansions points, as described above, in combination with these arguments is strong evidence for the absence of inhomogeneous condensates in all models described by Eq. (5.1) – or, vice versa, the effective action (5.6) – with $\vec{\mathcal{C}} = \vec{\mathcal{C}}_s$ and $\lambda_j = \lambda_S$ or $\lambda_j = 0$. Moreover, we showed the absence of a moat regime in both the SP and the HBP of the respective models.

DIFFERENT MODELS AND SYMMETRIES In Table 5.3, we present examples of four-fermion models where the condensates do not develop an instability towards inhomogeneous perturbations and, thus, it is improbable that an IP exists in their respective phase diagram. All presented models can be obtained from the action (5.1), or the effective action (5.6), by using $\vec{\mathcal{C}} = \vec{\mathcal{C}}_s$ (5.2) and setting $\lambda_j = \lambda_S$ or $\lambda_j = 0$. This allows to study different theories invariant under different symmetry groups. The main purpose of Table 5.3 is to illustrate that the non-existence of IPs and moat regimes in $(2+1)$-dimensional four-fermion models is independent of the number of considered interaction channels and the respective (chiral) symmetry group of the action. This is significantly different from findings in $1+1$-dimensions where the phase diagram of a theory can differ significantly when changing the

interaction channels and the respective symmetry group [201, 202, 245–248]. As already discussed above, the momentum-dependent part of the bosonic two-point vertex functions $\Gamma^{(2)}_{\phi_j}$ is given by $L_{2,+}$ when the parity quantum numbers (P_4, P_5) of the corresponding bosonic field ϕ_j are even whereas it is given by $L_{2,-}$ when the parity quantum numbers are odd.

The first row of Table 5.3 shows the GN model with one single (iso-)scalar interaction channel, c.f., Table 5.1. The momentum-dependent part of the bosonic two-point vertex function is proportional to $L_{2,+}$ as already shown in Ref. [241].

The second row considers the analogue of an NJL model in $(2+1)$-dimensions with three interaction channels, one isoscalar and two isovector interactions either of which is odd under P_4 or P_5. The axial symmetry transformations Eqs. (B.14) and (B.15) are broken by the isovector interactions similar to the axial U_1 symmetry breaking in the NJL model in $3+1$ dimensions[4] such that an invariance under combined isospin and axial symmetries Eqs. (B.20) and (B.21) remains. The γ_5 operator is ambiguous in $(2+1)$-dimensions such that it is sensible to construct an NJL model in this way. The momentum-dependence of the bosonic two-point vertex functions of the π-fields is given by $L_{2,-}$ while it is $L_{2,+}$ for the σ-field (similar to $(3+1)$ dimensions [10, 342]).

The third row introduces the chiral Heisenberg-Gross-Neveu (χHGN) model [267] with an additional $\left(\bar{\psi}\gamma_{45}\psi\right)^2$ interaction term that is invariant under the whole chiral symmetry group (B.19). The second-order contribution of this model (5.8) is only diagonal in the original field basis $(\sigma, \eta_4, \eta_5, \eta_{45})$ when $\bar{\eta}_{45} = 0$ which cannot be produced by a symmetry transformation of the homogeneous ground state. Thus, we showed how $\bar{\eta}_{45} = 0$ is obtained from the homogeneous effective potential below Eq. (5.9) such that there exist no off-diagonal contributions. Then, also for this model we found that the momentum-dependent parts of $\Gamma^{(2)}_{\phi_j}$ are either proportional to $L_{2,+}$ or $L_{2,-}$ such that homogeneous condensates are stable against inhomogeneous fluctuations.

The last row includes all interaction channels present in Eq. (5.1) with $\vec{\mathcal{C}} = \vec{\mathcal{C}}_s$ and $\lambda_j = \lambda_S$, $\forall j$, and is called complete Lorentz-(pseudo)scalar four-fermion (PSFF) model in this work. As discussed above, one finds by analytic arguments that $\bar{\eta}_{45} = \vec{\bar{\pi}}_{45} = 0$ such that the second-order contribution is diagonal in the original field basis $(\sigma, \eta_4, \eta_5, \eta_{45}, \vec{a}_0, \vec{\pi}_4, \vec{\pi}_5, \vec{\pi}_{45})$. Even though all interaction channels and the largest possible chiral symmetry group is considered, no bosonic two-point vertex function develops a minimum at $q \neq 0$ and the homogeneous condensates are stable against inhomogeneous fluctuations.

As discussed above, $\Gamma^{(2)}_{\phi_j}$ is proportional to $L_{2,\pm}$ independent of the symmetry group of the action and independent of the number of interaction channels considered. Therefore, according to the arguments summarized above, none of the models exhibits an instability towards an IP for any value of M^2, μ, T, q^2. This is strong evidence for the absence of IPs and a moat regime in $(2+1)$-dimensional four-fermion models, as argued above.

IMPLICATIONS FOR THE FULL QUANTUM THEORIES As for the whole chapter, the stability of homogeneous condensates is obtained in the mean-field approximation such that one needs to discuss the predictive power of the finding for the full quantum theory – given by the partition function (2.33) replacing $\mathcal{S}_{FF}$ by Eq. (5.1) with $\vec{\mathcal{C}} = \vec{\mathcal{C}}_s$. Typically, it is observed that bosonic fluctuations tend to disfavor and/or disorder any kind of condensation,

4 This symmetry is broken by a quantum anomaly in QCD [352]. As this anomaly is not broken by quantum effects in a theory without gauge fields, one constructs the NJL model such that the chiral symmetry resembles QCD, i.e., with a broken axial U_1 symmetry. Note that the occurence of an anomaly depends highly on the number of spacetime dimensions.

MODEL	USED CHANNELS c_j	FIELD BASIS $\vec{\varphi}_j$ DIAGONALIZING $\mathcal{S}^{(2)}_{\text{eff}}$	MOMENTUM DEPENDENCE OF $\Gamma^{(2)}_{\varphi_j}$		SYMMETRY GROUPS
			$L_{2,+}$	$L_{2,-}$	
GN	1	σ	σ		$\mathrm{U}_{\mathbb{I}_4}(N) \times$ $\mathrm{U}_{\gamma_{45}}(N) \times$ $Z_{\gamma_5}(2) \times$ $\mathrm{SU}_{\vec{\tau}}(2) \times P_4 \times P_5$
NJL	$1, \mathrm{i}\vec{\tau}\gamma_4, \mathrm{i}\vec{\tau}\gamma_5$	$\sigma, \vec{\pi}_4, \vec{\pi}_5$	σ	$\vec{\pi}_4, \vec{\pi}_5$	$\mathrm{U}_{\mathbb{I}_4}(N) \times$ $\mathrm{U}_{\gamma_{45}}(N) \times$ $\mathrm{SU}_{A,\gamma_4}(2N) \times$ $\mathrm{SU}_{A,\gamma_5}(2N) \times$ $\mathrm{SU}_{\vec{\tau}}(2) \times P_4 \times P_5$
$\chi\mathrm{HGN}_P$	$1, \mathrm{i}\gamma_4, \mathrm{i}\gamma_5, \gamma_{45}$	$\sigma, \eta_4, \eta_5, \eta_{45}$ (for $\bar{\eta}_{45} = 0$)	σ, η_{45}	η_4, η_5	$\mathrm{U}_{\gamma}(2N) \times$ $\mathrm{SU}_{\vec{\tau}}(2) \times P_4 \times P_5$
PSFF	$1, \mathrm{i}\gamma_4, \mathrm{i}\gamma_5, \gamma_{45},$ $\vec{\tau}, \mathrm{i}\vec{\tau}\gamma_4, \mathrm{i}\vec{\tau}\gamma_5, \mathrm{i}\vec{\tau}\gamma_{45}$	$\sigma, \eta_4, \eta_5, \eta_{45}$ $\vec{a}_0, \vec{\pi}_4, \vec{\pi}_5, \vec{\pi}_{45}$ (for $\bar{\eta}_{45} = \vec{\bar{\pi}}_{45} = 0$)	$\sigma, \eta_{45},$ $\vec{\varsigma}, \vec{\pi}_{45}$	$\eta_4, \eta_5,$ $\vec{\pi}_4, \vec{\pi}_5$	$\mathrm{U}_{\gamma}(2N) \times$ $\mathrm{SU}_{\vec{\tau}}(2) \times P_4 \times P_5$

Table 5.3: Examples of the bosonized four-fermion models given by the action (5.1), or the effective action (5.6), with $\vec{\mathcal{C}} = \vec{\mathcal{C}}_s$ (5.2) where no instability is observed for all homogeneous expansion points and all values of μ and T.. We allow for finite baryon chemical potential μ and finite temperature T. The first column gives the models abbreviations for their names for further reference (whenever available names existing in the literature are used). In the second column, the respective interaction channels kept from Eq. (5.1) are listed. The rest is removed by setting $\lambda_k = 0$. The third column lists the field basis φ_j, for which the second-order corrections (4.23) can be diagonalized and, thus, a meaningful stability analysis can be performed. The fourth column indicates whether the momentum dependence of $\Gamma^{(2)}_{\varphi_j}$ is given by $L_{2,+}(M^2, \mu, T, \boldsymbol{q}^2)$ or $L_{2,-}(M^2, \mu, T, \boldsymbol{q}^2)$. The fifth column gives the full symmetry group of the model. The group names are ´links to the definition of the symmetry group.

see Chapter 7 for a discussion. In $d = 1$ spatial dimensions and non-zero temperatures, a rather general argumentation is given excluding the spontaneous breaking of discrete symmetries in Ref. [323] and the breaking of a continuous symmetry is forbidden according to a no-go theorem [222, 223]. In higher dimensions, there exists no general argument forbidding the breaking of symmetries, but it is generically expected that bosonic quantum fluctuations disfavor any kind of ordering similar to thermal ones. This statement is supported multiple times in the literature [225, 226, 228, 229, 275, 325, 327]. See Section 3.3 and Chapter 7 for further discussions on the influence of bosonic quantum fluctuations on the phase diagram of QCD-inspired effective models. Based on these findings, we expect that the non-existence of IPs in $(2+1)$-dimensional four-fermion and Yukawa models (the generalization to Yukawa models is discussed below) in the mean-field approximation is a clear signal that inhomogeneous ground states are not present in the full quantum theory. The observation of an IPs – or other inhomogeneous order parameters / ground states –

in the full quantum theory that is not present within the mean-field approximation has so far not been observed.

5.2.2 *Stability analysis with multiple chemical potentials*

In this subsection, the discussion is extended towards theories that feature multiple imbalances introduced by the presence of multiple chemical potentials. In addition to the chemical potential for the fermion number density μ, which is introduced in Eq. (5.1) via the usual $\mu\bar{\psi}\gamma_3\psi$ term following Section 2.1, we consider an isospin as well as a chiral imbalance. Similar to non-vanishing fermion number, these imbalances are accounted for in the partition function through introduction of a finite isospin chemical potential with the term $\mu_I\bar{\psi}\gamma_3\tau_3\psi$, and a chiral chemical potential with $\mu_{45}\bar{\psi}\gamma_3\gamma_{45}\psi$. Although these additional imbalances in the system require a more sophisticated analysis, one can again identify the momentum-dependent part of the bosonic two-point vertex functions $L_{2,\pm}$ from Section 5.2.1 in particular simple cases. Thus, also the models discussed in this subsection do not exhibit instabilities towards an IP. Also, the existence of a moat regime is ruled out, as $Z \geq 0$ according to the discussion in Section 5.2.1.

In general, the introduction of multiple chemical potentials induces that multiple auxiliary fields ϕ_j have non-vanishing (homogeneous) expectation values; in contrast to the case of only $\mu \neq 0$ where the homogeneous ground state can be given by $\bar{\phi}_j = \delta_{j,0}\bar{\sigma}$. For example, a non-vanishing μ_{45} can lead to a non-vanishing $\bar{\eta}_{45}$ in addition to $\bar{\sigma} \neq 0$. An important example from QCD is the condensation of charged pions in the presence of an isospin chemical potential [353–355]. Thus, even when restricting to homogeneous phases, the phase structure of such a theory can be more involved, compare, e.g., Refs. [7, 304, 356].

Consequently, also the analysis of the bosonic two-point vertex functions in a stability analysis is more involved, although in principle the method can be applied as introduced in Section 4.1.2. The main difficulty is the diagonalization of the second-order contribution, see Eq. (4.23), since the fermion propagator $\bar{\mathrm{Q}}^{-1}$ contains the above introduced chemical potentials as well as multiple non-vanishing expectation values $\bar{\phi}_j$. For many of the scalar interaction channels contained in Eq. (5.2) it can become impossible to analytically diagonalize this expression and numerical diagonalization is required (see Chapter 6 where a numerical diagonalization is performed due to the presence of vector interactions). Thus, a general analysis of the model described by Eq. (5.1) with $\vec{\mathcal{C}} = \vec{\mathcal{C}}_s$ with multiple chemical potentials is not possible in a straightforward way similar to Section 5.2.1. However, for certain combinations of multiple chemical potential and interaction terms, the momentum dependence of the bosonic two-point vertex functions can be obtained by a comparatively straightforward diagonalization procedure through a suitable choice of field coordinates $\vec{\varphi}$. In this case, one chooses φ_j such that the fermion propagator (D.1) is diagonal in this basis and decomposes into 2×2 blocks – each corresponding to an irreducible spinor representation. Then, the contribution of the fermion loop (proportional to $\mathrm{Tr}\,(\bar{\mathrm{Q}}^{-1}\Delta\mathrm{Q}\bar{\mathrm{Q}}^{-1}\Delta\mathrm{Q})$, see Eq. (4.15)) also decomposes when $\Delta\mathrm{Q}$ is rewritten as a function of the corresponding perturbations $\delta\vec{\varphi}$. The bare interaction vertices for the $\bar{\psi}\psi\varphi_j$ term – that are proportional to the original four-fermion vertices $c_j \in \vec{\mathcal{C}}_s$ – project out either one or multiple of the 2×2 blocks and diagonalize the field space matrix in brackets in Eq. (D.3). This allows to proceed with the analysis as described in Section 4.1.2 and Appendix D.1.

Table 5.4 contains all models, where such an analysis with respect to the stability of homogeneous condensates against inhomogeneous fluctuations was performed by us with the presence of two or more non-vanishing chemical potentials. All bosonic two-point vertex functions obtained in the models in Table 5.4 are proportional to $L_{2,+}$. This stems from the choice of $\vec{\varphi}$ such that block-diagonal structures are obtained in the homogeneous fermion propagator (D.1). These blocks behave as contributions from the homogeneous propagator in the $(2+1)$-dimensional GN model (whose bosonic two-point vertex function is proportional to $L_{2,+}$) with a single effective chemical potential and either a single field φ_j or a linear combination of the fields φ_j. The effective chemical potentials are linear combinations of μ, μ_I, μ_{45}. The momentum dependence of the obtained bosonic two-point vertex functions is given by linear combinations of $L_{2,+}$ with effective masses and chemical potentials.

The first row in Table 5.4 contains an extension of the GN model with an additional $(\bar{\psi}\gamma_{45}\psi)^2$ interaction term and is subjected to both an ordinary fermionic and a chiral chemical potential. Without the additional interaction channel such a model was already studied in Ref. [7]. Due to the non-vanishing μ_{45} the homogeneous expectation value $\bar{\eta}_{45} \neq 0$ breaking both P_4 and P_5 (B.25) and (B.26) spontaneously. As described above, the field basis $\phi_{L/R}$ decouples the theory into two independent GN-type theories with chemical potentials $\mu_{L/R} = \mu \pm \mu_{45}$ leading to bosonic two-point vertex functions whose momentum dependence is given by $L_{2,+}$. A similar procedure can be performed for the model in the second row where instead of the $(\bar{\psi}\gamma_{45}\psi)^2$ one considers an isovector-component interaction channel $(\bar{\psi}\tau_3\psi)^2$ (corresponding to an auxiliary bosonic field $a_{0,3}$ in the bosonized action) and an isospin chemical potential μ_I instead of a chiral imbalance. In the third row, one studies both isospin and chiral imbalance in addition to the fermion chemical potential in a model with both $(\bar{\psi}\psi)^2$ and $(\bar{\psi}\gamma_{45}\tau_3\psi)^2$ interaction channels. Again, the diagonalized field basis is given by a linear combination of the bosonic fields σ and $\pi_{45,3}$. Due to the introduction of both chemical potential, the momentum dependence of the bosonic two-point vertex functions is given by a sum of two $L_{2,+}$ terms that differ in the value of the effective chemical potential. In the forth row, one considers all interactions present in the first two rows and the chemical potentials μ, μ_I, μ_{45}. Interestingly, the diagonalizing field basis contains $\phi_L, \phi_R, a_{0,3}$, i.e., the isovector-component interaction is not part of the diagonalization procedure although an isospin chemical potential is considered. The momentum dependent part of $\Gamma^{(2)}_{\phi_{L/R}}$ is again given by sums of two $L_{2,+}$ contributions each with different effective chemical potentials and masses $M^2 = (\phi_{L/R} \pm a_{0,3})^2$. The bosonic two-point vertex function of $a_{0,3}$, however, is proportional to the sum of $\Gamma^{(2)}_{\phi_L}$ and $\Gamma^{(2)}_{\phi_R}$.

Summarizing, all presented four-fermion model in Table 5.4 do not exhibit an instability of the homogeneous ground state towards inhomogeneous condensates and we consider it unlikely that their phase diagrams feature an IP or a moat regime, cf. the discussion in Section 5.2.1. Nevertheless, we want to note that in this investigation of four-fermion models subjected to multiple imbalances we restricted ourselves to a very limited set of interaction channels. This also restricts the predictive power of the used models for high-energy phenomenology. For example, at non-vanishing isospin chemical potential one needs to account for charged pion condensation [353–355]. Attentive readers may notice that the relevant channels for pion condensation are not present in the discussed models in Table 5.4. In order to take such a phenomenon into account in our analysis, one certainly has to extend this study to the relevant interaction channels. To study a larger set of interactions

with several of the chemical potentials μ, μ_I, μ_{45} or other axial imbalances[5], the diagonalization procedure is certainly more involved than what is described above and, probably, a numerical diagonalization is required. Such a numerical diagonalization is, for example, performed in Chapter 6 where it is necessitated by the inclusion of vector interactions. However, the present analysis should be understood as a first step in the stability analysis of four-fermion models with the presence of multiple imbalances in fermion densities. Certainly, our investigation shows that the presence of multiple chemical potentials does not generically favor the existence of inhomogeneous ground states. The numerical analysis of the $(2+1)$-dimensional GN model at non-vanishing μ_I or μ_{45} in Ref. [7] rather suggest that the introduction of another chemical potential in addition to the fermion chemical potential μ disfavors the existence of inhomogeneous condensates.

5.2.3 *Generalization to Yukawa models*

When the models are studied with a baryon chemical potential without the presence of other imbalances, it is directly possible to generalize the findings in the stability analysis in Section 5.2.1 to Yukawa models defined as generic extensions of the four-fermion models following Eq. (2.48).

The derivation is similar to the one outlined in Section 4.1.2 and in Section 5.2 for the general four-fermion model (5.1) with $\vec{\mathcal{C}} = \vec{\mathcal{C}}_s$. After an expansion of the effective action $\mathcal{S}_Y$ in powers of inhomogeneous perturbations $\delta\vec{\chi}$ of the Yukawa fields $\vec{\chi}$, one identifies again $\mathcal{S}_Y^{(0)}$ as the homogeneous effective action, proportional to the homogeneous effective potential, see Section 2.4.4. Applying the stability analysis to Eq. (2.48), the second-order contribution is again the first non-vanishing correction to the homogeneous effective action $\mathcal{S}_Y^{(0)}$ when the homogeneous expansion point is a solution of the gap equation. This is, again, due to the fact that the first-order correction $\mathcal{S}_Y^{(1)}$ is proportional to the gap equations. For the second-order corrections we find

$$\begin{aligned}\frac{\mathcal{S}_Y^{(2)}}{N_f} = \frac{\beta}{2}\sum_{j\in\vec{\mathcal{C}}_s}\frac{1}{h\lambda_j}\int \mathrm{d}^2x\,\delta\chi_j^2(\boldsymbol{x}) - \mathrm{Tr}\left[\bar{\mathrm{Q}}^{-1}\,h\Delta\mathrm{Q}\bar{\mathrm{Q}}^{-1}\,h\Delta\mathrm{Q}\right] + \\ + \frac{1}{2}\sum_{j\in\vec{\mathcal{C}}_s}\left\{\int \mathrm{d}^2x\,\left(\partial_\nu\delta\chi_j(\boldsymbol{x})\right)\left(\partial_\nu\delta\chi_j(\boldsymbol{x})\right) + \sum_{n>1}\kappa_n 2n\left(\vec{\bar{\chi}}^2\right)^{n-1}\int \mathrm{d}^2x\,\delta\chi_j^2(\boldsymbol{x})\right\} + \\ + 2\sum_{j,k\in\vec{\mathcal{C}}_s}\sum_{n>1}\kappa_n n(n-1)\bar{\chi}_j\bar{\chi}_k\left(\vec{\bar{\chi}}^2\right)^{n-2}\int \mathrm{d}^2x\,\delta\chi_j(\boldsymbol{x})\delta\chi_k(\boldsymbol{x}),\end{aligned} \tag{5.14}$$

where the second and third line contain the additional terms from the extensions to Yukawa models while all other expressions are similar to the ones in Eq. (4.23) when replacing $\bar{\phi}$ by $h\bar{\chi}$ and $\delta\vec{\phi}$ by $h\delta\vec{\chi}$. Thus, $\Delta\mathrm{Q} = \sum_k c_k\delta\chi_k$. Note that the third line contains non-diagonal contributions from the self-interaction terms of the $\vec{\chi}$ fields. These are, however, proportional to $\bar{\chi}_j\bar{\chi}_k$ and, consequently, vanish when the homogeneous expansion can be chosen such that only one of the Yukawa fields develops a non-vanishing expectation value. Since the Yukawa-type models given by Eq. (2.48) with a baryon chemical potential possess the same chiral symmetries as the respective four-fermion model, this is always possible. This is the case for the models in Table 5.3. If this choice is not allowed, e.g., due to the

5 For example, one could introduce chemical potentials for the conserved currents $\bar{\psi}\gamma^\nu\gamma_5\psi$ or $\bar{\psi}\gamma^\nu\gamma_4\psi$ as in Ref. [107].

USED CHANNELS c_j	BOSONIC AUXILIARY FIELDS ϕ_j	NON-ZERO CHEMICAL POTENTIALS	FIELD BASIS $\vec{\varphi}_j$ DIAGONALIZING $\mathcal{S}^{(2)}_{\text{eff}}$	MOMENTUM DEPENDENCE OF $\Gamma^{(2)}_{\varphi_j}$ $f(M^2,\mu) =$ $L_{2,+}(M^2,\mu,T,\boldsymbol{q}^2)$	UNDERLYING SYMMETRY GROUP
$1, \gamma_{45}$	σ, η_{45}	$\mu_L{=}(\mu+\mu_{45})$ $\mu_R{=}(\mu-\mu_{45})$	$\phi_L{=}(\sigma+\eta_{45})$ $\phi_R{=}(\sigma-\eta_{45})$	$f(\bar{\phi}^2_L,\mu_L)$ $f(\bar{\phi}^2_R,\mu_R)$	$\mathrm{U}_{\mathbb{I}_4}(N)\times$ $\mathrm{U}_{\gamma_{45}}(N)\times$ $Z_{\gamma_5}(2)\times$ $\mathrm{SU}_{\vec{\tau}}(2)\times P_4\times$ P_5
$1, \tau_3$	$\sigma, a_{0,3}$	$\mu_\uparrow{=}(\mu+\mu_I)$ $\mu_\downarrow{=}(\mu-\mu_I)$	$\phi_\uparrow{=}(\sigma+\varsigma_3)$ $\phi_\downarrow{=}(\sigma-\varsigma_3)$	$f(\bar{\phi}^2_\uparrow,\mu_\uparrow)$ $f(\bar{\phi}^2_\downarrow,\mu_\downarrow)$	$\mathrm{U}_{\mathbb{I}_4}(N)\times$ $\mathrm{U}_{\gamma_{45}}(N)\times$ $Z_{\gamma_5}(2)\times$ $\mathrm{U}_{\tau_3}(1)\times P_4\times P_5$
$1, \tau_3\gamma_{45}$	$\sigma, \pi_{45,3}$	$\mu_{L,\uparrow}{=}(\mu_L+\mu_I)$ $\mu_{L,\downarrow}{=}(\mu_L-\mu_I)$ $\mu_{R,\uparrow}{=}(\mu_R+\mu_I)$ $\mu_{R,\downarrow}{=}(\mu_R-\mu_I)$	$\varphi_+ =$ $(\sigma+\pi_{45,3})$ $\varphi_- =$ $(\sigma-\pi_{45,3})$	$f(\bar{\varphi}^2_+,\mu_{L,\uparrow})$ $+f(\bar{\varphi}^2_+,\mu_{R,\downarrow})$ $f(\bar{\varphi}^2_-,\mu_{L,\downarrow})$ $+f(\bar{\varphi}^2_-,\mu_{R,\uparrow})$	$\mathrm{U}_{\mathbb{I}_4}(N)\times$ $\mathrm{U}_{\gamma_{45}}(N)\times$ $Z_{\gamma_5}(2)\times$ $\mathrm{U}_{\tau_3}(1)\times P_4\times P_5$
$1, \tau_3, \gamma_{45}$	$\sigma, a_{0,3}, \eta_{45}$	$\mu_{L,\uparrow}$, $\mu_{L,\downarrow}$, $\mu_{R,\uparrow}$, $\mu_{R,\downarrow}$	ϕ_L ϕ_R $a_{0,3}$	$f((\bar{\phi}_L+\bar{a}_{0,3})^2,\mu_{L,\uparrow})$ $+f(\bar{\phi}_L-\bar{a}_{0,3})^2,\mu_{L,\downarrow})$ $f((\bar{\phi}_R+\bar{a}_{0,3})^2,\mu_{R,\uparrow})$ $+f(\bar{\phi}_R-\bar{a}_{0,3})^2,\mu_{R,\downarrow})$ $\Gamma^{(2)}_{\phi_L}+\Gamma^{(2)}_{\phi_R}$	$\mathrm{U}_{\mathbb{I}_4}(N)\times$ $\mathrm{U}_{\gamma_{45}}(N)\times$ $Z_{\gamma_5}(2)\times$ $\mathrm{U}_{\tau_3}(1)\times P_4\times P_5$

Table 5.4: Examples of the bosonized four-fermion models with multiple chemical potentials and interaction channels where no instability is observed for all homogeneous expansion points and all values of the chemical potentials and the temperature. The first column describes the used four-fermion interaction vertices (compare Eq. (5.2)) in the model. The second column gives the corresponding auxiliary bosonic fields after bosonization, that correspond to the fermion bilinear via the Ward identity (5.5). The third column lists the used chemical potentials. In the fourth column, the field basis φ_j is defined, which diagonalizes the second-order correction. Then, the momentum dependence of the two-point functions $\Gamma^{(2)}_{\varphi_j}$ is given in the fifth column, next to the field definition. The last column givens an overview of the present symmetries in the model. The group names are links to the definition of the symmetry group.

presence of additional chemical potentials, these additional contributions need to be taken into account and an explicit diagonalization procedure is necessary.

In the present case of one chemical potential μ for the fermion number, we can directly identify the second-order contribution to the effective action as being diagonal in the original field basis $\vec{\chi}$. We find

$$\frac{\mathcal{S}_Y^{(2)}}{N_f} = \frac{\beta}{2} \int \frac{\mathrm{d}^2 q}{(2\pi)^2} \left[\sum_{j \in \vec{\mathcal{C}}_s} |\delta\tilde{\chi}_j(\mathbf{q})|^2 \, \Gamma_{\chi_j}^{(2)} \left(M^2, \mu, T, q \right) \right], \tag{5.15}$$

with the bosonic two-point vertex functions

$$\begin{aligned} \Gamma_{\chi_j}^{(2)} \left(M^2, \mu, T, q \right) = \frac{1}{\lambda} - \ell_1 \left(M^2, \mu, T \right) + L_{2,\chi_j}(M^2, \mu, T, q^2) + \\ + \frac{1}{2} q^2 + \sum_{n>1} \kappa_n n \left[2 \left(\vec{\bar{\zeta}}^2 \right)^{n-1} + 4(n-1) \bar{\zeta}_j^2 \left(\vec{\bar{\zeta}}^2 \right)^{n-2} \right]. \end{aligned} \tag{5.16}$$

Again, one finds for the momentum-dependence of $\Gamma_{\chi_j}^{(2)}$ the monotonically increasing functions $L_{2,\pm}$ (5.11). As obvious from Eq. (5.16), the additional terms compared to the bosonic two-point vertex functions in the four-fermion model (5.10) are either constant or monotonically increasing in q^2. These terms cannot facilitate the appearance of an instability towards inhomogeneous fluctuations. Thus, the reasoning of the previous subsection applies also to the Yukawa models (2.48) with the effective action given by Eq. (5.6) where $\vec{\mathcal{C}} = \vec{\mathcal{C}}_s$ and either $\lambda_j = \lambda_S$ or $\lambda_j = 0$. For these models, no instabilities towards an IP is observed for all values of $T, \mu, \vec{\bar{\chi}}, q^2$ similar to the four-fermion models. In particular, this is the case for the Yukawa extensions of all models presented in Table 5.3. However, one has to note that the respective phase diagrams of the Yukawa models can significantly differ form the phase diagrams of the four-fermion model depending on the parameter setting of the additional couplings. Also, the effect of bosonic fluctuations can certainly be different due to nature of the dynamical bosonic fields. However, it is certainly also not expected that IPs are absent within the mean-field approximation but present in the full quantum theory, similar to the discussion in Section 5.2.1.

YUKAWA MODELS WITH MULTIPLE CHEMICAL POTENTIALS The extension of the findings from four-fermion models subjected to multiple chemical potentials to Yukuwa models is not straightforward – in contrast to the models with one, fermion chemical potential in Table 5.3 whose analysis can be extended to Yukawa extensions according to Eq. (2.48) as argued above. For the models in Table 5.4, we already showed that the respective bosonic two-point vertex functions are proportional to $L_{2,+}$ such that no instabilities towards an IP are observed and also no moat regime is present. Due to the multiple chemical potentials, multiple homogeneous expectation values $\bar{\chi}_j$ are non-vanishing (similar to multiple $\bar{\phi}_j$ in the four-fermion models). As discussed above, the Yukawa self-interactions of the bosonic fields cause non-vanishing second-order contributions proportional to $\bar{\chi}_j \bar{\chi}_k$, which are off-diagonal in the field perturbations $\delta\vec{\chi}$, c.f., the third line of Eq. (5.14), in addition to the off-diagonal fermion contributions, see Eq. (D.17) for an example. In the stability analysis of such a model the whole second-order contribution (5.14) needs to be diagonalized, i.e., one needs to find a field basis $\vec{\zeta}$ such that the whole second-order contribution is diagonal in the field perturbations $\delta\vec{\zeta}$, see for example Eq. (4.26). In the case of the four-fermion models in Table 5.4, this basis is given by $\vec{\phi}$ which is determined as discussed in Section 5.2.2. The basis transformations of the four-fermion part, however, is

not suitable for the corresponding Yukawa model, as one still needs to diagonalize the additional off-diagonal contributions from the bosonic self-interactions. This diagonalization can become very involved by analytic means, even when using symbolic diagonalization tools such as, e.g., *Mathematica* [349] or *Matlab* [22].

An example for this procedure is provided in Appendix D.2, where we discuss the Yukawa extension of the model in the first row of Table 5.4. In the analysis of this model, the bosonic two-point vertex functions exhibit a more complicated functional dependence and the diagonalizing field basis $\vec{\zeta}$ depends on the studied momentum $q = |\boldsymbol{q}|$ of the perturbation as well as on the homogeneous expectation values of the bosonic fields in addition to the external parameters such as the temperature and the chemical potentials. Nevertheless, we were able to show that the obtained bosonic two-point vertex functions are monotonically increasing functions in q and, thus, no instabilities toward inhomogeneous perturbations are observed. For the other models in Table 5.4, we refrain from performing an explicit calculation as the expressions become lengthy and the analysis is rather involved. However, we expect that also these Yukawa models do not develop any instabilities towards inhomogeneous condensates, since the off-diagonal contributions coming from the bosonic self-interactions are not dependent on the external momentum $\boldsymbol{q}$.

5.3 STABILITY OF THE SYMMETRIC PHASE WHEN INCLUDING VECTOR INTERACTIONS

In this section, we also consider vector interactions in the four-fermion models, i.e., we study the action (5.1) with $\vec{\mathcal{C}} = \vec{\mathcal{C}}_c$, see Eq. (5.3). It is important to note that there is no symmetry constraint relating the coupling for the scalar interactions to the vector couplings, such that we, in general, allow for $\lambda_j = \lambda_S$ for $c_j \in \vec{\mathcal{C}}_s$ and $\lambda_k = \lambda_V$ for $c_k \in \vec{\mathcal{C}}_v$. The action of this theory can be written as

$$\mathcal{S}[\bar{\psi},\psi] = \int \mathrm{d}^3x \Big[\bar{\psi}\left(\not{\partial} + \gamma_3\mu\right)\psi - \sum_{c_j\in\vec{\mathcal{C}}_s} \Big[\tfrac{\lambda_S}{2N_f}\left(\bar{\psi}c_j\,\psi\right)^2 + \tfrac{\lambda_V}{2N_f}\left(\left(\bar{\psi}\,c_j \mathrm{i}\gamma_3\,\psi\right)^2 + \left(\bar{\psi}\,c_j \mathrm{i}\boldsymbol{\gamma}\,\psi\right)^2\right)\Big]\Big] \tag{5.17}$$

where we used the definition of the tupel of scalar interaction vertices $\vec{\mathcal{C}}_s$ in Eq. (5.2) in order to illustrate the different signs of scalar and vector terms. Note that, especially when vector interactions including $\gamma_\nu = (\boldsymbol{\gamma}, \gamma_3)$ are studied, the signs and prefactors of i of interaction terms depend on the conventions used for the gamma matrices and the wick rotation. Our conventions for the gamma matrices and the Wick rotation are given in Appendix A.3 and Appendix A.2, a concrete example for the Wick rotation is given in Appendix A.2.2.

In the action (5.17) the vector coupling is treated as a free parameter and will not be affected by renormalization. This is further discussed in Chapter 6 where a simplified version of this model is studied in more detail, involving the computation of the homogeneous effective potential, the gap equations as well as the homogeneous phase diagram. Therein, we show that the vector interactions in combination with a non-vanishing chiral condensate can lead to mixing effects between the auxiliary scalar and vector fields. In certain parameter regions, this leads to the existence of a QπL in the phase diagram of the model. In the following, however, we focus on the stability analysis of the SP of the model where no mixing effects are present. In the case of vanishing chiral condensate, i.e., $\bar{\Sigma} = 0$, the absence of instabilities towards inhomogeneous condensates can be shown. Consequently, this analysis is in line with the stability analysis of models with Lorentzscalar interactions

in Section 5.2. The models discussed in Section 5.2.1, that neither feature a moat regime nor instabilities to an IP, can directly be obtained by setting $\lambda_V = 0$ in the action (5.17).

5.3.1 *Reducing the number of relevant interaction channels in the stability analysis*

In this subsection, we argue that the stability analysis can be performed with a reduced set of interaction channels, as present in the simpler model (6.1) from Chapter 6. Therefore, we use the Hubbard-Stratonovich transformation and the expression for the Hessian matrix (4.23) involving the expression (4.24) of the model described by the action (5.17).

We start with the bosonized effective action of the model (5.17) following Eq. (5.6)

$$\frac{1}{N_f}\mathcal{S}_{\text{eff}}[\vec{\phi},\vec{v}] = \int \mathrm{d}^3x \sum_{j,c_j\in\vec{\mathcal{C}}_s}\left[\frac{v_{j,\nu}v_{j,\nu}}{2\lambda_j}+\frac{\phi_j^2}{2\lambda_j}\right] - \mathrm{Tr}\ln\beta\mathrm{Q} \tag{5.18}$$

with Dirac operator

$$\mathrm{Q}[\vec{\phi},\vec{v}_\nu] = \gamma_\nu\partial_\nu + \gamma_3\mu + \sum_{c_a\in\vec{\mathcal{C}}_s}\left(c_a\phi_a + \mathrm{i}c_j\gamma_\nu v_{a,\nu}\right). \tag{5.19}$$

The set of interaction vertices $\vec{\mathcal{C}}_s$ is defined in Eq. (5.2). The auxiliary bosonic fields $\vec{\phi}$ and $\vec{v}$ are used to replace the scalar and vector four-fermion interaction terms in the four-fermion action (5.17), respectively, and follow the Ward identities (5.5).

HOMOGENEOUS EXPANSIONS POINTS FOR THE STABILITY ANALYSIS The homogeneous phase diagram of this theory is in detail discussed in Chapter 6. For the stability analysis in the SP, i.e., with $\vec{\phi} = 0$, we additionally assume that the homogeneous expectation values of the spatial components of the vectors fields vanish, i.e.,

$$\langle v_{a,j}\rangle = 0 \quad \text{for} \quad j = 1,2. \tag{5.20}$$

This assumption is, however, natural when considering homogeneous ground states. The system retains its invariance under rotations of the spatial coordinates $\boldsymbol{x} = (x_1, x_2)$ only if the expectation values of the spatial components of the vector fields vanish. While in an IP it is often observed that in addition to translational invariance also rotational invariance is spontaneously broken, this is expected when the ground state is assumed to be homogeneous in space. Therefore, the assumption of $\bar{v}_{a,j} = 0$ with $j = 1,2$ is justified for the homogeneous expansion points of the stability analysis.

Moreover, for the scalar fields we already motivated in Section 5.2 that one can choose $\bar{\phi}_j = \delta_{j,0}\bar{\sigma}$ by using chiral symmetry transformations. Consequently, for the homogeneous expansion point only σ and $v_{a,3}$ need to be considered as non-vanishing. At this point, a further assumption is made in the analysis. In this chapter we consider a non-vanishing fermion chemical potential μ. Then, it is natural that the homogeneous field $\bar{\omega}_3$ is non-vanishing, since its expectation value is proportional to $\langle\bar{\psi}\gamma_3\psi\rangle$ according to Eq. (5.5). However, all other fields $\langle v_{a,3}\rangle$ could in principle also develop a non-vanishing expectation value. We assume in the present analysis that this is not the case,i.e. $\langle v_{a,3}\rangle \sim \delta_{v_{a,3},\omega_3}$. Note that chiral and isospin symmetry transformations (B.19) can be applied also to the vector fields. This allows to rotate the vector $\vec{v}$ such that all other homogeneous expectation values of the vector fields are vanishing besides the ones of ω_3 and the temporal component of $\vec{a}_{1,45}$. Thus, our assumption, that only ω_3 has a non-vanishing homogeneous expectation

value, amounts to setting the third component of $\langle \vec{a}_{1,45} \rangle = 0$ by hand. This is rather natural since the temporal components of the vector fields are proportional to charges of the theory, which are conserved classically according to the Noether theorem. Since no chemical potential associated to the density $\psi^\dagger \gamma_{45} \psi$ is introduced within this section, it is natural to assume that the expectation value of the temporal component of $\vec{a}_{1,45}$ vanishes which is proportional to $\langle \psi^\dagger \gamma_{45} \psi \rangle$ via Eq. (5.5).

Summarizing, the appropriate homogeneous expansion points for the stability analysis are $\bar{\phi}_j = \delta_{\phi_j,\sigma} \bar{\sigma}$ and $\bar{v}_{j,a} = \delta_{v_{j,a},\omega_3} \bar{\omega}_3$. From the Ward identity for $\omega_\nu = (\boldsymbol{\omega}, \omega_3)$

$$\langle \omega_3 \rangle(x) = -\tfrac{\lambda_V}{N_f} \mathrm{i} \langle \bar{\psi} \gamma_3 \psi \rangle(x), \qquad \langle \boldsymbol{\omega} \rangle(x) = -\tfrac{\lambda_V}{N_f} \mathrm{i} \langle \bar{\psi} \boldsymbol{\gamma} \psi \rangle(x), \tag{5.21}$$

the temporal component of ω_ν is proportional to the fermion density $n(x) = -\bar{\psi} \gamma_3 \psi / N_f$.[6] Following Eq. (5.21), one finds for the homogeneous expectation values

$$\bar{\omega}_3 = \lambda_V \mathrm{i} \bar{n}. \tag{5.22}$$

This purely imaginary expectation values allows to conveniently absorb the vector condensate into an effective chemical potential $\bar{\mu} = \mu + \mathrm{i}\bar{\omega}_3 = \mu - \lambda_V \bar{n}$ where $\bar{n}$ is the homogeneous fermion number density per fermion species.

The properties of the homogeneous expectation values are crucial for the stability analysis. They can be chosen such that the bare fermion propagator $\bar{\mathrm{Q}}^{-1}$ corresponds to the propagator of free fermions with mass given by $\bar{\sigma}$ and effective chemical potential $\bar{\mu} = \mu + \mathrm{i}\bar{\omega}_3$ such that one can directly follow the analysis from Section 4.1.2, see the discussion around Eq. (4.36).

HESSIAN MATRIX After expanding around the homogeneous field configurations

$$\vec{\phi}(\boldsymbol{x}) = \bar{\vec{\phi}} + \delta\vec{\phi}(\boldsymbol{x}), \qquad \vec{v}(\boldsymbol{x}) = \bar{\vec{v}} + \delta\vec{v}(\boldsymbol{x}) \tag{5.23}$$

and identifying the leading second-order terms in the expansion of the effective actions in orders of the inhomogeneous perturbations following Section 4.1.2, one obtains the second-order correction and Hessian matrix of the theory $\Gamma^{(2)}_{\phi_j,\phi_k}(q)$ given by Eq. (4.23) and Eq. (4.24) where the bosonic fields in both of these eqs. can take the value of both ϕ_j and v_j, respectively, and the vertices c_j can, consequently, come from both $\vec{\mathcal{C}}_s$ (5.2) and $\vec{\mathcal{C}}_v$ (5.4). Here, q is the respective momentum in the Fourier decomposition of the inhomogeneous perturbation, i.e., the expression (4.23) is diagonal in momentum space. In a model with repulsive vector interactions (as mediated by the temporal component of the vector fields), one must treat the fluctuations in Eq. (5.23) carefully. For the saddle point approximation[7] to be well-defined, one has to consider perturbations with respect to the temporal components of the vector fields $v_{a,3}$ in the complex plane, since the homogeneous condensates, such as $\bar{\omega}_3 \sim \mathrm{i}\bar{n}$, can be purely imaginary. As discussed in Ref. [189], fluctuations must be in the direction of the steepest descent of the effective action as this amounts to following the stable Lefshetz thimble. While the real-valued condensates $\bar{\phi}_a$ and the spatial components of the vector fields $\bar{v}_{a,\nu}$ are perturbed with real-valued perturbations as expected, one has to perturb the purely imaginary condensates $\bar{v}_{a,3}$ with real-valued fluctuations δv_3 in order to follow the steepest descent of the effective action

6 Note that signs and factors of i may be different for different conventions of the Wick rotation and Gamma matrices.

7 Considering second-order fluctuations about the homogeneous expecation values in the mean-field approximation amounts to a saddle-point approximation about these extrema of the effective action.

(5.18). Especially, this is important for ω_3 whose homogeneous expectation value is purely imaginary, $\bar{\omega}_3 = \mathrm{i}\lambda_V \bar{n}$, and the steepest descent is in the direction parallel to the real axis. This is demonstrated in Figure 5 of Ref. [128] where a similar NJL-type model with vector interactions in 3 spatial dimensions is studied and the Lefshetz thimble in the field space of the temporal vector component is depicted. The corresponding bare fermion-boson vertices $c_j \in \vec{\mathcal{C}}_c$ relevant for the computation of the Hessian matrix (4.24) are modified according to the direction of the fluctuations in the complex plane, i.e., all vertices of the form $\bar{\psi} c v_{a,3} \psi$ pick up an additional factor of i compared to their definition in $\vec{\mathcal{C}}_v$ (5.4).

The resulting Hessian matrix $H_{\phi_j \phi_k} = \Gamma^{(2)}_{\phi_j,\phi_k}$ can be decomposed into sixteen, identical 4×4 blocks that contain matrix elements given by $H_{\sigma\sigma}, H_{\sigma\omega_\nu}, H_{\omega_\nu\omega_\xi}$. Consequently, the Hessian matrix of Eq. (5.17) is identical to the one of the action (6.2) proposed in Chapter 6

$$\mathcal{S}[\bar{\psi}, \psi, \sigma, \omega_\nu] = \int \mathrm{d}^3x \left[\bar{\psi}\, \mathrm{Q}\, \psi + \frac{\omega_\nu \omega_\nu}{2\lambda_V} + \frac{\sigma^2}{2\lambda_S} \right], \tag{5.24}$$

$$Z = \int \prod_{\phi = \{\bar{\psi}, \psi, \sigma, \omega_\nu\}} \mathcal{D}\phi\, \mathrm{e}^{-S[\bar{\psi}, \psi, \sigma, \omega_\nu]} \tag{5.25}$$

with Dirac operator

$$\mathrm{Q}[\sigma, \omega_\nu] = \gamma_\nu \partial_\nu + \gamma_3 \mu + \sigma + \mathrm{i}\gamma_\nu \omega_\nu. \tag{5.26}$$

The partition function of this partially bosonized action is equivalent to the one of a four-fermion model with interaction terms $\sim (\bar{\psi}\psi)^2$ and $\sim (\bar{\psi}\mathrm{i}\gamma_\nu\psi)^2$, see Eq. (6.1).

In the following we show explicitly that the decomposition of $H = \Gamma^{(2)}$ of the effective action (5.18), given by Eq. (4.23), into a block-diagonal structure containing multiple copies of the Hessian of the simpler model (5.24) is possible. Therefore, we consider the one-loop diagram (4.24) contained in the Hessian matrix H, which is proportional to

$$\sum_n \int \frac{\mathrm{d}^2 p}{(2\pi)^2} \mathrm{Tr} \left(\bar{\mathrm{Q}}^{-1}(p + (\boldsymbol{q}, 0)) c_j \bar{\mathrm{Q}}^{-1}(p) c_k \right) \tag{5.27}$$

with $p = (\boldsymbol{p}, \nu_n)$, and use properties of the bare fermion-boson vertices $c_j \in \vec{\mathcal{C}}_c$ (5.3). From the global $\mathrm{U}(4N_f)$ symmetry (B.19) one can choose the values of the homogeneous expansion points such that $\phi_a = \delta_{\phi_a,\sigma}\bar{\sigma}$ which implies $H_{\phi_a\phi_b} \sim \delta_{a,b}$, i.e., no off-diagonal terms are observed in the terms involving only perturbations in the scalar fields $\vec{\phi}$. This is a result already used in Section 5.2. Inspecting the trace over the spinor degrees of freedom in Eq. (5.27) one can also infer that $H_{\phi_a, v_{b,\nu}} = 0$ for $a \neq b$ as the additional Gamma matrix in the Dirac trace compared to the purely scalar matrix elements $H_{\phi_a\phi_b}$ does not lead to a non-vanishing result of the trace. Thus, one obtains off-diagonal matrix elements only for each respective 4×4 block in H with $a = b$, i.e., only $H_{\phi_{a,\nu} v_{a,\nu}}$, $H_{\phi_{a,\nu}\phi_{a,\nu}}$, and $H_{v_{a,\nu} v_{a,\nu}}$ can be non-zero. Again, inspecting the trace in Eq. (5.27) and using the commutation relations between the $c_j \in \vec{\mathcal{C}}_c$ (5.3) with each other and the Gamma matrices, one can derive that the matrix elements of these respective 4×4 blocks are identical to the 4×4 Hessian matrix that stems from doing the perturbative expansion Eq. (5.23) for the model (5.24) with $\vec{\phi} = (\sigma)$ and $\vec{v} = (\omega_\nu)$. Thus, the Hessian matrix derived from the effective action (5.18) is block-diagonal consisting of 16 matrices of size 4×4, which are identical to the Hessian matrix derived from the stability analysis of the simpler model (5.24).

PRACTICAL COMPUTATIONS In this section we investigate only the SP, i.e., $\vec{\bar{\phi}} = 0$. According to the above paragraph, we can simplify the stability analysis of the full model

described by the effective action (5.18) to the computation of the 4×4 Hessian matrix which is obtained for a model containing only σ and ω_ν interactions. Inserting the bare fermion propagator given by

$$\bar{\mathrm{Q}}^{-1}(\nu_n, \mathbf{p}) = \frac{-\mathrm{i}\tilde{\not{p}} + \bar{\Sigma}}{\tilde{p}^2 + \bar{\Sigma}^2}, \qquad \tilde{p} = (\nu_n - \mathrm{i}\bar{\mu}, \mathbf{p})^T \tag{5.28}$$

with $\bar{\mu} = \mu + \mathrm{i}\bar{\omega}_3$ as well as the vertices

$$\vec{c} = (1, -\gamma_3, \mathrm{i}\gamma_1, \mathrm{i}\gamma_2) \tag{5.29}$$

for the fields $(\sigma, \omega_3, \omega_1, \omega_2)$, respectively, into the Hessian matrix (4.24) according to the above discussion and using the homogeneous minima of the effective action $(\bar{\sigma}, \bar{\omega}_\nu) = (\bar{\Sigma}, \bar{\Omega}_3 \delta_{\nu,3})$, one finds the matrix elements (D.27) to (D.31), which need to further evaluated by performing the Matsubara summation and the angle integration in d^2p. In the above formulae we choose $\boldsymbol{q} = (q, 0)$ which is possible by appropriately rotating the momentum space integration variable $\mathbf{p}$. The resulting formulae can be found in Appendix D.3. From these explicit computations, one finds that $\Gamma^{(2)}_{\omega_1,\omega_2} = \Gamma^{(2)}_{\omega_3,\omega_2} = \Gamma^{(2)}_{\omega_3,\omega_1} = 0$, see Appendix D.3. Moreover, the matrix elements $\Gamma^{(2)}_{\sigma,\omega_\nu} \sim \bar{\Sigma}$, as obvious from Eq. (D.29), such that they vanish in the SP since $\bar{\Sigma} = 0$. Consequently, the Hessian matrix $\Gamma^{(2)}$ is diagonal in the field basis $\vec{\varphi} = (\sigma, \omega_3, \omega_1, \omega_2)^T$ in the SP and the eigenvalues are given by the diagonal elements $\Gamma^{(2)}_{\sigma,\sigma}, \Gamma^{(2)}_{\omega_\nu,\omega_\nu}$, which in turn correspond to the bosonic two-point vertex functions $\Gamma^{(2)}_\sigma$ and $\Gamma^{(2)}_{\omega_\nu}$, respectively. For non-vanishing T and any value of μ, we compute these diagonal elements numerically using *Python3* with various libraries [19, 350, 357]. The implemented formulae for $\Gamma^{(2)}_{\omega_j,\omega_j}$ can be found in Eqs. (D.32), (D.38) and (D.39), while $\Gamma^{(2)}_{\sigma,\sigma}$ is the bosonic two-point vertex function of the GN model and contains ℓ_1 and $L_{2,+}$, so see Appendix C.4 and Appendix D.1.1 for its evaluation.[8]

5.3.2 *Results in the symmetric phase*

In the following, we present the behavior of the bosonic two-point vertex functions $\Gamma^{(2)}_\sigma$ and $\Gamma^{(2)}_{\omega_\nu}$ which are given by the diagonal elements of the Hessian matrix according to the discussion above. Due to the absence of mixing effects, the bosonic two-point vertex functions are real-valued and, consequently, can directly be studied with respect to the (absence of) instabilities of the SP towards inhomogeneous fluctuations and the existence of the moat regime.

In the left plot of Fig. 5.2, $\Gamma^{(2)}_{\varphi_j}$ with $\vec{\varphi} = (\sigma, \omega_3, \omega_1, \omega_2)$ are plotted as functions of the momentum q of the perturbation $\delta\varphi_j$ for $\lambda_V \bar{\Sigma}_0/\pi = 0.1$ and $(\mu/\bar{\Sigma}_0, T/\bar{\Sigma}_0) = (1.051, 0.238)$. This point in the phase diagram lies directly on the second-order phase boundary between the SP and HBP, as shown in Chapter 6. The bosonic two-point vertex function of the order parameter σ, that characterizes the phase transition, is zero at $q = 0$. Since $\Gamma^{(2)}_{\varphi_j}(q)$ can be interpreted as the curvature of the effective action of the model (5.24) in the direction of $\varphi_j(q)$, it is expected that this curvature goes to zero for $q = 0$ and $\varphi_j = \sigma$ at the second-order homogeneous phase transition. The field ω_ν is not an order parameter and, thus, the corresponding bosonic two-point vertex functions are insensitive to the transition.

The bosonic two-point vertex functions $\Gamma^{(2)}_{\phi_j}(q)$ are monotonically increasing functions for any value of μ, T and λ_V by numerical computations. For $T = 0$, this can be seen

8 The bosonic two-point vertex function of the GN model is calculated multiple times in published work, e.g., in Refs. [211, 212, 241], see also Appendix B of Ref. [2] for the evaluation in various limits of $\bar{\Sigma}$, T and q.

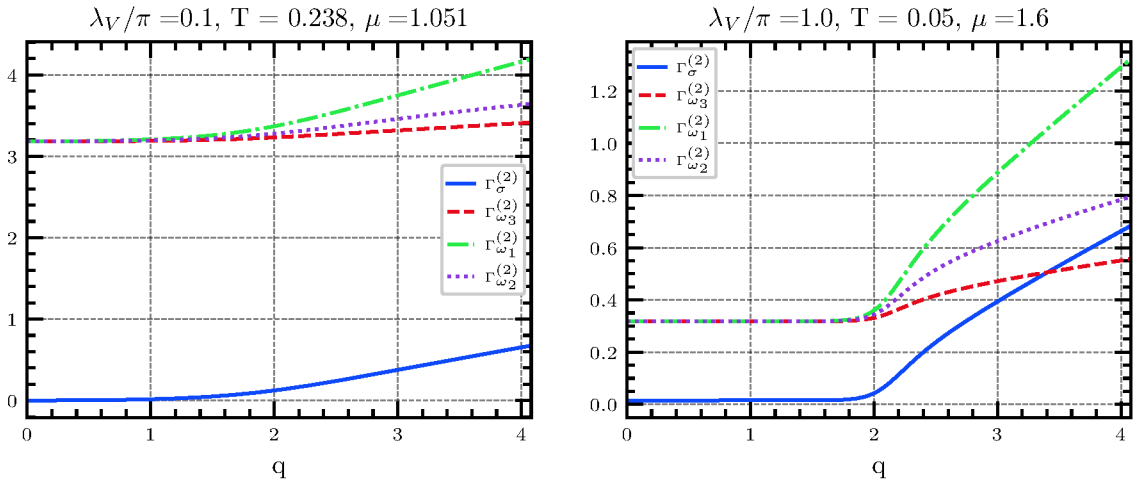

Figure 5.2: The bosonic two-point vertex functions $\Gamma^{(2)}_{\varphi_j}(q)$ as functions of the momentum of the perturbation q with $\vec{\varphi} = (\sigma, \omega_3, \omega_1, \omega_2)^T$. *((left))* At the homogeneous second-order phase transition for $\lambda_V \bar{\Sigma}_0/\pi = 0.1$. *((right))* Within the SP for $\lambda_V \bar{\Sigma}_0/\pi = 1.0$.

analytically by taking the zero temperature limit for all diagonal elements of the Hessian using the formulae in Appendix D.3 and setting $\bar{\Sigma} = 0$. An example for the bosonic two-point vertex functions within the SP is plotted on the right side of Fig. 5.2. In the plot, we used $\lambda_V \bar{\Sigma}_0/\pi = 1.0$ which is the largest vector coupling studied in this work. A non-monotonic behavior of the bosonic two-point vertex functions is not observed within in the SP within the large range of chemical potentials, temperatures and vector couplings we studied numerically. For $\Gamma^{(2)}_{\sigma}$, this result was already presented in Ref. [2], while in this work we also studied the two-point vertex functions $\Gamma^{(2)}_{\omega_\nu}(q)$, that become relevant within the mean-field approximation when including vector interactions. In the SP, however, our analysis yields the same conclusion as the one in Ref. [2]. We do neither observe an instability towards an IP nor a moat regime for all studied vector couplings. Together with the argument that in all model investigations in the literature (see Section 3.2 and Ref. [197] for a review) IPs feature a second-order phase boundary towards the SP which would be detected by the stability analysis [1], we consider the absence of such an instability a strong indication for the non-existence of an IP within this model.

As discussed in Section 5.2, there still exists a degeneracy between inhomogeneous condensates and homogeneous phases at zero temperature as found with a particular ansatz function in the GN model [321]. This is also consistent with our analysis, where the bosonic two-point vertex function $\Gamma^{(2)}_{\sigma}(q)$ is flat and vanishes for a certain interval in q at the point $(\mu/\bar{\Sigma}_0 = 1.0, T/\bar{\Sigma}_0 = 0)$ as shown in Section 5.2 for $\lambda_V = 0$ – the same point in the phase diagram where also the homogeneous potential is flat. The flatness of $\Gamma^{(2)}_{\sigma}(q)$ also occurs at the critical chemical potential μ_c at any value of λ_V at $T = 0.0$, again indicating a similar degeneracy between the SP and the IP as before. This property could already be guessed from the right plot in Fig. 5.2, which is still at finite, but low enough temperatures such that $\Gamma^{(2)}_{\sigma}$ is almost flat for small q. We expect, however, that a degenerate condensate would not be given by the one-dimensional kink ansatz from Ref. [321] (see Figure 5.4 therein) for non-vanishing vector coupling λ_V, since its mean density $\bar{n}$ is smaller than $\bar{n}/\bar{\Sigma}_0^2 = 1/(2\pi)$, which is the density corresponding to $\bar{\Sigma} = 0.0$ when solving the gap equations (6.10) and (6.12) at $(\mu/\bar{\Sigma}_0 = 1.0, T/\bar{\Sigma}_0 = 0)$. Thus, the homogeneous solution

$(\bar{\Sigma}/\bar{\Sigma}_0 = 0.0, \bar{\Omega}_3/\bar{\Sigma}_0 = \mathrm{i}\lambda_V \bar{\Sigma}_0/(2\pi))$ is expected to be favored over the ansatz in Ref. [321], as the bosonized action favors solution of the gap eqs. with higher baryon number, compare Eq. (5.24) using $\bar{\Omega}_3 = \mathrm{i}\lambda_V \bar{n}$.

5.4 SUMMARY AND CONTEXTUALIZATION

In this chapter, the stability of homogeneous condensates in $(2+1)$-dimensional four-fermion and Yukawa models is shown at non-vanishing chemical potential and temperatures by computing and analyzing the bosonic two-point vertex functions $\Gamma^{(2)}_{\varphi_j}$ following Chapter 4. The investigation was performed in a general manner for all four-fermion and Yukawa models with Lorentzscalar interaction channels with sixteen different interaction vertices defined in Eq. (5.2) such that the findings are robust against model details – vector interaction channels were treated separately. The central results of the analysis are:

(1) Homogeneous condensates are stable against inhomogeneous perturbations for every homogeneous expansion point and any value of μ and non-vanishing T when studying only Lorentzscalar interactions with sixteen different interaction vertices as defined in Eq. (5.2). This stability emerges from the monotonically increasing behavior of $\Gamma^{(2)}_{\varphi_j}$ as a function of the external, bosonic momentum for all homogeneous expansions points corresponding to the momentum of the inhomogeneous perturbation, as shown in Section 5.2. We refer to the central equations Eqs. (5.10), (5.11) and (5.13) including the analytic proof of the montonically increasing behavior for $T = 0$ and Fig. 5.1 for a visualization of the momentum dependence of $\Gamma^{(2)}_{\varphi_j}$ at $T \neq 0$.

(2) In the models specified in (1), the absence of moat regimes is obtained from the monotonically increasing momentum dependence of the $\Gamma^{(2)}_{\varphi_j}$.

(3) The inclusion of vector interactions in Section 5.3 yields the same findings as described above for the scalar channels when restricting the investigation to the SP within the homogeneous phase diagram, see Fig. 5.2 for a plot of the bosonic two-point vertex functions in this case. In the HBP mixing effects and symmetry arguments play an important role. The resulting phenomena are subject of Chapter 6.

(4) At zero temperature, there are hints for a degeneracy between the homogeneous phases and inhomogeneous condensates at $\mu/\bar{\Sigma}_0 = 1$ consistent with the earlier work [321]. At this point in the phase diagram, the homogeneous effective potential is also flat.

(5) The momentum dependence of the bosonic two-point vertex functions is proportional to $L_{2,\pm}$, see Eq. (5.11); $L_{2,+}$ is identical to the observed behavior of the bosonic two-point vertex function in the $2+1$-dimensional GN model, while $L_{2,-}$ just differs in a prefactor of the same integral as appearing in $L_{2,+}$. This implies that the behavior of $\Gamma^{(2)}_{\varphi_j}$, when introducing finite regulators, strongly depends on the used regularization scheme similar to the $2+1$-dimensional GN model [241]. This in turn results in a strong regularization dependence of IPs that possibly emerge at finite regulator values depending on the chosen regularization scheme [240, 241] in all of the investigated QCD-inspired models.

Further, we extended the above analysis by including multiple chemical potentials, implying a chiral and/or an isospin imbalance. Again, the stability of the homogeneous condensates

and the absence of the moat regime could be shown, but only for a restricted number of interaction channels, see Table 5.4 for the studied models. It has to be noted that the models investigated in this table are not very relevant for high energy physics phenomenology due to the restricted number of interaction terms, that result in, e.g., the absence of charged pions, which are expected to condense at a certain value of the isospin chemical potential.

CONCLUSIONS In Section 5.2.1, we argued that the absence of instabilities is a strong hint for the absence of IPs in mean-field investigations of the phase diagram in the above mentioned models. This statement is supported by literature findings from full minimizations of the effective action of the theory using LFT [7, 8, 240, 241, 344] and the central argument that all IPs in effective model investigations can be detected in some region of parameter space by a stability analysis since all of them feature a second-order transition to the SP. Under the assumption that an IP, if existent in the phase diagram, can be detected by the stability analysis at least in some region of the parameter space (to the knowledge of the author this has so far always been the case in effective model investigations, see, e.g., Refs. [1, 197, 342]), the findings and argumentation address the central aspect of **RO5** "What is the fate of inhomogeneous chiral condensates within $2+1$-dimensional four-fermion theories and related QCD-inspired models?". The findings suggest that IPs are non-existent for all four-fermion and Yukawa models in $2+1$ dimensions within the mean-field approximation (except for vector interactions in the HBP which are studied separately in Chapter 6). Naturally, the question arises whether the mean-field results have predictive power for the phase diagram of full quantum theories when computing the full partition function / path integral. The mean-field approximation according to our definition (see Section 2.4 for details) suppresses the bosonic quantum fluctuations. Bosonic quantum fluctuations that tend to disfavor and/or disorder any kind of condensation, see Refs. [216, 217, 219, 225, 226] and a detailed discussion in Section 1.2 (the paragraph on the quantum pion liquid and inhomogeous chiral condensates) and the findings in Chapter 7 . Thus, we consider the non-existence of IPs in the mean-field approximation a clear signal that inhomgoeneous ground states are absent also when including all quantum fluctuations in the partition function of $2+1$-dimensional four-fermion and Yukawa models.

Regarding the second part of the posed quesion in **RO5** with respect to "related QCD-inspired theories", the found momentum dependence of the bosonic two-point vertex functions implies that in all four-fermion and Yukawa models in two spatial dimensions that at (artifically introduced) finite regulators there is a strong dependence of the existence and extent of the IP on the respective regularization scheme and regulator value. This further supports the evidence in the literature that the extent and existence of IPs, especially in the parameter region of interest for QCD and QCD-inspired models, are very sensitive to regularization artifacts [10, 167, 211, 212, 240, 241] which implies that there is no predictive power of findings in four-fermion models in $3+1$ dimensions due to the found ambiguities [10, 167]. In these investigations, the regulator cannot be removed as four-fermion models are non-renormalizable in three spatial dimensions. Thus, the second part of **RO5** is not yet finally addressed and our findings rather suggest that this question cannot be answered at least for four-fermion / NJL-type model in $3+1$ dimensions. Also with respect to Yukawa / QM models, there are certain ambiguities regarding the renormalization of the results in mean-field investigations where unbounded potentials arise in the whole phase diagram [198]. This, however, is not subject of the present work and might be investigated in the future.

FUTURE RESEARCH PERSPECTIVES Our results suggest further that there might be a general argument behind the absence of IPs in $2+1$ dimensions, which might be of similar form as, e.g., Derrick's theorem [358] and could possibly be found by studying the properties of a appropriate general Ginzburg-Landau free energy as done in Ref. [359]. Therefore, this free energy functional would need to encode higher orders in a gradient expansion to represent the terms stemming from the fermion determinant in the four-fermion theories investigated in this chapter. An obvious direct research direction is the inclusion of vector interaction generically also within the HBP, as these are important for low-energy effective descriptions of QCD as they emerge from the quark-gluon interaction in a similar way as the scalar interactions [133, 148, 237] and are important to encode the $\mathcal{CK}$ symmetry of QCD at $\mu \neq 0$ in four-fermion models [189]. Yet, their analysis within the HBP is technically different from the one present here and is performed in Chapter 6.

With respect to high energy physics phenomenology, there are many ways to build on the present analysis – for example studying four-fermion models with an SU(3) flavor symmetry allowing for effects from strangeness or the dependence of the findings on explicit quark masses. However, from results in $3+1$ dimensions the effects of these aspects on IPs are negligible [200, 342] and, as outlined in Section 1.3, qualitative predictions for phenomenology were not part of the motivations for this work. Probably, other model approaches like QM models should be investigated first before incorporating the aforementioned aspects into $2+1$-dimensional four-fermion models. Further, this work contributes to the general understanding of the thermodynamics and phase transitions of strongly-interacting fermion in $2+1$ dimensions in equilibrium. From this point of view, it would be very interesting to study difermion interactions to allow for color-superconducting order parameters in order to study their competition with the chiral ones [107, 304, 356] or to investigate the interference and competition of different chiral chemical potentials (as possible in two spatial dimensions) via terms $\mu_{4/5}\bar{\psi}\gamma_3\gamma_{4/5}\psi$ corresponding to different charges. Both of these studies would, however, not change the conclusion with respect to the existence of IPs, as suggested by the findings in this chapter and in Ref. [7].

6

GENERATING A QUANTUM PION LIQUID FROM MIXING EFFECTS BETWEEN SCALAR AND VECTOR MESONS

DISCLOSURE The results of this chapter have been published in Ref. [3] and, thus, can be solely attributed to myself. The presentation and discussion of these results has been adapted to this thesis. However, some of the formulations in this chapter, especially in the results section, are similar to the ones of Ref. [3]. Also, all figures are taken from Ref. [3].

ABSTRACT AND RELATION TO THE RESEARCH OBJECTIVES In this chapter, we incorporate mixing effects between scalar and vector mesons as well as the $\mathcal{CK}$ symmetry at $\mu \neq 0$ into the investigation of four-fermion models as QCD-inspired models for the phase diagram at non-vanishing temperatures and chemical potentials. This allows to perform exploratory investigations in the direction of **RO1** and **RO2** which formulate the aim to investigate the implications of the combined $\mathcal{CK}$ symmetry at $\mu \neq 0$ and the incorporation of mixing effects between scalar and vector mesons, respectively, see Section 1.3 for the detailed formulation of these research objectives. We show that the incorporation of these features leads to the appearance of a QπL in $2+1$-dimensional four-fermion models, a regime that is not present in models without vector interactions.

OUTLINE In Section 6.1, we define a simple model with scalar and vector interactions and discuss its general properties on the level of its action and partition function. The homogeneous phase diagram of this model, as well as the renormalization procedure, is discussed in Section 6.2. Using the homogeneous condensates as expansion points, we perform an analysis of the Hessian matrix in field space in Section 6.3. We show how the QπL emerges from the complex-conjugate eigenvalue pairs of the static Hessian matrix.

6.1 MINIMAL FOUR-FERMION MODEL FOR THE INCLUSION OF MIXING EFFECTS

In this section, we incorporate the mixing of scalar and vector mesons – described by auxiliary fields in the four-fermion models – within our general approach to the phase diagram of strongly-interacting matter at non-vanishing temperatures and chemical potentials using QCD-inspired four-fermion models. This mixing is expected to be important for QCD at non-vanishing baryon density, since the emerging field in the isoscalar-vector channel couples directly to the vector current $\bar{\psi}\gamma_\mu\psi$ such that its expectation value is proportional to the baryon density. Consequently, at least this condensate as well as the chiral condensate is present in QCD matter at $\mu \neq 0$ and mixing between at least this scalar and the described vector channel occurs [360]. Moreover, Yukawa-type interactions between quarks and the effective scalar and vector degrees of freedom are rather dominant in the region of

intermediate and low temperatures and densities, as can be derived from FRG flows with dynamical hadronization [133, 361, 362]. In Chapter 1, a more detailed discussion of this and other relevant observations can be found. We consider the following action

$$\mathcal{S}_{\text{mix}}[\bar{\psi},\psi] = \int_0^\beta \mathrm{d}\tau \int \mathrm{d}^2x \left[\bar{\psi}\left(\partial\!\!\!/ + \gamma_3\mu\right)\psi - \left[\tfrac{\lambda_S}{2N_f}\left(\bar{\psi}\,\psi\right)^2 + \tfrac{\lambda_V}{2N_f}\left(\left(\bar{\psi}\,\mathrm{i}\gamma_3\,\psi\right)^2 + \left(\bar{\psi}\,\mathrm{i}\boldsymbol{\gamma}\,\psi\right)^2\right)\right]\right] \tag{6.1}$$

with $\boldsymbol{\gamma} = (\gamma_1, \gamma_2)$ as the simplest example of a four-fermion model that features both scalar and vector interactions as well as a generalized $\mathcal{PT}$ symmetry at $\mu \neq 0$, as is discussed in a separate paragraph below. Thereby, ψ contains N_f identical spinors with four components, see Section 2.3 for a general introduction of four-fermion models in this work and Appendix A.3 for the reducible representation of Gamma matrices used. The action (6.1) is invariant under the chiral symmetry group[1] $\mathrm{U}_1(N_f) \times \mathrm{U}_{\gamma_{45}}(N_f) \times Z_{\gamma_5}(2)$, see Eqs. (B.12), (B.13) and (B.23).

6.1.1 *Bosonization*

Following the usual bosonization procedure with a Hubbard-Statonovich transformation, we introduce auxiliary fields σ and $\omega_\nu = (\boldsymbol{\omega}, \omega_3)$ for the scalar and vector interactions, respectively. The partially bosonized action reads

$$\mathcal{S}[\bar{\psi},\psi,\sigma,\omega_\nu] = \int \mathrm{d}^3x \left[\bar{\psi}\,\mathrm{Q}\,\psi + \frac{\omega_\nu\omega_\nu}{2\lambda_V} + \frac{\sigma^2}{2\lambda_S}\right], \tag{6.2}$$

$$Z = \int \prod_{\phi=\{\bar{\psi},\psi,\sigma,\omega_\nu\}} \mathcal{D}\phi\; \mathrm{e}^{-S[\bar{\psi},\psi,\sigma,\omega_\nu]}, \tag{6.3}$$

with the Dirac operator

$$\mathrm{Q}[\sigma,\omega_\nu] = \gamma_\nu\partial_\nu + \gamma_3\mu + \sigma + \mathrm{i}\gamma_\nu\omega_\nu, \tag{6.4}$$

see Section 2.3.1 for details with respect to the bosonization procedure. Then, one obtains the following Ward identities according to Eq. (2.43) for the one-point functions of the auxiliary fields

$$\langle\sigma\rangle(x) = -\tfrac{\lambda_S}{N_f}\langle\bar{\psi}\psi\rangle(x), \quad \langle\omega_3\rangle(x) = -\tfrac{\lambda_V}{N_f}\mathrm{i}\langle\bar{\psi}\gamma_3\psi\rangle(x), \quad \langle\boldsymbol{\omega}\rangle(x) = -\tfrac{\lambda_V}{N_f}\mathrm{i}\langle\bar{\psi}\boldsymbol{\gamma}\psi\rangle(x). \tag{6.5}$$

such that the expectation value of the temporal component of ω_ν is proportional to the expectation value of the fermion density $n(x) = -\bar{\psi}\gamma_3\psi/N_f$ following Eq. (5.22). From this, one obtains that ω_3 yields purely imaginary expectation values and, in the mean-field approximation, is conveniently absorbed into an effective chemical potential $\bar{\mu} = \mu + \mathrm{i}\bar{\omega}_3$. This is directly linked to the repulsive nature of the Yukawa-type interaction between $\bar{\psi}, \psi$ and ω_ν in the action (6.2) and the corresponding four-fermion interaction.

GENERALIZED $\mathcal{PT}$ SYMMETRY It becomes evident through Eqs. (6.2), (6.4) and (6.5) that the model features an invariance under a combined $\mathcal{CK}$ transformation at non-vanishing μ while breaking both charge conjugation $\mathcal{C}$ and complex conjugation $\mathcal{K}$ separately through

1 The model is also invariant under $Z_{\gamma_4}(2)$ (B.23) but this transformation can be obtained by appropriate combination of $\mathrm{U}_{\gamma_{45}}$ and $Z_{\gamma_5}(2)$ such that it is no independent symmetry of the action (6.1).

a non-vanishing expectation value of $\omega_3 = \mathrm{i}\lambda_V n$, as always present at non-zero μ and T. This symmetry is also present in QCD at non-zero chemical potential and is a type of generalized $\mathcal{PT}$ symmetry [180, 190, 191, 193, 194, 309]. These symmetries give rise to exotic phenomena in the phase diagram [180, 190, 191], see Section 3.1.2 for a detailed discussion. Thus, the present analysis can be considered as an exploratory study of mixing effects between scalar and vector mesons in an effective model study as well as this symmetry that is present at finite density in the QCD phase diagram. Both of these phenomena are often not considered in typical NJL or quark-meson model investigations and only recently have received some attention [189, 191]. Although the $2+1$-dimensional four-fermion model (6.1) certainly is not suited to make phenomenological predictions, it serves as a first study of the consequence of both of these properties of QCD in a simple toy model that is free of regularization artifacts. Especially the latter is important, since NJL-type models in $3+1$ dimensions require regulator values that are in the order of the chemical potentials relevant for many exotic phenomena and regularization artifacts can strongly influence the resulting phase diagram [10], see Section 3.2 for a summary.

6.1.2 *Mean-field approximation*

Similar to Chapter 4 and Chapter 5, we employ the mean-field approximation, i.e., we suppress the bosonic quantum fluctuation in the partition function (6.2), see Section 2.4. This amounts to taking the limit $N_f \to \infty$ in the case of four-fermion models. Integrating out the fermion fluctuations in the partition function (since they appear as bilinears, c.f., Eq. (2.34)), one obtains the effective action

$$\frac{1}{N_f}\mathcal{S}_{\text{eff}}[\sigma,\omega_\nu] = \int \mathrm{d}^3x \left[\frac{\omega_\nu\omega_\nu}{2\lambda_V} + \frac{\sigma^2}{2\lambda_S}\right] - \operatorname{Tr}\ln\beta\mathrm{Q}. \tag{6.6}$$

Applying the mean-field approximation, observables can be computed by evaluating them on the global minimum of $\mathcal{S}_{\text{eff}}$, denoted by $\sigma = \Sigma$ and $\omega_\nu = \Omega_\nu$. Further we assume that rotational invariance remains intact whenever we explicitly determine ground states Σ, Ω_ν, which correspond to the global minima of $\mathcal{S}_{\text{eff}}$. This directly implies for the spatial components of the vector field

$$\langle \boldsymbol{\omega} \rangle = \boldsymbol{\Omega} = 0. \tag{6.7}$$

This assumption is only justified when studying homogeneous condensates, i.e., $\sigma = \bar{\sigma}$ and $\omega_\nu = \bar{\omega}_3$, such that also the ground states are homogeneous, $\sigma = \bar{\Sigma}$ and $\omega_\nu = \delta_{3,\nu}\bar{\Omega}_3$. When studying possible inhomogeneous condensates, we never actually perform the minimization of $\mathcal{S}_{\text{eff}}$ but instead analyze the stability of the homogeneous minima against inhomogeneous perturbations, see the discussion in Section 4.1.2. In this analysis, no assumption of the form of the inhomogeneous perturbation is made and, moreover, one finds that the result of the analysis only depends on the absolute value of the spatial momentum $\boldsymbol{q}$ of the inhomogeneous perturbation. Consequently, also this investigation respects rotational invariance of the spatial volume such that the assumption (6.7) remains valid whenever information about the ground state of the system is obtained. Note that in the stability analysis we also perturb about the spatial components of the vector field, such that rotational invariance could, in principle, be broken spontaneously. A minimization with respect to spatially dependent $\sigma(\boldsymbol{x}), \omega_\nu(\boldsymbol{x})$ using, e.g., ansatz functions for the functional dependence on the spatial coordinates would need to consider non-vanishing $\boldsymbol{\omega}(\boldsymbol{x})$, generally.

A non-vanishing expectation value of σ breaks the discrete chiral symmetry (B.23) of the model spontaneously, since it acts as a dynamically generated mass term for the fermions. Thus, we often refer to either $\langle\sigma\rangle$ or $\bar{\sigma}$ as the chiral condensate, as it is directly related through Eq. (6.5) to $\langle\bar{\psi}\psi\rangle$.

Implications of the study of phase diagrams within the mean-field approximation for the full quantum theory, described by the partition function (6.2), are discussed detailly in Section 2.4. In short, it is expected that whenever an ordered phase is absent in the mean-field approximation, it will also be absent in the full quantum theory.

6.2 HOMOGENEOUS PHASE DIAGRAM

In this section, we present methods for computing the thermodynamic ground state of the model (6.2) with the assumption of homogeneous condensates, $\sigma = \bar{\sigma}$ and $\omega_3 = \bar{\omega}_3\delta_{\nu,3}$. Thereby, we assume that the spatial components of the vector field respect the invariance of the partition function (6.2) under spatial rotations, i.e., $\boldsymbol{\omega} = 0$.

6.2.1 *Homogeneous effective potential and gap equations*

To perform our analysis, it is convenient to study the homogeneous effective potential (2.53) at fixed μ and T

$$\bar{U}(\bar{\sigma},\bar{\omega}_3) = \frac{1}{N_f}\frac{\mathcal{S}_{\text{eff}}[\bar{\sigma},\bar{\omega}_3]}{\beta V} \tag{6.8}$$

instead of the effective action (6.6), where V is the infinite spatial volume of the system (corresponding to the infinite axial extent of the cylindrical spacetime volume, see Section 2.1). In the case of homogeneous condensates, the eigenvalues of the Dirac operator (6.4) in the effective action (6.6) are momentum-independent. Following Section 2.4.4 and Appendix C, one obtains from Eq. (6.6)

$$\bar{U}(\bar{\sigma},\bar{\omega}_3) = \frac{\bar{\omega}_3^2}{2\lambda_V} + \frac{\bar{\sigma}^2}{2\lambda_S} - \frac{d_\gamma}{2}\int\frac{\mathrm{d}^2p}{(2\pi)^2}\left[E + \frac{1}{\beta}\left[\ln\left(1+\mathrm{e}^{-\beta(E+\bar{\mu})}\right) + \bar{\mu}\to-\bar{\mu}\right]\right], \tag{6.9}$$

where $E = \sqrt{\boldsymbol{p}^2+\bar{\sigma}^2}$ ($\boldsymbol{p}$ is the spatial momentum) and $d_\gamma = 4$ denotes the dimensionality of the spinors in $2+1$ dimensions. Thereby, we use the effective chemical potential $\bar{\mu} = \mu + \mathrm{i}\bar{\omega}_3 = \mu - \lambda_V\bar{n}$ which is convenient when ω_3 is homogeneous following the discussion above. The last two terms in Eq. (6.9) are identical to the effective potential of the GN model at chemical potential $\bar{\mu}$ and temperature T, see, e.g., Refs. [1, 240, 241, 249, 250] or the computation in Appendix C.

The computation of homogeneous condensates is performed by determining the extrema of the effective potential (6.9) with respect to the bosonic fields, i.e., by solving the gap equations

$$\frac{\partial\bar{U}^{(\mu,T)}}{\partial\bar{\sigma}} = 0 \qquad\Leftrightarrow\qquad \bar{\sigma}\left(\frac{1}{\lambda_S} - \ell_1(\mu,T,\bar{\sigma},\bar{\omega}_3)\right) = 0, \tag{6.10}$$

where

$$\ell_1(\mu,T,\bar{\sigma},\bar{\omega}_3) = \frac{d_\gamma}{2}\int\frac{\mathrm{d}^2p}{(2\pi)^2}\frac{1-n_F(E)-n_{\bar{F}}(E)}{E}, \tag{6.11}$$

and

$$\frac{\partial \bar{U}^{(\mu,T)}}{\partial \bar{\omega}} = 0 \qquad \Leftrightarrow \qquad \frac{\bar{\omega}_3}{\lambda_V} - \mathrm{i}\bar{n}(\mu, T, \bar{\sigma}, \bar{\omega}_3) = 0 \tag{6.12}$$

with

$$\bar{n}(\mu, T, \bar{\sigma}, \bar{\omega}_3) = \frac{d_\gamma}{2} \int \frac{\mathrm{d}^2 p}{(2\pi)^2} \left[n_F(E) - n_{\bar{F}}(E) \right] . \tag{6.13}$$

In the above expressions, we used the Fermi distribution functions (C.18) defined in Appendix C. Note that the gap equation for $\bar{\omega}_3$ does not contain a vacuum contribution from the Dirac sea, such that $\bar{\omega}_3 = 0$ is the only solution of Eq. (6.12) for $\mu = 0$. Solving this set of coupled equations, one can determine all extrema of Eq. (6.9) with respect to $\bar{\sigma}$ and $\bar{\omega}_3$ and computes the global minimum $(\bar{\Sigma}(\mu, T), \bar{\Omega}_3(\mu, T))$ by inserting all found extrema back into the effective potential (6.9).

The absorption of $\bar{\omega}_3$ into an effective chemical potential can be useful for the interpretation of results as well as for computational purposes. Moreover, since there is no way to distinguish between the dynamical contribution to the chemical potential through condensation of $\bar{\omega}_3$, $\bar{\mu}$ also is phenomenlogically relevant. Thus, one could argue to use $\bar{\mu}$ and T as external parameters of the model and, instead, treat the effective potential as a function of $\bar{\sigma}$ and μ, such as in Refs. [235, 236]. This would allow to directly solve Eq. (6.10) for $\bar{\sigma}$ at fixed $\bar{\mu}$ and T and inserting the solution into Eq. (6.12) which allows to directly compute $\bar{\omega}_3$ and, thus, the chemical potential from $\mu = \bar{\mu} - \mathrm{i}\bar{\omega}_3$. However, this procedure leads to ambiguities in the (μ, T) phase diagram, as multiple $(\bar{\sigma}, \bar{\mu})$ pairs can belong to the same chemical potential. Then, one would need to iterate through all computed tuples $(\bar{\sigma}, \bar{\mu})$ to get the correct global minimum of $\bar{U}$ for a certain (μ, T) in order to determine the phase diagram. Therefore, we prefer to keep μ and T as external parameters and solve the gap Eqs. (6.10) and (6.12) for $\bar{\sigma}$ and $\bar{\omega}_3$ directly in our numerical setup.

6.2.2 *Renormalization and parameter fixing*

The computation of homogeneous condensates in the model (6.1) involves the evaluation of integrals with linear UV divergences that require regularization, as obvious from analyzing the integrand of Eq. (6.10) with appropriate power counting. As originally demonstrated in Refs. [243, 244], four-fermion interactions are renormalizable order by order in $1/N_f$ in $(2+1)$ dimensions. This allows to remove divergences by imposing an appropriate renormalization condition, see Appendix C.2 for a detailed presentation in the context of the GN model in $2+1$ dimensions. By fixing $\bar{\Sigma}(\mu = 0, T = 0) = \bar{\Sigma}_0$ one can absorb the divergence using the coupling λ_S through the gap equation (6.10) in the vacuum. Using a Pauli villars regularization with parameter Λ for the UV divergence of the spatial loop momenta, we determine

$$\ell_1(0, 0, \bar{\sigma}, 0) = \frac{d_\gamma}{4\pi} \left(\Lambda - |\bar{\sigma}| \right) \tag{6.14}$$

such that one finds for $\bar{\Sigma}(\mu = 0, T = 0) = \bar{\Sigma}_0$

$$\frac{1}{\lambda_S} = \frac{d_\gamma}{4\pi} \left(\Lambda - |\bar{\Sigma}_0| \right) . \tag{6.15}$$

Note that we used that $\bar{\omega}_3 = 0$ in the vacuum, as can be read off directly from Eq. (6.12). Using this procedure and sending $\Lambda \to \infty$, we obtain

$$L_1(\mu, T, \bar{\sigma}, \bar{\omega}_3) \equiv \frac{1}{\lambda_S} - \ell_1(\mu, T, \bar{\sigma}, \bar{\omega}_3) = d_\gamma \left[\frac{|\bar{\sigma}| - |\bar{\Sigma}_0|}{4\pi} + \int \frac{\mathrm{d}^2 p}{(2\pi)^2} \frac{n_F(E) + n_{\bar{F}}(E)}{2E} \right], \tag{6.16}$$

which is finite. This procedure is all that is required to keep the effective potential (6.9) finite. The chiral condensate in the vacuum $\bar{\Sigma}_0$ will be used as the physical scale to construct dimensionless ratios for all other quantities, such as, e.g., $T/\bar{\Sigma}_0$, $\mu/\bar{\Sigma}_0$ and $n/\bar{\Sigma}_0^2$.

However, the gap Eq. for $\bar{\omega}_3$ (6.10) does not contain a vacuum contribution such that imposing a renormalization condition is not necessary. Since, $\bar{\omega}_3 = 0$ in the vacuum, there is thus no way of fixing λ_V in an analogous way to the scalar coupling λ_S. To the knowledge of the author, no alternative way of renormalizing this coupling is realized in the literatue and, in fact, a renormalization of the vector coupling is not necessary for the computation of the phase diagram. Alternatively, one could fix λ_V by working at $\mu \neq 0$, e.g., by imposing a value of $\bar{\omega}_3$ at a certain μ and $T = 0$. We consider the action (6.1) anyhow as a toy model for scalar-vector mixing effects in the (μ, T) phase diagram such that we do not fix λ_V according to some phenomenlogically motivated value. Instead, we treat it as a free parameter to study its influence on the phase diagram of the theory similar to Refs. [235, 236]. Moreover, the ratio λ_S/λ_V of the effectively generated four-fermion interaction vertices should anyhow change dynamically in QCD depending on μ and T as well as on the considered momentum exchange.

6.2.3 *Results*

In the following, we discuss our findings on the homogeneous phase diagram of the model (6.1) for different values of the vector coupling λ_V. We distinguish between the SP where $\bar{\Sigma} \neq 0$ and chiral symmetry is restored and the HBP where chiral symmetry is spontaneously broken by a non-vanishing chiral condensate $\bar{\Sigma} \neq 0$. By analyzing the gap Eq. (6.10) and the effective potential (6.9) we find that the phase boundary between those two phases in the $(\bar{\mu}, T)$ plane is identical to the one of the $2+1$-dimensional GN model in the (μ, T) plane, as first determined in Ref. [249] and later confirmed to be the full solution of the phase diagram in Refs. [240, 241]. The analytic expression for the critical chemical potential in the GN model, see Appendix C.3 for a derivation,

$$\mu_c(T) = T \operatorname{arcosh}\left(0.5 \mathrm{e}^{\bar{\Sigma}_0/T} - 1\right) \tag{6.17}$$

can be used as a cross-check for our numerical results also at $\lambda_V \neq 0$ by computing $\bar{\mu}_c = \mu_c + \mathrm{i}\bar{\Omega}_3(\mu_c, T)$ at the obtained phase boundary $\mu_c(\lambda_V, T)$ of the model (6.1). Then, the value of $\bar{\mu}_c/\bar{\Sigma}_0$ must be identical to the critical boundary $\mu_c(0.0, T)/\bar{\Sigma}_0$, as given by the right hand side of Eq. (6.17). The phase boundary in the GN model is of second-order, except for $\mu_c(T = 0)/\bar{\Sigma}_0 = 1$ where the effective potential is flat for $\bar{\sigma}/\bar{\Sigma}_0 \in [0.0, 1.0]$ which corresponds to a critical point.

In Fig. 6.1, the phase boundary lines of the model (6.1) are plotted for different values of the vector coupling $\lambda_V \bar{\Sigma}_0 \in [0.0, \pi]$. Similar to findings with NJL-type models with vector interactions [196, 208, 235] an enlargement of the phase with broken chiral symmetry is observed when increasing the vector coupling. The extent of the HBP grows monotonically with the vector coupling within the studied range. At larger vector couplings, a so-called

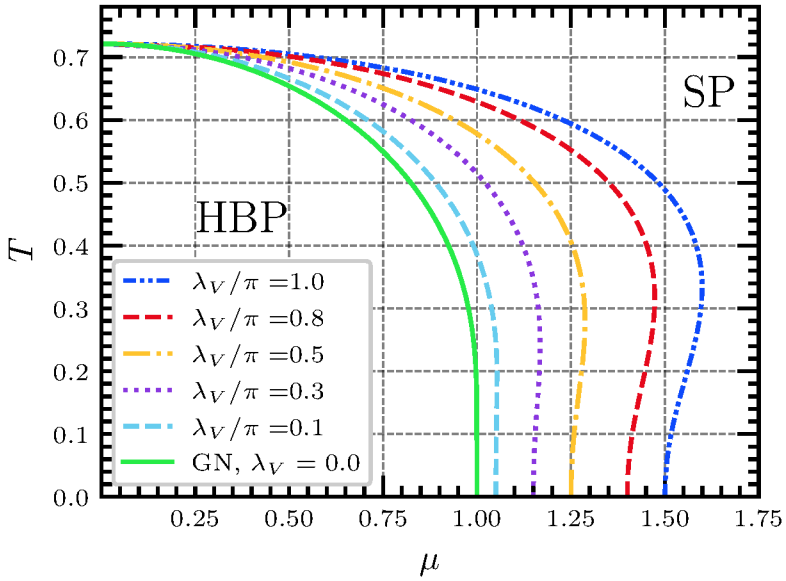

Figure 6.1: Phase boundary lines between the HBP and SP in the (μ, T) space for 5 different values of the vector coupling λ_V. The $\lambda_V = 0.0$ phase boundary corresponds to the known analytic solution of the GN model in $(2+1)$ dimensions [241, 249].

back-bending of the transition line is observed, i.e., the difference $\mu_c(\lambda_V, T) - \mu_c(0.0, T)$ for intermediate temperatures is larger than for zero or low temperatures. This reminds of a spinodal line in typical NJL or GN model phase diagrams [93] where no phase transition occurs but only the symmetric solution $\bar{\sigma} = 0.0$ becomes metastable. However, in the present investigation the left spinodal corresponds directly to the phase boundary line, since the phase transition is of second-order and the order parameter $\bar{\Sigma}(\mu, T)$ changes continuously from zero when crossing the boundary line from the SP at higher chemical potentials to the HBP.

This is investigated in more detail in Fig. 6.2 where the value of the order parameter $\bar{\Sigma}(\mu, T)$ is visualized in a triangulated contour color map for two different values of the vector coupling. For all studied values of λ_V one observes a continuous decrease of the chiral condensate $\bar{\Sigma}$ when increasing the temperature within the HBP. Thereby, by renormalization condition $\bar{\Sigma}(\mu = 0.0, T = 0.0) = \bar{\Sigma}_0$ which remains constant for all values of $\mu \leq \bar{\Sigma}_0$ in consistency with the Silver blaze property: observables are unaffected by chemical potential as long as the chemical potential is not large enough to create physical excitations, see Refs. [363–365] for a motivation why this is realized in QCD. Further increase of the chemical potential leads to a continuous decrease of $\bar{\Sigma}(\mu/\bar{\Sigma}_0 = 1, T = 0) = \bar{\Sigma}_0$ to $\bar{\Sigma}(\mu = \mu_c, T = 0) = 0$ at the phase transition. This can be analytically derived from the flatness of the GN model's effective potential at $\mu/\bar{\Sigma}_0 = 1$ and zero temperature. The flatness as a function of $\bar{\sigma}$ is also present in the effective potential (6.9) for non-vanishing λ_V at $(\mu/\bar{\Sigma}_0 = 1, T = 0)$. However, the additional contribution due to $\bar{\omega}_3$ causes solutions with higher densities to be favored, see Eq. (6.9). The coupled gap Eqs. (6.10) and (6.12) leads to a simultaneous decrease of the chiral condensate and a continuous increase of the density $\bar{N} = -\mathrm{i}\bar{\Omega}_3/\lambda_V$, when increasing $\mu \in [\bar{\Sigma}_0, \mu_c]$. For all chemical potentials in this interval and all values of $\lambda_V \neq 0$, one obtains $\bar{\mu} = 1.0$ which is the only value where the gap Eq. (6.10) allows for solutions other than $\bar{\Sigma}/\bar{\Sigma}_0 = 1.0$ or $\bar{\Sigma} = 0.0$. The solution of the gap

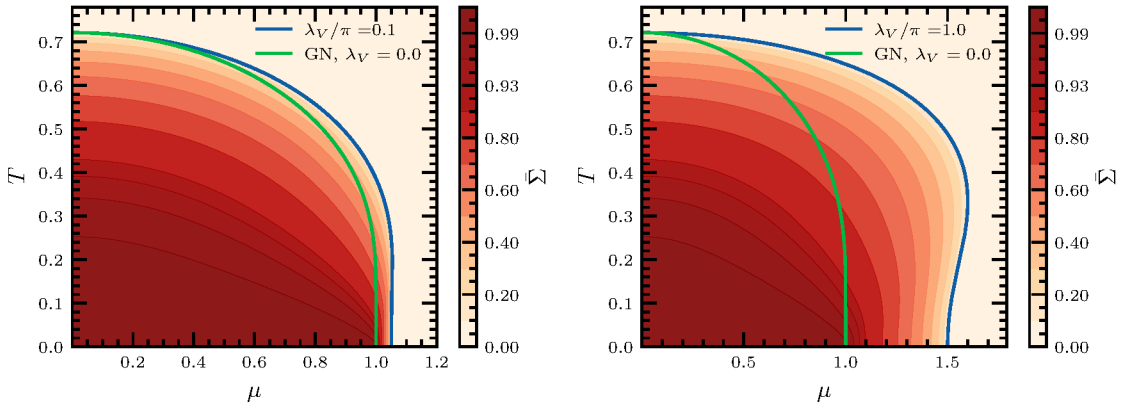

Figure 6.2: Contour color maps in the (μ, T) plane for the value of the chiral condensate $\bar{\Sigma}(\mu, T)$ for *(left)* $\lambda_V \bar{\Sigma}_0/\pi = 0.1$, *(right)* $\lambda_V \bar{\Sigma}_0/\pi = 1.0$. The green lines represent the second-order phase boundary of the $(2+1)$-dimensional GN model, while the blue lines correspond to the phase boundary of the model (6.1) for the respective value of λ_V. Continuous data for the contour plots is obtained using triangulation provided by *Matplotlib* in *Python3* [19, 20]. Note that the plot range in the μ and the T axis differs from plot to plot in order to make the contour lines visible.

eq. for $\bar{\Sigma}(\mu, T = 0)$ can directly be read of the plot for this range of chemical potentials. It is $\bar{\Sigma} = \mu - \bar{\mu}_c(T = 0) = \mu - \bar{\Sigma}_0$.

For $\lambda_V = 0.0$, the density jumps from 0 to $\bar{\Sigma}_0^2/(2\pi)$ when crossing the phase transition at zero temperature [321].[2] For non-vanishing vector coupling, a continuous transition of the density is obtained, as visualized also in Fig. 6.3, where the density $\bar{N}\pi/\bar{\Sigma}_0^2$ is plotted as a triangulated contour color map in the (μ, T) plane for two different values of the vector coupling. All values of $\bar{N}(\mu, T = 0)/\bar{\Sigma}_0^2 \in [0.0, 1/(2\pi))$ are obtained when continuously increasing the chemical potential from $\mu/\bar{\Sigma}_0 > 1.0$. At $\mu = \mu_c$, we obtain $\bar{N}/\bar{\Sigma}_0^2 = 1/(2\pi)$. The gap Eq. (6.12) allows a non-vanishing density only when $\mu/\bar{\Sigma}_0 > 1.0$ and $\bar{\Sigma}/\bar{\Sigma}_0 < 1.0$ such that at $\mu/\bar{\Sigma}_0 = 1.0$ the zero density solution is observed. This is another indication that the phase boundary is of second-order at zero temperature for non-vanishing vector coupling. At non-vanishing temperatures the relation of μ and the value of $\bar{\Omega}_3$ has to be determined numerically solving the gap Eqs. (6.10) and (6.12) and finding the global minimum of the effective potential (6.9). Compared to zero temperature, the density is non-vanishing also for $\mu/\bar{\Sigma}_0 < 1.0$. When comparing different values of λ_V, one generally observes that the density is smaller when increasing the vector coupling at fixed values of μ and T.

Note that one does not obtain a first-order phase transition for all values of λ_V within the (μ, T) phase diagram of this model, in contrast to NJL model results involving vector coupling [235]. In typical NJL model investigations, an IP can emerge that covers the region of the first-order phase transition between the HBP and SP that is present in the homogeneous phase diagram of the theory.

2 There is a factor of 2 difference in the value of the density between this work and Ref. [321] due to different conventions.

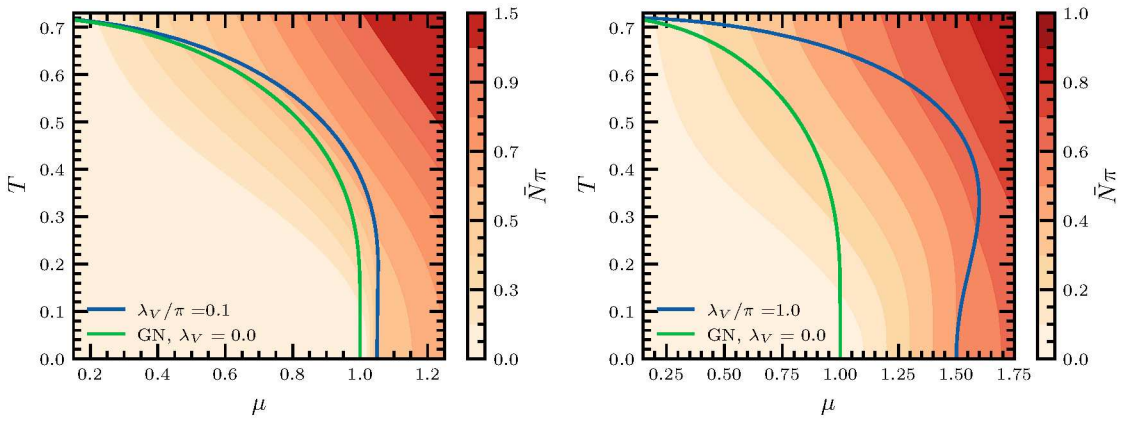

Figure 6.3: Contour color maps in the (μ, T) plane for the value of the density $\bar{N}(\mu,T)\pi = -\mathrm{i}\bar{\Omega}_3(\mu,T)\pi/\lambda_V$ for *(left)* $\lambda_V\bar{\Sigma}_0/\pi = 0.1$, *(right)* $\lambda_V\bar{\Sigma}_0/\pi = 1.0$. The green lines represent the second-order phase boundary of the $(2+1)$-dimensional GN model, while the blue lines correspond to the phase boundary of the model (6.1) for the respective value of λ_V. Continuous data for the contour plots is obtained using triangulation provided by *Matplotlib* in *Python3* [19, 20]. Note that the plot range in the μ axis, the T axis and the discrete color bar differs from plot to plot in order to make the contour lines visible. Also, the discrete contour levels are not necessarily linearily distributed.

6.3 MIXING EFFECTS IN THE HESSIAN MATRIX GENERATING THE QUANTUM PION LIQUID

In this section, we turn towards computing the Hessian matrix consisting of the bosonic two-point vertex functions $\Gamma^{(2)}_{\phi_j,\phi_k}$ in order to analyze the stability of the homogeneous ground states against inhomogeneous perturbations as well as the possible existence of the QπL over the whole (μ, T) phase diagram of the model (6.1).

6.3.1 *Hessian matrix analysis in field and momentum space*

The resulting Hessian for model (6.2) is given by

$$\Gamma^{(2)}_{\phi_j,\phi_k}\left(\bar{\phi},\mu,T,\boldsymbol{q}\right) = \frac{\delta_{j,k}}{\lambda_j} + T\sum_n \int \frac{\mathrm{d}^2p}{(2\pi)^2}\mathrm{tr}\left(\tilde{\bar{\mathrm{Q}}}^{-1}\left(p+(\boldsymbol{q},0)\right)c_j\tilde{\bar{\mathrm{Q}}}^{-1}\left(p\right)c_k\right) \tag{6.18}$$

where $\tilde{\bar{\mathrm{Q}}}^{-1}$ is the bare propagator of a free fermion with mass $\bar{\Sigma}$ at chemical potential $\bar{\mu} = \mu + \mathrm{i}\bar{\Omega}_3$ and temperature T. The matrices c_j stem from the bare fermion-boson vertices according to the action (6.2) with a slight, but important modification. Following the discussion about the expansion about homogeneous imaginary ground states, such as $\bar{\Omega}_3 = -\mathrm{i}\lambda_V\bar{n}$, in the paragraph about the Hessian matrix in Section 5.3.1, fluctuations in the complex plane have to be chosen along the steepest descent of the effective action in order to follow the stable Lefshetz thimble. For the real-valued $\bar{\sigma}$ as well as for the spatial components of the vector field $\boldsymbol{\omega}$, this is the case with real-valued perturbations, while one has to perturb the imaginary homogeneous expectation value $\bar{\omega}_3$ with real-valued fluctuations (instead of purely imaginary ones as one might naively expect). In the Hessian matrix, as computed generically in Eq. (4.24) and given in Eq. (6.18), the matrices $\vec{c} = (1, -\gamma_3, \mathrm{i}\gamma_1, \mathrm{i}\gamma_2)$ corresponding to the bare $\bar{\psi} - \psi - \phi_j$ for $\vec{\phi} = (\sigma, \omega_3, \omega_1, \omega_2)$ absorb the additional factor of i to account for the real-valued perturbation about the imaginary $\bar{\omega}_3$,

see Section 5.3.1 for details. Additionally, one has $\lambda_j = \lambda_S$ for $\phi_j = \phi_k = \sigma$ and $\lambda_j = \lambda_V$ for $\phi_j = \phi_k = \omega_\nu$.

The Hessian matrix (6.18) is already studied for $\bar{\Sigma} = 0$ in Section 5.3 in order to demonstrate the absence of an IP for all $2+1$-dimensional four-fermion models with local four-fermion interactions, see the discussion in Section 5.3.1. Therein, the individual matrix elements are given in Eqs. (D.27) to (D.31) using its rotational invariance to choose $\boldsymbol{q} = (q, 0)$ and are further evaluated in Appendix D.3. In practice, all elements of the Hessian matrix $\Gamma^{(2)}$ are evaluated numerically for fixed q at fixed μ and T using the previously computed homogeneous ground states $\bar{\Sigma}(\mu, T)$ and $\bar{\Omega}_3(\mu, T)$ as the appropriate expansion points. After computing all Hessian matrix elements for fixed q, we proceed by calculating the eigenvalues through numerical diagonalization. The numerics are implemented using *Python3* with various libraries [19, 350, 357].

$\mathcal{PT}$-TYPE SYMMETRY OF THE HESSIAN In the following, we analyze properties of the Hessian $\Gamma^{(2)}$ (6.18) using the generalized $\mathcal{PT}$ symmetry of the model (6.1) at non-zero μ which is given by $\mathcal{CK}$, i.e., combined charge conjugation and complex conjugation. Since ω_ν is a vector field, it picks up a sign under charge conjugation, $\mathcal{C}\omega_\nu\mathcal{C}^{-1} = -\omega_\nu$, see Ref. [274] for a construction of $\mathcal{C}$ in $2+1$ Euclidean spacetime dimensions. Thus, at non-vanishing density, as present according to Section 6.2.3 at non-vanishing μ and T, $\mathcal{C}$ is broken. This is expected from heuristic arguments due to the excess of particles over antiparticles. The Hessian matrix is non-Hermitian simultaneously with the broken $\mathcal{C}$ symmetry at $\mu \neq 0$ due to the non-vanishing, purely imaginary $\Gamma^{(2)}_{\sigma,\omega_3} = \Gamma^{(2)}_{\omega_3,\sigma}$. However, the Hessian still has a remaining invariance under the combined, anti-linear $\mathcal{CK}$ symmetry accordingly.

This symmetry of the Hessian gives rises to the property

$$\Gamma^{(2)} = A\Gamma^{(2)*}A \tag{6.19}$$

where * denotes complex conjugation and $A = \mathrm{diag}(1, -1, 1, 1)$. It directly follows that both $\Gamma^{(2)}$ and $\Gamma^{(2)*}$ have the same set of eigenvalues α_j and, consequently, these eigenvalues are either real-valued or come in complex conjugate pairs. In the former case, one can analyze the eigenvalues of the Hessian $\Gamma^{(2)}$ in a stability analysis of the homogeneous expansion points using an appropriate diagonalization according to Section 4.1.2. The latter case has been recently found as a so-called "$\mathcal{PT}$-broken" regime in the study of mixing in Euclidean field theories with $\mathcal{PT}$-type symmetries [180, 190]. The existence of complex-conjugate eigenvalue pairs in the Hessian matrix can lead to bosonic two-point correlation functions with spatial sine-like modulations in addition to the ordinary exponential decay, see the discussion in Section 4.4.

6.3.2 *Results*

Within the HBP where $\bar{\Sigma} \neq 0$, one obtains mixing between σ and ω_3 when inspecting the static Hessian $\Gamma^{(2)}_{\phi_j,\phi_k}(q = 0)$ since the matrix element for $\phi_j = \sigma$ and $\phi_k = \omega_3$ (or vice versa) is non-vanishing, see Eq. (D.29). When considering $q \neq 0$, there can also occur mixing involving the spatial components of ω_ν, see the discussion in Section 5.3.1 and Appendix D.3 for the Hessian matrix elements. We start by focusing on the static Hessian $\Gamma^{(2)}(q = 0)$, i.e., the mass matrix of the theory. To study these static mixing effects, one can consider the block of $\Gamma^{(2)}$ with $\phi_j, \phi_k \in (\sigma, \omega_3)$. Perturbations about the spatial components of the vector field are not relevant in this case, since the static Hessian is diagonal anyway

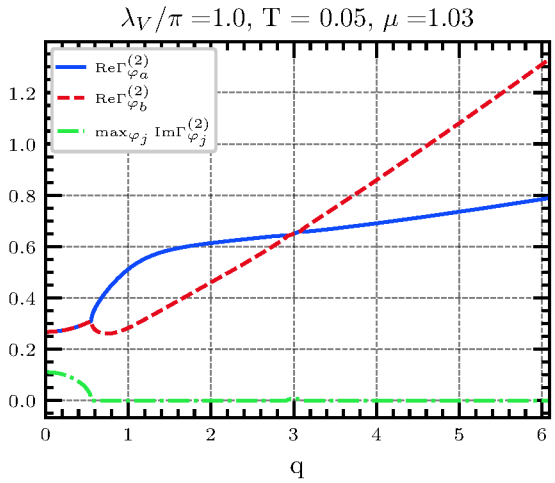

Figure 6.4: The real and imaginary part of the bosonic two-point vertex functions $\Gamma^{(2)}_{\varphi_j}(q)$ are plotted as functions of the momentum of the perturbation q. The bosonic two-point vertex functions are obtained as eigenvalues of H_{ϕ_j,ϕ_k} with $\phi_j, \phi_k \in \{\sigma, \omega_3\}$. Note that only $\mathrm{Im}\,\Gamma^{(2)}_{\varphi_j}(q)$ is plotted, since $\mathrm{Im}\,\Gamma^{(2)}_{\varphi_a} = -\mathrm{Im}\,\Gamma^{(2)}_{\varphi_b}$.

with respect to ω_1 and ω_2. Thus, no complex-conjugate eigenvalues can be obtained from these diagonal elements $\Gamma^{(2)}_{\omega_j,\omega_j}$ with $j = 1, 2$. The main finding of the following analysis is the observation of complex-conjugate eigenvalues of $\Gamma^{(2)}(q = 0)$ in the certain regions within the HBP through these mixing effects between σ and ω_3. As a consequence, we argue that the bosonic two-point correlation functions $\langle\varphi_j(0)\varphi_j(\boldsymbol{x})\rangle_c$, see Eq. (2.25) for its definition, are oscillatory, but exponentially suppressed according to the analysis of the propagator poles presented in Section 4.4. This regime is termed a QπL in analogy to quantum spin liquids in condensed matter systems, see Section 3.1.2 and Section 3.3.2 for further context.

At any non-vanishing T and μ within the HBP, one obtains mixing between σ and ω_3 such that the physical basis $\varphi_j \neq \phi_j$. This mixing, given that the non-diagonal elements of the Hessian are large enough compared to the diagonal ones, can lead to the appearance of complex-conjugate eigenvalues of $\Gamma^{(2)}_{\phi_j,\phi_k}$ depending on μ and T, and implicitly on the homogeneous expansion points $\bar{\Sigma}(\mu, T)$ and $\bar{\Omega}_3(\mu, T)$. An example of this phenomenon is shown in Fig. 6.4, where the real and imaginary eigenvalues of $\Gamma^{(2)}_{\phi_j\phi_k,(}q)$ with $\phi_j, \phi_k \in (\sigma, \omega_3)$ are plotted for $(\mu/\bar{\Sigma}_0 = 1.03, T/\bar{\Sigma}_0 = 0.05)$ and $\lambda_V\bar{\Sigma}_0/\pi = 1.0$. The eigenvectors φ_a and φ_b are given by q-dependent linear combinations of σ and ω_3, i.e., $\varphi_j(q) = c_j(q)\sigma + d_j(q)\omega_3(q)$. The imaginary part of the eigenvalues for $q = 0$ decreases as a function of q in this analysis until real-valued eigenvalues are obtained for $q/\bar{\Sigma}_0 \approx 0.5$. Then, also the degeneracy $\mathrm{Re}\,\Gamma^{(2)}_{\varphi_a} = \mathrm{Re}\,\Gamma^{(2)}_{\varphi_b}$ is no longer enforced by $\mathcal{CK}$ invariance (see the discussion in Section 6.3.1) resulting in an apparently non-analytic behavior of both bosonic two-point vertex functions at $q/\bar{\Sigma}_0 \approx 0.5$ and $q/\bar{\Sigma}_0 \approx 3.0$. Whenever the real parts of $\Gamma^{(2)}_{\varphi_{a/b}}(q)$ are equal to each other one also observes a non-vanishing imaginary part of $\Gamma^{(2)}_{\varphi_a}(q) = -\Gamma^{(2)}_{\varphi_b}(q)$ for $a \neq b$. In the static case with $q = 0$, the complex-conjugate eigenvalue pairs leads to bosonic propagators that are sinusoidal modulated alongside the usual exponential decay, see Section 4.4. A low-momentum expansion of the bosonic two-point vertex functions then yields the described behavior through the appearance of roots of the propagator with a non-vanishing real and imaginary part, see the discussions in Refs. [180, 188, 191]. Note the

bosonic two-point vertex functions behave quantitatively different from Fig. 6.4 at $q \neq 0$ when the $\Gamma^{(2)}_{\phi_j,\phi_k}$ is considered as a 4×4 matrix with $\vec{\phi} = (\sigma, \omega_3, \omega_1, \omega_2)$, i.e., perturbations about ω_1 and ω_2 are considered. The off-diagonal matrix elements proportional to ω_1 and / or ω_2 contribute at $q \neq 0$. Thus, Fig. 6.4 at non-vanishing q should be understood as an example for the effects of mixing and not as a full solution for the model (6.1). It would be the full solution of the momentum dependence of the Hessian matrix when only off-diagonal elements, i.e., mixing effects, proportional to σ and ω_3 are allowed.

To characterize the regime where complex-conjugate eigenvalue pairs appear in $\Gamma^{(2)}_{\phi_j,\phi_k}$ for $q = 0$, we use

$$k_0 = \max_{\varphi_j} \left(\operatorname{Im} \Gamma^{(2)}_{\varphi_j}(q = 0) \right), \tag{6.20}$$

i.e., the maximal imaginary part of the eigenvalues of the Hessian matrix at $q = 0$. This is an important scale for the momentum of the sinusoidal oscillation of the bosonic propagator, as a non-vanishing k_0 induces a non-vanishing real part of the propagator poles, see the discussion in Section 4.4. In Fig. 6.5, we plot k_0 in the (μ, T) plane using a color code for $\lambda_V \bar{\Sigma}_0 / \pi \in \{0.6, 0.8, 1.0\}$. A region with $k_0 \neq 0$ for chemical potentials $\mu/\bar{\Sigma}_0 > 1.0$ and rather small temperatures is observed for all three vector couplings. Whenever $k_0 \neq 0$, the QπL is observed, i.e., bosonic two-point correlation functions are oscillating, exponentially damped functions in this region. Note that the diagonalizing field basis for static perturbations $\vec{\varphi}(q = 0) = (z_1\sigma + z_2\omega_3, z_2^*\sigma + z_1^*\omega_3, \omega_1, \omega_2)$ with complex-valued coefficients z_1 and z_2 for all studied points in the phase diagram and all studied vector couplings λ_V.

The extent of the region with complex-conjugate eigenvalue pairs both in μ and in T direction depends monotonically on the value of the vector coupling. For $\lambda_V \bar{\Sigma}_0 / \pi = 0.6$, this region's extent is significantly smaller than for $\lambda_V \bar{\Sigma}_0 / \pi = 1.0$. For all studied vector couplings, the width in the μ direction of the regime with oscillating propagator behavior decreases for larger temperatures, until k_0 goes to zero. We expect that this is caused by thermal fluctuations suppressing the oscillatory behavior in the propagators. Such a behavior is typical for regimes with spatial oscillations, because the thermal fluctuations tend to destroy ordering and flatten short- and intermediate range correlations in general [219, 225, 226, 366]. For all three vector couplings, k_0 jumps from zero to a non-vanishing value when crossing $\mu/\bar{\Sigma}_0 > 1.0$ at zero temperature in consistency with the Silver Blaze property. This can also be derived from the formulas in Appendix D for the off-diagonal elements. As visible in Fig. 6.5, $k_0(\mu, T)$ seems to have a rapid but continuous onset from zero when increasing μ from the left of the regime with spatial oscillations at any $T \neq 0$. In the literature, the transition from $k_0 = 0$ to $k_0 \neq 0$ is also called disorder line [219], as the line where the propagator poles become degenerate and, subsequently, develop non-vanishing real parts.

In Fig. 6.6, we plot k_0 at zero temperature as a function of $\lambda_V \bar{\Sigma}_0$ and $\mu/\bar{\Sigma}_0$ and observe the above described non-analytic behavior at all $\lambda_V \bar{\Sigma}_0 > 0.5\pi$. Precisely at $\lambda_{V,c} \bar{\Sigma}_0 = 0.5\pi$, however, there is a continuous onset of k_0. For $\lambda_V \bar{\Sigma}_0 < 0.5\pi$, we do not find $k_0 \neq 0$ at all. The width of the region with $k_0 \neq 0$ in the μ direction is largest at $T = 0$ for all studied vector couplings such that we expect that one finds $k_0 = 0$ for all vector couplings lower than $\lambda_{V,c}$ both at zero and non-zero temperature. Consequently, for $q = 0$ we do not expect any complex-conjugate eigenvalues to appear in the Hessian matrix for $\lambda_V \bar{\Sigma}_0 < 0.5\pi$. From Fig. 6.6 it becomes clear that the extent of the region with complex-conjugate eigenvalues of $\Gamma^{(2)}$ at $q = 0$ grows with increasing vector coupling when $\lambda_V > \lambda_{V,c}$. Also, the value of k_0 grows monotonically when increasing λ_V from any value larger than $\lambda_{V,c}$. Both observations show that the increase of the vector coupling increases the mixing effects, which is expected

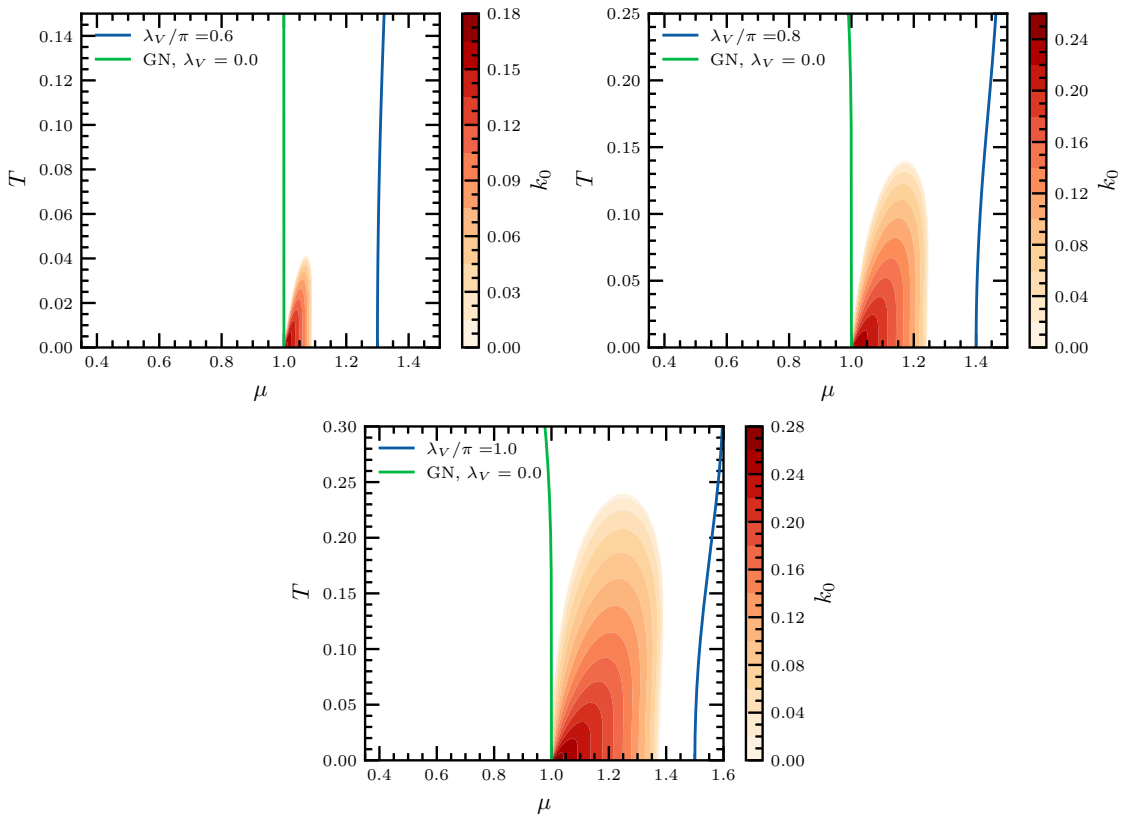

Figure 6.5: Contour color maps in the (μ, T) plane for the value of the maximal imaginary part of the eigenvalues at $q = 0$, denoted by k_0, for *(top left)* $\lambda_V \bar{\Sigma}_0/\pi = 0.6$, *(top right)* $\lambda_V \bar{\Sigma}_0/\pi = 0.8$, *(bottom)* $\lambda_V \bar{\Sigma}_0/\pi = 1.0$. The green lines represent the second-order phase boundary of the $(2+1)$-dimensional GN model, while the blue lines correspond to the phase boundary of the model (6.1) for the respective value of λ_V. Continuous data for the contour plots is obtained using triangulation provided by *Matplotlib* in *Python3* [19, 20]. Note that the plot range in the μ axis, the T axis and the discrete color bar differs from plot to plot in order to make the contour lines visible.

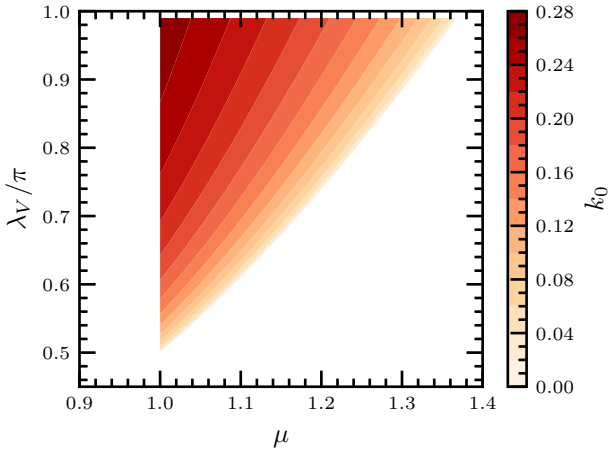

Figure 6.6: Contour color maps in the (λ_V, μ) plane for the value of the maximal imaginary part of the eigenvalues at $q = 0$, denoted by k_0, at zero temperature. Continuous data for the contour plots is obtained using triangulation provided by *Matplotlib* in *Python3* [19, 20].

since an increase of λ_V lowers the difference $\Gamma^{(2)}_{\sigma,\sigma}(q=0) - \Gamma^{(2)}_{\omega_3,\omega_3}(q=0)$. This difference between the two diagonal elements needs to be smaller than the product of the off-diagonal elements such that the eigenvalues of the corresponding 2×2 block are complex-conjugate eigenvalue pairs, as one can derive from the characteristic equation of any 2×2 matrix. Logically, the increase of mixing effects in terms of the off-diagonal elements $\Gamma^{(2)}_{\sigma,\omega_3}$ also amounts to a growth of the extent of the regime with spatially oscillating propagators.

Although k_0 is a useful observable to quantify the appearance of complex-conjugate eigenvalues, it is not the unique scale determining the spatial oscillation of the propagator $\langle \varphi_j(\boldsymbol{x}) \varphi_j k(0) \rangle_c$. Instead, the scales for the oscillation and the exponential decay of G_{φ_j} are given by the respective real and imaginary parts of the roots $q^{1,2}_{\varphi_j}$ of Eq. (4.61). These roots are given by

$$q^{1,2}_{\varphi_j} = \pm \mathrm{i} \sqrt{\frac{\Gamma^{(2)}_{\varphi_j}(0)}{Z_{\varphi_j}}}. \tag{6.21}$$

In order to compute these roots numerically, one can use the fact that $\varphi_j(q)$ has a weak dependence on q for small q. In practice, the computation of Z_{φ_j} involves the discrete differentiation of the eigenvalues of $\Gamma^{(2)}_{\phi_j,\phi_k}$ (compare Eq. (4.61) and Eq. (4.25)). Thus, its computation has to be performed by carefully taking into account the discretization error in q and the change of basis $\varphi_j(q)$ in this area. Also, the imaginary part of Z_{φ_j} is very small such that one also encounters problems with under-flowing of double precision. In test runs of this evaluation the maximum value for $\operatorname{Im} Z_{\varphi_j}$ encountered was on the order of 10^{-3}, while $\operatorname{Re} Z_{\varphi_j}$ is typically of order 10^{-1}. However, the problems involving the numerical evaluation of Z make a precise determination of the poles using Eq. (6.21) impractical with respect to the study of the whole phase diagram.

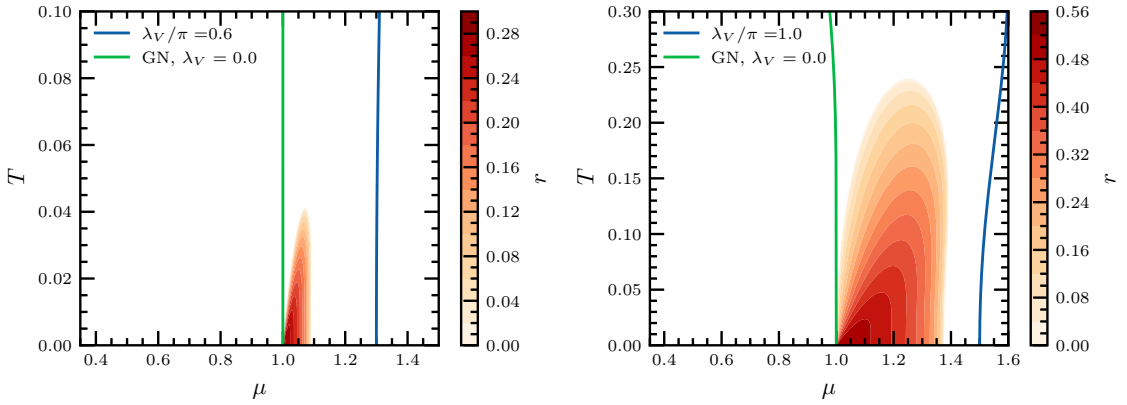

Figure 6.7: Contour color maps in the (μ, T) plane for the ratio r between the frequency of the spatial oscillation and the exponential decay rate of the exponential decay of the propagator. *(left)* $\lambda_V\bar{\Sigma}_0/\pi = 0.6$, *(right)* $\lambda_V\bar{\Sigma}_0/\pi = 1.0$. The green lines represent the second-order phase boundary of the $(2+1)$-dimensional GN model, while the blue lines correspond to the phase boundary of the model (6.1) for the respective value of λ_V. Continuous data for the contour plots is obtained using triangulation provided by *Matplotlib* in *Python3* [19, 20]. Note that the plot range in the μ axis, the T axis and the discrete color bar differs from plot to plot in order to make the contour lines visible.

Hence, we decided to use[3]

$$\theta = \arg\left(\sqrt{\frac{\Gamma_\chi^{(2)}(0)}{\operatorname{Re} Z_\chi}}\right) = \frac{1}{2}\arccos\left(\frac{\operatorname{Re}\Gamma_\chi^{(2)}(0)}{|\Gamma_\chi^{(2)}(0)|}\right) \tag{6.22}$$

with

$$\chi = \arg\max_{\varphi_j}\left(\operatorname{Im}\Gamma_{\varphi_j}^{(2)}(q=0)\right) \tag{6.23}$$

in order to compare the scales of oscillation and exponential decay. Equation (6.22) gives the complex argument θ of $q^{1,2}$ when setting the imaginary part of Z_{φ_j} to zero. As argued above, the error of this approximation is negligible due to the imaginary part of Z_{φ_j} being small. Using Eq. (6.22) does not require an evaluation of Z_{φ_j} and, thus, avoids the problems related to the underflow of the imaginary part of Z_{φ_j}.

We find $r = \tan\theta = \operatorname{Re} q_\chi^{1,2} / \operatorname{Im} q_\chi^{1,2}$ as the ratio of the oscillation frequency $\operatorname{Re} q_\chi^{1,2}$ and the decay rate $\operatorname{Im} q_\chi^{1,2}$. In Fig. 6.7, r is plotted for two different values $\lambda_V\bar{\Sigma}_0 = 0.6\pi$ and $\lambda_V\bar{\Sigma}_0 = \pi$. The maximal value of r is 0.58, obtained for the largest value of the vector coupling $\lambda_V\bar{\Sigma}_0 = \pi$, implying that the frequency of the oscillation is larger than half of the exponential decay rate at this point in the phase diagram. As expected from the decrease of k_0 for smaller vector couplings, also lower values of r are obtained in general when lowering λ_V. This is expected, since mixing effects will not be as drastic for lower vector couplings, see the discussion above. In general, the obtained contour lines for r are similar to the ones of k_0, see Fig. 6.5. The figure demonstrates that for large parts of the regime with oscillatory behavior the wavelengths are in the order of the inverse of the exponential decay rate.

3 Note that by definition of $\Gamma_\chi^{(2)}$ its imaginary part is always positive such that the determination of the argument in Eq. (6.22) is always valid.

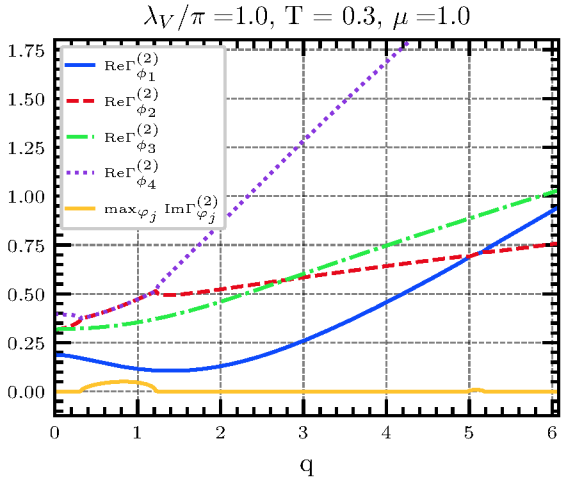

Figure 6.8: The real and imaginary part of the bosonic two-point vertex functions $\Gamma^{(2)}_{\varphi_j}(q)$ as functions of the momentum of the perturbation q. The bosonic two-point vertex functions are obtained as eigenvalues of H_{ϕ_j,ϕ_k} with $\phi_j, \phi_k \in \{\sigma, \omega_\nu\}$. Note that the non-vanishing imaginary part does not necessarily belong to similar eigenvectors $\varphi_j(q)$ and complex-valued two-point vertex functions appear as complex-conjugate pairs.

6.3.3 *Analysis of the Hessian matrix for larger external momenta*

In Fig. 6.4, where only mixing of σ and ω_3 was taken into account, one can observe the appearance of complex-conjugate eigenvalues of the Hessian at $q \neq 0$. However, considering a 4×4 Hessian matrix $\Gamma^{(2)}_{\phi_j,\phi_k}(q)$ with $\phi_j, \phi_k \in (\sigma, \omega_\nu)$ yields a more involved mixing pattern, since also ω_1 contributes to mixing effects with σ when studying $q \neq 0$. The other vector component ω_2 is not mixing with σ (but with the other components of ω_ν), since we choose $\mathbf{q} = (q, 0)$ in Eq. (6.18) by using the rotational invariance of the internal momentum integration in the Hessian matrix elements. The roles of ω_1 and ω_2 are exchanged if we choose $\mathbf{q}$ to be aligned with the x_2 axis. Since the stability analysis turns out to be invariant under spatial rotations (see the discussion in Section 6.3.1), the eigenvalues are independent of the chosen spatial direction $\mathbf{q}/|\mathbf{q}|$ (just the eigenvectors correspond to a different linear combination of ω_1 and ω_2 when changing the angle of $\boldsymbol{q}$).

The more complicated mixing pattern is depicted in Fig. 6.8. From the plot one obtains that $\Gamma^{(2)}$ has real eigenvalues for $q = 0$, but then develops complex-conjugate eigenvalue pairs at some value of $q = q_B$ where

$$q_B = \min_{q \in C} q, \quad C = \{q \in [0, \infty) | \mathrm{Im}\Gamma^{(2)}_{\phi_j}(q) \neq 0\}. \tag{6.24}$$

In this case, one obtains that only two of the four eigenvalues have non-vanishing imaginary parts for fixed q, while the other two are real-valued. As can also be seen from Fig. 6.8, complex-conjugate eigenvalue pairs can be obtained for multiple, disconnected intervals in q. This leads to the rather complicated behavior of the bosonic two-point vertex functions after diagonalization with the real-parts of different eigenvalues becoming degenerate depending on the value of q. Since complex-conjugate eigenvalue pairs can occur for all of the $\Gamma^{(2)}_{\varphi_j}$ with $j \in \{1, 2, 3, 4\}$, the yellow line in the plot always only describes the appearance of the maximal imaginary part in any of those eigenvalues. Since the eigenvectors of $\Gamma^{(2)}$ in field space can be strongly q-dependent especially for large $q/\bar{\Sigma}_0$, one might even argue that the association of the eigenvalues using functions $\Gamma^{(2)}_{\varphi_j}(q)$ is not very insightful. Nev-

ertheless, Fig. 6.8 certainly demonstrates the involved mixing effects between scalar and vector modes. Also, it shows that there is non-monotonic behavior of the real parts of the bosonic two-point vertex functions such that one cannot exclude the appearance of moat regime. However, also the bosonic wave-function renormalization Z_{φ_j} can become complex, see its definition involving $\Gamma^{(2)}_{\varphi_j}$ (4.25), and might not be a decent criterion for a moat regime where $\arg\min_q \operatorname{Re}\Gamma^{(2)}_{\varphi_j}(q) \neq 0$. This is caused by non-analytic behavior of $\Gamma^{(2)}_{\varphi_j}(q)$ around the regions with non-vanishing imaginary parts leading also to non-monotonic behavior. For these reasons we refrain from studying the moat regime within the HBP and focus on the complex-valued eigenvalues instead.

Overall, to the best of the author's knowledge there is no clear interpretation for the appearance of complex-conjugate eigenvalues of $\Gamma^{(2)}$ appearing at fixed $q \neq 0$, especially for $q/\bar{\Sigma}_0 > 1$, in the literature. Also, this work marks the first observation of this phenomenon in the literature – again to the knowledge of the author. For small q_B, a similar interpretation as in the static case of correlation functions with sinusoidal modulations might be meaningful, again performing a low-momentum expansion of the bosonic two-point vertex functions, compare Eq. (4.61) around some non-vanishing q and determining propagator poles similar to Eq. (6.21). However, whenever $q_B/\bar{\Sigma}_0 > 1.0$ such an expansion is certainly not sensible. We document the values of q_B in the following.

In the left plot of Fig. 6.9, we plot a color map in the (T, μ) plane encoding q_B for $\lambda_V \bar{\Sigma}_0/\pi$. In the right plot of this figure we visualize

$$k_{\max} = \max_{j,q} \left(\operatorname{Im} \Gamma^{(2)}_{\phi_j}(q) \right) \tag{6.25}$$

also using a color code. Fig. 6.9 demonstrates that complex-conjugate eigenvalues appear in large parts of the HBP except for a rather small region at small temperatures and chemical potentials. For some parts of this region the obtained imaginary parts are rather small. In consistency with the Silver Blaze property, $k_{\max} = 0$ for $T = 0$ and $\mu/\bar{\Sigma}_0 < 1.0$. For rather small chemical potentials, $k_{\max}/\bar{\Sigma}_0$ is of the order of 10^{-3} and $q_B/\bar{\Sigma}_0 \gg 1$. Accordingly, the interpretation in terms of oscillating propagators as in the static case is not possible, since the argumentation involves a low-momentum expansion which is not sensible here. However, if existent, any oscillating effects in this region should be negligible anyhow given that any relevant imaginary part should be smaller than $k_{\max}/\bar{\Sigma}_0 \sim 10^{-3}$. For larger chemical potentials, one obtains $q_B/\bar{\Sigma}_0 < 1.0$ making a low-momentum expansion of the inverse propagator more sensible. We note that due to the computational demands of computing multiple momentum integrals for the determination of the matrix entries of $H(q)$ and its diagonalization, the resolution in q for the computation of the data in Fig. 6.9 was chosen as $\Delta q = 0.2$. The rather coarse resolution in q results in inaccuracies in the determination of q_B and $k_{\max}$, because the intervals, where complex-valued eigenvalues occur, can be smaller than Δq. This is evident for some data points around the homogeneous phase boundary as well as small μ and $T/\bar{\Sigma}_0 \in [0.5, 0.7]$, where q_B appears to have jumps when changing μ or T. At these data points, it is likely that for some intervals in q, which are smaller than Δq, complex-valued $\Gamma^{(2)}_{\varphi_j}(q \neq 0)$ appear, that where missed such that the correct q_B differs from the depicted data point. Anyhow, the value of $k_{\max}$ is likely to be small anyhow within these intervals.

Again, we note that there is no clear interpretation for the appearance of complex-conjugate eigenvalues of $\Gamma^{(2)}$ appearing at fixed $q/\bar{\Sigma}_0 > 1$ in the literature. An inversion and Fourier-transformation of the obtained $\Gamma^{(2)}_{\varphi_j}$ to compute $G_{\varphi_j}(x, y)$ within these regions yields an ordinary exponential decay in the HBP. This is expected, since $k_{\max}$ is rather

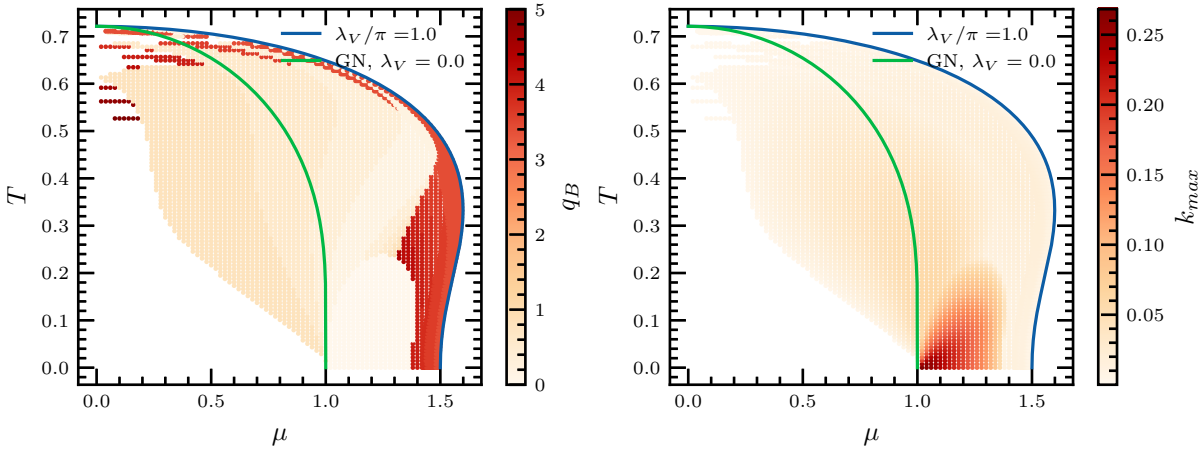

Figure 6.9: Contour color maps in the (μ, T) plane for $\lambda_V \bar{\Sigma}_0/\pi = 1.0$ encoding *(left)* q_B (see Eq. (6.24)) *(right)* $k_{\max}$ (see Eq. (6.25)). The green lines represent the second-order phase boundary of the $(2+1)$-dimensional GN model, while the blue lines correspond to the phase boundary of the model (6.1). Note that the plot range in the discrete color bar differs from plot to plot. The color bar for q_B is cut off at $q_B/\bar{\Sigma}_0 = 5.0$ such that the behavior of lower q_B could be visualized accurately. The discretization of q is given by $\Delta q = 0.2$ resulting in discretization errors in the computation of q_B and $k_{\max}$.

small compared to the real-part of the bosonic two-point vertex functions in these parameter regions (see Fig. 6.9) such that the effect of this phenomenon is negligible when studying bosonic two-point correlation functions. A search for propagator poles in the complex plane by studying $q \in \mathbb{C}$ as an argument of the bosonic two-point vertex functions would be a more appropriate method to finally determine the behavior of bosonic two-point correlation functions in the regime with complex-conjugate eigenvalues at $q \neq 0$.

6.4 SUMMARY AND CONTEXTUALIZATION

In this chapter, the phase diagram of a $2+1$-dimensional four-fermion model was computed in order to investigate the effects of mixing effects between scalar and vector mesons as well as the incorporation of the $\mathcal{CK}$ symmetry at $\mu \neq 0$ in a QCD-inspired theory. Thereby, the vector coupling λ_V was treated as a free parameter and varied in units of the chiral condensate in the vacuum $\bar{\Sigma}_0$. In line with the findings in Chapter 5, no instabilities of homogeneous ground states are observed such that the absence of inhomogeneous chiral condensates is expected in all $2+1$-dimensional four-fermion models with local interaction channels in line with the argumentation presented in Section 5.4 (and the more lengthy analysis in Chapter 5, in general). However, a QπL, i.e., a regime with spatially oscillating, yet exponentially damped mesonic two point correlation function, is observed within the HBP at low temperatures and intermediate chemical potentials for vector couplings $\lambda_V \bar{\Sigma}_0 > \pi/2$. Moreover, an enhancement of the HBP is observed with growing vector coupling λ_V, see Fig. 6.1.

The QπL regime was detected by the appearance of complex-conjugate eigenvalues when computing the bosonic two-point vertex functions $\Gamma^{(2)}_{\varphi_j}(\mathbf{q}) = \left(\langle \varphi_j \varphi_j \rangle_c(\mathbf{q})\right)^{-1}$ as a function of the external momentum $\mathbf{q}$, following the discussion in Section 4.4. See Fig. 6.5 for a visualization of the region in the phase diagram that corresponds to the QπL, where these complex-conjugate eigenvalues are observed, for three different values of the vector coupling.

The argumentation that the QπL arises from these complex-conjugate eigenvalues pairs, corresponding to a so-called $\mathcal{PT}$-broken regime, originates to studies of scalar theories with $\mathcal{PT}$-type symmetry [180, 188, 190], the same type of symmetry as the $\mathcal{CK}$ operation in QCD at $\mu \neq 0$, see the corresponding paragraph in Section 1.2 for a discussion. It has to be noted that the complex-conjugate eigenvalues are observed for both $q \neq 0$ and $q = 0$ in $\Gamma^{(2)}_{\varphi_j}(q)$, but a sensible interpretation through the emergence of a QπL was only possible for $q = 0$ through a low momentum expansion of $\Gamma^{(2)}_{\varphi_j}(q)$. Further, an estimate on the ratio r of the frequency of the oscillation and the exponential decay rate of the mesonic bosonic two-point correlation functions was computed in the whole QπL regime for two different vector couplings demonstrating that this ratio can be of order 10^{-1} to 1 for a large region, c.f. Fig. 6.7 for a visualization of the value of r within the QπL.

CONCLUSIONS This study represents one of the first investigations incorporating the presence of the combined $\mathcal{CK}$ symmetry at $\mu \neq 0$ as well as the mixing effects between scalar and vector mesons. Both effects are expected to play a crucial role in QCD at intermediate densities and temperatures [133, 191]. Thus, it serves as one of the first explorations of **RO1** "What are the implications of the presence of the combined $\mathcal{CK}$-symmetry at $\mu \neq 0$ for the existence of exotic phases?" and **RO2** "What are the implications of mixing effects between scalar and vector mesons for the existence of exotic phases at $\mu \neq 0$?". The finding of the QπL is to the best of our knowledge the first finding of this regime in a four-fermion model generated by the interplay of a attractive, scalar and repulsive, vector four-fermion interaction – apart from the report in the parallel work [189]. We note that Ref. [189] also incorporates both of the above mentioned features. Therein, complex-conjugate eigenvalues are also observed when computing the bosonic two-point vertex functions, which are, however, only studied for homogeneous perturbations (the external spatial momentum $q = 0$ in Eq. (6.18)), i.e., only static mixing effects in the mean-field approximation are considered. Further, Ref. [189] does not quantitatively investigate these complex-conjugate eigenvalues but only reported about their appearance near the CP of the phase diagram and their implicit relation to the QπL regime as stemming from the analysis of scalar theories with a $\mathcal{PT}$-type symmetry (as the $\mathcal{CK}$ operation is) [180, 188, 190] . These works already concluded that this type of symmetry can imply the existence of a QπL. However, these scalar theories can feature both IPs as well as QπLs while only the latter is realized in $2+1$-dimensional four-fermion models. Thus, our results together with the findings in Section 5.4 suggest that the latter seems to be the more robust phenomenon in QCD-inspired models.

Consequently, our findings and Refs. [189, 191] suggest that the QπL is relevant in the phase diagram of QCD at intermediate chemical potential and temperatures both from the above mentioned competition of repulsive and attractive forces as well as its direct relation to the emergent $\mathcal{CK}$ symmetry at $\mu \neq 0$ – both phenomena are relevant for QCD. The competition between an attractive and repulsive interaction is realized in the QCD phase diagram not only through emergent scalar and vector quark-meson exchange diagrams and corresponding four-fermion resonances [133, 148] but also directly from the lifted degeneracy between the Polyakov-loop and its conjugate at $\mu \neq 0$ [189, 191]. The latter suggest that gluon interactions might further favor the existence of a QπL.

Note that the QπL is realized at low temperatures in the case of the $2+1$-dimensional four-fermion model, but at higher temperatures near the CP in the QM model from Ref. [189]. We suspect that this is the case, because the analogue to a CP in four-fermion

models in two spatial dimensions is located at the zero temperature transition line where the homogeneous effective potential becomes flat. Thus, in QCD the QπL and a possibly related moat regime might be present near the suspected CP and the possible first-order phase transition line. They might leave an even more distinct imprint on observables such as two-particle correlations [232–234] and dilepton production [11].

FUTURE RESEARCH PERSPECTIVES With respect to QCD, effective model computations in three spatial dimensions would be even more relevant, although these are possibly spoiled by regularization artifacts present in four-fermion models [10, 210], as in detail discussed in Section 5.4 and multiple times throughout this thesis. Also in QM models / Yukawa-type models, certain ambiguities regarding unbounded potentials appear in the mean-field investigations of the phase diagram through a negative coupling of the mesonic self-interaction as well as an imaginary Yukawa coupling when including the vacuum fluctuations in the renormalization procedure [198] (something that does not occur in the aforementioned Ref. [189] where only effects of mixing in the medium are studied). A study of a fully-fletched QM model with vector mesons would be a logical next step to get closer to QCD and provide phenomenologically interesting results on the scales of the oscillation within the QπL. A promising tool for the renormalization of this theory, while still matching QCD observables in the vacuum such as the pion decay constant, the consistent quark mass and the σ mass, could possibly be provided by the framework of $\mathcal{PT}$ symmetric field theory. Although such QFTs are still rather novel [185, 186, 312, 313, 367], encouraging results for negative couplings have been found in this framework [368–370] – including the non-triviality of scalar ϕ^4 theory for $N > 2$ components and (possibly) for $N = 1$ and negative quartic couplings [371]. Moreover, a non-Hermitian $\mathcal{PT}$-symmetric four-fermion theory could be renormalizable [369].

Further, the investigations in Chapter 5 and Chapter 6 are performed within the mean-field approximation. Certainly, it would be interesting to study the effect of bosonic quantum fluctuations on the QπL. There exist LFT simulations [255] of the $2+1$-dimensional GN model observing oscillatory mesonic correlation function, although the model does not include vector interactions. These findings could be remnants of the IP that is present at finite lattice spacing in the GN model or could be generated by mixing effects stemming from off-diagonal fermion doubler interactions that have quantum numbers of a vector interaction, which are present in naive and staggered lattice discretizations at finite lattice spacing [226, 372]. Going beyond the mean-field approximation in the model (6.1) with LFT is not straightforward as complex weights appear in the path integral [128, 373]. Thus, one would have to either rely on Lefshetz thimble approaches [126, 127], the FRG [121], non-abelian bosonization techniques [228, 229] or $1/N_f$-expansion techniques [272, 273]. All of these approaches pose certain drawbacks, since the latter two analytical approaches are not yet developed to deal with complex actions while the FRG can tackle non-Hermitian problems but has to apply uncontrolled approximations to the bosonic two-point vertex functions (and it is not guaranteed that the method is numerically stable at these low temperatures [286]). Meanwhile, Lefshetz thimbles have been applied to an NJL model with vector interactions similar to model (6.1), see Ref. [128], but numerical instabilities from singular points and cuts in the integration plane have spoiled the simulations. In Chapter 7, the influence of bosonic fluctuations on exotic phase in general is nevertheless investigated using LFT, but using a simple enough, scalar field theory to study their effect with traditional lattice techniques.

As discussed in Section 1.2, oscillatory regimes can have effects on the propagation of pions in heavy-ion-collisions leaving imprints on the two-particle correlation functions of pions [233, 234] and dilepton production rates [11]. However, these findings are based on a generic moat dispersion relation. To extract similar observables from the QπL, one would have to think about a sensible model for this regime that allows their computation. Yet, further information about the scales of the oscillatory behavior in relation to the exponential decay of typical pion correlation functions would be helpful in this process and could be extracted from a Polyakov-Loop QM model, as discussed above.

7

ON THE EFFECTS OF BOSONIC QUANTUM FLUCTUATIONS ON INHOMOGENEOUS CONDENSATES AND THE MOAT REGIME

DISCLOSURE The results presented in this chapter stem from the conference proceedings contribution [6] and an on-going research project by the author together with S. Valgushev. Thus, these results can be attributed to myself and S. Valgushev. The underlying lattice simulation code was implemented solely by S. Valgushev. The production of the presented data was performed solely by myself. Further, useful discussions with R. D. Pisarski are acknowledged. A lot of the results stemming from mean-field and large-N_s approximation are reproduced from Ref. [219]. The presentation of the material has been rewritten and adapted to fit the context of this thesis.

ABSTRACT AND RELATION TO THE RESEARCH OBJECTIVES In this chapter, we investigate a scalar $\mathrm{O}(N_s)$ model incorporating higher-order, spatial kinetic terms to account for the possible existence of exotic phases, like an IP, a moat regime or a QπL, using LFT. Inhomogeneous condensates arise as solutions of the classical equations of motion of this model. We examine the impact of bosonic quantum fluctuations on inhomogeneous condensates through a fully-fledged LFT simulation using the Hybrid Monte Carlo (HMC) algorithm, as proposed in **RO3** (see Section 1.3). Furthermore, we review findings from the large-N_s limit where a mechanism for the disordering of IPs through the Goldstone mode fluctuations from $\mathrm{O}(N_s)$ symmetry breaking is proposed.

The main finding is that IPs are absent in the phase diagram for the investigated finite, spatial volumes independent of the chosen value of $N_s = 1, 2, 4, 8$. Instead, a QπL is observed for negative Z. The question posed in **RO4** about possible disordering mechanisms of IPs through bosonic quantum fluctuations is explored. In the LFT simulations, we systematically vary the number of scalar fields such that Goldstone modes from $\mathrm{O}(N_s)$ symmetry breaking are either present or absent. This demonstrates that IPs are not stable at finite spatial volumes independent of N_s. In line with **RO4**, an appropriate detection method of the breaking of translational invariance (and rotational invariance) in the thermodynamic limit is constructed and a proof-of-concept is presented.

OUTLINE In Section 7.1, the used model for spatially modulated phases is presented. Then, an extensive review of the findings in Ref. [219] for the mean-field approximation, amounting to classical field theory in the present case, and for the large-N_s limit is given. These findings build the foundation for the following LFT simulations for $N_s = 1, 2, 4, 8$. The setup of the HMC algorithm and investigated observables are discussed in Section 7.3. Then, the simulation results are presented in Section 7.4. More specifically, observables for fixed finite spatial volumes suggesting the disordering of the IP into a QπL at negative Z are discussed in Section 7.4.1, while preliminary findings for an extrapolation to the thermo-

dynamic limit are presented in the following subsections. A summary and contextualization of the results with the literature and **RO**s is provided in Section 7.5.

7.1 AN EFFECTIVE MODEL FOR EXOTIC REGIMES BASED ON MESONIC DEGREES OF FREEDOM

A scalar $O(N)$ model in $3+1$ Euclidean spacetime dimensions with spatial higher-derivative terms is considered at finite temperature $\beta = 1/T$,

$$\mathcal{S}[\vec{\phi}] = \int_0^\beta \mathrm{d}\tau \int \mathrm{d}^3x \left[\frac{1}{2}(\partial_0\vec{\phi})^2 + \frac{Z}{2}(\partial_j\vec{\phi})^2 + \frac{m^2}{2}\vec{\phi}^2 + \frac{\lambda N_s}{4}(\vec{\phi}^2)^2 \right], \tag{7.1}$$

where $\vec{\phi} = (\phi_1, \ldots, \phi_{N_s})$ is an N_s-component scalar field such that the theory has a global $\mathrm{O}(N_s)$ symmetry modeling chiral symmetry of QCD, which is isomorphic to $\mathrm{O}(4)$ for two flavors. The model is originally constructed in Ref. [219]. This action is considered an effective model emerging from an underlying theory (such as QCD or a four-fermion model) at non-vanishing μ and T, whose action is expanded in mesonic fields and their gradients. Such an expansion naturally arises also in the stability analysis in Section 4.1.2. There, the bosonic two-point vertex functions contains coefficients of up to all orders in spatial momenta but second-order in the amplitude of the meson fields, see, e.g., Ref. [342] for an explicit expansion of the thermodynamic potential. In Eq. (7.1), Z is the bare bosonic wave function renormalization[1], m^2 the bare mass, λ the quartic coupling of the scalar self-interaction term and M corresponds to a large mass scale. A negative Z implies the existence of the moat regime in the classical theory. This specific choice of a model can be motivated from the occurrence of the moat regime in four-fermion models [1, 9, 167] and in FRG investigations of QCD [121, 166].

At non-vanishing temperatures, the temporal momenta of bosonic fields are discretized as Matsubara frequencies $\omega_n = 2\pi T n$, $n = 0, \pm1, \pm2, \ldots$. In this case, the static Matsubara mode $\beta\omega_0 = 0$ is dominating the effective theory such that an effective 3-dimensional Lagrangian is given by[2]

$$L_{\text{eff}} = \frac{Z}{2}\left(\partial_j\vec{\phi}\right)^2 + \frac{1}{2M^2}\left(\sum_j \partial_j^2\vec{\phi}\right)^2 + \frac{m^2}{2}\vec{\phi}^2 + \frac{\lambda}{4}(\vec{\phi}^2)^2 \tag{7.2}$$

with the effective action $\mathcal{S}_{\text{eff}}[\vec{\phi}] = \beta\int \mathrm{d}^3x L_{\text{eff}}$ and partition function

$$Z = \int \mathscr{D}\vec{\phi}\, \mathrm{e}^{-\mathcal{S}_{\text{eff}}[\vec{\phi}]}. \tag{7.3}$$

This effective action can directly be obtained from Eq. (7.1) when restricting the bosonic fields to be time-independent. The bare parameters are varied in the following to explore the parameter space and the possible existence of exotic regimes within the model in different approximation and in LFT. Varying these parameters of the effective model should be though of as varying T and μ in the underlying theory.

Note that, in general, the used model is restrictive in the considered terms of higher energy dimension, for example one could consider a higher-order self-interaction $(\vec{\phi}^2)^3$ or

1 Its emergence from the bosonic two-point vertex functions of a four-fermion theory is presented in Section 4.1.

2 In this chapter, we use $\left(\partial_j\vec{\phi}\right)^2$ as a short-hand notation for $(\partial_j\vec{\phi})(\partial^j\vec{\phi})$ with summation over j.

other terms of mass dimension six that involve two spatial derivatives and four $\vec{\phi}$ operators, see Ref. [11] where all terms of mass dimension six involving higher spatial derivatives are listed.[3] However, as shown in Ref. [219], the terms considered in Eq. (7.6) are the relevant ones in the study of exotic regimes in the present context while the additional terms yield negligible contributions. See equations (1)-(3) in Ref. [219] for all further terms, and Chapters II and III of Ref. [219] for the discussion of the neglected terms.

SUPER-RENORMALIZABILITY AND ITS IMPLICATIONS The model (7.6) is super-renormalizable since each bare propagator contributes a factor of $\boldsymbol{p}^{-4}$ to the all perturbative calculations, rendering all Feynman diagrams finite. Therefore, commonly used power-counting arguments regarding renormalizability based on the dimension of coupling constants does not work, as seen explicitly in Section 7.2 where in tadpole diagrams are discussed. The super-renormalizability of the model implies that quantum corrections are finite, making effects from a finite UV regulator weaker than in renormalizable theories. As a first instructive study of this model, we fix M and λ, the couplings of the two terms with the highest order in mass dimension, and treat the model as an effective theory. Then, we vary Z and m^2 as the effective parameters of the theory in order to map out a phase diagram in this restricted parameter region. This is instructive because the Lagrangian (7.6) features a Mexican hat potential in both the field amplitude $\rho = \sqrt{\vec{\phi}^2}$ (corresponding to quartic and quadratic terms in $\vec{\phi}$) and the field momenta (corresponding to quartic and quadratic terms in the spatial derivatives). The physics of this potential is determined by the ratio of the quadratic and quartic coefficient and not by their respective amplitudes. Stability, obviously, requires $M > 0$ and $\lambda > 0$. Due to the super-renormalizablity of the theory and its function as a model for translational and chiral symmetry breaking, we start the investigation by considering the theory at a fixed energy scale (corresponding to fixed λ and M). This is further discussed in Section 7.4 and Section 7.5. A continuum limit or a removal of this limitation is not performed in this work.

7.2 DISCUSSION OF RESULTS FROM ANALYTICAL APPROXIMATIONS

The model (7.6) can be analyzed in the mean-field approximation, where bosonic quantum fluctuations are completely neglected (see Section 2.4). For a purely bosonic theory, the mean-field approximations amounts to reducing the QFT to the classical field theory. Note that the mean-field approximation is equivalent to the large-N_f limit of four-fermion models *but not* equivalent to the large-N_s limit of scalar O(N_s) models, see Section 2.5. The large-N_s limit for the scalar model contains (quantum) fluctuations of the scalar fields in a saddle-point approximation of the partition function (7.17) under the assumption that O(N_s)-invariant observables self-average in the partition function and have small fluctuations, see Ref. [302] for a review and Section 2.5. Note the findings discussed in this section stem from Ref. [219].

3 When coupling the moat regime to photons via imposing gauge invariance, as in Ref. [11], more caution is required.

7.2.1 *Mean-field approximation – Classical field theory*

Equation (7.6) consists only of scalar fields such that the mean-field approximation amounts to studying the classical field theory defined by the effective Lagrangian (7.6). The field equations from the Lagrange formalism read

$$\frac{1}{M^2}\left(-\sum_{j=1}^{3}\partial_j^2\right)^2\phi_k + Z\left(-\sum_{j=1}^{3}\partial_i^2\right)\phi_k + (m^2+\lambda\vec{\phi}^2)\phi_k = 0. \tag{7.4}$$

The solutions of these equations are found depending on the values of Z and m^2 for fixed values of M and λ.

In general, the mathematical structure of a Mexican hat potential arises both in spatial derivatives and in the field amplitude, i.e., one obtains vanishing or non-vanishing minima of the potential depending on the coefficient of the respective quadratic term.

POSITIVE Z For positive Z, the field $\phi^2(\mathbf{x}) = \phi_0^2$ is expected to be homogeneous in space since the potential is a monontonically increasing function of the momentum of the field. Thus, we distinguish between a phase with a non-zero expectation value of the field $\vec{\phi}$ for negative m^2 and a phase with $\vec{\phi} = 0$ for positive m^2. The latter corresponds to a SP where $\mathrm{O}(N_s)$ symmetry is restored. For negative m^2, one obtains a constant condensate given by $\phi_0 = \pm\sqrt{-m^2/\lambda}$ corresponding to the HBP. At $m^2 = 0$ there is a line of second-order phase transitions for any positive Z between the SP and the HBP.

NEGATIVE Z For negative Z, we expect that $\partial_j\phi \vec{\neq} 0$, i.e., a spatially inhomogeneous condensate is generated. Consequently, the theory features a Lifshitz point at $Z = 0$ and $m^2 = 0$ where three phases meet: the HBP with $\phi = \phi_0^2 \neq 0$ ($m^2 < 0, Z > 0$), the SP with $\phi = 0$ ($m^2 > 0, Z > 0$) and an IP ($Z < 0$). The form of Eq. (7.4) suggest that there is a single mode with momentum $k_0 \neq 0$ that minimizes the potential for the spatial derivatives. A simple ansatz for inhomogeneous condensates with a single Fourier mode is the chiral spiral

$$\vec{\phi} = \phi_0\left(\cos(k_0 z), \sin(k_0 z), \vec{\phi}_\perp = 0\right) \tag{7.5}$$

for $N_s \geq 2$. The parameters k_0 and ϕ_0 can be determined by solving Eq. (7.4) and minimizing the action (7.6). The $N_s - 2$ field components $\vec{\phi}_\perp$ are set to zero and, in the case of condensation, play the role of the Goldstone bosons of the theory. Note that the chiral spiral ansatz does not only break translational invariance spontaneously, but also rotational symmetry due to its dependence on only one of the three cartesian coordinates. The chiral spiral is only a specific ansatz and more general solutions can be given by sums of multiple or even infinitely different modes in the Fourier spectrum. In the present case, the chiral spiral is only used to construct an analytical solution as a starting point for the LFT simulations, making the analytical computations rather simple. Thus, the limitations of this ansatz can be seen as a further restriction of analytical computations, that are later overcome through using LFT.

PROPERTIES OF THE CHIRAL SPIRAL SOLUTION With the chiral spiral ansatz, the Lagrangian (7.5) equates to

$$L_{\text{eff}}(k_0, \phi_0) = \frac{Z}{2}k_0^2\,\phi_0^2 + \frac{1}{2M^2}k_0^4\,\phi_0^2 + \frac{m^2}{2}\,\phi_0^2 + \frac{\lambda}{4}\,\phi_0^4. \tag{7.6}$$

Minima with respect to k_0 are determined by differentiation with respect to k_0

$$\frac{\partial L_{\text{eff}}}{\partial k_0} = 0 \tag{7.7}$$

resulting in the solutions

$$k_0^2 = -Z\frac{M^2}{2} \qquad \text{or} \qquad k_0 = 0. \tag{7.8}$$

Since k_0^2 must be positive by definition, Z must be negative whenever a non-vanishing k_0^2 is obtained. Thus, an IP is observed in the mean-field approximation whenever $Z < 0$. For negative Z, a resubstitution of the non-trivial solution for k_0 yields

$$L_{\text{eff}}(k_0, \phi_0) = \frac{1}{2}\left(m^2 - \frac{Z^2M^2}{2}\right)\phi_0^2 + \frac{\lambda}{4}\phi_0^4. \tag{7.9}$$

When minimizing with respect to ϕ_0, one consequently obtains

$$\frac{\partial L_{\text{eff}}}{\partial \phi_0} = \left(m^2 - \frac{Z^2M^2}{2}\right)\phi_0 + \lambda N_s \phi_0^3 = 0, \tag{7.10}$$

i.e., the development of an inhomogeneous condensate at $Z < 0$ affects the scalar couplings involving contributions to the bare mass term. Thus, an IP is realized in form of a chiral spiral (7.5) if $2m^2 < Z^2M^2$ and $Z < 0$.

7.2.2 *Divergences in perturbation theory*

The inverse propagator for the static, transverse modes $\vec{\phi}_\perp$ is

$$\Delta^{-1}_{\vec{\phi}_\perp}(\mathbf{k}) = \frac{1}{M^2}(\mathbf{k}^2)^2 + Z\mathbf{k}^2 + m^2 + \lambda\phi_0^2 \tag{7.11}$$

which can be rewritten to

$$\Delta_{\vec{\phi}_\perp}(\mathbf{k}) = \frac{1}{M^2}(\mathbf{k}^2 - k_0^2)^2 + \frac{1}{\phi_0}\frac{\partial L_{\text{eff}}}{\partial \phi_0} = \frac{1}{M^2}(\mathbf{k}^2 - k_0^2)^2 \tag{7.12}$$

using Eq. (7.8) and Eq. (7.10). Thus, at $\mathbf{k}^2 = k_0^2$ the propagator vanishes. The traditional version of the Goldstone theorem would be that the mass squared vanishes for the *transverse modes at zero momentum*, i.e., the propagator at $\mathbf{k} = 0$ vanishes [44, 45]. Here, this vanishing is observed at the preferred momentum k_0 of the chiral spiral. Thus, $N_s - 2$ massless Goldstone modes of the broken $\mathrm{O}(N_s)$ symmetry group arise for $k = k_0$.

Perturbative contributions to the propagator of the transverse field components involve tadpole diagrams proportional to the bare propagator at the classical minimum

$$\int \mathrm{d}^3k \frac{1}{\frac{1}{M^2}(\mathbf{k}^2 - k_0^2) + \frac{1}{\phi_0}\frac{\partial L_{\text{eff}}}{\partial \phi_0}} \sim M^2 \int_{\mathbf{k}=k_0\hat{\boldsymbol{k}}+\delta\boldsymbol{k}} \frac{\mathrm{d}k}{(|\boldsymbol{k}| - k_0)^2} \tag{7.13}$$

where we use that the integral is dominated by the contributions of the integrand near $|\mathbf{k}| = k_0$, i.e., $|\delta\boldsymbol{k}|/k_0 < 1$. This diagram has an IR divergence at $|\mathbf{k}| = k_0$ such that the tadpole diagram diverges and the chiral spiral ansatz is destablized once quantum corrections are included using perturbation theory. However, in a perturbative analysis it is unclear whether this divergence is canceled by higher order diagrams or other non-perturbative effects that are missing. We revisit the fluctuations of transverse modes in the following discussion applying the large-N_s limit for non-perturbative access to the transverse propagator.

7.2.3 *Large-N_s analysis: General methodology*

In the analysis of the model (7.6), one has to distinguish between the case of homogeneous and inhomogeneous condensation in the methodology of the large-N_s limit. Therefore, we employ a constraint field approach for the dynamical variable $\vec{\phi}^2$, which is expected to have small fluctuations as $N_s \to \infty$, see Section 2.5 for a brief introduction. Keep in mind that we still restrict any possible IP to the chiral density wave ansatz (7.5).

HOMOGENEOUS CASE We treat both SP and HBP simultaneously by defining

$$\vec{\phi} = (\sigma, \vec{\chi}) \tag{7.14}$$

where we only allow condensation in σ, i.e., a spontaneously broken symmetry is obtained through $\langle\sigma\rangle \neq 0$. This is a common choice in semi-classical approximations, see, e.g., Refs. [93, 137]. With this restriction, we use the constraint field approach for $\vec{\phi}^2$ following Section 2.5. Auxiliary fields ω and ϵ are introduced in an $\mathrm{O}(N_s)$-invariant constraint for $\vec{\phi}^2$, where ω is the dynamical field enforced to have the value $\vec{\phi}^2$ and ϵ is introduced in the technical realization of this constraint, see Eq. (2.60).

The resulting action for introduction of the constraint fields reads

$$\mathcal{S}_{\text{constr}} = \int \mathrm{d}^3x \frac{\mathrm{i}\epsilon}{2}\left(\omega - \vec{\phi}^2\right). \tag{7.15}$$

By introducing this action in the partition function (7.17), each occurrence of $\vec{\phi}^2$ can be exchanged by ω due to the insertion of the identity (2.60). One obtains the effective action

$$\begin{aligned}\mathcal{S}_{\text{eff}}[\vec{\phi},\epsilon,\omega] = \int \mathrm{d}^3x \Bigg\{ &\frac{1}{2M^2}\left[\Big(\sum_j \partial_j^2\sigma\Big)^2 + \Big(\sum_j \partial_j^2\vec{\chi}\Big)^2\right] + \frac{Z}{2}\left[(\partial_j\sigma)^2 + (\partial_j\vec{\chi})^2\right] + \\ &+ \frac{m^2}{2}\omega + \frac{\lambda}{4}\omega^2 + \frac{\mathrm{i}\epsilon}{2}(\omega - \sigma^2 - \vec{\chi}^2)\Bigg\}\end{aligned} \tag{7.16}$$

and partition function

$$Z = \int \mathscr{D}\vec{\phi}\mathscr{D}\omega\mathscr{D}\epsilon\, \mathrm{e}^{-\mathcal{S}_{\text{eff}}[\vec{\phi},\epsilon,\omega]}, \tag{7.17}$$

where we use the substitution of ω such that $\vec{\chi}$ only appears in bilinears. An integral identity for operators appearing as $\vec{\chi}^T A\vec{\chi}$, see Eq. (2.63), can be applied to obtain the determinant of the corresponding operator A. The effective action then reads

$$\begin{aligned}\mathcal{S}_{\text{eff}}[\sigma,\epsilon,\omega] = \int \mathrm{d}^3x \Bigg\{ &\frac{1}{2M^2}\Big(\sum_j \partial_j^2\sigma\Big)^2 + \frac{Z}{2}(\partial_j\sigma)^2 + \frac{m^2}{2}\omega + \frac{\lambda}{4}\omega^2 - \frac{\mathrm{i}\epsilon}{2}(\omega - \sigma^2) + \\ &+ \frac{N_s - 1}{2}\ln\mathrm{Det}\left[\frac{1}{M^2}\Big(-\sum_j \partial_j^2\Big)^2 + Z\Big(-\sum_j \partial_j^2\Big) + \mathrm{i}\epsilon\right]\Bigg\}.\end{aligned} \tag{7.18}$$

Since $\sigma \sim \sqrt{\vec{\phi}^2} \sim \sqrt{N_s}$, $\omega \sim N_s$ and $\epsilon \sim 1$, all terms in $\mathcal{S}_{\text{eff}}$ are of order N_s (as long as λ is tuned to scale as $1/N_s$) and can be calculated in a large-N_s limit by a saddle point approximation, see the discussion in Section 2.4. The respective, global minimum with respect to σ, ϵ and ω dominates the path integral and needs to be determinant through

inserting the solutions of the gap equation, denoted by $(\sigma_0, \epsilon_0, \omega_0)$, in the effective action.[4] These saddle point conditions

$$\left.\frac{\partial \mathcal{S}_{\text{eff}}}{\partial(\sigma,\epsilon,\omega)}\right|_{(\sigma,\epsilon,\omega)=(\sigma_0,\epsilon_0,\omega_0)} = 0 \tag{7.19}$$

can be expressed as

$$\epsilon_0 \sigma_0 = 0, \tag{7.20}$$

and

$$\frac{\mathrm{i}}{2}\epsilon_0 + \left.\frac{\partial V}{\partial \omega}\right|_{\omega=\omega_0} = 0 \tag{7.21}$$

with $V(\omega) = \frac{m^2}{2}\omega + \frac{\lambda}{4N_s}\omega^2$ as well as

$$\omega_0 - \sigma_0^2 + (N_s - 1)\mathrm{Tr}\left(\frac{1}{\left(-\sum_j \partial_j^2\right)^2 / M^2 + Z\left(-\sum_j \partial_j^2\right) + \mathrm{i}\epsilon_0}\right) = 0. \tag{7.22}$$

From these equations, the common properties of spontaneous symmetry breaking can be deduced. For example, in the HBP one finds $\sigma_0 \neq 0$ and $\epsilon_0 = 0$, which ensures that the transverse modes are Goldstone bosons, i.e., have a vanishing pole mass, see Eq. (7.22). To determine the respectively observed phase, i.e., to distinguish an HBP with the global minimum $\Sigma \neq 0$ and SP with $\Sigma = 0$, one would need to reinsert the solutions into the effective action and compute its global minima. However, we follow a simpler approach for determination of the phase transition line below such that we refrain from doing this computation here.

INHOMOGENEOUS CASE With the chiral spiral ansatz (7.5), the two first components of $\vec{\phi}$ can be non-vanishing. Therefore, we decompose $\vec{\phi}$ into a two-component field $\vec{\sigma}$ and $N_s - 2$ component vector of the transverse modes $\vec{\chi}$,

$$\vec{\phi} = (\vec{\sigma}, \vec{\chi})\,. \tag{7.23}$$

This decomposition is related to the chiral spiral ansatz (7.5) where the first two-components of $\vec{\phi}$ can be non-vanishing. We use the constraint field approach for both $\vec{\chi}^2$ and $\left(\partial_j \vec{\phi}\right)^2$ in order to study the fluctuations of the transverse modes with respect to both magnitude and the derivatives.

Auxiliary fields ω and ϵ are introduced in an $\mathrm{O}(N_s)$-invariant constraint for $\vec{\chi}^2$, that holds for each point in space $\mathbf{x}_j$, using the identity

$$1 = \int \mathrm{d}\omega_j\, \delta(\vec{\chi}^2(\mathbf{x}_j) - \omega_j) = \frac{1}{4\pi}\int \mathrm{d}\omega \mathrm{d}\epsilon_j\, \mathrm{e}^{\mathrm{i}\epsilon_j(\vec{\chi}^2 - \omega_j)/2} \tag{7.24}$$

where $\omega_j = \omega(\mathbf{x}_j)$ and $\epsilon_j = \epsilon(\mathbf{x}_j)$, similar to Eq. (2.60). A similar constraint for $\left(\partial_j \vec{\phi}\right)^2$ using the auxiliary fields $\tilde{\omega}$ and $\tilde{\epsilon}$ is implemented.

The resulting action stemming from these constraints reads

$$\mathcal{S}_{\text{constr}} = \int \mathrm{d}^3x \left[\frac{\mathrm{i}\epsilon}{2}\left(\omega - \vec{\chi}^2\right) + \frac{\mathrm{i}\tilde{\epsilon}}{2}\left(\tilde{\omega} - (\nabla\chi)^2\right)\right] \tag{7.25}$$

4 Note that this notation is a bit sloppy as, in principle, one needs to label each solution with an index to properly distinguish each individual solution of the gap equation from each other. In this case, we refrained from complicating the notation with multiple indices and stayed with the notation from Ref. [219] where this analysis is performed originally.

and is introduced directly into the partition function (7.17), where every occurrence of $\vec{\chi}^2$ and $\left(\partial_j\vec{\phi}\right)^2$ can consequently be replaced by ω and $\tilde{\omega}$. Following the same strategy as above, one obtains

$$\begin{aligned}\mathcal{S}_{\text{eff}}[\vec{\phi},\epsilon,\omega,\tilde{\epsilon},\tilde{\omega}] = \int \mathrm{d}^3x \Bigg\{ &\frac{1}{2M^2}\left(\sum_j \partial_j^2\vec{\sigma}\right)^2 + \frac{Z}{2}(\partial_j\vec{\sigma})^2 + \frac{m^2}{2}\vec{\sigma}^2 + \frac{\lambda}{2}\omega\vec{\sigma}^2 + \frac{\lambda}{2}\left(\vec{\sigma}^2\right)^2 + \\ &- \frac{\mathrm{i}}{2}(\epsilon\omega + \tilde{\epsilon}\tilde{\omega}) + \frac{Z}{2}\tilde{\omega} + \frac{m^2}{2}\omega + \frac{\lambda}{4}\omega^2 + \\ &+ \frac{(N_s-2)}{2}\ln\mathrm{Det}\left[\frac{1}{M^2}\Big(-\sum_j\partial_j^2\Big)^2 - \mathrm{i}\partial_j\left(-\tilde{\epsilon}\partial_j\right) + \mathrm{i}\epsilon\right]\Bigg\}.\end{aligned} \tag{7.26}$$

Thereby, we consider ω, $\tilde{\omega}$ as well as ϵ and $\tilde{\epsilon}$ as being homogeneous. This restriction is sensible due to the simplicity of the chiral spiral ansatz (7.5) where the gradient squared of $\vec{\phi}$ is homogeneous. Again, the expectation values are denoted by ω_0, ϵ_0, and so on. For ω, one obtains

$$2\frac{\partial\mathcal{S}_{\text{eff}}}{\partial\omega}\bigg|_{(\vec{\sigma},\epsilon,\omega,\tilde{\epsilon},\tilde{\omega})=(\vec{\sigma}_0,\epsilon_0,\omega_0,\tilde{\epsilon}_0,\tilde{\omega}_0)} = -\mathrm{i}\epsilon_0 + m^2 + \lambda(\omega_0+\vec{\sigma}_0^2) = 0 \tag{7.27}$$

where we define the effective mass

$$m_{\text{eff}}^2 = \mathrm{i}\epsilon_0 = m^2 + \lambda(\omega_0+\vec{\sigma}_0^2) \tag{7.28}$$

in analogy to the discussion in the homogeneous case. For $\tilde{\omega}$, in turn, one obtains

$$2\frac{\partial\mathcal{S}_{\text{eff}}}{\partial\tilde{\omega}}\bigg|_{(\vec{\sigma},\epsilon,\omega,\tilde{\epsilon},\tilde{\omega})=(\vec{\sigma}_0,\epsilon_0,\omega_0,\tilde{\epsilon}_0,\tilde{\omega}_0)} = -\mathrm{i}\tilde{\epsilon}_0 + Z = 0 \tag{7.29}$$

fixing $\mathrm{i}\tilde{\epsilon}_0 = Z$. Thus, while ϵ_0 acts as the effective mass for $\vec{\chi}^2$, $\tilde{\epsilon}_0$ describes the quadratic coefficient of $\left(\partial_j\vec{\phi}\right)^2$. This is confirmed by

$$\frac{\partial\mathcal{S}_{\text{eff}}}{\partial\vec{\sigma}}\bigg|_{(\vec{\sigma},\epsilon,\omega,\tilde{\epsilon},\tilde{\omega})=(\vec{\sigma}_0,\epsilon_0,\omega_0,\tilde{\epsilon}_0,\tilde{\omega}_0)} = \left[\frac{1}{M^2}\Big(-\sum_j\partial_j^2\Big)^2 + Z\Big(-\sum_j\partial_j\Big)^2 + m_{\text{eff}}^2\right]\vec{\sigma}_0 = 0 \tag{7.30}$$

where we reinserted the above findings. From the gap equation for ϵ, one finds

$$-\omega_0 + (N_s-2)\mathrm{Tr}\left[\frac{1}{\frac{1}{M^2}(-\sum_j\partial_j^2)^2 + Z(-\sum_j\partial_j)^2 + m_{\text{eff}}^2}\right] = 0. \tag{7.31}$$

and, from the one of $\tilde{\epsilon}$,

$$-\tilde{\omega}_0 + (N_s-2)\mathrm{Tr}\left[\frac{(-\sum_j\partial_j)^2}{\frac{1}{M^2}(-\sum_j\partial_j^2)^2 + Z(-\sum_j\partial_j)^2 + m_{\text{eff}}^2}\right] = 0. \tag{7.32}$$

The functional traces can be performed by inserting Fourier representations similar to the procedure in Section 4.1.2. Then one can identify the inverse propagator of the static, transverse modes

$$\Delta_\chi^{-1}(\boldsymbol{k}) = \frac{1}{M^2}(\boldsymbol{k}^2)^2 + Z\boldsymbol{k}^2 + m_{\text{eff}}^2 \tag{7.33}$$

in the above equations. One obtains

$$-\omega_0 + (N_s - 2) \int \frac{\mathrm{d}^3 k}{(2\pi)^3} \Delta_\chi^{-1}(\boldsymbol{k}) = 0 \tag{7.34}$$

for ϵ and

$$-\tilde{\omega}_0 + (N_s - 2) \int \frac{\mathrm{d}^3 k}{(2\pi)^3} \boldsymbol{k}^2 \Delta_\chi^{-1}(\boldsymbol{k}) = 0 \tag{7.35}$$

for $\tilde{\epsilon}$. Recall that the theory is formulated as an effective one for the static fields at non-zero temperature such that integrals only involve the spatial momenta. For the chiral spiral ansatz (7.5), one obtains from Eq. (7.30) either

$$\frac{1}{M^2} k_0^4 + Z k_0^2 + m_{\mathrm{eff}}^2 = 0. \tag{7.36}$$

Thus, one obtains two solutions for a non-vanishing k_0^2 or the trivial solution $\phi_0 = 0$ corresponding to an SP with $\vec{\sigma}_0 = 0$. Equation (7.36), however, is of the same structure as the inverse propagator $\Delta_\chi(\boldsymbol{k})$ of the transverse modes. Consequently, it vanishes at $\boldsymbol{k} = k_0 \hat{\boldsymbol{k}}$, see also the discussion in the perturbative analysis at the end of Section 7.2.1.

For the ground state solution, the inverse propagators should be positive to avoid instabilities, cf. Section 4.1. Since Eq. (7.33) is positive for large $\boldsymbol{k}^2$ and at $\boldsymbol{k} = 0$ if $m_{\mathrm{eff}}^2 > 0$, the case of the saddle point solution (7.36) having two non-vanishing roots k_0^+ and k_0^- implies negativity of the inverse propagator in the interval $k_0^- < k < k_0^+$. Thus, Eq. (7.36) can be satisfied in a stable theory only if there is a double zero of the inverse propagator at $k_0 = k_0^- = k_0^+$, which also implies that the propagator is minimal at $k = k_0$. At this point, note that this degenerate double pole of the propagator is enforced simply by the saddle point equation and the requirement of a stable ground state (otherwise the theory would be unbounded from below). The same double pole arises in the brief discussion of perturbation theory of the same model, see the last paragraph of Section 7.2.1. This leads to a destabilization of the chiral spiral, that is expected from the mean-field approximation for negative Z.

This large-N_s analysis should hold for any effective theory obtained for light mesons, e.g., from some approximation to QCD or other fermionic models, that features an IP dominated by a single mode. Further, we suspect that similar properties do also hold for multi-mode solutions, although this remains unclear unless a more profound analytical approach is developed to investigate these. In the following analysis of the whole (m^2, Z) parameter region of the model (7.6) in the large-N_s limit we show how a self-consistent solution for the groundstate is obtained in a disorder phase, the QπL.

7.2.4 *Explicit solution in the (m^2, Z) plane*

We briefly discuss the explicit solution of the phase diagram for $\lambda N_s = 1$ and $M = 1$. These parameters of the highest order terms are fixed, i.e., they are treated as the largest energy scales in the system. Therefore, we perform a slight variation of the constraint field approach discussed previously. We introduce the constraint field ω as

$$1 = \int \mathrm{d}\omega_j \delta(\vec{\phi}^2 - \omega_j) = \frac{1}{4\pi} \int \mathrm{d}\omega_j \mathrm{d}\epsilon_j \, \mathrm{e}^{\mathrm{i}\epsilon_j (\omega_j - \vec{\phi}^2(\mathbf{x}_j))/2} \tag{7.37}$$

with $\omega_j = \omega(\boldsymbol{x}_j)$ and $\epsilon_j = \epsilon(\boldsymbol{x}_j)$ for each point in space $\boldsymbol{x}_j$ but integrate over all N_s components of $\vec{\phi}$ (instead of only $N_s - 1$ transverse modes as above), as discussed in Section 2.5.

Here, we only briefly summarize the procedure. In this case, the effective action only contains $\epsilon(\boldsymbol{x})$ and up to quadratic powers in ω, similar to Eq. (2.64). In the mass-squared term, we do not replace ϕ^2. Subsequently, we integrate over $\vec{\phi}$ which only occurs in quadratic terms. Then, also ω can be integrated over in the partition function since it occurs as a Gaussian integral similar to Eq. (2.63), but with a shift given by the term $\sim \epsilon\omega$. After using the identities for Gaussian integrals with respect to both $\vec{\phi}$ and ω, one obtains an effective action only in terms of the auxiliary field ϵ

$$\mathcal{S}_{\text{eff}}[\epsilon] = \int \mathrm{d}^3x \left[\frac{\epsilon^2}{4\lambda} + \frac{N_s}{2} \ln \mathrm{Det} \left(\frac{1}{M^2} \left(-\sum_j \partial_j^2 \right)^2 + Z \left(-\sum_j \partial_j^2 \right) + m^2 + \mathrm{i}\epsilon \right) \right]. \tag{7.38}$$

This formalism does not yield access to the expectation value of $\vec{\phi}^2$, since ω is integrated out, but to the effective mass squared m_{eff}^2. This is sufficient to determine the transition line between the homogeneous phases when it is of second-order. A homogeneous, first-order transition is not classically not possible from the ansatz for the potential that contains only up to fourth orders of $\vec{\phi}$ (terms of at least sixth order would be needed). From the above analysis, it can also not occur in the large-N_s limit.

Using the saddle point approximation, i.e., the limit of $N_s \to \infty$, we obtain through the gap equation, see the previous subsection,

$$\epsilon_0 - \mathrm{i}\frac{\lambda N_s}{2} \mathrm{Tr} \left[\frac{1}{\frac{1}{M^2}\left(-\sum_j \partial_j^2 \right)^2 + Z\left(-\sum_j \partial_j^2 \right) + m_{\text{eff}}^2} \right] = 0 \tag{7.39}$$

identifying the effective mass squared

$$m_{\text{eff}}^2 = m^2 + \epsilon_0 \tag{7.40}$$

for the extrema $\epsilon = \epsilon_0$ of the effective action. Simple solutions with homogeneous ϵ_0 involve either homogeneous phases or a chiral spiral with a single mode (7.5). Then, the transverse propagator Δ is similar to Eq. (7.33) and one needs to evaluate

$$\begin{aligned} \mathrm{Tr}\Delta = \int \frac{\mathrm{d}^3k}{(2\pi)^3} \Delta(\mathbf{k}) &= \frac{M^2}{4\pi^2} \int \mathrm{d}k \frac{k^2}{(k^2+m_+^2)(k^2+m_-^2)} \\ &= \frac{M^2}{4\pi^2} \frac{1}{m_+^2 - m_-^2} \int \mathrm{d}k \left(\frac{m_+^2}{k^2+m_+^2} - \frac{m_-^2}{k^2+m_-^2} \right) \end{aligned} \tag{7.41}$$

where $k = |\boldsymbol{k}|$ and the poles $\mathrm{i}m_\pm^2$ can be expressed in terms of m_{eff}^2 and the parameters of the theory,

$$m_\pm^2 = \frac{ZM^2}{2}(1 \pm \sqrt{1-\alpha^2}), \qquad \alpha = \frac{2m_{\text{eff}}}{|Z|M}. \tag{7.42}$$

One needs to take care about the position of these poles in the complex plane when evaluating the trace.

If $\alpha \leq 1$, $m_\pm^2$ is real and positive and one finds

$$\mathrm{Tr}\Delta = \frac{M^2}{4\pi} \frac{1}{m_+ + m_-}. \tag{7.43}$$

By solving $(k^2+m_+^2)(k^2+m_-^2) = (k^2)^2 + ZM^2k^2 + m_{\text{eff}}^2M^2 = 0$ one obtains

$$(m_+ + m_-)^2 = 2m_{\text{eff}}M + ZM^2 \tag{7.44}$$

independent of the sign of Z. Eq. (7.39) becomes

$$m_{\text{eff}}^2 - m^2 = \lambda_0 \frac{M^{3/2}}{\sqrt{2m_{\text{eff}} + ZM}} \tag{7.45}$$

with the rescaled quartic coupling $\lambda_0 = \lambda N_s/8\pi$. This equation can be solved for m_{eff}^2 in the (m^2, Z) plane when fixing λ_0 and M. When $m_{\text{eff}}^2 = 0$, a second-order phase transition between the SP (where $m_{\text{eff}}^2 > 0$) and the HBP (where $m_{\text{eff}}^2 < 0$) is obtained. Since we consider no self-interaction terms of higher order than the quartic ones, a first-order phase transition cannot be expected, unless these terms are generated from quantum fluctuations. From the analysis above, this is not the case in the large-N_s limit.

It is interesting to study the line with $m^2 = 0$. In the mean-field analysis in Section 7.2.1, one obtains a line of second-order phase transitions at $Z > 0$, a LP at $Z = 0$ and an IP at $Z < 0$. Neither of this is the case in the large-N_s limit. Instead, m_{eff} stay positive for any value of Z and $m^2 = 0$ in the large-N_s limit The second-order phase transition happens only for negative m^2 and positive Z at the value

$$m_{\text{c}}^2 = -\frac{\lambda_0 M}{\sqrt{Z}} \tag{7.46}$$

obtained by setting $m_{\text{eff}}^2 = 0$ in Eq. (7.45). As discussed above, in the broken phase we have to employ the constraint field method following Section 7.2.3 to compute the value of ϕ_0 and show that the transverse modes indeed are Goldstone modes, but this is not of interest here.

OBSERVATION OF QUANTUM PION LIQUID At $m^2 = 0$ one obtains a value of Z where m_+^2 and m_-^2 become degenerate. This is the case when $\alpha = 1$, which for $m^2 = 0$ occurs at $Z = (2^{3/2}\frac{\lambda_0}{M})^{2/5}$. Similarly, one can find $\alpha = 1$ for any $m^2 \in \mathbb{R}$ and a positive value of Z. The point of $\alpha = 1$ marks the degeneracy of m_+^2 and m_-^2, which we will later recover as the onset of the QπL, where spatial correlation functions of the ϕ_j fields are oscillatory on top of the exponential falloff. Thus, the line of $\alpha = 1$ as a function of Z and m^2 corresponds to the disorder line.

To discuss properties of correlation functions, we study first the SP with $m^2 > 0$ although one, in general, can also treat negative bare masses by recognizing the above discussed transition to the HBP. At large, positive Z, one finds $\alpha < 1$, c.f. Eq. (7.42). The propagator poles are $k = \pm \mathrm{i} m_+$ and $k = \pm \mathrm{i} m_-$. Consequently, a Fourier-transformation of Eq. (7.33) yields a sum of two-exponential as the long-range behavior, i.e.,

$$\langle \phi_i(\boldsymbol{x}) \phi_j(\boldsymbol{y}) \rangle \Big|_{|\boldsymbol{x}-\boldsymbol{y}|\to\infty} = \delta_{i,j} \left[c_- \mathrm{e}^{-m_-|\boldsymbol{x}-\boldsymbol{y}|} + c_+ \mathrm{e}^{-m_+|\boldsymbol{x}-\boldsymbol{y}|} \right]. \tag{7.47}$$

At large Z, one obtains separation of the masses, m_+^2 becomes large while m_-^2 becomes small, compare Eq. (7.42). Physically, this corresponds to one light and one heavy excitation of the scalar field ϕ_i. When decreasing Z both poles remain on the imaginary axis and the values of m_+ and m_- are getting closer to each other, since α increases. At the point $Z_{\alpha=1}(m^2)$, the masses merge, $m_+ = m_- = \sqrt{m_{\text{eff}} M} \equiv m_0$. Then, the poles are located at $k = \pm \mathrm{i} m_0$ and the spectrum of the two excitations becomes degenerate.

Below this point, m_+^2 and m_-^2 develop real and imaginary parts such that the poles of the propagator are

$$k = m_0 \exp\left[\pm \mathrm{i} \left(\frac{\pi}{2} \pm \frac{\theta}{2} \right) \right], \qquad \tan\theta = \sqrt{\alpha^2 - 1} \tag{7.48}$$

with $\alpha > 1$, as described above. These are four distinguished poles, but, however, two of the respective poles only differ by a global sign. The complex-conjugate pairs of the poles can be identified through the sign flip in front of the exponential. Propagator poles become degenerate and, subsequently, develop non-vanishing real and imaginary parts, as also observed in so-called $\mathcal{PT}$-broken regions of scalar theories [180], see Section 3.1.2, and in the four-fermion model with scalar and vector mesons studied in Chapter 6, where the bosonic two-point vertex functions appear in complex-conjugate pairs. In both of these cases, QπLs arise.

In the present case, one specifically obtains

$$\langle \phi_i(\boldsymbol{x})\phi_j(\boldsymbol{y})\rangle\Big|_{|\boldsymbol{x}-\boldsymbol{y}|\to\infty} = \delta_{i,j}\mathrm{e}^{-m_r|\boldsymbol{x}-\boldsymbol{y}|}\left[c_1\cos(m_i x) + c_2\sin(m_i x)\right] \tag{7.49}$$

for $\alpha \geq 1$, where

$$m_r = m_0\cos\left(\frac{\theta}{2}\right), \qquad m_i = m_0\sin\left(\frac{\theta}{2}\right) \tag{7.50}$$

for $Z > 0$, while

$$m_r = m_0\sin\left(\frac{\theta}{2}\right), \qquad m_i = m_0\cos\left(\frac{\theta}{2}\right) \tag{7.51}$$

for $Z < 0$. The two-point correlation functions are always real-valued, as ensured by the properties of the poles discussed above.

The case of $Z \to 0$ is special, since α diverges and $\theta \to \pi/2$. Then, $m_r = m_i = m_0/\sqrt{2}$, which is consistent with Eq. (7.51) and Eq. (7.50). The effective mass remains non-zero at $Z = 0$ at any $m^2 = 0$ and neither a LP nor a second-order transition is observed. One obtains a symmetric regime with $\phi^2 = 0$ in contrast to the mean-field findings, see Section 7.2.1. Considering $Z \to -\infty$, one finds $m_0 \sim |Z|^{1/2}M$ and $\theta \sim \lambda_0/(M|Z|^{5/2})$ such that $m_r \sim Z^{-2}$ and $m_i \sim \sqrt{Z}$, i.e., the exponential suppression gets weaker while the frequency of the oscillations increases.

SUMMARY AND "PHASE DIAGRAM" The findings of the large-N_s analysis in this chapter and Ref. [219] are summarized in Fig. 7.1. The second-order phase transition between the HBP and SP is obtained by numerical solution of Eq. (7.45) for effective mass $m_{\text{eff}}^2 = 0$. Analyzing the poles of the bosonic two-point correlation functions (7.42), one finds that the poles on the imaginary axis become degenerate at the so-called disorder-line (dashed blue line in Fig. 7.1). Beyond this line, one obtains complex-conjugate propagator poles with non-vanishing real and imaginary parts. As a consequence, one obtains a QπL where correlations functions are oscillatory in space while falling off exponentially, see Eq. (7.49).

The results for the phase diagram suggest that the quantum fluctuations of transverse modes, which can be incorporated in the large-N_s method, disorder the inhomogeneous condensate that is obtained for negative Z within the mean-field approximation, which is equivalent to classical field theory in the case of scalar field theory. In Ref. [219], it is argued that this disordering remains the dominant mechanism for $N_s > 2$, where Goldstone bosons from $\mathrm{O}(N_s)$ (chiral) symmetry breaking are present. This argumentation leads to the conclusion that an IP might be favored for $N_s = 1$ and $N_s = 2$, where for a chiral spiral ansatz no Goldstone modes are present. With respect to **RO4**, see Section 1.3, this is a considered disordering mechanism in the context of bosonic quantum effects in general. As

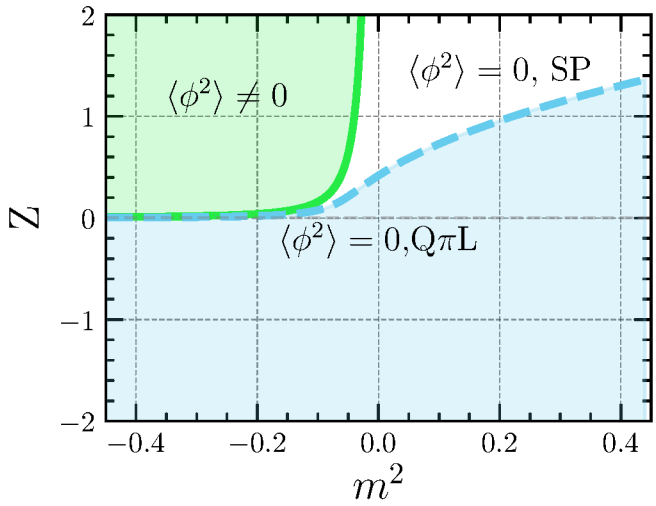

Figure 7.1: Phase diagram of the effective model (7.6) with the chiral spiral ansatz (7.5) in the (m^2, Z) plane, originally obtained in Ref. [219]. The solid green line describes the second-order phase transition between the HBP and the SP. The dashed blue line describes the disorder line where the two poles of the spatial propagator become degenerate. Beyond the disorder line, one obtains the QπL regime with spatially oscillating correlations functions (7.49).

proposed in **RO3**, this question is answered using LFT simulations with the setup presented in the following section. LFT allows to study the impact of quantum fluctuations in full simulations of the effective theory (7.6) for different values of the bare parameters and possibly detecting an IP as well as a QπL according to the findings above.

7.3 LATTICE SETUP, MONTE-CARLO ALGORITHM AND OBSERVABLES

In order to study the partition function

$$Z = \int \mathscr{D}\vec{\phi}\, \mathrm{e}^{-\mathcal{S}_{\mathrm{eff}}[\vec{\phi}]} \tag{7.52}$$

with the effective Lagrangian given by Eq. (7.6), we discretize the theory on a finite spatial lattice $\Lambda_{a,L}$ with lattice spacing a and periodic boundary conditions $\vec{\phi}(\boldsymbol{x}) = \vec{\phi}(\boldsymbol{x} + (La)e_j)$ for $j = 1, 2, 3$, where $e_j = a\hat{e}_j$ using the cartesian unit vector $\hat{e}_j$ in the j-th direction. Thereby, we use an isotropic lattice with L^3 lattice points $\boldsymbol{x_n} = \boldsymbol{n}a$ in our numerical computation, where $\boldsymbol{n} = (n_1, n_2, n_3)^T$ and $n_j \in 0, \ldots, L-1$. This causes the integration measure to be discretized,

$$\mathscr{D}\vec{\phi} \to \prod_{\boldsymbol{n}} \prod_{j=1}^{N_s} \mathrm{d}\phi_{j,\boldsymbol{n}} \tag{7.53}$$

with $\phi_{j,\boldsymbol{n}} = \phi_j(\boldsymbol{x_n})$. A suitable Lagrangian for numerical calculations on the lattice can be obtained by partially integrating the kinetic term proportional to Z in Eq. (7.6) such that the term reads $-Z\vec{\phi}\sum_j \partial_j^2\vec{\phi}$.

In order to write down a Lagrangian suitable for numerical calculations we discretize the second derivatives by the replacement

$$\partial_j^2 \to \sum_{\boldsymbol{m}} [\Delta_j]_{\boldsymbol{x}_n,\boldsymbol{y}_m} = \tag{7.54}$$

$$= \sum_{\boldsymbol{m}} \frac{1}{12a^2} \left(-\delta_{\boldsymbol{y}_m,\boldsymbol{x}_n+2e_j} + 16\delta_{\boldsymbol{y}_m,\boldsymbol{x}_n+e_j} - 30\delta_{\boldsymbol{y}_m,\boldsymbol{x}_n} + 16\delta_{\boldsymbol{y}_m,\boldsymbol{x}_n-e_j} - \delta_{\boldsymbol{y}_m,\boldsymbol{x}_n-2e_j} \right). \tag{7.55}$$

Moreover, the spatial integration in the effective action is replaced by a sum over the lattice points $\mathbf{x}_{\boldsymbol{n}}$. The resulting, lattice discretized action is

$$\mathcal{S}_{\text{eff}}[\vec{\phi}, a, L] = \sum_{\boldsymbol{n}} a^3 \Bigg[-\frac{Z}{2}\vec{\phi}(\boldsymbol{x_n}) \sum_j \sum_{\boldsymbol{m}} [\Delta_j]_{\boldsymbol{x}_n,\boldsymbol{y}_m} \vec{\phi}(\boldsymbol{y_m}) + \frac{1}{2M^2} \left(\sum_j \sum_{\boldsymbol{m}} [\Delta_j]_{\boldsymbol{x}_n,\boldsymbol{y}_m} \vec{\phi}(\boldsymbol{y_m}) \right)^2 + \tag{7.56}$$

$$+ \frac{m^2}{2}\vec{\phi}^2(\boldsymbol{x_n}) + \frac{\lambda}{4}\left(\vec{\phi}^2(\boldsymbol{x_n})\right)^2 \Bigg]$$

and the partition function

$$Z_{a,L} = \int \prod_{\boldsymbol{n}} \prod_{j=1}^{N_s} \mathrm{d}\phi_{j,\boldsymbol{n}}\, \mathrm{e}^{-\mathcal{S}_{\text{eff}}[\vec{\phi},a,L]}, \tag{7.57}$$

which can be studied with statistical simulation methods. Throughout the computation, we expressed all dimensinful quantities in units of the lattice spacing, i.e., a is never specifically determined. In a continuum extrapolation, obviously, one would need to physically fix the value of the lattice spacing by imposing, e.g., a fixed value of the chiral condensate $\sqrt{\vec{\phi}^2}$ for a certain parameter set. In this exploratory, qualitative investigation of quantum fluctuation effects on IPs and moat regimes, we focus on choosing specific bare parameters at one fixed lattice spacing a. In this setup, the dependence on the spatial volume is explored by varying the value of L while keeping other parameters of the action fixed.

7.3.1 *Monte-Carlo algorithm*

Monte Carlo methods are algorithms based on the sampling of random numbers to obtain numerical results. A typical application is the computation of (high-dimensional) integrals. Therefore, one draws N samples of random numbers within the integration domain and evaluates the integrand at these samples. In the limit of $N \to \infty$, the value of the integral is given by the average of the integrand over samples. For finite N, an approximate value for the integral is obtained, contaminated with a statistical error of $N^{-1/2}$ given that the integration domain is appropriately sampled. Monte Carlo integration is one of the most efficient methods for the computation of high-dimensional integrals. In LFT simulations, one typically uses importance sampling in Monte-Carlo integration algorithms, where the random numbers are not drawn uniformly but according to the probability distribution density given by the weight $\exp(-\mathcal{S})$, where $\mathcal{S}$ is the lattice-discretized action of the respective theory, such as, e.g., Eq. (7.56). This can be realized by an appropriate change of variables in the original integral. This strategy prevents the problem of underestimation of the integral that is caused by the integrand being approximately 0 within large regions

of the high-dimensional integration domain. In the integration procedure, the action of the theory of interest must be real-valued and positive such that the integral can be interpreted as a probability distribution. This requirement makes the simulation of QCD at $\mu \neq 0$ using LFT Monte-Carlo simulations impossible with the standard techniques, see, e.g., Ref. [117]. Equation (7.56) is real-valued and positive such that Monte-Carlo techniques are directly applicable. In this part of the chapter, we briefly present the HMC algorithm used for our specific case. This is a standard method in LFT and many details are omitted. For an introduction to Monte Carlo simulations in LFT context we refer to the textbooks [59, 284].

HYBRID MONTE-CARLO ALGORITHM The specialty of the HMC algorithm is the Molecular dynamics update step, which are is based on the numerical solutions of the field equations from the Hamilton formalism. This is typically more efficient than local algorithms due to the global update step changing the whole field configuration.[5] Therefore, one introduces the conjugate momenta $\vec{\pi}$ to the bosonic fields ϕ to the partition function, which integrates over the lattice-discretized fields $\vec{\phi}$ and $\vec{\pi}$. The probability weight for the integration is given by the exponential of the Hamiltonian

$$H[\vec{\phi}, \vec{\pi}, a, L] = \frac{1}{2} \sum_{\boldsymbol{n}} \pi^2(\boldsymbol{x_n}) + \mathcal{S}_{\text{eff}}[\vec{\phi}, a, L]. \tag{7.58}$$

One derives Hamiltonian field equations

$$\dot{\pi}_j(\boldsymbol{x_n}) = -\frac{\partial H}{\partial \phi_j(\boldsymbol{x_n})}, \qquad \dot{\phi}_j(\boldsymbol{x_n}) = \frac{\partial H}{\partial \pi_j(\boldsymbol{x_n})} = \pi(\boldsymbol{x_n}) \tag{7.59}$$

where the time derivatives, represented by the dot, are taken with respect to the artificially introduced Molecular dynamics time t. The following global update algorithm is based on the so-called ergodic hypothesis, which says that time averages of a statistical system are equal to statistical ensemble averages. Given an initial configuration of the field values $\vec{\phi}(\boldsymbol{x_n})$, one proceeds by

1. Generating new conjugate momenta $\vec{\pi}_j$: For each step the conjugate momenta are drawn according to a Gaussian distribution $\sim \exp(-\vec{\pi}^2/2)$.

2. Proposal step: Numerical integration step of the field $\vec{\phi}$ and $\vec{\pi}$ via Eq. (7.59) for a Molecular dynamics step of size dt: The numerical integration of Eq. (7.59) gives a proposal for the next field configurations $\vec{\phi}'$ and $\vec{\pi}'$. We use an Omelyan integrator algorithm, see Ref. [374] for their construction. Obviously, the numerical integration introduces an error to the computation, which is, however, compensated by the following acceptance step.

3. Acceptance step: The proposed configurations $\vec{\phi}'$ and $\vec{\pi}'$ are accepted with the probability

$$P(\vec{\phi} \to \vec{\phi}', \vec{\pi} \to \vec{\pi}') = \min\left[1, \exp\left(H[\vec{\phi}, \vec{\pi}, a, L] - H[\vec{\phi}', \vec{\pi}', a, L]\right)\right]. \tag{7.60}$$

   This transition is numerically implemented by drawing another random number lying between 0 and 1 and comparing to the value of P in the following way: If $P = 1$, the

5 A typical introduction to Monte-Carlo methods discusses the Metropolis update step, where one step updates the value of only one of the integration variables (the value of a field on a specific lattice point $\boldsymbol{x_n}$). This is considered a local update step.

proposal is immediately accepted. If not, one compares the value of P to the random number r that is drawn. Given $r < P$, the proposal is also accepted. If the proposal is rejected, the initial configuration for the field values $\vec{\phi}(\boldsymbol{x_n})$ are taken as the new configuration and one continues the generation of samples with step 1.

The combination of these algorithms meets the required condition of detailed balance [284], which ensures the normalization of all transition probabilities between the configurations. Details on the required properties of Monte-Carlo methods can be found in Refs. [59, 284].

An explicit dependence of the results on the numerical parameters of this setup such as, e.g., the discretization of the integration algorithm in step 2 was explored. Thereby, the acceptance rate of the HMC algorithm is tuned such that an average acceptance rate of roughly $80 - 90\%$ of proposed configurations is achieved. This choice leads to a fast enough thermalization process while guaranteeing that the whole configuration space can, in principle, be sampled. The tuning procedure needs to be repeated whenever the lattice setup changes and is specifically sensitive to the lattice volume L^3 and N_s.

Initial field configurations are produced either using the random number generator *ranlux* [375] or setting $\vec{\phi} = 0$. With this starting configuration, 200 initial Metropolis sweeps for thermalization are performed. Further, the first 200 update steps of the HMC algorithm are also identified as part of the thermalization and, consequently, not used in the computation of observables.

7.3.2 *Observables*

From the analytical investigation in Section 7.2, one expects different exotic phases to emerge within the (m^2, Z) parameter space of the theory, such as an IP or the QπL. Moreover, a liquid crystal-like scenario might also arise where correlation functions have quasi-long range order, see Section 3.3 for a motivation of this expectation. But also typical homogeneous phases are expected. The IP as well as the QπL are characterized by a particular behavior of bosonic correlations functions. Also, direct access of $\langle\vec{\phi}(x)\rangle$ or $\langle|\vec{\phi}|(x)\rangle$ is not suitable for detecting IPs due to destructive interference [226]. Thus, a straightforward choice for an observable, which allows to search for these different phenomena, are the spatial correlation functions between the bosonic fields $\vec{\phi}$

$$C^{ij}(\boldsymbol{x_n}) = \langle c^{ij}(\boldsymbol{x_n})\rangle = \tfrac{1}{L^3}\sum_{\boldsymbol{m}}\langle\phi_i(\boldsymbol{y_m}+\boldsymbol{x_n})\phi_j(\boldsymbol{y_m})\rangle\,, \tag{7.61}$$

where the sum over lattice point $\boldsymbol{y_m}$ is used to get more statistics. The brackets $\langle.\rangle$ denote the statistical averaging of the observable over all used field configurations, produced in the HMC algorithm. In order to characterize the different regimes, we use fits of C^{jj} for the respective regimes. Thereby, we focus first on one-dimensional slices of the correlator defined in Eq. (7.61), i.e., we choose $\boldsymbol{n}$ as a unit vector in one of the three spatial dimensions. The fit functions used are:

- Decaying oscillations $C^{ij}(x) \sim \delta_{ij}e^{-m_r x}\cos(kx)$ for the QπL, SP (using $k \approx 0$) and the IP (using $m_r \approx 0$).
- Algebraically decaying oscillations $C^{ij}(x) \sim \delta_{ij}\frac{\cos(kx)}{x^\alpha}$ for possible quasi-long range order, as in a liquid crystal.

For fitting, we use the *Scipy* package [357]. As a criterion to compare the fit qualities we use the coefficient of determination, defined for observables $O(x_{n_j})$ depending on one spatial direction on the lattice $x_{n_j} = n_j$ as

$$R_i^2 = 1 - \frac{\sum_{n_j=0}^{L} \left(O(x_{n_j}) - F_O(x_{n_j})\right)^2}{\sum_{n_j=0}^{L} \left(O(n_j) - \bar{O}\right)^2} \tag{7.62}$$

with the spatially mean $L\,\bar{O} = \sum_{n_j} O(x_{n_j})$ and the values of the fit function $F_O(x = x_{n_j})$ produced by *Scipy*.

As a further observable to check the dominating freuquency in the case of an oscillating correlator, we use the Fourier-transform of c^{ij} as an observable

$$\tilde{C}^{ij}(\boldsymbol{k_n}) = \langle \mathcal{F}\{c^{ij}\}(\boldsymbol{k_n}) \rangle \tag{7.63}$$

where $\boldsymbol{k_n} = 2\pi \boldsymbol{n}/L$ are the momenta available in the cubic, spatial volume L^3.

Moreover, we use the expectation value

$$\Phi^2 = \frac{1}{N_s L^3} \langle \sum_{\boldsymbol{x_n}} \vec{\phi}^2 \rangle \tag{7.64}$$

to determine whether the system is in the SP, where Φ^2 should have a small, non-vanishing value generated by statistical noise, or the HBP where $\Phi^2 \neq 0$.

REMARKS ON NUMERICAL PARAMETERS We run the calculations for $N_s = 1, 2, 4, 8$ and lattice sizes $L^3 = 12^3, 16^3, 20^3, 30^3$ (the largest lattice size is only studied for $N_s = 1$) as well as various values of the bare parameters. Between $2000 - 12000$ independent configurations are generated for the computation of the plotted observables, respectively. Except for the preliminary results in Section 7.4.3, all presented computations are thermalized and the statistical errors, estimated with the Jackknife method implemented in the *Astropy* package [376] and indicated by error bars, are typically so small that they are hardly visible in the plotted data.

7.4 RESULTS FROM LATTICE FIELD THEORY

As discussed above, one expects different scenarios alternative to an IP from analytical approximations to the partition function of model (7.6) that should be taken into account when simulating the full quantum theory. In our first, qualitative analysis we evaluate the spatial bosonic correlator $C^{ii}(\boldsymbol{x_n})$ using Eq. (7.61). Fits to the correlator allow to distinguish between QπL, SP, IP and quasi-long range order, see Section 7.3.2. For a first, qualitative effect of the quantum fluctuations on the phase diagram of the theory, we keep the bare parameters $M^2 = 1.0$, $\lambda N_s = 1.0$ fixed[6] and study the phase diagram within the (m^2, Z) plane, analogous to the large-N_s findings [219] summarized in Section 7.2.3. We use the phase structure presented in Fig. 7.1 as a reference for our simulations.

7.4.1 *Phase diagram for fixed spatial volumes*

In the following, we present results for the spatial volume $L^3 = 20^3$. However, we note that our findings are stable among different volumes $L^3 = 10^3, 16^3, 20^3, 30^3$ except for

6 The rescaling of λ with N_s is necessary in order to ensure that the lattice results can converge to the large-N_s findings when increasing the number of scalar fields.

very small, negative Z, where the decay rates of spatial correlators are getting small and larger volumes are needed. For the largest volume $L^3 = 30^3$, only few parameter sets are computed for $N_s = 1$ such that we use generally $L = 20$ for the discussion of our results. The error bars on computed observables estimated based on the Jackknife analysis are typically smaller than the dots used for visualization.

We begin by investigating the correlator C^{11} using Eq. (7.61) for different values of N_s and fixed $Z = -1.0, m^2 = 0.0$. In Fig. 7.2, the result for C^{11} as well as the preferred fit scenario is plotted for $N_s = 1, 2, 4, 8$. Note that we choose to plot always C^{11} but the simulations results for C^{jj} are independent of the choice of j, i.e., we could have chosen also, for example, $j = 2$ for $N_s = 2, 4, 8$ or $j = 6$ for $N_s = 8$. As obvious from the individual figures, the QπL fit function is preferred independent of N_s and the individually computed functional behaviors of $C(x)$ are qualitatively similar. From Ref. [219], one would have expected to obtain an IP at least for $N_s = 1$ since there is no disordering through Goldstone modes of $\mathrm{O}(N_s)$ symmetry breaking for the symmetry group $\mathrm{O}(1) = Z(2)$. The independence of the phase structure, determined by fits and measurements, on N_s repeatedly is observed in the present analysis, which is entirely unexpected. The structure of the model (7.6) contains off-diagonal terms $\sim \phi_j \phi_k$ with $j \neq k$ in the quartic self-interactions as well as in the higher order derivative term. However, we find, in general, that $C^{jk} \approx 0$ for $j \neq k$ within the statistical errors of the simulation, which are on the order ov 10^{-4}, i.e., i.e., the off-diagonal correlations of the fields ϕ_j are vanishing. This factorization of the correlator suggests that the mechanism of disordering inhomogeneous condensates through Goldstone modes might not be the relevant one for the observation of the QπL. The plots in Fig. 7.2 infer, instead, that generically including bosonic quantum fluctuations leads to disordering of inhomogeneous condensates independent of N_s.

For $N_s = 1$, we demonstrate how varying the parameters m^2 and Z changes the correlator. As discussed above, the qualitative behavior of the correlator is independent of N_s, as we checked by producing similar plots for $N_s = 2$ and $N_s = 4$. Therefore, $C(x) = C^{11}((x, 0, 0))$ is plotted in Fig. 7.3 in the top row of Fig. 7.3. In consistency with the predictions from large-N_s the obtained exponential decay rate gets smaller when decreasing Z to $Z = -2.0$, see the top left plot of Fig. 7.3. Moreover, when increasing Z for fixed m^2, the oscillatory behavior is stronger suppressed and finally vanishes. This can also be seen in the expectation value of the Fourier-transform (7.63) of the correlator, as plotted in Fig. 7.3. For small Z, there is a single mode, corresponding to the spatial momentum $k = 8\pi/L$ that dominates the Fourier spectrum, while lower frequencies are rather suppressed. It is expected that, when further lowering Z, this single dominant Fourier mode gets enhanced even more significantly compared to the other modes until, in the limit $Z \to -\infty$ an IP might emerge [219]. A diverging negative wave function renormalization, however, is not observed in typical QCD-inspired models [1, 10] or in the FRG [121, 166]. Within the SP, one observes the typical Fourier spectrum of a function proportional to $\exp(-m|x|)$ as is expected from the fit, cf. the right column of Fig. 7.3.

When varying m^2 between $m^2 = -0.4$ and $m^2 = 0.4$ in lattice units for fixed $Z = -1.0$, one obtains a QπL behavior of the correlator, see Fig. 7.4. However, the behavior of $C(x)$ still changes quantitatively, as the value of $C(0)$ in lattice units is significantly smaller for larger m^2. Moreover, the exponential decay rate is higher for larger m^2. Nevertheless, this behavior still amounts to the QπL such that no strong dependence of m^2 of the qualitative effects is observed. Therefore, in the exploratory analysis for the thermodynamic volume in the following sections we start by focusing on a single value of m^2 to reduce the computational costs.

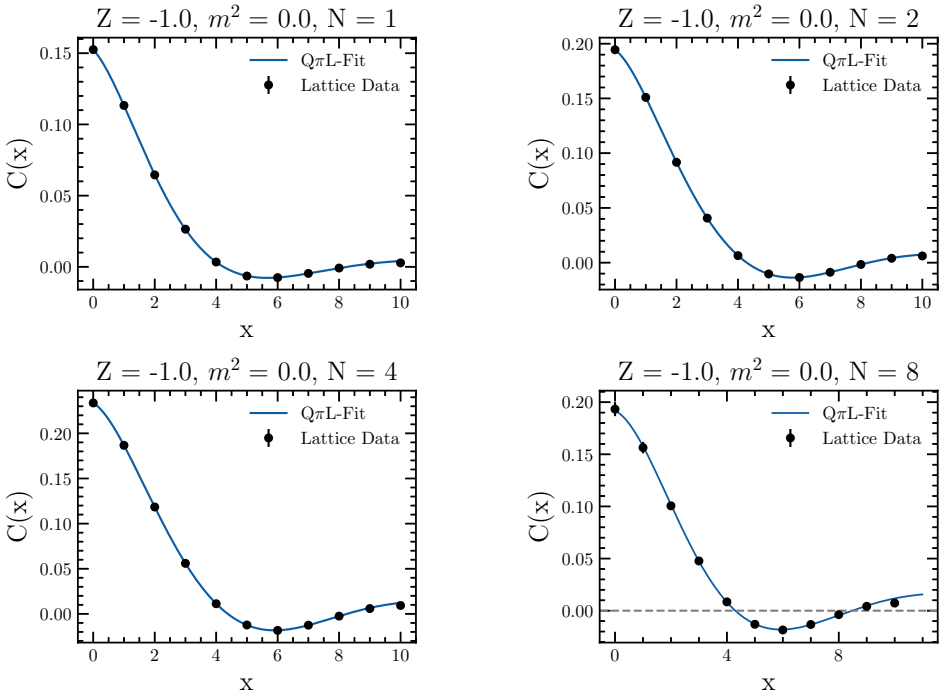

Figure 7.2: Plot of the spatial correlator $C(x) = C^{11}((x,0,0))$ for $Z = -1.0, m^2 = 0.0$ and $L = 20$. The preferred fit scenario is determined using the coefficient of determination. *(top left)* $N_s = 1$. *(top right)* $N_s = 2$. *(bottom left)* $N_s = 4$ *(bottom right)* $N_s = 8$.

.

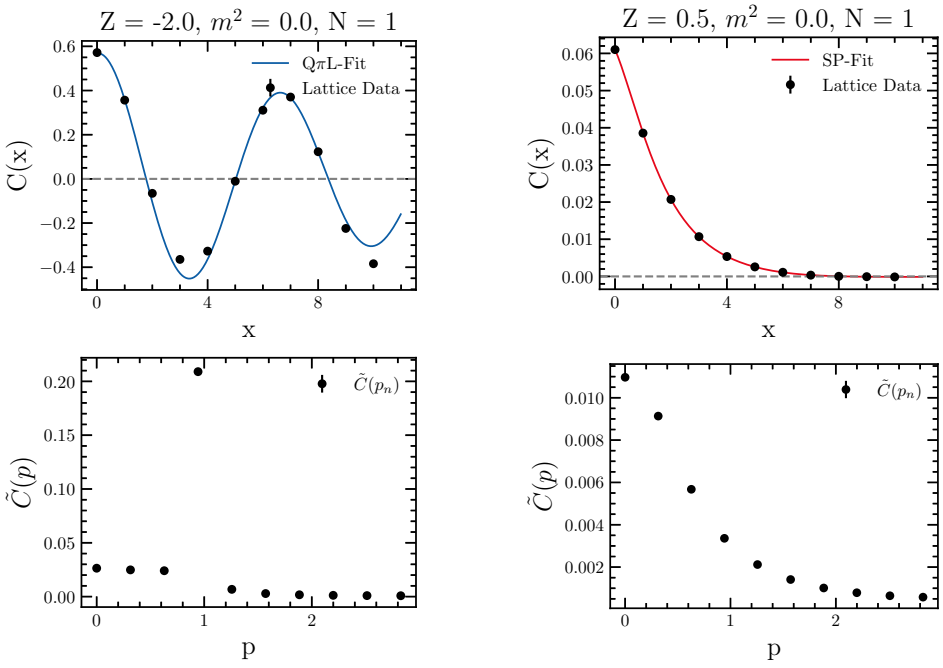

Figure 7.3: Plot of the *(top row)* spatial correlator $C(x) = C^{11}((x,0,0))$ (7.61) and *(bottom row)* its Fourier-transform $\tilde{C}(k) = \tilde{C}((k,0,0))$ for $N_s = 1$ and $L = 20$. The preferred fit scenario is determined using the coefficient of determination. *(left)* $m^2 = 0.0, Z = -2.0$. *(right)* $m^2 = 0.0, Z = 0.5$.

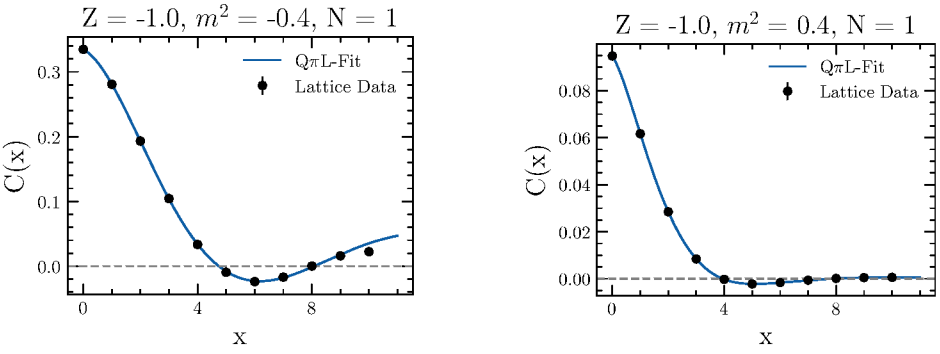

Figure 7.4: Plot of $C(x) = C^{11}((x,0,0))$ (7.61) for $N_s = 1$. The preferred fit scenario is determined using the coefficient of determination. *(bottom left)* $m^2 = -0.4, Z = -1.0$. *(bottom right)* $m^2 = 0.4, Z = -1.0$.

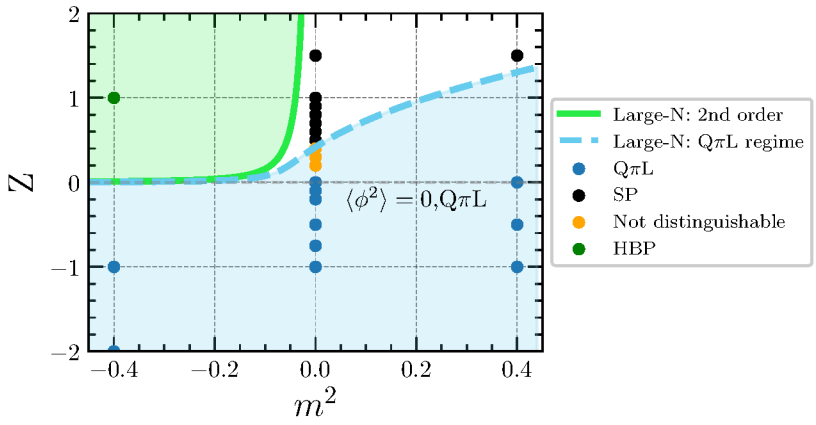

Figure 7.5: Phase diagram of the scalar lattice model (7.56) from fits for $N_s = 1$ with $\lambda N_s = 1.0, M = 1.0$. The color shaded regions represent the large-N_s findings from Ref. [219] for the phases: green — HBP, white — SP and blue — QπL.

In Fig. 7.5, we summarize our findings using fit functions for different values of m^2 and Z by depicting the observed regimes for $N_s = 1$ using LFT, represented by dots in different colors, in comparison to the large-N_s boundary lines. This illustrates that the simulation results are in agreement with the large-N prediction, although one has to note that the comparison of different fit scenarios does not yield conclusive results near any of the phase boundaries. As discussed in Section 7.3.2, we checked to correctly detect the HBP for one fixed parameter set using the observable defined in Eq. (7.64). The phase diagram in the (m^2, Z) plane seems to be identical for all studied values of N_s up to the current status of investigation. Investigations of the correlators for $N_s = 2, 4, 8$ yield similar phase diagrams as Fig. 7.5 (although admittedly less different tupels (m^2, Z) are studied), which we do not plot to avoid redundancy of the figures.

Summarizing, there is remarkable agreement between the LFT simulation results and the large-N_s phase structure. This could be an indication that the inclusion of bosonic quantum fluctuations themselves leads to disordering and it is not necessary to have any kind of Goldstone modes in order to form a QπL. Thus, the mechanism of disordering through transverse Goldstone modes discussed in Ref. [219] might not be the correct one for all finite N_s, although the resulting phase diagram could look similar. At $N_s = 1$, there

exist no Goldstone modes in the system and still the QπL could be observed instead of an IP.. However, symmetry breaking (as a transition from a SP to an IP would be) requires careful study, especially when recalling that phase transition in the strict mathematical sense, i.e., due to a diverging correlation length, can only occur in an infinite volume. This is explored in the following subsection.

7.4.2 *Explicit symmetry breaking through external field*

The above findings can be seen as an indication that the IP does not exist in the (m^2, Z) phase diagram of the full quantum theory with effective action (7.6) at respectively fixed spatial volume. However, the thermodynamic limit, i.e. $V \to \infty$, is required in order to properly identify phase transitions. Moreover, a removal of the artificially introduced spatial volume is interesting for the phase diagram in thermodynamic equilibrium. Within our simulations, however, the restriction to finite spatial volumes is always present. Thus, an extrapolation method of the results to the infinite volume is required. A straightforward approach is the finite volume scaling of an observable relevant for the distinction between IP and QπL, such as the exponential decay rate m_r in the QπL. The scaling of this quantity is, however, plagued by huge, systematic errors from the bias introduced through fitting and from the statistical errors of the simulation. Thus, we decide to use the traditional method of studying phase transitions by introducing an external symmetry breaking parameter, which we need to modify to study translational symmetry breaking.

Since we are interested not only in the spontaneous breaking of the $\mathrm{O}(N_s)$ symmetry but also of the remaining translational invariance and possibly of the discrete rotational symmetry on the lattice, we use an external field that specifically breaks these symmetry. Thus, we modify Eq. (7.56)

$$\mathcal{S}_{\text{eff}}^{(h_0)}[\vec{\phi}] = \mathcal{S}_{\text{eff}}[\vec{\phi}] - \sum_{\boldsymbol{n}} \vec{h}(\boldsymbol{x_n})\phi_1(\boldsymbol{x_n}) \tag{7.65}$$

with $h_j = \delta_{j,1} h_1$, where

$$h_1(\boldsymbol{x_n}) = h_1(x_3) = \frac{h_0}{\sqrt{2\pi} L\, \sigma_0} \sum_{n=0}^{L-1} \mathrm{e}^{-\frac{1}{2\sigma}(p_n - k_0)^2} \cos(p_n x_3), \tag{7.66}$$

for $N_s = 1$ and $\vec{h} = \vec{h}_{\text{spiral}}$, where

$$\vec{h}_{\text{spiral}}(\boldsymbol{x_n}) = \vec{h}_{\text{spiral}}(x_3) = \frac{h_0}{\sqrt{2\pi} L\, \sigma_0} \sum_{n=0}^{L-1} \mathrm{e}^{-\frac{1}{2\sigma}(p_n - k_0)^2} \left(\cos(p_n x_3), \sin(p_n x_3)\right) , \tag{7.67}$$

for $N_s = 2$ as well as $\vec{h} = \left(\vec{h}_{\text{spiral}}, 0\right)$ for $N_s > 2$. This ansatz resembles the chiral spiral (7.5), but additional one sums over lattice momenta $p_n = 2\pi n / L$ and $\sigma_0 = 0.1$, each spiral weighted by a Gaussian. In order to determine the peak of the Gaussian in momentum space, we extract k_0 from the fits to C^{11} with $h_0 = 0$, which are described in Section 7.4.1.

The Gaussian distribution of the present momenta is used in order to allow the system to adapt differing frequencies when translational symmetry is explicitly broken. Nevertheless, the peak of the Gaussian is extracted from the "physical situation" where the external field is supposed to be absent. In the end, we want to learn how the system behaves for $L \to \infty$ and $h_0 \to 0$.

Since the introduction of the external symmetry breaking term does not only break translational but also rotational invariance for $h_0 \neq 0$ in the modified action (7.65), we

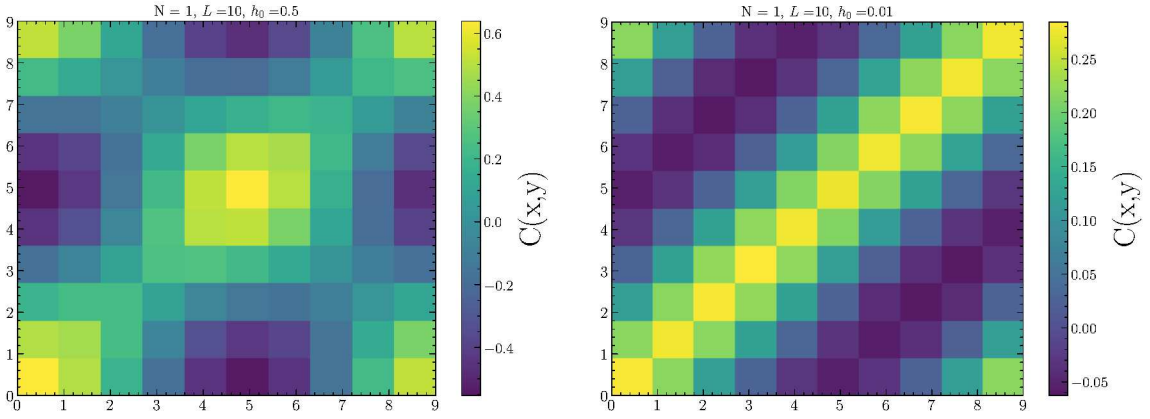

Figure 7.6: Color coded value of $C(0,0,x,y)$, see Eq. (7.68), for $N_s = 1, Z = -1.5, m^2 = 0.0, L = 10$ with an external symmetry breaking field (7.66) introduced to the action according to Eq. (7.65). Note that the scaling of the color bar differs in both plots. *(left)* $h_0 = 0.5$. *(right)* $h_0 = 0.01$.

expect that the correlation function still depends on the relative differences in the x_1 and x_2 directions. Translational symmetry breaking should then have an impact on its dependence on the x_3 directions, i.e., one expects

$$C(x_1 - y_1, x_2 - y_2, x_3, y_3) = \langle c^{11}(\boldsymbol{x}, \boldsymbol{y}) \rangle = \frac{1}{L^3} \langle \phi_1(\boldsymbol{y}) \phi_1(\boldsymbol{x}) \rangle \tag{7.68}$$

where the spatial coordinates are obviously restricted to the lattice points with coordinates $\boldsymbol{x_n} = \boldsymbol{n}a$ with $n_j = 0, \ldots, L-1$ for $j = 1, 2, 3$. compare to the definition of the correlator (7.61), which assumes translational invariances.

In Fig. 7.6, we plot $C(0,0,x,y)$ as a color map for $Z = -1.5, m^2 = 0.0$ and $L^2 = 10^3$. In this figure, we use an external field (7.66) with $k_0 = 0.63 \approx 3 \times 2\pi/20$. This serves to illustrate the effects of the external field introduced in Eq. (7.56) and draw consequences for the following analysis. For the left plot with $h_0 = 0.5$, one can directly see the signs of translational symmetry breaking due to the external field. Clearly, the correlator C follows an oscillatory pattern following an inhomogeneous ground state, that is sine-like in the x_2 direction. Thus, for this parameter set the ground state is expected to be inhomogeneous, reflecting the translational symmetry breaking stemming from the term proportional to h in the action (7.65). On the other hand, translational invariance is at least approximately intact for $h_0 = 0.01$, since the color pattern shows a dependence of C only on $x - y$. Thus, in between those two values a phase transition between the QπL and the IP must occur. Determining the critical value $h_{0,c}$ of the external field amplitude for this transition as a function of the volume V can provide the basis for the infinite-volume extrapolation.

Qualitatively, one can observe a color map similar to the right panel of Fig. 7.6 when computing the correlator (7.68) for vanishing external field, which is a consistency check and confirms that the translational symmetry, indeed, is intact for these parameter sets. In the following subsection, the inspection of plots similar to Fig. 7.6 is used for exploratory studies of the possibility of translational symmetry breaking in the thermodynamic limit.

7.4.3 *Preliminary studies of the finite-volume scaling*

The idea of the infinite-volume extrapolation is to determine the critical amplitude of the external field $h_{0,c}$ for the onset of the IP at fixed parameters of the effective action

$\mathcal{S}_{\text{eff}}[\vec{\phi}, a, L]$ and, specifically, for fixed L. The computation of $h_{0,c}$ for different values of L would then allow to get an idea of the functional behavior of $h_{0,c}(L)$. An extrapolation to $L \to \infty$ could then clarify whether translational symmetry breaking for the infinite volume theory and the physically interesting theory, i.e., for $L = \infty$ and $h_0 = 0.0$. For example, if the fit to $h_{0,c}$ is a monotonically decreasing function of L, hitting the $h_0 = 0$ axis for a finite value of L, one can expect that an IP is realized in the thermodynamic limit. On the other hand, the disordering of the IP in a QπL remains present in the infinite volume limit when, e.g., the fit to $h_{0,c}(L)$ is a constant or monotonically increasing function.

Unfortunately, investigations performing these extrapolations are not finalized yet. Larger values of L and large amplitudes of the external field significantly complicate the LFT simulations by significantly increasing autocorrelations and thermalization time. Additionally, huge amounts of memory storage are required, since the size of the spatial correlator observable (7.68) scales with L^4. Thus, only low statistics result are available for large L. Therefore, we present computations of Eq. (7.68) for a selected number of data points in the following without explicitly studying the finite volume scaling. Instead, the amplitude h_0 of the external field, given by Eq. (7.66) or Eq. (7.67) depending on the value of N_s, is fixed and L is increased in order to visualize a generic tendency of the system of either remaining in the disordered QπL or breaking translational invariance for larger L. Note that we refrain from analyzing these following findings with respect to the fate of IPs in the infinite-volume since these are preliminary results without proper thermalization at larger volumes.

In Fig. 7.7, we present color coded results for the correlator (7.68) for simulations with an external field using $h_0 = 0.1$, $k_0 = 0.62$ for three different volumes $L^3 = 10^3, 20^3, 30^3$. Specifically that the findings for $L = 20$ and $L = 30$ suffer from the long autocorrelation and thermalization times and are produced on rather low statistics. Within these configurations, thermalization effects are still present such that the plotted result probably does not entirely represent the value of the observable in equilibrium. Nevertheless, comparing the three different color maps one can clearly see that the translational invariance, which is intact in the x_3 direction for $L = 10$ where $C(0, 0, x, y) \sim f(x - y)$, is getting broken already for $L = 20$. We note that thermalization effects might be the reason that the oscillating structure in the color map is not periodic over the whole lattice. These findings could be an indication, given that fully thermalized configurations confirm these figures, that the system tends to break translational invariance when increasing the spatial volume, at least for $N_s = 1$. On the other hand, one could argue that the quantum fluctuations have not yet fully destroyed the inhomogeneous ordering provided by the external field and further thermalization would lead to an intact translational symmetry. Investigations for larger N_s and different values of h_0 are on-going and will be reported on in a later publication.

7.4.4 *Remarks regarding the line of constant physics*

One can argue that the above investigations suffer from technical problems regarding the scale setting. As outline above and in Section 7.3, we always set $a = 1$. No observable such as the absolute value of the chiral condensate Φ (7.64) or the diagonal elements of the spatial correlator $\sum_i C^{ii}(0)$, see Eq. (7.61) for its definition, is used to set a physical scale. Such a scale is used in LFT simulations to ensure that one remains on a line of constant physics while varying the lattice spacing a. This is a strategy that should be pursued in further investigation of this type. Nevertheless, the presented simulation results are at an

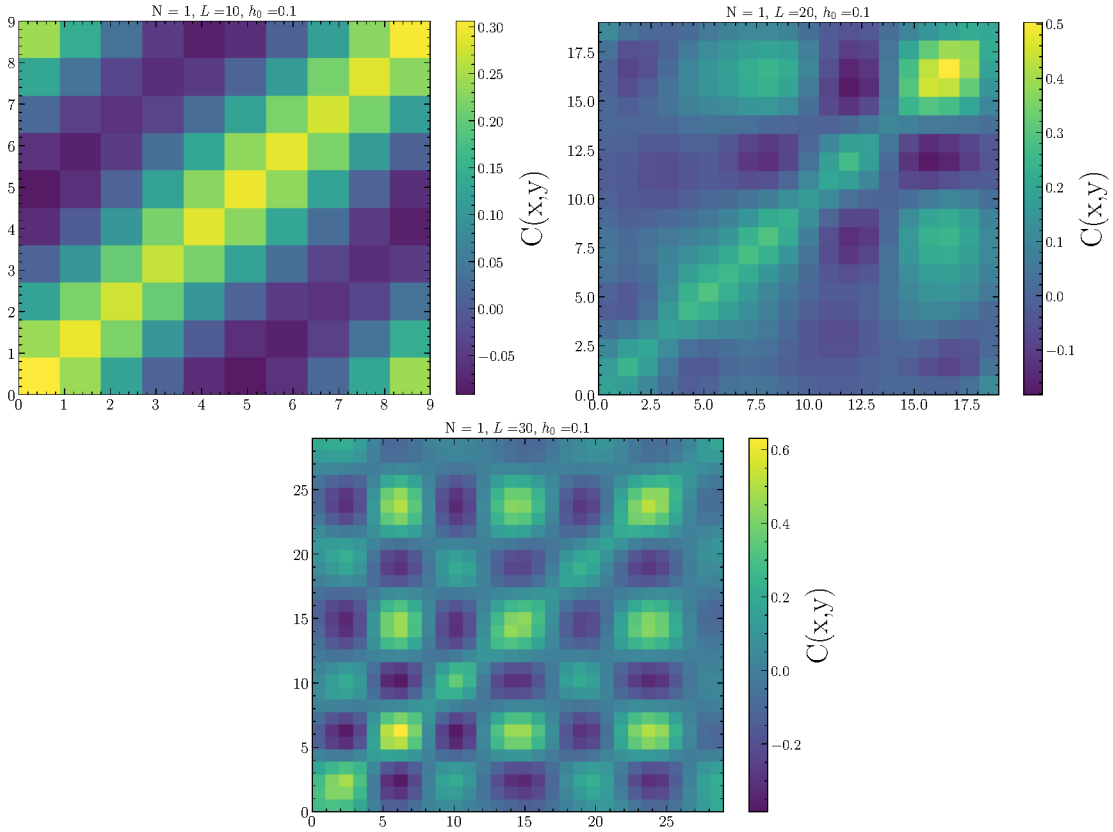

Figure 7.7: Color coded value of $C(0,0,x,y)$, see Eq. (7.68), for $N_s = 1, Z = -1.5, m^2 = 0.0$ with an external symmetry breaking field (7.66) introduced to the action according to Eq. (7.65). Note that the scaling of the color bar differs in both plots. The results for $L = 20$ and $L = 30$ suffer from long autocorrelation and thermalization times and are produced on rather low statistics. *(top left)* $L = 10$. *(top right)* $L = 20$. *(bottom)* $L = 30$.

intermediate stage and computed for a specific model setup with fixed bare parameters of the action at one fixed lattice spacing a. Especially, as motivated in the beginning of this chapter, the scalar model is considered as an effective theory for symmetry breaking patterns in QCD. Thus, it can naturally be considered as an theory with an inherit UV cutoff. If this UV cutoff is associated with the lattice spacing a, a continuum limit must not be necessary, especially since our findings are anyhow of qualitative nature and focus on the investigation of quantum effects in general. A strategy for a correct continuum limit of the above investigation is already developed and will be reported upon in subsequent publications.

7.5 SUMMARY AND CONTEXTUALIZATION

In this chapter, we presented an investigation of the effect of bosonic quantum fluctuations on spatially modulated phases using a scalar $O(N_s)$ model, which is constructed to feature a moat regime and an IP classically. We reviewed literature findings from the large-N_s limit as indications that bosonic quantum fluctuations of Goldstone modes stemming from the $O(N_s)$ symmetry breaking disorder the IP and, instead, a QπL is observed. The presented LFT simulation results demonstrate that this disordering is also observed for $N_s = 1, 2, 4, 8$

at finite spatial volumes. Thus, a QπL is always preferred over an IP in the LFT investigation (at finite spatial volume), independent of the studied model parameters, see Fig. 7.5 for the phase diagram in the parameter space of the theory.

For the study of spontaneous translational symmetry breaking in the thermodynamic limit, an external symmetry breaking approach was developed and first results for finite amplitude of the symmetry breaking term were discussed. In the developed approach, one introduces an external, static field, that explicitly breaks translational invariance, and determines the critical value of its amplitude that leads to the observation of an IP. Preliminary findings are presented, but the statistics are rather low such that no conclusions can be drawn from these simulations.

CONCLUSIONS At the current stage, our analysis suggests that, at finite spatial volume, a QπL is favored over an IP, even if the fermionic fluctuation effects, here encoded in the effective model Lagrangian as higher order kinetic terms, favor inhomogeneous condensation. This yields a clear picture in the sense of **RO3** and **RO4**, that disordered phases like a liquid-crystal regime with quasi-long range order or a QπL are preferred over crystalline structures like IPs. The model (7.6) classically features an IP and (trivially) a moat regime. However, from our lattice results it seems that the QπL is favored over quasi-long range or long-range ordering. Thus, in a computation of the phase diagram of QCD at non-vanishing μ, if possible in the future, we would rather expect the emergence of a QπL instead of an IP, given the presence of bosonic fluctuations in the system.

Our results are obtained for a fixed lattice spacing. No continuum limit is performed. However, the continuum limit might not be very insightful given that the used theory is super-renormalizable and can, anyhow, be considered an effective theory. This investigation focuses on qualitative effects of quantum fluctuations in LFT simulations such that keeping a UV cutoff for this purely scalar theory seems natural and practical in the first place. Nevertheless, it is important to check the stability of our findings against numerical parameters, such as the lattice spacing, in following investigations.

In the context of **RO4**, our analysis challenges the mechanism of the disordering of inhomogeneous condensates through the Goldstone modes stemming from $\mathrm{O}(N_s)$ symmetry breaking, proposed in Ref. [219]. The LFT simulations reveal that the observed regime remains independent of N_s, demonstrating that the existence of Goldstone bosons is not responsible for the absence of IPs in correlation functions. Instead, our findings suggest that bosonic quantum fluctuations alone are the primary cause of disordering, making the previously proposed mechanism unlikely.

To study the fate of the IP in the thermodynamic limit of a LFT simulation, we propose a method based on the external breaking of translational invariance, a key technical aspect of **RO4**. Albeit the method is rather intensive in both processing time and memory storage, as it increases the dimensionality of the to-be-explored parameter space as well as thermalization times significantly, we consider this the best available method for performing finite-size scaling in the context of spontaneous symmetry breaking – especially in contrast to studying the scaling of fit parameters. A rather drastic systematic limitation of the current approach is its reliance on the visual inspection of Eq. (7.68) using color maps, as in Fig. 7.6, to determine whether translational invariance is broken or not. Thus, this method lacks a sensible observable to determine the critical external field amplitude for the transition between IP and QπL at finite spatial volumes.

The finding of a moat regime with FRG computations of the QCD phase diagram in Ref. [121] can be interpreted as a signal for the existence of spatially modulated, chiral

observables in the phase diagram, see Section 3.1. Unfortunately, our investigation, so far, did not allow the computation of the coefficient of the spatial kinetic terms in the quantum effective action, the full bosonic wave function renormalization of the scalar fields. However, we expect that, within the observed QπL in Fig. 7.5, the oscillatory behavior in the correlators is caused by the presence of a moat regime in the quantum effective action. It is likely that the appearance of the moat regime and of the complex-conjugate bosonic two-point vertex functions around the CP in model computations [189] are related to each other in the sense that the moat regime is a precursor of the oscillatory behavior of mesonic correlation functions realized in the QπL.

FUTURE RESEARCH PERSPECTIVES The research project, that resulted in the LFT findings presented in this chapter, is on-going such that we only comment on direct follow-up steps, which are planned for the completion of the corresponding publication. Obviously, an extrapolation to the thermodynamic limit is mandatory to make clear statements about the fate of translational symmetry breaking in the thermodynamic limit. This, however, requires more data points with a lot of statistics in the plane of external field amplitude and the cubic, spatial volume L^3. The production of this data is rather cost intensive in terms of computer time but also memory storage, since the respective correlator, that needs to be computed and stored for each field configuration, scales with L^4. Moreover, the configurations at non-vanishing external field suffer from high autocorrelation and thermalization times. The analysis would further greatly be simplified by a construction of a local observable allowing to determine the transition between QπL and IP. However, we were unable to come up with an improvement of this method so far.

A further interesting research aspect is the investigation of the breaking of discrete rotational symmetry on the lattice. Findings without external symmetry breaking indicate that the QπL leaves rotational symmetry intact. This should be further investigated in the approach with external symmetry breaking, according to Eq. (7.65), that clearly breaks also the discrete rotational invariance on the lattice. The correlator observable, used so far in this investigation, can provide hints if one inspects its dependence on spatial coordinates transverse to the direction of external symmetry breaking. This analysis is left for future works.

Finally, there is also the above discussed aspect of performing a continuum limit. We argued above that a continuum limit, albeit the theory can be non-trivial according to Ref. [371] in the continuum, might not be very relevant for the qualitative effects, that we are interested in. A tuning of the observables to fix a phenomenlogical observable and the analysis of two or three different lattice spacings, however, is still a sensible approach, since the used parameter sets can be compared to more elaborate QCD-inspired models based on fermions. Moreover, it is, in general, important to check the numerical stability of the simulations also against the lattice spacing. Studying further lattice spacings, however, is, again, very intensive in terms of computer time and memory such that this is the last aspect from the ones discussed here, that will be improved upon.

8

SUMMARY, CONCLUSIONS AND OUTLOOK

8.1 SUMMARY

In this work, relevant mechanisms and properties for the existence of exotic regimes with spatial modulations in QCD at non-vanishing baryon chemical potentials and temperatures were investigated using so-called QCD-inspired models, i.e., QFTs that share particular features with QCD. First principle computations in QCD directly are not available at non-zero baryon chemical potential, see Chapter 1 for details. As the title of this thesis suggests, the approach is rather of exploratory nature and quantitative predictions for observables are not made. We focused on the incorporation of important aspects relevant in finite-density QCD and on the consequences of these aspects on the phase structure of the models used. In the following, let us briefly summarize the central findings:

The findings in Chapter 5 and Chapter 6 suggest the absence of IPs in all $2+1$-dimensional four-fermion models with local interactions and a variety of Yukawa models at non-vanishing chemical potentials and temperatures. The absence of instabilities of homogeneous ground states against inhomogeneous perturbations was rigorously proven in these models within the mean-field approximation, where bosonic quantum fluctuations are completely suppressed and only the fermionic ones are taken into account. Moreover, we argued that this finding is strong evidence that IPs are absent also in the full quantum theories. Also, our findings strongly support the claims in the literature that IPs have a strong dependence on the regularization scheme and value of the respective regulator [9, 10, 211, 240, 241], see also Section 3.2 for a discussion.

In Chapter 6, we showed that the mixing effects between scalar and vector mesons leads to the generation of a QπL, a regime with spatially oscillating, exponentially damped two point correlation functions of mesonic fields, within the HBP of $2+1$-dimensional four-fermion models. The appearance of the QπL is related to the interplay of the attractive scalar interactions and repulsive vector interaction channels and could have been expected through the existence of the combined $\mathcal{CK}$ symmetry of the model at non-vanishing chemical potential – a symmetry that is also realized in QCD. The $\mathcal{CK}$ transformation is of $\mathcal{PT}$-type, and theories with this symmetry are expected to exhibit exotic regimes [180, 185, 189, 191]. The mixing terms are proportional to the constituent quark masses, or, equivalently in the chiral limit, to the chiral condensate, an artifact from the mean-field approximation that was used in Chapter 6. The studied effects, however, are also expected to be the dominant mixing contributions in the full quantum theory.

The study in Chapter 7 is conceptually different from Chapters 5 and 6 since the effect of bosonic quantum fluctuations on exotic regimes is explored using LFT theory. Therefore, a scalar O(N_s) model is used that classically features both a moat regime as well as an IP. Our initial findings suggest that quantum fluctuations entirely disorder IPs in the LFT

results for $N_s = 1, 2, 4, 8$, where $N_s = 4$ is the relevant symmetry group isomorphic to the chiral $\mathrm{SU}(2) \times \mathrm{SU}(2)$ symmetry of two-flavor QCD in the chiral limit. These results are obtained at finite spatial volumes. The thermodynamic limit is essential to study the symmetry breaking in the strict sense, i.e., through diverging correlation lengths. Therefore, a method involving an inhomogeneous, external field that breaks translational invariance was developed.

8.2 CONCLUSIONS

In this section, the results are interpreted first in the context of the research program that the author set up and followed during the completion of this thesis, characterized through five **RO**s defined in Section 1.3. In the second part of this section, we also make an attempt to derive hints for the phase structure of QCD at intermediate temperatures and densities with respect to exotic, chiral regimes. This part should be rather seen as an educated speculation, influenced by the opinion and perspective of the author, than an evidence-based prediction for the phase structure. As admitted multiple times throughout this thesis, QCD-inspired model computations are not able to provide a solid basis for predicting the phase structure of QCD itself.

8.2.1 *Implications with respect to the research objectives*

RO1 focuses on the influence of the combined $\mathcal{CK}$ symmetry of QCD at $\mu \neq 0$ on the formation of exotic regimes. From the findings in Chapters 5 and 6 we conclude that the emergence of this symmetry at non-vanishing densities strongly favors the generation of QπLs. In these chapters, we first of all observed the absence of IPs in all kinds of $2+1$-dimensional four-fermion models both with and without the realization of the $\mathcal{CK}$ symmetry in four-fermion models. When including vector interactions and, as a consequence, allowing for condensation in the temporal component of a vector meson channel, however, the QπL is observed in the phase diagram at a sufficient strength of the vector coupling. The condensation of the vector meson, in turn, leads to the emergence of the $\mathcal{CK}$ symmetry in four-fermion models, supporting the claim that this symmetry pattern of the QCD action, mixing effects between scalar and vector mesons and the QπL regime are closely related to each other. Computations in QCD-inspired models have so far mostly neglected the effect of the $\mathcal{CK}$ symmetry in the investigation of the phase diagram. Our analysis is one of the first computations (together with the parallel work [189]) that the QπL can arise in the phase diagram when a model features the $\mathcal{CK}$ symmetry. Thereby, this result is obtained in an entirely renormalizable, unambiguous and consistent QFT used as a QCD-inspired model.[1]

RO2 concerns the mixing effects between scalar and vector mesons and their effect on the phase diagram. Yukawa-type interactions and four-fermion resonances in the respective channels play an important role at intermediate baryon densities and temperatures [133].

1 We briefly comment on the important findings in Ref. [191] and Ref. [189]. In the first of these two works, an NJL-type models with Polyakov-loops was used such that the results investigated parameter regions might be affected by regularization artifacts [10], unknown of at the publication of Ref. [191]. However, they find clear signals of the QπL. Ref. [189] uses a renormalizable QM model and also finds signals of the QπL, but neglects the effects of vacuum fluctuations such that the model computation is not based on an entirely consistent QFT setup. Given these remarks, we consider both of these works seminal to the above made arguments.

As outlined already in the above paragraph, the incorporation of both scalar and vector channels in four-fermion models implements the $\mathcal{CK}$ symmetry at $\mu \neq 0$ and, thus, is closely related to the existence of the QπL. The findings of the above mentioned Refs. [189, 191] together with the results in this thesis, consequently, provide arguments for the existence of a QπL in QCD. We note at this point, that both Refs. [189, 191] also incorporate mixing effects stemming from the gluon fields in terms of Polyakov loop potentials in addition to the mixing between scalar and vector mesons.

The work of the above mentioned chapters and many of the phase diagram calculations in QCD-inspired models in the literature are restricted to the mean-field approximation, where bosonic quantum fluctuations are suppressed. **RO3** is about the effect of the bosonic quantum fluctuations on these exotic regimes. Regarding **RO3**, our LFT investigations of a scalar O(N_s) model in Chapter 7 for $N_s = 1, 2, 4$ suggest that bosonic quantum fluctuations disorder inhomogeneous condensates. The corresponding classical theory features an IP but in the LFT simulations the QπL is obtained instead, as a remnant of the IP, for all studied N_s. This result is independent of N_s and consistent with predictions from the large-N_s limit [219]. The simulation results are in line with investigations and arguments in the literature [222, 223, 225, 227–229, 323, 328, 329] that support the statement that bosonic quantum fluctuations disorder phases with spontaneous symmetry breaking such as the HBP or the IP. The simulation results are obtained for a fixed lattice spacing and three different spatial volumes. Consequently, there are still a lot of open questions regarding the findings in Chapter 7 with respect to the infinite-volume and continuum extrapolation. Especially, the infinite-volume limit is crucial, since phase transitions (with critical behavior) and spontaneous symmetry breaking can in a strict sense only be observed in the thermodynamic limit. Together with further literature results, one can certainly conclude that QπLs are more stable with respect to quantum fluctuations than IPs, which can be disordered through different mechanisms [216, 217, 219].

Disordering mechanisms are in detail studied under **RO4**. Our findings suggest that inhomogeneous condensates are disordered purely by quantum fluctuations independent of the number of scalar fields N_s used in the lattice simulation. The relevant mechanism is not necessarily the disordering through Goldstone modes from the O(N_s) symmetry breaking, as suggested in Ref. [219], since the QπL is also favored for $N_s = 1$ and $N_s = 2$ where the Goldstone mode should be non-existent or strongly-suppressed, respectively (for $N_s = 2$ the mechanism of Goldstone mode fluctuations is only applicable depending on which modulation is realized). The present status of our analysis suggests that indeed the QπL is favored whenever quantum fluctuations are included. We note that in fermionic models, like the $1+1$-dimensional GN model whose discrete chiral symmetry $Z(2) = \mathrm{O}(1)$ corresponds to $N_s = 1$ in our scalar model, oscillating bosonic two-point correlation functions were observed, but translational symmetry breaking could not be proven [226]. In the chiral GN model, corresponding to the symmetry breaking pattern of the scalar model with $N_s = 2$, however, disordering was clearly observed [227]. **RO4** also formulates the technical goal of developing an efficient method to detect translational symmetry breaking appropriately in a LFT simulation. Our current approach to this problem is based on inspecting whether the bosonic two-point correlation functions break translational invariance when an explicit breaking through an inhomogeneous external field is introduced to the action. Then, an extrapolation of the critical, external field amplitude for translational symmetry in the correlator observable to an infinite volume should reveal the fate of translational symmetry in the absence of the external field. This approach is expected to provide sensible results, although it is highly inefficient due to the additional numerical costs and the non-locality

of the used observable. One possible approach is to define an observable for the translation symmetry breaking through a combination of matrix elements of the chosen correlator. However, a key challenge is ensuring that this observable is uniquely defined, regardless of the lattice spacing and the number of spatial lattice points used.

For **RO5**, we come back to the findings in Chapters 5 and 6 in $2+1$-dimensional four-fermion models. The question about the fate of inhomogeneous chiral condensates in $2+1$-dimensional four-fermion models was answered through the evidence for the absence of IPs provided by the results in these chapters. The question about the fate of IPs in related, QCD-inspired model is broader and can, thus, not be answered entirely within this thesis. As in detail described in Section 1.3 and Section 3.2, there is evidence for a strong regularization scheme and regulator dependence of IPs [211, 212, 240, 241] in the literature, which is particularly severe for predictions based on non-renormalizable four-fermion models such as the NJL model [10, 167]. As a side effect of our analysis in Chapter 5, the formulae for the bosonic two-point vertex functions – the object of relevance for the detection of IPs using stability analyses – can be identified with similar computations in the $2+1$-dimensional GN model [241] where also a strong regularization scheme and regulator dependence is observed. Thus, our results support the above mentioned literature that a strong regularization scheme and regulator dependence of IPs exists also in all $2+1$-dimensional four-fermion models. From this, one may conclude that there is no predictive power from findings in four-fermion models in three spatial dimension for QCD in the parameter regions relevant for the IP.

8.2.2 *Implications for the QCD phase diagram: A speculation on the phase structure*

By no means does the author suggest that the findings in this thesis provide direct predictions for the QCD phase diagram. The model approaches serve as a foundation for further investigations and are able to identify mechanisms for the formation of exotic phenomena in the QCD phase diagram. Thus, the results of this thesis should serve as a guideline for future studies of QCD at non-vanishing baryon densities, possibly experimentally through astrophysical observations or heavy-ion collision experiments, or theoretically with functional methods, like DSEs or the FRG, or other novel approaches that could be developed in the future. The motivation is to provide hints for interesting phenomena and give input to the more elaborate approaches to the QCD phase diagram at intermediate temperatures and densities. Also for experimental comparison, exotic regimes, observed in QCD-inspired model computations, can be incorporated in phenomenological approaches such that signatures of these regimes for experimental observables can be obtained without first-principles calculations, see, for example, Refs. [11, 231–233] for experimental signatures of the moat regime.

This subsection summarizes the subjective opinion of the author on the "most probable" scenario for the QCD phase diagram with respect to exotic, chiral regimes at intermediate temperatures and chemical potentials, based on the findings of this thesis and related literature. Thus, it should be interpreted as a speculative comment rather than a scientific prediction.

In Section 1.2.1, we discussed possible scenarios for the phase structure of QCD with respect to chiral symmetry breaking and related, exotic regimes. In Fig. 1.2, two different scenarios are proposed: One of these features the typical scenario of a first-order phase transition between HBP and SP at low temperatures with a CP, from which the transition

turn second-order (matching the second-order transition of two flavor QCD in the chiral limit at $\mu = 0$). In the other scenario, an IP at low temperatures and chemical potentials is observed instead of the first-order phase transition between HBP and SP, which was motivated by findings in NJL models [195, 197]. Both of these scenarios commonly feature a moat regime, as its existence in QCD is strongly suggested by the results stemming from the FRG [121, 166] and the robustness of the moat regime in NJL model calculations [9, 10, 167]. Moreover, the moat regime is often related to the appearance of the disorder line, the onset of the QπL [180, 192] (note that there is no rigorous proof for the connection between the two) which is also contained in this scenario. The disorder line is observed in recent model computations [189, 191], also in the present work, c.f. Chapter 6.

The findings in this thesis suggest that the scenario of the IP is likely not realized since we expect the IP to be destroyed by quantum fluctuations. Evidence for this mechanism is obtained in this thesis but also further evidence in the literature [216, 217, 219]. If an IP is realized, then it is expected at very low and/or zero temperatures where bosonic flucutations are milder. Consequently, the replacement of the CP and the chiral first-order phase transition through an IP is considered unlikely. The QπL could be formed both from mixing effects between scalar and vector mesons, which are relevant at these intermediate densities, but also from effects from the gluon dynamics, see Refs. [189, 191]. Moreover, at low temperatures it could be a remnant of the disordering of inhomogeneous condensates, as also suggested by the LFT simulation in Chapter 7. Thus, the phase diagram in the left sketch of Fig. 1.2 seems to be a more probably scenario in the eyes of the author. However, slight modifications are warranted. Although a disorder line is also obtained in the $1+1$-dimensional GN model [377], a model without mixing effects (the disorder line in the GN model resembles closely the sketch in Figure 1 of Ref. [11]), we suggest that parts of the QπL that are generated by mixing effects lie dominantly within the HBP. They are expected to appear also close around the CP, such that large parts of the HBP around the chemical potential of the CP and within temperature ranges between 0 and $T = T_{CP}$ could be covered with the QπL regime. Thus, also the onset of the QπL would be different to the proposed scenario in Fig. 1.2.

8.3 OUTLOOK

In this section, an outlook on the individual research projects, presented in this manuscript, but also on the broader investigation of the QCD phase diagram in the region of interest for this thesis is provided. For the former, the interested reader is referred also to the respective last sections of the results Chapters 5 to 7 where detailed research perspectives for the individual research projects are given. Nevertheless, we briefly comment here on interesting follow-up research perspectives in the context of the overall findings in this work.

8.3.1 *Possibilities for following projects*

As in detail motivated in Section 5.4, the absence of IPs in $2+1$-dimensional four-fermion and Yukawa models could be implied through a general principle, similar to Derrick's theorem [358]. A first attempt to formulate such a theorem could be made using a general enough Ginzburg landau free energy, similar to the approach in Ref. [359] but also including higher order kinetic terms.

For investigations of QCD-inspired theories in three spatial dimensions (which are in this respect certainly closer to QCD compared to the four-fermion models studied in the present work), one first has to tackle either the problem of non-renormalizability of four-fermion models in $3+1$ dimensions or technical problems in Yukawa-type models like unbounded potentials and imaginary Yukawa coupling [198], which arise when studying the theories properly including the vacuum fluctuations and imposing certain values of QCD observables in the renormalization procedure. The latter is sensible to obtain relevant phenomenological results in a fully consistent QFT. In terms of studying QCD inspired models, overcoming these technical problems and perform relevant investigations in three spatial dimensions would, however, be appropriate next steps for phenomenologically interesting findings, e.g., on the relevant scales of oscillations in the QπL. An interesting approach for both the issue of non-renormalizability as well as the issues with the renormalization of Yukawa / QM models is the application of $\mathcal{PT}$-symmetric field theory. The study of these QFTs is still rather novel [186, 312, 313, 367]; encouraging results involving negative quartic couplings, however, have been found regarding the non-triviality of the O(N_s) theory [371]. Also, a $\mathcal{PT}$-symmetric four-fermion theory could be renormalizable [369] which is a promising first finding for further QCD-inspired model computations. The drawback of this approach, however, is that it often involves non-Hermitian actions, which severely complicates LFT investigations. First, studies in a mean-field or large-N approximation should be conducted. Further, it is yet unclear whether these theories can reproduce QCD phenomenology. Investigations in these directions would be logical next steps with respect to the investigation of exotic regimes involving model approaches.

Further, going beyond the mean-field approximation is another important aspect. As outlined above, the issues in three spatial dimensions need to be solved first before LFT simulations are sensible. However, if the developed theories with $\mathcal{PT}$ symmetry are non-Hermitian, one will have to deal with their respective sign problem, i.e., with complex weights appearing in the partition function. Methods to deal with sign problems are in development and involve Lefshetz thimble approaches [126–128] or complex Langevin methods [129–131]. Presently, the methods are far from producing reliable results for QCD at non-vanishing densities. Thus, their application to $\mathcal{PT}$-symmetric theories that are developed according to the discussion above is only sensible if the appearing non-Hermiticities are mild. Otherwise, it would be more fruitful to try to apply developed methods directly in QCD.

Thus, it is currently sensible only to investigate scalar field theories, that incorporate IPs or QπLs as simple models using a gradient expansion, directly with LFT. This is the approach followed in Chapter 7 and is presently still under investigation. However, this study investigates the disordering of IPs and technical issues regarding spontaneous translational symmetry breaking on a finite spacetime lattice. It is not sensible to expect quantitative predictions from the investigation of scalar O(N_s) theories. The study in Chapter 7 is not complete and next steps in this project are discussed above.

8.3.2 *Future research perspectives: Exotic regimes in the QCD phase diagram*

The non-perturbative nature of QCD and its non-Hermiticity at intermediate temperatures and baryon densities make the investigation of these regions of the phase diagram an incredibly challenging task. To quote the PhD thesis of M. Steil [52], a highly appreciated

collaborator: "[The QCD phase diagram] ... is still to an extent a terra incognita of challenges and mysteries: *Here be dragons* and maybe even three-headed ones."[2]

Although the author certainly agrees to this statement, this region of the phase diagram is also of incredibly interesting and is more and more approached from the experimental side in terms of astrophysical approaches like direct gravitational wave detection or from heavy-ion collisions, like the planned CBM experiment at FAIR. Thus, complementary theoretical approaches are urgently needed and, still, as outline above, mostly consist of effective model calculations and functional methods like DSEs and FRG. The latter approaches are likely to be the ones that can provide the most accurate quantitative predictions for experimental observables, although uncontrolled artifacts are introduced into the findings, through restrictive ansatzes for the quantum effective action (or field derivatives of it) required in the FRG and through truncations of the DSEs. Thus, ideally, calculations from both methods should provide consistent estimates, as in the recent determination of the CP [121, 124, 159]. If this is not possible, the effect of the uncontrolled approximations must be carefully investigated by performing multiple computations involving different approximation schemes. Therefore, the further development of new numerical and analytical approaches within functional methods for the study of this region in the phase diagram is subject to a lot of research, see, e.g., Refs. [213–215, 378–383]. Still, it requires probably a lot of collaborative work combining experimental data analysis and theoretical modeling to tackle this region of the phase diagram, where first-principles results from theory are not available.

Since quantitative, theoretical computations can be incredibly involved both in terms of complexity as well of numerical sophistication, effective model calculations can provide hints for the appearance of novel phenomena. These investigations can be thought of as exploratory works focusing on the discovery of novel mechanism to provide guidelines for more involved studies. This is motivated also by the findings in this thesis, see Section 8.2.1, where multiple new aspects of exotic regimes were covered under the formulated **RO**s. These results can be build upon in the future to tackle the phase structure of QCD from different sides.

For example, findings from model calculations can lead to the development of new approaches within functional methods, see, for example, Refs. [102, 215] for the search for inhomogeneous chiral condensates. Further, model calculations can provide substantial weight for the focus of further involved experimental and theoretical investigations. This is achieved by providing novel experimental signatures of exotic regimes, such as the enhancement of dilepton production in the moat regime [11]. The quantitative precision of these signatures can later be improved upon using functional methods, see Ref. [166] for first attempts in this direction.

Nevertheless, one has to admit that all of these approaches always only provide tiny steps towards a realistic picture of the QCD phase diagram. The quality of predictions is far away from state-of-the-art LFT predictions for QCD at non-zero temperatures but zero density. In the end, to get accurate first-principles results in the (μ, T) plane, developments in the hardware and algorithmic side of quantum computing are necessary to provide a platform for these computations in the next decades. This technology is expected to provide the solution to the sign problem of lattice QCD in the end [132].

2 The formatting of the sentence in quotation marks is modified compared to the original text in the thesis.

APPENDIX

A

CONVENTIONS, DEFINITIONS AND MORE

This chapter summarizes the unit system, the wick rotation from Minkowski to Euclidean spacetime and chosen representations of the Clifford algebra in $1+1$ and $2+1$ spacetime dimensions. This serves as supplementary material for the main part of the thesis. Moreover, we briefly discuss the representation theory of the Poincaré group for standard spin-0 and spin-$1/2$ fields in $1+1$ and $2+1$ Euclidean spacetime dimensions. Due to the nature of this appendix, none of its content is original to this thesis and can be found elsewhere. A decent effort was put into referencing appropriate publications whenever possible, but much of the content in this chapter is repetitively used in the community such that it is difficult to identify original works. In these cases, the reader shall refer to common textbooks and lecture notes on QFT such as Refs. [278–281].

A.1 UNITS

In this section, the used unit system is briefly introduced. Note, however, that we typically work with ratios of dimensionful quantities and avoid quantifying the absolute values of physical observables and thermodynamic parameters. The reason for this is that this thesis mostly deals with qualitative behaviors of strongly-interacting systems at non-vanishing temperatures and chemical potentials. As discussed in Chapter 1, QCD is not accessible in this regime and, thus, our models are only effective descriptions for certain aspects of QCD. We do not aim to provide quantitative predictions but instead investigate underlying mechanisms for the generation of exotic phases in QCD at non-vanishing temperatures and chemical potentials. Consequently, the choice of unit system is not relevant in terms of the prediction of quantitative values of observables. It plays, however, a major role when comparing formulae from within this thesis to other literature results with different conventions.

A variant of natural units is used in this work. These are defined by setting the Boltzmann constant $k_B = 1$, the speed of light in vacuum $c = 1$ as well as $\hbar = 1$, i.e., all of these constant are chosen to be dimensionless. This unit system is rather standard in high energy physics as it massively reduces the number of constants in equations and allows to express all quantities in this thesis in terms of their energy dimensions. For example, temperatures, chemical potentials and masses have the dimension of an energy, while length and time are given in units of inverse energy. Thereby, this unit system implicitly implements the concept from special relativity of treating space and time equally. For conversion to SI units, one typically uses $\hbar c \approx 197.329\ldots$ MeVfm. In natural units, actions are dimensionless such that the path integral formalism does not require dimensionful prefactors in front of the action of the theory, see Chapter 2.

A.2 WICK ROTATION

In this section, we present examples for the changes in the path integral formulation of QFTs from the analytical continuation from real to imaginary spacetime. The starting point is the formulation of the QFT in Minkowski spacetime, see Eqs. (2.1) and (2.2), with metric

$$\eta_{\mu\nu} = \text{diag}\,(1, -1, \ldots, -1) \tag{A.1}$$

for $\mu, \nu = 0, 1, \ldots, d$. As outlined in Section 2.1.1, we perform the substitution $\tau = \mathrm{i}x_0^M$ and leaving the spatial coordinates to transform from $x_M = (x_0, \boldsymbol{x})^T$ to Euclidean spacetime coordinates $x_E = (\boldsymbol{x}, \tau)^T$. Thereby, τ is real-valued such that the original time coordinate must be purely imaginary. From this substitution stems the name "imaginary time formalism". The metric of Euclidean spacetime is defined as $\eta_{\mu\nu,E} = \delta_{\mu,\nu}$ such that one finds $\mathrm{d}s_M^2 = -\left(\mathrm{d}s_E\right)^2$ for the Minkowski and Eucilidean spacetime differences, see Eq. (2.8).

A.2.1 *Consequences for the action of common field theories*

In this subsection, we present the application of the Wick rotation to the action and partition function of common free field theories. We start with the free Dirac action without a bare mass term

$$\mathcal{S}_M[\bar{\psi}, \psi] = \int \mathrm{d}^{d+1}x_M \bar{\psi}\mathrm{i}\not{\partial}_M\psi = \bar{\psi}\gamma_M^\mu\partial_{\mu,M}\psi \tag{A.2}$$

where the γ_M^μ matrices fulfill the Clifford algebra

$$\{\gamma_M^\mu, \gamma_M^\nu\} = \gamma_M^\mu\gamma_M^\nu + \gamma_M^\nu\gamma_M^\mu = 2\eta_M^{\mu\nu}1, \quad \mu, \nu = 0, \ldots, d. \tag{A.3}$$

In order to define a similar relation for the Euclidean Gamma matrices with the Euclidean metric, one needs to make the substitution

$$\gamma_E^{d+1} = \gamma_M^0, \qquad \gamma_E^j = \mathrm{i}\gamma_M^j, \qquad j = 1, \ldots, d, \tag{A.4}$$

i.e., the spatial Gamma matrices pick up an additional factor of i. This leads to the Euclidean Gamma matrices fulfill a similar relation to Eq. (A.3), but with the Euclidean metric, see Appendix A.3 for details. Thus, we get for the kinetic term of the fermions

$$\not{\partial}_M = -\gamma_M^i\partial_m^i + \gamma_M^0\partial_{0,M} = \mathrm{i}\gamma_E^i\partial_E^i + \mathrm{i}\gamma_E^{d+1}\partial_E^{d+1} = \mathrm{i}\not{\partial}_E \tag{A.5}$$

which is inserted into Eq. (A.6) resulting in

$$\mathcal{S}_M[\bar{\psi}, \psi] = -\mathrm{i}\int \mathrm{d}^{d+1}x_E\bar{\psi}\left[-\gamma_E^\mu\partial_{\mu,E}\right]\psi \equiv \mathrm{i}\mathcal{S}_E[\bar{\psi}, \psi]. \tag{A.6}$$

Thus, the path integral transforms as

$$Z \sim \int \mathscr{D}\bar{\psi}\mathscr{D}\psi \mathrm{e}^{\mathrm{i}\mathcal{S}_M[\bar{\psi},\psi]} = \int \mathscr{D}\bar{\psi}\mathscr{D}\psi \mathrm{e}^{-\mathcal{S}_E[\bar{\psi},\psi]}, \tag{A.7}$$

i.e., the difficult to evaluate oscillatory, complex-valued integrand is transformed into a real-valued integrand that can be interpreted as a probability distribution for the fermionic fields.

Similar transformations can be performed, e.g, for scalar, spin-0 fields where the Klein-Gordon operators $\partial_{0,M}^2 - \nabla_M^2$ changes to $-\partial_E^2 - \nabla_E^2$ leading to a similar transformation of the respective path integral to a probability distribution. This leads, together with the transformation of the spacetime integration measure and the definition of a Euclidean action, to a change of the sign of the bare mass term in the action.

A.2.2 *Example: Four-fermion model with both scalar and vector interactions*

For interacting theories, one has to be careful to properly handle the signs and prefactors of coupling constants. We briefly discuss the Wick rotation at the example of the four-fermion model (6.1) studied in Chapter 6. Here, it is particularly important to be clear about the used conventions in Minkowski spacetime and for the Wick rotation (especially for the Euclidean Gamma matrices) since the applied conventions might results in different prefactors and signs in the theory. This subsection is adapted from Appendix A of Ref. [3].

In $(2+1)$-dimensional spacetime with the metric $\eta_{\mu\nu} = \mathrm{diag}(1,-1,-1)$ we demonstrate the Wick rotation using the action (6.1) and partition function

$$\mathcal{S}_{M,\mathrm{mix}}[\bar{\psi},\psi] = \int \mathrm{d}x_0 \int \mathrm{d}^2x \Big\{ \bar{\psi}\left(\mathrm{i}\gamma_M^\nu\, \partial_{\nu,M}\right)\psi + \left[\tfrac{\lambda_S}{2N_f}\left(\bar{\psi}\,\psi\right)^2 + \tfrac{\lambda_V}{2N_f}\left(\bar{\psi}\,\mathrm{i}\gamma_M^\nu\,\psi\right)\left(\bar{\psi}\,\mathrm{i}\gamma_{M,\nu}\,\psi\right)\right]\Big\}, \tag{A.8}$$

$$Z = \int \mathscr{D}\bar{\psi}\mathcal{D}\psi\, \mathrm{e}^{\mathrm{i}\mathcal{S}_{M,\mathrm{mix}}[\bar{\psi},\psi]} \tag{A.9}$$

with appearing variables as defined below Eq. (6.1) and in Section 2.3. The Gamma matrices γ_M^ν fulfill Eq. (A.3) for $d = 2$ as usual. For the Wick rotation we use the conventions discussed above, such that one obtains $(\gamma_{\nu,E})^2 = 1$. This changes the vector interaction term in the following way

$$\left(\bar{\psi}\,\mathrm{i}\gamma_M^\nu\,\psi\right)\left(\bar{\psi}\,\mathrm{i}\gamma_{M,\nu}\,\psi\right) = \left(\bar{\psi}\,\mathrm{i}\gamma_M^0\,\psi\right)^2 - \left(\bar{\psi}\,\mathrm{i}\gamma_M^j\,\psi\right)^2 = \left(\bar{\psi}\,\mathrm{i}\gamma_3\,\psi\right)^2 + \bar{\psi}\left(\,\mathrm{i}\gamma_j\,\psi\right)^2 \tag{A.10}$$

where the additional factor $(-\mathrm{i})^2 = -1$. Moreover, there is an overall additional "-" sign in front of the Euclidean interaction terms stemming from the factor of $-\mathrm{i}$ that comes from $\mathrm{d}^3x_M = -\mathrm{i}\mathrm{d}^3x_E$. With the other standard changes of the action and the definition $\mathcal{S}_{M,\mathrm{mix}} = \mathrm{i}\mathcal{S}_{E_,\mathrm{mix}}$ one obtains the Euclidean action Eq. (6.1).

A.3 GAMMA MATRICES AS REPRESENTATIONS OF THE CLIFFORD ALGEBRA

In this chapter, we already introduced the Gamma matrices γ_μ as representations of the Clifford algebra (A.3) in $d+1$ spacetime dimensions with Minkowski metric $\eta_{\mu\nu} = \mathrm{diag}(1,-1,\ldots,-1)$. The size of the Gamma matrices d_γ is closely connected to the number of spacetime dimensions. As we restrict ourselves to $d = 1,2$, we have $d_\gamma = 2$ and $d_\gamma = 4$.

For the most part of this thesis we work in Euclidean spacetime, i.e., the metric is given by $\delta_{\mu\nu} = \mathrm{diag}(1,1,\ldots,1)$, see Section 2.1 and Appendix A.2 for a discussion of the Wick rotation. The anti-commutation relation (A.3) is then replaced by

$$\{\gamma_\mu,\gamma_\nu\} = 2\delta_{\mu\nu}1, \quad \mu,\nu = 1,\ldots d+1. \tag{A.11}$$

where $\mu = d+1$ describes the Euclidean time component. Typically, one searches for irreducible representations of the algebra Eq. (A.3) or Eq. (A.11) in order to define the Gamma matrices. In odd spacetime dimensions, this is not necessarily the case as we will discuss below at the example of $2+1$ dimensions.

The Gamma matrices behave fundamentally different in even and odd spacetime dimensions, see, e.g., Ref. [384] for a compact presentation of representations of the Clifford algebra in different spacetime dimensions. When $d+1$ is even and an irreducible representation of the Clifford algebra is used, there generically exists one matrix that anti-commutes

with all γ matrices.[1] This matrix is typically called the chiral gamma matrix or chiral operator, denoted by γ_{ch} in this thesis, as it can be used to define so-called chiral projectors $\sim (1 \pm \gamma_5)$. A generic definition of γ_5 in even spacetime dimensions is

$$\gamma_{\text{ch}} = -(-\mathrm{i})^{\frac{d+1}{2}-d} \gamma_M^1 \dots \gamma_M^d \gamma_M^0 = -(-\mathrm{i})^{\frac{d+1}{2}} \gamma_1 \dots \gamma_{d+1} \tag{A.12}$$

where we used both the Gamma matrices in Minkowski and Euclidean spacetime with conventions from the Wick rotation given in Section 2.1. The chiral projectors can be used to project out the parts of a spinor ψ with left- or right-handed chirality. Left- and right-handed spinors transform differently under chiral symmetry transformations. The free Dirac Lagrangian is only invariant under chiral symmetry transformations when the mass term is set to zero, i.e., for massless fermions. This is because a mass term mixes left- and right-handed components of the spinor breaking chiral symmetry. The particular definition of chirality is specific to the number of spacetime dimensions and the dimensionality of the representation of the Clifford algebra, as discussed in Appendix B.

In odd spacetime dimensions, the irreducible representation of the Clifford algebra corresponds to the one from one dimension lower where the "missing" Gamma matrix is chosen to be proportional to the chiral Gamma matrix from one dimension lower. In this case, no chirality operator γ_{ch} can be defined, i.e., one cannot find a matrix that anti-commutes with all γ_μ [385]. Consequently, no axial chiral symmetry can be defined in this case and spinors cannot be decomposed into left- and right-handed components. In irreducible representations of the Clifford algebra in odd spacetime dimensions, it is, thus, not possible to define chirality and chiral symmetry. Moreover, there typically exist two independent irreducible representations in odd spacetime dimensions that cannot be related by such transformations. In even spacetime dimensions, in contrast, different irreducible representations of the Clifford algebra can be related through similarity transformations involving γ_{ch}, which is not present in odd spatial dimensions. We are unaware whether a rigorous proof of this statement exists for arbitrary odd spatial dimensions, but below an example for $2+1$ dimensions is given. Since we are interested in the study of regimes that also involve the possibility of spontaneous chiral symmetry breaking, it is instructive to use reducible representations of the Clifford algebra. This is common in the literature of $2+1$-dimensional QFTs involving fermions that feature an internal symmetry group, see Appendix B.2. In particular, this approach is also relevant for the study of condensed matter systems involving the description of electrons[2]. In the reducible representation, it is possible to define chiral symmetry and chiral projectors appropriately. Of course, the usage of a reducible representation comes at the price of introducing ambiguities in these definitions as well as in the definition of other spacetime symmetries, e.g., of parity, time-reversal and charge conjugations transformation, on the level of spinors. This becomes relevant at the example of the spinors in $2+1$ dimensions, see below and Appendix B.2.

1 When using a reducible representation, the Gamma matrices are typically taken from a representation of the Clifford algebra of two dimensions higher. Then, there exists multiple matrices that anti-commute with all γ matrices.

2 For example, these applications involve effective field theories for graphene and other planar systems [262–266, 271].

A.3.1 $1+1$ *dimensions*

We start with the irreducible representation of the Clifford algebra in $1+1$ dimensions. In Minkowski spacetime with metric $\eta_{\mu\nu} = \mathrm{diag}(1,-1)$, the Gamma matrices are chosen to be in Weyl basis, i.e.,

$$\gamma^0_M = \sigma_1, \qquad \gamma^1_M = -\mathrm{i}\sigma_2, \tag{A.13}$$

with the Pauli matrices (extended by the identity matrix)

$$\sigma_0 = \begin{pmatrix} +1 & 0 \\ 0 & +1 \end{pmatrix}, \quad \sigma_1 = \begin{pmatrix} 0 & +1 \\ +1 & 0 \end{pmatrix}, \quad \sigma_2 = \begin{pmatrix} 0 & -\mathrm{i} \\ \mathrm{i} & 0 \end{pmatrix}, \quad \sigma_3 = \begin{pmatrix} +1 & 0 \\ 0 & -1 \end{pmatrix}, \tag{A.14}$$

There exists another, additional matrix that anti-commutes with all γ matrices, the chirality operator denoted by γ_{ch} in analogy to the usual notation in $3+1$ dimensions. In $1+1$ dimensions, it is proportional to the "unused" Pauli matrix, i.e., in our conventions

$$\gamma_{\mathrm{ch}} = \gamma^0_M \gamma^1_M = -\gamma^1_M \gamma^0_M = \sigma_3. \tag{A.15}$$

This operator can be used to define axial symmetries of theories, e.g., of the free Dirac Lagrangian as discussed in Appendix B.1.

The Euclidean γ matrices are then given by

$$\gamma_1 = \sigma_2, \qquad \gamma_2 = \sigma_1, \tag{A.16}$$

where we used that the definition of the chirality operator does not change under Wick rotation. The chirality operator is similar to the one in Minkowski spacetime, i.e., $\gamma_{\mathrm{ch}} = \mathrm{i}\gamma_1\gamma_2 = \sigma_3$, as discussed above. Moreover, we define chiral projectors

$$\gamma_{R/L} = \frac{1}{2}(1 \pm \gamma^5) \tag{A.17}$$

such that

$$\gamma_R = \begin{pmatrix} 1 & 0 \\ 0 & 0 \end{pmatrix}, \quad \gamma_L = \begin{pmatrix} 0 & 0 \\ 0 & 1 \end{pmatrix}. \tag{A.18}$$

These are in particular relevant in the analysis of the chiral GN model in Section 4.3.

A.3.2 $2+1$ *dimensions*

In odd spacetime dimensions, there exists an ambiguity in the representation of Clifford algebra, i.e., two independent irreducible representations which cannot be related by a similarity transformation. In Minkowski spacetime the two, irreducible representations are

$$\gamma^0_M = +\sigma_1, \qquad \gamma^1_M = -\mathrm{i}\sigma_2, \qquad \gamma^2_M = -\mathrm{i}\sigma_3 \tag{A.19}$$

and

$$\tilde{\gamma}^0_M = -\sigma_1, \qquad \tilde{\gamma}^1_M = +\mathrm{i}\sigma_1, \qquad \tilde{\gamma}^2_M = +\mathrm{i}\sigma_2. \tag{A.20}$$

Since there exist no further anti-commuting matrix in both of these representations, one cannot define a chirality operator and chiral projectors in these representations. Thus, one

cannot define chirality and chiral symmetry in $2+1$ dimensions. Consequently, irreducible representations are not suited for the study of chiral symmetry breaking in $2+1$ dimensions which is crucial for the study of exotic phases in fermionic systems at non-zero densities.

In investigations of chiral symmetry breaking in $2+1$ dimensions, one therefore typically chooses a 4×4 representation of the Clifford algebra [274, 385], corresponding to using Gamma matrices from $3+1$ dimensions. Whenever needed, we choose for the basis of Gamma matrices in $2+1$ dimensions specifically as

$$\gamma_M^0 = \sigma_3 \otimes \sigma_1, \qquad \gamma_M^1 = \sigma_3 \otimes (-\mathrm{i}\sigma_2)\,, \qquad \gamma_M^2 = \sigma_3 \otimes (-\mathrm{i}\sigma_3)\,. \tag{A.21}$$

After Wick rotation, the Euclidean γ matrices are

$$\gamma^1 = \sigma_3 \otimes \sigma_2, \quad \gamma^2 = \sigma_3 \otimes \sigma_3, \quad \gamma^3 = \sigma_3 \otimes \sigma_1. \tag{A.22}$$

Using this reducible representation leaves two anticommuting matrices, i.e., the chirality operator is ambiguous. These two matrices are the chirality operator from $3+1$ dimensions as well as proportional to one leftover spatial Gamma matrix from $3+1$ dimensions. In the above basis (A.22), these are[3]

$$\gamma_4 = \sigma_1 \otimes \sigma_0, \qquad \gamma_5 = -\sigma_2 \otimes \sigma_0. \tag{A.23}$$

Both of these matrices generate axial symmetry transformations that leave the free Dirac lagrangian invariant, compare Appendix B.2. Additionally, there exists a further, independent matrix

$$\gamma_{45} = \mathrm{i}\gamma_4\gamma_5 = \sigma_3 \otimes \sigma_0. \tag{A.24}$$

that commutes with the Gamma matrices and generates a vector symmetry transformation (B.8). Note that γ_4, γ_5 and, consequently, also γ_{45} are not affected by the Wick rotation, i.e., both Eq. (A.23) and Eq. (A.24) would be appropriate operators in Minkowski spacetime as well. We chose γ_4, γ_5 and γ_{45} to be self-inverse and hermitian. All three matrices can be used to define chiral projectors similar to Eq. (A.17).

A.4 FIELDS AS REPRESENTATIONS OF THE POINCARÉ GROUP

In this section, we present representations of the Poincaré group in $1+1$ and $2+1$ Euclidean spacetime dimensions for bosonic fields with spin 0 and fermionic fields with spin $1/2$. This discussion is mostly based on the Appendix B of Ref. [344] and not original to this thesis. Moreover, representation theory of the Poincaré group is covered in many textbooks, lecture notes and reviews such as, e.g., Refs. [278, 279, 386].

For the purpose of this discussion, we only concentrate on the Poincaré symmetry on a single field, that transforms according to its respective spin. The transformations contained as elements in the Poincaré group can be categorized as (Euclidean) Lorentz transformations and spacetime translations. Moreover, only proper Lorentz transformations are discussed, while discrete spacetime symmetries are neglected. Note that in Euclidean spacetime it is possible to define the Lorentz transformations as a product of proper transformations, i.e.,

3 This choice is not unique. With reducible representations, a Weyl basis (which is used in $1+1$ dimensions) is, unfortunately, not sensible since both γ_4 and γ_5 generate axial transformations and spinors can be decomposed according to both matrices. A Weyl basis is defined by having a diagonal chirality operator such that chiral projectors project out certain components of the spinor. This is not possible to guarantee for both both choices of projectors corresponding to γ_4 and γ_5, respectively.

with determinant 1, and a discrete Z_2-symmetry. This discrete symmetry can for example be chosen as time reversal or parity (the latter has to be defined as the inversion of an odd number of cartesian coordinate axes; otherwise it is part of the proper Lorentz transformations for two spatial dimensions). From now, we always discuss transformations in Euclidean spacetime and do not specifically mention it the geometry of spacetime. At first, we discuss general properties of Poincaré transformations in d dimensions.

We start by defining a Poincaré transformation T through its action on spacetime vectors or, equivalently, spin 1 fields, i.e.

$$x' = T(\Lambda, a)x = \Lambda x + a\,. \tag{A.25}$$

with a spacetime vector $a = (a_0, \ldots, a_{d-1})^T$. The proper Lorentz transformation Λ is element of $\mathrm{SO}(d)$. An infinitesimal Lorentz transformation is given by

$$\Lambda_{\mu\nu} = \delta_{\mu\nu} + \epsilon_{\mu\nu} \tag{A.26}$$

with arbitrary small parameters $\epsilon_{\mu\nu} = -\epsilon_{\nu\mu}$.

Then, we consider the representation $U(\Lambda, a)$ of the Poincaré group on another vector space, i.e., on other physical entities. The elements $U(\Lambda, a)$ are written as

$$U(\Lambda, a) = \mathrm{e}^{-\frac{\mathrm{i}}{2}\epsilon_{\mu\nu}M_{\mu\nu}}\mathrm{e}^{-\mathrm{i}a_\mu P_\mu} = 1 - \frac{\mathrm{i}}{2}\epsilon_{\mu\nu}M_{\mu\nu} - \mathrm{i}a_\mu P_\mu + \ldots\,, \tag{A.27}$$

where $M_{\mu\nu}$ denote the anti-symmetric generators for Lorentz transformations. These generate rotations in Euclidean spacetime. Moreover, P_μ denote the generators for translations and a_μ is the parameter for the translation. The operators $M_{\mu\nu}$ and P_μ form a Lie algebra, the Poincaré algebra, whose commutation relations are given by[4]

$$[M_{\alpha\beta},\, M_{\gamma\delta}] = \mathrm{i}\left(\delta_{\beta\gamma}M_{\alpha\delta} + \delta_{\alpha\delta}M_{\beta\gamma} - \delta_{\alpha\gamma}M_{\beta\delta} - \delta_{\beta\delta}M_{\alpha\gamma}\right), \tag{A.28a}$$

$$[P_\alpha,\, P_\beta] = 0, \tag{A.28b}$$

$$[P_\alpha,\, M_{\beta\gamma}] = \mathrm{i}\left(\delta_{\alpha\beta}P_\gamma - \delta_{\alpha\gamma}P_\beta\right). \tag{A.28c}$$

A specific representation for the generators can be[5]

$$M_{\mu\nu} = \mathrm{i}\left(x_\mu\partial_\nu - x_\nu\partial_\mu\right) + S_{\mu\nu}, \qquad P_\mu = -\mathrm{i}\partial_\mu\,, \tag{A.29}$$

where $S_{\mu\nu}$ is a spin structure that vanishes for scalar fields. In general, $S_{\mu\nu} = -S_{\nu\mu}$. A scalar field ϕ transforms under Lorentz transformations under this specific representation with $S_{\mu\nu} = 0$

$$\phi'(x') = U(\Lambda, 0)\phi(\Lambda x) = \mathrm{e}^{-\frac{\mathrm{i}}{2}\epsilon_{\mu\nu}M_{\mu\nu}}\phi(\Lambda x). \tag{A.30}$$

Considering only infinitesimal transformation, this expression is expanded up to $O(\epsilon^2)$ corrections to

$$\begin{aligned}\phi'(x') &\approx \left(1 - \frac{\mathrm{i}}{2}\epsilon_{\mu\nu}M_{\mu\nu}\right)\left[\phi(x) + \epsilon_{\mu\nu}x_\nu\partial_\mu\phi(x)\right] \\ &= \phi(x) + \frac{1}{2}\epsilon_{\mu\nu}\left(x_\mu\partial_\nu - x_\nu\partial_\mu\right)\phi(x) + \epsilon_{\mu\nu}x_\nu\partial_\mu\phi(x) = \phi(x),\end{aligned} \tag{A.31}$$

4 These relations can, for example, be derived from the condition $U(\Lambda, a)\,U\left(\Lambda', a'\right)U^{-1}(\Lambda, a) = U\left(\Lambda\Lambda'\Lambda^{-1}, a + \Lambda a' - \Lambda\Lambda'\Lambda^{-1}a\right)$, which follows the composition rules for the representation $T(\Lambda, a)$. One inserts infinitesimal transformations (A.27) and keeps only linear terms in all group parameters.

5 The generators are chosen such that we obtain transformations of spin 0 and spin 1/2 fields. One can also obtain the spacetime transformation (A.25). Then each of the $M_{\mu\nu}$ has a matrix structure in spacetime.

where in the last step we use the anti-symmetry of the parameters $\epsilon_{\mu\nu}$ and relabel the summation indices. As we can express general Lorentz transformations via infinitesimal transformations, we obtain the expected invariance of scalar fields.[6]. One can perform the same calculation for translations $U(\mathbb{I}, a)$ and obtain

$$\phi'(x') = \phi'(x + a) = \phi(x). \tag{A.32}$$

Spin-1/2 fermion fields transform under Poincaré transformations as

$$\psi'(x') = U(\Lambda, 0)\psi(\Lambda x) = \mathrm{e}^{-\frac{\mathrm{i}}{2}\epsilon_{\mu\nu}S_{\mu\nu}}\psi(x) \tag{A.33}$$

with parameters $\omega_{\mu\nu} = -\omega_{\nu\mu}$, where we implicitly used the invariance of the spinor field under the part of the transformation generated by $M_{\mu\nu}$. This invariance can be derived similar to Eq. (A.31). Here, in the last step we used Eq. (A.31). The additional spin structure $S_{\mu\nu}$ of the generators can be constructed using representations of the Clifford algebra, c.f. Appendix A.3,

$$S_{\mu\nu} = \frac{\mathrm{i}}{4}\left[\gamma_\mu, \gamma_\nu\right]. \tag{A.34}$$

Then, the spinor transformations U fulfill

$$U^{-1}(\Lambda)\gamma_\mu U(\Lambda) = \Lambda_{\mu\nu}\gamma_\nu \tag{A.35}$$

such that the Lagrangian of free spinor fields is invariant under (Euclidean) Lorentz transformations.

A.4.1 $1+1$ *dimensions*

The Lorentz transformation Λ is an element of SO(2). An element O of SO(2) can be expressed as

$$O = \mathrm{e}^{\mathrm{i}\theta\sigma_2} = \cos(\theta) + \mathrm{i}\sin(\theta)\sigma_2\,, \text{t} \tag{A.36}$$

where τ_2 is the second Pauli matrix and θ is a real parameter. Hence, the group elements are connected continuously and can be represented by iterative application of infinitesimal transformations.

In $1+1$ dimensions, an irreducible representation of the Euclidean Clifford algebra is given by Eq. (A.16). The transformation behavior of fermion fields (A.33) can be explicitly written as

$$\psi'(x') = \mathrm{e}^{\frac{\mathrm{i}}{2}\epsilon_{01}\sigma_3}\psi(x). \tag{A.37}$$

using the one, independent generator $S_{01} = -\frac{\sigma_3}{2}$ With parameter $\epsilon = \epsilon_{01}$ the transformation matrix is given by

$$\mathrm{e}^{\frac{\mathrm{i}}{2}\epsilon\sigma_3} = \begin{pmatrix} \mathrm{e}^{\frac{\mathrm{i}\epsilon}{2}} & 0 \\ 0 & \mathrm{e}^{-\frac{\mathrm{i}\epsilon}{2}} \end{pmatrix}. \tag{A.38}$$

6 Besides the non-vanishing spin structure $S_{\mu\nu}$ when considering fields with a spin, this transformation shall also hold for all higher spin fields.

A.4.2 $2+1$ *dimensions*

In $2+1$ dimensions the Lorentz transformation Λ is element of SO(3), as demonstrated in the following. Elements $R \in \mathrm{SO}(3)$ can be expressed by

$$R = \mathrm{e}^{\mathrm{i}\theta_j T_j} \tag{A.39}$$

with three parameters θ_j and generators

$$T_0 = \mathrm{i}\begin{pmatrix} 0 & 0 & 0 \\ 0 & 0 & -1 \\ 0 & +1 & 0 \end{pmatrix}, \quad T_1 = \mathrm{i}\begin{pmatrix} 0 & 0 & 1 \\ 0 & 0 & 0 \\ -1 & 0 & 0 \end{pmatrix}, \quad T_2 = \mathrm{i}\begin{pmatrix} 0 & -1 & 0 \\ +1 & 0 & 0 \\ 0 & 0 & 0 \end{pmatrix}. \tag{A.40}$$

The commutation relation between the generators are

$$[T_j, T_k] = \mathrm{i}\epsilon_{jkl} T_l \tag{A.41}$$

with the three-dimensional Levi-Civita symbol, which is the Lie algebra of SO(3). This commutation relations are similar to the ones of orbital angular momentum operators, i.e., the specific choice of the generators T_j generate rotations in a three-dimensional Euclidean space.

There exist three independent generators for Lorentz transformations $M_{\mu\nu}$ and three generators for spacetime translations P_μ in $2+1$ spacetime dimensions. One can unambiguously map the matrix-valued $M_{\mu\nu}$ to vectors

$$L_\alpha = -\frac{\epsilon_{\alpha\beta\gamma}}{2} M_{\beta\gamma} \qquad \leftrightarrow \qquad M_{\alpha\beta} = -\epsilon_{\alpha\beta\gamma} L_\gamma \,. \tag{A.42}$$

The Poincaré algebra (A.28) translates to

$$[L_\mu, L_\nu] = \mathrm{i}\epsilon_{\mu\nu\rho} L_\rho \,, \tag{A.43a}$$
$$[P_\mu, L_\nu] = \mathrm{i}\epsilon_{\mu\nu\rho} P_\rho \,, \tag{A.43b}$$
$$[P_\mu, P_\nu] = 0 \,, \tag{A.43c}$$

i.e. the generators of Lorentz transformations L_α fulfill the algebra (A.41).

Fermion fields transform as

$$\psi'(x') = \mathrm{e}^{-\frac{\mathrm{i}}{2}\epsilon_{\mu\nu} S_{\mu\nu}} \psi(x) \tag{A.44}$$

where we now have three independent generators

$$S_{\mu\nu} = \frac{\mathrm{i}}{4} [\gamma_\mu, \gamma_\nu] \,. \tag{A.45}$$

As $S_{\mu\nu}$ involves the Gamma matrices, i.e., representations of the Clifford algebra (A.11), the transformation behavior of spinors will differ between irreducible representations, such as Eq. (A.19) (up to Wick rotation to Euclidean spacetime), and reducible ones, such as Eq. (A.22).

TWO-COMPONENT SPINOR REPRESENTATIONS In the irreducible, 2×2 representations with Pauli matrices the generators $S_{\mu\nu}$ are given by

$$S_{01} = -\frac{\sigma_1}{2}, \qquad S_{02} = \frac{\sigma_3}{2}, \qquad S_{12} = -\frac{\sigma_2}{2}, \tag{A.46}$$

i.e., they fulfill the algebra of SU(2)

$$\mathrm{su}(2) = \left\{ A \in \mathbb{C}^{2\times 2} : A + A^\dagger = 0, \mathrm{tr}(A) = 0 \right\}, \tag{A.47}$$

which is isomorphic to the one of SO(3) (A.41). Consequently, the matrices

$$U = \mathrm{e}^{-\frac{\mathrm{i}}{2}\epsilon_{\mu\nu}S_{\mu\nu}} = e^{\frac{\mathrm{i}}{2}\varepsilon_\alpha\sigma_\alpha} \tag{A.48}$$

are elements of SU(2). We define $\varepsilon = (\epsilon_{01}, \epsilon_{12}, -\epsilon_{02})$ and $\sigma = (\sigma_1, \sigma_2, \sigma_3)$ in the last step to choose a standard basis of SU(2) generators.

As well known (see, e.g., Ref. [278]), SU(2) is a double cover of SO(3), which is equivalent to the group of proper Euclidean Lorentz transformations in $2+1$ spacetime dimensions. This is demonstrated by considering rotations (A.48) and (A.39) around the x_1 axis ($\theta_0 = 0, \theta_2 = 0$ and $\varepsilon_0 = 0, \varepsilon_2 = 0$, respectively) for a spacetime vector a and a spinor ψ

$$a'(x') = \mathrm{e}^{\mathrm{i}2\pi T_2} a(x) = \begin{pmatrix} +\cos(2\pi) & 0 & -\sin(2\pi) \\ 0 & 1 & 0 \\ +\sin(2\pi) & 0 & +\cos(2\pi) \end{pmatrix} a(x) = a(x) \tag{A.49a}$$

$$\psi'(x') = \mathrm{e}^{\frac{\mathrm{i}}{2}2\pi\tau_2}\psi(x) = \begin{pmatrix} +\cos(\pi) & +\sin(\pi) \\ -\sin(\pi) & +\cos(\pi) \end{pmatrix} \psi(x) = -\psi(x)\,. \tag{A.49b}$$

Thus, after a full rotation around the x_1-axis the spinor is not mapped to itself. However, as one can easily see from the above calculation, performing a rotation with angle 4π results in $\psi'(x') = \psi(x)$. In general, a spinor rotates through half the angle that the spacetime vectors rotates through. Increasing a generic rotation angle by 2π one obtains $U \to -U$, $R \to R$. However, U and $-U$ both correspond to the rotation R, i.e., there is a two to one mapping of elements of SU(2) to elements of SO(3).

This is closely connected to the existence of two independent irreducible representations for the Clifford algebra, see Appendix A.3.1. Indeed, if one restricts the angles of rotation in (A.48) and (A.39) to $[0, 2\pi)$, one obtains the complete group of proper Lorentz transformation on spacetime vectors. To regain the complete group of spinor transformations one can use a second basis of generators $\sigma' = (-\sigma_1, -\sigma_2, -\sigma_3)^T$ in addition to the set of Pauli matrices defined in Eq. (A.48). Both choices of generator representations are not not equivalent but fulfill both the Clifford algebra (A.11) in $2+1$ spacetime dimensions as well as the SU(2) algebra (A.47).

FOUR-COMPONENT SPINOR REPRESENTATIONS In the reducible representation (A.21) the generators $S_{\mu\nu}$ are given by

$$S_{01} = \mathbb{1}_2 \otimes -\frac{\sigma_1}{2}, \qquad S_{02} = \mathbb{1}_2 \otimes \frac{\sigma_3}{2}, \qquad S_{12} = \mathbb{1}_2 \otimes -\frac{\sigma_2}{2}. \tag{A.50}$$

Consequently, the spinor transformation (A.44) takes the form of

$$U = \mathrm{e}^{-\frac{\mathrm{i}}{2}\epsilon_{\mu\nu}S_{\mu\nu}} = \mathrm{e}^{\frac{\mathrm{i}}{2}(\mathbb{1}_2\otimes\sigma)_\alpha\varepsilon_\alpha}. \tag{A.51}$$

with $\varepsilon = (\epsilon_{01}, \epsilon_{12}, -\epsilon_{02})^T$ and $\tau = (\tau_1, \tau_2, \tau_3)^T$. Using the matrix exponential we can rewrite

$$U = \begin{pmatrix} \mathrm{e}^{\frac{\mathrm{i}}{2}\epsilon_\mu \sigma_\mu} & 0 \\ 0 & \mathrm{e}^{\frac{\mathrm{i}}{2}\epsilon_\mu \sigma_\mu} \end{pmatrix}, \tag{A.52}$$

where the 2×2 blocks are again elements of SU(2). For four-component spinors, axial transformations, as, for example, Eq. (B.10) can be applied to obtain the full SU(2) group, even with the restriction $\epsilon \in [0, 2\pi)$, which is not possible when choosing one of the two differing irreducible two-component representations.

B

SYMMETRIES OF FERMIONS IN $d+1$ DIMENSIONS

In this chapter, we are going to discuss the symmetry transformations leaving the free, massless Dirac Lagrangian

$$\mathcal{L} = \bar{\psi}\left(\gamma_\mu \partial_\mu\right)\psi \tag{B.1}$$

in $d+1$ Euclidean spacetime dimensions invariant with $d = 1, 2$, as relevant for this dissertation. Note that the respectively used representations of the Dirac algebra for fixed d are given in Appendix A.3. Moreover, we show how certain interaction channels as well as (bare or dynamically generated) mass terms break these symmetries. Subgroups of symmetries, that are relevant for models discussed in Chapters 3 to 5, are defined as supplementary materifal for these chapters.

B.1 FERMIONS IN $1+1$ DIMENSIONS

In $1+1$ dimensions, the irreducible representation of the Dirac algrebra (A.11) is given by 2×2 matrices, see Eq. (A.16). The internal, chiral symmetry group of one species of fermions consists of the vector transformation

$$\mathrm{U}_V(1): \qquad \psi \to \mathrm{e}^{\mathrm{i}\alpha 1}\psi, \qquad \bar{\psi} \to \bar{\psi}\mathrm{e}^{-\mathrm{i}\alpha 1} \tag{B.2}$$

and the axial transformation

$$\mathrm{U}_A(1): \qquad \psi \to \mathrm{e}^{\mathrm{i}\beta\gamma_5}\psi, \qquad \bar{\psi} \to \bar{\psi}\mathrm{e}^{\mathrm{i}\beta\gamma_5} \tag{B.3}$$

with real parameters α, β. Thus, the full, internal symmetry group of Eq. (B.1) is given by $\mathrm{U}_V(1)\times\mathrm{U}_A(1)$.

B.1.1 *Generalization to N_f fermion species*

Often, we consider N_f identical copies of spinors, that are all contained in the field ψ. Thus, in the following (and also in the majority of this thesis) ψ implicitly represents $\left(\psi_1, \ldots, \psi_{N_f}\right)$ where each ψ_j is a 2-component spinor for $d = 1$. Consequently, symmetry transformation can always also be combined with any kind of rotation in the internal space of the N_f fermion species, as long as the action is diagonal in this space. This is always the case within this thesis. Thus, the full symmetry transformation, that leaves the free fermion action (B.1) invariant in this case, is given by $\mathrm{U}_V(N_f)\times\mathrm{U}_A(N_f)$ with

$$\begin{aligned}
&\mathrm{U}_V(N_f): && \psi \to \mathrm{e}^{\mathrm{i}\alpha^a 1 T^a}\psi, && \bar{\psi} \to \bar{\psi}\mathrm{e}^{-\mathrm{i}\alpha^a 1 T^a};\\
&\mathrm{U}_A(N_f): && \psi \to \mathrm{e}^{\mathrm{i}\beta^a\gamma_5 T^a}\psi, && \bar{\psi} \to \bar{\psi}\mathrm{e}^{\mathrm{i}\beta^a\gamma_5 T^a},
\end{aligned}$$

where T^a with $a = 1, \ldots, N_f^2 - 1$ are generalized $N_f \times N_f$ Gell-Mann matrices [387] and $T^{N_f^2} = 1$ is the $N_f \times N_f$ identity matrix. Moreover, α^a and β^a are real parameters.

B.1.2 *Subgroups*

In case of the GN model interaction term $\sim (\bar{\psi}\psi)^2$, the axial symmetry transformation of Eq. (B.3) is broken to a discrete subgroup. This is demonstrated in the following. Consider the application of the axial transformation $\mathrm{U}_A(N_f)$ (B.3) to the interaction term

$$(\bar{\psi}\psi)^2 \to \left(\bar{\psi}\mathrm{e}^{2\mathrm{i}\beta\gamma_5}\psi\right)^2 = \left[\bar{\psi}\left(\cos(2\beta) + \mathrm{i}\sin(2\beta)\gamma_5\right)\psi\right]^2 . \tag{B.4}$$

Thus, the interaction term is transformed into a combination of the original interaction term and the interaction term $(\bar{\psi}\mathrm{i}\gamma_5\psi)^2$ and a mixed term, which is not present in the original action (but is considered in the chiral GN model which is invariant under $\mathrm{U}_A(N_f)$). For the GN model, only an invariance is obtained when $\beta = n\frac{\pi}{2}$, $n \in \mathbb{Z}$. For even n the invariance is trivial, while for odd n one obtains the discrete subgroup

$$\psi \to \mathrm{i}^n\gamma_5\psi, \qquad \bar{\psi} \to \psi\mathrm{i}^n\gamma_5. \tag{B.5}$$

When combined with the vector transformation (B.2), this is written in the typical form in the literature

$$Z(2): \qquad \psi \to \gamma_5\psi, \qquad \bar{\psi} \to -\bar{\psi}\gamma_5. \tag{B.6}$$

Thus, the full symmetry group of the GN model is given by $\mathrm{U}_V(N_f) \times Z_2$.

B.2 FERMIONS IN 2 + 1 DIMENSIONS

The content of this section is mostly taken from Appendix A of Ref. [2]. In this section, we elaborate on the symmetries of free fermions in $2+1$ dimensions that are chosen as 4-component spinors in the reducible representation (A.22) of the Dirac algebra. This choice of Gamma matrices allows to define axial symmetries involving operators similar to the chirality operator in $3+1$ dimensions, which would not be possible using the irreducible representation. Apart from this, 4-component spinors in two spatial dimensions dimensions are chosen for applications where spontaneous internal symmetry breaking occurs, see, e.g., Refs. [259, 261, 268, 270, 274, 385]. First, we discuss symmetries of the free fermion action (B.1) in $2+1$ dimensions for $N_f = 1$ species of fermions without any additional degree of freedom.

B.2.1 *Chiral symmetry*

The free fermion action in $2+1$ Euclidean spacetime dimensions is invariant under the chiral symmetry group $U(2)$, in addition to the invariance under Poincaré transformations that is a priori present. This chiral symmetry group has 4 generators given by $1, \gamma_4, \gamma_5, \gamma_{45}$ (see Eqs. (A.23) and (A.24) for the definition of the additional matrices that are no representation of the Dirac algebra). Thereby, one distinguishes between the vector transformations

$$\mathrm{U}_1(1): \qquad \psi \to \mathrm{e}^{\mathrm{i}\alpha 1}\psi, \qquad \bar{\psi} \to \bar{\psi}\mathrm{e}^{-\mathrm{i}\alpha 1}; \tag{B.7}$$

$$\mathrm{U}_{\gamma_{45}}(1): \qquad \psi \to \mathrm{e}^{\mathrm{i}\beta\gamma_{45}}\psi, \qquad \bar{\psi} \to \bar{\psi}\mathrm{e}^{-\mathrm{i}\beta\gamma_{45}} \tag{B.8}$$

with real parameters α, β and the axial transformations

$$\mathrm{U}_{\gamma_4}(1): \qquad \psi \to \mathrm{e}^{\mathrm{i}\zeta\gamma_4}\psi, \qquad \bar{\psi} \to \bar{\psi}\mathrm{e}^{\mathrm{i}\zeta\gamma_4}; \tag{B.9}$$

$$\mathrm{U}_{\gamma_5}(1): \qquad \psi \to \mathrm{e}^{\mathrm{i}\iota\gamma_5}\psi, \qquad \bar{\psi} \to \bar{\psi}\mathrm{e}^{\mathrm{i}\iota\gamma_5} \tag{B.10}$$

with real parameters ζ, ι. The whole chiral symmetry group of one fermion species without an isospin degree of freedom is

$$\mathrm{U}_\gamma(2) : \psi \to U\psi \tag{B.11}$$

where U is a matrix element of the group $U(2)$.

B.2.2 *Generalization to N_f fermion species*

In order to adequately perform a large-N_f limit, we typically study N_f fermion species, i.e., ψ implicitly represents $\left(\psi_1, \ldots, \psi_{N_f}\right)$ where ψ_i each is a 4-component spinors for $d = 2$. Thus, each of the above chiral transformations is combined with rotation within the internal space of fermion species generated by $N_f \times N_f$ generalized Gell-Mann matrices T^a with $a = 1, \ldots, N_f^2 - 1$ and the $N_f \times N_f$ identity matrix $T^{N_f^2} = 1$. As above, we define the chiral transformations as

$$\mathrm{U}_1(N_f) : \qquad \psi \to \mathrm{e}^{\mathrm{i}\alpha^a 1 T^a}\psi, \qquad \bar\psi \to \bar\psi \mathrm{e}^{-\mathrm{i}\alpha^a 1 T^a}; \tag{B.12}$$

$$\mathrm{U}_{\gamma_{45}}(N_f) : \qquad \psi \to \mathrm{e}^{\mathrm{i}\beta^a \gamma_{45} T^a}\psi, \qquad \bar\psi \to \bar\psi \mathrm{e}^{-\mathrm{i}\beta^a \gamma_{45} T^a}; \tag{B.13}$$

$$\mathrm{U}_{\gamma_4}(N_f) : \qquad \psi \to \mathrm{e}^{\mathrm{i}\zeta^a \gamma_4 T^a}\psi, \qquad \bar\psi \to \bar\psi \mathrm{e}^{\mathrm{i}\zeta^a \gamma_4 T^a}; \tag{B.14}$$

$$\mathrm{U}_{\gamma_5}(N_f) : \qquad \psi \to \mathrm{e}^{\mathrm{i}\iota^a \gamma_5 T^a}\psi, \qquad \bar\psi \to \bar\psi \mathrm{e}^{\mathrm{i}\iota^a \gamma_5 T^a}; \tag{B.15}$$

with real parameters $\alpha^a, \beta^a, \zeta^a, \iota^a$. The chiral symmetry group of N_f fermion species without considering isospin is then

$$\mathrm{U}_\gamma(2N_f) : \psi \to U\psi \tag{B.16}$$

where U is a matrix element of the group $\mathrm{U}(2N_f)$.

B.2.3 *Isospin symmetry*

In Chapter 5, we also introduce an isospin degree of freedom allowing to additionally classify the fermion fields with isospin quantum numbers $I = \pm 1/2$. This additional degrees of freedom allows for the definition of isospin rotations of the group $\mathrm{U}_I(2)$, which is composed of $\mathrm{U}(1)$ axial transformation generated by the identity in isospin space and the vector transformation

$$\mathrm{SU}_{\vec\tau}(2) : \qquad \psi \to \mathrm{e}^{\mathrm{i}\vec\chi\vec\tau}\psi, \qquad \bar\psi \to \bar\psi \mathrm{e}^{-\mathrm{i}\vec\chi\vec\tau}. \tag{B.17}$$

Combined with the chiral symmetry group $\mathrm{U}_\gamma(2)$ (B.11) a single fermion species is invariant under the full symmetry group

$$\mathrm{U}(4) \cong \mathrm{U}_\gamma(2) \times \mathrm{U}_I(2). \tag{B.18}$$

Thus, for N_f fermion species, the full symmetry group is

$$\mathrm{U}(4N_f) \cong \mathrm{U}_\gamma(2N_f) \times \mathrm{U}_I(2) \tag{B.19}$$

under which the free fermion action (B.1) is invariant for $d = 2$ spatial dimensions.

B.2.4 *Subgroups*

However, when one adds interaction terms to the action, these terms possibly break the invariance under the full symmetry group. To avoid this, it is necessary to introduce a Fierz-complete set of four-fermion interaction channels with identical coupling constants. Then, each of the respective interaction terms is either invariant under Eq. (B.19) or transformed into another interaction term that is also present. This is, e.g., the case when using $\vec{\mathcal{C}} = \vec{\mathcal{C}}_s$ (5.2), $\vec{\mathcal{C}} = \vec{\mathcal{C}}_v$ (5.4) or $\vec{\mathcal{C}} = \vec{\mathcal{C}}_c$ (5.3) in the action (5.1) and $\lambda_j = \lambda_S$, $\forall j$.

However, sometimes it is necessary for phenomenological purposes to break the chiral symmetry group. For example, in QCD the axial $U_A(1)$ symmetry is broken by a quantum anomaly, which is typically modelled by hand in the Lagrangian of NJL-type models. In the following we provide a list of the relevant symmetry transformations as a reference for Table 5.3 and Table 5.4. Choosing a set of interaction channels such that one of the axial transformations (B.14) or (B.15) is broken (as in the second row of Table 5.3), the full symmetry group is reduced to a combined isospin and chiral rotation

$$\mathrm{SU}_{A,\gamma_4}(2N): \qquad \psi \to \mathrm{e}^{\mathrm{i}\zeta^{\vec{\prime}a}\vec{\tau}\gamma_4 T^a}\psi, \qquad \bar{\psi} \to \bar{\psi}\mathrm{e}^{\mathrm{i}\zeta^{\vec{\prime}a}\vec{\tau}\gamma_4 T^a}; \tag{B.20}$$

$$\mathrm{SU}_{A,\gamma_5}(2N): \qquad \psi \to \mathrm{e}^{\mathrm{i}\iota^{\vec{\prime}a}\vec{\tau}\gamma_5 T^a}\psi, \qquad \bar{\psi} \to \bar{\psi}\mathrm{e}^{\mathrm{i}\iota^{\vec{\prime}a}\vec{\tau}\gamma_5 T^a} \tag{B.21}$$

where $\zeta^{\vec{\prime}a}, \iota^{\vec{\prime}a}$ are real-valued, three-component isovectors and $a = 1, \ldots, N_f^2$. Typically, the isovector symmetry (B.17) remains intact. Some choices of interaction channels, e.g., in the GN model, break the continuous axial symmetries to discrete subgroups (see Appendix B.1.2 for a discussion of the mechanism)

$$Z_{\gamma_4}(2): \qquad \psi \to \gamma_4\psi, \qquad \bar{\psi} \to -\bar{\psi}\gamma_4; \tag{B.22}$$

$$Z_{\gamma_5}(2): \qquad \psi \to \gamma_5\psi, \qquad \bar{\psi} \to -\bar{\psi}\gamma_5. \tag{B.23}$$

Either of Eq. (B.22) or Eq. (B.23) can be reproduced by a combination of Eq. (B.8) and the other of the two discrete symmetries. In the three last models in Table 5.4, a remnant of the isospin symmetry (B.17) is present, namely

$$\mathrm{U}_{\tau_3}(1): \qquad \psi \to \mathrm{e}^{\mathrm{i}\chi\tau_3}\psi, \qquad \bar{\psi} \to \bar{\psi}\mathrm{e}^{-\mathrm{i}\chi\tau_3} \tag{B.24}$$

where τ_3 is the third Pauli matrix and χ is a real parameter.

B.2.5 *Discrete symmetries*

Apart of continuous elements of the Euclidean Poincaré group, there always exist discrete ones that can be combined with the continuous elements to form improper Lorentz transformations. On the level of spinor transformations, one can typically apply the parity transformation P, time reversal T and charge conjugation C. In the reducible 4×4 representation, the definition of this discrete operations comes with an ambiguity due to the enlarged symmetry group, see Ref. [274] for further details.

In this thesis, we particularly need to define the parity transformation for the classifications of quantum numbers of fermionic bilinears in Chapter 5. For an odd number of spacetime dimensions, parity must be defined as the inversion of an odd number of axes (otherwise it is an element of the continuous Poincaré group). Our convention is to flip all axis $x \to -x$. Then, two Parity transformations can be defined

$$P_4: \qquad \psi(x) \to \gamma_4\psi(-x), \qquad \bar{\psi}(x) \to \bar{\psi}(-x)\gamma_4; \tag{B.25}$$

$$P_5: \qquad \psi(x) \to \gamma_5\psi(-x), \qquad \bar{\psi}(x) \to \bar{\psi}(-x)\gamma_5. \tag{B.26}$$

C

EFFECTIVE POTENTIAL, GAP EQUATIONS AND RENORMALIZATION OF THE (2 + 1)-DIMENSIONAL GROSS-NEVEU MODEL

In Chapters 4 and 5, variants of fermionic theories with four-fermion self-interaction are studied in $2+1$ spacetime dimensions. These theories are renormalizable in a $1/N_f$ expansion [243, 244] that incorporates non-perturbative effects. In this section, the renormalization of these theories in the large-N_f limit (or, equivalently, in the mean-field approximation) is presented at the example of the $2+1$-dimensional GN model. Thereby, we also touch the computation of the homogeneous, effective potential of the theory as well as the gap equations. Various limits of relevant integrals within the computations are derived. Many of the below computations can be found in Refs. [2, 241, 249].

The effective action of this model is

$$\frac{\mathcal{S}_{\text{eff}}}{N_f} = \int \mathrm{d}^3x \, \frac{\sigma^2}{2\lambda} - \ln \operatorname{Det}(\beta \mathrm{Q}) \,, \qquad \mathrm{Q}[\sigma] = \partial\!\!\!/ + \gamma_3 \mu + \sigma, \tag{C.1}$$

where σ is the auxiliary field introduced to get rid of the $(\bar{\psi}\psi)^2$ self-interaction term and λ is the respective coupling constant with dimension of a length. The GN model is chosen on purpose, as it contains the relevant four-fermion coupling, which is subject of the renormalization procedure, and the effective action is of the form of Eq. (2.39) that is common to all four-fermion models studied in Chapters 4 and 5.

As described in Section 2.4, the quantum effective action is given by the minimum of $\mathcal{S}_{\text{eff}}$ with respect to σ, which is also easy to determine in the vacuum $T = \mu = 0$ where the assumption of $\sigma = \hom \sigma = \text{const.}$ for the ground state is fulfilled. The more practical object to study is, however, the homogeneous, effective potential $\bar{U}$ defined according to Eq. (2.53). The essential object, that is left to determine, is the fermion determinant DetQ. However, with the assumption of homogeneous $\bar{\sigma}$ the evaluation is similar to the computation of the fermion determinant of free fermions with mass $m = \bar{\sigma}$.

C.1 FERMION DETERMINANT

We briefly recapitulate the evaluation of the expression $\ln \operatorname{Det}\mathrm{Q}$ in Eq. (C.1). This is a textbook computation relevant for the pressure of the free-fermi gas and can be found in, e.g., Section 2.5 in Ref. [64] or Section 3.7 in Ref. [285] for the case of three spatial dimensions. As a first step, we perform a Fourier-expansion of the fermionic fields before integrating them out to obtain the Fourier representation of the Dirac operator $\bar{\mathrm{Q}} = \mathrm{Q}[\bar{\sigma}]$, given by

$$\tilde{\bar{\mathrm{Q}}} = \mathrm{i}\gamma_\nu \left(p_\nu - \mathrm{i}\mu\delta_{\nu,d+1}\right) + \bar{\sigma}. \tag{C.2}$$

After using the identity $\ln \mathrm{Det}\tilde{\tilde{\mathrm{Q}}} = \mathrm{Tr}\ln\tilde{\tilde{\mathrm{Q}}}$, one inserts the functional trace (4.16) to obtain

$$\begin{aligned}\frac{1}{\beta V N_f}\mathrm{Tr}\ln\beta\tilde{\tilde{\mathrm{Q}}} &= T\sum_n\int\frac{\mathrm{d}^2p}{(2\pi)^2}\,\mathrm{tr}\ln\beta\left[\mathrm{i}\gamma_\nu\left(p_\nu-\mathrm{i}\mu\delta_{\nu,d+1}\right)+\bar{\sigma}\right] \\ &= T\sum_n\int\frac{\mathrm{d}^2p}{(2\pi)^2}\ln\det\beta\left[\mathrm{i}\gamma_\nu\left(p_\nu-\mathrm{i}\mu\delta_{\nu,d+1}\right)+\bar{\sigma}\right] \\ &= T\sum_n\int\frac{\mathrm{d}^2p}{(2\pi)^2}2\ln\beta^2\left[E_{\boldsymbol{p}}^2+(\mathrm{i}\nu_n-\mu)^2\right]^2 \\ &= T\sum_n\int\frac{\mathrm{d}^2p}{(2\pi)^2}\left\{\ln\beta^2\left[\mathrm{i}\nu_n^2+(E_{\boldsymbol{p}}-\mu)^2\right]+\ln\beta^2\left[\mathrm{i}\nu_n^2+(E_{\boldsymbol{p}}+\mu)^2\right]\right\}\end{aligned} \tag{C.3}$$

with the energies $E_{\boldsymbol{p}}=\sqrt{\boldsymbol{p}^2+\bar{\sigma}^2}$. From the first to the second line, we reuse the identity $\ln\det M = \mathrm{tr}\ln M$ for the discrete operations on the level of spinor indices. In the third line, we insert the Gamma matrices in the representation (A.22) and compute the respective determinant in Dirac space for fixed $\boldsymbol{p}$ and ν_n. Then, we use a mathematical trick by restricting the integration and summation just to positive ν_n and $\boldsymbol{p}$ and grouping together terms with opposite signs in p together. After a few, arithmetic manipulations one obtains back the original integration domain, since the resulting integrand in the fourth line only depends on $\boldsymbol{p}^2$ and ν_n^2.

The respective integrand can be rewritten in another integral expression,

$$\ln\beta^2\left(\mathrm{i}\nu_n^2+(E_{\boldsymbol{p}}\pm\mu)^2\right)=2\int_1^{\beta(E_p\pm\mu)}\mathrm{d}x\frac{x}{x^2+\beta^2\nu_n^2}+C \tag{C.4}$$

with an irrelevant integration constant. This expression combined with the Matsubara sum can be evaluated using the identity

$$\sum_{n=-\infty}^{\infty}f(k_0=\mathrm{i}\nu_n)=\frac{1}{2\pi\mathrm{i}}\oint_{\mathcal{C}}\mathrm{d}k_0 f(k_0)\frac{1}{2T}\tanh\frac{k_0}{2T} \tag{C.5}$$

with a contour $\mathcal{C}$ that consists of an infinite number of small circles around $\mathrm{i}\nu_n=\mathrm{i}(2n+1)\pi T$ for $n\in\mathbb{Z}$. Equation (C.5) holds for functions $f(k_0)$ that are analytic on the imaginary k_0 axis, such that the residue theorem can be applied for the poles $x=(2n+1)\pi i$ of $\tanh x=(\mathrm{e}^x-1)/(\mathrm{e}^x+1)$. For $f(k_0)=T/(T^2x^2-k_0^2)$, one finds

$$\begin{aligned}&T\sum_{n=-\infty}^{\infty}f(k_0=\mathrm{i}\nu_n)= \\ &\quad=\frac{1}{2\pi i}\int_{-\mathrm{i}\infty+\delta}^{+\mathrm{i}\infty+\delta}\mathrm{d}k_0\,f(k_0)\left(\frac{1}{2}-\frac{1}{1+\mathrm{e}^{\beta k_0}}\right)+\frac{1}{2\pi i}\int_{-\mathrm{i}\infty+\delta}^{+\mathrm{i}\infty+\delta}\mathrm{d}k_0 f(k_0)\left(-\frac{1}{2}+\frac{1}{1+\mathrm{e}^{-\beta k_0}}\right)\end{aligned} \tag{C.6}$$

where we deformed the original integration contour. One of the contours is shifted away from the imaginary axis with a small positive real part, while the other is shifted in the opposite direction, leading to different expressions for $\tanh k_0/2T$. This deformation is legit because enlarging the circles until they merge is allowed according to the residue theorem, as they still enclose the poles. Then, parts of the contour are crossing the imaginary axis in opposite directions such that they cancel each other. We refer to Section 3 of Ref. [285] for a nice visualization of the contour deformations described in this section.

These integration contours can respectively be closed in a half-circle "at infinity" connecting $+\mathrm{i}\infty\pm\delta$ and $-\mathrm{i}\infty\pm\delta$ since $f(k_0)\sim k_0^{-2}$ is suppressed there. Then, however, this

contour only encloses the poles at $k_0 = \pm x$. Before doing so, however, we merge both expressions by substituting $k_0 \to -k_0$ in the second term such that we obtain

$$T \sum_{n=-\infty}^{\infty} f(k_0 = \mathrm{i}\nu_n) = \tag{C.7}$$
$$= \frac{1}{2\pi i} \int_{-\mathrm{i}\infty}^{+\mathrm{i}\infty} \mathrm{d}k_0 \, \frac{1}{2}(f(k_0 + f(-k_0))) + \frac{1}{2\pi i} \int_{-\mathrm{i}\infty+\delta}^{+\mathrm{i}\infty+\delta} \mathrm{d}k_0 \, \frac{1}{2}(f(k_0 + f(-k_0))) \frac{1}{\mathrm{e}^{\beta k_0} + 1}.$$

In the first integral we are allowed to set $\delta = 0$ since the poles are contained in the second term. Reinserting this into Eq. (C.4), one observes that, depending on the values of E and μ, either $k_0 = +x$ or $k_0 = -x$ is within the integration contour. However, we can treat both cases simultaneously with the residue theorem resulting in

$$T \sum_n f(k_0 = \mathrm{i}\nu_n) = \frac{1}{|x|} \left(\frac{1}{2} - \frac{1}{\mathrm{e}^{|x|} + 1} \right) = \frac{1}{2|x|} \tanh \frac{|x|}{2} \tag{C.8}$$

and, overall,

$$\frac{1}{\beta V N_f} \mathrm{Tr} \ln \beta \tilde{\tilde{\mathrm{Q}}} = T \sum_n \int \frac{\mathrm{d}^2 p}{(2\pi)^2} \left\{ \ln \beta^2 \left[\mathrm{i}\nu_n^2 + (E_{\boldsymbol{p}} - \mu)^2 \right] + \ln \beta^2 \left[\mathrm{i}\nu_n^2 + (E_{\boldsymbol{p}} + \mu)^2 \right] \right\} \tag{C.9}$$
$$= 2T \int \frac{\mathrm{d}^2 p}{(2\pi)^2} \sum_n \int \frac{\mathrm{d}^2 p}{(2\pi)^2} \left\{ \int_1^{\beta(E_{\boldsymbol{p}} - \mu)} \mathrm{d}x \frac{x}{x^2 + \nu_n^2} + \int_1^{\beta(E_{\boldsymbol{p}} + \mu)} \mathrm{d}x \frac{x}{x^2 + \nu_n^2} \right\}$$
$$= 2T \int \frac{\mathrm{d}^2 p}{(2\pi)^2} \left\{ \int_1^{\beta(E_{\boldsymbol{p}} - \mu)} \mathrm{d}x \left(1 - \frac{2}{\mathrm{e}^x + 1} \right) + \int_1^{\beta^2(E_{\boldsymbol{p}} + \mu)} \mathrm{d}x \left(1 - \frac{2}{\mathrm{e}^x + 1} \right) \right\}.$$

This last expression can be integrated to obtain

$$\frac{1}{\beta V N_f} \mathrm{Tr} \ln \beta \tilde{\tilde{\mathrm{Q}}} = 2 \int \frac{\mathrm{d}^2 p}{(2\pi)^2} \left[E_{\boldsymbol{p}} + T \ln \left(1 + \mathrm{e}^{-\beta(E_{\boldsymbol{p}} - \mu)} \right) + T \ln \left(1 + \mathrm{e}^{-\beta(E_{\boldsymbol{p}} + \mu)} \right) \right] \tag{C.10}$$

which is the well-known expression for the pressure of the free fermi gas in the vacuum [64]. This last expression contains a cubical UV divergence from the vacuum energy.

Reinserting this result into the homogeneous potential per fermion flavor, one obtains

$$\bar{U}(\bar{\sigma}, \mu, T) = \frac{1}{\beta V N_f} \mathcal{S}_{\mathrm{eff}}[\bar{\sigma}] = \tag{C.11}$$
$$= \frac{\bar{\sigma}}{2\lambda} - 2 \int \frac{\mathrm{d}^2 p}{(2\pi)^2} \left[E_{\boldsymbol{p}} + T \ln \left(1 + \mathrm{e}^{-\beta(E_{\boldsymbol{p}} - \mu)} \right) + T \ln \left(1 + \mathrm{e}^{-\beta(E_{\boldsymbol{p}} + \mu)} \right) \right]$$

which still contains the divergence. Dealing with the divergence by imposing a proper renormalization condition is subject of the following section.

C.2 RENORMALIZATION

In order to renormalize the effective potential (C.11), we choose a fixed value $\bar{\Sigma}_0$ for the vacuum expectation value of σ, i.e.,

$$\bar{\Sigma}(\mu = 0, T = 0) = \bar{\Sigma}_0 \tag{C.12}$$

where $\bar{\Sigma}(\mu, T)$ is the minimum of the homogeneous potential for fixed values of μ and T.

C.2.1 *Gap equation and definition of Fermi-Dirac distribution functions*

To determine $\bar{\Sigma}$, the gap equation of the GN model

$$\frac{\partial}{\partial\bar{\sigma}}\bar{U}(\bar{\sigma},\mu,T)=0 \tag{C.13}$$

is used, i.e., the extrema of the effective potential with respect to $\bar{\sigma}$ are determined. This evaluates to

$$\bar{\sigma}\left(\frac{1}{2\lambda}-\ell_1(\bar{\sigma},\mu,T)\right)=0 \tag{C.14}$$

with the integral expression

$$\ell_1(\bar{\sigma},\mu,T)=\frac{1}{\beta V}\mathrm{Tr}\left(\bar{\mathrm{Q}}^{-1}\right)=d_\gamma\int\frac{\mathrm{d}^2p}{(2\pi)^2}T\sum_{n=-\infty}^{\infty}\frac{1}{(\nu_n-\mathrm{i}\mu)^2+E_{\boldsymbol{p}}^2} \tag{C.15}$$

and the dimensionality of the Gamma matrices $d_\gamma = 4$.[1] This expression can directly be obtained from the derivative of the effective potential using representation (C.3) for the $\ln\mathrm{Det}\tilde{\mathrm{Q}}$ expression. Equation (C.14) always allows for the solution $\bar{\sigma}=0$ and, for a non-trivial solution, one has to find the solution of

$$\frac{1}{2\lambda}=\ell_1(\bar{\sigma},\mu,T). \tag{C.16}$$

It is practical to perform the summation over n using the Residue theorem, as discussed at the end of this section, such that

$$\ell_1(\bar{\sigma}(\mu,T),\mu,T)=d_\gamma\int\frac{\mathrm{d}^2p}{(2\pi)^2}\frac{1}{2E}\left[1-n_F(E)-n_{\bar{F}}(E)\right] \tag{C.17}$$

where we defined $E\equiv E_{\boldsymbol{p}}$ as well as the Fermi-Dirac distribution functions

$$n_F(E)=\frac{1}{\mathrm{e}^{\beta(E-\mu)}+1},\quad n_F(E)=\frac{1}{\mathrm{e}^{\beta(E+\mu)}+1}. \tag{C.18}$$

REGULARIZATION However, Eq. (C.17) contains a linear UV divergence, that we properly regularize with a Pauli-Villars regularization

$$\int\frac{\mathrm{d}^2p}{(2\pi)^2}f(\bar{\sigma})\to\int\frac{\mathrm{d}^2p}{(2\pi)^2}\left(f(\bar{\sigma})-f(\sqrt{\bar{\sigma}^2+\Lambda^2})\right), \tag{C.19}$$

i.e., we substract a term with an artificially introduced "Pauli-Villars mass" $\bar{\sigma}^2+\Lambda^2$.[2] This prescription, albeit it might seem arbitrary, is applied only to the vacuum parts of

1 A brief comment on the introduction of d_γ at this point: In principle, one can evaluate the whole effective potential also for irreducible representations with $d_\gamma = 2$, as, e.g., given in Eq. (A.19) for Minkowski spacetime. However, then the evaluation of the discrete determinant in Dirac space in Eq. (C.3) differs slightly to the one discussed, albeit the result deviates from Eq. (C.3) by a factor of 1/2. This is proven in Section 2 of Ref. [241]. Since ℓ_1 can in principle directly be obtained from deriving the effective action (C.1) with respect to $\bar{\sigma}$, ℓ_1 can be calculated without an explicit representation of Gamma matrices until the trace over $\bar{\mathrm{Q}}^{-1}$ needs to be evaluated. Thus, we define d_γ to indicate that the final result only differs by a global factor depending on whether the 4×4 or 2×2 representations are used.

2 The term "Pauli-Villars mass" stems from the fact that $\bar{\sigma}$ acts as a dynamically generated mass term for the fermions, such that the Pauli-Villars regularization introduces fermionic terms with a heavy mass $\sqrt{\sigma^2+\Lambda^2}$ artificially.

the integrals – the parts where neither μ nor T appear – allowing to perform some of the medium integrals analytically. For example, in this prescription

$$\ell_1(\bar{\sigma}(\mu,T),\mu,T) \to d_\gamma \int \frac{\mathrm{d}^2p}{(2\pi)^2}\left[\frac{1}{2E}(1-n_F(E)-n_{\bar{F}}(E)) - \frac{1}{2\sqrt{E^2+\Lambda^2}}\right] \tag{C.20}$$

$$= \frac{d_\gamma}{4\pi}\left[\sqrt{\bar{\sigma}^2+\Lambda^2} - |\bar{\sigma}| - T\ln\left(1+\mathrm{e}^{-\beta(|\bar{\sigma}|-\mu)}\right) - T\ln\left(1+\mathrm{e}^{-\beta(|\bar{\sigma}|-\mu)}\right)\right]. \tag{C.21}$$

C.2.2 *Gap equation in the vacuum*

Inserting this result into the gap equation (C.14) for $\mu = T = 0$ and imposing the renormalization condition (C.12), one finds

$$\lambda = \frac{4\pi}{d_\gamma\left(\sqrt{\bar{\Sigma}_0^2+\Lambda^2} - |\bar{\Sigma}_0|\right)} \tag{C.22}$$

as the scaling of the coupling constant with the regularization parameter to ensure that $\bar{\Sigma}(\mu=0,T=0) = \bar{\Sigma}_0$. The gap equation (C.14) at non-vanishing μ and T amounts to

$$L_1(\bar{\sigma},\mu,T) \equiv \frac{1}{\lambda} - \ell_1 = \frac{d_\gamma}{4\pi}\left[|\bar{\sigma}| - |\bar{\Sigma}_0| + T\ln\left(1+\mathrm{e}^{-\beta(|\bar{\sigma}|-\mu)}\right) + T\ln\left(1+\mathrm{e}^{-\beta(|\bar{\sigma}|-\mu)}\right)\right] = 0 \tag{C.23}$$

from which the extrema of $\bar{U}(\bar{\Sigma},\mu,T)$ can be determined for all μ and T. The extremum $\bar{\Sigma} = 0$ follows directly from the factorization of Eq. (C.14) and is not necessarily a solution of Eq. (C.23). The non-trivial part of the gap equation (C.23) is, thus, finite. The above prescription is suitable to remove divergences of all other observables studied in this work.

For $T = 0$, one can simplify L_1 to

$$L_1(\bar{\sigma},\mu,T=0) = \frac{d_\gamma}{4\pi}\left[|\bar{\Sigma}| - |\bar{\Sigma}_0| + \Theta(\mu^2-\bar{\sigma}^2)\left(|\mu| - |\bar{\Sigma}|\right)\right], \tag{C.24}$$

from which the other limits $\mu \to 0$ and / or $\bar{\sigma} \to 0$ follow trivially.

C.2.3 *Renormalization of the effective potential*

Inserting Eq. (C.22) for λ is not sufficient to render the cubic UV divergence of the effective potential finite. However, the physically relevant object is the difference $\Delta U(\bar{\sigma},\mu,T) = U(\bar{\sigma},\mu,T) - U(0,\mu,T)$ which is finite. This differences is used to determine the homogeneous ground state $\bar{\Sigma}$, by inserting the solutions of Eq. (C.14) into ΔU and determining the global minimum. Inserting Eq. (C.22) with $d_\gamma = 4$,[3] one finds for the effective potential

$$U(\bar{\sigma},\mu,T) = \frac{\sigma^2}{2\pi}\left(\sqrt{\bar{\Sigma}_0^2+\Lambda^2} - |\bar{\Sigma}_0|\right) + \tag{C.25}$$

$$- \frac{1}{\pi}\int_0^\infty \mathrm{d}p\left[E + T\ln\left(1+\mathrm{e}^{-\beta(E_p-\mu)}\right) + T\ln\left(1+\mathrm{e}^{-\beta(E_p+\mu)}\right)\right].$$

In the vacuum, one obtains after some calculation[3]

$$\Delta U(\bar{\sigma},\mu=0,T=0) = \frac{\sigma^2}{6\pi}\left(2\sigma - 3|\bar{\Sigma}_0|\right). \tag{C.26}$$

3 This result can only be obtained if one, in addition to the Pauli-Villars regulator, introduces a further artifical UV cutoff in the vacuum integrals of $U(\bar{\sigma},0,0)$ and $U(0,0,0)$. After integration, one has to carefully cancel the cubically diverging terms, expressed as functions of the UV cutoff, and, subsequently, remove the Pauli-Villars regulator.

This is consistent with the vacuum renormalization condition (C.12), since $\Delta U(0,0,0) = 0$ and $\Delta U(\bar{\Sigma}_0, 0, 0) = -\bar{\Sigma}_0^3/6\pi$, i.e., $\bar{\Sigma}_0$ is the minimum of the renormalized, effective potential. In practical computations in the medium, one has to add the medium integrals from the second row of Eq. (C.25) to Eq. (C.26). The medium contributions can be evaluated numerically, which can be simplified by expressing them in terms of Polylogarithms [348], as done in Ref. [241].

C.3 HOMOGENEOUS PHASE DIAGRAM OF THE GN MODEL

In Sections 5.2 and 6.2, the homogeneous phase diagram of the $2+1$-dimensional GN model is discussed multiple times, as a limit emerging from the model with vector interactions (6.1) or as the solution for the homogeneous ground states of the four-fermion models (5.1) with scalar interactions (5.2).

The chiral condensate $\bar{\Sigma}(\mu, T)$ as a function of μ and T can be obtained by finding the solutions of the gap equation (C.14) and inserting them into $\Delta U(\bar{\Sigma}, \mu, T)$, see Appendix C.2.3, to find the global minimum of ΔU with respect to $\bar{\Sigma}$ for fixed μ and T. This can be done numerically using *Python3* [19] , similar to the procedure discussed in Section 6.2.

We briefly want to discuss how the second-order phase boundary line (6.17) can be obtained analytically. One performs a stability analysis, as outlined in Section 4.1.2, but only for homogeneous fluctuations. This corresponds to studying the bosonic two-point vertex function of the GN model $\Gamma_\sigma^{(2)}$ for vanishing spatial momenta. Thereby, $\Gamma_\sigma^{(2)}$ is given by Eq. (5.10) with $L_{2,\phi_j} = L_{2,+}$ (5.11). For the homogeneous phase transition between SP and HBP, it is sensible to consider the stability of $\bar{\Sigma} = 0$ ($M^2 = 0$ in Eq. (5.10)) around homogeneous fluctuations, i.e., $q^2 = 0$. One obtains the condition

$$\Gamma_\sigma^{(2)}(\bar{\sigma}^2 = 0, \mu, T, q^2 = 0) = \frac{1}{\lambda} - \ell_1(\bar{\Sigma} = 0, \mu, T) = 0 \tag{C.27}$$

for the phase boundary, which corresponds to setting the curvature of the quantum effective action (that corresponds to the effective action in the mean-field approximation) to zero. This expression is, of course, only valid when there is no first-order phase transition which one does only know from the numerical analysis described above or from the findings in Ref. [249].

Inserting Eq. (C.22) into Eq. (C.27) for $\bar{\sigma} = 0$, one finds

$$T \ln\left(1 + \mathrm{e}^{\beta\mu}\right) + T \ln(1 + \mathrm{e}^{-\beta\mu}) = \bar{\Sigma}_0. \tag{C.28}$$

This can be solved for the chemical potential to obtain the phase transition line, one finds

$$\mu_c(T) = T \operatorname{arcosh}\left(\frac{1}{2}\mathrm{e}^{\beta\bar{\Sigma}_0} - 1\right), \tag{C.29}$$

which is the expression given for the phase boundary in Eq. (6.17).

C.4 EVALUATION OF THE MATSUBARA SUM IN THE GAP EQUATION

In Appendix C.2.1, the solution (C.17) of the Matsubara sum appearing in the expression for $\ell_1(\bar{\Sigma}, \mu, T)$ (C.15) is given without derivation. This derivation is outlined within this chapter. Thereby, the strategy of computation is taken from the lecture notes [285] and from Ref. [57], which provided an helpful, compact overview when the author first faced different types of Matsubara sums.

Equation (C.15) contains the sum

$$T \sum_{n=-\infty}^{\infty} \frac{1}{(\nu_n - \mathrm{i}\mu)^2 + E^2} \equiv \frac{1}{T} \sum_{n=-\infty}^{\infty} f(z_n) \tag{C.30}$$

with the complex function $f(z) = 1/((\beta E)^2 - z^2)$ and $z_n = \mathrm{i}2\pi(n + 1/2) - \beta\mu$. Thereby, the Matsubara frequencies $\nu_n = 2\pi(n + 1/2)T$ are obtained from the anti-periodic boundary conditions (2.12) for the fermionic fields, see Eq. (2.13) and Eq. (2.15). Note that we focus on the fermionic Matsubara sum exclusively in this section, although a formula with the replacement $\nu_n \to \omega_n$ (2.14) can be solved with a similar strategy.

The following strategy is followed: One expresses the sum as a contour integral over an integrand containing $f(z)$ multiplied with a function that has poles in the complex plane at $z = z_n$. Then, the contour integral in the complex plane can be deformed and closed such that the residue theorem can be applied over the poles of $f(z)$, while the poles of the multiplying function are avoided.

First, we prove that the searched function for the residue theorem is

$$g(z) = \frac{1}{2} - \frac{1}{\mathrm{e}^{z+\beta\mu} + 1} \tag{C.31}$$

where the second term reminds of the Fermi-Dirac distribution defined in Eq. (C.18). One can directly see from Eq. (C.18) that $g(z)$ has its poles at z_n, just by inserting z_n into the expression and using the Euler identity $\exp(\mathrm{i}2\pi(n + 1/2)) = -1$. Thus, we obtain

$$\sum_n f(z_n) = \frac{1}{2\pi\mathrm{i}} \oint_{\mathcal{C}} \mathrm{d}z f(z) g(z) \tag{C.32}$$

where the contour $\mathcal{C}$ consists of multiple, positively oriented[4] circles around the z_n, see Section 3 of [285] for a nice visualization. Then, the residue theorem

$$\frac{1}{2\pi\mathrm{i}} \oint_{\mathcal{C}} \mathrm{d}z\, h(z) = \sum_{n=1}^{m} \mathrm{Res}\,(h, z_n) \chi(\mathcal{C}; z_n) \tag{C.33}$$

with simple poles and a contour $\mathcal{C}$ with winding numbers

$$\chi(\mathcal{C}; z_n) = \frac{1}{2\pi\mathrm{i}} \oint_{\mathcal{C}} \mathrm{d}z \frac{1}{z - z_n} \tag{C.34}$$

around these poles ensures that Eq. (C.32) holds. Thereby, n labels the number of poles enclosed by the contour $\mathcal{C}$ and the residue for the simple pole is

$$\mathrm{Res}(h, z_n) = \lim_{z \to z_n} h(z)(z - z_n). \tag{C.35}$$

The integration contour $\mathcal{C}$ is now deformed into two contours (again, we refer to Ref. [285] for the visualization) into two paths

$$\mathcal{C}_1 : \qquad z(t) = -\beta\mu + \epsilon + \mathrm{i}t, \qquad t \in (-\infty, +\infty)\,, \epsilon \in \mathbb{R}, \epsilon \ll 1, \tag{C.36}$$

$$\mathcal{C}_2 : \qquad z(t) = -\beta\mu - \epsilon + \mathrm{i}t, \qquad t \in (\infty, -\infty)\,, \epsilon \in \mathbb{R}, \epsilon \ll 1. \tag{C.37}$$

Thus, $\mathcal{C}_1$ goes along the imaginary axis with a small, positive shift away from the real part of the poles $\mathrm{Re}\, z_n = -\beta\mu$, while $\mathcal{C}_2$ goes along the imaginary axis in the opposite direction

4 In mathematics, positively oriented means that the integration path winds around the pole in counterclockwise direction.

with a small, negative shift. These contours can be closed at infinity without additional contribution, since $f(z) \sim z^{-2}$ for large $|z|$. Now, the residue theorem (C.33) can again be applied, but now for the poles of $f(z) = \pm\beta E$ taking into account the negative winding numbers. One finds

$$\begin{aligned}\sum_{n=-\infty}^{\infty} f(z_n) &= \frac{1}{2\pi \mathrm{i}} \oint_{\mathcal{C}} \mathrm{d}z f(z) g(z) = \\ &= -\mathrm{Res}\left[f(z)g(z), z = \beta E\right] - \mathrm{Res}\left[f(z)g(z), z = -\beta E\right] \\ &= -\lim_{z\to\beta E} \frac{(z-\beta E)}{(\beta E - z)(\beta E + z)} \left(\frac{1}{2} - \frac{1}{\mathrm{e}^{z+\beta\mu}+1}\right) + \\ &- \lim_{z\to-\beta E} \frac{(z+\beta E)}{(\beta E - z)(\beta E + z)} \left(\frac{1}{2} - \frac{1}{\mathrm{e}^{z+\beta\mu}+1}\right) \\ &= \frac{1}{2\beta E}\left(\frac{1}{2} - n_{\bar{F}}(E)\right) - \frac{1}{2\beta E}\left(\frac{1}{2} - n_{\bar{F}}(-E)\right) \\ &= \frac{1}{2\beta E}\left(1 - n_F(E) - n_{\bar{F}}(E)\right)\end{aligned} \tag{C.38}$$

where we identified the Fermi-Dirac distribution functions (C.18) and used that

$$-\left(\frac{1}{2} - n_{\bar{F}}(-E)\right) = \frac{1}{2} - n_F(E). \tag{C.39}$$

This is the expression used in Eq. (C.17) taking into account that the factor of $1/\beta$ is canceled by the prefactor in Eq. (C.30).

Summarizing, one finds

$$T \sum_{n=-\infty}^{\infty} \frac{1}{(\nu_n - \mathrm{i}\mu)^2 + E^2} = \frac{1}{2E}\left(1 - n_F(E) - n_{\bar{F}}(E)\right) \tag{C.40}$$

which is used in Eq. (C.15) to obtain Eq. (C.17). Formulae for expressions of the form

$$T \sum_{n=-\infty}^{\infty} \frac{1}{\left[(\nu_n - \mathrm{i}\mu)^2 + E^2\right]^n} \tag{C.41}$$

can be obtained by iteratively applying $\frac{1}{E}\frac{\partial}{\partial E}$ to both sides of Eq. (C.40). Formulae with differing energies of the form

$$T \sum_{n=-\infty}^{\infty} \frac{1}{(\nu_n - \mathrm{i}\mu)^2 + E_1^2} \frac{1}{(\nu_n - \mathrm{i}\mu)^2 + E_2^2} \tag{C.42}$$

requires a computation that works analogous as for Eq. (C.40) but one has to take care of four different poles stemming from the energies $E_1 \neq E_2$. The strategy is, however, similar and we refrain from performing it explicitly.

D

STABILITY ANALYSIS IN 2 + 1 DIMENSIONS: DERIVATIONS AND IMPORTANT FORMULAE

This appendix consists of supplementary material for Chapters 5 and 6 regarding the stability analysis. The basic derivation for this analysis, that is based on the bosonic two-point vertex functions of auxiliary field in four-fermion models, can be found in Section 4.1.2. The following section provides model specific details of the computation of the bosonic two-point vertex functions in the above mentioned chapters and appearing formulae in the analysis. Also, selected limits for arguments of bosonic two-point vertex functions are performed and resulting formulae are given.

D.1 GENERAL FOUR-FERMION MODEL WITH LORENTZSCALAR INTERACTIONS

In this section, the computation of the bosonic two-point vertex functions for the general, $2+1$-dimensional four-fermion theory (5.1) from Chapter 5 with $\vec{\mathcal{C}} = \vec{\mathcal{C}}_s$ (5.2) subjected to a baryon chemical potential is performed in more depth. The basic principles of the expansion are presented in Section 4.1.2. Here, only specific aspects of the computation for Section 5.2 and Section 5.2.3 are discussed. Thus, this calculation can be understood as the logical bridge between the generic expression (4.23) and the formulae in Eq. (5.8) and Eq. (5.10) for $\vec{\mathcal{C}} = \vec{\mathcal{C}}_s$, $\lambda_j = \lambda$ and $d = 2$. Further, we provide formulae for the integral expressions $L_{2,\pm}$ appearing in Eq. (5.10), including the integral ℓ_2. Computations and formulae are originally derived in Ref. [2].

Following the expansion of fields $\vec{\phi}$ around a homogeneous expansion point $\vec{\bar{\phi}}$ with inhomogeneous perturbations $\delta\vec{\phi}$ according to Eq. (4.7) and, subsequently, expanding the effective action in orders of $\delta\vec{\phi}$, see Eq. (4.8), one obtains the second order correction (4.15) involving the bosonic two-point vertex functions (4.24) for $d = 2$ spatial dimensions. In order to evaluate the traces over spinor indices appearing in Eq. (4.24), it is instructive to consider the Fourier representation of the homogeneous propagator

$$\bar{\mathrm{Q}}^{-1}(x,y) = \frac{1}{\beta}\sum_{n=\infty}^{\infty}\int \frac{\mathrm{d}^2p}{(2\pi)^2}\,\mathrm{e}^{\mathrm{i}[\nu_n(\tau_x-\tau_y)+\boldsymbol{p}(\boldsymbol{x}-\boldsymbol{y})]}\tilde{\bar{\mathrm{Q}}}^{-1}(p), \tag{D.1}$$

which can be obtained by Fourier-transformation of the fermion fields the bilinear $\bar{\psi}\bar{\mathrm{Q}}\psi$ and inverting the obtained expression for $\tilde{\bar{\mathrm{Q}}}$. One obtains

$$\tilde{\bar{\mathrm{Q}}}^{-1}(\boldsymbol{p},\nu_n)_{\boldsymbol{\cdot}} = \frac{-\mathrm{i}\gamma_i\tilde{p}_i + \sum_k c_k^{\star}\bar{\phi}_k}{\tilde{\nu}_n^2 + \boldsymbol{p}^2 + M^2} \tag{D.2}$$

where $\tilde{\nu}_n = (\nu_n - \mathrm{i}\mu)$, $\nu_n = 2\pi(n-\frac{1}{2})/\beta$ are the fermionic Matsubara frequencies. The quantities M and $c^{\star}$ are given in Eq. (5.9).

As outlined in Section 4.1.2, the second order term is the first non-zero correction when using expansion points $\vec{\phi}$ that are solutions of the gap equation. This is the case for homogeneous, global minimum $\vec{\bar{\Phi}}$, which is the appropriate expansion points for searching instabilities towards an IP. We evaluate the trace in Eq. (4.23) to

$$\frac{1}{\beta}\sum_n \int \frac{\mathrm{d}^2p}{(2\pi)^2}\,\mathrm{tr}\left(c_j\,\tilde{\bar{\mathrm{Q}}}^{-1}(\boldsymbol{p}+\boldsymbol{q},\nu_n)\,c_k\,\tilde{\bar{\mathrm{Q}}}^{-1}(\boldsymbol{p}),\nu_n\right) = \tag{D.3}$$

$$= -\frac{1}{\beta}\sum_n \int \frac{\mathrm{d}^2p}{(2\pi)^2}\,\frac{A_{c_jc_k}}{[\tilde{\nu}_n^2+\boldsymbol{p}^2+M^2][\tilde{\nu}_n^2+(\boldsymbol{p}+\boldsymbol{q})^2+M^2]}$$

with

$$A_{c_jc_k} = (\tilde{\nu}_n^2+\boldsymbol{p}^2+\boldsymbol{p}\cdot\boldsymbol{q})\mathrm{tr}\left[c_j\gamma_i c_k\gamma_j\right] - \sum_{l,m\in\vec{\mathcal{C}}}\bar{\phi}_l\bar{\phi}_m\mathrm{tr}\left[c_jc_l^\star c_k c_m^\star\right] = \tag{D.4}$$

$$= \delta_{j,k}8(\tilde{\nu}_n^2+\boldsymbol{p}^2+\boldsymbol{p}\cdot\boldsymbol{q}) - \sum_{l,m\in\vec{\mathcal{C}}}\bar{\phi}_l\bar{\phi}_m\mathrm{tr}\left[c_jc_l^\star c_k c_m^\star\right],$$

where we used that $\mathrm{tr}(\gamma_i c_j c_k c_l) = 0$, $c_j^2 = \pm\mathbb{1}$ and that the anti-commutator $\{\gamma_i, c_k\}$ evaluates to 0 or $2c_k\gamma_i$ for all considered c_j. In order to make statements about the stability of a homogeneous field configuration one has to determine a basis $\varphi_j(\vec{\phi})$ for which $\Gamma^{(2)}_{\phi_j,\phi_k}$, containing the above trace, cf. (4.24), is diagonalized. This is not possible in general and depends on the present chemical potentials and the interactions of the model. In the present case, i.e., model (5.1) for $\vec{\mathcal{C}} = \vec{\mathcal{C}}_s$, $\lambda_j = \lambda$ and $d = 2$ at finite baryon chemical potential, one computes (D.4) and obtains for Eq. (4.23)

$$\frac{\mathcal{S}^{(2)}_{\mathrm{eff}}}{N_f} = \frac{\beta}{2}\int\frac{\mathrm{d}^2q}{(2\pi)^2}\left[\sum_{j\in\vec{\mathcal{C}}_s}|\delta\tilde{\varphi}_j(\mathbf{q})|^2\,\Gamma^{(2)}_{\varphi_j}\left(M^2,\mu,T,q\right)\right] \tag{D.5}$$

with

$$\Gamma^{(2)}_{\varphi_j}\left(M^2,\mu,T,q\right) = \frac{1}{\lambda} - \frac{8}{\beta}\sum_n\int\frac{\mathrm{d}^2q}{(2\pi)^2}\left(\frac{\tilde{p}^2+\boldsymbol{p}\cdot\boldsymbol{q}+a'_{\varphi_j}M^2}{[\tilde{\nu}_n^2+\boldsymbol{p}^2+M^2][\tilde{\nu}_n^2+(\boldsymbol{p}+\boldsymbol{q})^2+M^2]}\right), \tag{D.6}$$

where a'_{φ_j} is a coefficient that is determined by the considered field φ_j. In this diagonalized form, we identify $\Gamma^{(2)}_{\varphi_j}(q^2)$ as the curvature of the effective action for an inhomogeneous perturbation in field direction φ_j with momentum $\boldsymbol{q}$. By writing the denominator of the integrand in Eq. (D.6) in a partial fraction, we can split the integral and obtain the final form of the bosonic two-point function as given in Eq. (5.10), where $a_{\varphi_j} = 2(a'_{\varphi_j}-1)$.

D.1.1 *The momentum dependent part $L_{2,\pm}$*

In order to calculate the momentum dependent part of the two-point function (5.10), we start by carrying out the Matsubara summation in ℓ_2, see Eq. (5.10) for its definition.[1]

1 This Matsubara sum can be performed in a similar fashion as the integral for ℓ_1 performed in Appendix C.4. The only difference in the computation is that one has to consider four different poles (two of the poles can be assigned to the energy $E_{\boldsymbol{q}}$ while the other two stem from E, respectively) instead of two. Besides this, the procedure is completely analogue and is, thus not repeated here.

The summation of such expressions is standard in textbooks on thermal QFT, see, e.g., Ref. [64] or Appendix C.4 for examples. One obtains

$$\ell_2(M^2,\mu,T,q) = d_\gamma \int \tfrac{\mathrm{d}^2p}{(2\pi)^2} \frac{1}{2\boldsymbol{p}\cdot\boldsymbol{q}+q^2}\left[\frac{1-n_F(E)-n_{\bar F}(E)}{2E} - \frac{1-n_F(E_{\boldsymbol{q}})-n_{\bar F}(E_{\boldsymbol{q}})}{2E_{\boldsymbol{q}}}\right], \tag{D.7}$$

where $E_{\boldsymbol{q}} = \sqrt{M^2+(\boldsymbol{p}+\boldsymbol{q})^2}$ and $d_\gamma = 8$ is the dimension of the spinor index due to the reducible, 4×4 Gamma matrices used and the additional isospin degree of freedom, cf. Eq. (5.2). This integral is UV-finite and, thus, we do not have to apply a regularization scheme. However, the integrand has a divergence at $2\boldsymbol{p}\cdot\boldsymbol{q} = -q^2$, which has to be treated with a Cauchy principal value prescription. The vacuum contribution can be calculated analytically and we obtain

$$\ell_2(M^2,\mu,T,q) = \frac{8}{4\pi q}\left[\arctan\left(\frac{q}{2|M|}\right) - \int_0^{q/2}\mathrm{d}p\,\frac{p}{E}\frac{n_F(E)+n_{\bar F}(E)}{\sqrt{q^2/4-p^2}}\right]. \tag{D.8}$$

At any non-vanishing T, the medium contribution needs to be calculated numerically. However, taking the zero temperature limit enables us to also calculate the medium contribution analytically and we find Eq. (5.13). From this expression, we can take either the limit $q\to 0$ to obtain

$$\ell_2(M^2,\mu,T=0,q=0) = \frac{1}{\pi}\begin{cases} 0\,, & \mu^2 > M^2 \\ \frac{1}{|M|}\,, & \mu^2 < M^2 \end{cases} \tag{D.9}$$

or the limit $|M|\to 0$ to obtain

$$\ell_2(M^2=0,\mu,T=0,q) = \frac{2}{\pi q}\begin{cases} 0\,, & \mu^2 > q^2/4 \\ \arctan\left(\frac{\sqrt{q^2-4\mu^2)}}{2\mu}\right)\,, & 0<\mu^2\le q^2/4\,. \\ \frac{\pi}{2}\,, & \mu^2 = 0 \end{cases} \tag{D.10}$$

While ℓ_2 is not defined for $M=q=T=0$ for some values of μ, the whole momentum-dependent contribution to the two-point functions $L_{2,\pm}$ (5.11) yields

$$L_{2,\pm}(M^2=0,\mu,T=0,q=0) = 0. \tag{D.11}$$

D.2 STABILITY ANALYSIS FOR YUKAWA MODEL WITH MULTIPLE CHEMICAL POTENTIALS

In this section, we demonstrate an example that consists of off-diagonal contributions from the Yukawa self-interactions (compare the third line of Eq. (5.14)). This makes the diagonalization of $\mathcal{S}_Y^{(2)}$ harder to perform analytically. However, we will also demonstrate that this $\boldsymbol{q}$-independent contribution does not alter the predictions coming out of the analysis. This section is mostly taken from the appendix in the original publication [2].

The model that we will study is defined as the Yukawa model extension according to Eq. (2.48) of the four-fermion model in the first row of Table 5.4. Thus, the four-fermion

model contains the σ and η_{45} fields as well as a baryon chemical potential μ and a chiral chemical potential μ_{45}. As documented in Table 5.4 and Ref. [5], the four-fermion part of the model is diagonalized by

$$(\sigma \pm \eta_{45})\,. \tag{D.12}$$

In analogy to the four-fermion model, we study the effective action

$$\begin{aligned}\frac{\mathcal{S}_{\text{eff}}[\chi_L,\chi_R]}{N} = &-\operatorname{Tr}\ln\left[\not{\partial} + \gamma_3\left(P_L\mu_L + P_R\mu_R\right) + hP_L\chi_L + hP_R\chi_R\right] + \\ &+\int \mathrm{d}^3x\, h^2\Bigg[\tfrac{\chi_L^2+\chi_R^2}{2\lambda} + \tfrac{1}{2}\left(\partial\chi_L\right)^2 + \tfrac{1}{2}\left(\partial\chi_R\right)^2 + \\ &+\sum_{n>1}\kappa_n h^{2(n-1)}\left(\chi_L^2+\chi_R^2\right)^n\Bigg]\end{aligned} \tag{D.13}$$

of a Yukawa theory, i.e., $\chi_{L/R}$ are fields of canonical dimension and proportional to the dynamical scalar fields χ_σ and $\chi_{\eta_{45}}$ according to

$$\chi_L = \tfrac{1}{\sqrt{2}}\left(\chi_\sigma + \chi_{\eta_{45}}\right), \quad \chi_R = \tfrac{1}{\sqrt{2}}\left(\chi_\sigma - \chi_{\eta_{45}}\right). \tag{D.14}$$

This definition is completely analogous to the diagonalization of the four-fermion model. We, again, introduced a Yukawa coupling h as well as couplings κ_n for the self-interactions and define projectors and chemical potentials accordingly

$$P_L = \tfrac{1}{\sqrt{2}}\left(1+\gamma_{45}\right), \quad P_R = \tfrac{1}{\sqrt{2}}\left(1-\gamma_{45}\right), \tag{D.15}$$

$$\mu_L = \tfrac{1}{\sqrt{2}}\left(\mu+\mu_{45}\right), \quad \mu_R = \tfrac{1}{\sqrt{2}}\left(\mu-\mu_{45}\right). \tag{D.16}$$

All terms except for the last row in Eq. (D.13) either contain only χ_L or only χ_R.[2] Thus, the second order correction is given by

$$\begin{aligned}\frac{\mathcal{S}_{\text{eff}}^{(2)}}{N_f} = \frac{\beta}{2}\int\tfrac{\mathrm{d}^2q}{(2\pi)^2}\Bigg\{&\sum_{j=L,R}|\delta\chi_j(\boldsymbol{q})|^2\Bigg[h^2\Gamma^F_{\chi_j} + q^2 + \\ &+\sum_{n>1}\kappa_n n\left(2(M^2)^{n-1} + 4(n-1)\bar{\chi}_j^2(M^2)^{n-2}\right)\Bigg] + \\ &+\delta\chi_L(-\boldsymbol{q})\delta\chi_R(\boldsymbol{q})4\kappa_n n(n-1)\bar{\chi}_L\bar{\chi}_R(M^2)^{n-2} + L\leftrightarrow R\Bigg\},\end{aligned} \tag{D.17}$$

where $M^2 = \bar{\chi}_\sigma^2 + \bar{\chi}_{\eta_{45}}^2 = \bar{\chi}_L^2 + \bar{\chi}_R^2$ and

$$\Gamma^F_{\chi_j} = \frac{1}{\lambda} - \ell_1 + L_{2,+}(h^2\bar{\chi}_j^2, \mu_j, T, q^2) \tag{D.18}$$

is the contribution, that also appears in the corresponding four-fermion model (see Table 5.4 and Ref. [5]). The integrals ℓ_1 and $L_{2,+}$ are defined in Eqs. (5.10) and (5.11).

The last row of Eq. (D.17) contains the off-diagonal contribution stemming from the self-interaction of the dynamical fields. This contribution is not dependent on the spatial momentum $\mathbf{q}$ of the perturbation, but it makes the diagonalization more complicated

2 The Dirac operator within the Tr ln can be decomposed into a block-diagonal form, where each block only contains either μ_L and χ_L or μ_R and χ_R. In this sense, the fermionic contributions completely decouples χ_L and χ_R.

(compare Eq. (5.14) for the form of this contribution in the more general case). In fact, we are only able to diagonalize this symbolically using `Matlab` [22]. Using the definitions

$$Y_j = q^2 + \sum_{n>1} \kappa_n n \left(2(M^2)^{n-1} + 4(n-1)\bar{\chi}_j^2 (M^2)^{n-2}\right), \tag{D.19}$$

with $j = L, R$ as well as

$$I = \sum_{n>1} 4\kappa_n n(n-1)\bar{\chi}_L \bar{\chi}_R (M^2)^{n-2} \tag{D.20}$$

and

$$A = \sqrt{(h^2\Gamma^F_{\chi_L} - h^2\Gamma^F_{\chi_R} + Y_L - Y_R)^2 + (2I)^2} \tag{D.21}$$

we write the diagonalization of $\mathcal{S}^{(2)}_{\text{eff}}$ in the $(\delta\chi_L(\boldsymbol{q}), \delta\chi_R(\boldsymbol{q}))$-space

$$\begin{aligned}\frac{\mathcal{S}^{(2)}_{\text{eff}}}{N} = \frac{\beta}{2}\int \tfrac{\mathrm{d}^2 q}{(2\pi)^2} \left(\delta\chi_L(-\boldsymbol{q}), \delta\chi_R(-\boldsymbol{q})\right) B(q, \bar{\chi}_L, \bar{\chi}_R, \mu_L, \mu_R, T) \times \\ \times \begin{pmatrix} \frac{h^2}{2}\left(\Gamma^F_{\chi_L} + \Gamma^F_{\chi_R}\right) + \frac{1}{2}(Y_L + Y_R) - \frac{1}{2}A & \\ & \frac{h^2}{2}\left(\Gamma^F_{\chi_L} + \Gamma^F_{\chi_R}\right) + \frac{1}{2}(Y_L + Y_R) + \frac{1}{2}A \end{pmatrix} \times \\ \times B^{-1}(q, \bar{\chi}_L, \bar{\chi}_R, \mu_L, \mu_R, T) \left(\delta\chi_L(\boldsymbol{q}), \delta\chi_R(\boldsymbol{q})\right)^T,\end{aligned} \tag{D.22}$$

where $B(q, \bar{\chi}_L, \bar{\chi}_R, \mu_L, \mu_R, T)$ is a basis changing matrix determined by `Matlab`, whose form is not relevant for our analysis. In this form one can determine, whether the diagonal entries of the matrix in Eq. (D.22) are non-negative. For the physically relevant homogeneous expansion point $\mathcal{M}$ both entries are non-negative for $\boldsymbol{q} = 0$, since otherwise the expansion point would not be a minimum when only considering homogeneous field values. Therefore, in order to prove positivity for all $q = |\boldsymbol{q}|$ it suffices again to show that the entries are monotonically increasing functions of q. We take the derivative of the entries with respect to q and require it to be non-negative

$$\frac{h^2}{2}\left[(L_{2,L})' + (L_{2,R})'\right] + 2q \mp \frac{h^2}{2}\left[(L_{2,L})' - (L_{2,R})'\right] \frac{h^2\Gamma^F_{\chi_L} - h^2\Gamma^F_{\chi_R} + Y_L - Y_R}{A} \overset{!}{\geq} 0, \tag{D.23}$$

where $L_{2,L/R} = L_{2,+}(h^2\bar{\chi}^2_{L/R}, \mu_{L/R}, T, q^2)$ and its derivative with respect to q is non-negative, i.e., $\frac{\mathrm{d}}{\mathrm{d}q} L_{2,L/R} = (L_{2,L/R})' \geq 0$, since it is a monotonically increasing function of q (compare Section 5.2). We can rearrange Eq. (D.23) and square it to obtain

$$\left(\left[(L_{2,L})' + (L_{2,R})'\right] + \frac{2q}{h^2}\right)^2 \geq \left[(L_{2,L})' - (L_{2,R})'\right]^2 \frac{\left(h^2\Gamma^F_{\chi_L} - h^2\Gamma^F_{\chi_R} + Y_L - Y_R\right)^2}{(h^2\Gamma^F_{\chi_L} - h^2\Gamma^F_{\chi_R} + Y_L - Y_R)^2 + (2I)^2} = \tag{D.24}$$

$$= \left[(L_{2,L})' - (L_{2,R})'\right]^2 c^2, \tag{D.25}$$

where obviously $0 \leq c^2 \leq 1$ and, thus, the inequality is fulfilled for all q.

Summarizing this lengthy and delicate analysis: We diagonalized the second order corrections (D.17) of a Yukawa model with multiple chemical potentials given by Eq. (D.13) using computer algebra systems such as `Matlab` [22]. Analyzing the resulting expression,

we find that both eigenvalues of the relevant curvature matrix in the second order corrections are positive, monotonically increasing functions of the momentum squared q^2 of the inhomogeneous perturbation. Thus, we do not observe instabilities of the homogeneous condensates in the Yukawa model given by Eq. (D.13). By the same reasoning, a negative wave-function renormalization (proportional to the second derivative of the two eigenvalues with respect to q), i.e., a so-called moat regime is not observed in the model. Similar behavior is expected for the other Yukawa models that correspond to the four-fermion models in Table 5.4 in Section 5.2.3.

D.3 STABILITY ANALYSIS FOR THE MODEL WITH SCALAR AND VECTOR MESONS

In this section, we collect formulae needed for the computation of the bosonic two-point vertex functions $\Gamma^{(2)}_{\phi_j,\phi_k} = \Gamma^{(2)}_{\phi_k,\phi_j}$ with $\vec{\phi} = (\sigma, \omega_\nu)$, compare Eq. (4.24). A similar collection can be found in the appendix of Ref. [3].

Inserting the homogeneous fermion propagator

$$\tilde{\bar{\mathrm{Q}}}^{-1}(\mathbf{p}, \nu_n) = \frac{-\mathrm{i}\tilde{\not{p}} + \bar{\Sigma}}{\tilde{p}^2 + \bar{\Sigma}^2}, \qquad \tilde{p} = (\nu_n - \mathrm{i}\bar{\mu}, \mathbf{p})^T \tag{D.26}$$

with $\bar{\mu} = \mu + \mathrm{i}\bar{\omega}_3$ and homogeneous expansions points $(\sigma, \omega_\nu) = (\sigma, \delta_{3,\nu}\bar{\omega}_3)$ and the respective vertex $\vec{c} = (1, -\gamma_3, \mathrm{i}\gamma_1, \mathrm{i}\gamma_2)$ for $\vec{\phi} = (\sigma, \omega_3, \omega_1, \omega_2)$ in Eq. (4.24), respectively, one obtains for the diagonal elements

$$\Gamma^{(2)}_{\sigma,\sigma} = \frac{1}{\lambda_S} + \frac{d_\gamma}{\beta} \int \frac{\mathrm{d}^2 p}{(2\pi)^2} \sum_n \frac{-\tilde{p}^2 - \mathbf{pq} + \bar{\Sigma}^2}{(\nu_n - \mathrm{i}\bar{\mu})^2 + (\mathbf{p}+\mathbf{q})^2 + \bar{\Sigma}^2} \frac{1}{(\nu_n - \mathrm{i}\bar{\mu})^2 + \mathbf{p}^2 + \bar{\Sigma}^2}, \tag{D.27}$$

$$\begin{aligned}\Gamma^{(2)}_{\omega_\nu,\omega_\nu} = \frac{1}{\lambda_V} + (1 - 2\delta_{\nu,3}) \frac{d_\gamma}{\beta} \times \\ \times \int \frac{\mathrm{d}^2 p}{(2\pi)^2} \sum_n \frac{(2\delta_{\nu,\alpha} - 1)\tilde{p}_\alpha \tilde{p}_\alpha + (2\delta_{\nu,1} - 1) p_1 q - \bar{\Sigma}^2}{(\nu_n - \mathrm{i}\bar{\mu})^2 + (\mathbf{p}+\mathbf{q})^2 + \bar{\Sigma}^2} \frac{1}{(\nu_n - \mathrm{i}\bar{\mu})^2 + \mathbf{p}^2 + \bar{\Sigma}^2},\end{aligned} \tag{D.28}$$

where we choose the angle integration such that q lies on the x_1 axis. The off-diagonal elements are given by

$$\begin{aligned}\Gamma^{(2)}_{\sigma,\omega_\nu} = \\ = \Big(\delta_{\nu,3}\,(-\mathrm{i} - 1) + 1\Big)\bar{\Sigma}\, \frac{d_\gamma}{\beta} \int \frac{\mathrm{d}^2 p}{(2\pi)^2} \sum_n \frac{2\tilde{p}_\nu + \delta_{\nu,1} p_1 q}{(\nu_n - \mathrm{i}\bar{\mu})^2 + (\mathbf{p}+\mathbf{q})^2 + \bar{\Sigma}^2} \frac{1}{(\nu_n - \mathrm{i}\bar{\mu})^2 + \mathbf{p}^2 + \bar{\Sigma}^2},\end{aligned} \tag{D.29}$$

$$\Gamma^{(2)}_{\omega_1,\omega_2} = \frac{d_\gamma}{\beta} \int \frac{\mathrm{d}^2 p}{(2\pi)^2} \sum_n \frac{2p_1 p_2 + q p_2}{(\nu_n - \mathrm{i}\bar{\mu})^2 + (\mathbf{p}+\mathbf{q})^2 + \bar{\Sigma}^2} \frac{1}{(\nu_n - \mathrm{i}\bar{\mu})^2 + \mathbf{p}^2 + \bar{\Sigma}^2}, \tag{D.30}$$

$$\Gamma^{(2)}_{\omega_3,\omega_j} = -\frac{d_\gamma}{\beta} \int \frac{\mathrm{d}^2 p}{(2\pi)^2} \sum_n \frac{2\tilde{p}_3 p_j + \delta_{j,1}\tilde{p}_3 q}{(\nu_n - \mathrm{i}\bar{\mu})^2 + (\mathbf{p}+\mathbf{q})^2 + \bar{\Sigma}^2} \frac{1}{(\nu_n - \mathrm{i}\bar{\mu})^2 + \mathbf{p}^2 + \bar{\Sigma}^2}, \quad j \in \{1, 2\}. \tag{D.31}$$

Note that in consistency with the repulsive nature of the Yukawa interaction $\bar{\psi}\omega_3\psi$, the Hessian matrix elements with only one ω_3 index are purely imaginary.

D.3.1 *Finite temperature expressions for non-vanishing q*

In order to evaluate the Hessian at finite temperatures and chemical potentials, we perform the Matsubara summation, see Appendix C.4 for an explicit calculation of such a sum. Further examples can be found for example in Refs. [64, 285]. For some of the above expression,

one needs to do some additional manipulations in order to perform the summation in an easier way or to circumvent problems in the contour integration stemming from $\tilde{p}_3^2$ terms in the numerator. Equation (D.27) is exactly the bosonic two-point vertex function of the auxiliary bosonic field appearing the GN model, and was calculated multiple times, e.g., in Refs. [211, 212, 241], see Appendix B of Ref. [2] for the evaluation in various limits of $\bar{\Sigma}$, T and q. The other entries, however, have to our knowledge not be computed.

Using some manipulation of the numerator of Eq. (D.28) for $\nu = 3$ as well as rewriting the denominator in a partial fraction (see Eqs. $(4.14-16)$ in Ref. [138] for the general idea) one finds that

$$\Gamma^{(2)}_{\omega_3,\omega_3} = \frac{1}{\lambda_V} - \ell_1(\mu, T, \bar{\Sigma}, \bar{\Omega}_3) + L_{2,+}(\bar{\mu}, T, \bar{\Sigma}, q) + \ell_3(\mu, T, \bar{\Sigma}, q), \tag{D.32}$$

where ℓ_1 is known from the GN model and appears in the gap equation (C.16) or (6.10),

$$L_{2,+}(\bar{\mu}, T, \bar{\Sigma}, q) = \frac{1}{2}\int \frac{\mathrm{d}^2 p}{(2\pi)^2} \sum_{n=-\infty}^{\infty} \frac{d_\gamma}{\beta} \frac{(q^2 + 4\bar{\Sigma}^2)}{(\nu_n - \mathrm{i}\bar{\mu})^2 + \mathbf{p}^2 + \bar{\Sigma}^2} \frac{1}{(\nu_n - \mathrm{i}\bar{\mu})^2 + (\mathbf{p}+\mathbf{q})^2 + \bar{\Sigma}^2} = \tag{D.33}$$

$$\equiv \frac{1}{2}\left(q^2 + 4\bar{\Sigma}^2\right) \ell_2(\mu, T, \bar{\Sigma}, q)$$

is (up to a factor of 2) the momentum dependence of the bosonic two-point vertex function in the GN model [241] plus the novel contribution

$$\ell_3(\bar{\mu}, T, \bar{\Sigma}, q) = \tfrac{2d_\gamma}{\beta} \int \frac{\mathrm{d}^2 p}{(2\pi)^2} \sum_{n=-\infty}^{\infty} \frac{\mathbf{p}^2 + \mathbf{pq}}{(\nu_n - \mathrm{i}\bar{\mu})^2 + \mathbf{p}^2 + \bar{\Sigma}^2} \quad \frac{1}{(\nu_n - \mathrm{i}\bar{\mu})^2 + (\mathbf{p}+\mathbf{q})^2 + \bar{\Sigma}^2}. \tag{D.34}$$

The Matsubara summation can be performed as usual by analytic continuation and a contour integral. Then, one obtains

$$\ell_3(\bar{\mu}, T, \bar{\Sigma}, q) = 2d_\gamma \int \frac{\mathrm{d}^2 p}{(2\pi)^2} \frac{(p^2 + \mathbf{pq})}{q^2 + 2\mathbf{pq}} \left[\frac{1}{2E}\left(1 - n_F(E) - n_{\bar{F}}(E)\right) - (E \to E_q)\right] \tag{D.35}$$

with $E = \sqrt{\boldsymbol{p}^2 + \bar{\sigma}^2}$, $n_F(x)$, $n_{\bar{F}}(x)$ defined in Eq. (C.18) and $E_q = \sqrt{(\boldsymbol{p}+\boldsymbol{q})^2 + \bar{\Sigma}^2}$. This expression can be split up between $p_1 < q/2$ and $p_1 > q/2$ (remember that $\boldsymbol{q} = (q, 0)$), manipulated and evaluated using a Cauchy-Principal value (similar to how L_2 can be evaluated) and amounts to

$$\ell_3(\bar{\mu}, T, \bar{\Sigma}, q) = \tag{D.36}$$

$$= \frac{d_\gamma}{(4\pi)}\left[\int_0^{q/2} \mathrm{d}p \quad \frac{p}{E}\frac{p^2 - q^2/2}{q\sqrt{q^2 - 4p}}\left[1 - n_F(E) - n_{\bar{F}}(E)\right] + \int_0^{\infty} \mathrm{d}p \frac{p}{E}\left[1 - n_F(E) - n_{\bar{F}}(E)\right]\right],$$

where the latter term is linearly divergent and identical to ℓ_1. Thus, the divergences of ℓ_1 and ℓ_3 exactly cancel each other out such that Eq. (D.32) is finite. We are aware that these divergences occur because of splitting up the numerator of Eq. (D.28) for $\nu = 3$, as described above. However, this procedure is easier than dealing with the $(\nu_n - \mathrm{i}\mu)^2$ term in the numerator, since the standard method of analytic continuation and contour integration cannot be done as usual, since the asymptotic behavior of the integrand is not suppressed strong enough at the boundaries of the contour at infinity.

In turn, the other diagonal elements are evaluated in a straight forward manner

$$\Gamma^{(2)}_{\omega_j,\omega_j} = \tag{D.37}$$
$$= \frac{1}{\lambda_V} - \ell_1 + \frac{q^2}{2}\ell_2 + \frac{2N_\gamma}{\beta}\int \frac{\mathrm{d}^2p}{(2\pi)^2}\sum_n \frac{p_j^2 + \delta_{j,1}p_1 q}{(\nu_n - \mathrm{i}\bar{\mu})^2 + \mathbf{p}^2 + \bar{\Sigma}^2}\frac{1}{(\nu_n - \mathrm{i}\bar{\mu})^2 + (\mathbf{p}+\mathbf{q})^2 + \bar{\Sigma}^2}.$$

Splitting up the numerator and treating the remaining integrals with standard techniques (shifts, inversions of the integration variable) allow to identify already known integral structures for $j = 1$ and one obtains

$$\Gamma^{(2)}_{\omega_1,\omega_1} = \frac{1}{\lambda_V} - \ell_1 + \frac{1}{2}q^2\ell_2 + \ell_1 + q^2\ell_2 = \frac{1}{\lambda_V} + \frac{3}{2}q^2\ell_2(\mu, T, \bar{\Sigma}, q). \tag{D.38}$$

Also, one finds for $j = 2$

$$\Gamma^{(2)}_{\omega_2,\omega_2} = \frac{1}{\lambda_V} + \frac{N_\gamma}{2\pi q}\int_0^{q/2} \frac{p^3}{E\sqrt{q^2 - 4p^2}}\left[1 - n_F(E) - n_{\bar{F}}(E)\right], \tag{D.39}$$

which is again finite. Note that the differences in the expression for $H_{\omega_1\omega_1}$ and $H_{\omega_1\omega_1}$ come from the choice on $\mathbf{q} = (q, 0)$. The matrix elements $H_{\omega_2\omega_2}$ and $H_{\omega_1\omega_1}$ would be exchanged if we would have chosen $\mathbf{q} = (0, q)$, as expected since the analysis is invariant under spatial rotations. The limit of zero temperature in the above expressions is rather straightforward.

The mixing between σ and ω_3 is given by

$$\Gamma^{(2)}_{\sigma,\omega_3} = -\mathrm{i}\bar{\Sigma}\frac{2N_\gamma}{\beta}\int \frac{\mathrm{d}^2p}{(2\pi)^2}\sum_{n=-\infty}^{\infty} \frac{\tilde{p}_3}{(\nu_n - \mathrm{i}\bar{\mu})^2 + \mathbf{p}^2 + \bar{\Sigma}^2}\frac{1}{(\nu_n - \mathrm{i}\bar{\mu})^2 + (\mathbf{p}+\mathbf{q})^2 + \bar{\Sigma}^2}. \tag{D.40}$$

This expression can be evaluated using a contour integral, as the analytic continuation of the integrand is well-behaved when closing the contour at infinity. The result is

$$\Gamma^{(2)}_{\sigma,\omega_3}(q) = \mathrm{i}\bar{\Sigma}N_\gamma\int \frac{\mathrm{d}^2p}{(2\pi)^2}\frac{1}{\mathbf{q}^2 + 2\mathbf{pq}}\left[(n_F(E) - n_{\bar{F}}(E)) - (n_F(E_q) - n_{\bar{F}}(E_q))\right] \tag{D.41}$$
$$= -\mathrm{i}\bar{\Sigma}N_\gamma\int_0^{q/2}\frac{\mathrm{d}p}{2\pi}\frac{p}{q\sqrt{q^2 - 4p^2}}\left[n_F(E) - n_{\bar{F}}(E)\right] \equiv -\mathrm{i}\bar{\Sigma}\ell_4(\mu, T, \bar{\Sigma}, q),$$

where one can directly see that this expression vanishes in the SP and for $\mu = 0$.

Also, one obtains

$$\Gamma^{(2)}_{\sigma,\omega_1} = 2\bar{\Sigma}|q|\ell_2(\mu, T, \bar{\Sigma}, q) \tag{D.42}$$

and $H_{\sigma\omega_2} = 0$, where the term with $j = 2$ vanishes using symmetry arguments in the angle integration[3] (compare Eq. (D.29) for $\nu = 2$). Again, the two matrix elements $H_{\sigma\omega_1}$ and $H_{\sigma\omega_1}$ would be exchanged, if we would setup the momentum integration such that $\mathbf{q}$ would be aligned with the p_2 axis. In a similar way as for $H_{\sigma\omega_2}$, we obtain that $H_{\omega_1\omega_2} = H_{\omega_3\omega_2} = 0$. Lastly, one obtains

$$\Gamma^{(2)}_{\omega_3,\omega_1} = 0 \tag{D.43}$$

through splitting up the integral in Eq. (D.31) into two integrals, where each integral contains one of the summands in the numerator. Both integrals turn to be proportional to ℓ_4, but with different signs and prefactors such that both contributions cancel each other.

3 At first glance, this seems to be a trivial integration, but one still needs to perform a Cauchy principal value before using symmetry arguments.

D.3.2 *Finite temperature expressions for $q = 0$*

For the $q = 0$ expressions (and even more limits) of $H_{\sigma\sigma}$ and all integrals related to it, we refer again to Ref. [9]. Note that several of the integrals in the beginning of Appendix D.3 vanish, when the limit of q going to zero is taken. More precisely, we find

$$\Gamma^{(2)}_{\sigma,\omega_j}(q=0) = 0, \qquad \Gamma^{(2)}_{\omega_1,\omega_2}(q=0) = 0, \qquad \Gamma^{(2)}_{\omega_3,\omega_j}(q=0) = 0, \qquad j \in \{1,2\}, \tag{D.44}$$

as can be seen from going into polar coordinates after Matsubara summation and performing the angle integration, respectively. The Hessian $\Gamma^{(2)}_{\phi_j,\phi_k}$ becomes diagonal w.r.t. the 2×2 block with $\phi_j, \phi_k \in \{\omega_1, \omega_2\}$. Thus, complex-conjugate eigenvalue pairs can only be generated by mixing of σ and ω_3 at $q = 0$, allowing to study this phenomenon by only taking the respective 2×2 block. For the rest of the diagonal elements, we find

$$\begin{aligned}
\Gamma^{(2)}_{\omega_j,\omega_j}(q=0) &= \frac{1}{\lambda_V} - \ell_1(\mu,T,\bar{\Sigma}) + \ell_3(\mu,T,\bar{\Sigma},q=0) \\
&= \frac{1}{\lambda_V} - \ell_1 + \frac{N_\gamma}{8\pi}\int_0^\infty \mathrm{d}p \frac{p^3}{E^3}\Big[1 - (1+\beta E)\left(n_F(E) + n_{\bar{F}}(E)\right) + \\
&\qquad\qquad + \beta E\left(n_F^2(E) + n_{\bar{F}}^2(E)\right)\Big] \\
&= \frac{1}{\lambda_V} + \frac{N_\gamma}{8\pi}\int_{|\bar{\Sigma}|}^\infty \mathrm{d}E \Big[\beta E\left[n_F^2(E) + n_{\bar{F}}^2(E) - n_F(E) - n_{\bar{F}}(E)\right] + \\
&\qquad - \frac{\bar{\Sigma}^2}{E^2}\left[1 - (1+\beta E)\left(n_F(E) + n_{\bar{F}}(E)\right) + \beta E\left(n_F^2(E) + n_{\bar{F}}^2(E)\right)\right]\Big],
\end{aligned} \tag{D.45}$$

which is finite due to the suppression of high momenta in the first summand of the integrand, and

$$\Gamma^{(2)}_{\omega_3,\omega_3}(q=0) = \frac{1}{\lambda_V} - \ell_1 + 2\bar{\Sigma}^2\ell_2 + \ell_3, \tag{D.46}$$

which is identical to $\Gamma^{(2)}_{\omega_j,\omega_j}$ up to an additional contribution of $2\bar{\Sigma}^2\ell_2$. The diagonal element $\Gamma^{(2)}_{\sigma,\sigma}$ is given by the bosonic two-point vertex function $\Gamma^{(2)}_\sigma(q)$ in the $(2+1)$-dimensional GN model and studied in this limit in Refs. [2, 241]. For the remaining off-diagonal element we find

$$\Gamma^{(2)}_{\sigma,\omega_3} = -\mathrm{i}\bar{\Sigma}\frac{d_\gamma}{\pi}\int_0^\infty \mathrm{d}E \left\{\beta E\left[n_F^2(E) - n_{\bar{F}}^2(E)\right] - \left[n_F(E) - n_{\bar{F}}(E)\right]\right\}. \tag{D.47}$$

BACK MATTER

BIBLIOGRAPHY

[1] Adrian Koenigstein, Laurin Pannullo, Stefan Rechenberger, Martin J. Steil, and Marc Winstel. "Detecting inhomogeneous chiral condensation from the bosonic two-point function in the (1 + 1)-dimensional Gross–Neveu model in the mean-field approximation*." In: *J. Phys. A* 55.37 (2022), p. 375402. DOI: 10.1088/1751-8121/ac820a. arXiv: 2112.07024 [hep-ph] (cit. on pp. 8, 10, 12, 39, 40, 44, 54, 57, 65–68, 76, 89, 102, 104, 109, 128, 144).

[2] Laurin Pannullo and Marc Winstel. "Absence of inhomogeneous chiral phases in (2+1)-dimensional four-fermion and Yukawa models." In: *Phys. Rev. D* 108.3 (2023), p. 036011. DOI: 10.1103/PhysRevD.108.036011. arXiv: 2305.09444 [hep-ph] (cit. on pp. 54, 57, 60, 81, 88, 101, 102, 173, 176, 184, 186, 190, 192).

[3] Marc Winstel. "Spatially oscillating correlation functions in (2+1)-dimensional four-fermion models: The mixing of scalar and vector modes at finite density." In: *Phys. Rev. D* 110.3 (2024), p. 034008. DOI: 10.1103/PhysRevD.110.034008. arXiv: 2403.07430 [hep-ph] (cit. on pp. vi, 81, 106, 163, 189).

[4] Adrian Koenigstein and Marc Winstel. "Revisiting the spatially inhomogeneous condensates in the (1 + 1)-dimensional chiral Gross–Neveu model via the bosonic two-point function in the infinite-N limit." In: *J. Phys. A* 57.33 (2024), p. 335401. DOI: 10.1088/1751-8121/ad6721. arXiv: 2405.03459 [hep-th] (cit. on pp. 14, 54, 57, 74–76).

[5] Marc Winstel and Laurin Pannullo. "Stability of homogeneous chiral phases against inhomogeneous perturbations in 2+1 dimensions." In: *PoS* LATTICE2022 (2023), p. 195. DOI: 10.22323/1.430.0195. arXiv: 2211.04414 [hep-ph] (cit. on pp. 58, 187).

[6] Marc Winstel and Semeon Valgushev. "Lattice study of disordering of inhomogeneous condensates and the Quantum Pion Liquid in effective $O(N)$ model." In: *Excited QCD 2024 Workshop*. 2024. arXiv: 2403.18640 [hep-lat] (cit. on p. 127).

[7] Laurin Pannullo, Marc Wagner, and Marc Winstel. "Inhomogeneous Phases in the Chirally Imbalanced 2 + 1-Dimensional Gross-Neveu Model and Their Absence in the Continuum Limit." In: *Symmetry* 14.2 (2022), p. 265. DOI: 10.3390/sym14020265. arXiv: 2112.11183 [hep-lat] (cit. on pp. 56, 58, 60, 86, 89, 92–94, 104, 105).

[8] Marc Winstel, Laurin Pannullo, and Marc Wagner. "Phase diagram of the 2+1-dimensional Gross-Neveu model with chiral imbalance." In: *PoS* LATTICE2021 (2022), p. 381. DOI: 10.22323/1.396.0381. arXiv: 2109.04277 [hep-lat] (cit. on pp. 56, 58, 89, 104).

[9] Laurin Pannullo, Marc Wagner, and Marc Winstel. "Inhomogeneous phases in the 3+1-dimensional Nambu-Jona-Lasinio model and their dependence on the regularization scheme." In: *PoS* LATTICE2022 (2023), p. 156. DOI: 10.22323/1.430.0156. arXiv: 2212.05783 [hep-lat] (cit. on pp. 11, 39, 128, 153, 157, 192).

[10] Laurin Pannullo, Marc Wagner, and Marc Winstel. "Regularization effects in the Nambu–Jona-Lasinio model: Strong scheme dependence of inhomogeneous phases and persistence of the moat regime." In: *Phys. Rev. D* 110.7 (2024), p. 076006. DOI: 10.1103/PhysRevD.110.076006. arXiv: 2406.11312 [hep-ph] (cit. on pp. 8, 11, 12, 14, 15, 39, 48, 49, 56, 57, 65, 90, 104, 108, 125, 144, 153, 154, 156, 157).

[11] Zohar Nussinov, Michael C. Ogilvie, Laurin Pannullo, Robert D. Pisarski, Fabian Rennecke, Stella T. Schindler, and Marc Winstel. "Dilepton production from moaton quasiparticles." 2024. arXiv: 2410.22418 [hep-ph] (cit. on pp. 13, 125, 126, 129, 156, 157, 159).

[12] André Miede. *classicthesis v4.2*. Sept. 2015. URL: https://bitbucket.org/amiede/classicthesis/ (cit. on p. vi).

[13] R. Bringhurst. *The Elements of Typographic Style*. Elements of Typographic Style. Hartley & Marks, Publishers, 2004. ISBN: 9780881792065. URL: https://books.google.de/books?id=940sAAAAYAAJ (cit. on p. vi).

[14] Philip Kime, Moritz Wemheue, Audrey Boruvka, Joseph Wright, and Philipp Lehman. *CTAN: Package BibLATEX v3.20*. 2024. URL: https://ctan.org/pkg/biblatex (cit. on p. vi).

[15] Francois Francois Charette and Philip Kime. *CTAN: biber v2.20*. 2024. URL: https://ctan.org/pkg/biber (cit. on p. vi).

[16] Nicola Talbot. *CTAN: Package glossaries v4.55*. 2024. URL: https://ctan.org/pkg/glossaries (cit. on p. vi).

[17] Nicola Talbot. *CTAN: Package glossaries-extra v1.56*. 2025. URL: https://ctan.org/pkg/glossaries-extra (cit. on p. vi).

[18] Toby Cubitt. *CTAN: Package cleveref v0.21.4*. 2018. URL: https://ctan.org/pkg/cleveref (cit. on p. vi).

[19] Guido Van Rossum and Fred L. Drake. *Python 3 Reference Manual*. Scotts Valley, CA: CreateSpace, 2009. ISBN: 1441412697 (cit. on pp. vi, 76, 101, 113–115, 118–120, 181).

[20] John D. Hunter. "Matplotlib: A 2D Graphics Environment." In: *Computing in Science & Engineering* 9.3 (2007), pp. 90–95. DOI: 10.1109/MCSE.2007.55 (cit. on pp. vi, 113, 114, 118–120).

[21] ISO. *ISO/IEC 14882:2014 Information technology — Programming languages — C++*. Fourth. Dec. 2014. URL: http://www.iso.org/iso/home/store/catalogue_ics/catalogue_detail_ics.htm?csnumber=64029 (cit. on p. vi).

[22] The MathWorks Inc. *MATLAB version: 9.13.0 (R2022b)*. Natick, Massachusetts, United States, 2022. URL: https://www.mathworks.com (cit. on pp. vi, 97, 188).

[23] Benito van der Zander, Jan Sundemeyer, Daniel Braun, and Tim Hoffmann. *TeXstudio v4.8.1*. 2024. URL: https://www.texstudio.org (cit. on p. vi).

[24] Microsoft. *Visual studio code v1.97.2*. 2025. URL: https://code.visualstudio.com (cit. on p. vi).

[25] OpenAI. *ChatGPT 4o*. 2024. URL: https://chatgpt.com (cit. on p. vii).

[26] Github, Microsoft, and OpenAI. *Github Copilot v0.24*. 2025. URL: https://github.com/features/copilot (cit. on p. vii).

[27] Murray Gell-Mann. "The Eightfold Way: A Theory of strong interaction symmetry." In: (Mar. 1961). DOI: 10.2172/4008239 (cit. on p. 1).

[28] Yuval Ne'eman. "Derivation of strong interactions from a gauge invariance." In: *Nucl. Phys.* 26 (1961). Ed. by R. Ruffini and Y. Verbin, pp. 222–229. DOI: 10.1016/0029-5582(61)90134-1 (cit. on p. 1).

[29] Murray Gell-Mann. "Symmetries of baryons and mesons." In: *Phys. Rev.* 125 (1962), pp. 1067–1084. DOI: 10.1103/PhysRev.125.1067 (cit. on p. 1).

[30] G. Zweig. "An SU(3) model for strong interaction symmetry and its breaking. Version 2." In: *Developments in the Quark Theory of Hadrons, Vol. 1., 1964 - 1978.* 1964, pp. 22–101. DOI: 10.17181/CERN-TH-412 (cit. on p. 1).

[31] G. Zweig. "An SU(3) model for strong interaction symmetry and its breaking. Version 1." In: *Developments in the Quark Theory of Hadrons, Vol. 1., 1964 - 1978.* Jan. 1964. DOI: 10.17181/CERN-TH-401 (cit. on p. 1).

[32] M. Y. Han and Yoichiro Nambu. "Three Triplet Model with Double SU(3) Symmetry." In: *Phys. Rev.* 139 (1965), B1006–B1010. DOI: 10.1103/PhysRev.139.B1006 (cit. on p. 1).

[33] H. Fritzsch, Murray Gell-Mann, and H. Leutwyler. "Advantages of the Color Octet Gluon Picture." In: *Phys. Lett. B* 47 (1973), pp. 365–368. DOI: 10.1016/0370-2693(73)90625-4 (cit. on p. 1).

[34] William A. Bardeen and R. B. Pearson. "Local Gauge Invariance and the Bound State Nature of Hadrons." In: *Phys. Rev. D* 14 (1976), p. 547. DOI: 10.1103/PhysRevD.14.547 (cit. on p. 1).

[35] O. W. Greenberg and C. A. Nelson. "Color Models of Hadrons." In: *Phys. Rept.* 32 (1977), pp. 69–121. DOI: 10.1016/0370-1573(77)90035-7 (cit. on p. 1).

[36] David J. Gross and Frank Wilczek. "Ultraviolet Behavior of Nonabelian Gauge Theories." In: *Phys. Rev. Lett.* 30 (1973), pp. 1343–1346. DOI: 10.1103/PhysRevLett.30.1343 (cit. on pp. 2, 3, 7, 43).

[37] H. David Politzer. "Reliable Perturbative Results for Strong Interactions?" In: *Phys. Rev. Lett.* 30 (1973). Ed. by J. C. Taylor, pp. 1346–1349. DOI: 10.1103/PhysRevLett.30.1346 (cit. on pp. 2, 3).

[38] Peter W. Higgs. "Broken symmetries, massless particles and gauge fields." In: *Phys. Lett.* 12 (1964), pp. 132–133. DOI: 10.1016/0031-9163(64)91136-9 (cit. on p. 2).

[39] Peter W. Higgs. "Broken Symmetries and the Masses of Gauge Bosons." In: *Phys. Rev. Lett.* 13 (1964), pp. 508–509. DOI: 10.1103/PhysRevLett.13.508 (cit. on p. 2).

[40] Peter W. Higgs. "Spontaneous Symmetry Breakdown without Massless Bosons." In: *Phys. Rev.* 145 (1966), pp. 1156–1163. DOI: 10.1103/PhysRev.145.1156 (cit. on p. 2).

[41] R. L. Workman et al. "Review of Particle Physics." In: *PTEP* 2022 (2022), p. 083C01. DOI: 10.1093/ptep/ptac097 (cit. on p. 2).

[42] Yoichiro Nambu and G. Jona-Lasinio. "Dynamical Model of Elementary Particles Based on an Analogy with Superconductivity. 1." In: *Phys. Rev.* 122 (1961). Ed. by T. Eguchi, pp. 345–358. DOI: 10.1103/PhysRev.122.345 (cit. on pp. 2, 7).

[43] Yoichiro Nambu and G. Jona-Lasinio. "Dynamical model of elementary particles based on an analogy with superconductivity. II." In: *Phys. Rev.* 124 (1961). Ed. by T. Eguchi, pp. 246–254. DOI: 10.1103/PhysRev.124.246 (cit. on pp. 2, 7).

[44] J. Goldstone. "Field Theories with Superconductor Solutions." In: *Nuovo Cim.* 19 (1961), pp. 154–164. DOI: 10.1007/BF02812722 (cit. on pp. 2, 74, 131).

[45] Jeffrey Goldstone, Abdus Salam, and Steven Weinberg. "Broken Symmetries." In: *Phys. Rev.* 127 (1962), pp. 965–970. DOI: 10.1103/PhysRev.127.965 (cit. on pp. 2, 74, 131).

[46] F. Gursey. "On the Symmetries of strong and weak interactions." In: *Nuovo Cim.* 16 (1960), pp. 230–240. DOI: 10.1007/BF02860276 (cit. on p. 2).

[47] Henning Heiselberg and Morten Hjorth-Jensen. "Phases of dense matter in neutron stars." In: *Phys. Rept.* 328 (2000), pp. 237–327. DOI: 10.1016/S0370-1573(99)00110-6. arXiv: nucl-th/9902033 (cit. on p. 3).

[48] James M. Lattimer and Madappa Prakash. "The Equation of State of Hot, Dense Matter and Neutron Stars." In: *Phys. Rept.* 621 (2016), pp. 127–164. DOI: 10.1016/j.physrep.2015.12.005. arXiv: 1512.07820 [astro-ph.SR] (cit. on p. 3).

[49] Gordon Baym, Tetsuo Hatsuda, Toru Kojo, Philip D. Powell, Yifan Song, and Tatsuyuki Takatsuka. "From hadrons to quarks in neutron stars: a review." In: *Rept. Prog. Phys.* 81.5 (2018), p. 056902. DOI: 10.1088/1361-6633/aaae14. arXiv: 1707.04966 [astro-ph.HE] (cit. on p. 3).

[50] V. Vovchenko, V. V. Begun, and M. I. Gorenstein. "Hadron multiplicities and chemical freeze-out conditions in proton-proton and nucleus-nucleus collisions." In: *Phys. Rev. C* 93.6 (2016), p. 064906. DOI: 10.1103/PhysRevC.93.064906. arXiv: 1512.08025 [nucl-th] (cit. on pp. 3, 40).

[51] L. Adamczyk et al. "Bulk Properties of the Medium Produced in Relativistic Heavy-Ion Collisions from the Beam Energy Scan Program." In: *Phys. Rev. C* 96.4 (2017), p. 044904. DOI: 10.1103/PhysRevC.96.044904. arXiv: 1701.07065 [nucl-ex] (cit. on pp. 3, 40).

[52] Martin Jakob Steil. "From zero-dimensional theories to inhomogeneous phases with the functional renormalization group." PhD thesis. Technische Universität Darmstadt, 2024. DOI: 10.25534/tuprints-00009485. URL: https://tuprints.ulb.tu-darmstadt.de/27380/ (cit. on pp. 3, 17, 51, 66, 158).

[53] Dirk H. Rischke. "The Quark gluon plasma in equilibrium." In: *Prog. Part. Nucl. Phys.* 52 (2004), pp. 197–296. DOI: 10.1016/j.ppnp.2003.09.002. arXiv: nucl-th/0305030 (cit. on pp. 3–5).

[54] P. Braun-Munzinger and J. Wambach. "The Phase Diagram of Strongly-Interacting Matter." In: *Rev. Mod. Phys.* 81 (2009), pp. 1031–1050. DOI: 10.1103/RevModPhys.81.1031. arXiv: 0801.4256 [hep-ph] (cit. on p. 3).

[55] Kenji Fukushima and Tetsuo Hatsuda. "The phase diagram of dense QCD." In: *Rept. Prog. Phys.* 74 (2011), p. 014001. DOI: 10.1088/0034-4885/74/1/014001. arXiv: 1005.4814 [hep-ph] (cit. on pp. 3, 4).

[56] Kenji Fukushima and Chihiro Sasaki. "The phase diagram of nuclear and quark matter at high baryon density." In: *Prog. Part. Nucl. Phys.* 72 (2013), pp. 99–154. DOI: 10.1016/j.ppnp.2013.05.003. arXiv: 1301.6377 [hep-ph] (cit. on pp. 3, 4).

[57] Adrian Koenigstein. private communications (cit. on pp. 4, 181).

[58] P. Petreczky. "Lattice QCD at non-zero temperature." In: *J. Phys. G* 39 (2012), p. 093002. DOI: 10.1088/0954-3899/39/9/093002. arXiv: 1203.5320 [hep-lat] (cit. on p. 3).

[59] Christof Gattringer and Christian B. Lang. *Quantum chromodynamics on the lattice.* Berlin: Springer, 2010. ISBN: 978-3-642-01849-7, 978-3-642-01850-3. DOI: 10.1007/978-3-642-01850-3 (cit. on pp. 3, 141, 142).

[60] John C. Collins and M. J. Perry. "Superdense Matter: Neutrons Or Asymptotically Free Quarks?" In: *Phys. Rev. Lett.* 34 (1975), p. 1353. DOI: 10.1103/PhysRevLett.34.1353 (cit. on p. 4).

[61] Edward V. Shuryak. "Quantum Chromodynamics and the Theory of Superdense Matter." In: *Phys. Rept.* 61 (1980), pp. 71–158. DOI: 10.1016/0370-1573(80)90105-2 (cit. on p. 4).

[62] Paul Stankus, David Silvermyr, Soren Sorensen, and Victoria Greene, eds. *Proceedings, 21st International Conference on Ultra-Relativistic nucleus nucleus collisions (Quark matter 2009): Knoxville, USA, March 30-April 4, 2009.* Vol. 830. 2009, pp.1c–968c (cit. on p. 4).

[63] Andrei D. Linde. "Infrared Problem in Thermodynamics of the Yang-Mills Gas." In: *Phys. Lett. B* 96 (1980), pp. 289–292. DOI: 10.1016/0370-2693(80)90769-8 (cit. on p. 4).

[64] Joseph I. Kapusta and Charles Gale. *Finite-temperature field theory: Principles and applications.* Cambridge Monographs on Mathematical Physics. Cambridge University Press, 2011. ISBN: 978-0-52182082-0. DOI: 10.1017/CBO9780511535130 (cit. on pp. 4, 17, 18, 20, 33, 56, 78, 176, 178, 186, 189).

[65] R. Hagedorn. "Statistical thermodynamics of strong interactions at high-energies." In: *Nuovo Cim. Suppl.* 3 (1965), pp. 147–186 (cit. on p. 4).

[66] Larry D. McLerran and Benjamin Svetitsky. "Quark Liberation at High Temperature: A Monte Carlo Study of SU(2) Gauge Theory." In: *Phys. Rev. D* 24 (1981), p. 450. DOI: 10.1103/PhysRevD.24.450 (cit. on p. 4).

[67] G. Boyd, J. Engels, F. Karsch, E. Laermann, C. Legeland, M. Lutgemeier, and B. Petersson. "Thermodynamics of SU(3) lattice gauge theory." In: *Nucl. Phys. B* 469 (1996), pp. 419–444. DOI: 10.1016/0550-3213(96)00170-8. arXiv: hep-lat/9602007 (cit. on p. 4).

[68] Y. Aoki, G. Endrodi, Z. Fodor, S. D. Katz, and K. K. Szabo. "The Order of the quantum chromodynamics transition predicted by the standard model of particle physics." In: *Nature* 443 (2006), pp. 675–678. DOI: 10.1038/nature05120. arXiv: hep-lat/0611014 (cit. on p. 4).

[69] Y. Aoki, Szabolcs Borsanyi, Stephan Durr, Zoltan Fodor, Sandor D. Katz, Stefan Krieg, and Kalman K. Szabo. "The QCD transition temperature: results with physical masses in the continuum limit II." In: *JHEP* 06 (2009), p. 088. DOI: 10.1088/1126-6708/2009/06/088. arXiv: 0903.4155 [hep-lat] (cit. on pp. 4, 6).

[70] Szabolcs Borsanyi, Zoltan Fodor, Christian Hoelbling, Sandor D Katz, Stefan Krieg, Claudia Ratti, and Kalman K. Szabo. "Is there still any T_c mystery in lattice QCD? Results with physical masses in the continuum limit III." In: *JHEP* 09 (2010), p. 073. DOI: 10.1007/JHEP09(2010)073. arXiv: 1005.3508 [hep-lat] (cit. on pp. 4, 6).

[71] P. Petreczky and H. -P. Schadler. "Renormalization of the Polyakov loop with gradient flow." In: *Phys. Rev. D* 92.9 (2015), p. 094517. DOI: 10.1103/PhysRevD.92.094517. arXiv: 1509.07874 [hep-lat] (cit. on p. 5).

[72] A. Bazavov, N. Brambilla, H. -T. Ding, P. Petreczky, H. -P. Schadler, A. Vairo, and J. H. Weber. "Polyakov loop in 2+1 flavor QCD from low to high temperatures." In: *Phys. Rev. D* 93.11 (2016), p. 114502. DOI: 10.1103/PhysRevD.93.114502. arXiv: 1603.06637 [hep-lat] (cit. on p. 5).

[73] David Anthony Clarke, Olaf Kaczmarek, Frithjof Karsch, Anirban Lahiri, and Mugdha Sarkar. "Sensitivity of the Polyakov loop and related observables to chiral symmetry restoration." In: *Phys. Rev. D* 103.1 (2021), p. L011501. DOI: 10.1103/PhysRevD.103.L011501. arXiv: 2008.11678 [hep-lat] (cit. on p. 5).

[74] Anirban Lahiri. "Aspects of finite temperature QCD towards the chiral limit." In: *PoS* LATTICE2021 (2022), p. 003. DOI: 10.22323/1.396.0003. arXiv: 2112.08164 [hep-lat] (cit. on p. 5).

[75] Axel Maas. "On the spectrum of the Faddeev-Popov operator in topological background fields." In: *Eur. Phys. J. C* 48 (2006), pp. 179–192. DOI: 10.1140/epjc/s10052-006-0003-y. arXiv: hep-th/0511307 (cit. on p. 5).

[76] Axel Maas. "Instantons, monopoles, vortices, and the Faddeev-Popov operator eigenspectrum." In: *Nucl. Phys. A* 790 (2007). Ed. by Lauro Tomio, S. Adhikari, and G. Krein, pp. 566–569. DOI: 10.1016/j.nuclphysa.2007.03.096. arXiv: hep-th/0610011 (cit. on p. 5).

[77] L. Ya. Glozman. "$SU(2N_F)$ symmetry of QCD at high temperature and its implications." In: *Acta Phys. Polon. Supp.* 10 (2017), p. 583. DOI: 10.5506/APhysPolBSupp.10.583. arXiv: 1610.00275 [hep-lat] (cit. on p. 5).

[78] L. Ya. Glozman. "Chiral spin symmetry and hot/dense QCD." In: *Prog. Part. Nucl. Phys.* 131 (2023), p. 104049. DOI: 10.1016/j.ppnp.2023.104049. arXiv: 2209.10235 [hep-lat] (cit. on p. 5).

[79] T. Hatsuda and T. Kunihiro. "Fluctuation Effects in Hot Quark Matter: Precursors of Chiral Transition at Finite Temperature." In: *Phys. Rev. Lett.* 55 (1985), pp. 158–161. DOI: 10.1103/PhysRevLett.55.158 (cit. on p. 5).

[80] Carleton E. Detar. "A Conjecture Concerning the Modes of Excitation of the Quark-Gluon Plasma." In: *Phys. Rev. D* 32 (1985), p. 276. DOI: 10.1103/PhysRevD.32.276 (cit. on p. 5).

[81] C. Rohrhofer et al. "Symmetries of spatial meson correlators in high temperature QCD." In: *Phys. Rev. D* 100.1 (2019), p. 014502. DOI: 10.1103/PhysRevD.100.014502. arXiv: 1902.03191 [hep-lat] (cit. on p. 5).

[82] C. Rohrhofer, Y. Aoki, L. Ya. Glozman, and S. Hashimoto. "Chiral-spin symmetry of the meson spectral function above T_c." In: *Phys. Lett. B* 802 (2020), p. 135245. DOI: 10.1016/j.physletb.2020.135245. arXiv: 1909.00927 [hep-lat] (cit. on p. 5).

[83] Leonid Ya. Glozman, Owe Philipsen, and Robert D. Pisarski. "Chiral spin symmetry and the QCD phase diagram." In: *Eur. Phys. J. A* 58.12 (2022), p. 247. DOI: 10.1140/epja/s10050-022-00895-4. arXiv: 2204.05083 [hep-ph] (cit. on p. 5).

[84] Peter Lowdon and Owe Philipsen. "Pion spectral properties above the chiral crossover of QCD." In: *JHEP* 10 (2022), p. 161. DOI: 10.1007/JHEP10(2022)161. arXiv: 2207.14718 [hep-lat] (cit. on p. 5).

[85] Bertrand C. Barrois. "Superconducting Quark Matter." In: *Nucl. Phys. B* 129 (1977), pp. 390–396. DOI: 10.1016/0550-3213(77)90123-7 (cit. on p. 5).

[86] Steven C. Frautschi. "Asymptotic freedom and color superconductivity in dense quark matter." In: *Workshop on Theoretical Physics: Hadronic Matter at Extreme Energy Density*. Oct. 1978 (cit. on p. 5).

[87] R. Rapp, Thomas Schäfer, Edward V. Shuryak, and M. Velkovsky. "Diquark Bose condensates in high density matter and instantons." In: *Phys. Rev. Lett.* 81 (1998), pp. 53–56. DOI: 10.1103/PhysRevLett.81.53. arXiv: hep-ph/9711396 (cit. on p. 5).

[88] Mark G. Alford, Krishna Rajagopal, and Frank Wilczek. "Color flavor locking and chiral symmetry breaking in high density QCD." In: *Nucl. Phys. B* 537 (1999), pp. 443–458. DOI: 10.1016/S0550-3213(98)00668-3. arXiv: hep-ph/9804403 (cit. on p. 5).

[89] Mark G. Alford, Andreas Schmitt, Krishna Rajagopal, and Thomas Schäfer. "Color superconductivity in dense quark matter." In: *Rev. Mod. Phys.* 80 (2008), pp. 1455–1515. DOI: 10.1103/RevModPhys.80.1455. arXiv: 0709.4635 [hep-ph] (cit. on p. 5).

[90] D. T. Son. "Superconductivity by long range color magnetic interaction in high density quark matter." In: *Phys. Rev. D* 59 (1999), p. 094019. DOI: 10.1103/PhysRevD.59.094019. arXiv: hep-ph/9812287 (cit. on p. 5).

[91] Thomas Schäfer and Frank Wilczek. "Superconductivity from perturbative one gluon exchange in high density quark matter." In: *Phys. Rev. D* 60 (1999), p. 114033. DOI: 10.1103/PhysRevD.60.114033. arXiv: hep-ph/9906512 (cit. on p. 5).

[92] Thomas Schäfer. "Patterns of symmetry breaking in QCD at high baryon density." In: *Nucl. Phys. B* 575 (2000), pp. 269–284. DOI: 10.1016/S0550-3213(00)00063-8. arXiv: hep-ph/9909574 (cit. on p. 5).

[93] Michael Buballa. "NJL model analysis of quark matter at large density." In: *Phys. Rept.* 407 (2005), pp. 205–376. DOI: 10.1016/j.physrep.2004.11.004. arXiv: hep-ph/0402234 (cit. on pp. 6, 7, 29, 36, 112, 132).

[94] Stefan B. Ruester, Verena Werth, Michael Buballa, Igor A. Shovkovy, and Dirk H. Rischke. "The Phase diagram of neutral quark matter: Self-consistent treatment of quark masses." In: *Phys. Rev. D* 72 (2005), p. 034004. DOI: 10.1103/PhysRevD.72.034004. arXiv: hep-ph/0503184 (cit. on p. 6).

[95] D. Blaschke, S. Fredriksson, H. Grigorian, A. M. Oztas, and F. Sandin. "The Phase diagram of three-flavor quark matter under compact star constraints." In: *Phys. Rev. D* 72 (2005), p. 065020. DOI: 10.1103/PhysRevD.72.065020. arXiv: hep-ph/0503194 (cit. on p. 6).

[96] Hiroaki Abuki and Teiji Kunihiro. "Extensive study of phase diagram for charge neutral homogeneous quark matter affected by dynamical chiral condensation: Unified picture for thermal unpairing transitions from weak to strong coupling." In: *Nucl. Phys. A* 768 (2006), pp. 118–159. DOI: 10.1016/j.nuclphysa.2005.12.019. arXiv: hep-ph/0509172 (cit. on p. 6).

[97] Jens Braun and Benedikt Schallmo. "From quarks and gluons to color superconductivity at supranuclear densities." In: *Phys. Rev. D* 105.3 (2022), p. 036003. DOI: 10.1103/PhysRevD.105.036003. arXiv: 2106.04198 [hep-ph] (cit. on p. 6).

[98] Jens Braun, Andreas Geißel, and Benedikt Schallmo. "Speed of sound in dense strong-interaction matter." In: *SciPost Phys. Core* 7 (2024), p. 015. DOI: 10.21468/SciPostPhysCore.7.2.015. arXiv: 2206.06328 [nucl-th] (cit. on p. 6).

[99] Hosein Gholami, Marco Hofmann, and Michael Buballa. "Renormalization-group consistent treatment of color superconductivity in the NJL model." In: *Phys. Rev. D* 111.1 (2025), p. 014006. DOI: 10.1103/PhysRevD.111.014006. arXiv: 2408.06704 [hep-ph] (cit. on pp. 6, 56).

[100] Hosein Gholami, Ishfaq Ahmad Rather, Marco Hofmann, Michael Buballa, and Jürgen Schaffner-Bielich. "Astrophysical constraints on color-superconducting phases in compact stars within the RG-consistent NJL model." Nov. 2024. arXiv: 2411.04064 [hep-ph] (cit. on p. 6).

[101] Dominik Nickel, Jochen Wambach, and Reinhard Alkofer. "Color-superconductivity in the strong-coupling regime of Landau gauge QCD." In: *Phys. Rev. D* 73 (2006), p. 114028. DOI: 10.1103/PhysRevD.73.114028. arXiv: hep-ph/0603163 (cit. on p. 6).

[102] Daniel Müller, Michael Buballa, and Jochen Wambach. "Dyson-Schwinger Approach to Color-Superconductivity: Effects of Selfconsistent Gluon Dressing." In: (Mar. 2016). arXiv: 1603.02865 [hep-ph] (cit. on pp. 6, 159).

[103] Mark G. Alford, Jeffrey A. Bowers, and Krishna Rajagopal. "Crystalline color superconductivity." In: *Phys. Rev. D* 63 (2001), p. 074016. DOI: 10.1103/PhysRevD.63.074016. arXiv: hep-ph/0008208 (cit. on p. 6).

[104] R. Casalbuoni, M. Ciminale, M. Mannarelli, G. Nardulli, M. Ruggieri, and Raoul Gatto. "Effective gap equation for the inhomogeneous LOFF superconductive phase." In: *Phys. Rev. D* 70 (2004), p. 054004. DOI: 10.1103/PhysRevD.70.054004. arXiv: hep-ph/0404090 (cit. on p. 6).

[105] Roberto Anglani, Roberto Casalbuoni, Marco Ciminale, Nicola Ippolito, Raoul Gatto, Massimo Mannarelli, and Marco Ruggieri. "Crystalline color superconductors." In: *Rev. Mod. Phys.* 86 (2014), pp. 509–561. DOI: 10.1103/RevModPhys.86.509. arXiv: 1302.4264 [hep-ph] (cit. on p. 6).

[106] Lap-Ming Lin. "Torsional oscillations of crystalline color-superconducting hybrid stars: Possible sources for Advanced LIGO?" In: *Phys. Rev. D* 88.12 (2013), p. 124002. DOI: 10.1103/PhysRevD.88.124002. arXiv: 1311.2654 [astro-ph.HE] (cit. on p. 6).

[107] D. Ebert, T. G. Khunjua, K. G. Klimenko, and V. Ch. Zhukovsky. "Competition and duality correspondence between inhomogeneous fermion-antifermion and fermion-fermion condensations in the NJL$_2$ model." In: *Phys. Rev. D* 90.4 (2014), p. 045021. DOI: 10.1103/PhysRevD.90.045021. arXiv: 1405.3789 [hep-th] (cit. on pp. 6, 15, 94, 105).

[108] Philippe Chomaz. "The nuclear liquid gas phase transition and phase coexistence." In: *AIP Conf. Proc.* 610.1 (2002), p. 167. DOI: 10.1063/1.1469927. arXiv: nucl-ex/0410024 (cit. on p. 6).

[109] Jürgen Eser and Jean-Paul Blaizot. "Thermodynamics of the parity-doublet model: Symmetric nuclear matter and the chiral transition." In: *Phys. Rev. C* 109.4 (2024), p. 045201. DOI: 10.1103/PhysRevC.109.045201. arXiv: 2309.06566 [nucl-th] (cit. on p. 6).

[110] Jürgen Eser and Jean-Paul Blaizot. "Thermodynamics of the parity-doublet model. II. Asymmetric and neutron matter." In: *Phys. Rev. C* 110.6 (2024), p. 065205. DOI: 10.1103/PhysRevC.110.065205. arXiv: 2408.01302 [nucl-th] (cit. on p. 6).

[111] Larry McLerran and Robert D. Pisarski. "Phases of cold, dense quarks at large N(c)." In: *Nucl. Phys. A* 796 (2007), pp. 83–100. DOI: 10.1016/j.nuclphysa.2007.08.013. arXiv: 0706.2191 [hep-ph] (cit. on pp. 6, 46, 69).

[112] Larry McLerran. "Quarkyonic Matter and the Revised Phase Diagram of QCD." In: *Nucl. Phys. A* 830 (2009). Ed. by Paul Stankus, David Silvermyr, Soren Sorensen, and Victoria Greene, pp. 709C–712C. DOI: 10.1016/j.nuclphysa.2009.10.063. arXiv: 0907.4489 [nucl-th] (cit. on p. 6).

[113] Larry McLerran. "FAQS about quarkyonic matter." In: *Acta Phys. Polon. Supp.* 4 (2011), pp. 537–542. DOI: 10.5506/APhysPolBSupp.4.537 (cit. on p. 6).

[114] Dyana C. Duarte, Saul Hernandez-Ortiz, Kie Sang Jeong, and Larry D. McLerran. "Quarkyonic effective field theory, quark-nucleon duality, and ghosts." In: *Phys. Rev. D* 104.9 (2021), p. L091901. DOI: 10.1103/PhysRevD.104.L091901. arXiv: 2103.05679 [nucl-th] (cit. on p. 6).

[115] Toru Kojo, Yoshimasa Hidaka, Larry McLerran, and Robert D. Pisarski. "Quarkyonic Chiral Spirals." In: *Nucl. Phys. A* 843 (2010), pp. 37–58. DOI: 10.1016/j.nuclphysa.2010.05.053. arXiv: 0912.3800 [hep-ph] (cit. on p. 6).

[116] Larry McLerran. "A Pedagogical Discussion of Quarkyonic Matter and Its Implication for Neutron Stars." In: *Acta Phys. Polon. B* 51 (2020), pp. 1067–1077. DOI: 10.5506/APhysPolB.51.1067 (cit. on p. 6).

[117] Philippe de Forcrand. "Simulating QCD at finite density." In: *PoS* LAT2009 (2009), p. 010. DOI: 10.22323/1.091.0010. arXiv: 1005.0539 [hep-lat] (cit. on pp. 7, 19, 41, 141).

[118] R. Bellwied, S. Borsanyi, Z. Fodor, J. Günther, S. D. Katz, C. Ratti, and K. K. Szabo. "The QCD phase diagram from analytic continuation." In: *Phys. Lett. B* 751 (2015), pp. 559–564. DOI: 10.1016/j.physletb.2015.11.011. arXiv: 1507.07510 [hep-lat] (cit. on p. 7).

[119] A. Bazavov et al. "Chiral crossover in QCD at zero and non-zero chemical potentials." In: *Phys. Lett. B* 795 (2019), pp. 15–21. DOI: 10.1016/j.physletb.2019.05.013. arXiv: 1812.08235 [hep-lat] (cit. on p. 7).

[120] Claudio Bonati, Massimo D'Elia, Francesco Negro, Francesco Sanfilippo, and Kevin Zambello. "Curvature of the pseudocritical line in QCD: Taylor expansion matches analytic continuation." In: *Phys. Rev. D* 98.5 (2018), p. 054510. DOI: 10.1103/PhysRevD.98.054510. arXiv: 1805.02960 [hep-lat] (cit. on p. 7).

[121] Wei-jie Fu, Jan M. Pawlowski, and Fabian Rennecke. "QCD phase structure at finite temperature and density." In: *Phys. Rev. D* 101.5 (2020), p. 054032. DOI: 10.1103/PhysRevD.101.054032. arXiv: 1909.02991 [hep-ph] (cit. on pp. 7, 8, 12, 39, 40, 48, 64, 65, 73, 125, 128, 144, 151, 157, 159).

[122] Christian S. Fischer, Jan Luecker, and Christian A. Welzbacher. "Phase structure of three and four flavor QCD." In: *Phys. Rev. D* 90.3 (2014), p. 034022. DOI: 10.1103/PhysRevD.90.034022. arXiv: 1405.4762 [hep-ph] (cit. on p. 7).

[123] Christian S. Fischer. "QCD at finite temperature and chemical potential from Dyson–Schwinger equations." In: *Prog. Part. Nucl. Phys.* 105 (2019), pp. 1–60. DOI: 10.1016/j.ppnp.2019.01.002. arXiv: 1810.12938 [hep-ph] (cit. on p. 7).

[124] Fei Gao and Jan M. Pawlowski. "QCD phase structure from functional methods." In: *Phys. Rev. D* 102.3 (2020), p. 034027. DOI: 10.1103/PhysRevD.102.034027. arXiv: 2002.07500 [hep-ph] (cit. on pp. 7, 8, 159).

[125] Fei Gao and Jan M. Pawlowski. "Chiral phase structure and critical end point in QCD." In: *Phys. Lett. B* 820 (2021), p. 136584. DOI: 10.1016/j.physletb.2021.136584. arXiv: 2010.13705 [hep-ph] (cit. on pp. 7, 8).

[126] M. Cristoforetti, F. Di Renzo, A. Mukherjee, and L. Scorzato. "Quantum field theories on the Lefschetz thimble." In: *PoS* LATTICE2013 (2014), p. 197. DOI: 10.22323/1.187.0197. arXiv: 1312.1052 [hep-lat] (cit. on pp. 7, 125, 158).

[127] Marco Cristoforetti, Francesco Di Renzo, Abhishek Mukherjee, and Luigi Scorzato. "Monte Carlo simulations on the Lefschetz thimble: Taming the sign problem." In: *Phys. Rev. D* 88.5 (2013), p. 051501. DOI: 10.1103/PhysRevD.88.051501. arXiv: 1303.7204 [hep-lat] (cit. on pp. 7, 125, 158).

[128] Yuto Mori, Kouji Kashiwa, and Akira Ohnishi. "Lefschetz thimbles in fermionic effective models with repulsive vector-field." In: *Phys. Lett. B* 781 (2018), pp. 688–693. DOI: 10.1016/j.physletb.2018.04.018. arXiv: 1705.03646 [hep-lat] (cit. on pp. 7, 100, 125, 158).

[129] Gert Aarts. "Complex Langevin dynamics and other approaches at finite chemical potential." In: *PoS* LATTICE2012 (2012), p. 017. arXiv: 1302.3028 [hep-lat] (cit. on pp. 7, 158).

[130] Gert Aarts, Felipe Attanasio, Benjamin Jäger, and Dénes Sexty. "Results on the heavy-dense QCD phase diagram using complex Langevin." In: *PoS* LATTICE2016 (2016), p. 074. DOI: 10.22323/1.256.0074. arXiv: 1610.04401 [hep-lat] (cit. on pp. 7, 158).

[131] Felipe Attanasio, Benjamin Jäger, and Felix P. G. Ziegler. "Complex Langevin simulations and the QCD phase diagram: Recent developments." In: *Eur. Phys. J. A* 56.10 (2020), p. 251. DOI: 10.1140/epja/s10050-020-00256-z. arXiv: 2006.00476 [hep-lat] (cit. on pp. 7, 158).

[132] Lena Funcke, Tobias Hartung, Karl Jansen, and Stefan Kühn. "Review on Quantum Computing for Lattice Field Theory." In: *PoS* LATTICE2022 (2023), p. 228. DOI: 10.22323/1.430.0228. arXiv: 2302.00467 [hep-lat] (cit. on pp. 7, 159).

[133] Jens Braun, Leonard Fister, Jan M. Pawlowski, and Fabian Rennecke. "From Quarks and Gluons to Hadrons: Chiral Symmetry Breaking in Dynamical QCD." In: *Phys. Rev. D* 94.3 (2016), p. 034016. DOI: 10.1103/PhysRevD.94.034016. arXiv: 1412.1045 [hep-ph] (cit. on pp. 7, 13, 105, 107, 124, 154).

[134] Jens Braun, Marc Leonhardt, and Martin Pospiech. "Fierz-complete NJL model study III: Emergence from quark-gluon dynamics." In: *Phys. Rev. D* 101.3 (2020), p. 036004. DOI: 10.1103/PhysRevD.101.036004. arXiv: 1909.06298 [hep-ph] (cit. on p. 7).

[135] Jens Braun, Marc Leonhardt, Jan M. Pawlowski, and Daniel Rosenblüh. "Chiral and effective $U(1)_A$ symmetry restoration in QCD." In: (Dec. 2020). arXiv: 2012.06231 [hep-ph] (cit. on p. 7).

[136] Holger Gies and Christof Wetterich. "Renormalization flow of bound states." In: *Phys. Rev. D* 65 (2002), p. 065001. DOI: 10.1103/PhysRevD.65.065001. arXiv: hep-th/0107221 (cit. on p. 7).

[137] M. Asakawa and K. Yazaki. "Chiral Restoration at Finite Density and Temperature." In: *Nucl. Phys. A* 504 (1989), pp. 668–684. DOI: 10.1016/0375-9474(89)90002-X (cit. on pp. 7, 8, 29, 36, 132).

[138] S. P. Klevansky. "The Nambu-Jona-Lasinio model of quantum chromodynamics." In: *Rev. Mod. Phys.* 64 (1992), pp. 649–708. DOI: 10.1103/RevModPhys.64.649 (cit. on pp. 7, 48, 49, 190).

[139] Deog Ki Hong. "An Effective field theory of QCD at high density." In: *Phys. Lett. B* 473 (2000), pp. 118–125. DOI: 10.1016/S0370-2693(99)01472-0. arXiv: hep-ph/9812510 (cit. on p. 7).

[140] Deog Ki Hong. "Aspects of high density effective theory in QCD." In: *Nucl. Phys. B* 582 (2000), pp. 451–476. DOI: 10.1016/S0550-3213(00)00330-8. arXiv: hep-ph/9905523 (cit. on p. 7).

[141] O. Scavenius, A. Mocsy, I. N. Mishustin, and D. H. Rischke. "Chiral phase transition within effective models with constituent quarks." In: *Phys. Rev. C* 64 (2001), p. 045202. DOI: 10.1103/PhysRevC.64.045202. arXiv: nucl-th/0007030 (cit. on pp. 7, 8, 29, 36, 56).

[142] Giuseppe Nardulli. "Effective description of QCD at very high densities." In: *Riv. Nuovo Cim.* 25N3 (2002), pp. 1–80. arXiv: hep-ph/0202037 (cit. on p. 7).

[143] Thomas Schäfer. "Hard loops, soft loops, and high density effective field theory." In: *Nucl. Phys. A* 728 (2003), pp. 251–271. DOI: 10.1016/j.nuclphysa.2003.08.028. arXiv: hep-ph/0307074 (cit. on p. 7).

[144] Jens Braun, Marc Leonhardt, and Martin Pospiech. "Fierz-complete NJL model study: Fixed points and phase structure at finite temperature and density." In: *Phys. Rev. D* 96.7 (2017), p. 076003. DOI: 10.1103/PhysRevD.96.076003. arXiv: 1705.00074 [hep-ph] (cit. on p. 7).

[145] Jens Braun, Marc Leonhardt, and Martin Pospiech. "Fierz-complete NJL model study. II. Toward the fixed-point and phase structure of hot and dense two-flavor QCD." In: *Phys. Rev. D* 97.7 (2018), p. 076010. DOI: 10.1103/PhysRevD.97.076010. arXiv: 1801.08338 [hep-ph] (cit. on p. 7).

[146] Kie Sang Jeong, Fabrizio Murgana, Ashutosh Dash, and Dirk H. Rischke. "Functional Renormalization Group analysis of the quark-condensation pattern on the Fermi surface: A simple effective-model approach." July 2024. arXiv: 2407.13589 [nucl-th] (cit. on p. 7).

[147] Reinhard Alkofer, Axel Maas, Walid Ahmed Mian, Mario Mitter, Jordi París-López, Jan M. Pawlowski, and Nicolas Wink. "Bound state properties from the functional renormalization group." In: *Phys. Rev. D* 99.5 (2019), p. 054029. DOI: 10.1103/PhysRevD.99.054029. arXiv: 1810.07955 [hep-ph] (cit. on p. 8).

[148] Kenji Fukushima, Jan M. Pawlowski, and Nils Strodthoff. "Emergent hadrons and diquarks." In: *Annals Phys.* 446 (2022), p. 169106. DOI: 10.1016/j.aop.2022.169106. arXiv: 2103.01129 [hep-ph] (cit. on pp. 8, 13, 105, 124).

[149] Friederike Ihssen and Jan M. Pawlowski. "Physics-informed renormalisation group flows." Sept. 2024. arXiv: 2409.13679 [hep-th] (cit. on p. 8).

[150] Nathan Weiss. "The Effective Potential for the Order Parameter of Gauge Theories at Finite Temperature." In: *Phys. Rev. D* 24 (1981), p. 475. DOI: 10.1103/PhysRevD.24.475 (cit. on p. 8).

[151] Kenji Fukushima and Koichi Ohta. "Stability of the perturbative vacuum against spatial variations of the Polyakov loop." In: *J. Phys. G* 26 (2000), pp. 1397–1415. DOI: 10.1088/0954-3899/26/9/309. arXiv: hep-ph/0011108 (cit. on p. 8).

[152] Kenji Fukushima. "Chiral effective model with the Polyakov loop." In: *Phys. Lett. B* 591 (2004), pp. 277–284. DOI: 10.1016/j.physletb.2004.04.027. arXiv: hep-ph/0310121 (cit. on p. 8).

[153] C. Ratti, Simon Roessner, M. A. Thaler, and W. Weise. "Thermodynamics of the PNJL model." In: *Eur. Phys. J. C* 49 (2007), pp. 213–217. DOI: 10.1140/epjc/s10052-006-0065-x. arXiv: hep-ph/0609218 (cit. on p. 8).

[154] H. Hansen, W. M. Alberico, A. Beraudo, A. Molinari, M. Nardi, and C. Ratti. "Mesonic correlation functions at finite temperature and density in the Nambu-Jona-Lasinio model with a Polyakov loop." In: *Phys. Rev. D* 75 (2007), p. 065004. DOI: 10.1103/PhysRevD.75.065004. arXiv: hep-ph/0609116 (cit. on p. 8).

[155] Misha A. Stephanov, K. Rajagopal, and Edward V. Shuryak. "Signatures of the tricritical point in QCD." In: *Phys. Rev. Lett.* 81 (1998), pp. 4816–4819. DOI: 10.1103/PhysRevLett.81.4816. arXiv: hep-ph/9806219 (cit. on p. 8).

[156] Robert D. Pisarski and Frank Wilczek. "Remarks on the Chiral Phase Transition in Chromodynamics." In: *Phys. Rev. D* 29 (1984), pp. 338–341. DOI: 10.1103/PhysRevD.29.338 (cit. on p. 8).

[157] Juergen Berges and Krishna Rajagopal. "Color superconductivity and chiral symmetry restoration at nonzero baryon density and temperature." In: *Nucl. Phys. B* 538 (1999), pp. 215–232. DOI: 10.1016/S0550-3213(98)00620-8. arXiv: hep-ph/9804233 (cit. on p. 8).

[158] Adam Miklos Halasz, A. D. Jackson, R. E. Shrock, Misha A. Stephanov, and J. J. M. Verbaarschot. "On the phase diagram of QCD." In: *Phys. Rev. D* 58 (1998), p. 096007. DOI: 10.1103/PhysRevD.58.096007. arXiv: hep-ph/9804290 (cit. on p. 8).

[159] Pascal J. Gunkel and Christian S. Fischer. "Locating the critical endpoint of QCD: Mesonic backcoupling effects." In: *Phys. Rev. D* 104.5 (2021), p. 054022. DOI: 10.1103/PhysRevD.104.054022. arXiv: 2106.08356 [hep-ph] (cit. on pp. 8, 159).

[160] Gokce Basar. "QCD critical point, Lee-Yang edge singularities, and Padé resummations." In: *Phys. Rev. C* 110.1 (2024), p. 015203. DOI: 10.1103/PhysRevC.110.015203. arXiv: 2312.06952 [hep-th] (cit. on p. 8).

[161] David A. Clarke, Petros Dimopoulos, Francesco Di Renzo, Jishnu Goswami, Christian Schmidt, Simran Singh, and Kevin Zambello. "Searching for the QCD critical endpoint using multi-point Padé approximations." May 2024. arXiv: 2405.10196 [hep-lat] (cit. on p. 8).

[162] M. S. Abdallah et al. "Measurements of Proton High Order Cumulants in $\sqrt{s_{\mathrm{NN}}} = 3$ GeV Au+Au Collisions and Implications for the QCD Critical Point." In: *Phys. Rev. Lett.* 128.20 (2022), p. 202303. DOI: 10.1103/PhysRevLett.128.202303. arXiv: 2112.00240 [nucl-ex] (cit. on p. 8).

[163] Jens Braun, Bertram Klein, and Piotr Piasecki. "On the scaling behavior of the chiral phase transition in QCD in finite and infinite volume." In: *Eur. Phys. J. C* 71 (2011), p. 1576. DOI: 10.1140/epjc/s10052-011-1576-7. arXiv: 1008.2155 [hep-ph] (cit. on p. 8).

[164] Fei Gao and Jan M. Pawlowski. "Phase structure of (2+1)-flavor QCD and the magnetic equation of state." In: *Phys. Rev. D* 105.9 (2022), p. 094020. DOI: 10.1103/PhysRevD.105.094020. arXiv: 2112.01395 [hep-ph] (cit. on p. 8).

[165] Julian Bernhardt and Christian S. Fischer. "QCD phase transitions in the light quark chiral limit." In: *Phys. Rev. D* 108.11 (2023), p. 114018. DOI: 10.1103/PhysRevD.108.114018. arXiv: 2309.06737 [hep-ph] (cit. on p. 8).

[166] Wei-jie Fu, Jan M. Pawlowski, Robert D. Pisarski, Fabian Rennecke, Rui Wen, and Shi Yin. "The QCD moat regime and its real-time properties." Dec. 2024. arXiv: 2412.15949 [hep-ph] (cit. on pp. 8, 39, 128, 144, 157, 159).

[167] Laurin Pannullo. "Inhomogeneous phases and the Moat Regime in Nambu-Jona-Lasinio-Type models." PhD thesis. Frankfurt U., 2024. DOI: 10.21248/gups.82274 (cit. on pp. 8, 11, 12, 14, 15, 17, 45, 48, 66, 104, 128, 156, 157).

[168] A. Yoshimori. "A New Type of Antiferromagnetic Structure." In: *J. Phys. Soc. Jpn.* 14 (1959), p. 805 (cit. on p. 9).

[169] R. M. Hornreich, M. Luban, and S. Shtrikman. "Critical Behavior at the Onset of $\vec{k}$-Space Instability on the λ Line." In: *Phys. Rev. Lett.* 35 (1975), p. 1678 (cit. on p. 9).

[170] Michael Seul and David Andelman. "Domain Shapes and Patterns: The Phenomenology of Modulated Phases." In: *Science* 267.5197 (1995), pp. 476–483. DOI: 10.1126/science.267.5197.476 (cit. on p. 9).

[171] S. Chakrabarty and Z. Nussinov. "High temperature correlation functions: universality, extraction of exchange interactions, divergent correlation lengths and generalized Debye length scales." In: *Physical Review B* 84 (2011), p. 064124 (cit. on p. 9).

[172] Abrahams E. and I. E. Dzyaloshinskii. "A Possible Lifshitz Point for TTF_TCNQ*." In: *Solid State Commun.* 23 (1977), p. 883 (cit. on p. 9).

[173] Jonathan V. Selinger. "Director Deformations, Geometric Frustration, and Modulated Phases in Liquid Crystals." In: *Annual Review of Condensed Matter Physics* 13.1 (2022), pp. 49–71. DOI: 10.1146/annurev-conmatphys-031620-105712 (cit. on pp. 9, 51).

[174] S. A. Brazovskii. "Phase Transition of an Isotropic System to a Nonuniform State." In: *Zh. Eksp. Teor. Fiz.* 68 (1975), p. 175 (cit. on pp. 9, 40).

[175] Peter Fulde and Richard A. Ferrell. "Superconductivity in a Strong Spin-Exchange Field." In: *Phys. Rev.* 135 (3A 1964), A550–A563. DOI: 10.1103/PhysRev.135.A550 (cit. on pp. 9, 40).

[176] A. I. Larkin and Y. N. Ovchinnikov. "Nonuniform state of superconductors." In: *Zh. Eksp. Teor. Fiz.* 47 (1964), pp. 1136–1146 (cit. on pp. 9, 40).

[177] A. I. Larkin and Yu. N. Ovchinnikov. "Inhomogeneous state of superconductors." In: *Sov. Phys. JETP* 20 (1965), p. 762 (cit. on pp. 9, 40).

[178] Eduardo Fradkin and Steven A. Kivelson. "Liquid-crystal phases of quantum Hall systems." In: *Phys. Rev. B* 59 (12 Mar. 1999), pp. 8065–8072. DOI: 10.1103/PhysRevB.59.8065 (cit. on p. 9).

[179] Songyang Pu, Ajist C. Balrma, Joseph Taylor, Eduardo Fradkin, and Zlatko Papic. "Microscopic Model for Fractional Quantum Hall Nematics." In: *Phys. Rev. Lett.* 132 (2024), p. 236503 (cit. on p. 9).

[180] Moses A. Schindler, Stella T. Schindler, Leandro Medina, and Michael C. Ogilvie. "Universality of Pattern Formation." In: *Phys. Rev. D* 102 (2020), p. 114510. DOI: 10.1103/PhysRevD.102.114510. arXiv: 1906.07288 [hep-lat] (cit. on pp. 9, 10, 12, 13, 40–42, 78, 108, 115, 116, 124, 138, 153, 157).

[181] Carl M. Bender and Stefan Boettcher. "Real spectra in nonHermitian Hamiltonians having PT symmetry." In: *Phys. Rev. Lett.* 80 (1998), pp. 5243–5246. DOI: 10.1103/PhysRevLett.80.5243. arXiv: physics/9712001 (cit. on pp. 9, 41, 42).

[182] Ramy El-Ganainy, Konstantinos G. Makris, Mercedeh Khajavikhan, Ziad H. Musslimani, Stefan Rotter, and Demetrios N. Christodoulides. "Non-Hermitian physics and PT symmetry." In: *Nature Phys.* 14.1 (2018), pp. 11–19. DOI: 10.1038/nphys4323 (cit. on p. 9).

[183] Carl M. Bender et al. *PT Symmetry*. WSP, 2019. DOI: 10.1142/q0178 (cit. on pp. 9, 41).

[184] Carl M. Bender and Daniel W. Hook. "PT-symmetric quantum mechanics." Dec. 2023. arXiv: 2312.17386 [quant-ph] (cit. on pp. 9, 41).

[185] Peter N. Meisinger and Michael C. Ogilvie. "PT Symmetry in Classical and Quantum Statistical Mechanics." In: *Phil. Trans. Roy. Soc. Lond. A* 371 (2013), p. 20120058. DOI: 10.1098/rsta.2012.0058. arXiv: 1208.5077 [math-ph] (cit. on pp. 10, 12, 40–42, 78, 125, 153).

[186] Carl M. Bender, Alexander Felski, S. P. Klevansky, and Sarben Sarkar. "*PT* Symmetry and Renormalisation in Quantum Field Theory." In: *J. Phys. Conf. Ser.* 2038 (2021), p. 012004. DOI: 10.1088/1742-6596/2038/1/012004. arXiv: 2103.14864 [hep-th] (cit. on pp. 10, 41, 125, 158).

[187] Michael C. Ogilvie and Leandro Medina. "Simulation of Scalar Field Theories with Complex Actions." In: *PoS* LATTICE2018 (2018), p. 157. DOI: 10.22323/1.334.0157. arXiv: 1811.11112 [hep-lat] (cit. on pp. 10, 12).

[188] Moses A. Schindler, Stella T. Schindler, and Michael C. Ogilvie. "Finite-density QCD, $\mathcal{PT}$ symmetry, and exotic phases." In: *PoS* LATTICE2021 (2022), p. 555. DOI: 10.22323/1.396.0555. arXiv: 2110.07761 [hep-lat] (cit. on pp. 10, 12, 13, 40–42, 78, 116, 124).

[189] Maximilian Haensch, Fabian Rennecke, and Lorenz von Smekal. "Medium induced mixing, spatial modulations, and critical modes in QCD." In: *Phys. Rev. D* 110.3 (2024), p. 036018. DOI: 10.1103/PhysRevD.110.036018. arXiv: 2308.16244 [hep-ph] (cit. on pp. 10, 13, 79, 99, 105, 108, 124, 125, 152–155, 157).

[190] Moses A. Schindler, Stella T. Schindler, and Michael C. Ogilvie. "$\mathcal{PT}$ symmetry, pattern formation, and finite-density QCD." In: *J. Phys. Conf. Ser.* 2038.1 (June 2021), p. 012022. DOI: 10.1088/1742-6596/2038/1/012022. arXiv: 2106.07092 [hep-lat] (cit. on pp. 10, 13, 40–42, 78, 108, 115, 124).

[191] Hiromichi Nishimura, Michael C. Ogilvie, and Kamal Pangeni. "Complex Saddle Points and Disorder Lines in QCD at finite temperature and density." In: *Phys. Rev. D* 91.5 (2015), p. 054004. DOI: 10.1103/PhysRevD.91.054004. arXiv: 1411.4959 [hep-ph] (cit. on pp. 10, 13, 40, 78, 108, 116, 124, 153–155, 157).

[192] John Stephenson. "Ising Model with Antiferromagnetic Next-Nearest-Neighbor Coupling: Spin Correlations and Disorder Points." In: *Physical Review B* 1.11 (June 1970), pp. 4405–4409. DOI: 10.1103/PhysRevB.1.4405 (cit. on pp. 10, 157).

[193] Hiromichi Nishimura, Michael C. Ogilvie, and Kamal Pangeni. "Complex spectrum of finite-density lattice QCD with static quarks at strong coupling." In: *Phys. Rev. D* 93.9 (2016), p. 094501. DOI: 10.1103/PhysRevD.93.094501. arXiv: 1512.09131 [hep-lat] (cit. on pp. 10, 108).

[194] Hiromichi Nishimura, Michael C. Ogilvie, and Kamal Pangeni. "Liquid-Gas Phase Transitions and $\mathcal{CK}$ Symmetry in Quantum Field Theories." In: *Phys. Rev. D* 95.7 (2017), p. 076003. DOI: 10.1103/PhysRevD.95.076003. arXiv: 1612.09575 [hep-th] (cit. on pp. 10, 40, 108).

[195] Dominik Nickel. "Inhomogeneous phases in the Nambu-Jona-Lasino and quark-meson model." In: *Phys. Rev. D* 80 (2009), p. 074025. DOI: 10.1103/PhysRevD.80.074025. arXiv: 0906.5295 [hep-ph] (cit. on pp. 10, 12, 29, 39, 46, 47, 157).

[196] Stefano Carignano, Dominik Nickel, and Michael Buballa. "Influence of vector interaction and Polyakov loop dynamics on inhomogeneous chiral symmetry breaking phases." In: *Phys. Rev. D* 82 (2010), p. 054009. DOI: 10.1103/PhysRevD.82.054009. arXiv: 1007.1397 [hep-ph] (cit. on pp. 10, 11, 13, 39, 46, 47, 111).

[197] Michael Buballa and Stefano Carignano. "Inhomogeneous chiral condensates." In: *Prog. Part. Nucl. Phys.* 81 (2015), pp. 39–96. DOI: 10.1016/j.ppnp.2014.11.001. arXiv: 1406.1367 [hep-ph] (cit. on pp. 10, 12, 29, 36, 39, 43, 46, 69, 102, 104, 157).

[198] Stefano Carignano, Michael Buballa, and Bernd-Jochen Schaefer. "Inhomogeneous phases in the quark-meson model with vacuum fluctuations." In: *Phys. Rev. D* 90.1 (2014), p. 014033. DOI: 10.1103/PhysRevD.90.014033. arXiv: 1404.0057 [hep-ph] (cit. on pp. 10, 39, 49, 104, 125, 158).

[199] Michael Buballa and Stefano Carignano. "Inhomogeneous chiral symmetry breaking in dense neutron-star matter." In: *Eur. Phys. J. A* 52.3 (2016), p. 57. DOI: 10.1140/epja/i2016-16057-6. arXiv: 1508.04361 [nucl-th] (cit. on p. 10).

[200] Stefano Carignano and Michael Buballa. "Inhomogeneous chiral condensates in three-flavor quark matter." In: *Phys. Rev. D* 101.1 (2020), p. 014026. DOI: 10.1103/PhysRevD.101.014026. arXiv: 1910.03604 [hep-ph] (cit. on pp. 10, 46, 65, 105).

[201] Verena Schön and Michael Thies. "2-D model field theories at finite temperature and density." In: *At The Frontier of Particle Physics: Handbook of QCD, Boris Ioffe Festschrift* (Aug. 2000), pp. 1945–2032. DOI: 10.1142/9789812810458_0041. arXiv: hep-th/0008175 (cit. on pp. 10, 14, 45, 46, 90).

[202] Michael Thies and Konrad Urlichs. "Revised phase diagram of the Gross-Neveu model." In: *Phys. Rev. D* 67 (2003), p. 125015. DOI: 10.1103/PhysRevD.67.125015. arXiv: hep-th/0302092 (cit. on pp. 10, 12, 44, 65, 69, 90).

[203] Gokce Basar, Gerald V. Dunne, and Michael Thies. "Inhomogeneous Condensates in the Thermodynamics of the Chiral NJL(2) model." In: *Phys. Rev. D* 79 (2009), p. 105012. DOI: 10.1103/PhysRevD.79.105012. arXiv: 0903.1868 [hep-th] (cit. on pp. 10, 75).

[204] Francois Dautry and Ebbe M. Nyman. "Pion condensation and the σ-model in liquid neutron matter." In: *Nucl. Phys. A* 319 (May 1979), pp. 323–348. DOI: 10.1016/0375-9474(79)90518-9 (cit. on p. 10).

[205] Marek Kutschera, Wojciech Broniowski, and Andrzej Kotlorz. "Quark matter with neutral pion condensate." In: *Phys. Lett. B* 237 (Mar. 1990), pp. 159–163. DOI: 10.1016/0370-2693(90)91421-7 (cit. on p. 10).

[206] Marek Kutschera, Wojciech Broniowski, and Andrzej Kotlorz. "Quark matter with pion condensate in an effective chiral model." In: *Nucl. Phys. A* 516 (Oct. 1990), pp. 566–588. DOI: 10.1016/0375-9474(90)90128-9 (cit. on p. 10).

[207] H. G. Dobereiner and P. G. Reinhard. "Instabilities in the nonlinear relativistic mean field model." In: *Phys. Lett. B* 227 (1989), pp. 305–309. DOI: 10.1016/0370-2693(89)90934-9 (cit. on pp. 10, 57).

[208] Stefano Carignano, Marco Schramm, and Michael Buballa. "Influence of vector interactions on the favored shape of inhomogeneous chiral condensates." In: *Phys. Rev. D* 98.1 (2018), p. 014033. DOI: 10.1103/PhysRevD.98.014033. arXiv: 1805.06203 [hep-ph] (cit. on pp. 11, 13, 46, 111).

[209] Prabal Adhikari, Jens O. Andersen, and Patrick Kneschke. "Inhomogeneous chiral condensate in the quark-meson model." In: *Phys. Rev. D* 96.1 (2017). [Erratum: Phys.Rev.D 98, 099902 (2018)], p. 016013. DOI: 10.1103/PhysRevD.96.016013. arXiv: 1702.01324 [hep-ph] (cit. on p. 11).

[210] Jens O. Andersen and Patrick Kneschke. "Chiral density wave versus pion condensation at finite density and zero temperature." In: *Phys. Rev. D* 97.7 (2018), p. 076005. DOI: 10.1103/PhysRevD.97.076005. arXiv: 1802.01832 [hep-ph] (cit. on pp. 11, 125).

[211] Laurin Pannullo. "Inhomogeneous condensation in the Gross-Neveu model in non-integer spatial dimensions $1 \leq d < 3$." In: *Phys. Rev. D* 108.3 (2023), p. 036022. DOI: 10.1103/PhysRevD.108.036022. arXiv: 2306.16290 [hep-ph] (cit. on pp. 11, 14, 48–50, 54, 57, 101, 104, 153, 156, 190).

[212] Adrian Koenigstein and Laurin Pannullo. "Inhomogeneous condensation in the Gross-Neveu model in noninteger spatial dimensions 1≤d<3. II. Nonzero temperature and chemical potential." In: *Phys. Rev. D* 109.5 (2024), p. 056015. DOI: 10.1103/PhysRevD.109.056015. arXiv: 2312.04904 [hep-ph] (cit. on pp. 11, 14, 48, 54, 57, 101, 104, 156, 190).

[213] Theo F. Motta, Julian Bernhardt, Michael Buballa, and Christian S. Fischer. "Toward a stability analysis of inhomogeneous phases in QCD." In: *Phys. Rev. D* 108.11 (2023), p. 114019. DOI: 10.1103/PhysRevD.108.114019. arXiv: 2306.09749 [hep-ph] (cit. on pp. 11, 12, 59, 159).

[214] Theo F. Motta, Julian Bernhardt, Michael Buballa, and Christian S. Fischer. "Inhomogenuous instabilities at large chemical potential in a rainbow-ladder QCD model." In: (May 2024). arXiv: 2406.00205 [hep-ph] (cit. on pp. 11, 12, 59, 159).

[215] Theo F. Motta, Michael Buballa, and Christian S. Fischer. "New Tool to Detect Inhomogeneous Chiral Symmetry Breaking." Nov. 2024. arXiv: 2411.02285 [hep-ph] (cit. on pp. 11, 59, 159).

[216] Tong-Gyu Lee, Eiji Nakano, Yasuhiko Tsue, Toshitaka Tatsumi, and Bengt Friman. "Landau-Peierls instability in a Fulde-Ferrell type inhomogeneous chiral condensed phase." In: *Phys. Rev. D* 92.3 (2015), p. 034024. DOI: 10.1103/PhysRevD.92.034024. arXiv: 1504.03185 [hep-ph] (cit. on pp. 11, 51, 104, 155, 157).

[217] Yoshimasa Hidaka, Kazuhiko Kamikado, Takuya Kanazawa, and Toshifumi Noumi. "Phonons, pions and quasi-long-range order in spatially modulated chiral condensates." In: *Phys. Rev. D* 92.3 (2015), p. 034003. DOI: 10.1103/PhysRevD.92.034003. arXiv: 1505.00848 [hep-ph] (cit. on pp. 11, 51, 104, 155, 157).

[218] Robert D. Pisarski, Vladimir V. Skokov, and Alexei M. Tsvelik. "Fluctuations in cool quark matter and the phase diagram of Quantum Chromodynamics." In: *Phys. Rev. D* 99.7 (2019), p. 074025. DOI: 10.1103/PhysRevD.99.074025. arXiv: 1801.08156 [hep-ph] (cit. on p. 11).

[219] Robert D. Pisarski, Alexei M. Tsvelik, and Semeon Valgushev. "How transverse thermal fluctuations disorder a condensate of chiral spirals into a quantum spin liquid." In: *Phys. Rev. D* 102.1 (2020), p. 016015. DOI: 10.1103/PhysRevD.102.016015. arXiv: 2005.10259 [hep-ph] (cit. on pp. 11, 12, 14, 39, 52, 53, 64, 78, 104, 117, 127–129, 133, 138, 139, 143, 144, 146, 151, 155, 157).

[220] Efrain J. Ferrer and Vivian de la Incera. "Absence of Landau-Peierls Instability in the Magnetic Dual Chiral Density Wave Phase of Dense QCD." In: *Phys. Rev. D* 102.1 (2020), p. 014010. DOI: 10.1103/PhysRevD.102.014010. arXiv: 1902.06810 [nucl-th] (cit. on p. 11).

[221] E. J. Ferrer, W. Gyory, and V. de la Incera. "Thermal phonon fluctuations and stability of the magnetic dual chiral density wave phase in dense QCD." In: *Phys. Rev. D* 109.3 (2024), p. 036023. DOI: 10.1103/PhysRevD.109.036023. arXiv: 2307.05621 [nucl-th] (cit. on p. 11).

[222] N. D. Mermin and H. Wagner. "Absence of ferromagnetism or antiferromagnetism in one-dimensional or two-dimensional isotropic Heisenberg models." In: *Phys. Rev. Lett.* 17 (1966), pp. 1133–1136. DOI: 10.1103/PhysRevLett.17.1133 (cit. on pp. 11, 50, 51, 91, 155).

[223] Sidney R. Coleman. "There are no Goldstone bosons in two-dimensions." In: *Commun. Math. Phys.* 31 (1973), pp. 259–264. DOI: 10.1007/BF01646487 (cit. on pp. 11, 50, 51, 91, 155).

[224] Edward Witten. "Chiral Symmetry, the 1/n Expansion, and the SU(N) Thirring Model." In: *Nucl. Phys. B* 145 (1978), pp. 110–118. DOI: 10.1016/0550-3213(78)90416-9 (cit. on pp. 11, 50, 51).

[225] Jonas Stoll, Niklas Zorbach, Adrian Koenigstein, Martin J. Steil, and Stefan Rechenberger. "Bosonic fluctuations in the $(1+1)$-dimensional Gross-Neveu(-Yukawa) model at varying μ and T and finite N." Aug. 2021. arXiv: 2108.10616 [hep-ph] (cit. on pp. 11, 12, 51, 91, 104, 117, 155).

[226] Julian Lenz, Laurin Pannullo, Marc Wagner, Björn Wellegehausen, and Andreas Wipf. "Inhomogeneous phases in the Gross-Neveu model in 1+1 dimensions at finite number of flavors." In: *Phys. Rev. D* 101.9 (2020), p. 094512. DOI: 10.1103/PhysRevD.101.094512. arXiv: 2004.00295 [hep-lat] (cit. on pp. 11, 12, 51, 91, 104, 117, 125, 142, 155).

[227] Julian J. Lenz, Michael Mandl, and Andreas Wipf. "Inhomogeneities in the two-flavor chiral Gross-Neveu model." In: *Phys. Rev. D* 105.3 (2022), p. 034512. DOI: 10.1103/PhysRevD.105.034512. arXiv: 2109.05525 [hep-lat] (cit. on pp. 11, 51, 75, 155).

[228] Riccardo Ciccone, Lorenzo Di Pietro, and Marco Serone. "Inhomogeneous Phase of the Chiral Gross-Neveu Model." In: *Phys. Rev. Lett.* 129.7 (Aug. 2022), p. 071603. DOI: 10.1103/PhysRevLett.129.071603. arXiv: 2203.07451 [hep-th] (cit. on pp. 11, 51, 76, 91, 125, 155).

[229] Riccardo Ciccone, Lorenzo Di Pietro, and Marco Serone. "Anomalies and persistent order in the chiral Gross-Neveu model." In: *JHEP* 02 (2024), p. 211. DOI: 10.1007/JHEP02(2024)211. arXiv: 2312.13756 [hep-th] (cit. on pp. 11, 51, 76, 91, 125, 155).

[230] Joseph I. Kapusta and T. Toimela. "Friedel Oscillations in Relativistic QED and QCD." In: *Phys. Rev. D* 37 (1988), p. 3731. DOI: 10.1103/PhysRevD.37.3731 (cit. on p. 12).

[231] R. D. Pisarski, F. Rennecke, A. Tsvelik, and S. Valgushev. "The Lifshitz Regime and its Experimental Signals." In: *Nucl. Phys. A* 1005 (2021). Ed. by Feng Liu, Enke Wang, Xin-Nian Wang, Nu Xu, and Ben-Wei Zhang, p. 121910. DOI: 10.1016/j.nuclphysa.2020.121910. arXiv: 2005.00045 [nucl-th] (cit. on pp. 13, 64, 156).

[232] Robert D. Pisarski and Fabian Rennecke. "Signatures of Moat Regimes in Heavy-Ion Collisions." In: *Phys. Rev. Lett.* 127.15 (2021), p. 152302. DOI: 10.1103/PhysRevLett.127.152302. arXiv: 2103.06890 [hep-ph] (cit. on pp. 13, 64, 125, 156).

[233] Fabian Rennecke, Robert D. Pisarski, and Dirk H. Rischke. "Particle interferometry in a moat regime." In: *Phys. Rev. D* 107.11 (2023), p. 116011. DOI: 10.1103/PhysRevD.107.116011. arXiv: 2301.11484 [hep-ph] (cit. on pp. 13, 39, 125, 126, 156).

[234] Kenji Fukushima, Yoshimasa Hidaka, Katsuya Inoue, Kenta Shigaki, and Yorito Yamaguchi. "Hanbury-Brown–Twiss signature for clustered substructures probing primordial inhomogeneity in hot and dense QCD matter." In: *Phys. Rev. C* 109.5 (2024), p. L051903. DOI: 10.1103/PhysRevC.109.L051903. arXiv: 2306.17619 [hep-ph] (cit. on pp. 13, 125, 126).

[235] C. Sasaki, B. Friman, and K. Redlich. "Quark Number Fluctuations in a Chiral Model at Finite Baryon Chemical Potential." In: *Phys. Rev. D* 75 (2007), p. 054026. DOI: 10.1103/PhysRevD.75.054026. arXiv: hep-ph/0611143 (cit. on pp. 13, 110, 111, 113).

[236] K. Redlich, B. Friman, and C. Sasaki. "QCD phase diagram and charge fluctuations." In: *J. Phys. G* 34 (2007), S437–444. DOI: 10.1088/0954-3899/34/8/S32. arXiv: hep-ph/0702296 (cit. on pp. 13, 110, 111).

[237] Fabian Rennecke. "Vacuum structure of vector mesons in QCD." In: *Phys. Rev. D* 92.7 (2015), p. 076012. DOI: 10.1103/PhysRevD.92.076012. arXiv: 1504.03585 [hep-ph] (cit. on pp. 13, 105).

[238] P. M. Chaikin and T. C. Lubensky. *Principles of Condensed Matter Physics*. Cambridge University Press, 1995 (cit. on p. 13).

[239] Eduardo H. Fradkin. *Field Theories of Condensed Matter Physics*. Vol. 82. Cambridge, UK: Cambridge Univ. Press, Feb. 2013. ISBN: 978-0-521-76444-5, 978-1-107-30214-3 (cit. on p. 13).

[240] Rajamani Narayanan. "Phase diagram of the large N Gross-Neveu model in a finite periodic box." In: *Phys. Rev. D* 101.9 (2020), p. 096001. DOI: 10.1103/PhysRevD.101.096001. arXiv: 2001.09200 [hep-th] (cit. on pp. 14, 39, 46, 48, 89, 103, 104, 109, 111, 153, 156).

[241] Michael Buballa, Lennart Kurth, Marc Wagner, and Marc Winstel. "Regulator dependence of inhomogeneous phases in the (2+1)-dimensional Gross-Neveu model." In: *Phys. Rev. D* 103.3 (Feb. 2021), p. 034503. DOI: 10.1103/PhysRevD.103.034503. arXiv: 2012.09588 [hep-lat] (cit. on pp. 14, 39, 46–48, 54, 56–58, 60, 89, 90, 101, 103, 104, 109, 111, 112, 153, 156, 176, 179, 181, 190, 192).

[242] Marc Winstel, Jonas Stoll, and Marc Wagner. "Lattice investigation of an inhomogeneous phase of the 2 + 1-dimensional Gross-Neveu model in the limit of infinitely many flavors." In: *J. Phys. Conf. Ser.* 1667.1 (2020), p. 012044. DOI: 10.1088/1742-6596/1667/1/012044. arXiv: 1909.00064 [hep-lat] (cit. on pp. 14, 46).

[243] Baruch Rosenstein, Brian J. Warr, and Seon H. Park. "The Four Fermi Theory Is Renormalizable in (2+1)-Dimensions." In: *Phys. Rev. Lett.* 62 (Mar. 1989), pp. 1433–1436. DOI: 10.1103/PhysRevLett.62.1433 (cit. on pp. 14, 15, 46, 48, 86, 110, 176).

[244] G. Gat, A. Kovner, and B. Rosenstein. "Chiral phase transitions in d = 3 and renormalizability of four Fermi interactions." In: *Nucl. Phys. B* 385 (1992), pp. 76–98. DOI: 10.1016/0550-3213(92)90095-S (cit. on pp. 14, 15, 46, 110, 176).

[245] Michael Thies. "Non-Abelian twisted kinks in chiral Gross-Neveu model with isospin." In: *Phys. Rev. D* 93.8 (2016), p. 085024. DOI: 10.1103/PhysRevD.93.085024. arXiv: 1512.03894 [hep-th] (cit. on pp. 14, 90).

[246] Michael Thies. "Chiral spiral in the presence of chiral imbalance." In: *Phys. Rev. D* 98.9 (2018), p. 096019. DOI: 10.1103/PhysRevD.98.096019. arXiv: 1810.03921 [hep-th] (cit. on pp. 14, 46, 76, 90).

[247] Michael Thies. "Phase structure of the (1+1)-dimensional Nambu–Jona-Lasinio model with isospin." In: *Phys. Rev. D* 101.1 (2020), p. 014010. DOI: 10.1103/PhysRevD.101.014010. arXiv: 1911.11439 [hep-th] (cit. on pp. 14, 90).

[248] Michael Thies. "Duality study of the chiral Heisenberg-Gross-Neveu model in 1+1 dimensions." In: *Phys. Rev. D* 102.9 (2020), p. 096006. DOI: 10.1103/PhysRevD.102.096006. arXiv: 2008.13119 [hep-th] (cit. on pp. 14, 90).

[249] Konstantin G. Klimenko. "Phase Structure of Generalized Gross-Neveu Models." In: *Z. Phys. C* 37 (Sept. 1988), p. 457. DOI: 10.1007/BF01578141 (cit. on pp. 15, 56, 86, 109, 111, 112, 176, 181).

[250] Baruch Rosenstein, Brian J. Warr, and Seon H. Park. "Thermodynamics of (2+1)-dimensional Four Fermi Models." In: *Phys. Rev. D* 39 (May 1989), p. 3088. DOI: 10.1103/PhysRevD.39.3088 (cit. on pp. 15, 109).

[251] Simon Hands, Aleksandar Kocic, and John B. Kogut. "The Four Fermi model in three-dimensions at nonzero density and temperature." In: *Nucl. Phys. B* 390 (1993), pp. 355–378. DOI: 10.1016/0550-3213(93)90460-7. arXiv: hep-lat/9206024 (cit. on p. 15).

[252] T. Inagaki, T. Kouno, and T. Muta. "Phase structure of four fermion theories at finite temperature and chemical potential in arbitrary dimensions." In: *Int. J. Mod. Phys. A* 10 (1995), pp. 2241–2268. DOI: 10.1142/S0217751X95001091. arXiv: hep-ph/9409413 (cit. on pp. 15, 48, 50, 56).

[253] Luigi Del Debbio and Simon Hands. "Monte Carlo simulation of the three-dimensional Thirring model." In: *Phys. Lett. B* 373 (1996), pp. 171–177. DOI: 10.1016/0370-2693(96)00137-2. arXiv: hep-lat/9512013 (cit. on p. 15).

[254] Thomas Appelquist and Myck Schwetz. "The (2+1)-dimensional NJL model at finite temperature." In: *Phys. Lett. B* 491 (2000), pp. 367–374. DOI: 10.1016/S0370-2693(00)01046-7. arXiv: hep-ph/0007284 (cit. on p. 15).

[255] Simon Hands, John B. Kogut, Costas G. Strouthos, and Thao N Tran. "Fermi surface phenomena in the (2+1)-d four Fermi model." In: *Phys. Rev. D* 68 (2003), p. 016005. DOI: 10.1103/PhysRevD.68.016005. arXiv: hep-lat/0302021 (cit. on pp. 15, 50, 51, 125).

[256] Michael Mandl, Julian J. Lenz, and Andreas Wipf. "Magnetic catalysis in the 1-flavor Gross-Neveu model in $2+1$ dimensions." In: *PoS* LATTICE2022 (2023), p. 152. DOI: 10.22323/1.430.0152. arXiv: 2211.10333 [hep-lat] (cit. on p. 15).

[257] Julian J. Lenz, Michael Mandl, and Andreas Wipf. "Magnetic catalysis in the (2+1)-dimensional Gross-Neveu model." In: *Phys. Rev. D* 107.9 (2023), p. 094505. DOI: 10.1103/PhysRevD.107.094505. arXiv: 2302.05279 [hep-lat] (cit. on p. 15).

[258] Simon Hands, Biagio Lucini, and Susan Morrison. "Critical behavior in the dense planar NJL model." In: *Phys. Rev. Lett.* 86 (2001), pp. 753–756. DOI: 10.1103/PhysRevLett.86.753. arXiv: hep-lat/0008027 (cit. on p. 15).

[259] K. G. Klimenko, R. N. Zhokhov, and V. Ch. Zhukovsky. "Superconductivity phenomenon induced by external in-plane magnetic field in (2+1)-dimensional Gross-Neveu type model." In: *Mod. Phys. Lett. A* 28 (2013), p. 1350096. DOI: 10.1142/S021773231350096X. arXiv: 1211.0148 [hep-th] (cit. on pp. 15, 173).

[260] D. Ebert, T. G. Khunjua, K. G. Klimenko, and V. Ch. Zhukovsky. "Interplay between superconductivity and chiral symmetry breaking in a (2+1)-dimensional model with a compactified spatial coordinate." In: *Phys. Rev. D* 91.10 (2015), p. 105024. DOI: 10.1103/PhysRevD.91.105024. arXiv: 1504.02867 [hep-th] (cit. on p. 15).

[261] D. Ebert, T. G. Khunjua, K. G. Klimenko, and V. C. Zhukovsky. "Competition and duality correspondence between chiral and superconducting channels in (2+1)-dimensional four-fermion models with fermion number and chiral chemical potentials." In: *Phys. Rev. D* 93.10 (2016), p. 105022. DOI: 10.1103/PhysRevD.93.105022. arXiv: 1603.00357 [hep-th] (cit. on pp. 15, 173).

[262] Joaquin E. Drut and Timo A. Lahde. "Is graphene in vacuum an insulator?" In: *Phys. Rev. Lett.* 102 (2009), p. 026802. DOI: 10.1103/PhysRevLett.102.026802. arXiv: 0807.0834 [cond-mat.str-el] (cit. on pp. 15, 164).

[263] D. L. Boyda, V. V. Braguta, S. N. Valgushev, M. I. Polikarpov, and M. V. Ulybyshev. "Numerical simulation of graphene in external magnetic field." In: *Phys. Rev. B* 89.24 (2014), p. 245404. DOI: 10.1103/PhysRevB.89.245404. arXiv: 1308.2814 [hep-lat] (cit. on pp. 15, 164).

[264] V. V. Braguta, S. N. Valgushev, A. A. Nikolaev, M. I. Polikarpov, and M. V. Ulybyshev. "Interaction of static charges in graphene within Monte-Carlo simulation." In: *Phys. Rev. B* 89.19 (2014), p. 195401. DOI: 10.1103/PhysRevB.89.195401. arXiv: 1306.2544 [cond-mat.str-el] (cit. on pp. 15, 164).

[265] Carleton DeTar, Christopher Winterowd, and Savvas Zafeiropoulos. "Lattice Field Theory Study of Magnetic Catalysis in Graphene." In: *Phys. Rev. B* 95.16 (2017), p. 165442. DOI: 10.1103/PhysRevB.95.165442. arXiv: 1608.00666 [hep-lat] (cit. on pp. 15, 164).

[266] J. A. Gracey. "Loop calculations for models of graphene." In: *PoS* LL2018 (2018), p. 070. DOI: 10.22323/1.303.0070. arXiv: 1808.05030 [hep-th] (cit. on pp. 15, 164).

[267] J. A. Gracey. "Large N critical exponents for the chiral Heisenberg Gross-Neveu universality class." In: *Phys. Rev. D* 97.10 (2018), p. 105009. DOI: 10.1103/PhysRevD.97.105009. arXiv: 1801.01320 [hep-th] (cit. on pp. 15, 90).

[268] G. W. Semenoff, I. A. Shovkovy, and L. C. R. Wijewardhana. "Phase transition induced by a magnetic field." In: *Mod. Phys. Lett. A* 13 (1998), pp. 1143–1154. DOI: 10.1142/S0217732398001212. arXiv: hep-ph/9803371 (cit. on pp. 15, 173).

[269] D. Ebert, K. G. Klimenko, P. B. Kolmakov, and V. Ch. Zhukovsky. "Phase transitions in hexagonal, graphene-like lattice sheets and nanotubes under the influence of external conditions." In: *Annals Phys.* 371 (2016), pp. 254–286. DOI: 10.1016/j.aop.2016.05.001. arXiv: 1509.08093 [cond-mat.mes-hall] (cit. on p. 15).

[270] Benjamin Knorr. "Critical chiral Heisenberg model with the functional renormalization group." In: *Phys. Rev. B* 97.7 (2018), p. 075129. DOI: 10.1103/PhysRevB.97.075129. arXiv: 1708.06200 [cond-mat.str-el] (cit. on pp. 15, 173).

[271] Thomas C. Lang and Andreas M. Läuchli. "Quantum Monte Carlo Simulation of the Chiral Heisenberg Gross-Neveu-Yukawa Phase Transition with a Single Dirac Cone." In: *Phys. Rev. Lett.* 123.13 (2019), p. 137602. DOI: 10.1103/PhysRevLett.123.137602. arXiv: 1808.01230 [cond-mat.str-el] (cit. on pp. 15, 164).

[272] K. G. Klimenko. "Gross-Neveu model and optimized expansion method." In: *Z. Phys. C* 50 (1991), pp. 477–481. DOI: 10.1007/BF01551460 (cit. on pp. 15, 125).

[273] Jean-Loic Kneur, Marcus Benghi Pinto, Rudnei O. Ramos, and Ederson Staudt. "Updating the phase diagram of the Gross-Neveu model in 2+1 dimensions." In: *Phys. Lett. B* 657 (2007), pp. 136–142. DOI: 10.1016/j.physletb.2007.10.013. arXiv: 0705.0673 [hep-ph] (cit. on pp. 15, 125).

[274] Daniel D. Scherer and Holger Gies. "Renormalization Group Study of Magnetic Catalysis in the 3d Gross-Neveu Model." In: *Phys. Rev. B* 85 (2012), p. 195417. DOI: 10.1103/PhysRevB.85.195417. arXiv: 1201.3746 [cond-mat.str-el] (cit. on pp. 15, 115, 166, 173, 175).

[275] Julian J. Lenz, Björn H. Wellegehausen, and Andreas Wipf. "Absence of chiral symmetry breaking in Thirring models in 1+2 dimensions." In: *Phys. Rev. D* 100.5 (2019), p. 054501. DOI: 10.1103/PhysRevD.100.054501. arXiv: 1905.00137 [hep-lat] (cit. on pp. 15, 91).

[276] Claudio Bonati, Alessio Franchi, Andrea Pelissetto, and Ettore Vicari. "Chiral critical behavior of 3D lattice fermionic models with quartic interactions." In: *Phys. Rev. D* 107.3 (2023), p. 034507. DOI: 10.1103/PhysRevD.107.034507. arXiv: 2212.13932 [hep-lat] (cit. on p. 15).

[277] Jens Braun, Holger Gies, and Daniel D. Scherer. "Asymptotic safety: a simple example." In: *Phys. Rev. D* 83 (2011), p. 085012. DOI: 10.1103/PhysRevD.83.085012. arXiv: 1011.1456 [hep-th] (cit. on p. 15).

[278] L. H. Ryder. *Quantum Field Theory*. Cambridge University Press, June 1996. ISBN: 978-0-521-47814-4. DOI: 10.1017/CBO9780511813900 (cit. on pp. 17, 22, 161, 166, 170).

[279] Walter Greiner and Joachim Reinhardt. *Field Quantization*. Springer, 1996. ISBN: 978-3-642-61485-9. DOI: 10.1007/978-3-642-61485-9 (cit. on pp. 17, 22, 161, 166).

[280] Michele Maggiore. *A Modern introduction to quantum field theory*. Oxford Master Series in Physics. 2005. ISBN: 978-0-19-852074-0 (cit. on pp. 17, 161).

[281] Dirk H. Rischke. *Lecture notes on: Quantenfeldtheorie I + II*. [Online; accessed 2024.07.24]. 2021. URL: https://itp.uni-frankfurt.de/~drischke/Skript_QFT_I.pdf (cit. on pp. 17, 22, 26, 161).

[282] Michel Le Bellac. *Thermal Field Theory*. Cambridge Monographs on Mathematical Physics. Cambridge University Press, Mar. 2011. ISBN: 978-0-511-88506-8, 978-0-521-65477-7. DOI: 10.1017/CBO9780511721700 (cit. on pp. 17, 20, 33, 78).

[283] Mikko Laine and Aleksi Vuorinen. *Basics of Thermal Field Theory*. Lect. Notes Phys. 925. Springer, 2016, pp. 1–281. DOI: 10.1007/978-3-319-31933-9. arXiv: 1701.01554 [hep-ph] (cit. on pp. 17, 20).

[284] Andreas Wipf. *Statistical Approach to Quantum Field Theory: An Introduction*. Vol. 992. Lecture Notes in Physics. Springer, Oct. 2021. ISBN: 978-3-030-83262-9, 978-3-030-83263-6. DOI: 10.1007/978-3-030-83263-6 (cit. on pp. 17, 18, 20, 141, 142).

[285] Dirk H. Rischke. *Lecture notes on: Statistische Feldtheorie*. [Online; accessed 2024.07.24]. 2022. URL: https://itp.uni-frankfurt.de/~drischke/Skript_SFT.pdf (cit. on pp. 17, 20, 33, 56, 176, 177, 181, 182, 189).

[286] Adrian Koenigstein. "Non-perturbative aspects of (low-dimensional) quantum field theories." PhD thesis. Goethe U., Frankfurt (main), 2023. DOI: 10.21248/gups.74658 (cit. on pp. 17, 51, 66, 125).

[287] G. C. Wick. "Properties of Bethe-Salpeter Wave Functions." In: *Phys. Rev.* 96 (4 Nov. 1954), pp. 1124–1134. DOI: 10.1103/PhysRev.96.1124. URL: https://link.aps.org/doi/10.1103/PhysRev.96.1124 (cit. on p. 18).

[288] Konrad Osterwalder and Robert Schrader. "Axioms for Euclidean Green's functions." In: *Commun. Math. Phys.* 31 (1973), pp. 83–112. DOI: 10.1007/BF01645738 (cit. on p. 19).

[289] Konrad Osterwalder and Robert Schrader. "Axioms for Euclidean Green's Functions. 2." In: *Commun. Math. Phys.* 42 (1975), p. 281. DOI: 10.1007/BF01608978 (cit. on p. 19).

[290] C. Wetterich. "Spinors in euclidean field theory, complex structures and discrete symmetries." In: *Nucl. Phys. B* 852 (2011), pp. 174–234. DOI: 10.1016/j.nuclphysb.2011.06.013. arXiv: 1002.3556 [hep-th] (cit. on p. 19).

[291] Ryogo Kubo. "Statistical mechanical theory of irreversible processes. 1. General theory and simple applications in magnetic and conduction problems." In: *J. Phys. Soc. Jap.* 12 (1957), pp. 570–586. DOI: 10.1143/JPSJ.12.570 (cit. on p. 19).

[292] Christof Gattringer and Kurt Langfeld. "Approaches to the sign problem in lattice field theory." In: *Int. J. Mod. Phys. A* 31.22 (2016), p. 1643007. DOI: 10.1142/S0217751X16430077. arXiv: 1603.09517 [hep-lat] (cit. on p. 19).

[293] Barry A. Freedman and Larry D. McLerran. "Fermions and Gauge Vector Mesons at Finite Temperature and Density. 1. Formal Techniques." In: *Phys. Rev. D* 16 (1977), p. 1130. DOI: 10.1103/PhysRevD.16.1130 (cit. on p. 21).

[294] Joseph I. Kapusta. "Bose-Einstein Condensation, Spontaneous Symmetry Breaking, and Gauge Theories." In: *Phys. Rev. D* 24 (1981), pp. 426–439. DOI: 10.1103/PhysRevD.24.426 (cit. on p. 21).

[295] R. J. Rivers. *Path Integral Methods in Quantum Field Theory*. Cambridge Monographs on Mathematical Physics. Cambridge University Press, 1987 (cit. on p. 22).

[296] Ruslan L. Stratonovich. "On a Method of Calculating Quantum Distribution Functions." In: *Soviet Physics Doklady* 2 (July 1957), p. 416. URL: https://www.mathnet.ru/eng/dan22296 (cit. on p. 26).

[297] John Hubbard. "Calculation of partition functions." In: *Phys. Rev. Lett.* 3 (July 1959), pp. 77–80. DOI: 10.1103/PhysRevLett.3.77 (cit. on p. 26).

[298] John Clive Ward. "An Identity in Quantum Electrodynamics." In: *Phys. Rev.* 78 (1950), p. 182. DOI: 10.1103/PhysRev.78.182 (cit. on p. 27).

[299] Y. Takahashi. "On the generalized Ward identity." In: *Nuovo Cim.* 6 (1957), p. 371. DOI: 10.1007/BF02832514 (cit. on p. 27).

[300] Hosein Gholami. "On the Calculation of Pressure Derivatives in Mean-Field Thermal Field Theories." Jan. 2025. arXiv: 2501.05192 [hep-ph] (cit. on p. 29).

[301] H. E. Daniels. "Saddlepoint Approximations in Statistics." In: *The Annals of Mathematical Statistics* 25.4 (1954), pp. 631–650. DOI: 10.1214/aoms/1177728652. URL: https://doi.org/10.1214/aoms/1177728652 (cit. on p. 30).

[302] Moshe Moshe and Jean Zinn-Justin. "Quantum field theory in the large N limit: A Review." In: *Phys. Rept.* 385 (2003), pp. 69–228. DOI: 10.1016/S0370-1573(03)00263-1. arXiv: hep-th/0306133 (cit. on pp. 30, 34, 52, 129).

[303] Marc Wagner. *Lecture notes on: Theoretische Physik 3: Klassische Elektrodynamik*. [Online; accessed 2025.01.11]. 2021. URL: https://itp.uni-frankfurt.de/~mwagner/teaching/theo3_WS20/Theo3_ED.pdf (cit. on p. 34).

[304] Mariusz Sadzikowski. "Comparison of the non-uniform chiral and 2SC phases at finite temperatures and densities." In: *Phys. Lett. B* 642 (2006), pp. 238–243. DOI: 10.1016/j.physletb.2006.08.086. arXiv: hep-ph/0609186 (cit. on pp. 39, 46, 47, 92, 105).

[305] Paolo Alba, Wanda Alberico, Rene Bellwied, Marcus Bluhm, Valentina Mantovani Sarti, Marlene Nahrgang, and Claudia Ratti. "Freeze-out conditions from net-proton and net-charge fluctuations at RHIC." In: *Phys. Lett. B* 738 (2014), pp. 305–310. DOI: 10.1016/j.physletb.2014.09.052. arXiv: 1403.4903 [hep-ph] (cit. on p. 40).

[306] F. Becattini, J. Steinheimer, R. Stock, and M. Bleicher. "Hadronization conditions in relativistic nuclear collisions and the QCD pseudo-critical line." In: *Phys. Lett. B* 764 (2017), pp. 241–246. DOI: 10.1016/j.physletb.2016.11.033. arXiv: 1605.09694 [nucl-th] (cit. on p. 40).

[307] Anton Andronic, Peter Braun-Munzinger, Krzysztof Redlich, and Johanna Stachel. "Decoding the phase structure of QCD via particle production at high energy." In: *Nature* 561.7723 (2018), pp. 321–330. DOI: 10.1038/s41586-018-0491-6. arXiv: 1710.09425 [nucl-th] (cit. on p. 40).

[308] V. V. Sagun et al. "Hadron Resonance Gas Model with Induced Surface Tension." In: *Eur. Phys. J. A* 54.6 (2018), p. 100. DOI: 10.1140/epja/i2018-12535-1. arXiv: 1703.00049 [hep-ph] (cit. on p. 40).

[309] Hiromichi Nishimura, Michael C. Ogilvie, and Kamal Pangeni. "Complex saddle points in QCD at finite temperature and density." In: *Phys. Rev. D* 90.4 (2014), p. 045039. DOI: 10.1103/PhysRevD.90.045039. arXiv: 1401.7982 [hep-ph] (cit. on pp. 40, 108).

[310] Carl M. Bender, H. F. Jones, and R. J. Rivers. "Dual PT-symmetric quantum field theories." In: *Phys. Lett. B* 625 (2005), pp. 333–340. DOI: 10.1016/j.physletb.2005.08.087. arXiv: hep-th/0508105 (cit. on p. 41).

[311] Jean Alexandre, John Ellis, and Peter Millington. "Discrete spacetime symmetries and particle mixing in non-Hermitian scalar quantum field theories." In: *Phys. Rev. D* 102.12 (2020), p. 125030. DOI: 10.1103/PhysRevD.102.125030. arXiv: 2006.06656 [hep-th] (cit. on p. 41).

[312] N. E. Mavromatos, Sarben Sarkar, and A. Soto. "PT symmetric fermionic field theories with axions: Renormalization and dynamical mass generation." In: *Phys. Rev. D* 106.1 (2022), p. 015009. DOI: 10.1103/PhysRevD.106.015009. arXiv: 2111.05131 [hep-th] (cit. on pp. 41, 125, 158).

[313] Wen-Yuan Ai, Carl M. Bender, and Sarben Sarkar. "PT-symmetric -gφ4 theory." In: *Phys. Rev. D* 106.12 (2022), p. 125016. DOI: 10.1103/PhysRevD.106.125016. arXiv: 2209.07897 [hep-th] (cit. on pp. 41, 125, 158).

[314] Carl M. Bender and Philip D. Mannheim. "PT symmetry and necessary and sufficient conditions for the reality of energy eigenvalues." In: *Phys. Lett. A* 374 (2010), pp. 1616–1620. DOI: 10.1016/j.physleta.2010.02.032. arXiv: 0902.1365 [hep-th] (cit. on p. 41).

[315] Carl M. Bender and Philip D. Mannheim. "PT symmetry in relativistic quantum mechanics." In: *Phys. Rev. D* 84 (2011), p. 105038. DOI: 10.1103/PhysRevD.84.105038. arXiv: 1107.0501 [hep-th] (cit. on p. 41).

[316] U. Wolff. "The phase diagram of the infinite-N Gross-Neveu model at finite temperature and chemical potential." In: *Phys. Lett. B* 157 (1985), pp. 303–308. DOI: 10.1016/0370-2693(85)90671-9 (cit. on pp. 43, 44, 56).

[317] G. Sarma. "On the influence of a uniform exchange field acting on the spins of the conduction electrons in a superconductor." In: *Journal of Physics and Chemistry of Solids* 24.8 (Aug. 1963), pp. 1029–1032. ISSN: 0022-3697. DOI: 10.1016/0022-3697(63)90007-6 (cit. on p. 44).

[318] Oliver Schnetz, Michael Thies, and Konrad Urlichs. "Phase diagram of the Gross-Neveu model: Exact results and condensed matter precursors." In: *Annals Phys.* 314 (2004), pp. 425–447. DOI: 10.1016/j.aop.2004.06.009. arXiv: hep-th/0402014 (cit. on pp. 44, 45).

[319] F. W. J. Olver et al. *NIST Digital Library of Mathematical Function*. Release 1.1.2 of 2021-06-15. [Online; accessed 2024.12.20]. 2021. URL: http://dlmf.nist.gov/ (cit. on p. 44).

[320] Johannes Mertsching and Helmut J. Fischbeck. "The Incommensurate Peierls Phase of the Quasi-One-Dimensional Fröhlich Model with a Nearly Half-Filled Band." In: *Physica Status Solidi B-basic Solid State Physics* 103 (1981), pp. 783–795. URL: https://api.semanticscholar.org/CorpusID:97160063 (cit. on p. 45).

[321] Konrad Urlichs. "Baryons and baryonic matter in four-fermion interaction models." Doctoral thesis. Universität Erlangen, Feb. 2007 (cit. on pp. 45, 47, 81, 88, 102, 103, 113).

[322] Jens Braun, Marc Leonhardt, and Jan M. Pawlowski. "Renormalization group consistency and low-energy effective theories." In: *SciPost Phys.* 6.5 (2019), p. 056. DOI: 10.21468/SciPostPhys.6.5.056. arXiv: 1806.04432 [hep-ph] (cit. on p. 46).

[323] L. D. Landau and E. M. Lifshitz. *Statistical Physics, Part 1*. Vol. 5. Course of Theoretical Physics. Oxford: Butterworth-Heinemann, 1980. ISBN: 978-0-7506-3372-7 (cit. on pp. 50, 51, 91, 155).

[324] Walter E. Thirring. "A Soluble relativistic field theory?" In: *Annals Phys.* 3 (1958), pp. 91–112. DOI: 10.1016/0003-4916(58)90015-0 (cit. on p. 51).

[325] S. J. Hands, J. B. Kogut, and C. G. Strouthos. "The (2+1)-dimensional Gross-Neveu model with a U(1) chiral symmetry at nonzero temperature." In: *Phys. Lett. B* 515 (2001), pp. 407–413. DOI: 10.1016/S0370-2693(01)00885-1. arXiv: hep-lat/0107004 (cit. on pp. 51, 91).

[326] Simon Hands and David N. Walters. "Evidence for BCS diquark condensation in the (3+1)-d lattice NJL model." In: *Phys. Lett. B* 548 (2002), pp. 196–203. DOI: 10.1016/S0370-2693(02)02766-1. arXiv: hep-lat/0209140 (cit. on p. 51).

[327] David Nathan Walters. "The 3 + 1 dimensional lattice NJL model at non-zero baryon density." PhD thesis. Swansea University, 2003 (cit. on pp. 51, 91).

[328] V. L. Berezinsky. "Destruction of long range order in one-dimensional and two-dimensional systems having a continuous symmetry group. I. Classical systems." In: *Sov. Phys. JETP* 32 (1971), pp. 493–500 (cit. on pp. 52, 155).

[329] V. L. Berezinsky. "Destruction of Long-range Order in One-dimensional and Two-dimensional Systems Possessing a Continuous Symmetry Group. II. Quantum Systems." In: *Sov. Phys. JETP* 34.3 (1972), p. 610 (cit. on pp. 52, 155).

[330] J. M. Kosterlitz and D. J. Thouless. "Ordering, metastability and phase transitions in two-dimensional systems." In: *J. Phys. C* 6 (1973), pp. 1181–1203. DOI: 10.1088/0022-3719/6/7/010 (cit. on p. 52).

[331] Philippe de Forcrand and Urs Wenger. "New baryon matter in the lattice Gross-Neveu model." In: *PoS* LAT2006 (2006), p. 152. DOI: 10.22323/1.032.0152. arXiv: hep-lat/0610117 (cit. on p. 56).

[332] Marc Wagner. "Fermions in the pseudoparticle approach." In: *Phys. Rev. D* 76 (2007), p. 076002. DOI: 10.1103/PhysRevD.76.076002. arXiv: 0704.3023 [hep-lat] (cit. on p. 56).

[333] Achim Heinz, Francesco Giacosa, Marc Wagner, and Dirk H. Rischke. "Inhomogeneous condensation in effective models for QCD using the finite-mode approach." In: *Phys. Rev. D* 93.1 (2016), p. 014007. DOI: 10.1103/PhysRevD.93.014007. arXiv: 1508.06057 [hep-ph] (cit. on p. 56).

[334] R. Horst and H. Tuy. *Global Optimization: Deterministic Approaches*. Springer Berlin Heidelberg, 1996. ISBN: 9783540610380. URL: https://books.google.de/books?id=usFjGFvuBDEC (cit. on p. 56).

[335] M.I. Kamien and N.L. Schwartz. *Dynamic Optimization: The Calculus of Variations and Optimal Control in Economics and Management*. Calculus of Variation and Optimal Control in Economics and Management Series. North Holland, 1981. ISBN: 9780444004246. URL: https://books.google.de/books?id=y8V9yEF_P4kC (cit. on pp. 56, 57).

[336] D. Bertsekas. *Dynamic Programming and Optimal Control: Volume I*. Athena Scientific optimization and computation series. Athena Scientific, 2012. ISBN: 9781886529434. URL: https://books.google.de/books?id=qVBEEAAAQBAJ (cit. on pp. 56, 57).

[337] Jens Braun, Stefan Finkbeiner, Felix Karbstein, and Dietrich Roscher. "Search for inhomogeneous phases in fermionic models." In: *Phys. Rev. D* 91.11 (2015), p. 116006. DOI: 10.1103/PhysRevD.91.116006. arXiv: 1410.8181 [hep-ph] (cit. on pp. 56, 57, 73).

[338] R. L. S. Farias, Dyana C. Duarte, Gastão Krein, and Rudnei O. Ramos. "Thermodynamics of quark matter with a chiral imbalance." In: *Phys. Rev. D* 94.7 (2016), p. 074011. DOI: 10.1103/PhysRevD.94.074011. arXiv: 1604.04518 [hep-ph] (cit. on p. 56).

[339] Alejandro Ayala, Aritra Bandyopadhyay, Ricardo L. S. Farias, Luis A. Hernández, and José Luis Hernández. "QCD equation of state at finite isospin density from the linear sigma model with quarks: The cold case." In: (Jan. 2023). arXiv: 2301.13633 [hep-ph] (cit. on p. 56).

[340] Arthur E. B. Pasqualotto, Ricardo L. S. Farias, William R. Tavares, Sidney S. Avancini, and Gastão Krein. "Causality violation and the speed of sound of hot and dense quark matter in the Nambu–Jona-Lasinio model." In: *Phys. Rev. D* 107.9 (2023), p. 096017. DOI: 10.1103/PhysRevD.107.096017. arXiv: 2301.10721 [hep-ph] (cit. on p. 56).

[341] E. Nakano and T. Tatsumi. "Chiral symmetry and density wave in quark matter." In: *Phys. Rev. D* 71 (2005), p. 114006. DOI: 10.1103/PhysRevD.71.114006. arXiv: hep-ph/0411350 (cit. on p. 57).

[342] Michael Buballa, Stefano Carignano, and Lennart Kurth. "Inhomogeneous phases in the quark-meson model with explicit chiral-symmetry breaking." In: *Eur. Phys. J. ST* 229.22-23 (2020), pp. 3371–3385. DOI: 10.1140/epjst/e2020-000101-x. arXiv: 2006.02133 [hep-ph] (cit. on pp. 57, 90, 104, 105, 128).

[343] Ralf-Arno Tripolt, Bernd-Jochen Schaefer, Lorenz von Smekal, and Jochen Wambach. "Low-temperature behavior of the quark-meson model." In: *Phys. Rev. D* 97.3 (2018), p. 034022. DOI: 10.1103/PhysRevD.97.034022. arXiv: 1709.05991 [hep-ph] (cit. on pp. 57, 59).

[344] Marc Winstel. "Inhomogeneous phases in the 2 + 1-dimensional Gross-Neveu model via mean-field lattice field theory." Updated version from December 30, 2020 with minor corrections. Master thesis. Goethe University Frankfurt, Sept. 2020. URL: https://itp.uni-frankfurt.de/~mwagner/theses/MA_Winstel.pdf (cit. on pp. 58, 89, 104, 166).

[345] Takeo Matsubara. "A New approach to quantum statistical mechanics." In: *Prog. Theor. Phys.* 14 (1955), pp. 351–378. DOI: 10.1143/PTP.14.351 (cit. on p. 68).

[346] Michael Thies. "Nonperturbative phase boundaries in the Gross-Neveu model from a stability analysis." In: *Phys. Rev. D* 110.9 (2024), p. 096012. DOI: 10.1103/PhysRevD.110.096012. arXiv: 2408.09803 [hep-th] (cit. on p. 73).

[347] Gokce Basar and Gerald V. Dunne. "Self-consistent crystalline condensate in chiral Gross-Neveu and Bogoliubov-de Gennes systems." In: *Phys. Rev. Lett.* 100 (2008), p. 200404. DOI: 10.1103/PhysRevLett.100.200404. arXiv: 0803.1501 [hep-th] (cit. on p. 75).

[348] Don Zagier. "The Dilogarithm Function." In: *Les Houches School of Physics: Frontiers in Number Theory, Physics and Geometry*. 2007, pp. 3–65. DOI: 10.1007/978-3-540-30308-4_1 (cit. on pp. 76, 181).

[349] Wolfram Research Inc. *Mathematica, Version 14.1*. Champaign, IL, 2024. URL: https://www.wolfram.com/mathematica (cit. on pp. 76, 78, 97).

[350] Charles R. Harris et al. "Array programming with NumPy." In: *Nature* 585.7825 (Sept. 2020), pp. 357–362. ISSN: 1476-4687. DOI: 10.1038/s41586-020-2649-2. URL: http://dx.doi.org/10.1038/s41586-020-2649-2 (cit. on pp. 76, 101, 115).

[351] Simon Hands. *Planar Thirring Model in the U(2N)-symmetric limit*. May 2021. arXiv: 2105.09643 [hep-lat] (cit. on p. 83).

[352] Gerard 't Hooft. "Symmetry Breaking Through Bell-Jackiw Anomalies." In: *Phys. Rev. Lett.* 37 (1976), pp. 8–11. DOI: 10.1103/PhysRevLett.37.8 (cit. on p. 90).

[353] Bastian B. Brandt and Gergely Endrodi. "QCD phase diagram with isospin chemical potential." In: *PoS* LATTICE2016 (2016), p. 039. DOI: 10.22323/1.256.0039. arXiv: 1611.06758 [hep-lat] (cit. on pp. 92, 93).

[354] Xuanmin Cao, Hui Liu, Danning Li, and Guanning Ou. "QCD phase diagram at finite isospin chemical potential and temperature in an IR-improved soft-wall AdS/QCD model." In: *Chin. Phys. C* 44.8 (2020), p. 083106. DOI: 10.1088/1674-1137/44/8/083106. arXiv: 2001.02888 [hep-ph] (cit. on pp. 92, 93).

[355] Bastian B. Brandt, Francesca Cuteri, and Gergely Endrodi. "QCD thermodynamics at non-zero isospin asymmetry." In: *PoS* LATTICE2021 (2022), p. 132. DOI: 10.22323/1.396.0132. arXiv: 2110.14750 [hep-lat] (cit. on pp. 92, 93).

[356] Phillip Lakaschus, Michael Buballa, and Dirk H. Rischke. "Competition of inhomogeneous chiral phases and two-flavor color superconductivity in the NJL model." In: *Phys. Rev. D* 103.3 (2021), p. 034030. DOI: 10.1103/PhysRevD.103.034030. arXiv: 2012.07520 [hep-ph] (cit. on pp. 92, 105).

[357] Pauli Virtanen et al. "SciPy 1.0–Fundamental Algorithms for Scientific Computing in Python." In: *Nature Meth.* 17 (2020), p. 261. DOI: 10.1038/s41592-019-0686-2. arXiv: 1907.10121 [cs.MS] (cit. on pp. 101, 115, 143).

[358] G. H. Derrick. "Comments on nonlinear wave equations as models for elementary particles." In: *J. Math. Phys.* 5 (1964), pp. 1252–1254. DOI: 10.1063/1.1704233 (cit. on pp. 105, 157).

[359] Leonid P. Pryadko, Steven A. Kivelson, V. J. Emery, Yaroslaw B. Bazaliy, and Eugene A. Demler. "Topological doping and the stability of stripe phases." In: *Physical Review B* 60.10 (Sept. 1999), pp. 7541–7557. DOI: 10.1103/physrevb.60.7541. URL: https://doi.org/10.1103%2Fphysrevb.60.7541 (cit. on pp. 105, 157).

[360] Teiji Kunihiro. "Quark number susceptibility and fluctuations in the vector channel at high temperatures." In: *Phys. Lett. B* 271 (1991), pp. 395–402. DOI: 10.1016/0370-2693(91)90107-2 (cit. on p. 106).

[361] Jens Braun. "The QCD Phase Boundary from Quark-Gluon Dynamics." In: *Eur. Phys. J. C* 64 (2009), pp. 459–482. DOI: 10.1140/epjc/s10052-009-1136-6. arXiv: 0810.1727 [hep-ph] (cit. on p. 107).

[362] S. Floerchinger and C. Wetterich. "Exact flow equation for composite operators." In: *Phys. Lett. B* 680 (2009), pp. 371–376. DOI: 10.1016/j.physletb.2009.09.014. arXiv: 0905.0915 [hep-th] (cit. on p. 107).

[363] Thomas D. Cohen, R. J. Furnstahl, and David K. Griegel. "Quark and gluon condensates in nuclear matter." In: *Phys. Rev. C* 45 (1992), pp. 1881–1893. DOI: 10.1103/PhysRevC.45.1881 (cit. on p. 112).

[364] Thomas D . Cohen. "Functional integrals for QCD at nonzero chemical potential and zero density." In: *Phys. Rev. Lett.* 91 (2003), p. 222001. DOI: 10.1103/PhysRevLett.91.222001. arXiv: hep-ph/0307089 (cit. on p. 112).

[365] Pascal J. Gunkel, Christian S. Fischer, and Philipp Isserstedt. "Mesons at finite chemical potential and the Silver-Blaze property of QCD." In: *J. Phys. Conf. Ser.* 1667.1 (2020), p. 012011. DOI: 10.1088/1742-6596/1667/1/012011. arXiv: 1911.04399 [hep-ph] (cit. on p. 112).

[366] K. Kolehmainen and G. Baym. "Pion condensation at finite temperature. 2. Simple models including thermal excitations of the pion field." In: *Nucl. Phys. A* 382 (1982), pp. 528–541. DOI: 10.1016/0375-9474(82)90359-1 (cit. on p. 117).

[367] Lukas Grunwald, Volker Meden, and Dante M. Kennes. "Functional renormalization group for non-Hermitian and $\mathcal{PT}$-symmetric systems." In: *SciPost Phys.* 12.5 (2022), p. 179. DOI: 10.21468/SciPostPhys.12.5.179. arXiv: 2203.08108 [cond-mat.str-el] (cit. on pp. 125, 158).

[368] Paul Romatschke. "A solvable quantum field theory with asymptotic freedom in (3+1) dimensions." In: *Int. J. Mod. Phys. A* 38.28 (2023), p. 2350157. DOI: 10.1142/S0217751X23501579. arXiv: 2211.15683 [hep-th] (cit. on p. 125).

[369] Seth Grable and Max Weiner. "A fully solvable model of fermionic interaction in 3 + 1d." In: *JHEP* 09 (2023), p. 017. DOI: 10.1007/JHEP09(2023)017. arXiv: 2302.08603 [hep-th] (cit. on pp. 125, 158).

[370] Scott Lawrence, Ryan Weller, Christian Peterson, and Paul Romatschke. "Instantons, analytic continuation, and PT-symmetric field theory." In: *Phys. Rev. D* 108.8 (2023), p. 085013. DOI: 10.1103/PhysRevD.108.085013. arXiv: 2303.01470 [hep-th] (cit. on p. 125).

[371] Paul Romatschke. "What if $\phi 4$ theory in 4 dimensions is non-trivial in the continuum?" In: *Phys. Lett. B* 847 (2023), p. 138270. DOI: 10.1016/j.physletb.2023.138270. arXiv: 2305.05678 [hep-th] (cit. on pp. 125, 152, 158).

[372] Y. Cohen, S. Elitzur, and E. Rabinovici. "A Monte Carlo study of the Gross-Neveu model." In: *Nucl. Phys. B* 220 (1983), pp. 102–118. DOI: 10.1016/0550-3213(83)90136-0 (cit. on p. 125).

[373] Andrei Alexandru, Gokce Basar, Paulo F. Bedaque, Gregory W. Ridgway, and Neill C. Warrington. "Monte Carlo calculations of the finite density Thirring model." In: *Phys. Rev. D* 95.1 (2017), p. 014502. DOI: 10.1103/PhysRevD.95.014502. arXiv: 1609.01730 [hep-lat] (cit. on p. 125).

[374] I. P. Omelyan, I. M. Mryglod, and R. Folk. "Symplectic analytically integrable decomposition algorithms: classification, derivation, and application to molecular dynamics, quantum and celestial mechanics simulations." In: *Comput. Phys. Commun.* 151.3 (2003), pp. 272–314. DOI: 10.1016/S0010-4655(02)00754-3 (cit. on p. 141).

[375] Martin Luscher. "A Portable high quality random number generator for lattice field theory simulations." In: *Comput. Phys. Commun.* 79 (1994), pp. 100–110. DOI: 10.1016/0010-4655(94)90232-1. arXiv: hep-lat/9309020 (cit. on p. 142).

[376] Thomas P. Robitaille et al. "Astropy: A Community Python Package for Astronomy." In: *Astron. Astrophys.* 558 (2013), A33. DOI: 10.1051/0004-6361/201322068. arXiv: 1307.6212 [astro-ph.IM] (cit. on p. 143).

[377] Laurin Pannullo. private communications (cit. on p. 157).

[378] Adrian Koenigstein, Martin J. Steil, Nicolas Wink, Eduardo Grossi, Jens Braun, Michael Buballa, and Dirk H. Rischke. "Numerical fluid dynamics for FRG flow equations: Zero-dimensional QFTs as numerical test cases. I. The O(N) model." In: *Phys. Rev. D* 106.6 (2022), p. 065012. DOI: 10.1103/PhysRevD.106.065012. arXiv: 2108.02504 [cond-mat.stat-mech] (cit. on p. 159).

[379] Adrian Koenigstein, Martin J. Steil, Nicolas Wink, Eduardo Grossi, and Jens Braun. "Numerical fluid dynamics for FRG flow equations: Zero-dimensional QFTs as numerical test cases. II. Entropy production and irreversibility of RG flows." In: *Phys. Rev. D* 106.6 (2022), p. 065013. DOI: 10.1103/PhysRevD.106.065013. arXiv: 2108.10085 [cond-mat.stat-mech] (cit. on p. 159).

[380] Martin J. Steil and Adrian Koenigstein. "Numerical fluid dynamics for FRG flow equations: Zero-dimensional QFTs as numerical test cases. III. Shock and rarefaction waves in RG flows reveal limitations of the N→∞ limit in O(N)-type models." In: *Phys. Rev. D* 106.6 (2022), p. 065014. DOI: 10.1103/PhysRevD.106.065014. arXiv: 2108.04037 [cond-mat.stat-mech] (cit. on p. 159).

[381] Niklas Zorbach, Adrian Koenigstein, and Jens Braun. "Functional Renormalization Group meets Computational Fluid Dynamics: RG flows in a multi-dimensional field space." Dec. 2024. arXiv: 2412.16053 [cond-mat.stat-mech] (cit. on p. 159).

[382] Friederike Ihssen, Jan M. Pawlowski, Franz R. Sattler, and Nicolas Wink. "Towards quantitative precision for QCD at large densities." Sept. 2023. arXiv: 2309.07335 [hep-th] (cit. on p. 159).

[383] Friederike Ihssen, Jan M. Pawlowski, Franz R. Sattler, and Nicolas Wink. "Towards quantitative precision in functional QCD I." Aug. 2024. arXiv: 2408.08413 [hep-ph] (cit. on p. 159).

[384] Jeong-Hyuck Park. "Lecture note on Clifford algebra." In: *J. Korean Phys. Soc.* 81 (2022), p. 1. DOI: 10.1007/s40042-022-00493-z. arXiv: 2205.09509 [hep-th] (cit. on p. 163).

[385] Holger Gies, Lukas Janssen, Stefan Rechenberger, and Michael M. Scherer. "Phase transition and critical behavior of d=3 chiral fermion models with left/right asymmetry." In: *Phys. Rev. D* 81 (2010), p. 025009. DOI: 10.1103/PhysRevD.81.025009. arXiv: 0910.0764 [hep-th] (cit. on pp. 164, 166, 173).

[386] Marc Wagner. *Lecture notes on: Höhere Quantenmechanik, Advanced quantum mechanics*. [Online; accessed 2025.02.06]. 2023. URL: https://itp.uni-frankfurt.de/~mwagner/teaching/QM2_SS23/QM2.pdf (cit. on p. 166).

[387] Stephan Narison. *QCD spectral sum rules*. Vol. 26. 1989 (cit. on p. 172).

LIST OF FIGURES

LIST OF TABLES

ACRONYMS

χHGN	chiral Heisenberg-Gross-Neveu. 92, 93, 173, 182
RO	research objective. xiii, 8, 13, 16, 17, 55, 83, 132, 160, 165
CBM	Compressed Baryonic Matter. 8, 13
CP	critical point. v, 8–12, 41, 45, 49, 90, 127, 128, 156, 163, 165
DSE	Dyson-Schwinger equation. 7, 8, 11, 12, 162, 165
FAIR	Facility for Antiproton and Ion Research. 3, 8, 13
FRG	functional renormalization group. 7, 8, 12, 39–41, 49, 110, 128, 132, 150, 156, 162, 163, 165, 235
GN	Gross-Neveu. 7, 11, 14, 41, 44–52, 55, 57, 63, 66–70, 73–78, 80, 81, 87–91, 93–95, 103–105, 112, 114–116, 121, 123, 126, 128, 161–163, 182, 184, 185, 188, 190, 199, 201, 235, 236
HBP	homogeneous broken phase. 6, 9, 10, 16, 31, 44, 45, 47, 51–53, 70–74, 79, 83, 91, 103, 105, 106, 114, 115, 117–119, 125, 126, 134, 136, 138, 141–143, 147, 151, 157, 159, 161, 163, 190, 235
HMC	Hybrid Monte Carlo. 131, 145–147
IP	inhomogeneous phase. v, 9–16, 31, 34, 39–53, 55, 57–60, 64–66, 70, 72–74, 76, 78–81, 83, 87, 89–95, 98–100, 103–107, 117, 118, 127, 128, 131, 132, 134–136, 140, 141, 143–145, 147, 148, 150, 151, 153–157, 159–165, 194, 235
IR	infra-red. 77, 136
LFT	lattice field theory. v, 3, 5, 7, 11, 13, 14, 19, 22, 23, 42, 43, 47, 51, 54, 57–60, 79, 105, 128, 131, 133, 134, 144, 145, 150, 151, 153–156, 160–164, 166
LHC	Large Hadron Collider. 3
LP	lifshitz point. 11, 12, 45, 48, 49, 53, 73, 141, 143

NJL Nambu-Jona-Lasinio. 7, 8, 10–12, 14–16, 44, 47–50, 52, 66, 91–93, 101, 106, 111, 114, 115, 117, 128, 161–163, 184, 235

PSFF complete Lorentz-(pseudo)scalar four-fermion. 92, 93

QπL quantum pion liquid. v, 9–14, 16, 34, 39, 40, 42, 43, 53, 56, 79–81, 83, 99, 109, 117, 119, 120, 126–129, 131, 132, 140, 142–144, 147, 148, 150, 151, 153–157, 159–161, 163, 164

QCD quantum chromodynamics. v, xiii, 1–17, 19, 21, 29, 30, 39–42, 44, 49, 51–53, 60, 66, 75, 79, 81, 83, 92, 94, 105, 106, 109, 111, 114, 115, 126–128, 132, 140, 145, 150, 154, 156, 157, 159–166, 169, 184, 235

QED quantum electrodynamics. 1, 133

QFT quantum field theory. 1, 9–11, 13, 15, 17–23, 25, 27, 30, 31, 34, 42, 43, 50, 56, 79, 81, 133, 159, 161, 164, 169, 170, 172, 195

QM quark-meson. 7, 8, 10, 50, 51, 106, 107, 127–129, 161, 164

RHIC Brookhaven National Laboratory's Relativistic Heavy Ion Collider. 3, 4, 8, 41

SP symmetric phase. 6, 8–10, 16, 41, 45, 46, 49, 52, 53, 59, 70, 71, 73, 74, 76, 78–81, 83, 91, 99, 100, 102–105, 114, 115, 117, 134, 136, 138, 139, 141–143, 147, 148, 150, 151, 161, 163, 190, 200, 236

UV ultra-violet. 27, 49, 68, 77, 113, 133, 154, 156, 187–189, 195